APSU-1.1-PLN-002-02.1

Conceptual Design Report

May 2011

Advanced Photon Source Upgrade Project

Argonne NATIONAL LABORATORY

Table of Contents

List of Acronyms

µm	micron
µrad	microrad
µsec	microsecond
1-D, 2-D, 3-D	one-dimensional, three-dimensional, two-dimensional
2D-IR	two-dimensional infrared
AAO	Argonne Area Office
ACIS	access control interlock system
ACUFE	asymmetric canted undulator front end
ACWP	actual cost of work performed
ADC	analog to digital
ADSC	Area Detector Systems Corporation
AES	APS Engineering Support Division
AFM	atomic force microscope
ALCF	Argonne Leadership Computing Facility
ALD	(Argonne) Associate Laboratory Director
ALS	Advanced Light Source
AMP	antimicrobial peptides
AOPDF	acoustico-optic programmable dispersive filter
ANL	Argonne National Laboratory
APAD	analog pixel array detector
API	application programmers interface
APPLE	advanced planar polarized light emitter
APS	Advanced Photon Source
APS-U	Advanced Photon Source Upgrade project
ASCU	advanced superconducting undulator
ASO	Argonne Site Office
ASIC	Application-Specific Integrated Circuit
ATLAS	Argonne Tandem Linear Accelerator System
ATP	Adenosine Triphosphate
Au	Gold
BAT	beam arrival time
BCE	baseline cost estimate
BCWP	budgeted cost of work performed
BCWS	budgeted cost of work scheduled
BDA	beam-defining aperture
BDCM	branching double crystal monochromator
BES	Office of Basic Energy Sciences
BHJ-OPV	bulk heterojunction organic photovoltaic
BLM	beam loss monitor
BM	bending magnet
BNL	Brookhaven National Laboratory
BNP	biomolecular nanoparticles
Bph	bacteriophytochromes

BPLD	beam-position limits detector
BPM	beam position monitor
BTG	Beam Technology Group (at LBNL)
BW	bandwidth
CAD	computer-aided design
CAM	control account manager
CARS	Center for Advanced Radiation Sources
CAS	contingent additional scope
CAT	collaborative access team
CBI	coupled bunch instabilities
CCD	charge-coupled device
CDI	coherent diffractive imaging
CDR	Conceptual Design Report
CDS	Correlated Double Sampling
CdTe	Cadmium Telluride
CDW	charge density wave
CFE	canted front end
CHESS	Cornell High Energy Synchrotron Source
CHF	critical heat flux
CMOS	complimentary metal-oxide semiconductor
CMP	chemical-mechanical polishing
CMR	colossal magnetoresistance
CNM	Center for Nanoscale Materials
CNP	CryoNanoprobe
COBRA	coherent Bragg-rod analysis
CP	circularly polarized
CPA	chirped-pulse amplification
CPR	Cost Performance Report
CPU	central processing unit
CPU	circularly polarized undulator
CRL	compound refractive lens
CT	charge transfer
CT	computed tomography
CTR	crystal truncation rod
CUFE	canted undulator front end
Cu-K XRF	copper K-edge x-ray fluorescence
cw	continuous wave
DA	dynamic acceptance
DA	dynamic aperture
DAC	diamond-anvil cell
DAFS	diffraction anomalous fine structure
DCM	double-crystal monochromator
DESY	Deutsches Elektronen Synchrotron
DI	dionized
DMM	double multilayer monochromator

DOE	U.S. Department of Energy
DPPC	dipalmitoylphosphatidylcholine
DSP	digital signal processor
DSSC	dye-sensitized solar cells
EBIC	electron beam-induced current
EBS	electron backscatter contrast
ED&I	engineering design and inspection
EELS	electron energy loss spectroscopy
EFTEM	energy-filtered transmission electron microscopy
EHHL	extremely high heat load
EMBL	European Molecular Biology Laboratory
EMVPU	electromagnetic variable polarizing undulator
EMW	elliptical multipole wiggler
EPICS	Experimental Physics and Industrial Control System
EPS	equipment protection system
EPU	elliptical polarizing undulator
ESRF	European Synchrotron Radiation Facility
eV	electron-volt
EVMS	Earned Value Management System
EVPU	electromagnetic variable polarizing undulator
EXAFS	extended x-ray absorption fine structure
FE	front end
FEEPS	front-end equipment protection system
FEL	free-electron laser
FIB	focused ion beam
FMN	flavin mononucleotide
F-MT	fast monochromatic tomography
FNAL	Fermi National Accelerator Laboratory
FOE	first optics enclosure
FPGA	field-programmable gate array
FPLC	fast protein liquid chromatography
fs	Femtosecond
FTIR	Fourier transform infrared radiation
FWHM	full width half maximum
F-WT	fast white-beam tomography
FZP	Fresnel zone plate
Gb	gigabit
GB	gigabyte
GDA	generic data acquisition
GE	General Electric
GEOCARS	GeoSoilEnviro CARS
GISAXS – CDI	grazing-incidence coherent diffraction imaging
GISAXS	grazing-incidence small-angle x-ray scattering
GIWAXS	grazing incidence wide-angle x-ray scattering
GIXRD	grazing incidence x-ray diffraction

GIXS	grazing-incidence x-ray scattering
GPU	Graphics processing unit
GsAs	gallium arsenide
GUI	graphical user interface
H-DCM	horizontal-diffracting double-crystal monochromator
HEDM	high-energy diffraction microscopy
HER	high-energy ring (at KEK-B)
HERIX	High-Energy-Resolution Inelastic X-ray Scattering detector
HHL	high heat load
HHLFE	high heat load front end
HLRF	high-level rf
HOM	higher-order modes
HP	high pressure
HPC	high-performance computing
HPM	hybrid permanent magnet
HP-CAT	High Pressure Collaborative Access Team
HRM	high-energy-resolution monochromator
HT	high-throughput
HTS	high-temperature superconductors
HVPS	high-voltage power supply
HXPS	hard x-ray photoelectron spectroscopy
Hz	hertz
I/O	input/output
I/OC	input/output controller
IASCC	irradiation-assisted stress corrosion cracking
IB	in-board
IC	integrated circuit
IC	ion channels
ICE	interfaces in complex environments
IDVC	insertion device vacuum chamber
ID(s)	insertion device(s)
IEX	intermediate energy x-ray
IF	intermediate frequency
ILC	International Linear Collider
INP	*in situ* nanoprobe
InSb	indium antimonide
IOC	input/output controller
IPS	integrated project schedule
IPT	integrated project team
IR	infrared
ISMS	Integrated Safety Management System
IT	information technology
IVU	in-vacuum undulator
IXS	inelastic x-ray scattering
JLAB	Jefferson Accelerator Laboratory

K-B	Kirkpatrick-Baez
keV	kilo-electron-volt
kHz	kilohertz
kW	kilowatt
LBNL	Lawrence Berkeley National Laboratory
LCLS	Linac Coherent Light Source
LDRD	Laboratory Directed Research and Development
LEEM	low-energy electron microscopy
LER	low-energy ring (at KEK-B)
LERIX	Lower-Energy Resolution Inelastic X-ray scattering detector
LHe	liquid helium
Li-ion	lithium-ion
LITR	laser-initiated time-resolved
LL	low loss
LLNL	Lawrence Livermore National Laboratory
LLRF	low-level rf
LMA	local momentum acceptance
LMF	low-peak magnetic field
LMS	Laboratory Management System
LN2	liquid nitrogen
LNLS	Labratorio Nacional de Luz Sincrotron
LOM	lab/office module
LOM	lower-order mode
LOV	light, oxygen, or voltage
LR	load ratio
LRO	long-range order
LSS	long straight section
LTC	low-temperature combustion
LTS	low-temperature superconductors
M&O	management and operating
M&S	materials and services
m	meter
mA	milliampere
MBE	molecular beam epitaxy
MBE/CVD	molecular beam epitaxy/chemical vapor deposition
MCR	main control room
MDL	minimum detection limit
MEMS	microelectromechanical systems
MERIX	Medium Energy Resolution Inelastic X-ray detector
MeV	mega-electron-volt
MHz	megahertz
MKID	microwave kinetic inductance detector
MLL	multilayer Laue lens
MLM	multilayer mirror
MMC	metal-matrix composite

MMPA	mixed-mode pixel-array detector
MNP	micro/nanoprobe
MNS	Mission Need Statement
MOCVD	Metal-organic chemical vapor deposition
MPa	megaPascal
MPS	machine protection system
MS	magnetostriction
msec	millisecond
MTS	Materials Test Systems Corp.
NEPA	National Environmental Policy Act
neV	nano-electron-volt
NFS	nuclear forward scattering
NHMFL-PFF	National High Magnetic Field Laboratory's Pulsed Field Facility
NIH	National Institutes of Health
NIXS	nonresonant inelastic x-ray scattering
NXRS	nonresonant x-ray Raman scattering
Nm	nanometer
NMOS	negative-channel metal-oxide semiconductor
NO_x	nitrogen oxide
NRIXS	nuclear resonant inelastic x-ray scattering
NRS	nuclear resonant scattering
NRVS	nuclear resonance vibrational spectroscopy
ns	nanosecond
NSF	National Science Foundation
NSLS	National Synchrotron Light Source
NSLS-II	National Synchrotron Light Source II
NSRRC	National Synchrotron Radiation Research Center
ODH	oxgen-deficiency hazard
OECM	Office of Engineering and Construction Management
OSA	order-sorting aperture
P6	Oracle Primavera P6 Project Management Module
PAD	pixel array detector
PARS	Project Assessment and Reporting System
PDF	pair distribution function
PECVD	plasma-enhanced chemical vapor deposition
PEEM	photoemission electron microscope
PEO	polyethylene oxide
PES	photoelectron spectroscopy
PESAC	Project Scientific Advisory Committee
PETRA	Positron Electron Tandem Ring Accelerator
PF	pulsed field
pk-pk	peak-to-peak
PLC	programmable logic controller
PLD	pulsed laser deposition
PLS	Pohang Light Source

pm	picometer
PMCS	Project Management Controls System
PMOS	positive-channel metal-oxide semiconductor
PMT	photomultiplier tube
ppb	parts per billion
PR	phase retarders
ps	picosecond
PSAC	Project Scientific Advisory Committee
PSS	personnel safety system
PT	phase-contrast-enhanced tomography
P-T	pressure-temperature
PTV	peak to valley
PUP	partner user proposal
PWD	potential well distortion
PXRD	powder x-ray diffraction
QA	quality assurance
QCM	quartz crystal monitor
QE	quantum efficiency
QP	quasi-periodic
QXAFS	quick-scanning x-ray absorption fine structure
R&D	research and development
rf	radio frequency
rf/THz	radiofrequency/terahertz
RGA	residual gas analyzer
RHB	reduced horizontal beam size
RHEED	reflection high-energy electron diffraction
RIXS	resonant inelastic x-ray scattering
rms	root mean square
RRR	residual resistivity radio
RSS	radiation safety shielding
RTD	resistive thermal devices
RTFB	real-time feedback system
RTIL	room-temperature ionic liquids
RW	resistive wall
RXES	resonant inelastic x-ray emission
SAD	APS Safety Assessment Document
SAS	serial-attached Small Computer System Interface
SATA	Serial Advanced Technology Attachment
SAXS	small-angle x-ray scattering
SBCA	spherically bent crystal analyzer
SBIR	Small Business Innovation Research (program)
SC	superconducting
SCM	superconducting magnets
SCR	silicon-controlled rectifier
SCU	superconducting undulator

SCXS	surface coherent x-ray scattering
SDD	silicon drift detector
SDDS	self-describing data set
SDW	spin density wave
sec	second
SEM	scanning electron microscope
SFD	small form-factor pluggable
SGE	Sun Grid Engine
Si	silicon
SI	spark ignited
SiGe	silicon germanium
SLAC	SLAC National Accelerator Laboratory
SLS	Swiss Light Source
SMS	synchrotron Mössbauer spectroscopy
SNR	signal-to-noise ratio
SOFC	solid oxide fuel cell
SOM	same-order mode
SPM	scanning-probe microscope
SPX facility	Short-Pulse X-ray Facility
SPX	short-pulse x-ray
SR	storage ring
SR	synchrotron radiation
SRF	superconducting rf
SS	stainless steel
SSD	solid-state drive
SSRF	Shanghai Synchrotron Radiation Facility
STM	scanning tunneling microscope
sub-nm rms	sub-nanometer root mean square
SVD	singular value decomposition
SXRD	surface x-ray diffraction
SXRPD	*in situ* synchrotron x-ray powder diffraction
SXRPD	synchrotron x-ray powder diffraction
TA	transverse acoustic
TB	terabyte
TCSPC	time-correlated single-photon counting
TE	transferse electric
TEM	transmission electron microscope
TFT	thin-film transistor
THz	terahertz
TM	transverse magnetic
TMCI	transverse mode-coupling instability
TPB	three-phase boundary
TPC	total project cost
TPS	titanium sublimation pump
TRIXS	total-reflection nonresonant inelastic x-ray scattering

TR-XRD	time-resolved x-ray diffraction
TR-XRF	total reflection x-ray fluorescence
TXM	transmission x-ray microscope
U.S.	United States
UA	undulator A
UA33	3.3-cm-period undulator
UF-WT	ultrafast white-beam tomography
UHV	ultrahigh vacuum
USY	ultra-stable Y
UV	ultraviolet
UV-vis	ultraviolet-visible
V-DCM	vertical diffracting double-crystal monochromator
VHHL	very high head load
VHHLFE	very high heat load front end
VLS-PGM	varied line-spacing grating design
VSWR	voltage standing-wave ratio
WAXS	wide-angle x-ray scattering
WBS	white-beam slit
WBS	work breakdown structure
WDX	wavelength dispersive x-ray
WFI	wide-field imaging
XAFS	x-ray absorption fine structure
XANES	x-ray absorption near-edge structure
XAS	x-ray absorption spectroscopy
XBIC	x-ray beam induced current
XBPM	x-ray beam position monitor
XES	x-ray emission spectroscopy
XFELO	X-ray Free Electron Laser Oscillator
XHF	x-ray high field
XIS	x-ray interfacial science
XMCD	x-ray magnetic circular dichroism
XMLD	x-ray magnetic linear dichroism
XOMBE	x-ray oxide MBE
XOR-PNC	X-ray Operations and Research/Pacific Northwest Consortium
XPCS	x-ray photon correlation spectroscopy
XPS	x-ray photoelectron spectroscopy
XRD	x-ray diffraction
XRF	x-ray fluorescence
XRIM	x-ray interfacial microscopy
XRR	x-ray reflectivity (x-ray reflectometry)
XRS	x-ray Raman scattering
XSD	X-ray Science Division
XSW	x-ray standing wave
YSZ	yttrium-stabilized zirconium
ZP	zone plate

Chapter 1

Executive Summary

1.1 Introduction

On April 22, 2010, the U.S. Department of Energy (DOE) granted approval of Mission Need, Critical Decision 0 (CD-0) for the Advanced Photon Source Upgrade (APS-U) project (MIE-12-SC-APSU).

Following CD-0, Argonne National Laboratory has prepared a conceptual design for the upgrade of the APS as described in this conceptual design report (CDR). The upgrade will provide high-energy, high-average-brilliance, short-pulse, penetrating hard x-rays in the energy range above 20 keV; nanoscale focal spots approaching 5 nm for energies above 20 keV; time resolution approaching 1 ps; new and upgraded x-ray beamlines; and the infrastructure required to fully exploit all of the new and upgraded technical equipment.

The overall objective of the APS-U project is to provide current and future users of the APS with enhanced scientific tools to observe, understand, and ultimately control materials function on the nanoscale through two themes that reflect the scientific power of high-energy x-rays: mastering hierarchical structures through imaging, and understanding real materials under real conditions in real time.

The first version of the CDR is revision 0, issued on November 5, 2010. The second version of the CDR is revision 1, issued on March 10, 2011. The CDR has been revised with continued development of the conceptual design until this final version, revision 2, is submitted for review by the U.S. Department of Energy in preparation for obtaining approval for Critical Decision 1 (CD-1).

1.2 Scope

The APS-U project scope includes the design, procurement, assembly, installation, and testing of the accelerator hardware, beamline instrumentation, and enabling technical capabilities required to upgrade the existing APS synchrotron light source. Specifically, the main scope elements include:

- Upgrade technical equipment to increase the operating current to 150 mA.
- The addition of long straight sections in the APS storage ring lattice in order to accommodate long insertion devices, or to fit into one straight section a combination of a superconducting undulator and a permanent magnet undulator, or a combination of a permanent magnet undulator and a set of superconducting radio-frequency deflecting cavities.

- Superconducting insertion devices that will provide to APS users hard (energy greater than 20 keV) x-ray beams brighter than those available from any other third-generation synchrotron light source.
- New planar, revolver, and variable polarization insertion devices optimized for beamline missions.
- A Short-Pulse X-ray accelerator facility consisting of superconducting radio-frequency deflecting cavities with the capability to produce intense hard x-ray pulses almost two orders of magnitude shorter than those currently available from an electron storage ring for enhanced time resolution.
- Experimental facilities to exploit the hard x-ray pulses by combining picosecond temporal resolution with atomic-scale spatial resolution, elemental specificity, and nanoprobe capabilities in a suite of new x-ray beamlines and supporting laser instrumentation.
- Upgrades to existing APS beamlines, including addition of state-of-the-art hard x-ray focusing optics and greatly improved detectors.
- New or upgraded information technology and physical infrastructure.

The final APS-U project scope includes a subset of the hardware, instrumentation, and capabilities described in this CDR, depending on the total estimated cost of the scope elements and their prioritization during conceptual design planning. At this stage of planning, the intent of the CDR is to document the continuing development of the conceptual design for all of the potential elements of the APS-U project until the preliminary baseline scope has been established at CD-1. Those elements that are not included in the baseline scope may later become potential contingency tasks in the APS-U project or may be addressed by other APS enhancement projects or programs as part of the long term strategic planning of the APS.

1.3 Capabilities

The APS-U project will provide an unprecedented combination of high-energy, high-average-brilliance, and short-pulse penetrating hard x-rays, nanoscale focal spots, and time resolution beyond the reach of existing storage ring facilities, together with state-of-the-art x-ray beamline instrumentation. Table 1.3-1 shows the APS-U project accelerator upgrade components and Table 1.3-2 shows the APS-U project accelerator parameter improvements and trade-offs as described in this conceptual design. Scientific proposals for all potential proposed beamline improvements were submitted to and reviewed by the APS SAC in March 2011, and the final selection of beamline improvements has been incorporated into this version of the CDR, revision 2. Table 1.3-3 shows the proposed APS-U project beamline improvements as of May 2011. The current design supports the key performance parameters for the APS-U project as shown in Table 1.3-4.

Table 1.1-1. APS-U Project Accelerator Upgrade Components

	No. of Components
Long straight section	4
Beam stability	
BPM electronics	220
X-ray BPM system	34
Real-time feedback upgrade	1
Temperature regulation upgrade [CAS]	1
BPM mechanical motion sensing	2 × 34 = 68
Short-pulse x-ray	
Insertion devices	
Planar undulators	
Single-period	5
Dual-period revolver	6
Polarizing undulators	
EM variably polarizing undulator	1
APPLEII	1
Superconducting undulators	
1.6-cm period 2.0-m magnetic structure in 3-m cryostat	3
Canting sector magnets	5
ID loss monitors [CAS]	36
Front ends	21

Table 1.3-2. APS-U Project Accelerator Parameter Improvements and Trade-Offs

	Present	**Upgrade**
Electron energy (GeV)	7	7
Stored current (mA)	100	150
Number of long straight sections	0	4
Stability of current (%)	1	1
Horizontal emittance (nm)	3.15	<3.3
Vertical emittance (pm)	37	<50
Maximum brightness at 10 keV	1×10^{20}	2.0×10^{20}
Maximum brightness at 20 keV	5×10^{19}	11×10^{19}
Maximum brightness at 60 keV	0.5×10^{19}	3×10^{19}
Horizontal electron beam size (microns)	274	278
Horizontal electron beam divergence (microradians)	11.3	11.5
Vertical electron beam size (microns)	10.4	11.2
Vertical electron beam divergence (microradians)	3.6	3.6
Horizontal stability of electron beam in 0.1-200 Hz band as % of size or divergence	8	5
Vertical stability of electron beam in 0.1-200 Hz band as % of size or divergence	22	7

Table 1.3-3. APS-U Project Beamline Improvements

Upgraded	New
Short Pulse X-ray Imaging and Microscopy	Short Pulse X-ray Scattering and Spectroscopy
High Flux Pump-Probe	Wide Field Imaging
Resonant Inelastic X-ray Scattering	High Energy X-ray Tomography
Magnetic Spectroscopy (2 beamlines)	*In situ* Nanoprobe
High Energy X-ray Diffraction (existing beamlines)	High Energy X-ray Diffraction (new side-bounce beamline)
Sub-micron 3D Diffraction (2 beamlines)	X-Ray Interface Science
Beamline upgrades for higher storage ring current (as needed at all APS beamlines)	

Table 1.3-4. APS-U Key Performance Parameters

Key Performance Parameter	Thresholds (Performance Deliverable)	Objectives
SPX pulse width (10 keV)	observed pulse	2 ps
SPX number of rf cavities	4	8
Operating current	install components capable of 150 ma	150 ma
Improved stability	×2	×4
Undulators	12	21
X-ray brilliance at 25 keV*	install components capable of 11×10^{19}	11×10^{19}
X-ray brilliance at 60 keV*	install components capable of 3×10^{19}	3×10^{19}
New beamlines installed and ready for commissioning with x-ray beam	6	9
Beamlines upgraded and ready for commissioning with x-ray beam	6	6
Focus at 25 keV	deliver optics capable of 20 nm	20 nm

*photon/second/0.1%bw/mm^2/mrad^2

1.4 Cost and Schedule

The initial Total Project Cost range of the APS-U project is $300M to $400M. The project is planned to execute at the middle of the range with a Total Project Cost (TPC) of $355M. The initial cost range is based upon expert analysis and opinion from technicians, engineers, scientists, and accelerator physicists who have recently constructed and/or fabricated systems similar to those systems and components at the current facility that is being upgraded. They have used discussions with vendors and suppliers with whom they are familiar to assist in the estimating process. Acquisition and installation are scheduled for early completion at the end of FY 17, CD-4 is planned to occur at the end of FY 18, including one year of schedule contingency. The details of cost and schedule and the TPC are described in the APS-U Preliminary Project Execution Plan, and will continue to mature until approval of the performance baseline at Critical Decision-2.

1.5 Acquisition Strategy

The acquisition strategy relies on UChicago Argonne, LLC, the DOE M&O contractor for Argonne National Laboratory, to directly manage the APS-U project acquisition. The design, fabrication, assembly, installation, testing, and commissioning of technical components in the APS-U project will be performed by Argonne and APS scientific and technical staff. Much of the subcontracted work to be performed for the APS-U project consists of hardware fabrication and infrastructure additions. The acquisition strategy is described in greater detail in the APS-U Project Acquisition Strategy.

Chapter 2

Project Overview

2.1 Introduction

The DOE's Office of Basic Energy Sciences (BES) has a mission to support "fundamental research to understand, predict, and ultimately control matter and energy at the electronic, atomic, and molecular levels in order to provide the foundations for new energy technologies and to support DOE missions in energy, environment, and national security."

There is a particular need for studies of real materials under real conditions in real time by the use of groundbreaking scientific tools that observe, understand, and ultimately control the functions of materials on the nanoscale to develop new technologies. In order to sustain this nation's position at the frontier of science and technology, there is a need for BES to acquire a new, or to upgrade an existing third-generation, synchrotron light source facility that provides an unprecedented combination of high-energy, high-average-brilliance, and short-pulse x-rays together with state-of-the-art x-ray beamline instrumentation. Such a facility is specifically identified as a priority in the Office of Science strategic plan. In this context, the most practical alternative to achieve this mission is to upgrade the APS at Argonne National Laboratory.

Among the various BES user facilities, such as neutron sources, nanoscience centers, and electron microscopy centers, the synchrotron light sources have proven especially valuable. These light sources can be categorized as either storage ring type or free-electron laser (FEL) type, and as producing x-rays optimized in the low-energy (<3 keV) , medium-energy(<20 keV) or high-energy (>25 keV) ranges. Storage ring and FEL sources have complementary capabilities, as do light sources optimized for each of the three x-ray energy ranges. Storage ring sources typically have many beamlines and so can accommodate a large user community. To address its critical mission needs, the DOE expects to provide leading capabilities for each energy range and both source types.

The four DOE-operated, storage-ring-based light sources —APS, Advanced Light Source (ALS), National Synchrotron Light Source, and Stanford Synchrotron Radiation Lightsource (SSRL) — have provided research opportunities for an ever-expanding scientific user community of almost 10,000 scientists, leveraging individual research grants from DOE, the U.S. National Science Foundation, the National Institutes of Health, the U.S. Environmental Protection Agency, the U.S. Department of Agriculture, and many other U.S. federal agencies.

The APS is the only DOE light source in the U.S. Midwest; is the only modern high-energy storage ring source in the U.S.; and, after the APS-U project is complete, will be the best source for x-rays above 20-keV worldwide. The upgraded APS will complement the other existing and planned DOE light sources; the National Synchrotron Light Source II will be a high-performance storage ring radiation source located in the U.S. Northeast, and will be the brightest source of medium-energy x-rays

worldwide; the ALS is the only modern low-energy storage ring source in the U.S; the SSRL at the SLAC National Accelerator Laboratory, which has recently been modernized and offers medium- to high-energy x-rays, and the new FEL Linac Coherent Light Source (also at SLAC), the only operating source of its kind in the world, offering ultra-intense, ultra-short pulses of medium-energy x-rays.

Upgrading the APS will provide the U.S. with a suite of state-of-the-art, complementary research tools needed to carry out the revolutionary research described in the Basic Energy Sciences Advisory Committee report, New Science for a Secure and Sustainable Energy Future. In particular, the route to new functional materials involves better control during the synthesis and processing of materials. High-energy x-rays uniquely allow structural and chemical studies at the nanometer and picosecond scale under the realistic conditions of materials manufacturing. The vision of going beyond a "discovery" approach to a "controlled" approach for making functional materials will rely on a new high-energy x-ray capability with enough brilliance to provide nanoscale spatial resolution in such environments, which is not possible with any U.S. source today.

The upgraded APS will be able to continue to make major contributions in attacking energy problems. The BES report, Basic Research Needs for Clean and Efficient Combustion of 21st Century Transportation Fuels, notes that, "The evolution of fuel sprays plays a defining role … in determining both combustion efficiency and the formation of … pollutants. This level of understanding may permit extraordinary new technologies, such as smart fuel injectors." Gains already made at the APS in imaging high-speed sprays will be greatly improved with a state-of-the-art, high-energy x-ray source thanks to improved x-ray brilliance and field-of-view of very-high-speed imaging, paving the way for improved design of fuel injectors for internal combustion engines. The vast majority of chemical reactions are controlled by catalysts that determine energy and environmental efficiency. The action of catalysts occurs on the nanoscale, but can only be studied in environments of flowing gases and substrates. Through a better understanding of catalytic materials and processes gained from research at an advanced high-energy x-ray facility, engineered biomimetic catalysts can be designed that will have dramatic effects on our national energy and raw materials needs, and reduce effluent from materials synthesis and processing.

The APS provides a ready-made foundation for the upgraded facility, including $1.7B of scientific infrastructure and a vibrant user community already attuned to future needs. The APS facility includes an accelerator complex and photon delivery, as well as extensive beamlines and instrumentation, an experiment hall, computing, laboratories, offices, infrastructure, and expert staff. Therefore, upgrading the APS is the most logical, efficient, and cost-effective route to a high-energy x-ray source. Meeting these objectives can be accomplished by an operating electron storage ring current of at least 150 mA; long straight sections in the storage ring to accommodate the specialized undulators that would be the source of the high-energy x-ray beams; new, brighter undulators based on superconducting technology; an innovative scheme to produce short x-ray pulses; improved beam stability; beamlines optimized for scientific applications; new or improved detectors for data collection and other crucial beamline instruments; controls software; and fast data transfer, storage, and analysis.

The APS-U project will have the capability to produce x-rays that penetrate inside the environments where materials are synthesized and their function is determined, and to image with nanometer resolution. These capabilities are necessary for the design of new materials with emergent properties that require researcher access to significantly higher pressures, temperatures, and chemical activities—and to shorter time scales— than are currently available for studies of real materials under real conditions in real time. In addition, the upgraded high-energy x-ray source would fill a gap between picoseconds and seconds in the critically important time-resolved study of materials while they are being synthesized or processed.

The penetrating rays provided by the APS-U project will be a key tool for meeting the BES Grand Challenges facing the new "Control Age," which requires the development of materials and machines to satisfy our need for sustainable energy, healthy lives, and a thriving economy.

The following sections of this chapter will include:

- A description of the WBS shown at the third level and containing a complete definition of the APS-U project scope. WBS elements are defined as specific systems/deliverables.
- Initial cost and schedule estimates based on a preliminary target of $350M as total project cost.
- A description of the APS-U project management organization.

2.2 Work Breakdown Structure

All work required for completion of the APS-U project is included in the WBS and is shown in Figure 2.2-1, beginning with the first year of funding in FY10 (CD-0) and continuing through project completion in FY17 (CD-4). The development of the WBS and WBS Dictionary are consistent with the requirements set forth in DOE Order 413.3A, *Program and Project Management for the Acquisition of Capital Assets* and ANSI/748a, *Earned Value Management Systems*.

The organization of the WBS reflects a logical breakdown of the work by major system. Each lower level breaks down the previous level by subsystem and task. Each system captures all costs, resources, tasks, and activities necessary to complete each APS-U project system. Each system contains progressively lower levels to further define the sub-elements down to the lowest WBS.

Each element of the WBS has cost, manpower, and schedule associated with it and is the key element for planning, executing, and controlling project activities. The detailed activities to design, fabricate, construct, and install the APS-U project are described in the WBS Dictionary. The WBS Dictionary is maintained by the project as a separate document that defines the activities to the lowest WBS level. All changes to the WBS must be approved by the Project Director and the Configuration Change Board members prior to implementation.

A description of the second-level WBS elements is given below:

- U1.01 Project Management: Project Office administrative and management activities that integrate across the entire project, such as management, regulatory compliance, quality assurance, safety, project controls, etc.
- U1.02 Research and Development: R&D activities necessary to support delivery of project objectives. Includes SPX and superconducting undulators.
- U1.03 Accelerator Systems: Includes all phases of design, procurement, installation, and testing of the accelerator systems upgrades. Includes SPX, SR technical components (LSS), beam stability and insertion devices.
- U1.04 Experimental Facilities: Includes all phases of design, procurement, installation, and testing of new beamlines and upgrades to beamlines.
- U1.05 Infrastructure and Enabling Technologies: includes all phases of design, procurement, installation, and testing of front ends for beamlines, site services and design, procurement, and installation of computing requirements.

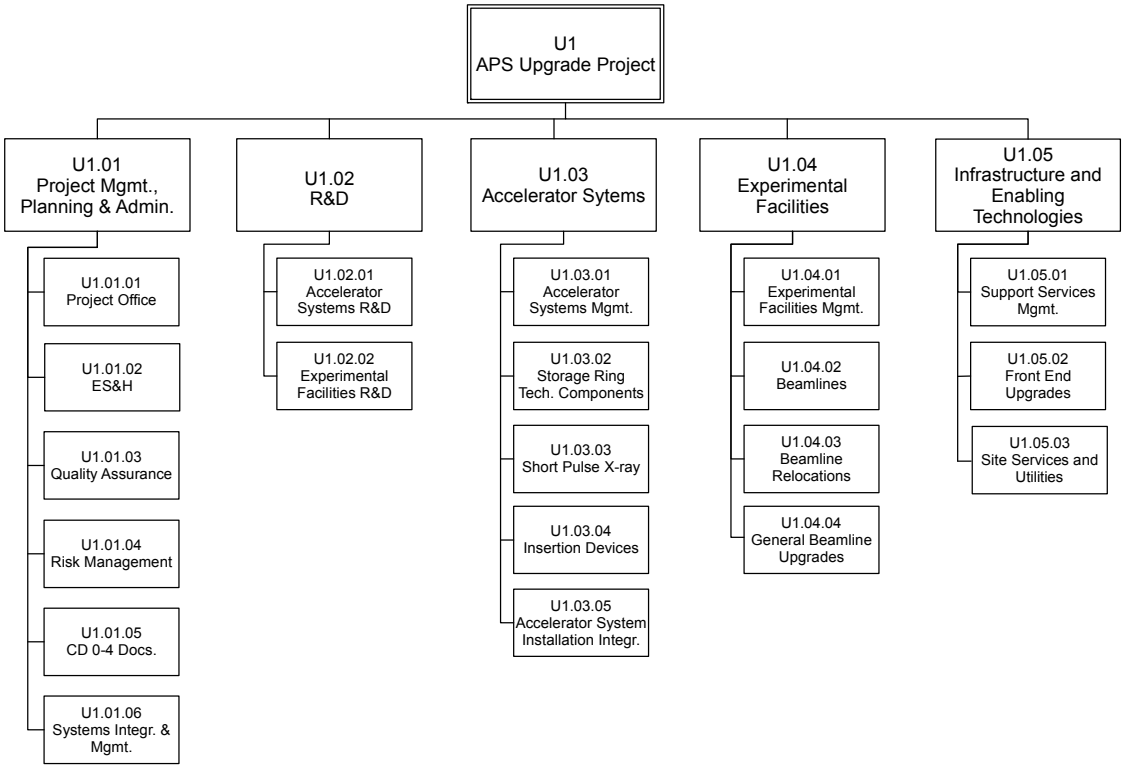

Figure 2.2-1. APS-U project work breakdown structure.

2.3 Project Cost and Schedule

2.3.1 Summary of Cost Estimate

The initial cost range of the APS-U project is $300M to $400M. The project is planned to execute near the middle of the range with a TPC of $350M. The APS-U cost and schedule baselines will consist of a BCE and the IPS, which will use a project-wide logic network, resource-loaded tasks, and a hierarchy of schedule milestones. Both the BCE and IPS will be maintained by the APS-U Project Management Controls System (PMCS) Group and are subject to change control under Configuration Management. Table 2.3-1 shows the TPC with initial estimates of the work breakdown at WBS Level 2 at CD-0.

Table 2.3-1. Target Budget Estimates at WBS Level 2*

WBS	Description	Budget ($M)
U1.01	Project Mgmt.	35
U1.02	R&D	12
U1.03	Accelerator Systems	122
U1.04	Experimental Facilities	119
U1.05	Enabling Technologies	37
	Escalation	25
	Total Project Cost	350

*Estimates include 35% Contingency

Based on a preliminary target of $350M as the total project cost estimate, Table 2.3-2 shows the initial project timeline and notional funding profile that is being used for planning purposes only and has not been approved.

Table 2.3-2. Initial Funding Profile

	FY10	FY11	FY12	FY13	FY14	FY15	FY16	FY17	Total
CDR and R&D (OPC)	$5M	$10M	$10M						$25M
Long-Lead Procurement (TEC)			$10M	$40M					$50M
Design & Construction (TEC)				$20M	$95M	$80M	$60M	$20M	$275M
Total Project Cost (TPC)	$5M	$10M	$20M	$60M	$95M	$80M	$60M	$20M	$350M

2.3.2 Cost Estimate by WBS Element

2.3.2.1 Basis of Estimate

The initial scope of the project includes alternate solutions to address the scientific challenges associated with the APS Upgrade. Initial cost estimates are shown in Table 2.3-3. The scope has been revised based on input from the APS-U project and APS management.

All cost estimates for the APS-U project conceptual design stage are based on the component layout developed for the Conceptual Design Report and expressed in FY2010 dollars. All costs are estimated by the APS staff. Various entries in the worksheet are designed to assist in future preparation of cost account plans for the Earned Value Management System in accordance with DOE Order 413.3A, *Program and Project Management for the Acquisition of Capital Assets* [2.3-1], and ANSI/748a, *Earned Value Management Systems* [2.3-2].

A standard Cost and Schedule Worksheet was utilized for the preliminary estimates; the worksheet features:

- Detailed cost sheets at the lowest level of WBS
- Rollup cost sheets for each system and “parent” WBS
- Summarized cost by ED&I (engineering design and inspection), Materials, and Fabrication
- Budget spread by start and finish date for each labor resource type
- Activity phase codes
- Fully burdened labor and material resources (i.e., applied overhead)
- Budgeted units for labor (hrs) and materials ($)

Table 2.3-3. Project Estimates

WBS Element	WBS Description	Non-Labor ($K)	Labor ($K)	Total Estimated Cost ($K)
U1	**APS Upgrade Project**	**221,429**	**135,319**	**356,748**
U1.01	Project Management	7,881	17,774	25,654
U1.02	Research & Development	5,615	9,555	15,170
U1.03	Accelerator Systems	45,199	25,521	70,720
U1.04	Experimental Facilities	68,232	23,036	91,268
U1.05	Infrastructure & Enabling Technologies	24,902	6,580	31,482
	Sub-total	151,830	82,464	234,294
	Escalation	12,192	17,772	29,964
	Contingency @ 35% (base + esc)	57,408	35,083	92,490
	Sub-total (Contingency + Escalation)	69,600	52,854	122,454

2.3.2.2 Contingency

At the conceptual stage of the APS-U project, 35% contingency was allocated to every WBS element based on an overall assessment of risks associated with cost estimates due to unforeseen job conditions, uncertainties of market conditions for labor and materials, and the level of design maturity. During preliminary engineering design phases, and as more information becomes available, continual contingency analysis will be performed that identifies risks and determines the appropriate levels of contingency and the percentage level will be adjusted accordingly. Contingency will be managed centrally and is not pre-allocated or pre-assigned to any item. Each sub-project must have adequate contingency to ensure successful completion without risk to the project as a whole. Scope contingency is also planned for both containing costs and addition of priority-based, enhanced scope. The decision to allocate such funds for either purpose can be justified in part by demonstrating that the project has sufficient confidence in the cost estimates. Significant risk is managed according to the contingency spend plan, and thus that adding any tasks to the project will leave sufficient contingency to mitigate the risks going forward.

2.3.2.3 Escalation

In order to manage escalation, it is necessary to understand its role in an MIE project. Escalation is the increase in costs from one time period to another. All Materials and Services (M&S) and labor costs are subject to escalation over the lifetime of the project. The initial cost estimate includes an escalation calculation for M&S using DOE rates from base year 2011 costs for scientific laboratories and are escalated accordingly. Values were taken from DOE-published escalation values found at: http://www.cfo.doe.gov/cf70/escalation.pdf. For greater accuracy, escalation labor costs were calculated from published Argonne labor escalation rates found at: http://inside.anl.gov/ocf/budget/escalation_percentages.html. A further study of escalation will be conducted using independent consultants prior to CD-2.

Table 2.3-4. Cost of Escalation through the Project

		FY10	FY11	FY12	FY13	FY14	FY15	FY16	FY17	FY18
Labor	incremental	0.0%	5.0%	4.2%	5.0%	5.0%	5.0%	5.0%	5.0%	5.0%
	compounded	1.000	1.050	1.094	1.149	1.206	1.267	1.330	1.396	1.466
Material	incremental	0.0%	0.0%	2.2%	2.4%	2.4%	2.4%	2.4%	2.4%	2.4%
	compounded	1.000	1.000	1.022	1.047	1.072	1.097	1.124	1.151	1.178

FY11 RATES (labor base FY10, nonlabor base FY11)

2.3.3 Schedule Summary

A preliminary summary schedule including the expected timeline and milestones is shown in Figure 2.3-1.At the approval of CD-0 in the 3rd quarter of FY 10, the project was estimated to be completed in the last quarter of FY 17. The current plan has additional float of 12 months with a CD4 date of the last quarter of FY18.

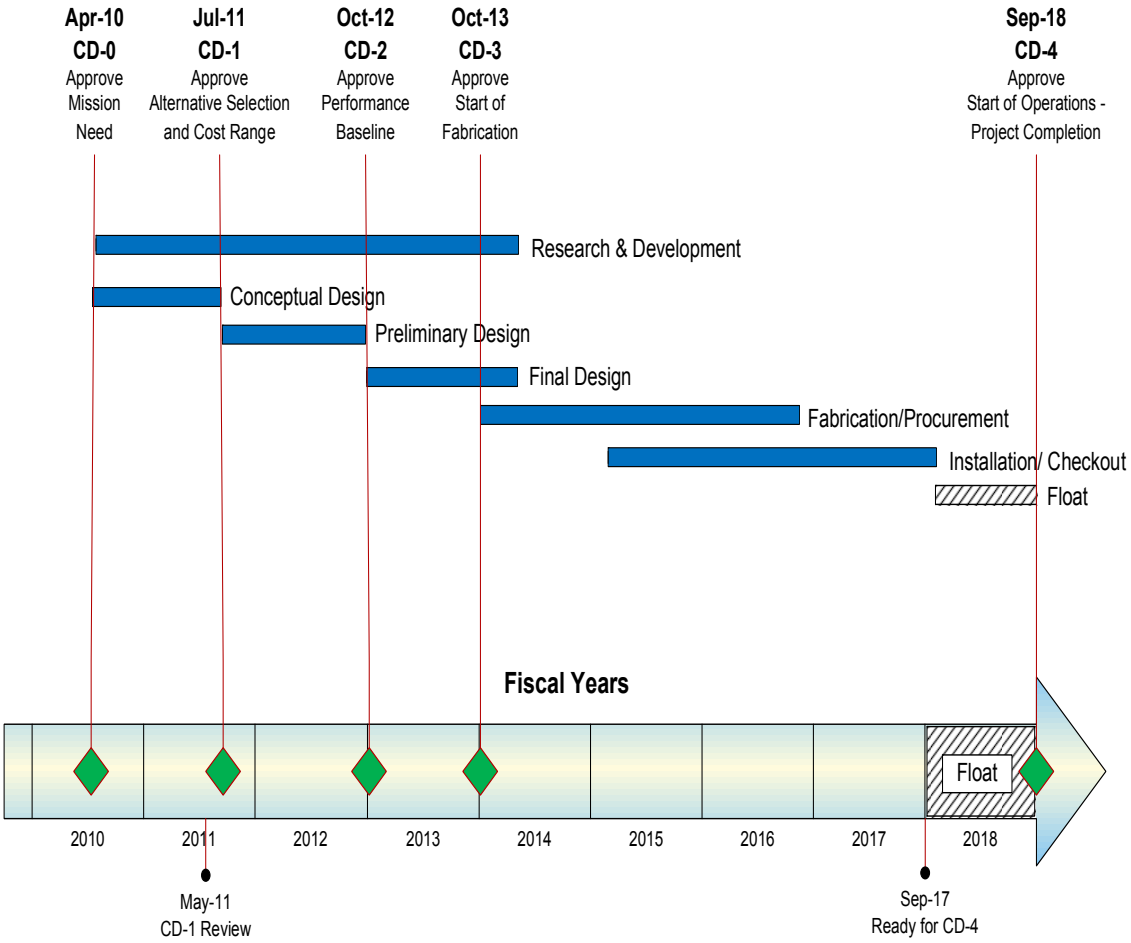

Figure 2.3-1. APS Upgrade expected timeline and milestones.

2.4 Project Management

The APS-U project has three major institutional participants: (1) DOE Headquarters, Office of Basic Energy Sciences; (2) Argonne Site Office; and (3) UChicago Argonne, LLC. Each of these institutions has important roles and responsibilities for project success. Figure 2.4-1 shows DOE's organization of the APS-U project.

Within the Chicago Operations Office, the ASO provides DOE's direct contractual link to the University of Chicago, which operates Argonne. The ASO Manager will partner with SC-10 and maintain regular communication on project status to ensure successful execution. The APS-U project Federal Project Director is positioned within ASO and is present full-time at the Argonne site. The APS-U project Federal Project Director is responsible for the requirements assigned to the Federal Project Director in DOE Order 413.3, *Program and Project Management for the Acquisition of Capital Assets*. The Federal Project Director will (1) submit key project documents and critical decisions to the respective Acquisition Executive for approval; (2) report project progress; (3) provide environment, safety, and health oversight; (4) coordinate approval of NEPA documentation; and (5) assess contractor performance on project execution. The IPT will support these responsibilities. The IPT is led by the APS-U project Federal Project Director, and its members include the MIE Project Program Manager in BES, the APS Director, the APS-U Project Director, the APS-U Project Manager, and members with expertise in ES&H, procurement, budget, financial, legal, and facilities management. The APS-U project will be accomplished by the IPT. The intent is to implement DOE Order 413.3 via a tailored approach that optimizes control, progress, and performance of the APS-U project.

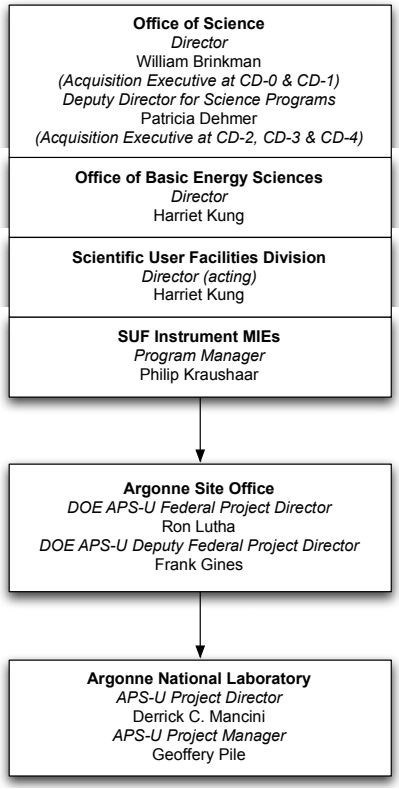

Figure 2.4-1. DOE APS-U project organization.

The UChicago Argonne, LLC manages and operates Argonne National Laboratory for DOE under the terms and conditions of Contract No. DE-AC02-06CH11357. The University of Chicago has provided the Laboratory Director with overall responsibility for all projects, programs, operations, and facilities at Argonne. Argonne plans to manage the APS-U project within cost and on schedule, and to deliver the promised technical scope and performance. The Laboratory is committed to maintaining the APS-U as a premier scientific user facility. Argonne's management organization is shown in Figure 2.4-2, and Argonne's organization for the APS-U project is shown in Figure 2.4-3.

The Laboratory Director has designated an APS-U Project Director and an APS-U Project Manager. The APS-U Project Director is responsible for the management and execution of the APS-U project. He will ensure that the project is successfully completed within its budget and on time, meeting the planned scope. In addition, the Laboratory Director has recruited distinguished external members for the high-level APS-U project PSAC, which advises him and the APS-U Project Director on scientific directions, programmatic themes, and equipment priorities for the APS-U project.

Argonne will establish a written Memorandum of Agreement between the APS-U project and all Laboratory organizations providing members of the IPT in order to explicitly define roles, responsibilities, relationships, authorities, resources, and deliverables. The IPT includes an Associate Project Manager for each WBS Level 2 system, as well as project controls staff, and specialists in procurement, ES&H, QA, facilities, NEPA compliance, and construction.

Argonne has an EVMS in place and is utilizing it on several projects. Currently, the EVMS is undergoing certification through the OECM. It is anticipated that the certification will be in place prior to the APS-U project receiving CD-2.

The APS-U project is utilizing several project management tools. Primavera Project Planner has been implemented for tracking project progress, schedule logic, and earned value capture. Primavera Cost Manager has been implemented for cost and earned value reporting.

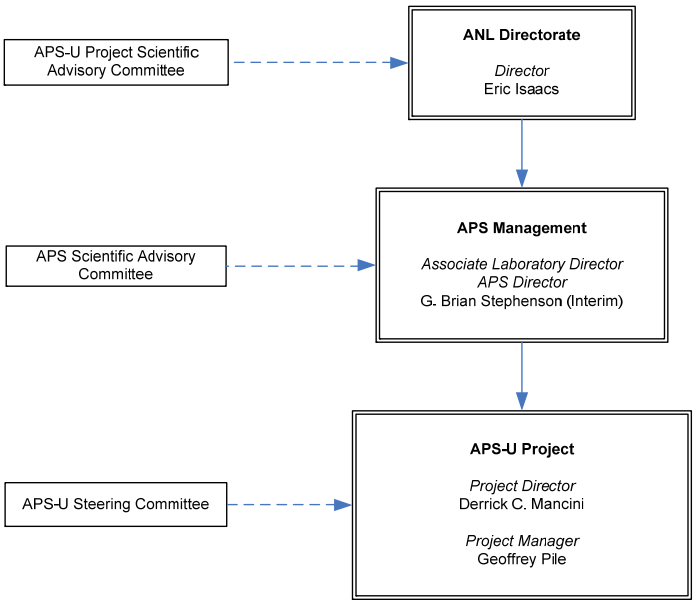

Figure 2.4-2. Argonne management organization.

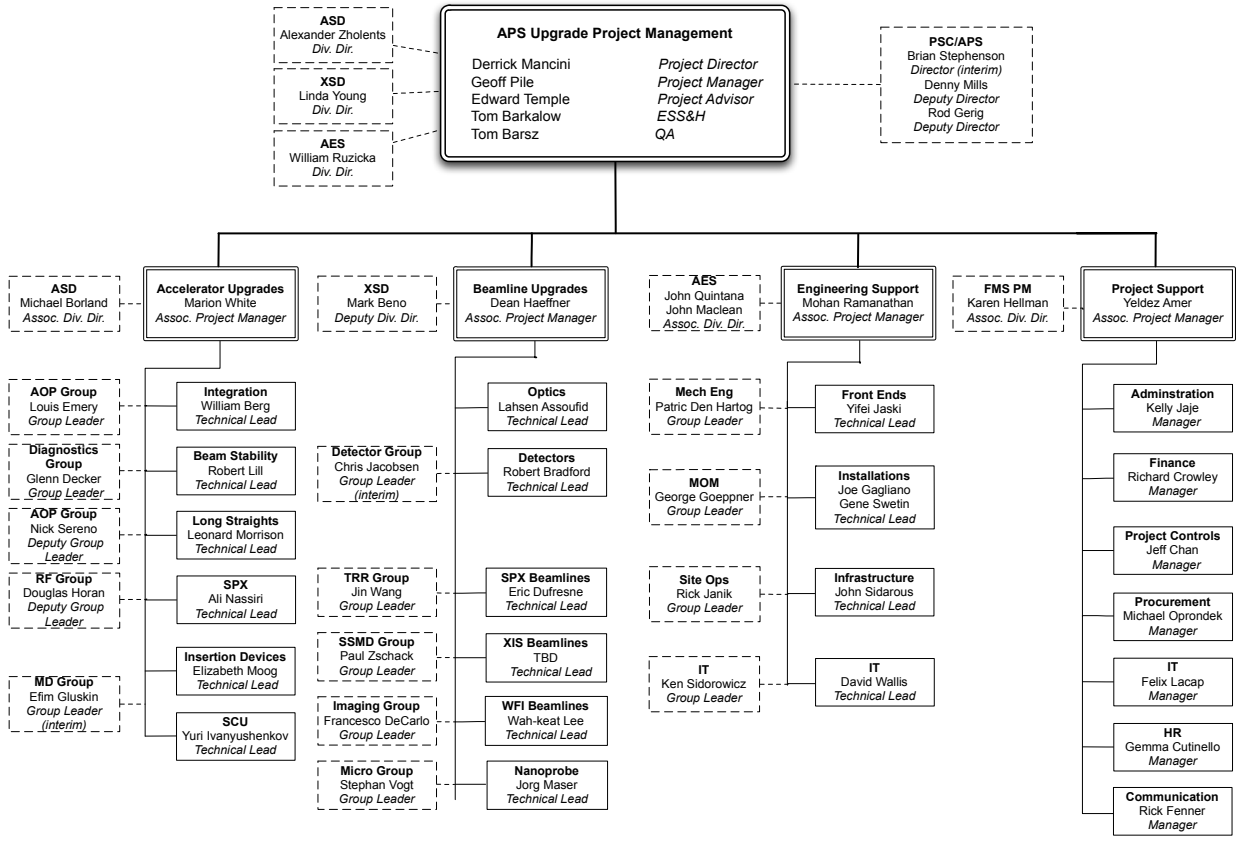

Figure 2.4-3. Argonne APS-U project organization.

Argonne will provide monthly technical and cost performance reports to the DOE. The APS-U project has been entered into the DOE PARS. For the APS-U project, the DOE APS-U Federal Project Director will provide quarterly reports to DOE Headquarters and monthly updates to PARS and later PARS-II, starting at CD-2. A monthly progress report on the APS-U project will be issued by the APS-U Project Director and distributed to appropriate DOE offices and other organizations outside the project. This report will provide information at WBS level 2 and higher and will discuss the overall status of the APS-U project. A Highlights (or equivalent) section will address the total project schedule overview and any significant project accomplishments. An Assessment and Issues (or equivalent) section will cite any areas of concern to the project management. The APS-U project monthly report will also document monthly and cumulative project cost and schedule performance at WBS level 2 and progress against DOE level 2 milestones. BES will charter major reviews of the APS-U project's overall technical, cost, schedule, and management.

Monthly performance measurement figures will be based on three quantities: schedule status submitted by the APS-U project Associate Program Managers each month, actual financial status (cost and commitments) for the month, and the cost and schedule baseline.

A CPR will be prepared and issued monthly by the PMCS Group. Reporting will be by WBS element at the project level to the control account level. For each element, the following data will be reported: actual cost of work performed, budgeted cost of work performed, and budgeted cost of work scheduled. Cost and schedule variances and cost and schedule performance indices will be documented in the CPR.

Chapter 3

Accelerator Upgrades

3.1 Overview

The Advanced Photon Source (APS) is the largest accelerator complex in the Western Hemisphere dedicated to the production of synchrotron radiation using electrons stored in a ring. With a 1104-m circumference and a 7-GeV beam energy [3.1-1], there are only three other sources in the world with a comparable size and electron beam energy [3.1-2–3.1-4]. APS consists of an injector and storage ring. The purpose of the injector is to supply beam to the storage ring. No changes to the injector are planned as part of the upgrade project. A number of upgrades to the storage ring will be undertaken, as detailed in subsequent chapters of this document. These upgrades are targeted at specific changes that will improve the scientific capabilities of the APS in order to address the mission needs described in Chapter 1.

In this section, we give an overview of the accelerator complex as it now exists and operates. We then briefly summarize the accelerator aspects of the upgrade and how these relate to mission need. These aspects are discussed in detail in subsequent sections of this chapter.

3.1.1 Accelerator Complex and Present Operations

The APS contains 40 largely identical sectors, each of which consists of accelerator components and a 5-m-long straight section. Five of these straight sections are reserved for accelerator systems required for beam injection, replenishing of the electron beam energy, and diagnostics. The remaining 35 straight sections are available for insertion devices, typically undulator magnets, that produce x-rays for user experiments. The maximum length available for such devices is 4.8 m. Each sector also contains two bending magnets, one of which is designed for use as an x-ray source.

The most fundamental parameters of the stored electron beam are the energy, current, and emittance. Light sources targeting hard x-ray applications tend to operate with high electron beam energy E, since the energy of x-rays produced in undulators scales like E^2. There is also a tendency to operate with moderate beam current to reduce rf power requirements and x-ray beam power loads on the beamline front ends to more manageable levels. APS presently operates at 100 mA, which is

fairly typical of sources in this energy range. The APS effective emittance,[1] 3.1 nm, is again typical for high-energy third-generation sources. The normal vertical emittance is 40 pm, which is somewhat higher than typical, resulting both from user requirements and the desire to operate routinely in few-bunch modes (see below). Of these basic parameters, only the beam current and emittance will change as part of the upgrade, as discussed below.

Besides total beam current, the electron beam bunch timing pattern is very important for many applications. For this reason, APS operates with various bunch patterns or modes (depicted in Figure 3.1-1):

- *24-bunch mode*: As the name suggests, this features 24 equispaced bunches. The time between bunches is about 150 ns, with a FWHM bunch duration of about 80 ps, which is suitable for certain time-resolved studies. This mode is used about 65% of the time.
- *Hybrid mode*: This features a single intense bunch of 16 mA together with a collection of 56 bunches crowded on the opposite side of the ring. There is a space of about 1.6 μs before and after the intense bunch that has a FWHM duration of about 120 ps, which again makes it suitable for certain time-resolved studies. This mode is used about 15% of the time.
- *324-bunch mode*: This features 324 equispaced bunches. This mode is used about 20% of the time.

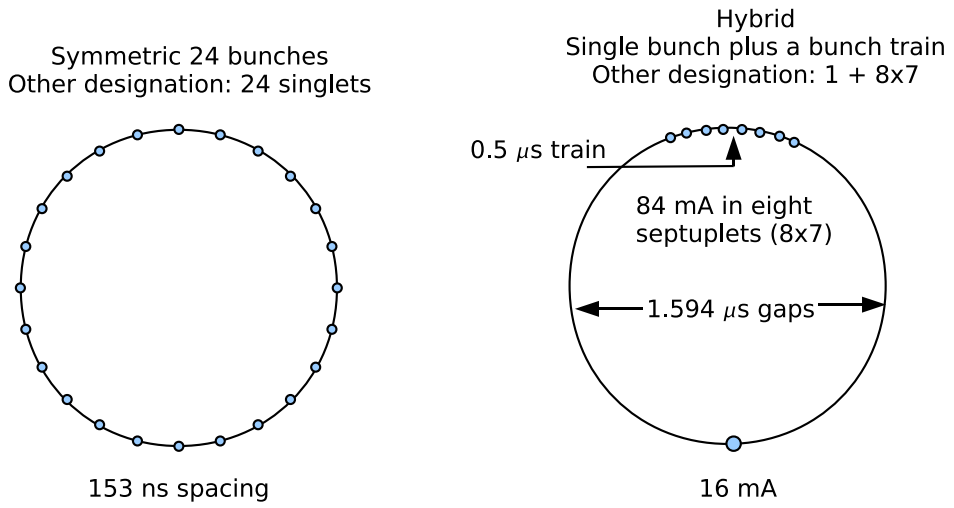

Figure 3.1-1. Depictions of two bunch patterns at present operating current of 100 mA.

One goal of the upgrade is to continue to support operation in all three modes.

Another important aspect of the beam is the partitioning of the effective emittance into the beam size and divergence in the horizontal and vertical planes. The electron beam size and divergence are nominally identical at all beamlines, a result of the 40-fold symmetry of the accelerator lattice.

[1] The effective emittance is the emittance including dispersion effects. At the center of a straight section with $\alpha_x = 0$ and $\eta_x' = 0$, it is given by $\sigma_x \sigma_{x'} = \epsilon_0 \sqrt{1 + (\sigma_\delta \eta_x)^2/(\epsilon_0 \beta_x)}$, where σ_x is the rms beam size, $\sigma_{x'}$ is the rms divergence, ϵ_0 is the raw natural emittance, and σ_δ is the fractional rms energy spread.

However, reduced horizontal beam size (RHB) can be delivered to one straight section, while leaving other straight sections unchanged. At present, each APS run includes some time operating with such a lattice. In principle, this can be provided to several sectors when there is demand. At present, there is little impact on machine operation from the broken symmetry. As discussed in subsequent sections, delivering this mode in the upgrade is more challenging because of other lattice changes.

The combination of low emittance and high charge per bunch in the 24-bunch and hybrid modes leads to short beam lifetimes. Even with a vertical emittance of 40 pm, the lifetime in 24-bunch mode at 100 mA is typically 8 hours, while the lifetime of the hybrid bunch is about 3 hours. Because of this, the beam intensity would decay rapidly, resulting not only in loss of x-ray intensity, but perhaps more importantly, in variation in beam-position-monitor (BPM) systematics and heat loads on x-ray optics. This would negatively impact experiments that demand high beam stability. For these reasons, APS pioneered top-up mode [3.1-5], which involves frequent injection of beam to make up for losses. At present, top-up injections occur at 2-minute intervals in 24-bunch mode and 1-minute intervals in hybrid mode. The 324-bunch mode has a sufficiently long lifetime that top-up is not required; instead, the beam is added every 12 hours to restore 100 mA. One additional attraction of this mode is that it provides valuable time for injector development and operator training.

APS operates for users for approximately 5000 hours per year, with typical mean time between faults of 50 to 100 hours and availability of 97 to 99%. There are three runs and three shutdowns per calendar year. During a run, weekly maintenance and study periods are scheduled, lasting for 24 to 48 hours. Much of this time is used to perform necessary repairs or studies that prepare the accelerator for an upcoming change in the fill pattern or lattice.

3.1.2 Accelerator Upgrade Components

The APS accelerator upgrade includes a number of components, several of which will be unique. These are driven by mission needs, including

- *The need for additional beamline capacity.*
- *The need for more stable beams to allow demanding, state-of-the-art experiments to be performed.*
- *The need to provide intense, tunable, few-picosecond x-ray pulses with high repetition rates for time-domain experiments.*
- *The need to provide higher brightness and flux in the hard x-ray regime (above 10 keV), with particular emphasis above 25 keV.*

Implementation of these upgrades will present many challenges, not the least of which is the intention to continue to operate the APS for 5000 hours per year. This implies that installation of components in the storage ring, as well as commissioning of new systems, will have to take place during existing maintenance and startup periods. In the remainder of this section, we briefly sketch our approach to each of these requirements. Details are given in appropriate sections below.

By and large, each of these upgrades could be pursued independently. That is, they are complementary, but not tightly linked. Where there are links, we've indicated what they are in the discussion below.

3.1.2.1 Capacity

The need for additional beamline capacity is addressed by provision of additional canted straight sections and long straight sections. At present, each straight section at APS accommodates a total of 4.8 m of insertion devices, which is suitable for canting two devices with a length of 2.1 m each. As described in section 3.2, we plan to provide four long straight sections for which the total length of insertion devices is increased to more than 7.7 m. This allows increased capacity with higher brightness and flux, due to the longer devices that are possible. Provision of long straights is also beneficial in order to implement the short-pulse x-ray (SPX) scheme without reducing capacity (i.e., the long straights are helpful in accommodating the SPX hardware and insertion devices in the same straight).

Provision of long straights has a modest negative effect on brightness because the horizontal emittance will increase. However, the increase is less than 10%, which is considered acceptable.

3.1.2.2 Stability

More stable beams will allow demanding, state-of-the-art experiments to be performed. This is addressed by a multipronged approach to improving electron beam stability, as described in section 3.3. The goal is to increase the short- and long-term beam stability by a factor of two to four.

Improved beam stability has essentially no negative impacts on other aspects of APS-U. Indeed, it is helpful in that it is in some cases equivalent to a brightness increase. The SPX project has the potential to negatively impact beam stability. As a result, specific steps are taken as part of SPX project that include setting tolerances on various errors and providing the diagnostics needed for control, feedback, and fine tuning.

3.1.2.3 Short X-ray Pulses

There is a need to provide intense, tunable, few-picosecond x-ray pulses with high repetition rates for time-domain experiments. This is addressed by the use of Zholents' deflecting-cavity scheme [3.1-6] for production of short x-ray pulses. This scheme, discussed in section 3.5, addresses one of the major deficiencies of storage ring light sources, namely, the inability to make intense, few-picosecond x-ray pulses.

As stated above and described in detail in section 3.5.3, the SPX system has the potential to negatively impact beam stability, both in terms of beam motion and emittance. Hence, upgrades to the beam stabilization systems, in particular the fast feedback system, are highly desirable as a complementary upgrade. In addition, a comprehensive suite of SPX-specific diagnostics are planned.

3.1.2.4 Brightness and Flux

There is a need to provide higher brightness and flux in the hard x-ray regime, above 10 keV, with particular emphasis above 25 keV. This is addressed in part by optimized insertion devices, as described in section 3.4, which includes planar undulators with customized periods, revolver undulators,

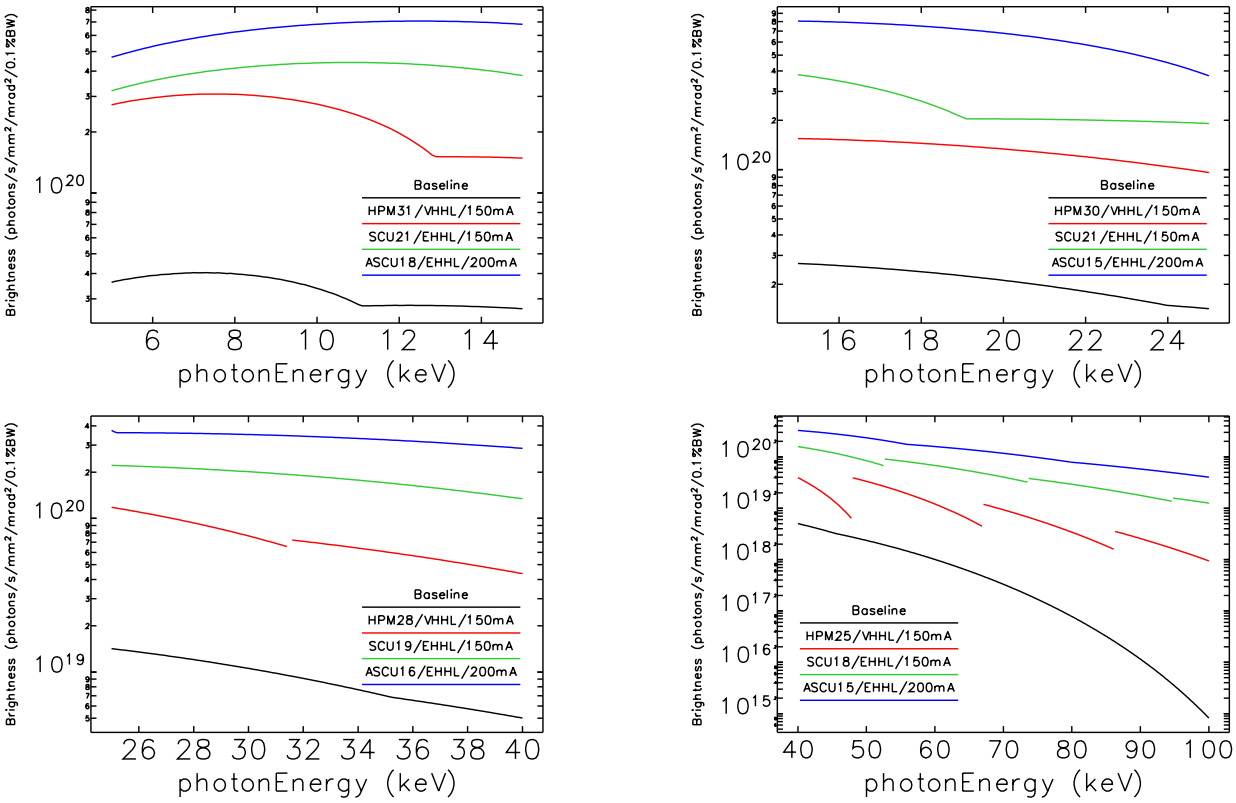

Figure 3.1-2. Illustration of potential brightness improvements in four energy bands for APS-U and beyond. The figures compare the brightness of a present-day U33 device at 100 mA with a canted front end to optimized HPM (hybrid permanent magnet), SCU (superconducting undulator), and ASCU (Advanced SCU) devices at 150 to 200 mA with front-end developments. The vertical scale is different for each energy band and is made to accommodate all the curves. Note that ASCU and 200 mA are not within the scope of the upgrade. The Extremely High Heat Load (EHHL) front end concept is described in section 3.4.8.

and short-period superconducting undulators. The need for higher brightness and flux is also addressed by provision of a number of long straight sections, as described in section 3.2, and by increasing the operating electron beam current from 100 mA to at least 150 mA.

The accelerator is presently capable of running at 150 mA but would require upgrades to run beyond that. In order to provide an option for enhanced brightness and flux, we have explored what would be required for 200-mA operation, as described in section 3.6. While this is not within the scope of the upgrade, we have adopted the principle that nothing should be done to preclude it. Hence, all new components will be designed to be compatible with 200 mA.

In order to perform user operations with current above 100 mA, e.g., at the 150-mA minimum upgrade level, we will have to upgrade the beamline front ends, as discussed in section 5.3, and the beamlines, as discussed elsewhere in this document.

In addition, improved control of the coupling will be implemented, which will also improve x-ray brightness by permitting lower vertical emittance and providing more predictable beam parameters.

These changes are described in more detail in section 3.2

Because brightness is such a prominent performance measure for synchrotron radiation sources, we end this introductory section with an illustration of the potential brightness gains from the APS upgrade. As shown in Figure 3.1-2, there is the potential for very significant brightness improvements in various energy bands as part of the APS upgrade and beyond. (Details of this analysis and the assumptions behind it are described in section 3.4.8.)

3.1.3 References

[3.1-1] J. N. Galayda. The Advanced Photon Source, Proc. of PAC 1995, pp. 4–8, (1996); http://www.JACoW.org.

[3.1-2] J. L. Laclare. Commissioning and Performance of the ESRF, Proc. of PAC 1993, pp. 1427–1431, (1993); http://www.JACoW.org.

[3.1-3] S. Date et al. Operation and Performance of the SPring-8 Storage Ring, Proc.of PAC 1999, pp. 2346–2348, (1999); http://www.JACoW.org.

[3.1-4] K. Balewski et al. PETRA III: A New High Brilliance Synchrotron Radiation Source at DESY, Proc. of EPAC 2004, pp. 2302–2304, (2004); http://www.JACoW.org.

[3.1-5] L. Emery and M. Borland. Upgrade Opportunities at the Advanced Photon Source Made Possible by Top-up Operations, Proc. of EPAC 2002, pp. 218–220, (2002); http://www.JACoW.org.

[3.1-6] A. Zholents et al. Generation of subpicosecond X-ray pulses using RF orbit deflection, Nuclear Instruments and Methods in Physics Research A, **425**, 385, (1999).

3.2 Lattice and Accelerator Physics

3.2.1 Introduction

One of the goals of the APS upgrade is to meet the need for higher-brightness x-ray beams, as well as the simultaneous need for additional beamline capacity. Provision of a number of long straight sections is an effective way to meet this need. Long straight sections are needed for long insertion devices (IDs) and in order to be able to fit in one straight section a combination of a superconducting undulator and a permanent magnet undulator or a combination of a permanent magnet undulator and a set of superconducting cavities. Hence, long straights are an important part of providing higher brightness, increased capacity, and short x-ray pulses (see section 3.5).

Specific details for all these goals are discussed in other sections of this report. Here we focus on the beam dynamics issues pertaining to establishing the APS lattice with four long straight sections. The most significant challenge of this task arises from a need for uneven distribution of long straight sections around the ring to meet user demands and practical constraints. The loss of lattice symmetry associated with this presents potentially severe consequences in terms of beam emittance increase, lifetime reduction, and loss of injection efficiency.

In 2003, APS accelerator scientists and engineers, in consultation with interested members of the user community, conducted an extensive study of various options for implementation of long straight sections. Several of these involved replacement of dipole magnets which, while very effective at lengthening the straight section, was determined to be too expensive for the benefit delivered. In the end, it was decided to make a long straight section by removing one quadrupole magnet on each side of the existing straight section.

This is conceptually simple and requires no additional magnets, which greatly reduces the cost. This scheme requires rebuilding the girders on either side of the straight section. These girders presently hold the quadrupole triplets, as well as two sextupoles, two steering magnets, and several beam position monitors. Although no additional magnets are needed, we must prepare girders ahead of time for rapid installation.

Because of the breaking of ring symmetry by the long straight sections, much effort has been spent in mitigating the adverse effects on beam dynamics by making adjustments to the strengths of the quadrupole and sextupole magnets, a unique opportunity offered by the existing power supply arrangement in which all quadrupoles and sextupole magnets have individual power supplies. Taking advantage of this opportunity, a new approach relying on a parallel genetic optimization algorithm for lattice optimization has been developed that allows us to largely regain the performance parameters of the original symmetric lattice. Discussion of the approach developed for the APS appears in the first part of this section. In addition to the arrangement of the long straight sections, a requested special sector with reduced horizontal beam size also reduces the symmetry of the lattice. The method of recovering the performance of a symmetric lattice is essentially the same as that employed when introducing the long straight sections.

Following the discussion of lattice design, we discuss experimental tests of mock-up lattices, which give confidence in our results. One outcome of these tests, as reported in section 3.2.2.6, is that we will have to restrict the extent of beam steering for users in order maintain good injection efficiency and lifetime.

Issues in correcting the vertical emittance will be discussed next. In the presence of errors, a storage ring produces a somewhat large vertical emittance that can be reduced to reasonable levels using standard techniques used at all light sources. In addition, the nonlinear properties of a lattice are usually worsened by the same errors that cause vertical emittance. Thus when the vertical emittance is corrected, the nonlinear properties are improved.

In the final part of this section, we review collective effects in the storage ring, which are well characterized in the present configuration. They define the practical operating limits for total current and for single-bunch charge. In particular, we look at the potential impact of lattice changes and longer insertion device chambers, with a view toward maintaining the existing operating limits and setting requirements for chamber gaps. (Other changes, such as the introduction of rf cavities for the short pulse x-ray (SPX) source, will potentially adversely impact collective effects, and are discussed in section 3.5. Requirements for higher current operation will also be discussed in section 3.6.)

3.2.2 Lattice Design

The APS magnetic lattice consists of 40 double-bend sectors, normally operated in an essentially translation- and reflection-symmetric configuration. (The symmetry is slightly broken by the use of Decker distortion in the user Sectors 1-35 [3.2-1], a feature that any upgrade must retain since it reduces backgrounds on x-ray beam position monitors.) Each sector has ten quadrupoles, seven sextupoles, and eight steering magnets per plane. In anticipation of the need to customize the electron optics, all quadrupoles and sextupoles have independent power supplies [3.2-2]. In addition to permitting optics correction [3.2-3], this feature has allowed provision of special reduced horizontal beam size (RHB) optics for several beamlines. Its importance to the APS upgrade is twofold: First, it permits us to entertain lattice customizations without the expense of additional power supplies and controls. Second, it permits us to mock-up many of these customizations before we commit to hardware changes.

The most important of these customizations will be provision of long straight sections (LSSs) to (nominally) four sectors. As described above, this will be accomplished by removing the long Q2 quadrupoles, one beam-position-monitor (BPM), and one corrector on either side of the target straight section, then moving other components away from the straight section into the empty locations.

Given that there are 40 straight sections in total and that we will nominally have four long straights, the most natural configuration is to make every tenth straight section a long one. This retains a high degree of symmetry in the lattice, which is traditionally considered necessary in order to obtain good dynamic and momentum acceptance.

However, such a configuration is less than ideal. First, it requires relocation of beamlines to match the locations of the LSSs, which would be expensive and would disrupt the beamlines' science programs. In addition, for implementation of SPX, we would ideally like to have two LSSs separated by a single short straight, since this permits accommodating the SPX cryomodules without excessively reducing the space available for undulators.

The last of these concerns could be addressed with a configuration that features two groups of two LSSs separated by a standard straight. This could be done in a two-fold symmetric fashion. However, the expense of moving beamlines is still present and should be avoided if possible.

Based on these considerations and recent progress in optimization of the nonlinear properties of lattices [3.2-4, 3.2-5], we have developed workable nonsymmetric configurations incorporating four and eight LSSs. In this document, we discuss the present preferred configuration of four LSSs. The remainder of this section is devoted to explaining the optimization methods and simulation predictions, as well as the results of experimental tests.

3.2.2.1 Installation Tasks and Schedule [U1.03.02.01]

As indicated, provision of an LSS is conceptually simple, since we are removing accelerator components. In practice, this requires pre-assembling new girders to be installed in place of the existing girders (known as girders 1 and 5) on either side of the straight. In addition, a new vacuum chamber must be prepared and installed for the straight section. These components, illustrated in Figure 3.2-1, must be installed during a standard APS shutdown, which lasts approximately one month. A

preliminary schedule, shown in Figure 3.2-2 has been worked out that indicates that this is feasible.

Table 3.2-1 summarizes the components that must be removed and installed. We see that sufficient spare magnets are available to build up the first set of required girders prior to installation. Although some reworking of aluminum spacers and utility connections may be required, it will not be necessary to build new magnets. After that, components will be harvested from the girders that are removed to build the next set of girders.

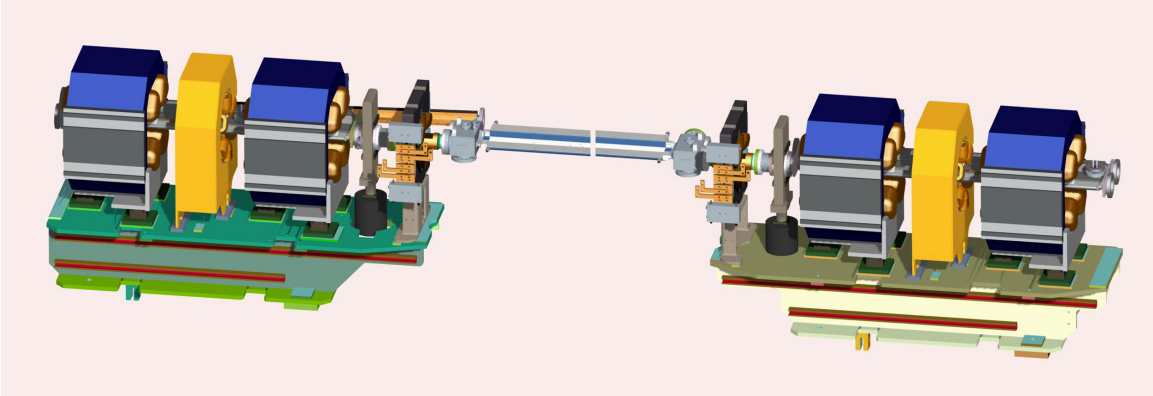

Figure 3.2-1. Conceptual layout of components that must be installed for a long straight.

	Activity Name	Duration (Hours)	Start Date	Finish Date
1	Long Straight Section Installation	258.00	4/28/11	5/30/11
2	Disconnect Power Systems	4.00	4/28/11	4/28/11
3	Disconnect Diagnostics	2.00	4/28/11	4/28/11
4	Disconnect Water	3.00	4/28/11	4/28/11
5	Disconnect Vacuum	7.00	4/29/11	4/29/11
6	Remove Girders	16.00	4/30/11	5/1/11
7	Survey & Alignment	16.00	5/2/11	5/3/11
8	Install Pedestals	8.00	5/4/11	5/4/11
9	Survey & Alignment	8.00	5/5/11	5/5/11
10	Install Girders	32.00	5/6/11	5/9/11
11	Survey & Alignment	24.00	5/10/11	5/12/11
12	Install Water	8.00	5/13/11	5/13/11
13	Connect Power Systems	4.00	5/14/11	5/14/11
14	Connect Vacuum & Bakeout	112.00	5/14/11	5/27/11
15	Survey & Alignment	16.00	5/28/11	5/29/11
16	Connect Diagnostics	2.00	5/30/11	5/30/11
		Tot: 262.00		

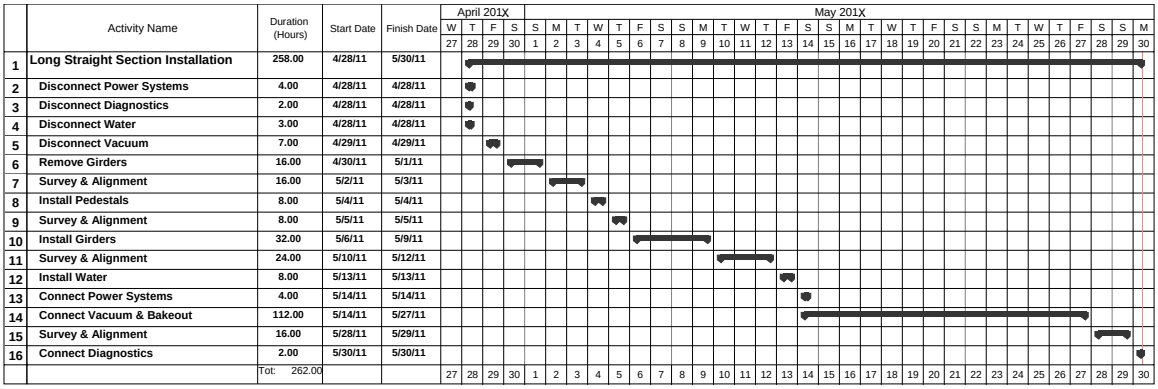

Figure 3.2-2. Preliminary schedule showing tasks required for installation of a long straight during a one-month shutdown, assuming eight-hour work days including weekends. (The April shutdown is used only as an example.)

As discussed in section 3.2.2.6, the new lattices are more sensitive to orbit displacement in sextupoles than the existing APS lattices. As a result, it will be necessary to center the orbit in the sextupoles, which is not presently required. This implies the need to improve the alignment of the accelerator and beamlines in those locations where the beamlines are now accommodated by large steering of the electron beam. This can be done gradually (i.e., a few sectors at a time). Steering tolerances are still under investigation, but preliminary estimates indicate that 23 insertion device beamlines and 14 bending magnet beamlines will require realignment. This is not part of project scope.

Table 3.2-1. Simplified Listing of Components that Must be Removed and Installed to Create a Single Long Straight Section

Component	Remove	Install	Spares available
Accelerator systems:			
0.5-m quadrupole	4	4	11
0.8-m quadrupole	2	0	n/a
h/v corrector	4	2	10
sextupole	2	2	11
beam position monitor	6	4	n/a (new components)
magnet girder	2	2	n/a (new components)
vacuum chamber assembly	2	2	n/a (new components)
vacuum system supports	-	16	n/a (new components)
ID systems:			
vacuum chamber extrusion	1	1	n/a (new components)
beam position monitors	2	2	n/a (new components)
transition end boxes	2	2	n/a (new components)
vacuum chamber supports	2	2	n/a (new components)
vacuum ion pumps	2	2	n/a (new components)
vacuum gauges	2	2	n/a (new components)

3.2.2.2 Lattice Constraints

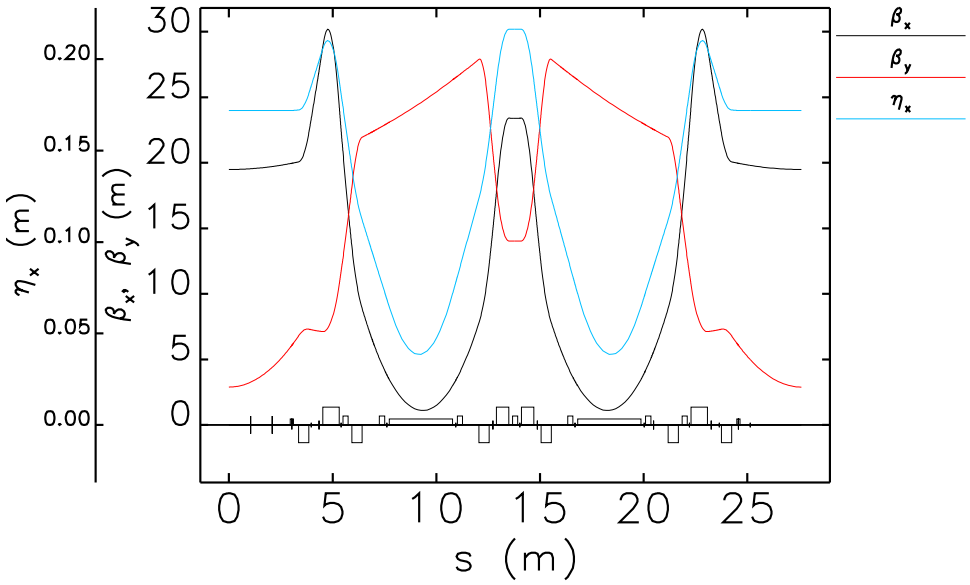

Figure 3.2-3. Present lattice functions for the first sector of the APS.

Before describing in detail how the new lattices are developed, we review the properties of

the present lattice and list constraints that must be satisfied by new lattices. The present APS lattice functions are shown in Figure 3.2-3. Constraints on new lattices include:

- Maximum beta functions in the horizontal and vertical planes of 40 m and 30 m, respectively. Ideally, maximum beta functions should be as small as possible, particularly at ID transitions, in order to reduce the effective chamber impedance (see section 3.2.4).
- Horizontal beta functions at the center of ID straights of between 15 and 25 m. In general, values close to 20 m are used now and are preferred.
- Vertical beta functions at the center of the ID straights within 50% of $\beta_{opt} = L/2$, where L is the length of the small gap chamber. ($L \approx 2.5$m for a normal straight.) This maximizes the vertical acceptance. The beta function β_e at the end of the chamber is relatively insensitive to the exact value $\beta_c = \beta_{opt} + \Delta\beta_c$ at the center, being governed by

$$\frac{\Delta\beta_e}{\beta_e} \approx \frac{1}{2}\left(\frac{\Delta\beta_c}{\beta_c}\right)^2, \tag{3.2-1}$$

  so that β_e is within 13% of the optimum value.
- At present the APS effective emittance is 3.1 nm, resulting from a 2.5-nm natural emittance combined with the presence of dispersion in the straight sections. Because the effective emittance has been optimized to the present low value, any changes are likely to result in an increase. This increase should be kept to under ~10%. In order to keep the emittance close to its present value, the horizontal integer tune should be 36 (the present value) or higher. There is little reason to raise it above this value, so we've elected to keep both tunes close to the present values, $\nu_x = 36.15$ and $\nu_y = 19.25$.
- Because of the need to run with high single-bunch current, APS operates with high chromaticities, which reduces the impact of the transverse mode coupling instability. In 100-mA, 24-bunch mode, we historically have needed $\xi_x \approx 7$ and $\xi_y \approx 6$, while in hybrid mode we require $\xi_x \approx \xi_y \approx 11$. A newly developed single-bunch feedback system has recently been put into routine operations [3.2-6]. With this system, the requirement for exceeding 16 mA per bunch is reduced to $\xi_x \approx \xi_y \approx 9$, while $\xi_x \approx \xi_y \lesssim 8$ will be needed for 24-bunch mode at 150 mA. Hence, we have targeted $\xi = 9$ in our designs.
- We do not intend to upgrade any main accelerator magnets or power supplies as part of the project. Hence, we must respect existing power supply limits, which give $K_1 \leq 0.9\mathrm{m}^{-2}$ for quadrupoles. For most sextupoles, we are limited to $K_2 \leq 21.6\mathrm{m}^{-3}$. We can, if necessary, add inexpensive "noses" to the sextupole poles as was done already for the S2 family, raising the limit to $29.8\mathrm{m}^{-3}$ [3.2-7].
- As described in detail below, sufficient dynamic acceptance (DA) is necessary in order to have efficient injection. Simulations of the present operating lattice indicate that our dynamic acceptance is -12 to -15 mm on the injection side, as shown in Figure 3.2-4. Hence, we attempt to achieve this value in optimization of new lattices. The dynamic acceptance on the positive side is less important; we attempt to achieve at least 7 mm. In the vertical plane, we target 1 mm, which is quite generous compared to the typical rms beam size of 10 μm for the stored beam and 0.2 mm for the injected beam (assuming 10% coupling in the booster).

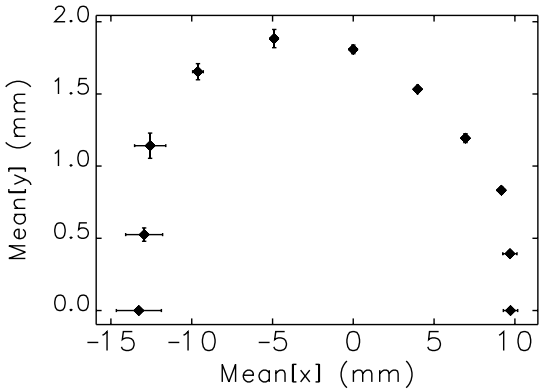

Figure 3.2-4. Nominal dynamic acceptance computed for 50 error ensembles for $\xi_x = 7$ and $\xi_y = 6$. The error bars show the standard deviation of the DA boundary location.

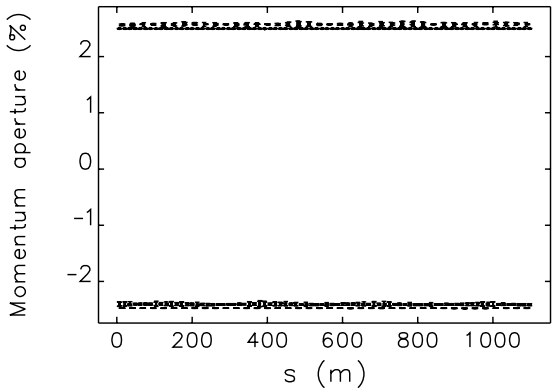

Figure 3.2-5. Nominal momentum acceptance computed for 50 error ensembles for $\xi_x = 7$ and $\xi_y = 6$. The error bars show the standard deviation of the boundary location. An rf voltage of 9 MV is assumed and is the limiting factor in determining the momentum acceptance.

- Although APS runs in top-up mode [3.2-8] and can therefore tolerate a somewhat short beam lifetime, there are limits both in the amount of charge and frequency of injections. Ideally, to avoid disturbing experiments, we would inject no more frequently than every 120 seconds, although in hybrid mode at present we inject every $\Delta T_i = 60$ s. While our injector is nominally capable of delivering $\Delta Q_i = 6$ nC per shot, a value of 3 nC is routinely available. The minimum workable lifetime is

$$\tau_{\min} = \frac{Q_s \Delta T_i}{\Delta Q_i \eta_i}, \tag{3.2-2}$$

  where Q_s is the total stored charge, and η_i is the injection efficiency. At 150 mA and 80% efficiency, this gives $\tau_{\min} = 3.8$ h for a 60-second top-up interval.

  Another consideration is the droop in the charge in each bunch between injections, which should be kept to a minimum. This is given by

$$D = 1 - e^{\frac{-B\Delta T_i}{\tau}}, \tag{3.2-3}$$

  where B is the number of stored bunches. If the lifetime is only 3.8 hours for 24 bunches, we would have $D = 0.1$, or a 10% droop. This is probably acceptable, but clearly having a longer lifetime is desirable, if for no other reason than to prevent radiation damage of components.

  The lifetime is strongly affected by the local momentum acceptance (LMA), described in detail below. The reference LMA for the present APS lattice is shown in Figure 3.2-5. This is sufficient to provide lifetimes of 8 to 9 hours at 100 mA in 24 bunches for our nominal vertical emittance of 40 pm.

3.2.2.3 Dynamic and Momentum Acceptance

As alluded to above, in addition to designing appropriate linear optics, we must control the nonlinear dynamics of the lattice in order to obtain adequate dynamic and momentum acceptances. We will begin with an explanation of the meaning and importance of these quantities.

Dynamic acceptance (DA) is characterized by the area in horizontal and vertical space into which particles may be injected and survive as stored beam. Thus, the importance of the dynamic acceptance is that it is a primary determinant of the injection efficiency. In the APS, we inject in the horizontal plane, i.e., with non-zero residual amplitude in the horizontal motion, so the horizontal dynamic acceptance needs to be much larger than the vertical. In addition, because we inject from inside the ring, the horizontal acceptance on the negative side is more important than on the positive side.

Dynamic acceptance is determined by tracking particles with increasing initial horizontal (x) and vertical (y) amplitudes until the boundary between survival and loss is found. This process is illustrated in Figure 3.2-6. A series of n line searches are conducted beginning at the origin. The coordinates along the lines are simply

$$x = R\cos\phi_n, \tag{3.2-4}$$

$$y = R\sin\phi_n, \tag{3.2-5}$$

where $\phi_n = n\pi/L$ for an L-line search. For each line, we wish to find the smallest R, R_{da}, at which a particle will be lost within N turns. To do this, R is increased in small steps ΔR until a loss is seen within N turns. The step interval ΔR is then subdivided to refine the determination of R_{da}. The set of (x, y) points resulting from the determination of R_{da} for each line defines the DA boundary.

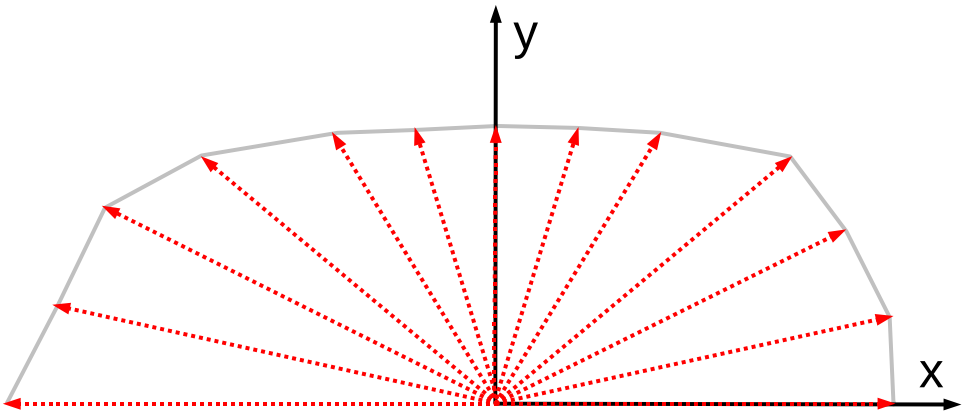

Figure 3.2-6. Illustration of the method used to determine dynamic acceptance. Particles are launched at intervals along a series of lines beginning at the origin. After a loss is seen, interval subdivision is used to refine the determination of the minimum acceptance required for loss. The (x, y) location of first particle loss defines a point on the dynamic acceptance boundary.

Momentum acceptance is characterized by the maximum momentum displacement that a particle can undergo and still survive. In general, this quantity varies as a function of position around the ring, as well as for negative and positive momentum displacements. Hence, we are interested in the

local momentum acceptance characterized by two functions $\delta_n(s)$ and $\delta_p(s)$. These give, respectively, the maximum fractional negative and positive momentum displacements that a particle may experience at location s and still survive a chosen number of turns. These functions are primary determinants of the Touschek lifetime, which is the dominant lifetime-limiting mechanism in the APS and other third-generation light sources.

The method used to determine $\delta_{n,p}(s)$ [3.2-9] is similar to that used for determining the dynamic acceptance. At the exit of selected elements (i.e., at selected s positions), particles are given increasing positive or negative momentum kicks, then tracked N turns. When a loss is seen, the step size is decreased to refine the determination of the boundary.

For both DA and LMA determination, particle tracking must include not only the effects of the magnets, but also longitudinal motion, radiation damping, physical apertures, and errors.

Longitudinal motion: The need for longitudinal motion (i.e., motion in the rf bucket) in the case of the LMA is clear, since the momentum acceptance may be determined either by transverse dynamics or the rf acceptance $\pm\epsilon_{\text{rf}}$. This is particularly the case with the APS, where we operate with relatively low rf voltage giving an $\epsilon_{\text{rf}} \approx \pm 2.3\%$. In the case of DA, we have observed some sensitivity to longitudinal motion, which results from the small path-length dependence on the betatron amplitude.

Radiation damping: Radiation damping must be included in the model for several reasons. First, it may increase the DA or LMA by damping the growth of particle motion near the stability boundary. Second, it stabilizes the determination of the acceptance by sweeping the particle's amplitude over a small range. This ensures that an unstable amplitude is not "stepped over" in the search. For this reason, in computing the LMA it is advisable to choose a momentum step size $\Delta\delta$ that is smaller than $\epsilon_{rf}(1 - e^{-NT_r/\tau_\delta})$, where T_r = 3.68 μs is the revolution time and $\tau_\delta = 4.8$ ms is the longitudinal damping time. For APS, we typically take $N = 400$, which means that over 25% of the initial momentum displacement decays away in the course of the simulation. A third reason for including damping in LMA simulations is that this large momentum slew potentially sweeps the particle past many resonances, the effect of which would be missed if radiation damping was omitted. Similar reasoning applies for DA determination, where radiation damping results in a rapid drop in amplitude that may result in sampling resonances due to the tune shift with amplitude.

Physical apertures: Although we commonly speak of the "dynamic aperture," what we are in fact interested in is the dynamic acceptance, which is the aperture including both dynamic and physical limits. Often, we find that the effective aperture is smaller than the physical aperture, which may lead to the erroneous conclusion that the physical aperture is not important. Including small vertical physical apertures is particularly important when there is coupling of horizontal and vertical motion, as it can result in significant reductions in the *horizontal* aperture. All simulations include realistic physical apertures unless otherwise stated. In particular, in the case of the long straight sections, the simulated apertures include the effect of the longer ID chamber.

Inclusion of errors: Inclusion of errors refers not only to multipole errors resulting from magnet imperfections, but, far more importantly in the case of APS, to random errors in the strength and

alignment of magnets. For example, without errors the effect even of the half-integer resonance may not be seen in a tracking simulation. Similarly, without errors we would not have coupling between the horizontal and vertical planes, which is well known to strongly affect the dynamic acceptance of light sources with small-vertical-gap insertion devices. Hence, we must include lattice errors in the simulations.

Effective methods exist for correcting linear optics [3.2-10] and coupling (e.g., [3.2-11–3.2-13]), which are important in light sources because of the small insertion device vertical apertures. In the APS, for example, we correct lattice function errors to the 1% rms level [3.2-3] and coupling to the 1% level. These are commonly achieved in modern storage rings.

It would seem that in order to be realistic, we must not only include errors, but also correct those errors using real-world techniques. However, correction is not essential in the simulations. Once correction is performed, we are left with residual errors of a certain level. Instead of modeling relatively large errors with correction, we can simply use smaller random errors that give lattice function and coupling errors at post-correction levels. This neatly sidesteps a considerable complication. We have found that assuming quadrupole and sextupole strength errors at the 0.02% rms level and tilt errors at the 0.05 mrad rms level give lattice errors at or above the desired level. It is then only necessary to apply a coupling correction algorithm to emulate our operational method of setting of the vertical emittance.

3.2.2.4 Optimization Technique

The requirements set down in the previous section are a mixture of linear optics constraints and constraints that depend on nonlinear properties of the lattice. The latter are, of course, controlled through adjustment of the sextupole magnets. A very common approach [3.2-14] to optimization of sextupole settings is to minimize various resonance driving terms, which in turn minimizes tune shifts with transverse amplitude $d^n\nu_{x,y}/dA^n_{x,y}$ and momentum offset $d^n\nu_{x,y}/d\delta^n$. However, as described in the last section, we operate the APS with chromaticities $d\nu_{x,y}/d\delta$ that are considerably different from zero. Hence, the utility of minimizing the higher-order chromaticities is doubtful. Indeed, we very likely need to employ significant higher-order terms to minimize the size of the tune footprint over the desired momentum acceptance.

The issue is less obvious in the case of the amplitude-dependent tune shifts. However, experience has shown that small amplitude-dependent tune shifts are not always optimal, depending on the proximity of the working point to strong resonances. In some cases, we have found that a large tune shift with amplitude can defuse a resonance by preventing quasi-stable particles from remaining on the resonance.

Even when it is applicable, the traditional method of sextupole optimization does not guarantee good DA and LMA. If it did, we would not need tracking simulations to validate the sextupole configuration, and yet such simulations are universally used. Informed by these observations, we have developed a new technique [3.2-4, 3.2-5] for sextupole optimization that relies on tracking simulations directly. It is made possible by the availability of relatively inexpensive computing clusters and fully scriptable accelerator simulations.

Although our method could use any tracking code, the ability to create fully scripted

simulations is essential, since matching and tracking must run without human intervention. Thus, we use the tracking program `elegant` [3.2-15, 3.2-16], as well as the SDDS Toolkit [3.2-17] and `geneticOptimizer` [3.2-18].

In this method we use many computers simultaneously to evaluate the DA and LMA for various lattice tunings (e.g., tunes and sextupole settings). As described above, DA and LMA computation includes radiation damping, synchrotron oscillations, and physical apertures. After completion of a sufficient number of evaluations, a genetic algorithm is used to "breed" more candidate configurations based on the best configurations seen so far. The process continues until a sufficiently good solution is obtained or until the results stop improving.

As mentioned above, it is important to include errors in the DA and LMA simulations. In order to have a hope that the optimization will converge, it is of course essential that the errors remain unchanged for each evaluation. Hence, we optimize with a single, fixed ensemble of errors. It is always possible that we may choose an error ensemble that happens to provide atypically good results. We guard against this possibility by evaluating the optimized configuration with a large number of ensembles.

Any optimization requires one or more penalty functions. In the work reported here, we used a multi-objective optimization. The objectives are derived from the DA and lifetime.

Dynamic Acceptance Penalty Function: While the DA is frequently computed, quantitative use of the acceptance is uncommon and can be fraught with uncertainty. Typically, we quote the horizontal acceptance as a single number but do not quantify the shape of the acceptance. Such a number could well be highly misleading. However, in order to optimize DA, we must obtain one or a few quantities that clearly indicate how good a solution is. Our approach is to use the area of the DA, but to compute it with certain restrictions that ensure it is a useful quantity.

One potential pitfall of using the DA area is that the optimizer might provide a useless solution with large vertical acceptance and small horizontal acceptance. This can be prevented by simply not scanning the vertical coordinate beyond the minimum requirement. This prevents the algorithm from "seeing" any vertical DA that exceeds requirements.

Another potential pitfall is that the acceptance may not have a smooth shape. In some instances depending, for example, on the strength of coupling resonances, one might find useless protrusions that enlarge the area but that are not useful for injection. We avoid this by applying a clipping algorithm to the DA boundary, as illustrated in Figure 3.2-7.

A third potential pitfall is that the acceptance may be enlarged at $x > 0$ at the expense of $x < 0$ (at APS, we inject on the $x < 0$ side). We avoid this by clipping off any DA that extends beyond $x = 7$ mm, which provides generous room for oscillation of the stored beam due to our mismatched kicker bump.

With these restrictions and modifications, we have found that the area of the DA, A_d, is a robust indicator of a good solution. Because we wish to maximize this area, the related objective function is $-A_d$.

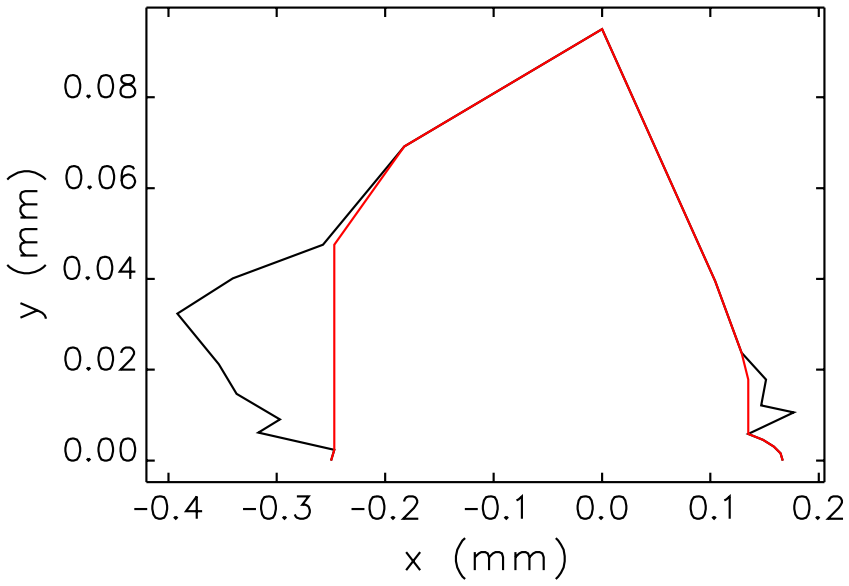

Figure 3.2-7. Illustration of the behavior of dynamic acceptance boundary clipping method. The black line shows the original dynamic acceptance boundary, while the red line shows the clipped boundary.

Lifetime Penalty Function: The Touschek lifetime can be computed from the LMA, the Twiss parameters, the beam emittances, and the bunch charge. We do this using the program `touschekLifetime` [3.2-19]. This program uses the Twiss parameters and LMA computed by `elegant` and applies Piwinski's formalism [3.2-20].

In order to reduce the computer resource requirements, we do not compute the LMA at the exit of every element. Instead, we compute the LMA at the exit of the S1, S3, and S4 sextupoles in the first six (of 40) sectors. Experience shows this is representative of the LMA around the ring. In order to compute the Touschek lifetime, we simply assume that the LMA repeats the same pattern in the subsequent 34 sectors. We check out results in ensemble evaluation by determining the LMA at the exit of all sextupoles.

The objective function related to the Touschek lifetime τ_T is $-\tau_T$, since we want to maximize the lifetime.

In many cases, optimization of the lifetime results in a relatively small momentum-dependent tune footprint that avoids major resonances, such as the integer, half-integer, and main coupling resonances. However, in some cases we have seen stable half-integer resonance crossings, which apparently are possible because of strong coupling between the planes and/or large tune shift with amplitude. Observation of phase-space trajectories for such crossings shows an exchange of amplitude between the planes, as well as mitigation of the effects of the resonances due to fairly rapid synchrotron motion and, presumably, large tune shifts with momentum and amplitude.

In spite of this, we elected to disallow crossing the half integer resonance. We did this by modifying the LMA computation to "cap" the momentum acceptance at the momentum deviation that corresponds to the resonance crossing, if any. This requires that we first track a series of off-momentum particles to determine their tunes. This adds only a small amount of additional running time. The

momentum acceptance cap is accepted as an additional parameter by `touschekLifetime`.

Tune Variation: Variation of the tunes is important in finding an optimal solution. In the case of complex lattices with many different types of sectors, this can be challenging. In the present APS lattice, we have three types of sectors: ordinary user sectors, which include Decker distortion [3.2-1]; special user sectors with reduced horizontal beam size (RHB); and non-user sectors, which do not have Decker distortion. Of the 40 sectors in the ring, a least 33 are ordinary user sectors while five are non-user sectors. Changing the working point is thus relatively simple, even using a quadrupole knob for the ordinary sectors.

When the lattice becomes more complex, this is not true. In particular, with long straights we have reduced the ability to change the tunes while satisfying other constraints, such as maximum beta functions, lattice functions at straight sections, and uniformity of phase advance, not to mention preventing the effective emittance from increasing appreciably. For complex lattices, the most robust approach is to perform matching of the entire ring at once, which can be time consuming. If we must perform such matching for each configuration during the optimization, it can easily add 25% to the running time.

Instead, we chose to make a grid of solutions covering the tune plane on $\nu_x : [36.1, 36.4]$ and $\nu_y : [19.1, 19.4]$ with a spacing of 0.01. We started by creating a single solution by matching individual sector types "by hand." We then gradually covered the tune plane by working our way outward from this starting solution, taking steps of no more than $\nu_x = 0.01$ and $\nu_y = 0.01$. This can be done on a cluster in a matter of a few hours, depending on the difficulty of the lattice. Once we had this grid of solutions, we created a table of quadrupole strengths as a function of tunes. We then created a new solutions by performing two-dimensional interpolation as a function of the tunes. Tests showed that the resulting interpolated solutions were very well behaved. This process was made relatively straightforward by the fact that `elegant` saves and loads lattice data in self-describing data set (SDDS) files [3.2-17, 3.2-21, 3.2-22], which allowed collation and interpolation of the quadrupole strength table without writing any new code, using the SDDS toolkit programs.

Details of the Algorithm: Having reliable objective functions is perhaps the most important part of any optimization. This has been covered in the previous subsections. Here, we discuss several details of the optimization algorithm itself, which is implemented in the `geneticOptimizer` Tcl script [3.2-18]. The algorithm is as follows:

1. Create N randomized configurations. Typically, these are "small" perturbations from a reasonable starting point, e.g., a previous similar configuration or the present operational configuration. N varies depending on the computing resources available. Typically, we have $N \sim 100$, but have used $N > 1000$ for some of the work reported here.

2. Submit N jobs to a cluster to evaluate the configurations.

3. Wait until at least M (e.g., 4 to 10) configurations are newly completed. (Note that the running time is not the same for all configurations, since a small DA/LMA takes less time to simulate.)

4. Collect information on all completed configurations.

5. If the best configuration is adequate, stop. Otherwise
   (a) Perform a nondominated sort to find the first-rank solutions.
   (b) Determine how many open slots P are available.
   (c) For each open slot:
      i. Randomly select two configurations from this group to act as "parents."
      ii. Randomly blend the attributes of the parents to "breed" a new configuration.
      iii. Submit a new job to evaluate this configuration.
6. Wait for at least one job to complete.
7. Return to step 4.

The quantities N, M, and P have been determined in only a rough fashion based on experience, rather than any systematic program of study.

3.2.2.5 Optimization Results

We began with optimization of a configuration with four LSSs in locations required for planned beamline upgrades. In particular, LSSs were placed in straight sections 1, 5, 7, and 11. Since the LSSs are nonsymmetric locations, we refer to this lattice as 4NLSS. The linear optics is reflection symmetric for the two sectors on either side of each LSS. For example, Sector 1 (a short-to-long sector) and Sector 2 (a long-to-short sector) quadrupoles are mirror images of each other. However, the sextupoles are allowed to vary without this symmetry constraint, which has been found to be essential in getting good solutions [3.2-16]. The sextupoles are not necessarily the same in all sectors with the same sequence of quadrupole strengths (as seen by the beam), although this is our starting assumption. Hence, since there are seven sextupoles per sector, we have at least 14 independent sextupole variables for the long-to-short and short-to-long sectors.

In addition to the sectors surrounding the LSSs, we need solutions for ordinary sectors having short straights at each end. Two such solutions are needed, one for the (normal) Decker-distorted sectors and one for the non-Decker sectors (which are used for machine operation and have no beamlines). Although the linear optics in these sectors are very similar, we allowed the sextupoles to vary independently. This provides 14 additional sextupole variables, two of which are used to set the chromaticities.

The physical aperture limit in APS is the small-gap ID vacuum chamber in Sector 4, which has a vertical aperture of $\pm$ 2.4 mm and a horizontal aperture limit of 15 mm on the inboard side. For reasons we'll see below, it is helpful to allow the sextupoles bracketing this straight section to vary independently of others, which adds a further 14 free sextupoles. Finally, as mentioned above, we also allow the tunes to vary, bringing the total number of variables for this optimization to 42.

Starting from the nominal, symmetric sextupoles for a symmetric linear solution, we optimized these sextupoles for target chromaticities of $\xi_x = \xi_y = 3$. Once a satisfactory solution was obtained, we raised the chromaticity in steps $\Delta\xi = 2$ up to $\xi = 9$. Figures 3.2-8 and 3.2-9 show the linear optics for this configuration, while Figures 3.2-10 and 3.2-11 show the dynamic and momentum acceptances.

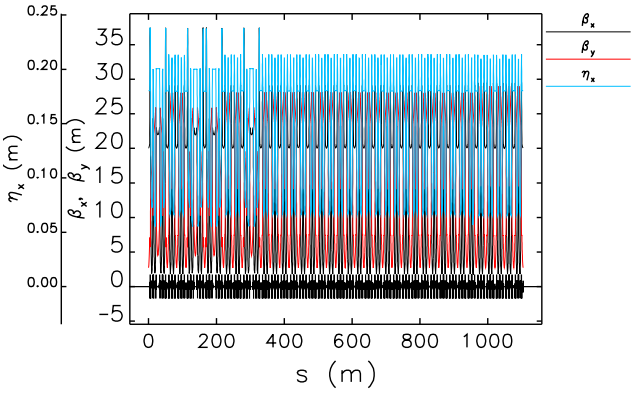

Figure 3.2-8. Optical functions for the full ring with four LSSs at nonsymmetric locations.

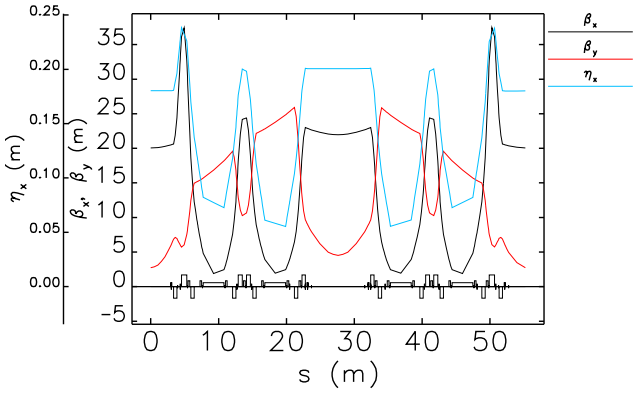

Figure 3.2-9. Detail of optical functions for solution with four LSSs. Here we show the functions for the first two sectors, which start and end with short straights while having a long straight in the center straight.

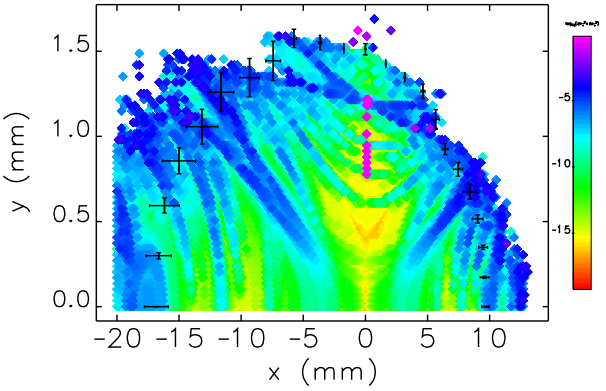

Figure 3.2-10. Dynamic acceptance from 50 ensembles for the lattice with four LSSs and $\xi_x = \xi_y = 9$, superimposed on the frequency map for the machine with no errors.

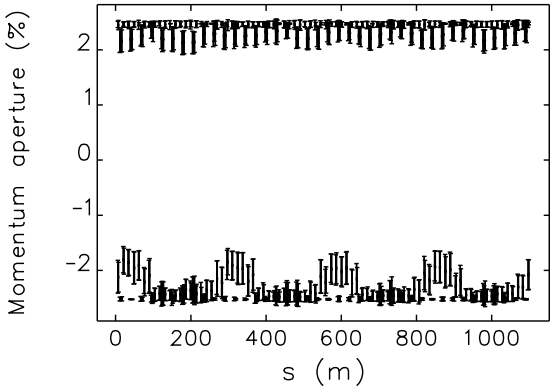

Figure 3.2-11. Momentum acceptance from 50 ensembles for the lattice with four LSSs and $\xi_x = \xi_y = 9$.

It is of interest that the dynamic acceptance in this lattice is enlarged on the negative x side compared to the lattice without long straight sections. Indeed, the dynamic acceptance is larger than the nominal limiting physical aperture (described above), which results from a curious distortion of the phase-space ellipses between the injection point at the end of Sector 40 and the location of the minimum aperture (which is -15 mm in the horizontal at straight section 4). This could only be brought about through adjustment of a significant number of sextupoles between the injection and limiting aperture points, which is what we have in the present case, as Figure 3.2-12 shows.

Since a workable 4NLSS lattice has been obtained, we move next to add the required optics for the short-pulse x-ray scheme (see section 3.5), known as SPX. The center of the SPX system will be straight section 6. Because of the length of the cryomodules for the deflecting cavities, we need long

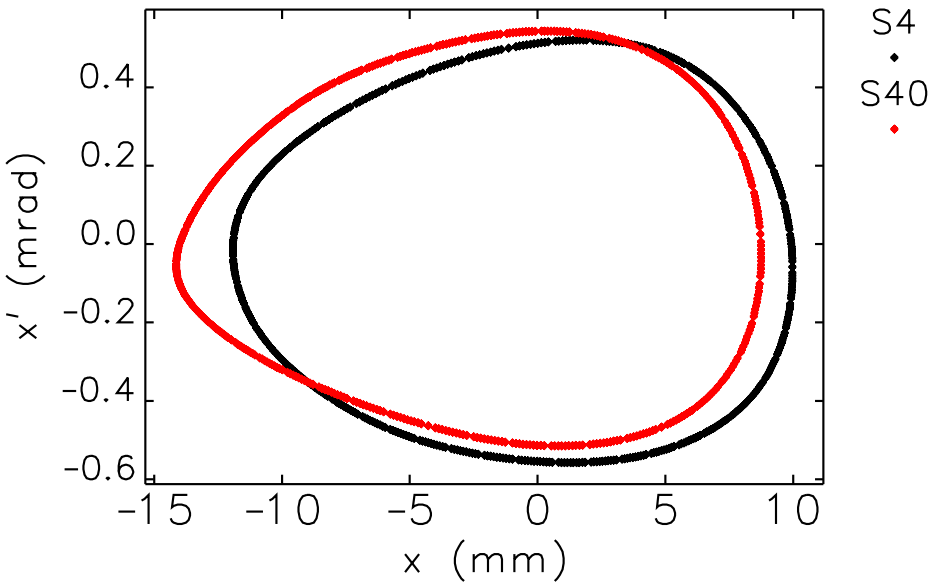

Figure 3.2-12. Distortion of horizontal phase space in the four LSS lattice with $\xi_x = \xi_y = 9$. Shown are the particle coordinates at the ends of Sectors 40 (injection point) and 4 (minimum aperture point). The phase space is distorted in such a way that the effect of the limiting horizontal aperture of -15 mm at S4 is diminished.

straights in Sectors 5 and 7. This not only allows accommodating the cryomodules but still permits sufficient space for insertion devices in those sectors. As discussed in section 3.5.1, the vertical betatron phase advance between the deflecting cavities in straights 5 and 7 must be 360°. Fortunately, the nominal vertical tune for the APS is 19.3, so we are close to this value already.

There are four possible placement options for the cavities. For example, we could have cavities in the upstream half of straights 5 and 7, which we refer to as US+US. We could also have DS+DS, DS+US, and US+DS. We present results here for the DS+DS configuration, which involves the least significant changes in the optics and minimizes interference between the cryomodules and the bending magnet beamline.

We started with the solution from the 4NLSS optimization and determined linear optics to satisfy the SPX requirements with tunes that are close to the previous optimum values. We then performed optimization of the 14 interior sextupoles (i.e., those in Sectors 6 and 7) to control vertical emittance growth due to the deflecting cavities (see section 3.5.3). We then developed full-ring linear optics for a tune grid, as described above. Finally, we performed optimization of the exterior sextupoles. During this optimization the interior sextupoles were fixed, which was found to be acceptable given the small changes in the linear optics of sectors 6 and 7 that are introduced as we change the overall tunes. The total number of independent variables in the optimization was again 42.

The linear optics for the region surrounding the SPX straight is shown in Figure 3.2-13. Figures 3.2-14 and 3.2-15 show the dynamic and momentum acceptance for 50 ensembles with $\xi_x = \xi_y = 8$. A solution also exists for $\xi_x = \xi_y = 9$, but it suffers from slightly marginal lifetime. Further optimization of this solution may be possible by introducing additional free sextupoles. One possibility is allowing

different short-to-long and long-to-short sectors to have different sextupole strengths.

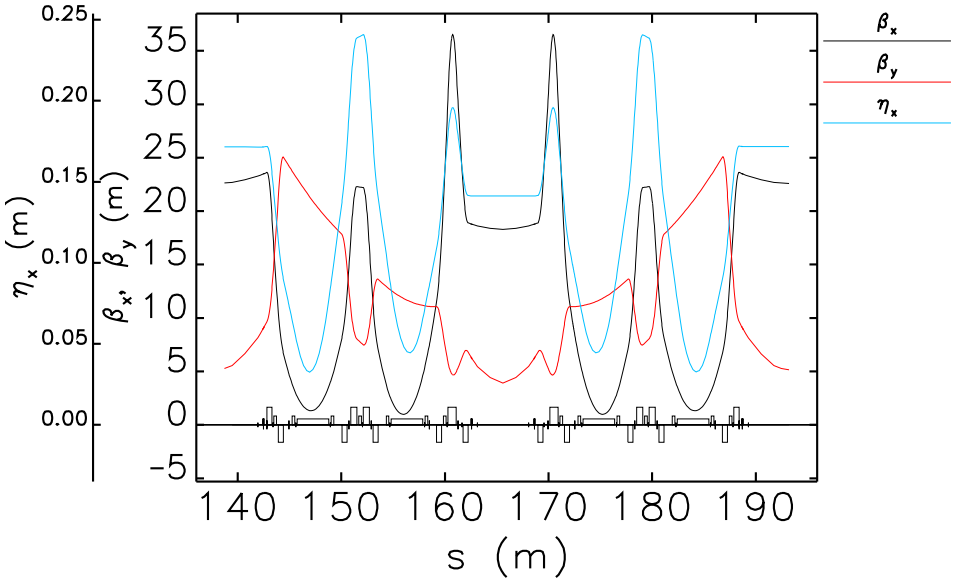

Figure 3.2-13. Detail of optical functions for solution with four LSS and SPX. Here we show the functions for the SPX sectors, which starts and ends with long straights while having a short straight in the center straight.

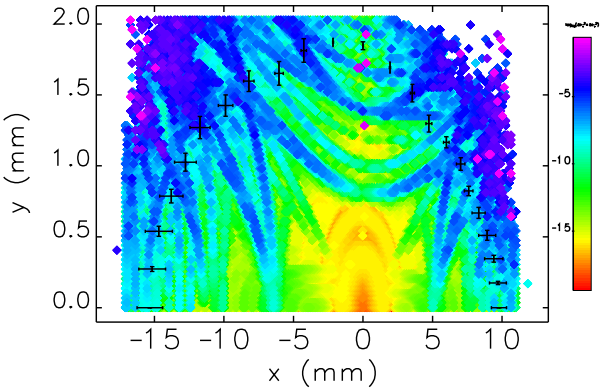

Figure 3.2-14. Dynamic acceptance from 50 ensembles for the lattice with four LSS + SPX and $\xi_x = \xi_y = 8$, superimposed on the frequency map for the machine with no errors.

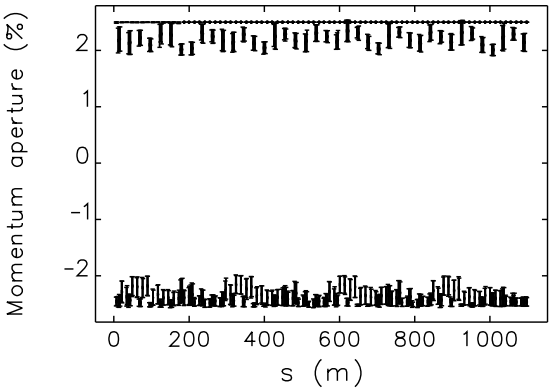

Figure 3.2-15. Momentum acceptance from 50 ensembles for the lattice with four LSS + SPX and $\xi_x = \xi_y = 8$.

Finally, we have performed optimization for the 4NLSS + SPX lattice with the addition of reduced horizontal beam size (RHB) in one location (Sector 20). Using the quadrupoles in Sectors 20 and 21, we adjusted the linear optics to target a horizontal beam size of 170 µm, which is about 60% of what is delivered in a normal straight section. The linear optics for the insertion is shown in Figure 3.2-16. The sextupoles in Sectors 20 and 21 were allowed to vary independently. This gives a total of 56 independent variables for the DA/LMA optimization. Figures 3.2-17 and 3.2-18 show the dynamic

and momentum acceptances, respectively, for chromaticities of 7. While the dynamic acceptance is sufficient, the momentum acceptance is noticeably reduced. Again, this has so far prevented raising the chromaticities to the desired value of 8. Work on this configuration continues.

Table 3.2-2 compares the parameters of the four lattices. We see that the effective emittance increases by less than 1% going from the present lattice to the final lattice. The split between the horizontal and vertical tunes is generally larger than is typical in operations. (See section 3.2.2.6 for more discussion of this point.)

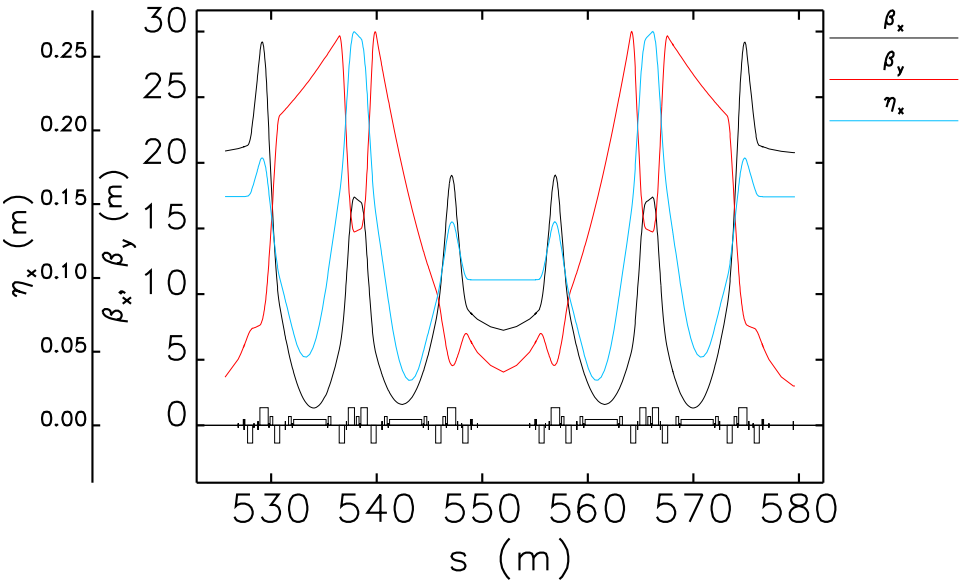

Figure 3.2-16. Detail of optical functions for solution with four LSSs, SPX, and RHB. Here we show the functions for the RHB sectors.

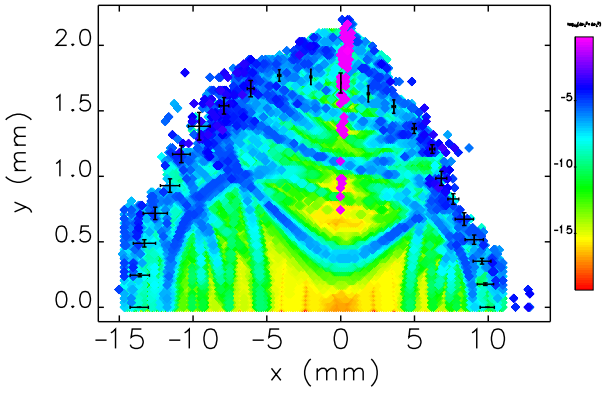

Figure 3.2-17. Dynamic acceptance from 50 ensembles for the lattice with four LSSs + SPX + RHB and $\xi_x = \xi_y = 7$, superimposed on the frequency map for the machine with no errors.

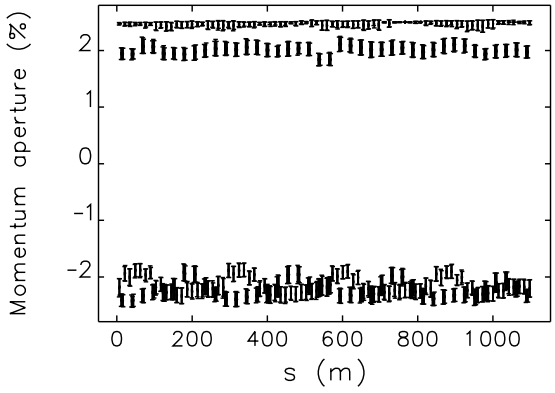

Figure 3.2-18. Momentum acceptance from 50 ensembles for the lattice with four LSSs + SPX + RHB and $\xi_x = \xi_y = 7$.

Table 3.2-2. Comparison of Major Parameters of the Four Lattices

	Now $\xi_{x,y} = 7, 6$	4NLSS $\xi = 9$	4NLSS+SPX $\xi = 8$	4NLSS+SPX+RHB $\xi = 7$	Units
Betatron Tunes					
Horizontal	36.127	36.100	36.119	36.112	
Vertical	19.248	19.352	19.295	19.246	
Lattice functions					
Maximum β_x	29.613	36.154	36.854	34.329	m
Maximum β_y	25.705	29.018	25.200	29.791	m
Maximum η_x	0.224	0.238	0.241	0.267	m
Average β_x	13.656	13.737	13.952	13.915	m
Average β_y	15.173	16.071	14.366	15.150	m
Average η_x	0.156	0.154	0.144	0.143	m
Radiation-integral-related quantities at 7 GeV					
Natural emittance	2.479	2.578	2.728	2.729	nm
Energy spread	0.096	0.096	0.096	0.096	%
Horizontal damping time	9.626	9.626	9.626	9.626	ms
Vertical damping time	9.631	9.631	9.631	9.631	ms
Longitudinal damping time	4.817	4.817	4.817	4.817	ms
Energy loss per turn	5.353	5.353	5.353	5.353	MeV
Standard ID Straight Sections					
Effective emittance	3.186	3.234	3.218	3.211	nm
β_x	20.092	20.058	20.547	20.814	m
η_x	0.189	0.180	0.155	0.155	m
β_y	3.088	2.724	3.180	2.994	m
Miscellaneous parameters					
Momentum compaction	2.831×10^{-4}	2.835×10^{-4}	2.819×10^{-4}	2.823×10^{-4}	
Damping partition J_x	1.001	1.001	1.001	1.001	
Damping partition J_y	1.000	1.000	1.000	1.000	
Damping partition J_δ	1.999	1.999	1.999	1.999	

Table 3.2-3 gives a comparison of the predicted lifetime for the four lattices for various fill patterns. For each lattice, the lifetime is computed for each of the 50 ensembles. Variations in lifetime result from variations in the momentum acceptance and the effectiveness of coupling correction. The median gives a prediction of the most likely lifetime in operations, while the 5$^{\text{th}}$ percentile gives a

prediction of the lowest likely lifetime. That is, the probability is 95% that we will have lifetime greater than this value. All the lattices have median and 5th percentile lifetimes above our requirement of 3.8 hours for the 150 mA, 24 bunch patterns.

However, the lattice with RHB does not clearly have sufficient chromaticity to be workable at 150 mA. Optimization of this configuration is on-going. This lattice also does not have sufficient chromaticity for hybrid mode. Given that SPX will not be operated in hybrid mode, one solution is to develop a 4NLSS+RHB lattice for use in hybrid mode. Such a configuration should be easier to optimize.

We list the 150-mA, 324-bunch mode evaluated with the high chromaticity required for the 24-bunch mode. The lifetime is quite long in spite of the excessively high chromaticity, which provides an operational convenience as it obviates the need to change sextupoles when changing between the 24- and 324-bunch fill patterns. Presently, the 324 bunch mode does not require top-up. However, if we reduced the vertical emittance to, say, 10 pm, the lifetime would drop to about 20 hours, which would require occasional top-up. This mode would provide significantly higher brightness than the other modes, owing to the low coupling.

Table 3.2-3. Comparison of Computed Lifetimes for Various Lattices and Fill Patterns. For each fill pattern, the median and 5th percentile lifetimes are shown for all lattices. The median vertical emittance is 35 pm. Note that SPX will not be operated in hybrid mode. In addition, the 324-bunch mode does not require significant chromaticity, but operationally it is convenient to use the same values as those used for the 24-bunch mode.

	Now $\xi_{x,y} = 7, 6$ h	4NLSS $\xi = 9$ h	4NLSS+SPX $\xi = 8$ h	4NLSS+SPX+RHB $\xi = 7$ h
100 mA/24				
median	9.2	8.1	8.7	7.3
5^{th} percentile	8.6	5.6	6.9	6.2
150 mA/24				
median	-	6.1	6.5	5.5
5^{th} percentile	-	4.2	5.2	4.6
16 mA (hybrid)				
median	-	3.2	-	-
5^{th} percentile	-	2.2	-	-
134 mA/56 (hybrid)				
median	-	12.1	-	-
5^{th} percentile	-	8.4	-	-
150 mA/324				
median	43.3	39.2	41.3	35.9
5^{th} percentile	40.9	28.9	34.3	31.6

3.2.2.6 Experimental Tests

Because the APS has independent power supplies for all quadrupoles and sextupoles, it is possible to mock up a long straight section. This is done by setting to zero the power supplies for the Q1 magnets on either side of the target straight section. This reduces the quadrupole strength to K_1 = -0.006 m^{-2}, compared to a maximum strength of 0.9 m^{-2} [3.2-7]. Using the same techniques as discussed in the previous section, we can optimize the linear and nonlinear properties of the lattice to obtain a configuration with large predicted dynamic acceptance and lifetime. Such optimizations were carried out for a series of mock-up lattices corresponding to each of the configurations described in the previous subsection. In addition, we have experimentally tested two of the mock-up lattices, known as 8NLSS and 8NLSS+SPX+RHB. These optimizations assumed eight LSS, because that was the original concept. Due to the time required to perform experimental studies, the lattices with four LSSs have not been tested. However, they will almost certainly have performance that is at least as good as the lattices with eight LSSs.

Here we need to mention that it has been APS policy from the beginning of operation to allow large user-requested beam steering. Over time the storage ring and beamlines have settled, and, at many locations, the steering has accumulated to several millimeters of orbit distortion. This orbit is called "user orbit" and deviates from the centers of magnets significantly. This would have been a big problem for the storage ring optics, but fortunately the APS has separate power supplies for all quadrupoles (and sextupoles). As long as the optics is regularly corrected, there seems to be no significant negative effects from operating on a significantly non-zero orbit.

The first step in our experiments was to test the simpler 8NLSS lattice. We started by setting this lattice up on the "user orbit." Lattice setup includes installing new quadrupole and sextupole setpoints, correcting the orbit, measuring and correcting the beta functions and dispersion, adjusting the coupling, and optimizing the injection efficiency. In this experiment, we found that we could not improve injection efficiency above 40% or store beam current above 40 mA. We performed a lifetime vs betatron tunes scan and found a strong resonance line at $2\nu_x - \nu_y = 53$. This is a skew-sextupole-type resonance that is excited when large coupling is present.

To reduce this resonance, we next set the lattice up on the "reference orbit," i.e., the orbit going through the centers of the magnets. We repeated the lifetime vs tunes scan and confirmed that the width of the resonance $2\nu_x - \nu_y = 53$ was reduced. We were able to achieve injection efficiency of 90%, which is almost as good as for the symmetric APS lattice. The lifetime was 9 hours at the operational values of 1.5% coupling and 100 mA current. Since we only need a lifetime of about 5 hours, in order to maintain 100 mA with top-up, this lattice looks quite workable. The inferred lifetime at 150 mA (scaling as $1/I^{2/3}$) is over 6 hours, which is workable with a 60-s top-up interval (see Equation (3.2-2)).

This result implies that we will have to realign beamlines to allow elimination of large orbit offsets in the accelerator magnets. Steering tolerances are still under investigation, but preliminary estimates indicate that 23 insertion device beamlines and 14 bending magnet beamlines will require realignment. This can be done gradually (i.e., a few sectors at a time) and could be started prior to installation of any long straights, in order to save time. This is not part of project scope.

Although the test was successful and shows that the 8NLSS lattice is suitable for user operation, there was one issue: The optimization process suggested betatron tunes of 36.11 and 19.28.

We first set up a lattice with such tunes but later found that moving the tunes to the usual APS working point of 36.16 and 19.22 provides for better lifetime. This was not the first time that the optimization suggested tunes that were not optimal for the real machine. We think there is some feature in the real machine not included in our model, that makes the usual APS working point better in terms of lifetime than the one suggested by the optimization. Several steps are being taken to investigate this issue:

- Addition of fringe field modeling for multipoles.
- Improvement of fringe field model for dipoles.
- Remeasurement of one quadruople and sextupole of each type to characterize fringe fields and excitation curves. There is some suspicion that the excitation curves for the S2 sextupole family may be in error.
- Improvement of the coupling correction algorithm used for the experiments.

The next step was to test the 8NLSS+SPX+RHB lattice. As a starting point, we used the 8NLSS lattice on the "reference orbit." We obtained better than 80% injection efficiency, but the lifetime was shorter than expected. We again performed the lifetime vs tunes scan and found that, at the best point, the lifetime was only 4.5 hours at 100 mA. We anticipate that having better coupling correction (using the response matrix fit, see section 3.2.3.2) might improve the lifetime, since this has been observed in simulations.

3.2.2.7 Remaining Work

The lattice work is well advanced and shows that the desired configuration with four nonsymmetrically placed long straight sections is generally workable. The configuration with SPX and RHB included is more challenging, and more work remains to obtain a fully satisfactory result. One possibility is that we will find that SPX and RHB combined are not compatible with high chromaticities (i.e., above 7). Hence, we will develop a lattice variant that includes only RHB for use during hybrid mode, since SPX cannot operate in hybrid mode in any case. It is also possible that hybrid mode may only be compatible with the "plain" 4NLSS lattice that lacks SPX and RHB. Since hybrid mode is used only a small part of the time and is incompatible with SPX operation in any case due to large phase transients, this should be an acceptable compromise.

In addition, we need to understand why the experimental test of 8NLSS+SPX+RHB gives shorter lifetime than the simulations. One reason could be that the experiments use a less sophisticated method for coupling correction, which can be readily improved (see section 3.2.3.2). Another unresolved issue is why the computer optimization always tends to place vertical betatron tune close to 19.3 while in the experiment we find that a lower tune gives better lifetime. This issue might not be very important as long as we are able to achieve suitable lifetime in the mock-up lattices.

One special issue that has to be addressed during the tests is the changed physical aperture at locations of LSSs. Presently the small-gap vacuum chambers have a length of 5 m; after the upgrade the small-gap vacuum chambers at LSS locations will have the length of 7.8 m. Due to the beta function increase in a drift space, that would lead to decreased acceptance of such vacuum chambers.

We will mock this up by moving the orbit closer to the vacuum chamber wall such that the distance from the beam orbit to the wall would be the same in terms of the beam size:

$$D_{new} = G\ \frac{\sigma_{2.5m}}{\sigma_{3.85m}}, \tag{3.2-6}$$

where G is vacuum chamber half-gap, σ is vertical beam sizes at 2.5 m or 3.85 m from the center of the long straight section. For an 8-mm vacuum chamber, it means moving the orbit towards one of the walls by 0.25 mm.

As a part of the experimental tests and investigation of the observed discrepancies, we plan to perform thorough benchmarking of our ability to predict nonlinear behavior of the lattice. We've performed comparisons of some parameters during various studies, and no significant disagreement was found. However, no systematic benchmarking has done recently. Crucial for any benchmarking is good knowledge of the linear lattice, and APS is well equipped with response-matrix-fit-based linear lattice calibration tools. A study plan has been developed to compare as many lattice parameters as possible with the model. This work is on-going. After completion we will better understand our ability to predict lattice performance.

3.2.3 Coupling Control

3.2.3.1 Introduction

The brightness of a synchrotron radiation source is inversely proportional to the transverse beam emittances. In third-generation synchrotron light sources the horizontal emittance is defined by the equilibrium between radiation damping and quantum excitation, and a great deal of research is devoted to the minimization of the horizontal emittance in storage rings.

In an ideal planar storage ring, there are no vertical bends and therefore no deliberately produced vertical dispersion. In a real machine, there are multiple sources of vertical dispersion, including small tilts of the horizontal bending magnets and coupling of the horizontal dispersion via tilted quadrupoles and vertically misaligned sextupoles. The spurious vertical dispersion is usually much smaller than the horizontal dispersion and can be made even smaller using correcting skew quadrupoles. Thus, the impact of quantum excitation and the subsequent emittance in the vertical plane is much smaller than in the horizontal. Another source of the vertical emittance is coupling between motion in the horizontal and vertical planes. Both of these effects can be minimized by performing better alignment of the storage ring magnets and by applying beam-based corrections using skew quadrupoles. The smaller these effects, the smaller the vertical emittance, and therefore the higher the brightness of the light source.

Another source of vertical emittance is coupling of betatron oscillations between the horizontal and vertical planes. This coupling also affects beam dynamics during injection. In third-generation light sources the vacuum chambers have very small vertical gaps (for installation of various insertion devices — undulators and wigglers). Since the injection process requires a large aperture, injection is performed in the horizontal plane, where insertion devices do not limit the available aperture. However, due to coupling between planes, large horizontal beam oscillations during injection can transfer into the

vertical plane, resulting in loss of beam on small-gap vacuum chambers. Again, skew quadrupoles can be used to reduce these effects, as can improved alignment of quadrupoles and sextupoles.

The coupling between horizontal and vertical planes is introduced by skew quadrupole gradients that can be generated by small tilts ϕ of quadrupoles:

$$K_{sq} = K\phi,$$

or with nonzero vertical orbit y_o in sextupoles:

$$K_{sq} = -\frac{1}{B\rho}\frac{\partial^2 B_y}{\partial x^2} y_o.$$

Some insertion devices can also be sources of coupling. Dedicated skew quadrupole magnets are used to compensate the effect of all unwanted coupling sources. They can also be used, of course, to increase the coupling and vertical dispersion.

Indeed, in a perfect machine we would be forced to do this in order to avoid extremely small vertical emittance. At the APS and other third-generation sources, the electron-beam lifetime is defined by the Touschek scattering and is proportional to the beam volume. Thus, having very small vertical beam size means having very short lifetime. Even though the APS can tolerate short lifetime due to top-up operation, there is still a limit on how short the lifetime can be. Therefore it is crucial to have a good control of both vertical dispersion and coupling of beam motion in order to maintain a careful balance between the contradicting requirements of good injection efficiency, high brightness, and long lifetime.

3.2.3.2 Issues for Upgrade

In order to control the vertical emittance and coupling, one must have a good measurement of both and the ability to control each separately. At the APS we deduce the emittance ratio from the ratio of horizontal and vertical beam sizes measured on the diagnostics beamline in Sector 35. We control it using 19 skew quadrupoles located in every second sector (with one missing in the injection area). The present coupling correction algorithm consists of three steps:

1. Minimize the vertical dispersion. This is done using the measured vertical dispersion by computing the required skew quadrupole strengths using singular value decomposition (SVD).
2. Minimize the vertical beam size. This is done by using an optimizer that adjusts the skew quadrupoles in a pattern determined by the two orthogonal phases of the main coupling harmonic ($\nu_x - \nu_y = 36 - 19 = 17$).
3. Add vertical dispersion to achieved desired vertical emittance. This is done by adding skew quadrupole current at the 0^{th} harmonic, which ideally gives the same pattern of vertical dispersion everywhere while driving the coupling resonance as little as possible.

This quick and convenient procedure allows us to control the global ratio of emittances but not the local beam tilts in each sector. The goal of the upgrade with respect to coupling is to enable local

measurement and control of the vertical emittance and beam tilts. Ideally, we'll provide the possibility of using lower coupling, presumably in 324-bunch mode where the lifetime will accommodate it.

Local measurement of the coupling is possible using a response matrix fit. The response matrix fit detects all skew quadrupole errors in the ring, which then can be used to calculate local beam sizes everywhere. It also can be used to minimize coupling by minimizing the cross-orbit responses. The APS has all the required experience and expertise to implement coupling minimization by minimizing cross-orbit responses. Existing tools for the response matrix measurement and fit will require minor modifications to speed up the measurement process and fitting. A tool to minimize coupling based on the results of the response matrix fit is being written and will be used for tests of upgrade mock-up lattices (see section 3.2.2.6). Simulations show that this "new" method of coupling correction may be crucial for achieving good lifetime in the new lattices.

As discussed above, presently the APS operating orbit has large vertical deviations at many sextupoles. This is the result of beam steering for user beamlines. Such an orbit results in large coupling with significant local variations of vertical beam size that is impossible to compensate using existing skew quadrupoles. Figure 3.2-19 shows variations of vertical beam size at ID locations as calculated using the response matrix fit. Sector 2 has the largest operating vertical orbit, and it also has the largest vertical beam size. Existing skew quadrupoles also don't allow for coupling minimization below emittance ratio of about 1% on the present user orbit.

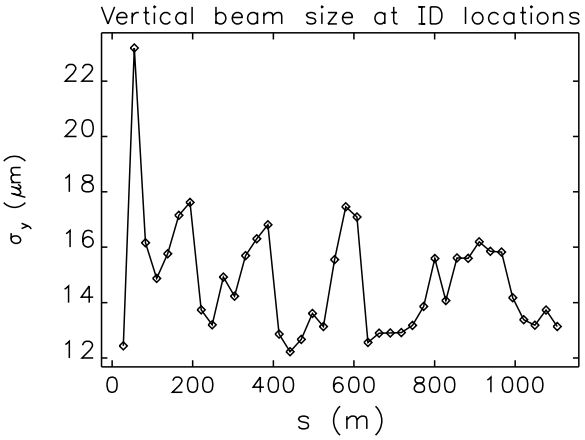

Figure 3.2-19. Variations of vertical beam size at ID locations (middle of ID straight sections) in the present APS.

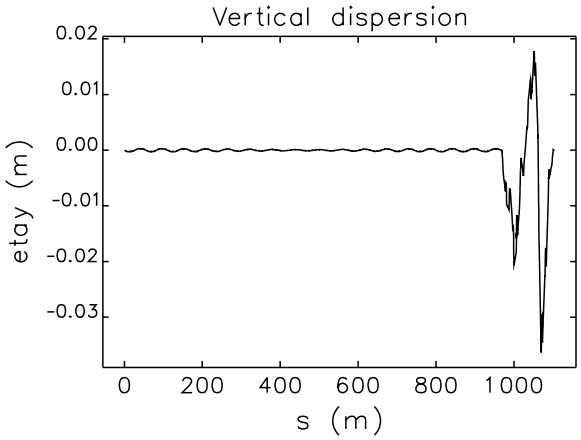

Figure 3.2-20. Vertical dispersion for the coupling bump lattice.

Our tests have shown that steering the orbit through the centers of sextupoles significantly decreases the coupling and beam-size variation while improving the beam dynamics. Simulations show that on this new orbit the emittance ratio can be minimized down to about 0.25% using existing skew quadrupoles. However, they would not be enough to provide local vertical beam size control in case this capability will ever be requested.

Maintaining low coupling is not only important for providing small vertical beam sizes for brighter x-ray beams. It is also required for improving beam dynamics. From experiments we know that presently the APS beam dynamics is affected by skew-sextupole resonance $2\nu_x - \nu_y = 53$. This

resonance is driven by a combination of nonzero coupling and sextupoles. Keeping coupling small minimizes the strength of that resonance.

However, APS storage ring cannot operate with arbitrary small coupling due to lifetime limitation. The lifetime at APS is defined by the Touschek scattering and therefore is getting shorter when the vertical beam size becomes smaller. Ideally, it is advantageous to be able to generate vertical beam size using vertical dispersion without creating too much coupling between the planes. We performed simulation studies of coupling control using skew quadrupole sources (skew quadrupoles or vertical orbit bumps inside sextupoles) in the area where there are no insertion devices installed (and therefore no small-gap vacuum chambers) — in Sectors 36 to 40 [3.2-23]. The idea here is to minimize coupling globally by steering through the centers of magnets and by using skew quadrupoles everywhere, then use local coupling sources in Sectors 36 to 40 to increase the global vertical emittance to increase lifetime, without generating global vertical dispersion and coupling.

We have found that it is possible to create a coupling bump in the nonuser sectors to control the vertical emittance without creating vertical dispersion and beam tilts all around the ring. Figure 3.2-20 shows the resulting vertical dispersion that generates the required vertical emittance. The dispersion outside of the bump in nonuser sectors is very small. This succeeded using 15 skew quadrupoles at the locations of the existing corrector magnets in sectors 36 through 40. However, there is one drawback to this approach: we have recently found experimentally that turning off all skew quadrupoles inside the injection orbit bump improves the injection efficiency. The injection bump spans Sectors 39 and 40, therefore limiting the above-described method of coupling control to only Sectors 36 through 38. The combination of the coupling bump and injection bump would need to be studied further.

As discussed in section 3.2.2.6, we have found that in order to improve the beam dynamics, the upgrade lattice will have to operate with orbit going through the centers of magnets. This will also allow for better control over coupling. Operating on this new orbit will require realignment of some user beamlines. It will also mean that user-requested steering will be limited. No position steering will be allowed, and the preliminary limits on the angle steering are ± 50 μrad in horizontal and ± 25 μrad in vertical planes.

3.2.3.3 Remaining Work

Simulations will need to be done to understand if more skew quadrupoles are required for better local coupling control. If necessary, the additional skew quadrupoles can be installed in some sectors upstream of the S3 sextupoles. Also, some orbit correctors can be combined with skew quadrupoles by using separate power supplies for each coil of the existing magnets. Use of a coupling bump in nonuser sectors for coupling control should also be studied further to minimize its possible effect on the injection efficiency. Limits on user-requested steering will need to be studied in more detail.

3.2.4 Collective Effects

3.2.4.1 Introduction

In the storage ring the limit on the single-bunch current is determined during injection, and its efficiency can be improved by adjusting the lattice, sextupoles, kickers, closed orbit, and rf voltages for its optimal condition.

The stored current reaches its limit during injection when the amount of charge lost by the stored beam equals the charge of the incoming beam that survives the process. The injection efficiency decreases with increasing stored bunch charge due to collective effects. Currently the APS delivers 16 mA in the single bunch during hybrid-fill for users. This amounts to 60 nC per bunch, which may be the largest charge producing x-rays per bunch in light sources around the world. In the upgrade we plan to deliver the same charge per bunch to the users.

The sources of collective effects may include electron cloud, ions, and impedance elements in the ring. The phenomena caused by the first two were observed in the ring with specially arranged bunch patterns; however, the magnitude of these effects is very small and does not affect nominal operations. On the other hand, the impedance elements in the ring cause various instabilities, which often limit the high-current operation. In the upgrade the same will be true, in that the impedance will dominate the collective effects on the stored beam. In order to predict the single-bunch limit, we will use the existing impedance model of the present ring, which can be extrapolated to cover the upgrade once we identify and estimate the additional impedance sources. Hence, we first describe the status of the impedance model which was used to reproduce the various impedance-driven collective effects observed in the ring [3.2-24–3.2-26]. The estimate of impedance and its consequences in the upgrade will be discussed following that.

3.2.4.2 Status of Impedance Model

The microwave instability blows up the longitudinal emittance of the beam not only by lengthening the bunch but also by widening the energy spread. The threshold current, based on the Boussard criteria, was predicted in the design stage of the APS to be 0.25 mA for an impedance budget Z/n of 0.5 Ω. The detailed computation by 3D modeling of impedance elements in the ring found Z/n to be close to 0.2 Ω. With the improved estimate of the impedance we predicted the threshold to be a little less than 1 mA. However, careful measurement by an x-ray pinhole camera showed it to be much higher, namely, 7-8 mA. The large discrepancy between theory and experiment was due to the significant bunch shape deformation, the effect of which cannot be fully included in the theory.

In order to overcome this deficiency, we modeled the interaction of beam and impedance as close to reality as possible by simulating macroparticles in longitudinal phase space; tracking includes the impedance up to a few hundred gigahertz, a particularly high range of frequency. One of the results was the anomalous energy spread due to the microwave instability, as shown in Figure 3.2-21. The experimental data and simulation results are in a good agreement, indicating an accurate impedance model.

The longitudinal profile of a bunch measured by the streak camera revealed an asymmetric distribution in time. The distortion of the bunch was due to the combined effect of potential well

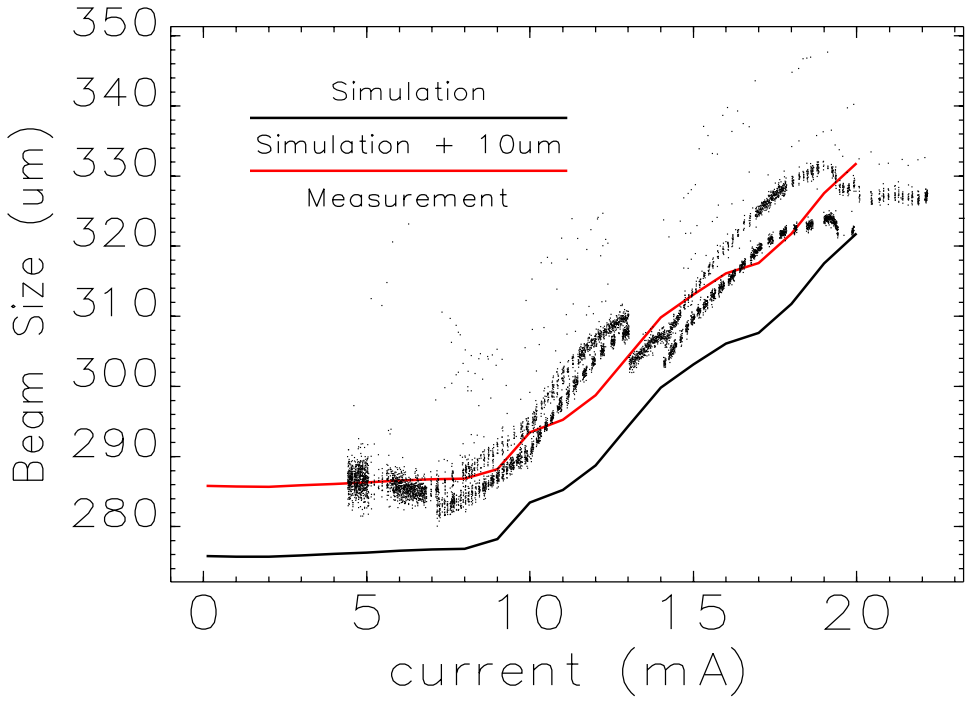

Figure 3.2-21. The dots represent two measurements of the horizontal beam size at an undulator where a dispersion of 17 cm contributes to the energy-dependent beam size. The black curve shows the simulation results with the impedance model. The agreement is very good considering the camera resolution of 40 μm. For better visual guidance we created the red curve by simply adding 10 μm to the simulation result.

distortion and energy loss caused by the imaginary and real parts of impedance, respectively. From the simulation that produced Figure 3.2-21 one can extract a longitudinal profile; this distribution and that of the streak camera overlap each other closely as shown in Figure 3.2-22. Since the only adjustable parameter in the simulation was cavity voltage, which can be estimated very accurately through synchrotron tune measurement, we have confidence not only in the impedance model but also in the simulation method using `elegant`.

We extended the simulation of phase space to 6D including the effect of transverse impedance. We found that the collective motion of a single bunch was strongly dependent on the sextupole settings.

Historically, we needed to understand the effect of small-gap chambers on the single-bunch current limit. Initially, with a few 12-mm gap chambers installed in the ring, we could store more than 20 mA in a bunch with moderate chromaticity (below 5) in the 7.5-nm high-emittance lattice. Later we installed more 8-mm-gap chambers, up to 29 in total, in the newly-commissioned low emittance lattice with nonzero dispersion at the straight section. We could not store more than 8 mA at moderate chromaticity (around 7), and the chromaticity was limited by the capabilities of the sextupole magnets. After modification of some of the sextupoles, we were able to increase the chromaticity to greater than 10, subsequently leading to the present ability to deliver 16 mA in a single bunch. From this we learned that the single-bunch current was strongly dependent on the chromaticity.

The main purpose of impedance modeling was to predict the single-bunch effects of any

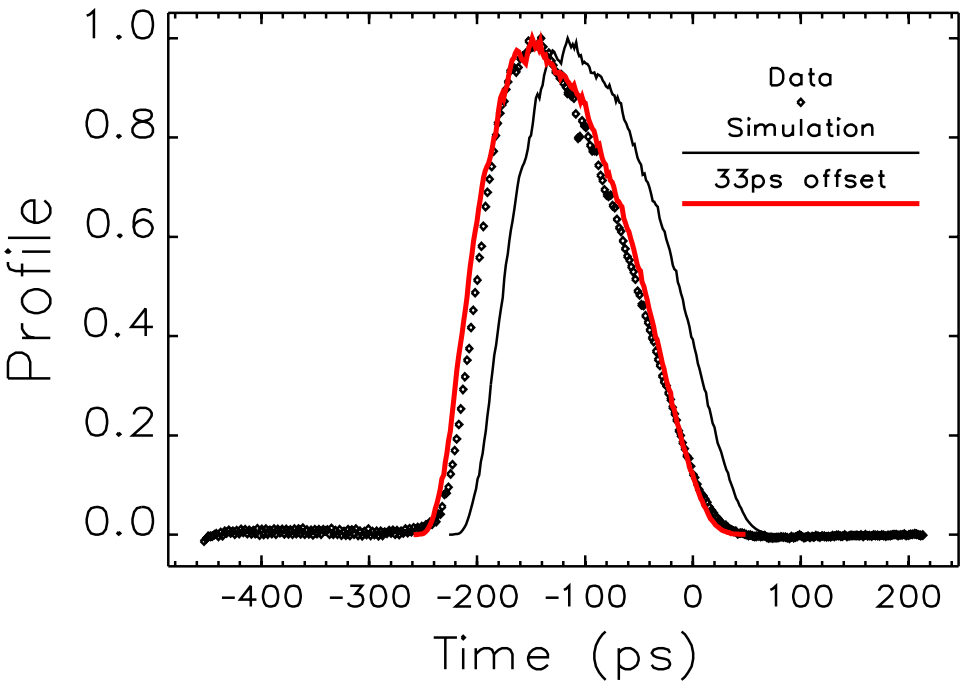

Figure 3.2-22. The open circles represent the streak camera data for 15 mA in the bunch, while the black curve is the simulation result. The red curve is offset by 33 ps from the direct simulation output for better comparison with the streak camera profile, whose reference time was not coincident with the simulation.

proposed new undulator chambers prior to installation in the ring. A practical question is, for example, what would happen to the single-bunch limit if we replaced all 8-mm chambers with 5-mm chambers? In order to answer this question correctly, we needed to validate the impedance model with the experimental data at hand or with the measurements specially designed for model validation purposes, prior to applying the model to predict the future performance of the ring.

Through the impedance modeling, we found and reproduced several aspects of coherent instability behavior in the transverse planes.

- We found that the transverse mode-coupling instability (TMCI) blows up the beam size in the vertical plane, resulting in scraping on the aperture of the small-gap chambers. During injection, this results in losing a fraction of the stored current in the bunch, which limits the total accumulation. An important prediction of the simulations is that the limit on the stored current and accumulated current is different. For instance, at a low chromaticity of 3, we could only *accumulate* up to 3 mA, but we could *store* more current in the bunch. We verified this experimentally by storing 20 mA with a chromaticity of 10, then showing that we could retain 5 mA when the chromaticity was gradually lowered to 3.
- The effect of vertical motion following injection was simulated by kicking the stored beam in the vertical plane, then determining the evolution of the centroid and beam size from the tracking data. The same situation was explored experimentally by using the vertical pinger magnet and recording the turn-by-turn beam image with a gated camera. The image was processed to extract

the beam size as function of turn. Simulation and experiment were compared, showing good agreement at low current (1 mA) as well as at medium current (5 mA), limited by the available chromaticity at the time of the experiment [3.2-26].

- The observed saw-tooth instability in the horizontal plane was reproduced. The driving impedance was identified in the simulation as the misalignment of the transverse impedance. This effect is similar to the misalignment of a quadrupole magnet except that the dipolar kick is time-dependent instead of static [3.2-24].

- The accumulation limit as a function of chromaticity was measured during two machine studies a week apart. The method was simple: we set the highest chromaticity and injected to 20 mA or more in one bunch. We fixed the injection conditions (rf cavity parameters and kicker strengths) at the optimum values for this case. Then we gradually decreased the chromaticity. For each chromaticity value, we injected from zero until the limit was determined. The results were compared with the simulation, where the sextupole effects were approximated as the combination of first-order chromaticity and amplitude-dependent tune shift [3.2-27]. (Subsequent work showed that this approximation did not impact the results.) The comparison is shown in Figure 3.2-23.

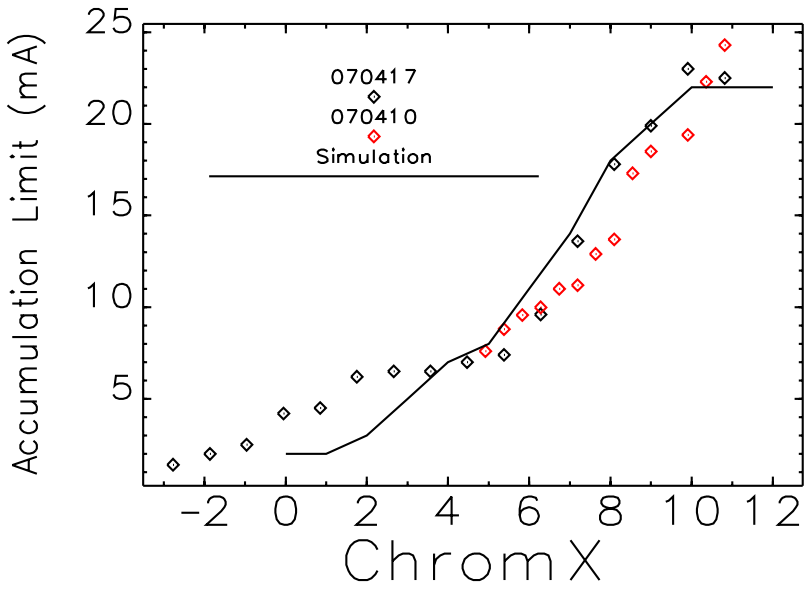

Figure 3.2-23. The symbols represent the measured accumulation limit collected in two machine studies separated by a week; the black curve is the simulation result.

In this way we demonstrated the predictive power of the three-dimensional APS impedance model [3.2-27], though we still consider it a working model in need of continual improvements.

We can utilize the above APS impedance model to predict the single-bunch current limit as a function of hypothetical impedance increase or decrease. Figure 3.2-24 shows the nonlinear change of single-bunch current limit as a function of ring vertical impedance (or wake potential) times a scaling factor Z_t. Actually, one might think that the product of I_{limit} and factor Z_t would be constant, but it is not because the bunch length varies with current.

It is worth noting that, even if the APS can now store 24 mA in a single bunch, the usable current with a good operational experience has been about 16 mA, a 2/3 “derating” factor. If this defines the usable limit, we have to minimize or eliminate any impedance increase in the upgrade. This is discussed in the next section.

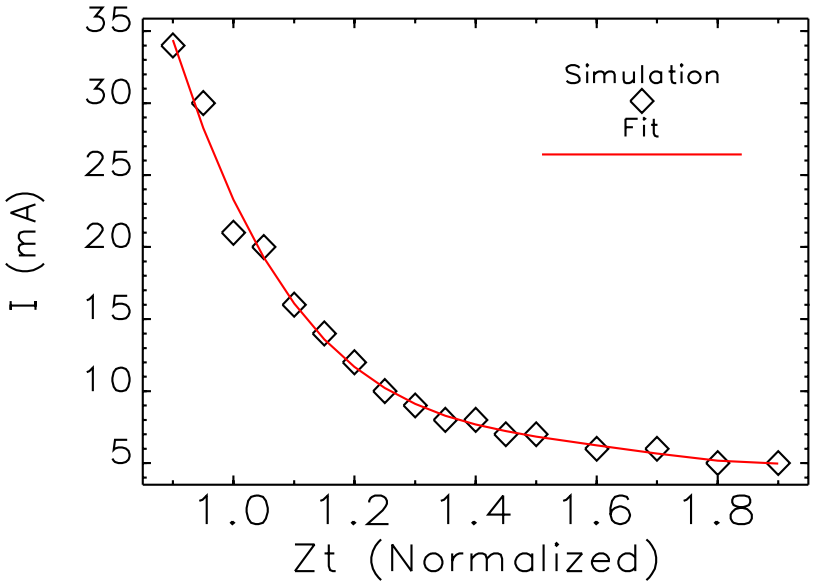

Figure 3.2-24. Single-bunch current limit as a function of vertical impedance. The symbols are simulation results. The line is a fit to guide the eye. The impedance axis is normalized to the value for the current APS storage ring.

3.2.4.3 Issues for Upgrade

The upgrade will utilize all the present vacuum chambers except the ones for the long-straight sections (LSSs). In addition, there will be deflecting cavities used for generating the short x-ray pulses (see section 3.5). These are the main impedance sources we need to consider in the upgrade. In this section we will discuss issues related to the impedance of undulator the chambers at the LSSs. The deflecting cavity will be treated separately in section 3.5.4.3.

There will be four LSSs, each about 8 m long, that will replace the 5-m standard chamber; this effectively increases the impedance of transition by 8/5 due to the increase in β_y at the taper. In order to keep the same accumulation limit, we need to reduce the geometric impedance at the LSSs by 5/8.

Since the impedance of the taper is generated at the transition connecting the regular chamber to the undulator chamber, achieving a smaller impedance will require designing a new transition. For this purpose we utilize the impedance formula of a rectangular chamber derived by Stupakov [3.2-28]

$$Z_y = j\frac{Z_0 w}{4}\int_{-\infty}^{\infty} dz \frac{h'(z)^2}{h(z)^3}, \tag{3.2-7}$$

where w is a (constant) half-width, and $h(z)$ is the half-height defining the vertical profile. We note that only the tapered section with nonzero $h'(z)$ contributes to the impedance. There are three parameters in the formula, namely, $h(z)$, w, and $h'(z)$. We first consider optimizing $h(z)$. The optimal profile to minimize the functional Z_y/w was found in [3.2-29] and is

$$h(z) = \frac{h_{\min}}{\left(1 + \left(\beta^{-1/2} - 1\right) z/L\right)^2}, \text{ where } \beta \equiv \frac{h_{\max}}{h_{\min}}. \tag{3.2-8}$$

We note that the profile in Equation 3.2-8 is nonlinear. The ratio of this impedance to that of the linear transition is [3.2-29]

$$\frac{Z_y^{\text{optimum}}}{Z_y^{\text{linear}}} = \frac{8\beta}{(1+\beta)\left(1+\sqrt{\beta}\right)^2}. \tag{3.2-9}$$

Note that the above impedance expressions have no dependence on frequency, as the theory is developed in the limit of low frequencies. Thus we should stay aware of the applicability range. For example, we should not expect any bunch-length dependence using such impedances.

For the APS 8-mm gap chamber where $h_{\max}$ = 21 mm and $h_{\min}$ = 4 mm, the predicted reduction by using a nonlinear taper is, coincidentally, very close to 5/8, which happens to compensate the increased impedance effect caused by the LSS.

In order to verify Equation (3.2-9) we numerically computed the wake potential of the nonlinear taper with `GdfidL` [3.2-30]. For a transition from 21 mm to 4 mm in the vertical plane and flat in the horizontal plane, the optimal profile predicted by Equation (3.2-8), $h(z)$, is shown in Figure 3.2-25.

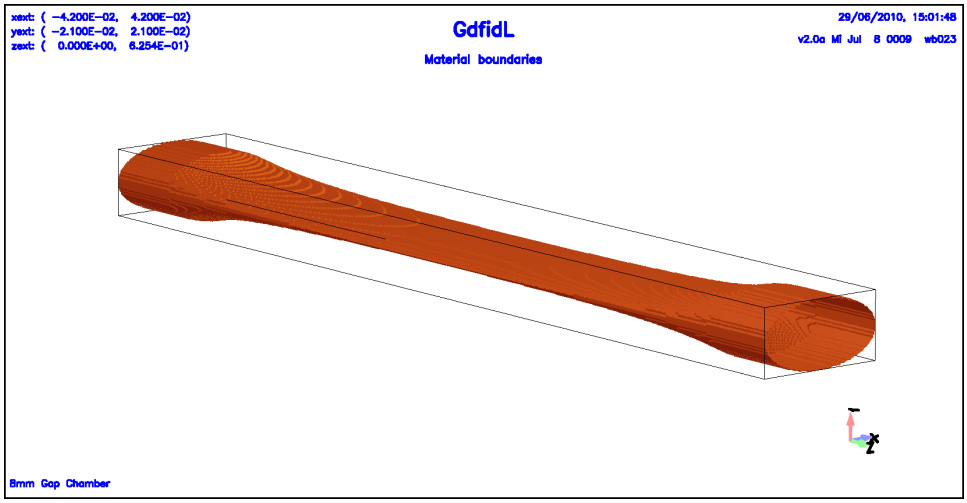

Figure 3.2-25. The vertical profile used in numerical simulation of an optimized nonlinear taper connecting a regular chamber to an undulator chamber with an 8-mm vertical gap.

Kick factors were calculated for bunches of different lengths using the wakefields computed with `GdfidL` for the nonlinear and linear taper. The ratio of kick factors is plotted in Figure 3.2-26.

Recall that the goal is to have a small ratio, so that the APS can benefit from the nonlinear taper. However, there seems to be a reduction in benefit as the bunch becomes shorter. For reference, the expected improvement for the nonlinear taper from Equation (3.2-9), is shown as a straight line (as mentioned before, there is no frequency or bunch length dependence in the above formulas). Thus, by using the nonlinear taper, we would fall short of our goal to reduce the impedance.

In addition we also found that the reduction could be much less if the horizontal profile was not flat. For the actual APS chamber, where the horizontal profile also varies, the optimization resulted in a reduction of less than 5% of the value for a linear taper, hardly justifying the modification. Hence, we decided not to adopt a nonlinear taper in the upgrade.

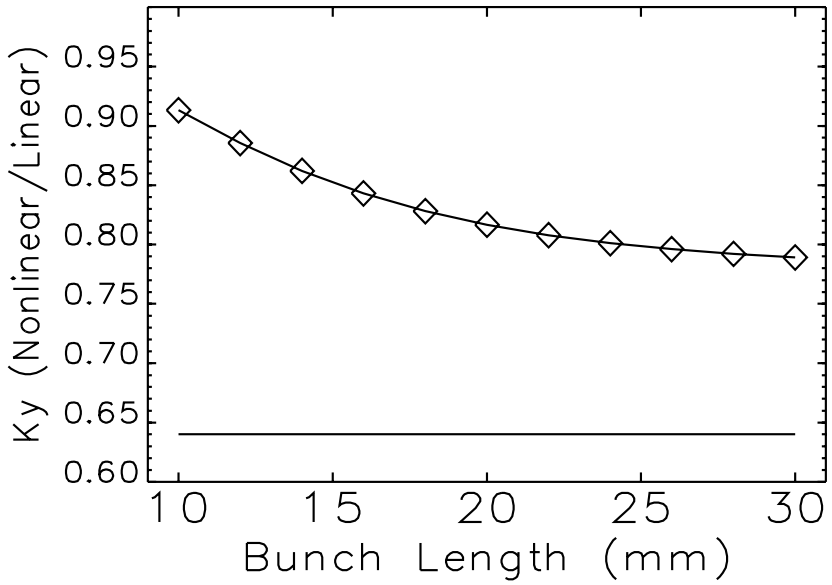

Figure 3.2-26. The ratio of vertical kick factors of nonlinear and linear taper for different bunch lengths. The straight line is the prediction by Equation (3.2-9), i.e., no frequency or bunch-length dependence.

Though an approximate expression, Equation (3.2-7) suggests that the horizontal half-width w strongly controls the vertical impedance. In the long-wave approximation this linear dependence could be correct, but for high frequencies the behavior is unknown. So we investigated the quantitative effect of width for the 8-mm-gap chamber. Figure 3.2-27 shows that widening increases the impedance until it reaches some maximum. From this we can estimate the impedance increase of a hypothetical in-vacuum undulator (IVU) chamber if installed (IVUs are noted for wide chambers).

Conversely, narrowing of the chamber decreases the impedance quite effectively. However, this decrease in aperture would require a smaller horizontal beta function to maintain injection, which would impose additional restrictions on the lattice design.

The last option is to simply make a longer linear transition. A detailed computation of vertical wakes showed that a transition length of over 50 cm is sufficient to achieve the target reduction of 5/8. In order to accommodate this long transition, the area needs to be redesigned as shown in Figure 3.2-28. The downstream will be mirrored with respect to the center of the straight section.

The new transition of the LSS chamber will reduce the effective transverse kick to a level equal

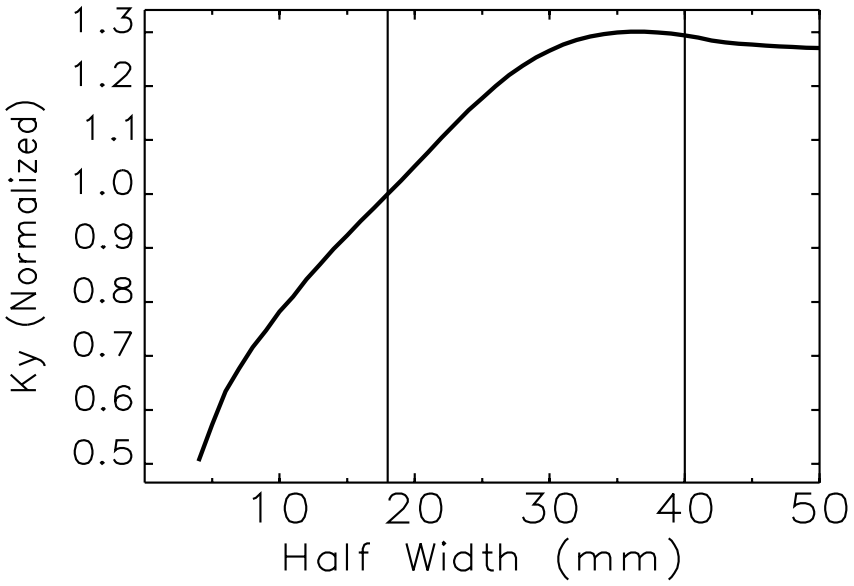

Figure 3.2-27. The vertical kick factor of bunched beam as a function of the half width, w, of an 8-mm small-gap chamber connected to the regular chamber in the ellipse of (4.2 cm, 2.1 cm).

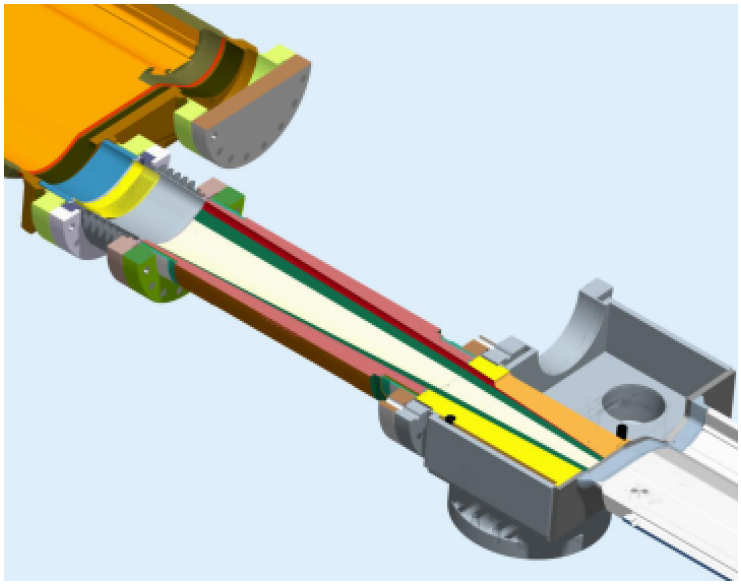

Figure 3.2-28. The new transition designed for the LSS will have 55-cm taper, which is significantly longer than the current taper with 18-cm effective length.

to or less than the regular 5-m-long straight section. However, an 8-m LSS chamber will increase the resistive wall impedance by 8/5 per sector. If we had to build such a chamber, we could reduce the impact of the resistive wall effect by using a strip of copper on the top and bottom inside surfaces of the chamber. However, in the LSS cases present in the upgrade, this will not be needed. In Sectors 1

and 11, a superconducting undulator with a cryogenically cooled chamber will occupy about 3 m of the straight. In Sectors 5 and 7, a set of superconducting cavities will occupy about 2.8 m of the straight. Hence, the resistive wall impedance should not increase.

In summary, in this section we determined that implementation of LSSs would significantly increase the effective impedance and reduce the single-bunch current, unless we devise a method of mitigating transverse instabilities. The method we chose for this mitigation was to control the impedance source by

- reducing the geometrical impedance transition by making the taper longer at both ends, and
- reducing the resistive wall wake by providing a chamber with a copper-lined beam path or some other configuration that avoids a long, room-temperature chamber.

This will leave the beam in the current storage ring unaffected impedance-wise by the LSSs.

3.2.5 Top-Up Injection

Lower lifetime in some of the operating modes will require more frequent top-up injection, which makes it very desirable to implement a much "quieter" injection. Presently our injection is not quiet: for a 20-ms duration after the injection pulse there is a 15 μm closed orbit bump and a $\sim 30\times$ stored-beam emittance jump that decays with the synchrotron radiation damping time (9.6 ms).

The main cause for the closed orbit is a leakage field through a pulsed dipole magnet in the transfer line (the "thick" septum magnet). The perturbation starts with the charging of the pulsed kicker magnets, 5 ms before the injection time. The orbit perturbation is alleviated about 90% through feedforward waveforms applied to two fast correctors near the time of injection.

The cause of emittance increase is the betatron oscillation initiated by the kickers. This in turn is caused by the requirement of a mismatched kicker bump for handling a small dynamic aperture, having a four-kicker bump covering two sectors of optics and nonlinear magnets, and the dependence of the kicker waveform on amplitude (i.e., saturation effects in the ferrite of the kickers).

The closed-orbit feedforward is done through the fast orbit feedback system in a simple way: we open the loop (suspend corrections) for 20 ms so that waveforms of predetermined values can be sent to two correctors. The waveform provides a sequence of current values that the two correctors must have to make a closed three-bump with the septum acting as the third corrector. Luckily there are no user beamlines within the bump. The optimum waveforms are obtained from scaled orbit measurements during open-loop conditions plus amplitude and time-delay adjustments.

The quality of the feedforward correction is limited by the ambient orbit noise during the orbit perturbation measurement and by the slight uncertainty of the timing (20 μs rms — equivalent to 5-μm worst-case orbit error) of the setpoint values sent to the correctors. We will improve the closed orbit feedforward by increasing the sample frequency from 1.5 kHz to 10 kHz (requested for general orbit stability in section 3.3.6), by reducing the uncertainty of the corrector timing and by integrating feedforward waveforms with closed-loop operation.

Whether we can reduce the betatron kick given to the stored beam depends on the injection aperture (dynamic aperture) of present and any future optics. Presently we impart a betatron kick to

the target bunch of the stored beam to reduce the betatron amplitude of the injection bunch and reduce injection losses. The kicker pulses are 4 μs long, which is slightly longer than the 3.68-μs revolution time. Thus all bunches are affected somewhat.

If we find that we *must* impart a betatron kick to the target bunch of the stored beam, then there are a limited number of things we could do to minimize the perturbation on the stored beam. On the other hand, if we do not need to impart a betatron kick to the target bunch, then a longer set of options are available to reach quiet injection.

To minimize the perturbation on the beam from a mismatched injection bump, we could:

1. Make the kicker pulses shorter so that only a fraction of bunches get a betatron kick. This would involve reducing the magnet length (inductance) and the capacitance of the charging circuit. We could realistically shorten the pulse by, say, 40%.
2. **Preferred:** Implement a correction kicker, a weaker and faster kicker that would give a supplemental kick only to the target bunch and nearby bunches for an otherwise matched bump. Thus only the target stored bunch is affected (assuming a 24-bunch pattern), while the rest of the bunches are unaffected.

   A supplemental kicker with 20% the strength and width of the the regular kickers would be feasible. The space needed is found immediately downstream of the rf cavities in the straight section of Sector 40. Ideally one would need two supplemental kickers at different betatron phase advances to optimize the available aperture for the injected bunch, but there is no other available space for a second supplemental kicker.

To minimize the perturbation on the beam in the case of a matched injection bump, we could:

1. Match all kicker waveforms. The presence of sextupoles in the two sectors complicates the matching. One could either:
   (a) find a special sextupole distribution to cancel to first-order the closure error dependence of the kick amplitude (this was done in 1995 in an easier optics),
   (b) somehow tune the kicker waveform time-dependence in the presence of sextupoles (tuning waveforms is difficult in general even in the absence of sextupoles), or
   (c) devise a small kicker that compensates the error by feedforward, such as was mentioned above. In this case the kicker waveform would need to be programmable.
   (d) discharge several short pulses into several short ferrite kickers (see above) at different times to create a longer arbitrarily shaped pulse for the beam. However this string of small kickers requires space that is not available.

   Items (a) and (b) interact with each other. On paper finding a sextupole distribution for (a) is possible for idealized kicker with matched circuit elements and whose waveform decays do not depend on pulsed height. Given this, we speculate that the dynamic aperture of the lattice can be re-optimized given the fixed solution for the injection section. Thus (a) is deemed the most feasible choice.

The tuning of kicker waveforms (b) will be difficult. The first step is to match properties of circuit elements like capacitors and resistors, which is feasible. But the following, compensating the variation of decay constant with pulse height, has not been done before, as far as we know.

Item (c) can not be done in general with a discharge circuit, nor with a regulated circuit, as the signal is too fast. Perhaps a rf circuit might accomplish this, but the amount of necessary current required for an rf output stage is too large. For example our bunch-by-bunch feedback system with a 500-W amplifier can only produce 0.8 μrad in one pass, much smaller than the 0.1 mrad required.

Item (d) is feasible technologically, but space is not available.

2. Place the four kickers in a long straight section, which would avoid the nonlinearities from sextupoles in the present situation. The four kicker waveforms would be closely matched because they are running at the same amplitude. This requires making very strong kickers, perhaps three times as strong as the present ones. The kicker's pulse lengths can remain the same (4 μs).

Top-up safety will have to be reassessed with the implementation of the long straight sections. Several tracking assumptions (i.e., addition and removal of apertures) will have to be changed.

3.2.6 Lattice Alternatives

A number of alternatives has been considered in detail as possible upgrades for the APS. Many of these are documented in the literature or in internal notes. Among the alternatives considered are

1. Lattices with more than four long straight sections.
2. Lattices with lower emittance that require replacing the storage ring.
3. Operation at lower energy in order to reduce the emittance.
4. Use of damping wigglers to lower the emittance.
5. Changing the damping partition number to reduce the emittance.

In this section, we survey these alternatives and indicate the advantages and drawbacks of each.

3.2.6.1 Lattices with More Long Straights

The wide-spread interest in revolver undulators (see section 3.4.3.5), reduced the demand for long straight sections. However, configurations have been developed for eight long straights, and these appear workable. As might be expected, obtaining acceptable dynamic acceptance and beam lifetime is somewhat harder than for configurations with four LSS, particularly when both SPX and the RHB insertion are added. Such configurations have also been tested in mock-ups, which largely confirmed their workability. However, at present there is no demand for additional long straights.

3.2.6.2 Replacement Lattices

Two possible replacement lattices were explored, both based on the use of a triple-bend cell and incorporating 10-m-long straight sections. Both require complete replacement of the storage ring magnets, girders, and vacuum system. Only the rf systems and presumably the injection hardware would be retained.

The first of these lattices [3.2-31] was optimized for low effective emittance, with a target of 1 nm. Detailed studies of this lattice indicated that an effective emittance of 0.9 nm should be possible. The magnet strengths were also judged to be possible, provided the bore radius for the quadrupoles and sextupoles was reduced to 20 mm. This would in turn require reducing the chamber size, which was found not to adversely impact instability issues [3.2-32].

In discussing this lattice with users, it emerged that a significant number of users were limited not by beam brightness but by capacity. Hence, we further developed the triple-bend concept to provide the possibility of an additional insertion device beamline [3.2-33]. This was found to be possible by adjusting the relative bend angles of the three dipoles such that the straight section between the second and third dipole was parallel to the existing bending magnet beamline. This new straight section would accommodate a new insertion device with an approximately 1-m length, delivering radiation to an existing bending magnet beamline. Drawbacks of this approach include the limitations on the minimum gap imposed by the relatively large vertical beta function at the location of the new insertion device. In addition, the effective emittance increases to 1.7 nm.

As far as the preliminary studies determined, both lattices are feasible. However, because of the relatively small number of quadrupoles in each sector (which results from the desire for long straight sections), it appears to be impossible to replace one sector at a time while maintaining operation of the ring. In order words, the entire ring would have to be replaced at once, which would require a shutdown of at least one year's duration. This was considered unacceptable by the user community.

3.2.6.3 Lower Energy Operation

It is well known that the equilibrium emittance scales as E^2, where E is the electron beam energy [3.2-34]. Hence, in the quest for higher x-ray brightness, one might anticipate some advantage from reducing the electron beam energy. This has been investigated several times at APS and was recently revisited under the assumption that, if we went to lower energy, we would simply use the present low-emittance lattice with optimized superconducting undulator choices.

The method of analysis is as follows:

1. Vary the beam energy from 3 GeV to 7.7 GeV in 0.1-GeV steps
   (a) Vary the device period from 10 mm to 30 mm in 1-mm steps
      i. Compute the maximum K value available for a NbTi-based device of the chosen period.
      ii. Compute the brightness and flux tuning curves for this device, subject to the high-heat-load front-end limits.

iii. Multiply the brightness for each harmonic by values that approximately account for the effect of typical phase errors [3.2-35].

iv. Compute the brightness envelope over all harmonics. This eliminates the overlap and gives a single curve of maximum brightness vs photon energy. Gaps in the spectrum are represented by zero values.

2. For a series of 5-keV-wide photon energy bands with starting points from 5 to 95 keV, find the best brightness performance available for each beam energy.

3. For each energy band, find the beam energy that maximizes the brightness performance.

4. For each beam energy, determine the number of photon energy bands for which the brightness performance is within a factor of two of the best available for any energy.

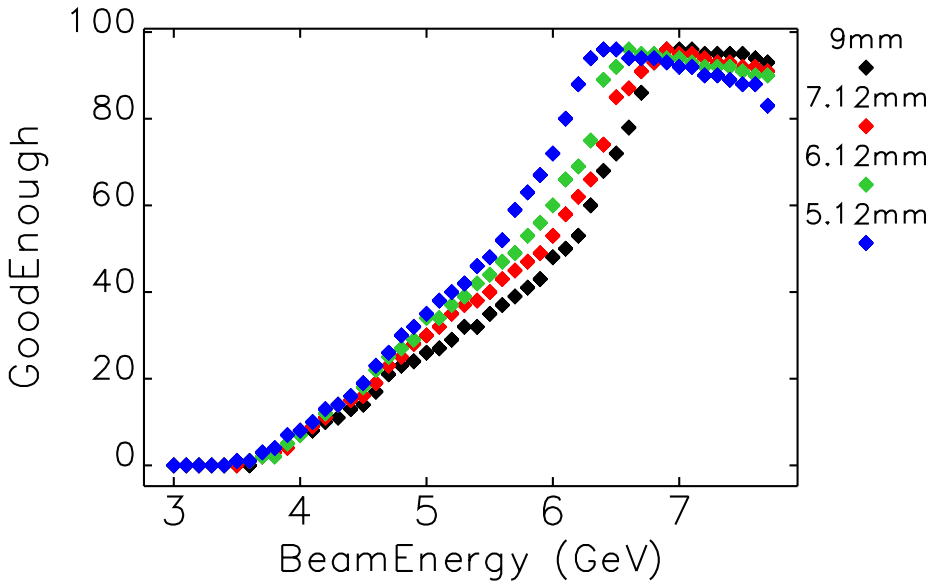

Figure 3.2-29. Number of 5-keV bands between 5 keV and 95 keV for which performance is "good enough," i.e., within a factor of two of the best available result, as a function of the electron beam energy.

Figure 3.2-29 shows the results of the analysis for several different assumed magnetic gaps. For magnetic gaps of 7.12 to 9 mm, operation at 7 GeV is very close to optimal. Indeed, even for the smallest gap explored (5.12 mm), 7 GeV is close to optimal in 90% of the cases. Our conclusion is that large gains in x-ray brightness cannot be obtained by using lower electron beam energy. It is always possible to get a nearly identical gain by simply optimizing the choice of undulator. In addition, higher energy has the advantage of higher instability thresholds, which is important given our emphasis on high single-bunch current for timing experiments.

3.2.6.4 Damping Wigglers

An increasingly popular way to reduce the emittance in a light source is through the use of damping wigglers. This was investigated [3.2-36] for APS from the standpoint of linear optics and rf

requirements. The wigglers must be placed in zero-dispersion straight sections, which means that the starting effective emittance will increase from the 3.1-nm value delivered now. (One might imagine that one could use zero-dispersion insertions for the wigglers and retain the distributed dispersion lattice elsewhere. However, we found that the increase in energy spread due to the wigglers would significantly reduce the anticipated emittance reduction.) The lowest-emittance zero-dispersion lattice we found, irrespective of nonlinear dynamics issues, has an emittance of 4.7 nm. If we imagine devoting the three remaining free straight sections to damping wigglers, we can obtain an effective emittance of 1.7 nm using a somewhat speculative 5-T superconducting wiggler design with a 60-mm period.

With such wigglers, the rf voltage requirements increase from about 9 MV to 21 MV. We have four 5-m-long straight sections available for rf. Analysis of the capabilities of existing superconducting rf systems [3.2-36] indicated that this space is not sufficient. Even conversion of the rf straight sections to a 7.7-m LSS configuration would not suffice. Hence, the use of damping wigglers seems to be ruled out for a number of reasons.

3.2.6.5 Damping Partition Change

Another well-known method for reducing the beam emittance is to increase the horizontal damping partition number J_x. Normally, $J_x + J_y + J_z = 4$, with $J_x = J_y \approx 1$. We can increase J_x at the expense of J_z, which decreases the emittance while increasing the energy spread. Since APS has dispersion in the straight sections, one must be careful to look at the effective emittance rather than the raw emittance when assessing the effect of such a change. In addition, the direct effect of the energy spread on the brightness may be significant for higher undulator harmonics h.

Adding gradients to the dipoles is one option for changing the damping partition. This can be done either by modifying the cores or adding pole-face windings. Using this method, the effective emittance might be reduced to 1.8 nm. However, this involves very high tunes in both planes (46 in the horizontal and 32 in the vertical), for which no satisfactory nonlinear dynamics solution could be found.

Another approach to changing the damping partition is to change the rf frequency. This results in a systematic orbit in the quadrupole magnets, which can change the damping partition just as the use of a gradient dipole magnet will. The disadvantage of this approach is that, because we have dispersion in the straight sections, changing the rf frequency causes significant changes in the orbit, requiring realignment of all the beamlines simultaneously, which simply isn't feasible. In addition, the effective emittance can only be decreased by about 20% with this method, because of the large dispersion value at the straight sections.

Since these methods are not satisfactory, we've looked into another method, namely, producing systematic orbit shifts between the dipoles using a combination of trim coils on the dipoles and steering correctors [3.2-37]. Developing this lattice is much more difficult than developing a normal lattice, because we have orbit in the quadrupoles and sextupoles. Hence, we must simultaneously optimize linear and nonlinear dynamics. Using the multi-objective optimization techniques described in section 3.2.2.4, we succeeded in obtaining a lattice with an effective emittance of 1.5 nm ($J_x = 2.34$, $J_z = 0.66$). The brightness increases by over a factor of 2 in the first harmonic, with slightly diminished gains for the higher harmonics. Dropping the coupling from the nominal 1% to 0.3% would further increase the brightness of the first harmonic, by about 50%.

The tunes, $\nu_x = 37.34$ and $\nu_y = 18.08$, are not too different from the present values. The chromaticities obtained, $\xi_x = 4.6$ and $\xi_y = 3.8$, are suitable for at least 100 mA in 324 bunches, for which the predicted Touschek lifetime is over 40 hours for a coupling of 1% and about 24 hours for a coupling of 0.3%. More work is needed to improve the dynamic acceptance, which is only 10 mm on the negative side. In addition, the lattice will no doubt be operationally challenging, since quadrupoles, skew quadrupoles, and sextupoles will be combined-function elements. However, the lattice shows considerable promise as a possible special operating mode. This would require integrating it with a configuration that includes long straight sections, which has not been attempted.

3.2.6.6 Conclusion

We've reviewed several of the lattice alternatives that have been studied as possibilities for an APS upgrade. In general, these suffer from significant drawbacks, including (variously) high cost, inability to implement gradually, and disappointing performance. Only one option, namely the change of damping partition via a systematic orbit, appears to hold much promise. It is being considered as a possible special high-brightness operating mode, provided it can be made workable in the context of the long straight section lattice.

3.2.7 Dependencies on Programmatic Work

Successful completion of the long-straight-section implementation depends on, or will benefit from, several programmatic tasks and resources, which we enumerate here.

1. *Development of lattices.* On-going lattice development and evaluation requires significant computing resources, which are available from APS, ANL's Laboratory Computing Resource Center, and the Argonne Leadership Computing Facility.

2. *Testing of mock-up lattices.* Testing of mock-up lattices is needed in order to provide confidence that changes will not affect APS operations in unanticipated ways. This is on-going using regular machine studies periods and existing staff.

3. *Improved collimation.* An improved collimation system is desirable in order to reduce beam losses at insertion devices. This will take on greater importance in the upgrade, since the lifetimes are expected to decrease significantly.

4. *Orbit Displacement Lattice testing.* Development and testing of the Orbit Displacement Lattice, described in Section 3.2.6.5, will require use of APS machine studies time and staff. This lattice is not part of project scope but represents a potentially worthwhile special operating mode.

3.2.8 References

[3.2-1] G. Decker and O. Singh. Method for reducing x-ray background signals from insertion device x-ray beam position monitors, Phys. Rev. ST Accel. Beams, **2**(11), 112801, (1999).

[3.2-2] G. Decker. APS Storage Ring Commissioning and Early Operational Experience, Proc. of PAC 1995, pp. 290–292, (1995); http://www.JACoW.org.

[3.2-3] V. Sajaev and L. Emery. Determination and Correction of the Linear Lattice of the APS Storage Ring, Proc. of EPAC 2002, pp. 742–744, (2002); http://www.JACoW.org.

[3.2-4] M. Borland et al. Direct Methods of Optimization of Storage Ring Dynamic and Momentum Aperture, Proc. of PAC 2009, (2010); http://www.JACoW.org.

[3.2-5] M. Borland et al. Application of Direct Methods of Optimizing Storage Ring Dynamic and Momentum Apertures, Proc. of ICAP 2009, (2010); http://www.JACoW.org.

[3.2-6] C. Y. Yao et al. Recent Progress of the Bunch-by-Bunch Feedback System at the Advanced Photon Source, Proc. of IPAC 2010, p. 2803; http://www.JACoW.org.

[3.2-7] V. Sajaev, ANL, (2010). Private communication.

[3.2-8] L. Emery and M. Borland. Top-up Operation Experience at the Advanced Photon Source, Proc. of PAC 1999, pp. 200–202, (1999); http://www.JACoW.org.

[3.2-9] M. Belgrounne et al. Proc. of PAC 2003, pp. 896–898, (2003); http://www.JACoW.org.

[3.2-10] J. Safranek. Experimental Determination of Linear Optics Including Quadrupole Rotations, Proc. of PAC 1996, pp. 2817–2819, (1996); http://www.JACoW.org.

[3.2-11] P. Bagley and D. L. Rubin. Correction of Transverse Coupling in a Storage Ring, Proc.of PAC 1989, pp. 874–876, (1989); http://www.JACoW.org.

[3.2-12] J. Safranek and S. Krinsky. Plans to Increase Source Brightness of NSLS X-ray Ring, Proc. of PAC 1993, pp. 1491–1493, (1993); http://www.JACoW.org.

[3.2-13] L. Emery et al. Use of a General-Purpose Optimization Module in Accelerator Control, Proc. of PAC 2003, pp. 2330–2332, (2003); http://www.JACoW.org.

[3.2-14] J. Bengtsson. The sextupole scheme for the Swiss Light Source (SLS): an analytic approach. Technical Report SLS-TME-TA-1997-0009, SLS, (1997).

[3.2-15] M. Borland. elegant: A Flexible SDDS-Compliant Code for Accelerator Simulation. Technical Report LS-287, Advanced Photon Source, (2000).

[3.2-16] M. Borland et al. Recent progress and plans for the code `elegant`, Proc. of ICAP 2009, (2010); http://www.JACoW.org.

[3.2-17] M. Borland. A Self-Describing File Protocol for Simulation Integration and Shared Postprocessors, Proc. of PAC 1995, pp. 2184–2186, (1996); http://www.JACoW.org.

[3.2-18] M. Borland and H. Shang. geneticOptimizer. Unpublished program.

[3.2-19] A. Xiao and M. Borland. Touschek Effect Calculation and Its Application to a Transport Line, Proc. of PAC 2007, pp. 3453–3455, (2007); http://www.JACoW.org.

[3.2-20] A. Piwinski. The Touschek Effect in Strong Focusing Storage Rings. Technical Report DESY 98-179, DESY, (1998).

[3.2-21] R. Soliday et al. New Features in the SDDS Toolkit, Proc. of PAC 2003, pp. 3473–3475, (2003); http://www.JACoW.org.

[3.2-22] M. Borland et al. SDDS-Based Software Tools for Accelerator Design, Proc. of PAC 2003, pp. 3461–3463, (2003); http://www.JACoW.org.

[3.2-23] M. Borland. Use of a Coupling Bump to Control APS Vertical Emittance. Technical Report OAG-TN-2008-006, APS, (2008).

[3.2-24] Y. Chae. Impedance Database and Its Application to the APS Storage Ring, Proc.of PAC 2003, pp. 3017–3019, (2003); http://www.JACoW.org.

[3.2-25] Y. Chae and Y. Wang. Impedance Database II for the Advanced Photon Source Storage Ring, Proc. of PAC 2007, pp. 4336–4338, (2007); http://www.JACoW.org.

[3.2-26] Y. Chae. The Impedance Database Computation and Prediction of Single Bunch Instabilities, Proc.of PAC 2007, (2007); http://www.JACoW.org.

[3.2-27] Y. Chae. Study of Impedance and Its Effect on Single-Bunch Instability at the Advanced Photon Source, ICFA Beam Dynamics Newsletter 45, (2008); http://www.JACoW.org.

[3.2-28] G. V. Stupakov. Geometrical Wake of a Smooth Flat Collimator. Technical Report SLAC-PUB-7167, SLAC, (1996).

[3.2-29] B. Podobedov and I. Zagorodonov. Impedance Minimization by Nonlinear Tapering, Proc. of PAC 2007, pp. 2006–2008, (2007); http://www.JACoW.org.

[3.2-30] W. Bruns. GdfidL on Massive Parallel Systems, Proc. of LINAC 2002, pp. 418–420, (2002); http://www.JACoW.org.

[3.2-31] A. Xiao et al. A 1-nm Emittance Lattice for the Advanced Photon Storage Ring, Proc. of PAC 2003, pp. 3447–3449, (2007); http://www.JACoW.org.

[3.2-32] Y.-C. Chae et al. Single-Bunch Instability Estimates for the 1-nm APS Storage Ring Upgrade with Smaller Vacuum Chamber, Proc. of PAC 2007, Albuquerque, NM, pp. 4330–4332, (2007); http://www.JACoW.org.

[3.2-33] V. Sajaev et al. New Lattice Design for APS Storage Ring with Potential Tri-fold Increase of the Number of Insertion, Proc. of PAC 2003, pp. 1139–1141, (2007); http://www.JACoW.org.

[3.2-34] M. Sands. The Physics of Electron Storage Rings: An Introduction. SLAC Report SLAC-121, SLAC, (1979).

[3.2-35] R. Dejus, ANL, (2011). Private communication.

[3.2-36] M. Borland and L. Emery. Evaluation of the Possibility of using Damping Wigglers in the Advanced Photon Source, Proc. of PAC 2003, pp. 1124–1126, (2007); http://www.JACoW.org.

[3.2-37] M. Borland. Potential Two-fold Reduction of Advanced Photon Source Emittance using Orbit Displacement, Proc. of PAC 2011, (to be published); http://www.JACoW.org.

3.3 Beam Stability [U1.03.02.02]

3.3.1 Introduction

One of the distinguishing features of 3rd-generation storage-ring light sources like the APS are the small beam emittances, which imply small beam size and divergence. Table 3.3-1 shows the typical dimensions for the APS electron beam at the ID location. Any beam motion that is significant compared to these dimensions will impact the ability of users to perform demanding experiments. In essence, fast beam motion washes out the brightness of the beam. Hence, controlling beam motion is effectively a brightness upgrade and serves an important role in delivering the mission requirements.

Table 3.3-1. APS Particle Beam Transverse Dimensions.

	Beam Size μm rms		**Angular Divergence** μrad rms	
	ID	BM	ID	BM
Horizontal	275.3	91.6	11.3	56.4
Vertical	8.5	25.5	3.0	1.1

In October of 2005, a white paper was written by John Carwardine, Frank Lenkszus, Glenn Decker, and Om Singh [3.3-1]. This paper enumerated specific goals and an upgrade path aimed at achieving these goals in a 5-year time frame. Since that time, a number of projects recommended in the white paper have been at least partially completed, while others were deferred. The intent of this section is to describe the present status of APS beam stability and beam stabilization systems, and to describe how best to proceed toward our ultimate goals.

At the time it was written, the white paper asserted that “the APS no longer provides the best orbit stability amongst the three large third-generation light source worldwide.” In the case of SPring-8, the focus has been on the passive elimination of beam disturbances, which has resulted in vertical rms motion 40% lower than the APS in at least one instance. At ESRF, a new fast global orbit feedback system was commissioned in 2004, resulting in closed-loop bandwidth extending up to 150 Hz, compared with the old APS system that has a bandwidth of about 60 Hz. As a result, rms noise at ESRF is a factor of 2 or more lower than at APS, in the frequency band from 0.1 to 200 Hz. In fact, ESRF has undergone a second upgrade, purchasing 224 channels of very low noise beam position monitor (BPM) electronics networked together to provide even lower levels of beam motion. Shown in Table 3.3-2 is a comparison of AC performance between the three facilities, evaluated at insertion device beamline source points.

Table 3.3-2. AC Beam Stability Comparison. Values are μm rms in the frequency band 0.1 - 200 Hz.

	APS 2008	**ESRF 2005**	**SPring-8 2004**
Horizontal (μm)	4.8	1.2 - 2.2	3 - 4
Vertical (μm)	1.6	0.8 - 1.2	1

For the APS, AC beam stability goals are derived to be 5% of the x-ray beam's rms phase-space dimensions (both beam size and angular divergence). The values in Table 3.3-1 are typical transverse beam size and divergence values for the particle beam at insertion device and bending magnet source points assuming 2.5-nm-rad natural emittance and 1% coupling. Note that for bending magnet (BM) sources, the x-ray beam's vertical angular divergence is dominated by the natural synchrotron radiation opening angle, which is approximately $1/\gamma = 73$ μrad.

Listed in Table 3.3-3 are APS upgrade beam stability goals for ID sources. Beam stability at BM sources is already sufficient.

Table 3.3-3. APS Beam Stability Goals.

		AC rms Motion, 0.01-200 Hz		**Long-term drift (One Week)**	
		μm rms	μrad rms	μm rms	μrad rms
Horizontal	Present	5.0	0.85	7.0	1.4
	Upgrade	3.0	0.53	5.0	1.0
Vertical	Present	1.6	0.80	5.0	2.5
	Upgrade	0.42	0.22	1.0	0.5

3.3.2 Beam-Stability Limitations

To arrive at a coherent stability improvement strategy, one must have a clear understanding of the fundamental mechanisms that limit the ability to precisely and accurately measure and correct beam disturbances. These mechanisms fall into a number of broad categories that impact beam stability over a variety of time / frequency scales. At the highest level, one can separate beam instability into three classes:

- Environmental, i.e., true sources of instability that actually disturb the particle beam,
- Systematic, i.e., erroneous readbacks from diagnostic devices, and
- Algorithmic, i.e., errors in how corrections to the particle beam are computed and / or applied.

The time / frequency scales of primary interest are dictated by the nature of x-ray experiments conducted at the APS. A large proportion of these involve photon counting, which effectively integrate the on-sample x-ray flux over some time period ranging from minutes or hours down to tens of milliseconds. In addition, experiments are conducted in such a fashion that one desires to achieve the same results tomorrow or even next week as were seen today, without performing major beamline adjustments.

Since the inception of the APS real-time orbit correction system c. 1998, one standard measure of AC beam stability has been the amount of rms motion within a frequency band from 0.01 to 30 Hz, averaged over a set of high-resolution rf beam position monitors located nearest to insertion device x-ray source points. As x-ray experiment integration times continue to fall, this measure needs to be

expanded to cover higher frequencies. As shown in Table 3.3-3, the proposed standard measure of AC beam stability for the APS upgrade will cover motions in the frequency range from 0.01 to 200 Hz.

On longer time scales, a number of difficulties arise, in that it is very difficult to distinguish between long-term drift resulting from electronics, real ground motion, and thermally induced mechanical component motion. In spite of these difficulties, a significant goal of the APS upgrade is to control long-term beam motion at x-ray source points using the rms motion in microns over a period of one week as a measure.

3.3.2.1 Environmental Disturbances

Major sources and magnitudes of beam motion and their respective amplitudes and time scales are as follows:

- Vacuum chamber water system temperature, 0.1 to 0.2 °F variation over minutes to hours.
- Tunnel air and electronics temperature, 0.8 to 1.2 °F variation over hours to days.
- Diffusive ground motion, 1.7 to 5.5 microns variation over weeks to months.
- Earth tides, tens of microns over hours.
- Girder / Magnet vibration, micron-scale, 1 to 100 Hz.
- Power-supply noise, submicron scale, 1 Hz to tens of kHz, this after years of efforts to identify and remediate problem components.
- Radio frequency phase / amplitude noise, micron-scale, 1 Hz to several kHz, but typically narrow band spectral lines at multiples of 60 Hz, with 360 Hz and 1800 Hz being most prominent.
- Insertion device field integral variation due to gap changes, 5 to 10 microradians in seconds.

Of these sources, many have already been sufficiently suppressed. Insertion device gap changes are strongly suppressed by the existing 10-Hz orbit correction algorithm, as are the effects of girder vibrations up to 60 Hz. Earth tides are dealt with using feedback of orbit circumference to the master oscillator rf frequency. Power supply noise has similarly been dealt with, but in addition recent efforts to reduce 20-kHz “chopper noise” affecting fast correctors have been instrumental in the commissioning of a fast multibunch transverse feedback system. In short, sources of environmental noise in the frequency band from 0.01 to 60 Hz have had the most attention, with good success. The challenge to AC noise suppression lies at the higher frequencies up to 200 Hz and beyond. Fortunately technological solutions including outstanding commercially available beam position monitoring electronics and feedback system components provide a clear path forward in this area.

More challenging, and the subject of early R&D efforts, are those sources active in the time frame from hours to days, specifically thermal variation and diffusive ground motion. Research has already begun in these areas, as described in sections 3.3.8 and 3.3.7.

3.3.2.2 Systematic Errors

The APS has the most diverse set of beam position monitor diagnostics used in feedback of any light source in the world. This has had many advantages but has come with its own costs. Among the advantages has been the ability to cross-check readings from different diagnostics, e.g., narrowband rf BPMs near the insertion device source points in comparison with photon BPMs located far downstream. A distinct disadvantage has been maintenance and support of the hardware and software needed to manage all of the different flavors of systematic errors affecting the different systems. The different BPM types and their most significant systematic errors are as follows:

- Narrowband rf BPMs near insertion device source points have the advantage of having good (micron-scale) long-term drift performance over days. The asynchronous switching between inputs, which underlies their operating principle, results in spurious spectral lines that can occasionally wander below 100 Hz where the real-time feedback system is active. Their AC noise floor is at best some tens of nm $/\sqrt{\text{Hz}}$.
- Broadband rf BPMs used between insertion device source points have excellent high-frequency performance, but suffer from intensity dependence and fill-pattern dependence, producing several microns of long-term drift and several-micron variations during top-up operation as the fill pattern changes with each shot from the injector. Also, these systems are impacted by a spurious microwave mode present in the large-aperture chambers that mimics a vertical beam position signal.
- Bending magnet photon BPMs are based on photoemission and use pairs of molybdenum blades located above and below the accelerator midplane near bending magnet beamline source points. Bending magnet photon BPMs are the most reliable diagnostic suffering from very few systematic errors, although they only provide vertical position information. They have excellent AC and DC performance, at the submicron level.
- Insertion device photon BPMs, while nearly identical in principle to the bending magnet variety, suffer from the fact that their signal sources, the insertion devices, are variable. Extensive work to compensate for gap-dependent variations in calibration factor and position offset provide correction only at the level of about 10 microns over the normal range of gap values. Their configuration and compensation has gotten even more complex with the advent of canted undulator beamlines, where cross-talk between BPMs in the same front end result from stray radiation and insertion device field integral variation. Very careful background subtraction is also necessary to deal with stray radiation from local steering corrector magnets.

3.3.2.3 Orbit-Correction Algorithms

Orbit correction at the APS uses two concurrently operating frequency-band-separated feedback algorithms. Motions slower than about 1 Hz are corrected by a singular value decomposition (SVD) algorithm operating at 10 Hz, with access to the full complement of 278 steering correctors in each plane and over 500 BPMs. Higher-frequency motions are suppressed by the real-time feedback system operating at 1.5-kHz sample rate, which uses a smaller response matrix with at most 38 steering correctors and 160 BPMs.

The 10-Hz algorithm typically uses between 80 and 120 steering correctors per plane and several hundred BPM channels. Performance of the nearly 15-year-old fast feedback is limited by processing power, system bus bandwidth, real-time network throughput, and the availability of fast-steering corrector magnets. All APS steering correctors are identical six-pole magnets wired as combined-function horizontal / vertical steering dipoles. The distinction between fast vs. slow correctors results from the type of vacuum chamber used. Slow correctors are mounted around thick-walled aluminum extrusions which limit their bandwidth to a few Hz as a result of strong eddy currents, while the 38 fast correctors have steel spool piece chambers.

One consequence of running parallel feedback algorithms is the existence of a frequency dead-band near 1 Hz. This has been compensated reasonably well using a feedforward algorithm that essentially informs the fast system what the slow system is about to do on each 10 Hz sample, to prevent the fast system from fighting against the slow system [3.3-2].

While SVD provides a method for inverting possibly near-singular rectangular matrices, standard practice for the slow feedback has been to restrict the number of steering correctors rather than omit modes with small eigenvalues. For the fast feedback, the number of correctors has necessarily been limited to 38, but in addition small-eigenvalue modes are eliminated, providing a robust and stable algorithm. Additionally, the capability exists to use weighted SVD that preferentially locks down specific sets of BPMs, however this capability has not been used during user beam operation.

There are a number of auxiliary algorithms that are independent of the fast and slow feedback. A very slow feedback varies the rf frequency in order to fight earth tides, which stretch the ring circumference. A fast transient feedforward algorithm drives fast steering correctors near the injection point to reduce the effects of pulsed injection during top-up operation.

One important element of the APS upgrade beam stabilization program will be to perform extensive simulations of different feedback system topologies, sample rates, and algorithms to arrive at a system optimized to meet long-term stability goals. Increasing the fast-feedback sample rate by an order of magnitude is expected to extend the closed-loop bandwidth from 60 Hz to 200 Hz or more [3.3-3] . Increasing the number and placement of fast correctors are similarly expected to produce substantially improved stability. These simulations will include the known dynamics of the different BPM systems, steering power supplies and magnets. In addition, the effects of different lattice functions and errors in the response matrix will be modeled. The effects of SPX will similarly need to be studied.

3.3.3 Upgrade Plan

The goals listed in Table 3.3-3 are challenging but achievable in the context of the APS upgrade. To achieve them, a substantial investment in BPM technology, real-time data networking, mechanical engineering, and high-level software will be required. Specific items addressing beam stability for the APS upgrade are as follows:

- New BPM Electronics — We will replace the obsolete BPM electronics for the narrowband rf and photon BPMs with modern systems, providing improved resolution and drift characteristics.
- X-ray BPM System Enhancement — We will augment the existing photon BPMs with BPMs based on hard x-ray fluorescence, providing improved immunity to background radiation and

improved long-term drift characteristics.

- Storage Ring Real-Time Feedback System Upgrade — We will upgrade the system to improve the bandwidth from approximately 60 Hz to 200 Hz. We will also double the number of fast corrector magnets that can be used.
- BPM Mechanical Motion Sensing System — We will instrument critical BPMs with sensors to allow compensation for temperature-induced motion of the monitors.

The scope of the effort and the benefit expected from each item are summarized in Table 3.3-4.

Table 3.3-4. Beam Stability Upgrades for APS-U

Item	Scope	Expected Improvement
New BPM electronics	80 narrowband rf BPMs, 70 ID photon BPMs, 70 BM photon BPMs	Factor of 2, AC noise floor
New hard x-ray BPMs	34 complete units installed in front ends	Factor of 2, long-term pointing stability
Real-time feedback system	Complete replacement with modern components	Extend closed-loop bandwidth from 60 to 200 Hz; reduce AC beam motion by a factor of 4
BPM mechanical motion sensing	Install for 34 photon and 34 rf BPMs	Factor of 2, long-term drift

3.3.4 New BPM Electronics [U1.03.02.02.01]

Table 3.3-5 is a list of the different types of BPM electronics presently in use to control APS beam stability [3.3-4].

Table 3.3-5. Installed APS BPM Electronics

Type	Location	Advantages	Disadvantages
Narrowband rf	ID source points	Long-term stability	Aliasing; micron-scale drift
Original broadband rf	Ring arcs	Large installed base	Obsolete; intensity dependence
FPGA-based broadband rf	Ring arcs	Low noise	Intensity dependence
Bending magnet photon BPMs	BM front ends	Long lever arm	Vertical only
Insertion device photon BPMs	ID front ends	Long lever arm	Gap-dependent errors

Narrowband rf BPM electronics (Commercial, Bergoz) monitor the particle beam and are attached to capacitive button pickup electrodes mounted on the small-aperture insertion device vacuum

chambers (IDVCs) in pairs (or triplets for canted undulators). Each insertion device source has an additional pair similarly instrumented but using electrodes mounted on the large 42 × 80 mm elliptical chambers closest to the insertion devices. These units are used to detect misaligned beams to trigger a fast beam abort (< 1 ms). The best AC performance for the Bergoz receivers using the most advantageous button geometry associated with the IDVCs is no better than about 30 nm /$\sqrt{\text{Hz}}$.

All other rf BPM electronics use the same broadband (10 MHz) rf monopulse receiver front end attached to the large elliptical chambers in the ring arcs. Using operating funds, their obsolete data acquisition is in the process of being replaced to include a modern field-programmable gate array (FPGA) design and fast sampling (14 bits, 88 MS/sec) [3.3-5]. The APS-designed data acquisition board used for this purpose is called the BSP-100 module (bunch signal processor).

One can acquire commercially available broadband rf BPM electronics from Instrumentation Technologies, Solkan, Slovenia, which have been deployed at the Diamond Light Source among many others. A set of these electronics, called Libera Brilliance, were procured for evaluation purposes. Shown in Figure 3.3-1 is a comparison of the achievable noise floor for Libera Brilliance vs the APS BSP-100 module. The electronics in this case were attached to opposite ends of the same small-aperture IDVC associated with the APS 35ID undulator source point.

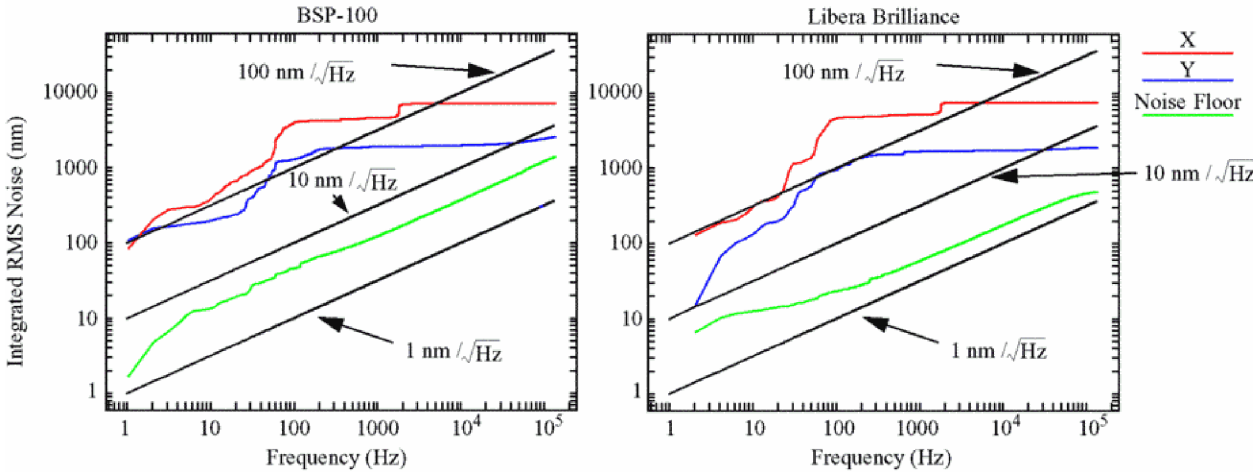

Figure 3.3-1. Comparison of AC performance of BSP-100 (left) and Libera Brilliance (right).

To determine the noise floor (green traces in Figure 3.3-1), a single button was split using a four-way rf splitter. In this case the conversion to microns corresponded to that for the horizontal plane, which in this case has the highest geometric sensitivity. Also shown are the present levels of real beam motion as a function of frequency both horizontally (X) and vertically (Y). The Libera module shows better noise performance, approaching 2 nm /$\sqrt{\text{Hz}}$ and in addition has shown long-term stability at the level of 200 nm p-p over a 24-hour period [3.3-6]. While the BSP-100 modules have the advantage of lower cost and acceptable AC performance, the monopulse rf BPM receivers they sample do not have good enough long-term drift performance and have unacceptably large intensity and fill-pattern dependence.

The Libera solution appears to satisfy the requirements and has been deployed at a large number of light sources but is relatively costly. There are new developments in BPM electronics design

supporting the NSLS-II project that will be watched closely as a cost-effective candidate solution for the APS upgrade [3.3-7]. In any case, because the insertion device source points are critically important, a pair of new BPM electronics will be deployed at each of the 35 APS ID sources, with three units for canted undulators.

With regard to photon BPMs, research is ongoing to determine the suitability of an FPGA data acquisition solution similar to the BSP-100 module for providing low-noise high-speed results. The present obsolete photon BPM data acquisition electronics is the same as that used by the installed Bergoz receivers, which will be retained for interlock purposes. It is planned to replace the data acquisition for both the Bergoz system and the photon BPM systems using a standardized platform. Alternatives are the BSP-100, a new in-house development, or a commercial solution.

Work remaining for BPM electronics:

- Determine whether to build vs buy new electron rf BPM electronics for IDVCs.
- Finalize design for replacement data acquisition for photon and Bergoz BPMs.

3.3.5 X-ray Beam Position Monitor System Enhancement [U1.05.02.02.10]

The x-ray beam position monitors (XBPMs) are farther away from the synchrotron radiation source points than the rf BPMs, and are uniquely suitable for detecting minute beam direction changes. Since the commissioning of the APS, we have used photoemission blade-based XBPMs. Their readings depend on the undulator gaps by as much as several hundred micrometers. They met the performance specifications only after extensive data processing work to compensate for the gap dependencies. It will be difficult to improve the compensation further for the more stringent requirements after the APS upgrade. Analyses show that the best way to improve the signal-to-noise ratio of the beam position monitor is to maximize the undulator x-ray flux intercepted and minimize the background radiation received [3.3-8]. This naturally leads to the solution of combining the XBPM with the limiting aperture of the front end. Many of the front ends will be rebuilt to increase their power-handling capabilities (see section 5.3), providing a good opportunity to implement this upgrade.

The left panel of Figure 3.3-2 shows the horizontal x-ray beam profiles calculated with the XOP program suite at a distance of 20 meters from the undulator source. The APS Undulator A was chosen as the x-ray source, and a typical set of parameters in Run 2010-1 was used for the electron beam: $\sigma_x = 0.27$ mm, $\sigma_y = 0.012$ mm, $\sigma_{x'} = 0.012$ mrad, and $\sigma_{y'} = 0.004$ mrad. The profiles are for the total x-ray power, the monochromatic x-ray at the first harmonic energy ω_1, at $\omega_1/140$ below the harmonic energy (near the peak of the x-ray flux), and at $\omega_1/70$ below the harmonic energy (near the spectral edge of pink beam users). Two vertical lines in the figure show the 2-mm-wide aperture that intercepts about $2/3$ of the x-ray power but allows over 99% of the useful x-rays to pass through. The right panel of Figure 3.3-2 shows the similarly calculated vertical x-ray beam profiles. Here a 1.5-mm-high aperture appears to intercept about 40% of the x-ray power and allow over 99% of the useful x-rays to pass through.

Due to its excellent thermal-mechanical properties, the copper alloy GlidCop will be used to construct the x-ray aperture. Since copious amounts of secondary electrons and x-ray photons

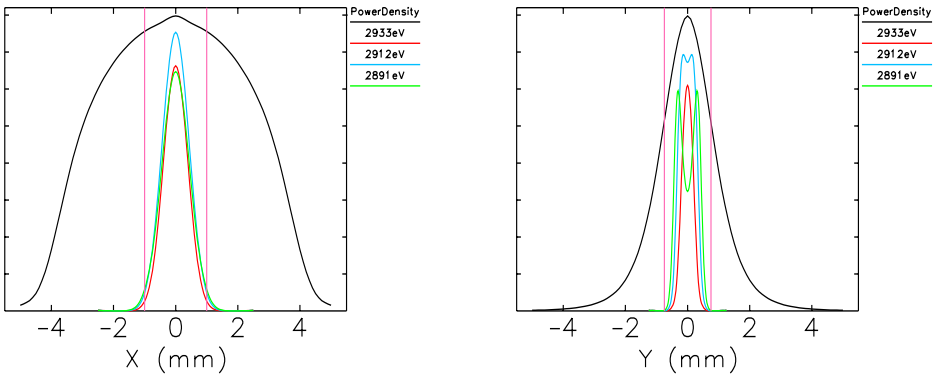

Figure 3.3-2. Horizontal (left) and vertical (right) x-ray beam profiles of Undulator A: shown are the total x-ray power density (black) along with the irradiance for three specific x-ray energies, where 2933 eV is the first-harmonic energy E_1, 2912 eV is below the first harmonic by $E_1/140$, and 2891 eV is below the first harmonic by $E_1/70$. The apertures of the grazing incidence XBPM are shown by the vertical lines.

are emitted by the aperture, we may use either particle to read out the x-ray footprint information. Our first choice will be the copper K-edge x-ray fluorescence (Cu-K XRF) photons, since they are not produced by the soft bending magnet radiation parasitic to the undulator beam. A prototype has been constructed and successfully demonstrated the basic design principle of the grazing incidence XBPM [3.3-9]. Silicon PIN diodes were used for the XRF intensity detectors. After the APS upgrade, two 3.3-cm-period undulators could generate up to 16 kW of x-ray power with 150 mA of stored beam, and several kW XRF power are expected in the extreme cases. We plan to use diamond detectors for the XBPM signal readout in the final product. These detectors are radiation hard and stable at high power load. The device will be designed to handle 200-mA operation with two 3.3-cm-period undulators.

Combining the functionality of a front-end fixed mask with that of an x-ray BPM has the primary advantage of providing a self-centering aperture. Integrating this concept into the design of high-heat-load insertion device beamline front ends will reduce the number of simple masks while providing enhanced long-term stability. Several concepts have been investigated already, with encouraging results [3.3-10, 3.3-11].

Figure 3.3-3 contains data showing the calibration of a prototype XRF-based BPM collected at diagnostic beamline 35-ID. Calibrations were performed either by displacing the detector (red) or steering the beam (black). The upper left frame shows horizontal difference over sum data, all others are for the vertical plane. A comparison between the performance of the existing photoemission-based photon beam position monitors and the new XRF detector is shown in Figure 3.3-4. At large gap values, the photoemission blade signals have relatively large and vastly different background signal levels. This effect is not seen for the XRF detector over a full three decades of signal amplitude.

Work remaining for x-ray beam position monitors:

- Determine optimum XBPM geometry for high power and sensitivity.

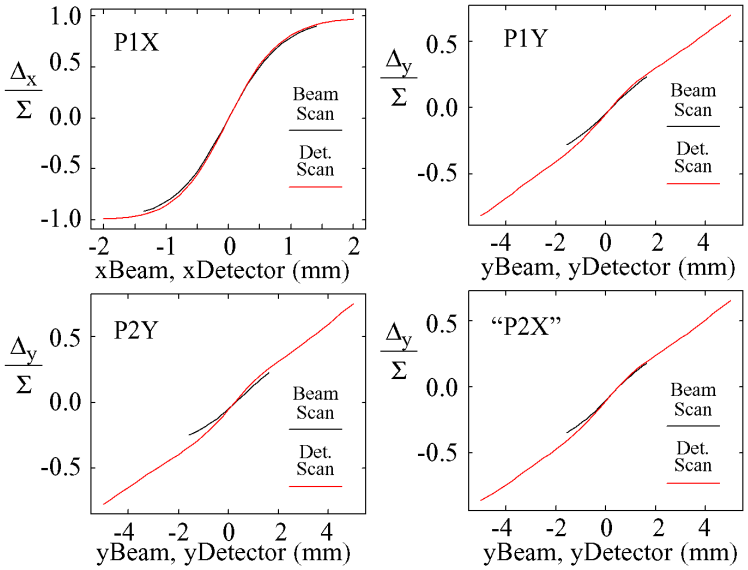

Figure 3.3-3. Calibration curves for an x-ray fluorescence-based BPM.

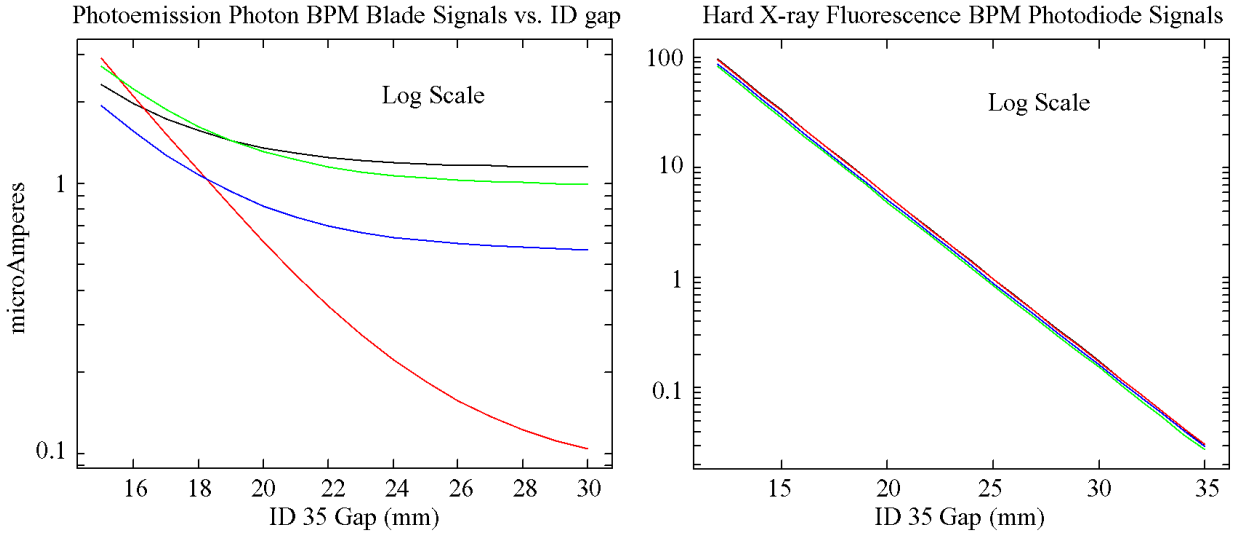

Figure 3.3-4. Response of photoemission BPM blades (left) and XRF BPM diode signals (right) vs gap.

- Develop suitable cost-effective diamond detectors.
- Develop a cost-effective mechanical design integrating a grazing-incidence x-ray BPM into high-heat-load front-end designs.

3.3.6 Storage Ring Real-Time Feedback System Upgrade [U1.03.02.02.03]

The present APS real-time feedback system operates at 1.534 kS/sec sample rate, and is limited to use a maximum of 38 steering correctors and 160 BPMs [3.3-12]. It was commissioned in 1997 and has had incremental code patches over the years, but uses many components (digital signal processors, reflective memory) that are 15 or more years old. The closed-loop bandwidth of this system is approximately 60 Hz. To achieve 200-Hz closed-loop bandwidth, an increase in sample rate by an order of magnitude is desirable, to the range from 10 to 20 kS/sec. In addition, access to the full complement of rf and photon BPMs together with approximately doubling the number of fast-steering correctors should allow reduction of beam motion by a factor of four or more.

Use of modern networking, digital signal processing, and FPGA technology should allow the creation of a reliable system with vastly enhanced capabilities for a modest investment. The development of such a system for NSLS-II will be closely monitored.

The present system is limited by the processing power of fifteen-year-old digital signal processors (DSP), limited bandwidth of the system bus through which all data must pass, and throughput of the reflective memory system that is used to communicate data between the 22 nodes that comprise the real-time feedback/orbit correction system.

Only 160 BPM values per plane (4 per sector) can be integrated into the present system. Each DSP must calculate corrector error values by multiplying the 160-value BPM vector by the 160-element row of the inverse response matrix corresponding to each corrector. The resulting computed corrector error is passed through a digital controller and then written to the corresponding corrector. This calculation taxes the computing power of the existing DSPs at the 1.5-kHz iteration rate.

The new system will double the number of BPMs and correctors used. This requires eight 320 $\times$ 320 dot products per double sector per iteration cycle for both planes. In addition, the complete algorithm requires scaling and digital filtering of input values, limit checking, feedback controller computations, etc. The present DSPs in a double-sector node have a combined rating of approximately 110 MFlops and are saturated at the 1.5-kHz iteration rate. Extrapolating the 110-MFlop figure by increasing the number of BPMs to 320, correctors to 2 per plane per sector, and sampling rate by a factor of 13 to 20 kHz infers a computational load of about 5 GFlops per double sector. This could possibly be achieved with an array of tightly coupled DSPs, but would likely be an expensive solution and still may be limited by the speed that data can be shuffled between processors.

The solution to the computation bottleneck is field-programmable gate arrays (FPGAs). These devices allow the implementation of highly parallel processing and are capable of clock rates exceeding 300 MHz. This offers a significant performance increase over traditional DSPs, which have limited parallel processing capability. For example, the eight 320 $\times$ 320 dot products, digital filters, and feedback controllers would be computed in parallel rather than sequentially. In addition, the FPGA may be programmed to optimize algorithm implementation to increase performance.

The present system transfers all data between data acquisition modules and DSPs via a system bus. At the existing 1.5-kHz iteration rate, this system bus is heavily loaded and near saturation. Newer BPM processors such, as the APS-developed BSP100 and the Libera units from Instrumentation Technologies, provide high-speed serial data streams via industry-standard small form-factor pluggable

(SFP) optical transceivers. Modern FPGAs provide support for these high-speed serial links. It is envisioned that individual high-speed data links would be provided for each BPM processor, connecting the data streams directly to the FPGA. This avoids the system bus bottleneck.

The existing reflective memory network that interconnects the feedback nodes is based on aging commercial modules that communicate with the DSPs via the system bus. The proposed system would use high-speed links similar to those used for the BPM data that connect directly to the FPGA to implement the equivalent of the reflective memory network. One or two (1 per plane) would be dedicated to transferring data required for the feedback algorithm. An additional network would be used to communicate global parameters, such as feedback gains, sampling rate, and loop status. This management network could transfer more data at a lower update rate for system control and monitoring.

The new system nodes will need to communicate to the APS control system This may be either via an embedded processor running EPICS or via a system bus to a modular processor that runs EPICS.

The existing real-time feedback system has a number of useful features, including DSP scope, which is essentially a 40-channel synchronous waveform acquisition system with access to any of the hundreds of available signals. In addition, the AC voltmeter application allows for convenient lock-in type measurements, for example when measuring response to sinusoidal excitations. The DSP scope function that presently is available via the feedback master node could be moved to the FPGA nodes. Other diagnostics, such as AC voltmeter and beam rms motion calculations that operate on BPM vectors spanning all sectors, will need to be computed at a central node.

A significant effort will be required to design, fabricate, and install this system while integrating it incrementally with existing hardware that must continue to function at their present level of performance or better through the course of the upgrade. Interfaces to new BPM electronics and power supply controls will need to be carefully defined very early in the project.

A simulator for the feedback system is under development following the original time-domain approach [3.3-13] for a 1995 SPEAR feedback upgrade. The time-domain approach allows analysis not possible or not convenient in the frequency domain, such as quantization noise, slew rate limits and use of time-series measurement of orbit response of correctors. Also our BPM types have different responses. Thus depending on which BPMs are predominately used, one would have different loop behavior. In addition we need to handle mixed discrete and continuous time responses. `Matlab Simulink` [3.3-14] software handles such real-world difficulties, but we found it practical only for low-dimension systems. Our correction system has up to 360 digital inputs and 76 outputs that are coupled, which is cumbersome to enter in a `Simulink` model. Thus our C program will handle the specific case of orbit correction in the same way `Simulink` would in the general case. Since the software will be (Self-Describing Data Sets) SDDS-compliant, much of the work preparing and analyzing a simulation is offloaded to existing GUIs (e.g. correction matrix creation used in operations) and to standard post-processing tools.

3.3.7 BPM Mechanical Motion-Sensing System [U1.03.02.02.04]

In order to achieve long-term beam stability goals, all sources of mechanical motion of critical in-tunnel beam position monitoring devices must be carefully evaluated and appropriately addressed. This includes the effects not only of water and air temperature, but in addition Earth tides and diffusive

ground motion.

Figure 3.3-5 shows the amount of circumference change of the APS storage ring over the course of a week resulting from Earth tides. In this case, the rf frequency is being continuously changed using feedback to keep the beam centered in the vacuum chambers horizontally at the high-dispersion points around the ring. This type of motion is mostly common to the entire facility and, as such, is inconsequential however, differential motions along any given beamline from source to sample caused by Earth tides could be a serious problem and are an important area of investigation.

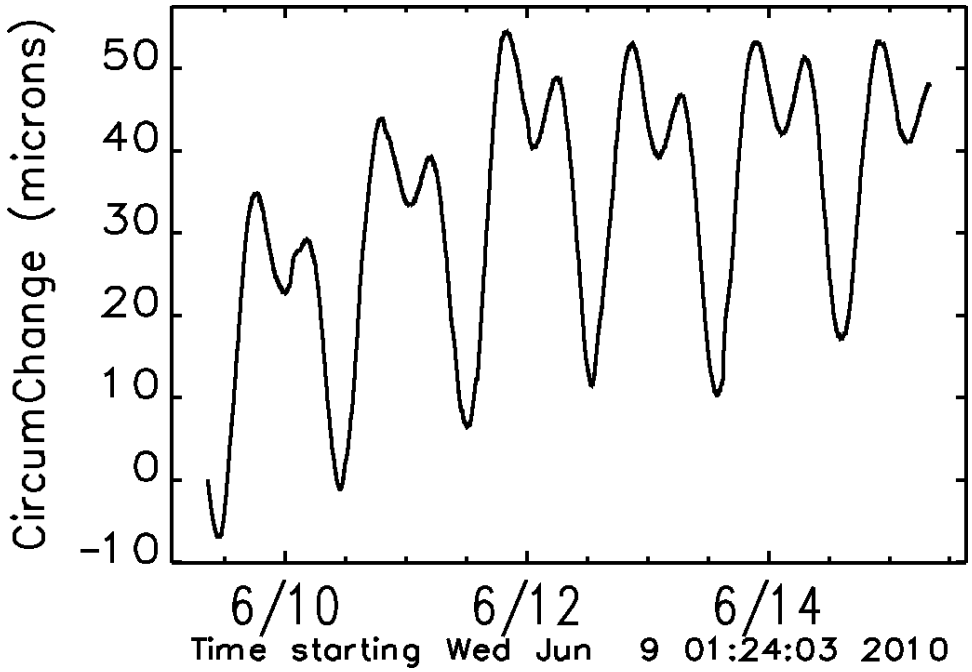

Figure 3.3-5. APS circumference changes due to Earth tides over a one-week time period.

A common measure of diffusive ground motion over extended time periods is the so-called ATL law whereby the mean square amount of ground motion taking place over a time period T between two points separated by a displacement L is proportional to their product, with proportionality constant A. This constant takes on values ranging from 10^{-8} to 10^{-4} μm^2/meter/second depending on the site. Research performed at Fermilab in relation to the next linear collider project indicate that a conservative range for A is between 10^{-6} and 10^{-5} μm^2/meter/second [3.3-15].

This means that the relative rms ground motion for 2 BPMs separated by 5 meters (the distance between BPMs mounted on an insertion device vacuum chamber) is in the range from 1.7 to 5.5 microns over a 1-week period. Dividing by the 5-meter lever arm results in ground-motion-induced angular instability between 350 nanoradians and 1.1 microradians rms, significantly exceeding the goals stated in Table 3.3-3. An active area of research will be to quantify this type of motion specifically for the APS accelerator tunnel and experiment hall floor under normal operating conditions using a hydrostatic level system and to develop a strategy for dealing with potentially large amounts of diffusive ground motion. There are reasons to believe that the above estimates are overly pessimistic. The APS accelerator enclosures have been in place for nearly 20 years, are largely monolithic (have very few

expansion joints), and have been temperature-regulated for most of those 20 years.

The use of XBPMs in beamline front ends is expected to further improve the ability to stabilize angular motion, being closer to the beamline point of use. The stability of the XBPM is affected by many factors at different time scales: (1) vibration of the XBPM body and its support structure excited by cooling water flow (from milliseconds to seconds), (2) distortion and expansion of the XBPM and its support structure due to temperature changes (from seconds to hours), and (3) diffusive motion of the floor/ground (from days to months). A good part of these changes can be monitored by a real-time position monitoring system that measures the XBPM position relative to the floor or to a reference surface defined for example by a hydrostatic level system. Figure 3.3-6 shows a proposed concept for such a position monitor [3.3-16]. For two pedestals solidly attached to the floor or hydrostatic level reference, the simple triangulation measures XBPM displacements in both horizontal and vertical directions, avoiding the difficulties of precisely transferring a horizontal reference from the floor to the XBPM. This system will be effective for monitoring XBPM motion from milliseconds to hours. However, its usefulness for the horizontal displacement measurement is questionable at time scales from weeks to months due to diffusive motion of the floor.

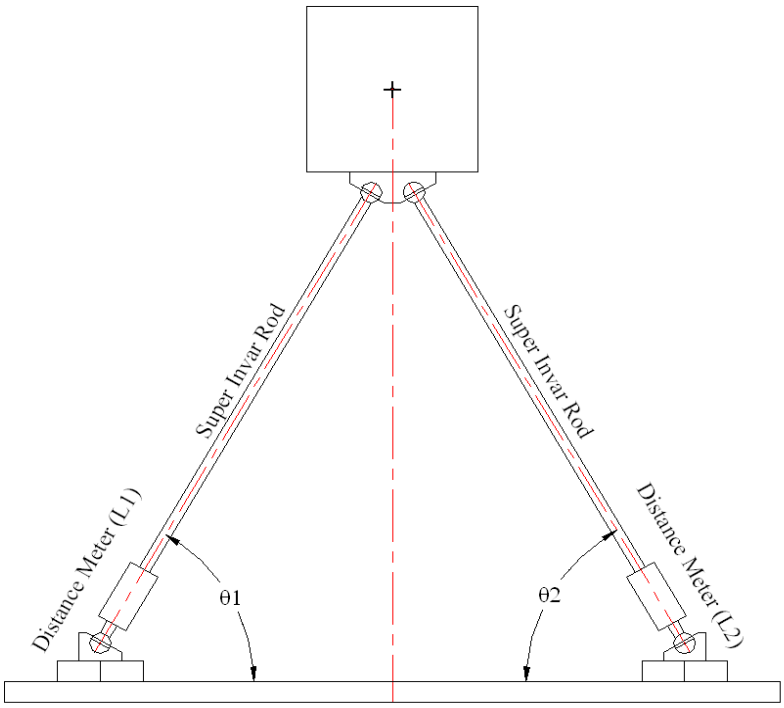

Figure 3.3-6. Real-time mechanical motion sensing concept: Two sub-100-nm-resolution length meters monitor the change of distance between the BPM and two points on a hydrostatic level reference system. The BPM x-y position change can be easily calculated from the two distance changes.

An analogous system will be developed for the rf BPM pickup electrodes nearest to the insertion device source points. In this case space constraints will require some nontrivial mechanical engineering.

Tunnel air-temperature variations have a significant impact on the support structure of the insertion device vacuum chambers upon which the rf BPM pickup electrodes are mounted. For that reason, a mechanical redesign of the support using materials such as Invar^{TM}and titanium could reduce sensitivity to air temperature fluctuations by as much as a factor of two. Coupled with a factor of two improvement in air-temperature regulation, this redesign could be a cost-effective alternative for improving overall BPM mechanical stability.

Work remaining for the BPM mechanical motion sensing system:

- Perform long-term stability measurements on the APS floor,
- Develop real-time BPM mechanical motion sensing system,
- Finalize cost / benefit analysis of deploying such a system vs investing in water and air temperature regulation improvements and mechanical support structure redesign.

3.3.8 Storage Ring Air and Water Temperature Regulation Upgrade [CAS]

Variation in storage ring air and water temperature are significant contributors to long-term beam motion. Shown in Figure 3.3-7 are typical tunnel air temperature data for one week of APS operation, with doors closed. It appears that 80 to 90% of the time the air temperature lies in a range of 0.6 °F, with temperatures wandering outside this range resulting in a peak-to-peak (pk-pk) or 100 percentile variation of 0.8 to 1.2 °F.

Given that the thermal expansion coefficient for materials like steel and aluminum is near 10^{-5} / °F, and that the accelerator magnets are 1.4 meters above the floor, Figure 3.3-7 implies that accelerator components will move relative to the floor on the order of 10 to 15 microns pk-pk due to air temperature variations over a one-week time period. Clearly, meeting the long-term drift stability goals stated in Table 3.3-3 will be quite challenging with the present amount of tunnel air temperature variation. Improving temperature regulation by an order of magnitude will likely be prohibitively expensive, and other means, such as the BPM mechanical motion sensing system described below, will need to be employed.

In any case, a goal of decreasing tunnel air temperature variation by a factor of two appears achievable with reasonable cost, which will improve the ultimate performance of the mechanical motion sensing system. It is planned to design a system similar to that being implemented for the NSLS-II project, which will employ silicon-controlled rectifier (SCR)-controlled electric reheat coils to fine tune and further stabilize supply air temperatures. The performance of the NSLS-II system will be closely monitored as that system is commissioned.

Recent measurements indicate that rf BPM pickup electrode assemblies mounted on small-aperture insertion device vacuum chambers move at the scale of tens of microns per °F of vacuum chamber water temperature change [3.3-16]. The specification for water temperature is 2 °F pk-pk; however, present typical performance is at the level of 0.2 °F pk-pk. This implies micron-scale motions of the vacuum chamber, exceeding the budget for long-term beam motion listed in Table 3.3-3. A new requirement placing a hard limit of 0.1 °F pk-pk on vacuum-chamber water-temperature regulation will

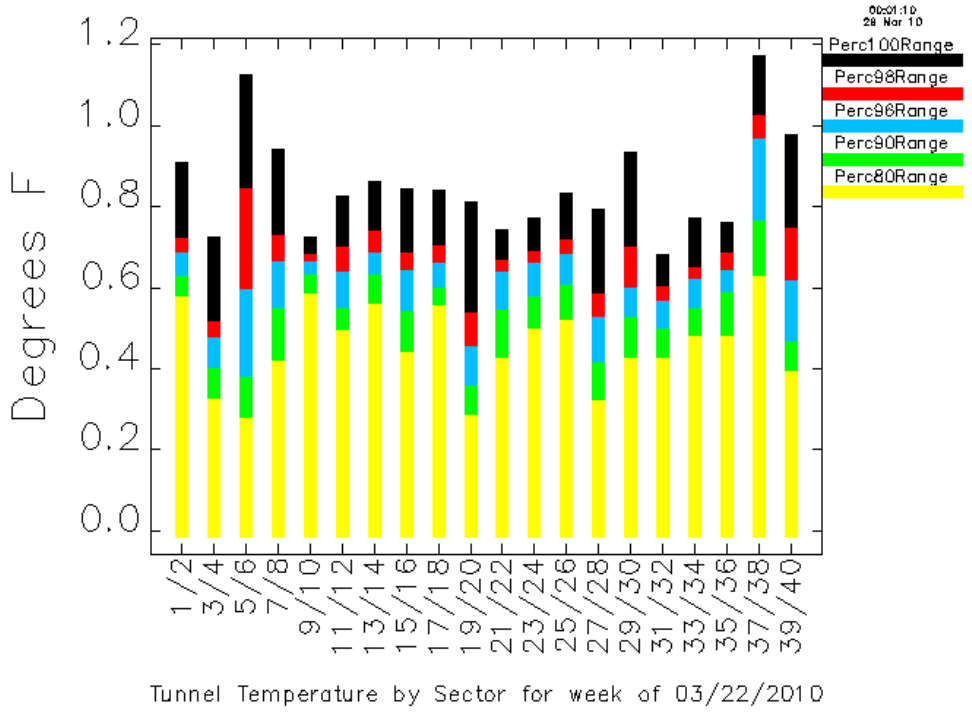

Figure 3.3-7. Statistical data showing ranges of APS tunnel air temperature excursions over a one-week time period.

reduce mechanical motion to the level of a few microns. Residual motions will need to be corrected using the mechanical motion-sensing system.

While tunnel air and water temperature variation place fundamental limits on the ability to stabilize long-term drift, of perhaps equal importance is the temperature stability of the electronics racks within which the sensitive beam position monitor electronics are located. Modern designs are relatively resistant to temperature variation, however even high-quality electronics performance has been demonstrated to improve when placed in temperature-regulated electronics racks, as is being done at NSLS-II [3.3-17]. A substantial amount of work will be required to assess the relative costs and benefits of incremental improvements to tunnel air, water, and rack air temperature regulation.

Finally, should temperature improvements be deferred, work with the mechanical motion monitoring systems is expected to improve long-term drift significantly.

3.3.9 Dependencies on Programmatic Work

There are a number of on-going projects at various degrees of completion being executed with programmatic funds that directly or indirectly impact the attainment of ultimate beam-stability goals. These include:

- Monopulse BPM data-acquisition system upgrade
- X-ray BPM first article
- Storage ring vacuum-chamber microwave mode dampers
- Storage ring corrector power-supply regulator upgrade
- Additional fast-steering corrector magnets

3.3.9.1 Monopulse BPM Data Acquisition System Upgrade

An AIP project was started c. 2005 to upgrade the data-acquisition portion of the aging broadband monopulse rf BPM system. To that end, a fast-sampling FPGA data-acquisition board, the BSP-100, was developed. As of May 2011, eight APS sectors had been upgraded with this new hardware, with hardware in hand for an additional 10 sectors. Provided sufficient funds become available, production of all hardware can be completed for the entire APS storage ring prior to major APS upgrade installation activities. Since some in-scope BPM electronics is envisioned to use the BSP-100 module, installation and checkout can be integrated in a straight-forward fashion between ongoing electronics upgrades and the new APS-U project scope.

While a partial monopulse system upgrade could in principle be made compatible with the new APS-U hardware without severe impact on ultimate AC beam stability, it would clearly be beneficial to have the ongoing work completed in a timely fashion, to avoid obvious inefficiencies.

3.3.9.2 X-ray BPM first article

A first article grazing-incidence x-ray BPM based on x-ray fluorescence is being constructed using programmatic funding for testing in late CY2011. The success of this test will add confidence in the design methodology and provide an improved basis for cost estimation. This project in addition will help in the identification of cost-saving strategies for the production units planned for the APS upgrade.

3.3.9.3 Storage Ring Vacuum Chamber Microwave Mode Dampers

A long-standing problem associated with the large-aperture APS storage ring vacuum chambers is a spurious microwave mode that mimics vertical beam position signals. Specifically this mode has a vertical component of electric field at the location of the BPM pickup electrodes and has a frequency that falls within the processing bandwidth of the monopulse BPM front-end electronics. A solution involving the insertion of conductive microwave gasket material into the chambers has been arrived at and installed in Sector 29. The impact of not completing this work for the whole ring will be that the affected sectors will have a reduced number of reliable beam position monitors. In any case, with the proposed BPM electronics upgrades, there will be adequate coverage to provide the desired improvements in beam stability. In addition, the presence of photon BPMs in the bending magnet beamlines provide high-quality vertical position information. This work will be completed as funding becomes available in coordination with other types of vacuum work on the large-aperture chambers as it is scheduled.

3.3.9.4 Storage Ring Corrector Power Supply Regulator Upgrade

Work is ongoing in the development of a new digital regulator for the storage ring steering corrector power supplies and hardware that interfaces to them from the outside world (specifically, from the real time feedback system). As things stand, a pair of fiber optics are run to each and every steering magnet power supply to directly its digital-to-analog converter. Once the signal arrives, there are certain time delay penalties associated with up/down counters, at the scale of tens of microseconds, before the power-supply output current begins to change. As a result, if the power-supply regulator work is not completed, it will impact the ultimately achievable closed-loop bandwidth of the real-time feedback system, however there is good reason to think that 200 Hz should still be achievable. This eventuality is also rather displeasing aesthetically, since a proper digital interface using modern components could simplify the fiber plant substantially and therefore improve reliability.

3.3.9.5 Additional Fast Steering Corrector Magnets

The 38 existing fast corrector magnets are mounted on steel spool pieces located between girders 1 and 2 in each sector. (Each APS sector comprises five girders plus an insertion device straight section). By relocating an existing slow corrector magnet downstream by one meter to the spool piece between girders 3 and 4, it will be possible to nearly double the number of available fast correctors with minimal cost. This has already been done in three sectors, with additional sectors funded. Completion of this task will improve the efficiency of the new real-time feedback system, allowing the suppression of orbit disturbances with shorter spatial wavelengths.

3.3.10 References

[3.3-1] J. Carwardine et al. Five-year plan for APS beam stabilization, (2005). https://icmsdocs.aps.anl.gov/docs/groups/aps/documents/report/aps_1192147.pdf.

[3.3-2] C. Schwartz and L. Emery. Compensating the Frequency Deadband of the APS Real-Time and DC Transverse Orbit Correction Systems, Proc. of PAC 2001, pp. 1234–1236, (2001); http://www.JACoW.org.

[3.3-3] O. Singh. Characterization of APS Real-Time Feedback, (2007). http://www.bnl.gov/nsls2/workshops/Stability_Wshop_4-18-07.asp.

[3.3-4] O. Singh and G. Decker. Beam Stability at the Advanced Photon Source, Proc.of PAC 2001, pp. 3268–3270, (2001); http://www.JACoW.org.

[3.3-5] H. Bui et al. Performance of FPGA-Based Data Acquisition for the APS Broadband Beam Position Monitor System, Proc. of BIW 2008, pp. 80–84, (2001); http://www.JACoW.org.

[3.3-6] G. Rehm. Recent Development of Diagnostics on 3rd Generation Light Sources, Proc.of EPAC 1908, pp. 1016–1020, (2008); http://www.JACoW.org.

[3.3-7] K. Vetter et al. NSLS-II Beam Position Monitor, Proc.of BIW 2010, (2010); http://www.JACoW.org.

[3.3-8] B.X.Yang et al. High-power Hard X-ray Beam Position Monitor Development at the APS, Proc. of BIW 2010, pp. 1000–1001, (2001); http://www.JACoW.org.

[3.3-9] G. Decker et al. APS Beam Stability Studies at the 100-Nanoradian Level, Proc. of BIW 2010, (2010); http://www.JACoW.org.

[3.3-10] G. Decker et al. Progress Toward a Hard X-ray Insertion Device Beam Position Monitor at the Advanced Photon Source, Proc. of PAC 2007, pp. 4342–4344, (2007); http://www.JACoW.org.

[3.3-11] S. Lee et al. Development of a Grazing-Incidence Insertion Device X-ray Beam Position Monitor at the APS, Proceedings of the 6th International Conference on Mechanical Engineering Design of Synchrotron Radiation Equipment and Instrumentation (MEDSI-6), (2010); http://www.JACoW.org.

[3.3-12] J. Carwardine and F. Lenkszus. Real-Time Orbit Feedback and the APS, BIW98, AIP Conference Proceedings 451, pp. 125–144, (1998); http://www.JACoW.org.

[3.3-13] J. Corbett et al. Digital Orbit Feedback Compensation for SPEAR, Proc. of PAC 1995, p. 2714, (1996); http://www.JACoW.org.

[3.3-14] Simulink by MathWorks. http://www.mathworks.com/products/simulink.

[3.3-15] V. Shiltsev and J. Lach. VLHC/NLC Slow Ground Motion Studies in Illinois, Proc. of PAC 2001, pp. 1470–1472, (2001); http://www.JACoW.org.

[3.3-16] R. Lill et al. Studies of APS storage Ring Vacuum Chamber Thermal Mechanical Effects and their Impact on Beam Stability, Proc. of BIW 2010, p. 1500, (2010); http://www.JACoW.org.

[3.3-17] O. Singh. BNL, Private communication, (2011).

3.4 Insertion Devices [U1.03.04]

3.4.1 Introduction

As described in section 3.1.2, providing higher flux and brightness in the hard x-ray regime, particularly at energies above 10 keV, is a significant aspect of the upgrade mission. The APS is a third-generation light source, so the highest flux and brightness come from insertion devices (IDs). As described below, many existing IDs at the APS are general-purpose devices that are not optimized for particular experiments.

Hence, an important aspect of the upgrade is to provide tailored devices that will maximize performance at the wavelengths of interest to particular experimental programs. In some cases, multiple devices, each with a different period, are indicated, which may be served by a canted configuration (section 3.4.7.2), long straight section (section 3.2), and/or a revolver ID (section 3.4.3.5). Beyond these approaches, which utilize conventional hybrid permanent magnet devices, we will develop and deliver three short-period superconducting undulators, as described in section 3.4.6. These are a key technology for enhancing brightness above 25 keV while maintaining other operating characteristics of the APS, such as the maximum single-bunch current.

Table 3.4-1. Summary of Undulator Types.

Type	Status	Special Features	Number for Upgrade
Planar hybrid permanent magnet (HPM), out-of-vacuum	Many in use at APS	Established technology	5
Planar revolver HPM, out-of-vacuum	In use elsewhere	Selection of periods	6
Superconducting planar	APS-U R&D development	Higher brightness, short period	3
APPLE	In use elsewhere	Polarization control, harmonic suppression, on-axis heat load suppression	1
EMVPU (Electromagnetic variably polarizing undulator)	New (to be developed as part of APS-U)	Polarization control, fast switching	1

There are many technological options for producing synchrotron radiation, allowing the radiation to be tailored to user requirements to a considerable degree. In the following subsections, we discuss those options that are included as part of the upgrade. Table 3.4-1 summarizes the basic device types, their status, and their applicability. At present, the quantities of new types of devices that will be part of the upgrade scope are known. In many cases, the period lengths are also known. For a few cases, the final period length has been set tentatively but may in the future be optimized based on the needs of the individual beamlines and globally to control cost.

Below is an overview of existing devices at APS, including their properties and some of their limitations. Following that is a description of the devices planned as a part of the upgrade, including conventional planar undulators, polarizing undulators, and superconducting planar undulators. There is no in-vacuum undulator included in the upgrade, and the reason for this is explained. Accelerator physics requirements and issues related to insertion devices are reviewed. Finally, plans for improved instrumentation to monitor and understand radiation damage to undulators are described.

3.4.2 Existing Devices

When the APS was originally built and undulators were being chosen for the beamlines, the decision was made to standardize on the 3.3-cm-period Undulator A. Undulator A would be tunable to produce a spectrum of radiation with neither big jumps in brightness nor gaps in the achievable photon energy and so would satisfy most users no matter what specific photon energy they might want. Standardizing on one type of undulator also allowed production efficiencies that lowered the cost per undulator and sped up the rate of undulator deliveries. A few users decided that they would be better served by a different period length (e.g., 2.7 cm or 5.5 cm) or type of undulator (e.g., an elliptical

wiggler, which has since been removed), but most chose Undulator A.

Since then, more focused consideration of individual users' experimental needs has resulted in a greater variety of insertion devices. Table 3.4-2 shows the variety of insertion devices presently installed.

Table 3.4-2. Breakdown of the 47 Presently Installed IDs. Device length includes the ends — approximately one period at each end is less than full field strength. The K value is at 10.5-mm gap unless stated otherwise.

Period length	**Number**	**Length (periods)**	$\mathbf{K_{eff}}$
33-mm (Undulator A)	26	72	2.74
33-mm	6	62	2.74
18-mm	1	198	0.46
23-mm	3	103	1.17[a]
27-mm	3	88	1.78
30-mm	2	79	2.20
30-mm	3	69	2.20
35-mm (SmCo)	1	67.5	3.08[b]
55-mm	1	43	6.57
128-mm (Circularly Polarized Und.)	1	16	$K_{x,y} < 2.8$

Gap set to: [a] 10.6 mm, [b] 9.5 mm.

The result of the early standardization on the 3.3-cm-period Undulator A is clear in that a total of 32 Undulators A are installed, of various lengths. In addition, a few as-yet-uninstalled Undulators A are on hand, waiting until beamlines whose users have requested another Undulator A are ready for them. Of the other devices, the shorter period lengths were chosen for higher brightness, especially at higher photon energies. This higher brightness came at the cost of the low-energy end of the tuning range, however. Longer period lengths were chosen to make even lower photon energies available.

The 3.5-cm-period undulator was made of SmCo magnets because of their better radiation resistance. That undulator is installed in the sector with the small-aperture ID vacuum chamber that serves as the effective scraper for the ring; the Undulator A previously installed in that sector suffered from an unmanageably high radiation damage rate.

The all-electromagnetic circularly-polarized undulator (CPU) has the added capability of producing different polarizations — left- or right-handed circular, or vertical or horizontal linear polarization — depending on the need of the user experiment. It can switch rapidly between the two circular polarizations, so that more sensitive difference measurements can reveal magnetic states of the sample. It can also go to lower photon energies.

The 1.8-cm-period undulator is a special-purpose device that delivers essentially a single photon energy (and its harmonics) with effectively no tuning range.

Tuning curves for these devices are shown in Figure 3.4-1. Note that, in general, devices with periods shorter than 3.3 cm deliver increasing brightness for 10 keV and above. However, as the period is reduced, gaps appear in the tuning curve. In addition, for sufficiently short periods, the device does not produce sufficient magnetic field to reach the $K \approx 1$ region needed for maximized brightness. (This

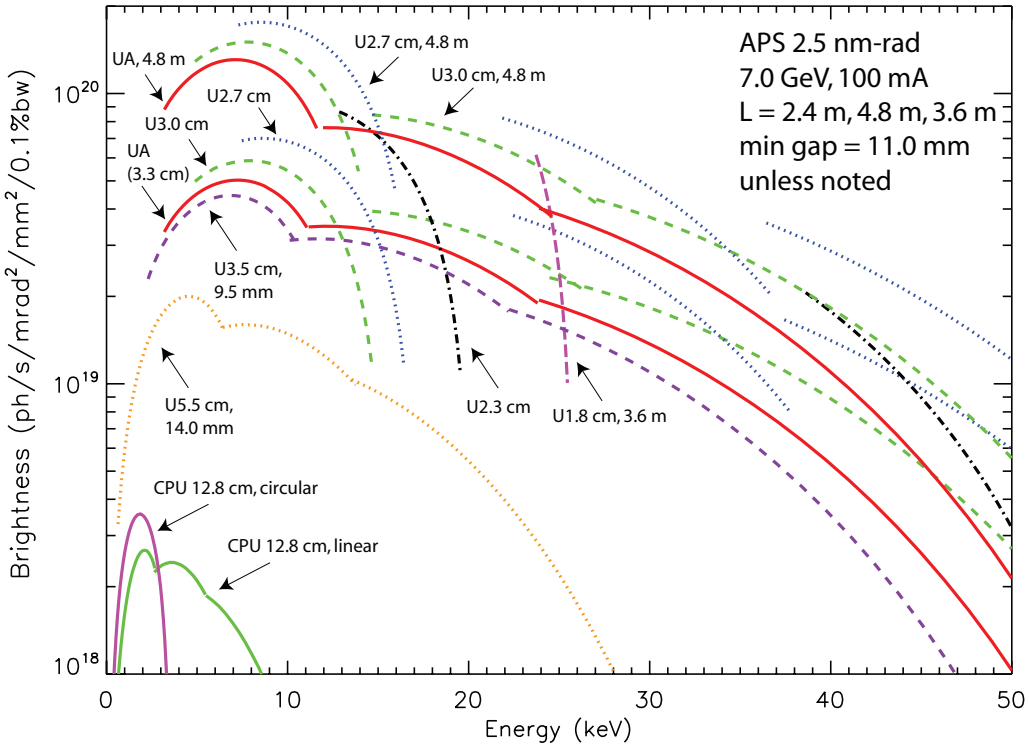

Figure 3.4-1. Tuning curves for the insertion devices presently installed in the storage ring. Different undulator lengths are shown where there are sectors with two in-line undulators installed. All undulators are 2.4-m long unless otherwise noted.

is particularly evident for the 1.8-cm-period device.) As we will argue in sections 3.4.3 and 3.4.6, in the context of APS operations, the use of superconducting technology addresses this issue more effectively than other options, allowing us to deliver on the bright promise of short-period devices.

In addition to these existing undulators, there is another type of undulator that is presently under construction for the Intermediate Energy X-ray (IEX) beamline. It is an all-electromagnetic, 12.5-cm-period undulator that will have a quasiperiodic capability. More information about it is given in section 3.4.4.

3.4.3 Conventional Planar Devices [U1.03.04.01]

3.4.3.1 Basic Properties

Nearly all of the insertion devices installed at the APS are conventional planar undulators, as can be seen in Table 3.4-2 above. The magnetic field of the undulator on axis is vertical, the wiggle of the electron beam is horizontal, and the photons that are produced are horizontally linear polarized, at least on axis. The magnetic field is produced by NdFeB permanent magnets in all of the planar devices (except for the single SmCo-based undulator) with poles between the magnets. The poles are made

of vanadium permendur (nominally 2% vanadium, 49% Fe, 49% Co), chosen because it has a higher magnetic permeability than iron when it is properly handled and annealed, leading to a higher on-axis undulator field. This called a hybrid permanent magnet design.

When assembled, the magnetization of the magnet blocks is parallel to the beam axis, with two adjacent magnets being magnetized in opposite directions; the poles between the magnets focus the magnetic flux across the gap. An advantage of this type of design is that the permanent magnet blocks can be sorted so the inevitable variation in magnetic moments between the blocks is averaged somewhat to even out the on-axis variation in magnetic field strength. This is the first step in magnetic tuning.

Occasionally interest is expressed in a planar undulator that produces vertical linear polarization, which would require a horizontal planar magnetic field. A planar horizontal field is impractical for a simple conventional planar undulator intended for a storage ring. As discussed in section 3.2.2, relatively large horizontal acceptance is required for injection, so the insertion device vacuum chamber must be wide, increasing the minimum magnetic gap. The magnetic field strength needed for a reasonable tuning range then becomes out of reach. More complicated pole configurations are possible and are used in circularly polarizing undulators where there is no other choice (see section 3.4.4), but the achievable field strength is still less.

3.4.3.2 Choice of Device Parameters

The important characteristics of planar undulators for users are the period length of the magnetic field and the maximum achievable strength of the field on the beam axis. In general, a shorter period length means the maximum photon brightness will be higher and will occur at a higher photon energy. This trend can be seen in Figure 3.4-2, which shows the tuning curves for the planar undulators presently installed at APS, assuming the same beam characteristics and the same overall undulator length. The first, third, and fifth harmonics are shown when they are within the range of the graph. Higher harmonics will also be present in the undulator spectrum but they are not included in the figure. The tuning ranges shown are those that are met by the installed undulators.

As discussed briefly in the introduction to this section, there is a tradeoff in shortening the period length in order to increase the brightness, in that the shorter the period length, the weaker the on-axis field of the undulator (at the same gap). The highest field strength that the undulator can produce on-axis, which is at the smallest gap permitted for the undulator, determines the lowest photon energy that can be reached. The implication of this, and the tradeoff, can be seen in the figure as the gaps between the first and third harmonics for period lengths shorter than 3.0 cm. For the 2.7-cm period undulator, there is a gap between about 16.5 keV and 22.5 keV that is not covered by either the 1st or 3rd harmonic. Even with the 3.0-cm-period undulator where there is continuous tunability between the first and third harmonics, there is a discontinuity in brightness slightly below 15 keV as the transition is made between harmonics. Some users find such a brightness discontinuity problematic, so they might prefer a slightly longer period length.

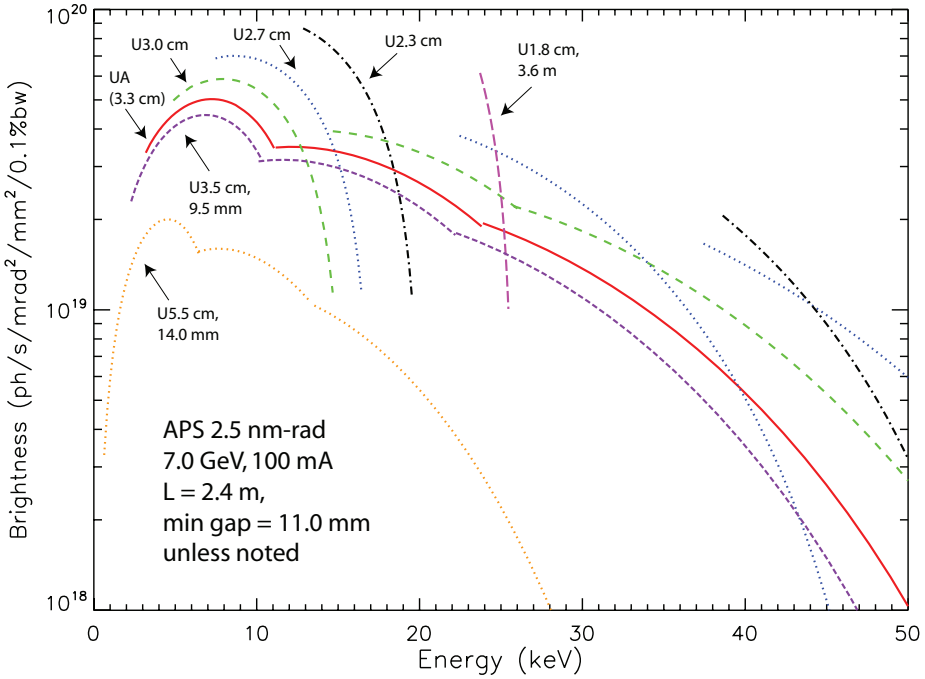

Figure 3.4-2. Tuning curves for undulators with a variety of different period lengths. The same overall magnetic length and beam parameters are assumed for each device to show the effect of just a change in period.

3.4.3.3 Power Load Considerations

The other consideration that must go into the choice of a period length is the power load from whatever undulators will be in the straight section and how that power will be distributed on the front end and beamline components. The total power and power density from planar undulators as a function of the first harmonic energy are shown in Figures 3.4-3 and 3.4-4. Note that even if it is the third (or higher) harmonic that is being used for experiments, the undulator is still producing the first and all other harmonics, and they are all contributing to the overall heat load.

Engineers will continue to work with individual beamlines in order to customize power handling for specific beamline and front-end configurations (see section 5.3). As a comparison point, though, the allowable limits for total power and on-axis power density from all the insertion devices that will be in simultaneous use in the straight section are 21 kW and 590 kW/mrad^2 for the highest-power installed front-end design. Recently, we have developed software for automatic optimization of ID choices, consistent with limits on power handling in the front ends. We have also developed a new concept for beamline operation that may significantly increase the power-handling capability. Both of these points are discussed in greater detail in section 3.4.8.

In the computations shown in Figure 3.4-3, a conservative minimum undulator gap of 10.5 mm is assumed for the variable-gap undulators. The ultimate limit is imposed by the outer dimension of the vacuum chamber. While 10.5 mm is in principle possible for the smallest ID vacuum chamber, it is not in general achievable. Additional information and a detailed table of the power and power density as a

function of gap for various planar IDs can be found in ref. [3.4-1].

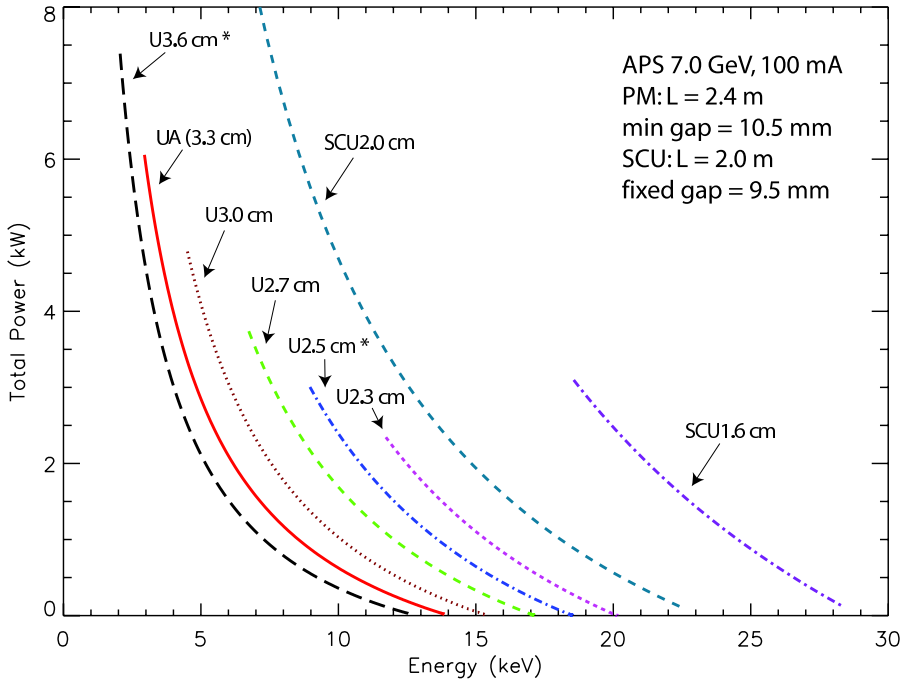

*Figure 3.4-3. Total power from different planar undulators plotted as a function of the first harmonic energy for a beam current of 100 mA. For the permanent-magnet undulators, a device length of 2.4 m and a minimum gap of 10.5 mm are assumed. Power densities for planar superconducting undulators are also included; for those, a magnetic length of 2.0 m is assumed. Neither the superconducting undulators nor the permanent-magnet undulators with a * have been built (yet), so the calculation is based on estimated magnetic fields.*

Note that the tuning curves given in Figures 3.4-2, 3.4-3, and 3.4-4 are relevant for undulators of a given period length independent of the technology used in the particular undulator. Using a technology that can produce a stronger magnetic field will not change the brightness or power for a given photon energy. What is gained by employing technologies that can produce a higher magnetic field is tuning range — the curves shown will extend to lower photon energies, with the minimum photon energy determined by the maximum field that is achievable.

3.4.3.4 Available Devices

New undulators with period lengths of 3.0, 2.7, and 2.3 cm can be readily provided to users, as these were designed and built at APS. The SmCo undulator is also an APS design. In addition, construction of a 3.6-cm-period undulator is presently underway, again to an APS design. There are a few as-yet uninstalled 3.3-cm-period undulators on hand at APS; it is anticipated that there are just enough to fulfill users' requests. Undulators with new period lengths that are not very different from the present undulators can be designed readily.

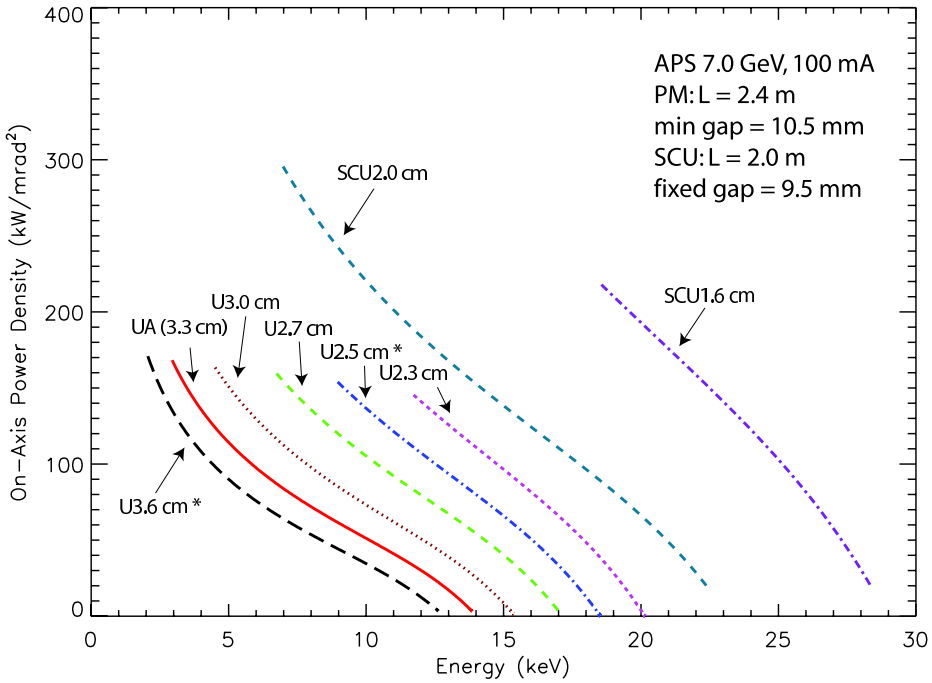

*Figure 3.4-4. On-axis power density from different planar undulators, as a function of the first harmonic energy for a beam current of 100 mA. For the permanent-magnet undulators, a device length of 2.4 m and a minimum gap of 10.5 mm is assumed. Power densities for planar superconducting undulators are also included; for those, a magnetic length of 2.0 m is assumed. Neither the superconducting undulators nor the permanent-magnet undulators with a * have been built (yet) so the calculation is based on estimated magnetic fields.*

While new period lengths can be designed and provided, issues can arise around the availability of spares. It is not financially feasible to keep spares for all devices when there are many different periods. The most common components to fail are the encoders, so a supply of replacement encoders is kept on hand.

Magnet blocks can become demagnetized as a result of radiation exposure, though this problem is less common now than in the past. For modest damage, we can taper the undulator, which works because of the pattern of the demagnetization. More significant damage requires removal of the undulator and, sometimes, replacement of damaged magnet blocks. For this reason, spare magnet blocks are kept on hand for each of the period lengths. If insufficient spares are available, magnets can be remagnetized, but disassembly, remagnetization, reassembly, and tuning requires more time than available in a normal shutdown. In such a case, we would install a spare Undulator A (or another available device) until the work is completed.

It may be helpful to users considering new period lengths to have some guidelines for what the expected minimum-gap field would be. A number of design studies in two dimensions were recently carried out for a variety of period lengths. A good fit for undulators using NdFeB magnets was found with the equation [3.4-2]

$$B_{\text{eff}}(\text{Tesla}) = 3.276e^{-4.51r+1.20r^2}, \tag{3.4-1}$$

where r is the ratio of the gap/period. This expression can be used with two caveats: 1) the three-dimensional (i.e., real-world) field is slightly lower than the 2-D calculation, possibly by 1%; and 2) various other real-world variables (e.g., construction tolerances, variation in pole heights that affect the accuracy and interpretation of a gap measurement, strength of as-delivered magnet blocks) result in a disagreement in the effective field between calculation and measurement of about 2%. More details of these estimates are given in ref. [3.4-3].

3.4.3.5 Revolver Undulators [U1.03.04.04]

A revolver-type undulator is another possibility for offering greater flexibility to a beamline. (See [3.4-4] and references therein, as well as [3.4-5].) A revolver undulator provides the user with the option to switch between two or more magnetic structures at will. Each structure can be optimized for a specific requirement or in order to cover a given spectral range with higher average brightness than would be possible with a single device.

In a revolver undulator, two or more magnetic structures of different period lengths are mounted together in a single undulator support. The upper and lower strongbacks both hold several magnet arrays, e.g., two arrays oriented at 90 degrees with respect to one another. The jaw revolves (at open gap) to select the desired magnet array, after which the gap may be closed so the selected period length is the one producing photons. Users can change between the two different period lengths as needed.

A preliminary analysis was conducted of the feasibility of revolver devices for APS. This revealed several challenges. The APS ID vacuum chambers and vacuum chamber supports are moderately bulky, as was needed to allow the present undulator gaps, and attention would be needed to ensure that the revolver stays clear of the chamber and supports. A special revolver strongback would be used instead of the present design and would require additional vertical space, so the achievable maximum gap might be limited to 150 mm. The present magnetic structure design has the magnets and poles mounted on a baseplate that is, in turn, mounted to the strongback. Mechanical shimming between the strongback and the baseplate is an important step in the magnetic tuning of the undulators. In a revolver, however, there would not be enough space for a baseplate, so magnetic tuning techniques would need adaptation.

As in the current devices, a minimum gap of 11 mm would still be achievable, so the individual magnetic arrays of a revolver would deliver comparable performance to a single undulator. Some aspects of the present undulator supports could also apply to specialized revolver supports, but many changes would be needed, including possible changes in materials. New constraints would be imposed. For instance, the less-rigid strongback would limit the magnetic structures to period lengths of 3.0 cm or less, and the overall undulator magnetic length would be limited to 2.4 m unless extensive design work is undertaken.

A preliminary cost estimate was undertaken based on the foregoing, assuming two hybrid permanent-magnet assemblies at 90-degree orientation, each having a length of 2.4 m. A rendering of a possible device is shown in Figure 3.4-5. We also assumed that the period of the devices was chosen to match an existing design (i.e., 2.3, 2.7, or 3.0 cm), with a minimum gap of 11 mm. Essentially the same gap-separation mechanism we currently employ is used, with extensive frame modifications. A unique strongback, possibly of stainless steel rather than aluminum, will be required. Existing magnet-assembly designs are used with the divider plates mounted either directly to the special revolver

strongback or to a full-length "baseplate," now more of a "mini-strongback." The existing discrete baseplates cannot be used as they consume scarce height without providing bending resistance, which has magnetic tuning implications. The gap control system will also require a redundant interlock that will inhibit gap motion while the revolver axis is moving.

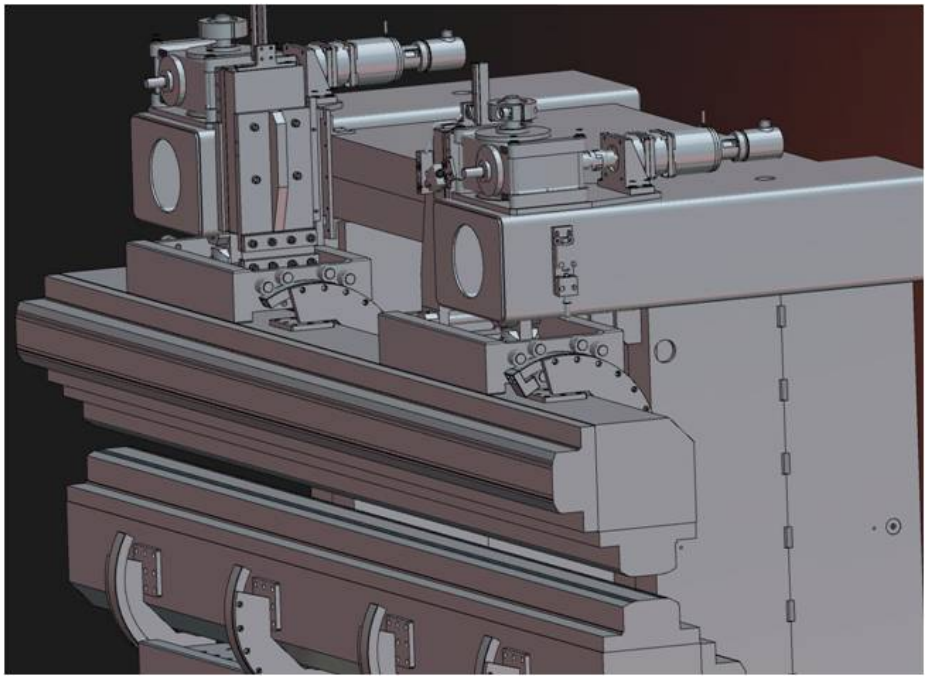

Figure 3.4-5. Rendering of a preliminary design concept for a two-period revolver undulator.

The ability to taper the gap of the magnetic structure is presently built into the gap separation mechanisms of the planar undulators. It will be retained in the revolver undulators, for two reasons. 1) Tapering proved to be essential with radiation-damaged undulators, when tapering the undulator gap was the first, and key, step for correcting for radiation damage. 2) Tapering an undulator results in changes in both the spatial and energy distributions of the photon beam produced. One APS beamline specifically requested the ability to broaden the spatial beam size in order to image a sample as large as a bug or a mouse heart. Calculations of the effect of tapering the undulator found, and measurements confirmed, that the desired spatial broadening can be achieved. While there is some associated loss in flux, it is at a level that is acceptable to the user. Details of the measurement and calculation will be published shortly [3.4-6].

There are of course possibilities for taking the design beyond the basis of this estimate. Use in a canted sector is possible but may require changes to existing canting magnets, supports, and vacuum chamber. Periods longer than 3.0 cm are possible but will require more costly frames and strongbacks.

Optimization of Revolvers Optimization of the periods on a revolver cannot take place without knowledge of the requirements of x-ray users, which have only recently been defined. However, we have developed a methodology and software for choosing revolver periods. This will be applied systematically to refine choices of revolver periods. The methodology is described in section 3.4.8.

Revolvers are well suited to providing highly tuned performance at a few energies, perhaps coupled with a broad, general-purpose capability. In addition, one can use two periods to provide better performance over a broad energy range than possible with a single period. By way of example, we consider two hypothetical cases, which demonstrate the value of both revolvers and the optimization technqiue.

1. Operation at 12.4 keV with broad tuning between 5 and 30 keV, shown in Fig. 3.4-6. The single-period optimization chooses a U30, which is a very versatile device. With a two-period optimization, a U24 is added, increasing performance at 12.4 keV by a factor of more than 2.
2. Operation with broad tuning between 40 and 100 keV, shown in Fig. 3.4-7. The single-period optimization chooses a U25. The two-period optimization adds a U26, significantly improving performance by filling in where the U25 performance falls off.

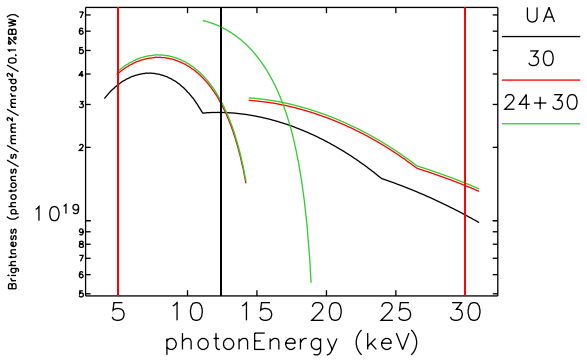

Figure 3.4-6. Comparison of optimized one- and two-period devices to a UA, assuming 2.1-m-long canted devices. The target energy bands were 12.4 keV and 5-30 keV, and are indicated by the vertical lines. The single-period 30-mm curve is offset slightly for visibility.

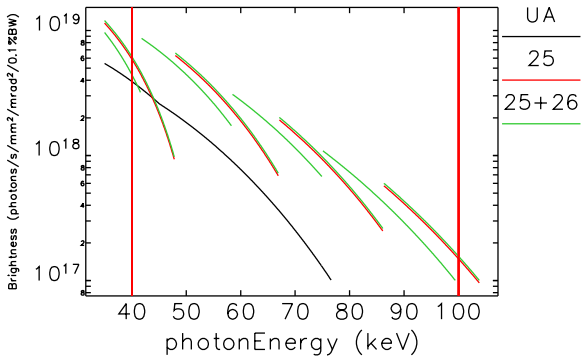

Figure 3.4-7. Comparison of optimized one- and two-period devices to a UA, assuming 2.1-m-long canted devices. The target energy band was 40.0 keV to 100 keV, as indicated by the vertical lines. The single-period 25-mm curve is offset slightly for visibility.

3.4.4 Devices for Polarized Radiation Production [U1.03.04.02]

3.4.4.1 Introduction

Nearly all of the presently installed insertion devices are conventional planar undulators. On the beam axis, they produce a magnetic field that is vertical and that varies in strength approximately sinusoidally along the axis. Off the beam axis, horizontal transverse and longitudinal field components begin to appear (and of course the inevitable field errors can introduce such small components on axis), but still the electrons travel through the undulator wiggle in the horizontal plane and produce horizontally linearly polarized photons.

Insertion devices can be built that produce both vertical and horizontal field components on axis. Often, the maxima in the horizontal field are midway between successive maxima in the vertical

field so that the field direction seen by the beam rotates along the length of the device. The resulting trajectory is no longer planar; if the magnitudes of the vertical and horizontal field components are the same, then the beam travels in a circular helix and produces circularly polarized photons. Circularly polarized light is often used in studies of magnetic properties of samples.

There are a number of alternatives available for producing polarized radiation. Those that are included in the upgrade project are an APPLE-type undulator and an electromagnetic variably-polarizing undulator (EMVPU) that can switch polarization rapidly. Their characteristics are discussed below. Following that is a brief description of the variably-polarizing undulator that is presently under construction for the IEX beamline. Although it is not part of the upgrade project, it is included here because its quasiperiodicity may be sought by other users in the longer-term future of APS.

3.4.4.2 Electromagnetic Variably Polarizing Undulator (EMVPU) [U1.03.04.02.01]

An undulator that is capable of producing variable polarization in the soft X-ray regime has been requested by a group of users for their magnetic studies. They want to be able to choose between left- and right-circular, and horizontal and vertical linear, polarization in an energy range below 2 keV. A minimum photon energy of 400 eV would offer access to the nitrogen edge at 409 eV. The optics for this beamline will be optimized at 800 eV after the upgrade.

A particular demand of the magnetic studies is the ability to switch between left- and right-circular polarization sufficiently rapidly that lock-in techniques can be employed. The request is for switching at 10 Hz; a switching speed below 5 Hz would not provide a sufficiently reliable XMCD signal given the users' present data-collection times. The circular polarizing undulator (CPU) [3.4-7] presently available to these users is only able to switch at 0.5 Hz.

Achieving such a high switching speed will require that the coils have both a low static resistance and a low reactive resistance. The EMVPU has not been designed yet, but it is anticipated that it may resemble the existing CPU. A cross-sectional view of the CPU magnetic structure is shown in Figure 3.4-8. The horizontal field component is produced by four poles. Two are shown in the figure; the other two are in symmetric positions below the axis. The vertical field is produced by two poles: the one shown in the figure and another in a symmetric position above the axis. The coils are large buss bars, to minimize the static resistance, and they follow a serpentine path among the poles, to minimize the inductive impedance. The CPU design will need revising, however, both to increase the switching speed and to decrease the minimum photon energy below its present 500 eV.

Experience with the CPU showed the importance of time-dependent corrections to the integrated field of the device. Feed-forward look-up tables were generated based on measured perturbation of the stored electron beam. An arbitrary function generator is used to provide time-dependent corrections.

3.4.4.3 APPLE (Advanced Planar Polarized Light Emitter) Undulator [U1.03.04.02.02]

Probably the most common variably polarizing type of undulator worldwide is the APPLE-style undulator. Though there are none at APS yet, some users have expressed interest in having an

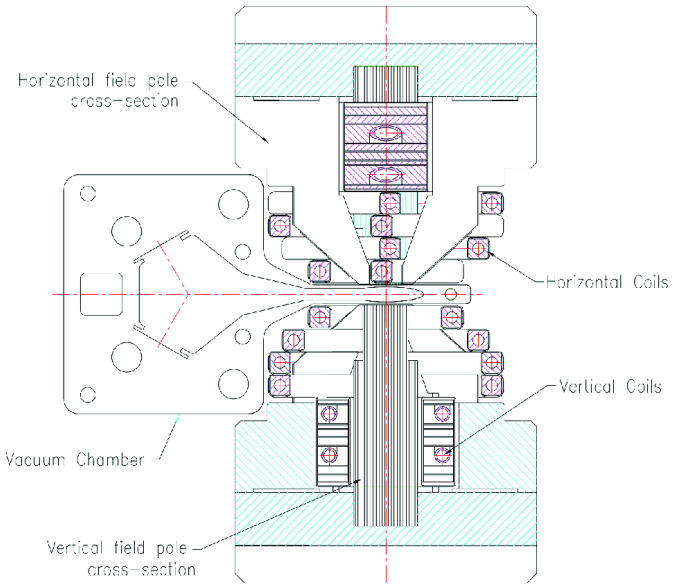

Figure 3.4-8. Cross section of the all-electromagnetic circularly polarizing undulator (CPU). The cross section through a vertical pole is shown in the lower half; the cross section through a horizontal pole is shown in the upper half. The assembled device is in reality symmetric top-to-bottom, with the vertical poles offset by a quarter-period in the beam direction from the horizontal poles. The CPU fits around a standard ID vacuum chamber.

APPLE-style device for their beamline, and one APPLE undulator is included in the scope of the upgrade. An APPLE undulator can be used when the period length of the desired undulator is too short to allow space for coils for an electromagnet. A sketch of the magnetic structure scheme is shown in Figure 3.4-9. Four arrays of permanent magnets are combined into two jaws — effectively, one jaw of a standard pure permanent magnet undulator is split in half longitudinally, with the split located immediately above (or below) the beam axis. The longitudinal arrays are then allowed to shift longitudinally with respect to one another. With one phase setting between the magnet arrays, it is a standard planar undulator. At another phase, the combined effect of the arrays produces circular polarization. The motion to change polarization is mechanical, so polarization changes are too slow for lock-in techniques. The gap of an APPLE undulator can also be changed, but since the vertical and horizontal field components change differently with gap, a longitudinal shift may be needed to preserve the polarization as the gap is changed.

There will be challenges in building and running an APPLE-style undulator. Mechanical design and construction are complicated by the magnetic forces between the jaws that change depending on the phase of the longitudinal shift. These forces can be particularly strong because the magnet arrays are so close to one another. The holders for the magnets can be made more robust but still need to fit around a vacuum chamber. An APPLE-style undulator provides challenges as well for stored beam control. The magnetic field at the position of the beam is not uniform in space, so it contributes to effects on the stored beam. The attention of accelerator specialists will be needed to ensure that changes in the settings of the APPLE do not affect the beam seen at other beamlines. These challenges have been met successfully at other storage rings, including many with electron beams that are less stiff than at APS,

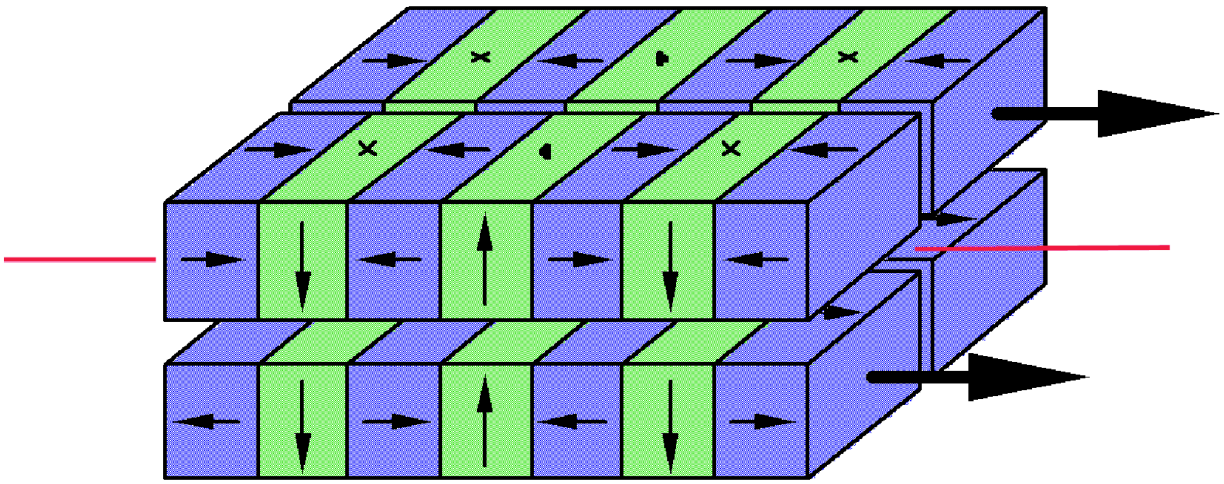

Figure 3.4-9. Magnetic structure scheme for an APPLE-style undulator. The red line represents the electron beam. The magnetic arrays can be shifted longitudinally with respect to one another to change the polarization.

however.

The use of APPLE undulators worldwide, especially at lower-energy rings, is so common today that several companies successfully produce APPLE undulators commercially. Since only one APPLE is included in the scope of the upgrade, we expect that we will purchase the device rather than attempt to develop a design ourselves.

3.4.4.4 IEX Undulator and Quasi-periodicity

Another undulator with variable polarization is under development outside of the APS upgrade for the intermediate energy x-ray (IEX) beamline. Although this is outside the upgrade, we cover it for completeness. “Intermediate” energy in this case is actually quite low for the APS: the undulator will be able to go as low as 0.25 keV in horizontal linear mode and as low as 0.44 keV in vertical linear or circular polarization mode. The more restrictive tuning range, when there is a vertical component to the electron motion, is due to the opening angle of the radiation output. A section of vacuum chamber downstream does not have high enough vertical clearance to avoid an unacceptable risk of overheating the chamber. At 12.5 cm, the period of this undulator is long enough that it can be all electromagnetic.

An advantage of an all electromagnetic undulator is that it can readily be made variably quasi-periodic. A few of the coils will be wired and powered separately from the rest. When those coils are operated at the same current as the rest, the device will be a standard periodic undulator. They can, however, be operated at a different current. The quasiperiodic poles will be chosen to be spaced apart by 6 or 7 poles, and the poles will come in pairs so there is no net steering of the electron beam.

The advantage of such a device can be seen in Figures 3.4-10 and 3.4-11. While the errors being introduced in the undulator field cause, not surprisingly, a decrease in the height of the first harmonic peak, they also cause the higher harmonics to shift in energy. With the downstream

monochromator set to transmit the first harmonic photon energy and its multiples, the shifted harmonics will be stopped. The effect is particularly noticeable in linear polarization mode, Figure 3.4-10, but also has an effect on the on-axis flux in circular mode, as can be seen in Figure 3.4-11. The decrease in current for the quasi-periodic poles can be made user-adjustable to allow the tradeoff between photon loss in the first harmonic and the reduction in higher-harmonic contamination to be optimized. Note that this quasi-period scheme does not give any reduction in power load hitting the monochromator.

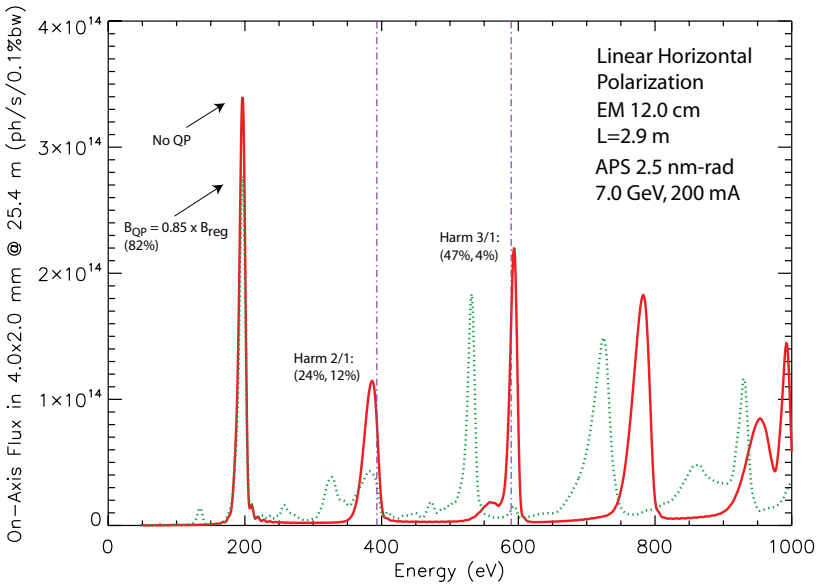

Figure 3.4-10. Effect of quasi-periodicity on the spectrum in linear polarization mode. The vertical lines mark the positions of integer multiples of the first harmonic. With quasi-periodicity turned on, the higher harmonics shift to lower energies.

3.4.5 In-Vacuum Undulators

At present, all APS undulators are out-of-vacuum. There is no plan to develop or acquire in-vacuum undulators as part of the upgrade. The explanation for this choice follows.

An out-of-vacuum undulator requires a vacuum chamber in the gap of the device, and means that the undulator magnetic gap will be considerably larger than the beam aperture. For a vertical beam aperture of 8 mm, the minimum undulator magnetic gap is generally 11 mm. Putting the undulator magnetic structure inside the vacuum chamber, however, allows a smaller magnetic gap. Such devices have been installed at other light sources, and technical challenges — such as providing a smooth conducting surface to reduce electron-beam impedance and the need to bake out in-vacuum components, including magnets that are susceptible to thermally induced demagnetization — have been met.

In light of this, it is natural to ask what might be achieved at APS with such devices. The critical issue [3.4-8] is maintaining the same beam impedance as those of out-of-vacuum undulator chambers to allow 16-mA operation in hybrid mode and 150-mA operation in 24-bunch mode. Since

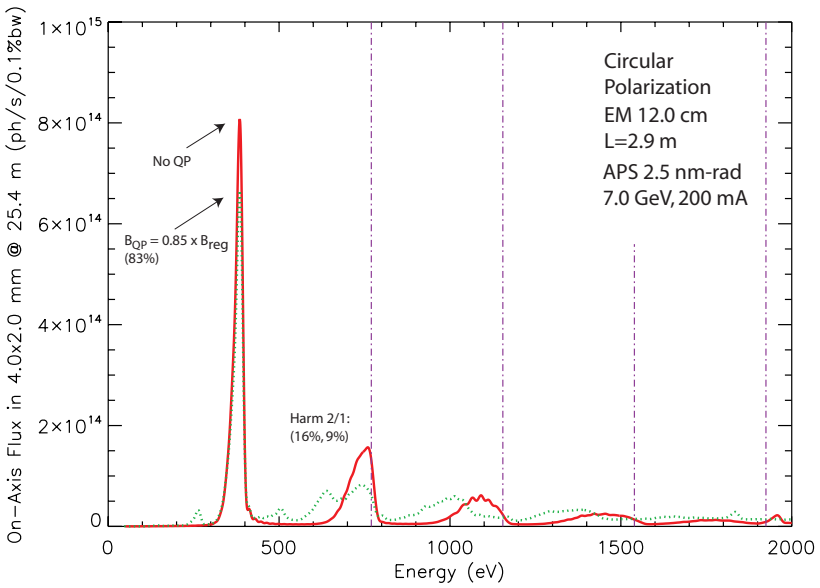

Figure 3.4-11. Effect of quasi-periodicity on the spectrum for circular polarization. The vertical lines mark the positions of integer multiples of the first harmonic. Although the harmonics start out with a lower flux rate than in the linear case shown in Figure 3.4-10, quasi-periodicity can still help reduce the harmonics further.

the IVUs require a movable taper of higher impedance than that of fixed taper, the required beam-stay-clear gap for an IVU is 8.75 mm or greater in order to ensure that the impedance does not increase relative to a standard APS chamber. With this constraint, the performance of IVUs is not much different than existing out-of-vacuum devices [3.4-3].

It is partly because of this issue that the APS upgrade is pursuing the use of superconducting undulators (SCUs), which offer superior performance to IVUs without increasing the impedance. However, if SCUs prove unworkable for some reason, we might wish to reconsider IVUs in a few locations. To support a beam stay clear of 7 mm in an IVU while still allowing 16 mA hybrid mode, it will be necessary to modify the straight section to control the impedance. Referring to the long-straight-section work on mitigating the increased impedance effect in section 3.2.4, we could combine a long 55-cm transition (Figure 3.2-28) with a movable taper having a much smaller maximum gap of 12 mm. Since the new movable taper will be of smaller slope and horizontal aperture, the combined impedance would be reduced to that of an 8-mm-gap fixed taper. However, R&D would be required to separate the conductive liner from the IVU when opening the magnetic gap past 12 mm. Though it would seem that an IVU could be installed without increasing the impedance, certainly the cost of an IVU will increase significantly due to the fabrication and installation of a new chamber with a long transition.

Another way to mitigate the impedance issue absent a combination taper design is to lengthen the bunch, either with a dedicated bunch-lengthening cavity or a full complement of (i.e., 16) deflecting cavities in the SPX system (see section 3.5.4.3). However, we have elected not to pursue this possibility, for four reasons. First, we do not intend to install the full complement of deflecting cavities as part of the upgrade, so the effect on bunch length or instability threshold is diminished. Further, installation of dedicated bunch-lengthening cavities is outside the scope of the upgrade. Second, we do

not wish to link the success of one upgrade (insertion devices) to the implementation of another (SPX). Third, in light of the mission need to better serve timing studies, a better use of a lengthened bunch would be to operate at even higher single-bunch current, which requires careful preservation of the transverse impedance. Finally, the potential benefit for APS from IVUs is less than the expected benefit from superconducting devices.

3.4.6 Superconducting Undulator [U1.03.04.03]

3.4.6.1 Introduction

A superconducting undulator (SCU) employs a set of superconducting coils to generate a periodic magnetic field. Due to the high current-carrying capacity of superconductors, magnetic flux densities near 1 T can be reached despite undulator period lengths as short as 1.5 to 2.0 cm. (In a conventional permanent magnet or hybrid device, reaching a 1-T field would typically require a period length closer to 3 cm.) Such short-period undulators are becoming very attractive because they produce high brightness at higher photon energies. According to our detailed analysis of various undulator types, including conventional hybrid technology and in-vacuum permanent magnet technology [3.4-9], superconducting undulators should outperform all other technologies in terms of peak magnetic field for a given period length and magnetic gap, as illustrated by Figures 3.4-12 and 3.4-13. Hence, superconducting undulators are the preferred method of satisfying the mission need to produce brighter x-rays at 25 keV and beyond.

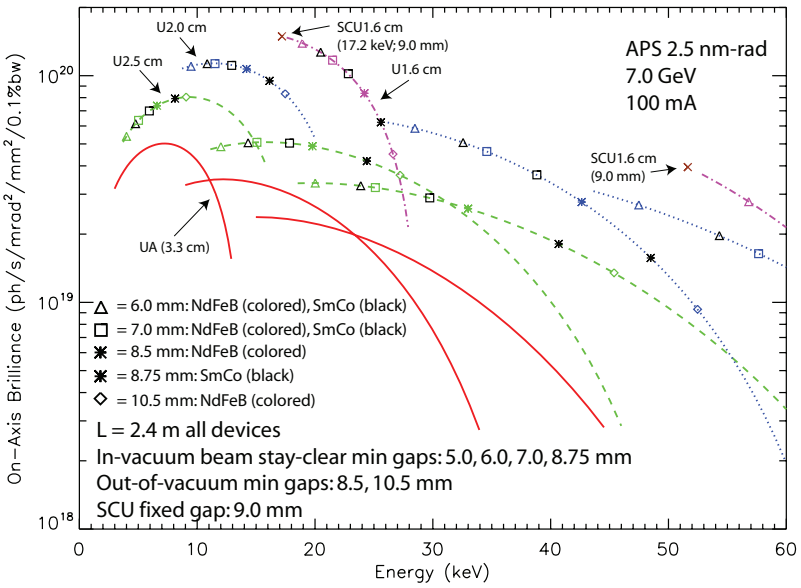

Figure 3.4-12. Comparison of the brightness from undulators with various period lengths, including hybrid permanent magnet undulators and a superconducting undulator with a 16-mm period. Beam parameters are for the present APS. See text for further explanation.

On-axis brilliance tuning curves for three in-vacuum undulators (1.6-cm, 2.0-cm, and 2.5-cm periods, each 2.4-m long) compared to the APS Undulator A for harmonics 1, 3, and 5 in linear

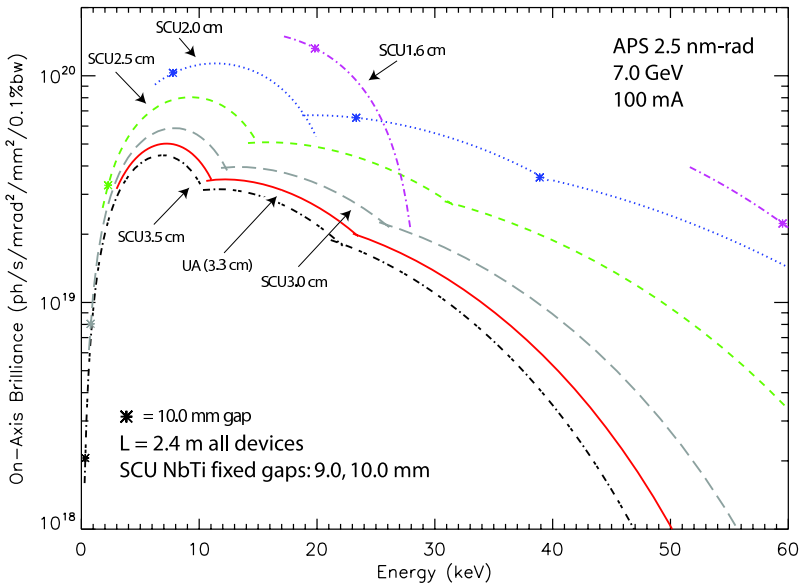

Figure 3.4-13. Comparison of the brightness from superconducting undulators with various periods. Beam parameters are for the present APS.

horizontal polarization mode for 7-GeV beam energy and 100-mA beam current are shown in Figure 3.4-12. The minimum reachable harmonic energies were calculated for in-vacuum undulators assuming SmCo magnets and a 5-mm beam stay-clear gap. For comparison, the data for a 1.6-cm superconducting undulator at 9-mm pole gap have been marked separately by the two crosses. As is seen from Figure 3.4-12, the 9-mm gap SCU at the first-harmonic energy of 17.2 keV nearly overlaps with the 5-mm gap in-vacuum SmCo undulator. A magnetic gap as small as 5 mm is impractical for the APS storage ring, while the 9-mm gap of the SCU allows enough room for a beam chamber. This issue is particularly important given the strong desire to continue to run with high single-bunch current, e.g., in hybrid mode (see sections 3.4.5 and 3.2.4).

In principle, superconducting undulators could be built with different period lengths. The on-axis brilliance tuning curves with the overlaps between harmonics removed for five superconducting undulators (1.6-cm, 2-cm, 2.5-cm, 3-cm, and 3.5-cm periods, each 2.4-m long) compared to Undulator A for harmonics 1, 3, and 5 in linear horizontal polarization mode for 7-GeV beam energy and 100-mA beam current are shown in Figure 3.4-13. The minimum reachable harmonic energies were calculated assuming a 9-mm magnetic pole gap. As in the previous example, ideal magnetic fields were assumed for the calculations. It should be noted that a variety of undulator types could be built with superconducting technology including planar, helical, and even a quasi-periodic device [3.4-10] that provides a nearly monochromatic photon flux.

(In these illustrations, we've assumed identical magnetic lengths for all devices, whereas in reality the SCU would have shorter magnetic length for the same available length due to the cryostat and cryogenic transitions. The case for the SCU performance advantage is presented more rigorously in section 3.4.8.)

3.4.6.2 Worldwide Status

The advantage of applying superconducting technology to undulators has long been recognized by both high-energy physicists and the synchrotron light source community. A superconducting helical undulator was developed at Stanford for the very first free-electron laser experiment in the 1970s [3.4-11]. In the 1980s, the use of such undulators for positron sources in high-energy physics was suggested, and the idea was demonstrated at Budker Institute, Russia [3.4-12]. Recently, a 4-m superconducting helical undulator module was built at the Rutherford Appleton Laboratory, UK, for the International Linear Collider positron source R&D program [3.4-13]. In Europe, a superconducting planar undulator built by ACCEL is in operation at the ANKA light source in Germany [3.4-14], and another device for ANKA is being built by Babcock Noell GmbH [3.4-15]. In Asia, R&D on a superconducting undulator is underway at the National Synchrotron Radiation Research Center, Taiwan [3.4-16]. As far as we are aware, there are no superconducting undulators currently in operation in the U.S.

3.4.6.3 Feasibility Study at the APS

Since there are no commercial vendors of superconducting undulators in the world except possibly a single company in Germany, an in-house R&D program was started at the APS to develop superconducting undulators. In 2008-09 our activity was focused on developing construction techniques. This phase involved magnetic modeling, developing manufacturing techniques, building, and testing short prototype magnets.

Magnetic simulation of the superconducting undulator was performed using the 2D and 3D OPERA software packages. The issues addressed were the field profile, the undulator peak field value (the maximum field on the undulator axis), design of the magnet ends including correction coils, and calculation of the load line of the superconductor [3.4-17]. The task of magnetic modeling was to find the shortest period length that would give the desired tuning range of 20-25 keV in the first harmonic without violating the APS storage ring required beam stay-clear of 7 mm in the vertical direction. Since the magnetic structure of the planar superconducting undulator consists of two half-magnets separated with a magnetic gap where a beam chamber is located, a magnetic gap of 9 mm was chosen for the modeling, taking into account the thickness of the beam chamber walls.

Despite the opportunities offered by the higher critical current density of a Nb_3Sn superconductor, we have chosen the widely used and robust NbTi superconductor for our first superconducting undulators. In particular, a round NbTi wire with 0.75-mm outside diameter available from Supercon Inc. was used for the modeling. The superconductor load line was calculated for a period length of 16 mm and a magnetic gap of 9 mm. The calculation showed that the on-axis field of 0.64 T required for the first harmonic energy of 20 keV could be achieved at a wire current of 429 A. At this current the superconductor is at 65% of its critical value at a temperature of 4.2 K. The calculated temperature margin was about 2.1 K. At a magnetic gap of 9.5 mm, the operational current rises to about 500 A, as was found in the tests of the prototype coils (see below).

In the undulator structure, the winding core (or the former) can be made of either nonmagnetic (e.g., an Al alloy) or magnetic material (e.g., a low carbon steel 1006-1010). The effect of a magnetic core on the undulator peak field and the superconductor peak field (the maximum field in the conductor) was analyzed using a 2D OPERA model. It was found that the ratio of the maximum field

in the conductor to the on-axis peak field is the lowest for the iron core case, at about 2.8, as compared to 3.3 for the nonmagnetic core case. According to the simulation, the magnetic core increases the undulator peak field value by about 7% as compared to that of the nonmagnetic core. However, only a relatively thin layer of magnetic material around the coil winding is required.

This conclusion has led us to the possibility of making the cores using an assembly technique such that magnetic poles are inserted into the grooves precisely cut on a magnetic or nonmagnetic central core part, as opposed to an approach in which the core is machined out of a single block of material. A number of short prototypes were built in the course of developing these manufacturing techniques, starting with coils about 100 mm in length (10-pole prototypes) and then moving to a length of about 330 mm (42-pole coils), as summarized in Table 3.4-3.

Table 3.4-3. Short Undulator Prototypes Summary.

Prototype	**1**	**2**	**3-5**	**Assembly 1**	**Assembly 2**	**Assembly 3**
No of poles	10	10	10	42	42	42
Core/pole material	Al/Al	Iron/Iron	Al/Al	Iron/Iron	Al/Iron	Iron/Iron
LHe test status	Tested	Tested	Used for impregnation study	Tested	Tested	Tested
Peak field				0.65 T at 500 A	0.61 T at 500 A	0.65 T at 500 A
Phase error				7.1° at 500 A; 3.3° at 200 A	5.0° at 500 A; 3.0° at 200 A	1.8° at 500 A; 1.6° at 200 A
Expected spectral performance				>75% of ideal in 3rd harmonic (60 keV); >55% of ideal in 5th harmonic (100 keV)		≈100% of ideal in 3rd harmonic (60 keV) ; >97% of ideal in 5th harmonic (100 keV)

It is worth mentioning that the manufacture of superconducting undulators is a technological challenge as it requires precise winding on precisely machined formers. We measured the geometry of the formers and found that a precision in the groove width of 9 μ rms and in the groove depth of 7 μ rms was achieved for a pair of 42-pole assembled cores. The coil winding onto these formers was performed on a specially built winding machine. Finally, the coils were impregnated with epoxy resin. Several small coils were used to develop vacuum impregnation techniques, in collaboration with experts from the Technical Division of Fermi National Accelerator Laboratory (FNAL). Our study confirmed that the quality of resin impregnation affects the training of a superconducting coil. Thus, a 42-pole coil with no visible cracks in the resin reached the plateau in tuning curve after only 4 quenches while another coil with cracks required substantial training.

Three 42-pole double-magnet assemblies were built with a 9.5-mm magnetic gap, two with

an iron core and iron poles, and one with an Al core and iron poles. All three assemblies were successfully tested in a vertical LHe bath cryostat, as shown in Figure 3.4-14 [3.4-18].

Figure 3.4-14. Photograph of a 42-pole prototype SCU assembly ready for testing in a vertical LHe dewar.

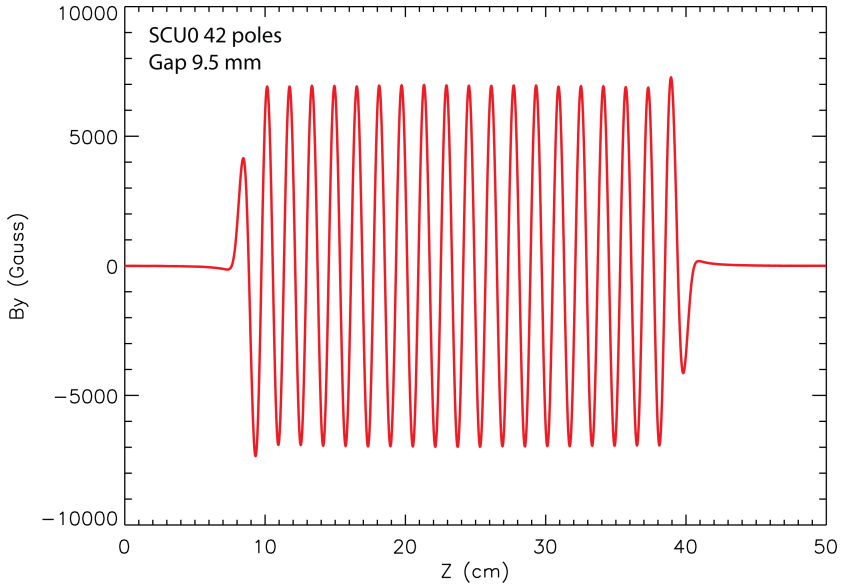

Figure 3.4-15. Measurements for a 42-pole prototype SCU assembly.

The coils were trained and reached critical currents of 720 A - 760 A, which compares very well to the required operational current between 200 A (for 25 keV in the first harmonic) and 500 A (for 20 keV in the first harmonic). Thus, the design undulator peak field between 0.38 T (at 200 A) and 0.65 T (at 500 A) was successfully achieved.

The magnetic field profile was measured with a cryogenic Hall probe. Results are shown in Figure 3.4-15. It was shown that a design that includes trim coils at each end of the magnet could meet magnetic field quality requirements for the first and second field integrals and for phase errors. For the first two test assemblies rms phase error ranging from 3 to 7 degrees were calculated for the measured field profiles such as those shown in Figure 3.4-15. We have recently measured the third assembly that has achieved the phase errors below 2 degrees rms without any magnetic shimming. This compares favorably to the original specifications developed during APS construction for Undulator A. The conclusion from our R&D experience is that the superconducting magnetic structure is intrinsically precise as soon as it is fabricated accurately.

3.4.6.4 Heat Load Estimates

A superconducting undulator employs coils wound with superconducting wire to generate high magnetic field and therefore requires the magnetic structure to be cooled to about 4 K when low-temperature superconductors (LTS), such as NbTi and Nb_3Sn, are used. For our first devices, NbTi superconductor was chosen because it is a more established technology and easier to implement. A challenge in successful implementation of low-temperature superconducting technology is the heating caused by the electron beam passing through the undulator beam chamber. Image currents and other effects may cause the coil temperature to rise above the critical temperature of the superconductor. Therefore, predictions of the heat load and appropriate design of the cooling system become highly important issues.

Estimates of the various contributions to the heat load due to the stored beam are shown in Table 3.4-4.

Table 3.4-4. Beam-Related Heat Loads.

Heat source	**Heat load on 2-m-long beam chamber**
Image current	2.44 W (at 100 mA) 4.88 W (at 200 mA) [3.4-19]
Electron cloud	2 W [3.4-19]
Wakefield heating in the beam chamber transition	0.093 W [3.4-19]
Synchrotron radiation from upstream magnet	~0.1 W (for wide chamber) (40 W for narrow chamber)
Injection losses	40 W (injection accident) 2 W (non-top-up mode) 0.1 W (normal top-up mode) [3.4-20]
Max heat load	~45 W (injection accident) ~6.6 W (non-top-up mode)

Sources of heat on the SCU beam chamber caused by an electron beam include wall heating due to beam-induced image currents, electron cloud or multipactor effects, direct beam strikes, and wakefield effects. The superconductor undulator beam chamber is made of extruded Al 6063T5 alloy and has a vertical aperture of 7.2 mm. For calculation of resistive wall heating, a simplified planar

geometry with 7-mm gap was used, and a residual resistivity ratio (RRR) of 45 was assumed for the wall material, giving wall heating of 1.22 W/m at 100-mA beam current. This value is scaled up to 4.88 W for a 2-m-long beam chamber and a beam current of 200 mA.

Electron cloud heating arises from electrons in the vacuum chamber being accelerated into the vacuum chamber wall because of repulsion from a passing beam bunch. When they strike the wall, secondary electrons are emitted. The secondaries will in turn be accelerated into the wall. The heating effect is estimated to be 2 W.

The SCU beam chamber has a vertical aperture smaller than the aperture of the storage ring chamber. The resulting transition from the standard chamber height down to the SCU chamber causes electromagnetic field perturbations, resulting in wakefield heating. In our design, the transitions are outside the SCU cryomodule in the room-temperature region, and therefore the estimated heat load in the cold region due to this effect is as small as 0.1 W.

Another source of SCU beam chamber heating is a flux of photons from an upstream bending magnet. This can cause substantial heating but is relatively easy to eliminate by masking off the photon beam upstream of the superconducting undulator and by increasing the horizontal aperture of the SCU beam chamber such that the photon beam passes cleanly through. The resulting heat load is then reduced to the level of 0.1 W.

Finally, there might be heating caused by the electron beam injection losses or losses of Touschek-scattered electrons on the SCU beam chamber. The heating due to the former is at most about 2 W under normal operation. The highest heat load on the SCU beam chamber is due to a possible injection accident resulting in a heating power as high as 45 W, which in principle could go on indefinitely. This is most likely to happen during machine studies but can be eliminated by adopting careful procedures for conducting studies. Also, the superconducting undulator magnet should be switched off during such an exercise to prevent quenching. We can also instrument the area around the undulator to allow us to detect beam losses promptly, as described in section 3.4.9.

Based on these analyses, the maximum heat load during normal operation is estimated to be under 7 W. The SCU cooling system, as described below, has a beam chamber cooling capacity of 40 W, which provides a comfortable margin for normal operation.

3.4.6.5 Cooling Scheme Concept

As indicated in Table 3.4-4, the heat load on the beam chamber from beam-related effects could be as high as about 45 W in the case of an injection accident. In order to prevent this heat from reaching the superconductor, the chamber will be thermally isolated from the superconducting coils and separately cooled by the two lower cryocoolers shown in Figure 3.4-16. These cryocoolers will hold the beam chamber at approximately 20 K and will also be used for cooling two radiation shields to 20 K and 60 K.

The superconducting coils are cooled by liquid He (LHe) that flows through channels in the center of the magnetic cores and is gravity driven in a thermosiphon loop. A cryocooler-cooled recondenser in the LHe tank reliquifies evaporated He, making it a closed system. This and another cryocooler mounted to the top of the cryostat are also used to cool the current lead assemblies.

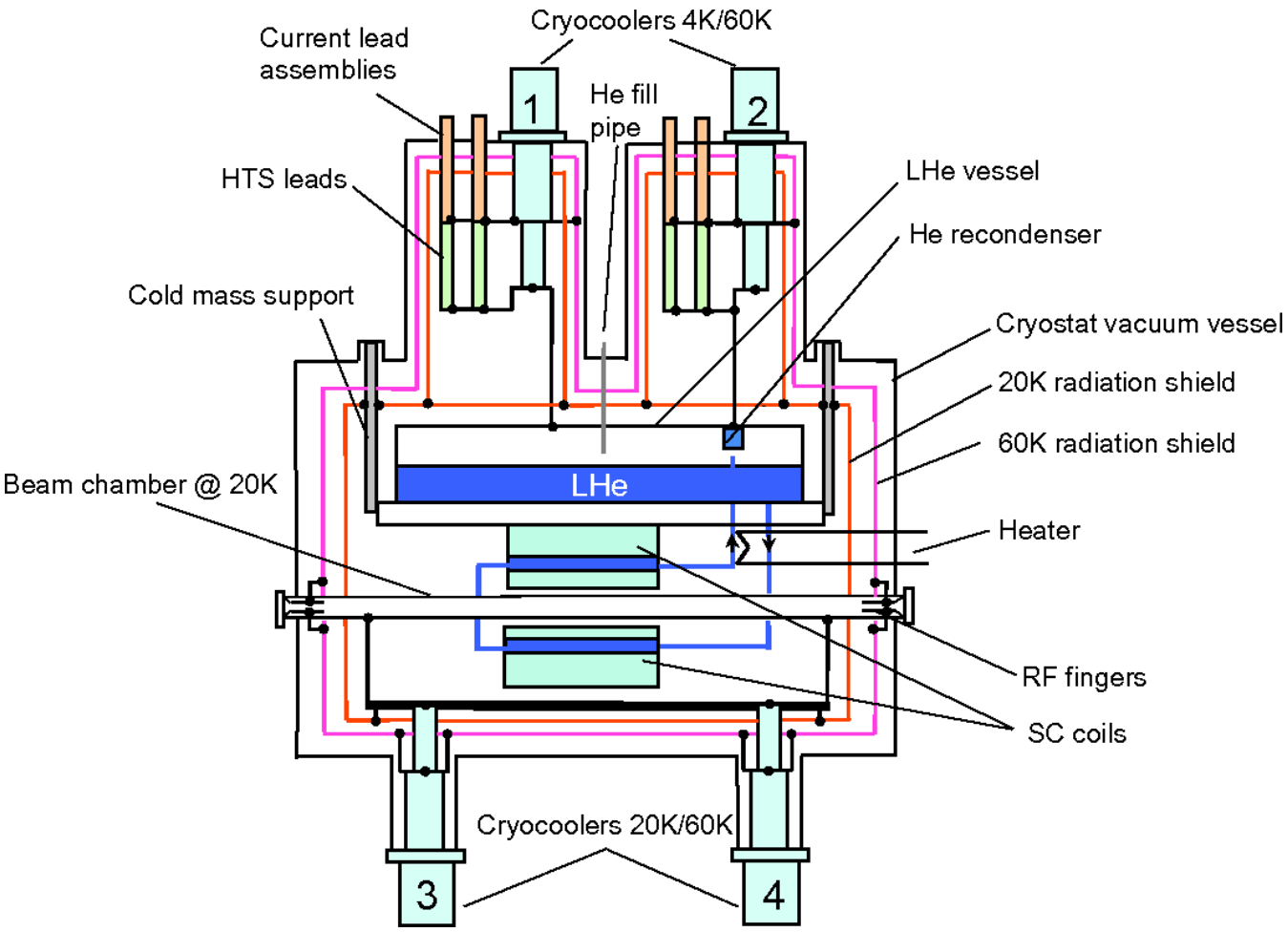

Figure 3.4-16. Superconducting undulator cooling scheme concept.

A listing of the heat loads and the temperatures at which the heat loads occur is shown in Table 3.4-5 along with the total cooling capacity of the four cryocoolers.

3.4.6.6 Cryostat Concept

The design of the superconducting undulator cryostat is based on the concept developed at the Budker Institute, Novosibirsk, Russia, and implemented in the superconducting wigglers that have been built for a number of institutions worldwide [3.4-21]. A view of the assembled cryostat is shown in Figure 3.4-17 with a cut-away view shown in Figure 3.4-18.

The cryostat is designed to hold a 1.15-m-long SCU magnet, but is shown holding the initial 42-pole-long magnetic structure selected for the first test undulator SCU0 to be built in the R&D phase of the project. The second undulator, SCU1, will use the same 2-m-long cryostat design, provided no flaws are found in testing with SCU0.

Table 3.4-5. Heat Loads. All values are in Watts.

Heat source	**Heat load** at 4 K	**Heat load** at 20 K	**Heat load** at 60 K
Beam		10	
Radiation	0.0116	1.21	4.2
Conduction through:			
beam chamber bellows			1.4
beam chamber supports	0.08		
He vent pipe bellows	0.006	0.07	0.9
He fill pipe	0.012		
cold mass support	0.005		
radiation shield supports		1.2	5.6
Current leads:			
total, current off			44
correction coil leads only, 100 A	0.12		22
main coil leads only, 500 A	0.45		52
Total at I = 500 A	0.685	12.5	86.1
Cooling capacity	3	40	224

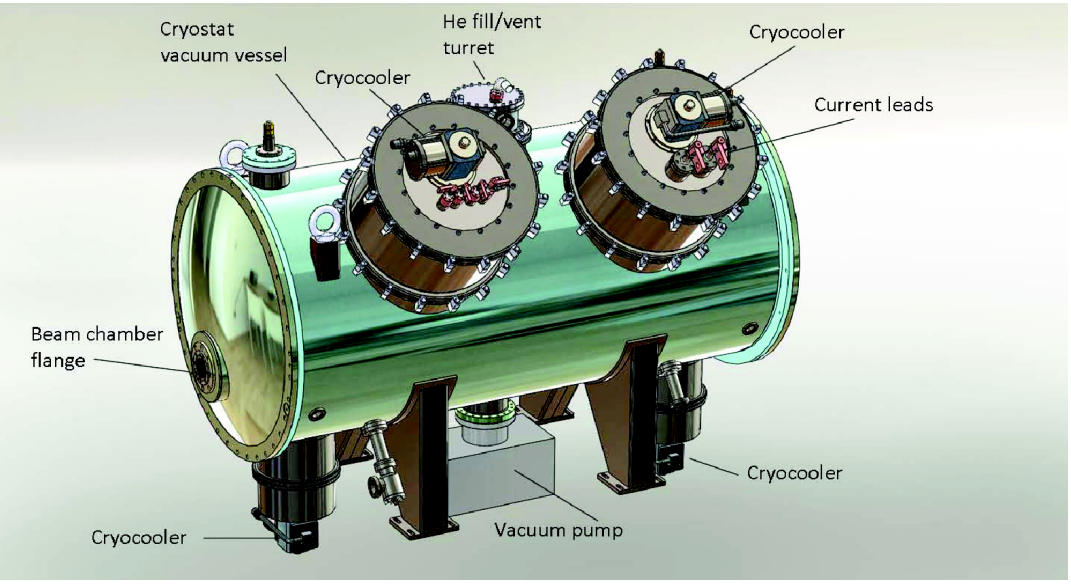

Figure 3.4-17. Drawing of the cryomodule for the superconducting undulator.

3.4.6.7 Measurement System

Performance characterization of the SCU is one of the key requirements to be satisfied before installation of the device in the APS storage ring. The procedure includes quality control of superconducting coils after their manufacture and before mounting into the cryostat, as well as final

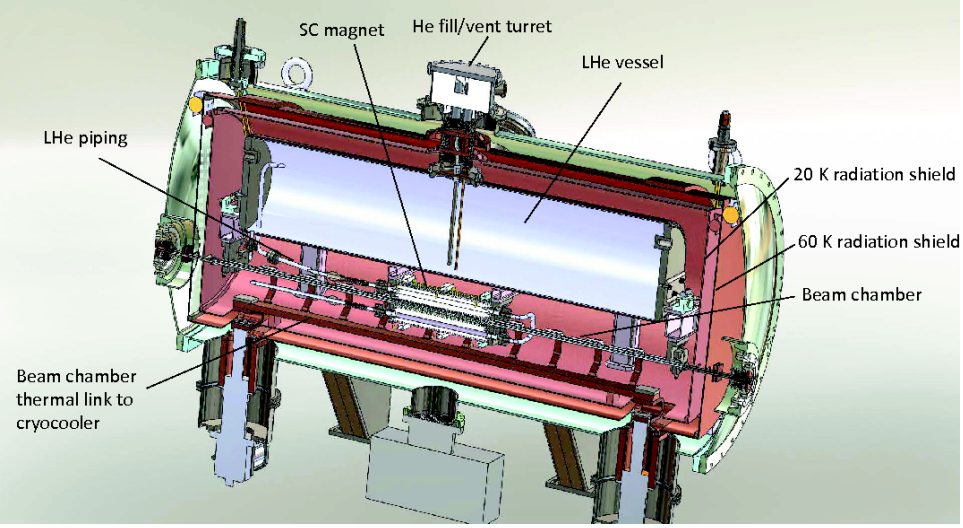

Figure 3.4-18. Cutaway view of the inside of the cryostat.

magnetic measurements of the undulator field once the undulator is assembled.

A vertical measurement system was developed for testing SCU magnetic structures up to 1 m long in a vertical LHe cryostat. This system was successfully employed to measure the short undulators listed in Table 3.4-3. It includes a movable Hall probe driven by a precise mechanical stage, power supplies for the magnets being tested, and a data acquisition system controlled by LabVIEW software. We are planning to use this system for cold tests of superconducting coils for our first three devices. An extended version of such a system will be required for cold tests of 2-m-long structures.

Once assembled into a cryostat, the superconducting undulators will also be measured with a horizontal measurement system. The specification for such a system has been recently developed. It will include a Hall probe assembly to measure magnetic field flux in the vertical and horizontal planes on and off axis. A rotating coil will be used for measuring both the field integrals and the multipole components of the magnetic field.

The mechanical concept for the system is based on the idea that a Hall probe is moving inside a vacuum-sealed, warm guide tube located in the cold-bore chamber. The Hall probe assembly is mounted on a carbon fiber rod that is pushed into the SCU by a high-precision mechanical stage located outside the SCU cryostat. Such a rod can also hold a rotating wire coil or even a pair of orthogonal wire coils. In this approach the Hall probe is operating at atmospheric pressure and at close to room temperature and would thus be easily replaceable. A conceptual design has been completed and is being detailed.

The issue of operating a Hall sensor at various temperatures has already been addressed [3.4-22]. A small cryostat was added to our Hall probe calibration facility to measure Hall sensor response at different temperatures including cryogenic temperatures. The measured calibration curves were used in our tests of the SCU magnet prototypes, reported above.

A novel three-sensor Hall probe is being developed for the superconducting undulator measurement system [3.4-23]. It includes a pair of Hall sensors to measure the vertical magnetic field

and an additional sensor to measure the horizontal component of the field. The vertical sensors will also be used to find the exact vertical position of the Hall probe assembly by measuring and comparing the field in two different locations. This idea has been successfully tested recently.

In carrying out this work, we will take full advantage of extensive experience at APS in magnetic measurements of conventional undulators. Existing methods of undulator field analysis and corresponding software packages are already being implemented into the data acquisition system for the superconducting undulator.

3.4.6.8 R&D Plan

According to our current plan, shown in Table 3.4-6, the R&D phase of the project will initially focus on the design and manufacture of SCU0, the first test undulator. This device will use the 42-pole, 1.6-cm-period magnetic structure design that was developed in 2008-2009.

The R&D plan is targeted to reduce risk by addressing critical issues. This will culminate in installation of a fully functional test device in the APS storage ring in late spring of 2012. Among the issues addressed are:

1. Measurement of the amount of beam-induced heating of the vacuum chamber under a full range of operating conditions.
2. Validation of the cryogenic design concept, in particular, the separation of cooling systems for the beam chamber and the magnet core, as well as cooling of the chamber using a cryogenic siphon.
3. Development and verification of methods of building a device with a sufficiently high-quality field. This includes development and verification of tuning techniques, if required.
4. Development of magnetic measurement techniques for an SCU in its cryostat at operating temperature, with sufficient precision to determine whether the device meets requirements for field integrals and phase errors.
5. Characterization of long-term stability.
6. Resolution of operational issues with integration of an SCU into the APS storage ring. For example, the response of the ring to an SCU quench, or the effect of a beam strike on the SCU.

The installation and successful operation of SCU0 in the APS storage ring will address most of the issues critical to the success of these devices. R&D on several other critical issues will run in parallel with the fabrication of the SCU0. Questions to be addressed include possible development of a beam chamber with reduced vertical aperture, the technology needed to make longer magnetic structures with a 1.6-cm period, the design of the cooling system and cryostat for a long undulator, and the possibility of reducing the period length of a NbTi-based superconducting undulator.

The R&D program will finished with the building of a second prototype device, SCU1, in the engineering development phase of the APS Upgrade. This 1.14-m-long, 144-pole device will will have the same number of magnetic poles as the popular APS Undulator A and will be accommodated by the then-existing SCU0 cryostat. The design of the SCU1 will be completed by summer of 2013. The undulator will be installed into the APS ring in late spring of 2014.

Table 3.4-6. Superconducting Undulator Road Map

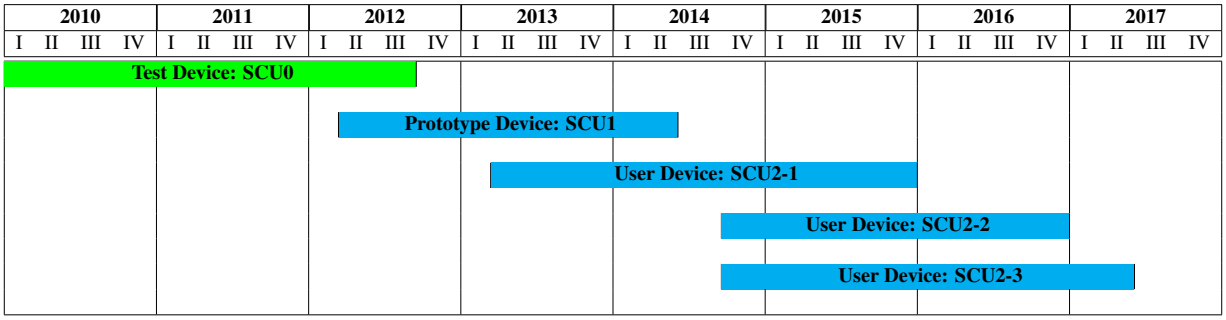

3.4.6.9 User Devices

In addition to the test device SCU0 and the prototype device SCU1, we will build and install three longer user devices SCU2-1, SCU2-2, and SCU2-3 that will deliver the promised enhanced brightness for hard x-rays. The parameters of the SCUs are listed in Table 3.4-7. While the parameters of SCU0 and SCU1 are defined, the specification for SCU2-1, SCU2-2 and SCU2-3 may change.

Table 3.4-7. Parameters of the Superconducting Undulators.

	SCU0	SCU1	SCU2-1, SCU2-2 and SCU2-3
Photon energy at 1^{st} harmonic, keV	20-25	20-25	$20 - 25^*$
Period length, mm	16	16	16^*
Magnetic gap, mm	9.5	9.5	9.5^*
Magnetic length, m	0.340	1.140	$\simeq 2.300^*$
Cryostat length, m	2.063	2.063	$\simeq 3.000^*$
			* preliminary

At the moment it is assumed that user devices SCU2-1, SCU2-2, and SCU2-3 are identical. In these undulators the magnetic length will be doubled compared to SCU1 and will reach about 2.3 meters. The cryostat length will correspondingly grow to about 3 meters. Commissioning and operating experience with the 1-m-long undulator will drive the design of the longer devices. Additional engineering development may be required before manufacturing.

3.4.6.10 Development of an Advanced SCU

We have already mentioned that application of Nb_3Sn superconductor, which has a higher critical current density than NbTi, may lead to development of an SCU with enhanced performance. In addition, by operating the undulator closer to the critical current, combined with lowering the superconductor temperature and using better magnetic material for the magnetic poles, one could almost double the peak field of a SCU, according to our estimation shown in Table 3.4-8. Such an “Advanced

SCU," which realizes the full potential of superconducting technology, is the ultimate purpose in pursuing this technology.

Table 3.4-8. Potential Field Enhancement from Various Aspects of an Advanced SCU

	Field enhancement factor
Using Nb_3Sn instead of NbTi	1.4
Operating closer to critical current	1.2
Operating below 4.2 K	1.1
Using better magnetic material for poles	1.1
Reducing magnetic gap	1.1
Total enhancement	2.2

Although it is outside the scope of the R&D being performed for the APS Upgrade, it is worth sketching the R&D plan for the Advanced SCU. This R&D plan will need to address the following issues:

1. Development of technology for manufacturing undulators using Nb_3Sn conductor, including techniques of making precise long magnetic formers and winding superconducting wire onto them, followed by heat treatment and resin vacuum impregnation.
2. Cooling scheme and cryostat design improvement including implementation of a method of lowering the temperature of liquid helium and reducing heat leaks into it.
3. Development of a thin-wall beam chamber that will allow reducing the magnetic gap and therefore enhancing the field.
4. Feasibility study of a cryogen-free undulator in a compact cryostat that utilizes direct cooling of superconducting coils by cryocoolers and eliminates liquid helium in the system.
5. Feasibility study of using high-temperature superconductors (HTS), once these conductors are developed up to a level where they produce a current density in the windings that is comparable with the low-temperature superconductors (LTS).

Such an R&D program is not a part of the APS upgrade project and therefore needs to be run in parallel with the upgrade and will require additional funding. The R&D being undertaken as part of the upgrade, in addition to creating high-performance devices, sets the stage for creation of these more advanced devices. We describe the potential benefits of both generations of devices in the next section.

It should also be noted that experience gained in development of planar devices is applicable to the development of a helical superconducting undulator that is of great interest for both the free-electron laser (FEL) community and the high energy linear collider community.

3.4.7 Accelerator Requirements and Issues

3.4.7.1 Perturbations

Insertion Devices (IDs) may have undesired effects on the beam. Much effort is spent in reducing these during the design and tuning stage. Table 3.4-9 shows the connection between the type of magnet error and beam effect. Limits on these integrals were determined in the early stage of the APS [3.4-24] and are reproduced in Table 3.4-10. It is presumed that the specification of linear errors refers to changes in time after an initial linear error is established and corrected. The limits for multipoles were determined from tracking 34 IDs in the original APS lattice, which had weaker focusing and larger dynamic aperture than the present or future APS-U lattice. A study done today would probably allow looser tolerances. Hence, we will revisit this analysis in light of present-day operating parameters. This may result in a relaxation of requirements with a possible beneficial cost and schedule impact.

Table 3.4-9. Effect from ID Errors.

Name	**Expression**	**Beam effect**
First field integral	$I_{1x,y} = \int B_{y,x} ds$	Beam position
Second field integral	$I_{2x,y} = \int \int B_{y,x} ds' ds$	Beam position
Quadrupole integral	$\int (dB_y/dx) ds$	Tune
Skew quadrupole integral	$\int (dB_y/dy) ds$	Vertical beam size
Higher-order multipole integrals	$\int (d^n B_y/dx^n) ds$, $\int (d^n B_y/dy^n) ds$	Dynamic aperture, lifetime

Table 3.4-10. ID Error Tolerance Specification in 1995.

(a) Steering

Order	**Limit**
I_{1x}	100 G-cm
I_{1y}	50 G-cm
$I_{2x,y}$	1×10^5 G-cm^2

(b) Multipole

Order	**Normal Component** $\mathbf{B_0 L b_n}$ [a]	**Skew component** $\mathbf{B_0 L a_n}$ [a]
1	50 G	50 G
2	200 G/cm	100 G/cm
3	300 G/cm^2	500 G/cm^2

[a] $\int (B_y + iB_x) dl = B_0 L \sum_{n=0}^{\infty} (b_n + ia_n)(x + iy)^n$

Presently installed IDs for the most part respect these limits individually because they are undulators (low K values). Since most IDs are under the limits, some particular IDs have been allowed to exceed the individual limits. Also special IDs (i.e., polarizing wigglers) may not be able to produce such low perturbations on the beam, so a special case has to be made for these.

We will comment below on the requirements for each type of perturbation, while occasionally referring to the three types of IDs present or planned at APS: hybrid undulators, superconducting undulators, and devices for polarized radiation (e.g., electromagnetic wigglers).

Steering Stability: The tolerances for first and second integrals developed in 1995 assumed that a feedforward compensation scheme would be 90% effective in maintaining stability of the orbit. Actually, we do not use a feedforward compensation because our "slow" orbit correction (a 1.3-Hz bandwidth (BW) feedback process) is much more effective.

This appears to make the tolerance for first and second integrals much looser. However we must still consider the pointing stability of the x-ray beam produced and any internal trajectory the electron beam takes while traversing the IDs, which reduces brightness of harmonics. The photon pointing error that occurs from scanning the ID gap, say, can only be removed by two pairs of correctors: one inside pair to direct the photon beam properly and one outside pair to remove the resulting orbit perturbation. However this four-corrector configuration would be impractical because we don't have sufficient space. Thus we maintain the original first and second integral tolerances and live with the present photon displacement.

Optics Perturbation: The IDs at the APS are mostly hybrid iron permanent magnet devices (e.g., Undulator A) that have little effect on the optical functions of the storage ring because of the high (7-GeV) energy of the stored beam. Normal quadrupole errors, which change the tune of the ring, are generally ignored because their effect is unnoticeable. The edge-focusing effect (affecting only the vertical plane tune) is small as well and is ignored. Skew quadrupole errors, which change the vertical beam size everywhere in the ring, are generally ignored because their effect is small. Local skew quadrupole correction could be considered for the worst offending IDs.

Nonlinear Perturbation: In general undulators have wide poles and therefore have relatively little higher-multipole content in the region of interest (injection aperture) near the beam axis. Multipole components are measured along a straight-line path, as is done for normal quadrupole and sextupole magnets.

Polarizing electromagnetic wigglers, on the other hand, have narrower poles because they have interleaved vertical and horizontal poles to provide the alternating B_y and B_x fields. These wigglers, in addition to their finite pole width, have longer period lengths and stronger fields, giving them the potential to contribute to all linear and nonlinear effects. Linear perturbing effects are observed in the APS CPU [3.4-7], which operates with specially designed local correction magnets for dipole and quadrupole perturbations.

Besides the usual multipole components that are measured along a straight-line path, there are also the so-called "dynamic multipoles," which are additional nonlinearities that the stored beam experiences because of the amplitude of the oscillation. These come about because in wigglers the stored beam executes relatively large oscillatory trajectories (in either or both planes), which makes the beam experience slightly different peak fields along one full period due to the finite-width poles. This results in a net (small) kick in either or both planes that is nonlinearly dependent on the trajectory of the beam, making a wiggler a nonlinear device. The nonlinearity is complex and cannot be described as a simple multipole or sum of multipole components. Since these nonlinear kicks emerge from the oscillation of the central trajectory, the kicks are sometimes called "dynamic multipoles," even though they are not really multipoles. Although methods to partially compensate the dynamic multipoles are advancing [3.4-25], we strive to design wigglers so that these would not be necessary.

A noted example of a nonlinear wiggler is the SPEAR device analyzed in [3.4-26]. The nonlinearity of this device was partially corrected by end-multipole magnets. Assuming a sinusoidal model of the magnetic field, the nonlinear kick in the x-plane for a horizontally deflecting wiggler is (the simplest case is selected for illustration):

$$\Delta x'(x) = -\frac{L_w}{(E/e)^2}\left(\frac{\lambda_w}{2\pi}\right)^2 B_{y0}^2 \frac{d}{dx}F^2(x), \tag{3.4-2}$$

where L_w is the length of the wiggler, E is the beam energy, λ_w is the period length, B_{y0} is the peak field, and $F(x) = B_y(x)/B_y(0)$. The nonlinearity comes from the roll-off in $F(x)$.

The overall strength of the nonlinearity goes as $L_w B_0^2 \lambda_w^2/E^2$. Fortunately the APS beam energy is high. However, electromagnetic wigglers are designed with a long period in order to reach lower photon energies. Also, a strong wiggler that operates in circular or vertical polarization requires narrow B_y poles, which worsens the roll-off term. When designing wigglers we must track the trajectories through the wigglers as accurately as possible to ensure that the dynamic aperture is maintained.

To evaluate nonlinear wigglers, we start by fitting field-expansion functions (harmonics) to the wiggler 3D field obtained from either measurement or model calculation. Fitting provides a certain degree of noise filtering of the data, which is beneficial as this noise can severely overstate the nonlinear effect. Another component of fitting residuals might be the error from an incomplete expansion of the field for high-order transverse spacial harmonics. An accurate canonical tracking method has been developed [3.4-27] and added to `elegant` [3.4-28] as element CWIGGLER. It accepts an arbitrary number of harmonic coefficients. However this method is relatively slow.

A now-standard method for quickly modeling the nonlinear effects of such devices is the use of kick maps [3.4-29]. The kick map $(x, y)_0 \rightarrow (x', y')_1$ for an optical element consists of two large 2D tables covering a uniform grid of initial $(x, y)_0$ values with $(x', y')_0 = (0, 0)$, which is obtained using an accurate tracking method (i.e., the method mentioned above). The grid covers all desired trajectories, in this case the vacuum chamber aperture of $\pm$ 17 mm $\times$ $\pm$ 2.5 mm. Only one period needs to be tracked because all periods are generally the same. Of the output coordinates only the angles $(x', y')_1$ are retained, to avoid nonsymplectic behavior. Ignoring changes in $(x, y)_1$ is valid since the position offsets in a single period are small. Nevertheless, position coordinates do change from the half-period drift that follows each kick and from all the drift components of the following periods.

A more common way of obtaining the kick map is using the direct, approximate formulae given in ref. [3.4-29]. Detailed comparisons have been made of this method to the method described above. We determined that the intermediate step of fitting the field data to a form that guarantees Maxwellian fields is beneficial. For the same field data, the fitting method provides results that are smoother and show additional detail. This detail emerges from the direct formulae only when the field data has finer grid spacing. This gives confidence that the approach used here provides a more reliable way to obtain a smooth, detailed kick map.

To track through the wiggler, a special wiggler element (UKICKMAP) in `elegant` was created requiring a kick map plus a length parameter and a number-of-period parameter. The tracking for one period is done by drifting through half the period length, then applying the (hopefully small) $\Delta x'$ and $\Delta y'$ kicks determined from linearly interpolating the 2D tables, then drifting through the second half of the period. Tracking continues with more drifts and kicks for all periods defined.

The kick maps for one period of two wigglers are shown in Figure 3.4-19 for the C-polarizing mode. Table 3.4-11 gives just a few basic wiggler parameters. The CPU kick map was calculated years after installation; it was already empirically determined that its nonlinearity, if any, had no effect on the beam. The Intermediate Energy X-ray (IEX) wiggler (section 3.4.4.4) has a stronger nonlinear field. Though this wiggler is not part of the APS Upgrade it is included here to illustrate our characterization method.

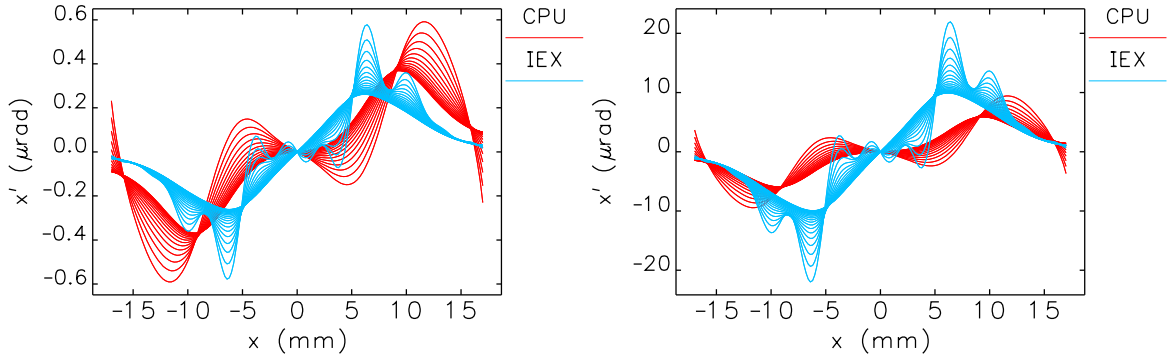

Figure 3.4-19. Kick map for one period of two wigglers (left) and for the full device (right) in C-polarizing mode. The full-device curve is just the one-period curve times the number of periods. The full-device curve is not actually used in tracking. Each group of lines represent a set of values for y_0.

Table 3.4-11. Wigglers Used in Tracking Simulations in APS.

Wiggler	**Peak fields on axis**[a] **B_y/B_x (T)**	**Period length (cm)**	**Periods**	**Length (m)**
CPU	0.30/0.36	12.8	16	2.048
IEX[b]	0.25/0.29	12.5	38	4.75

[a] In circular polarizing mode [b] A 4.8-m device not part of APS-U

Figure 3.4-19 shows that the nonlinear kick for each period is slightly larger for the CPU than for the IEX because of the higher peak fields on axis and longer period length. However, the total nonlinear kick from the entire IEX device is larger owing to its greater length. Similar curves can be obtained for the other dependency, y_1' as a function of $(x, y)_0$, but are not shown. There is no theory to predict dynamic acceptance (DA) or momentum acceptance (MA) outcome for such wigglers because their map is so nonlinear, so we rely heavily on tracking. Applying one nonlinear kick per wiggler period in tracking, we simulated DA (Figure 3.4-20) and MA (Figure 3.4-21), finding no significant negative impact. Kick maps for the other polarization modes (H and V) and their effects on DA and MA are also evaluated. Similar results are obtained but not shown here.

These techniques will be tested when the IEX device is installed and refined as needed. They will then be applied for new devices considered as part of the upgrade. In particular, we will look at the EMVPU and APPLE devices.

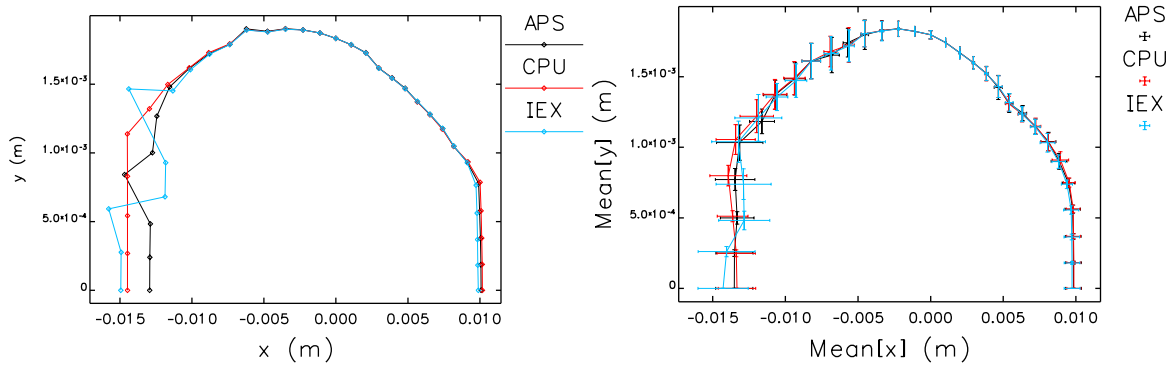

Figure 3.4-20. Dynamic aperture calculations for two wigglers with no errors (left) and with errors (right). One can see that in general the lattice is tolerant of errors. APS refers to the APS bare lattice with normal sextupoles.

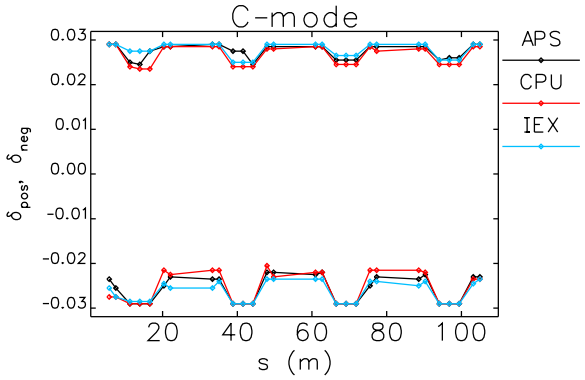

Figure 3.4-21. Momentum aperture calculations for two wigglers with no errors.

3.4.7.2 Canted Undulators

In a canted undulator section, two independent undulators separated by a 1-mrad horizontally and inboard-deflecting dipole magnet produce two photon beams separated by the same angle. The photon beams are "canted" by ± 0.5 mrad with respect to the original beam. Thus the number of possible simultaneous experiments at this sector is doubled.

Presently APS has four such pairs in 5-m straight sections. The undulators are shorter than the usual Undulator A because space is needed for additional components: one 1-mrad dipole, one mini-BPM, and one combined function H/V dipole corrector. The required opposite 0.5-mrad angle kicks at the ends are provided by storage ring corrector magnets.

Presently the orbit bump is symmetric with the 1-mrad dipole in the center. It is possible to have an unsymmetrical bump, in which the two legs are of unequal length. The angle separation would still be 1 mrad. This is applicable in the present 5-m straight section and in the future 7.7-m-long straight sections.

If we had a unsymmetrical bump with 1:2 length ratio, say, then the upstream-to-downstream

trajectory angle ratio would be 2:1. The canting angles would be $+0.67$ and -0.33 mrad.

The amount of unsymmetry is limited to how close we allow the two photon beams to pass by the dipole-fan photon absorbers located downstream. Presently for the symmetric canted straight section, the photon beam produced by the upstream undulator passes close to the outboard photon absorber, and the steering interlock in place has little margin of error. For any unsymmetric bump with upstream angle larger than $+0.5$ mrad, a relocation of an absorber or a redesign of the vacuum chamber will be required. For an unsymmetric bump with upstream angle smaller than +0.5 mrad, a redesign would not be required.

3.4.8 Optimization Methods and Ultimate Performance

The user requirements that will drive the choice of new insertion devices have only recently been defined. However, generally speaking, individual beamlines work within certain bands or ranges of photon energies and desire the highest possible brightness or flux within those bands. This suggests the possibility of automated selection of ID characteristics. In this section, we describe a method for automated selection and show predictions of ultimate performance for the APS Upgrade and beyond.

The APS presently operates at 100 mA, but will move to 150 mA as part of the upgrade, with 200 mA as a possible future upgrade. Due to power and power density limits in the front ends, the optimum for one current may well not be optimal for another. At the very least, we should optimize for 150 mA and keep an eye on performance at 200 mA. The software described here was configured to allow determining optimal choices for all three currents.

Another variable is the type of front end, since that determines the specific power and power density limits. We've investigated a number of possible combinations, as listed in Table 3.4-12. The canted front ends (CFEs) and high heat load (HHL) front ends exist now but, as we will see, they impose significant limits on the performance of advanced devices as the beam current and device length are increased. The VHHL (very high heat load) front end is an extrapolation of the existing HHL design, obtained by simply multiplying the HHL limits by 1.5.

Table 3.4-12. Potential Front End Options Used in Analysis.

Front End	**Power Limit** kW	**Power Density Limit** $\mathrm{kW/mrad^2}$
Canted	20	281
HHL	21	590
VHHL (extrapolation)	32	885
EHHL (new concept)	210	5900

The EHHL (extremely high heat load) case is something altogether different, with assumed power and power density limits that are ten times the HHL values. Analyzing the EHHL front end may seem pointless, since it is an order of magnitude beyond what we are doing today. However, we realized in the course of this analysis that for SCUs, such high limits may be possible. The power and power density limits for the front ends pertain to the first photon shutter, which must withstand the full power of the beam when the bremsstrahlung stopper is closed. The stopper is closed when the

user needs to enter the hutch to change samples, for example. Clearly, there is no need for the device to remain energized when the user is in the hutch. Hence, we realized that the SCU could simply be turned off, in which case the photon shutter will only see the comparatively weak bending magnet radiation. However, if the SCU is always off when the shutter is closed, the front-end limit will be much higher. The new limits on the front end will presumably originate with the fixed masks, which see the peripheral part of the beam. While these limits are as yet to be determined, it seems clear that they will be much higher than the present HHL limits, particularly if the masks are protected by beam steering interlocks. We chose a factor of 10 as a working assumption.

Of course, the photon shutter and bremsstrahlung stopper are not necessarily closed in a controlled fashion. One can imagine that the user might erroneously "break into" the hutch without going through proper procedures, causing the shutters to close immediately. In this case, the device needs to be shut off when the closing of the shutters is detected. The photon shutter may briefly see very high heat loads. If this is unacceptable, then the stored beam could be dumped instead.

One might wonder if similar thinking can be applied to HPM devices. While such devices cannot be turned off in the same way as an electromagnetic device, the gap can be opened, giving the same end result. Under controlled conditions, there is no difference. However, in an emergency an SCU can be forced to zero current in about 100 ms, while it may take longer to open an HPM device sufficiently. Even so, emergencies are by design rare. In such cases, one can always resort to dumping the stored beam to protect the shutter, should the opening of the gap be insufficiently rapid.

In addition to the choice of front end, the length of the straight section is potentially variable, as is the length of the device. In all, we have performed the analysis for six combinations of straight section length and front end:

1. Short canted straight with CFE, which accommodates two devices of up to 2.1 m length each.
2. Long canted straight with CFE, which accommodates two devices of up to 3.55 m length each.
3. Short straight with HHL front end, which accommodates one device of up to 4.8 m length.
4. Long straight with HHL front end, which accommodates one device of up to 7.7 m length.
5. Long straight with VHHL front end, which accommodates one device of up to 7.7 m length.
6. Long straight with EHHL front end, which accommodates one device of up to 7.7 m length.

To provide some flexibility to the algorithm, we allowed device lengths to either take the maximum value, or half of the maximum value. This provided a way to relieve power density limits in the case of the less capable front ends.

3.4.8.1 Optimization Method

The optimization method we are about to describe can be applied to single- and multi-period devices (i.e., revolvers). We'll describe the application of the method to revolvers, since this is the most complicated case. Application to single-period devices is very similar. Results were already shown for two revolver examples in section 3.4.3.5.

The starting point of our method is the assumption that each beamline will be interested in working over a specific set of photon energy bands, and that the desired quantity to optimize is the brightness. (If flux is the quantity of interest, the same technique can readily be applied.) The analysis has two steps: data preparation and choice of an optimum for a specific requirement.

For data preparation, we do the following for each combination of beam current, front-end type, and straight section length.

1. Vary the device period from 17 mm to 35 mm in 1-mm steps
   (a) Compute the maximum K value assuming NdFeB magnets according to Equation (3.4-1). A 10.75-mm magnetic gap is assumed. However, this equation is recognized as being somewhat conservative, so the results are valid for a slightly larger gap.
   (b) Run `sddsbrightness` and `sddsfluxcurve` to get power density and total power as a function of K, along with brightness and flux density for harmonics 1 through 9.
   (c) Limit the photon energy range for each harmonic to account for the power and power density limits of the chosen front end.
   (d) Multiply the brightness for each harmonic by values that approximately account for the effect of typical phase errors [3.4-30].
   (e) Compute the brightness envelope over all harmonics. This eliminates the overlap and gives a single curve of maximum brightness vs photon energy. Gaps in the spectrum are represented by zero values.
2. Choose in turn the data for each device period from 17 to 33 mm.
   (a) Loop over all periods that are shorter than or equal to the chosen period.
      i. For each pair of periods, compute the maximum brightness available from either undulator as a function of photon energy.

Having completed this step, we now have a large set of data files for each combination of beam current, front end, and straight section length. Each file tells us, for any pair of undulator periods, the maximum brightness available as a function of photon energy when the relevant front-end limits are taken into account.

The next step is to find the optimal pairs of periods for a specific set of photon energy bands. This is performed with another script that accepts the beam current, front-end type, and straight section type, as well as a list of lower and upper limits for any number of energy bands. It produces a list of the top combinations of periods, along with graphs of the performance for each. Because all the data are generated ahead of time, it takes less than 10 s to produce a result. (This algorithm has also been implemented for optimization of three-period revolvers. The amount of data is somewhat larger and, as a result, it takes about 60 s to find the best devices.) The algorithm for choosing the best pairs is as follows:

1. For each period pair p
   (a) For each band b determine the sum of the widths of any gaps in the brightness tuning curves. Call this W_{bp}.

(b) For each band b compute the minimum brightness and the average brightness. Call these $B_{bp,m}$ and $B_{bp,a}$, respectively

2. Perform a nondominated sort [3.4-31] of the results for all p in order to minimize W_{bp} while maximizing $B_{bp,m}$ and $B_{bp,a}$.

3. Select only the first-rank solutions, i.e., the Pareto-optimal set, for further review.

Depending on the number of bands, the algorithm may choose a single period pair or a handful of period pairs. These selections are equivalent in the sense that none is dominated in all performance measures by any other selection. Down-selection from this point requires introduction of an additional decisive criterion, or review by a potential user of the device. When a fully-automated selection is desired, a useful criterion to add is maximization of the minimum (for each p) over all bands.

The use of this algorithm for single-period devices is quite straightforward: we simply use the single-period files instead of the multi-period files. For SCUs and ASCUs (Advanced SCUs), we change item 1a in the data preparation stage to use the predicted performance curve for the SCUs, with conservative limits for the maximum current as described in earlier sections. In addition, the effective magnetic length of SCUs is reduced by 0.6 m from that for a HPM device, to account for the cryostat and warm-to-cold transitions. That is, we are looking at devices with fixed insertion length, not fixed effective length.

3.4.8.2 Optimized Performance Results

To illustrate what we can potentially gain from the upgrade and beyond, we chose six photon energy bands as examples: 5-15 keV, 15-25 keV, 25-40 keV, 40-100 keV, 25-26 keV, and 75-76 keV. For each, we found the optimum HPM, two-period revolver, SCU, and ASCU for various combinations of beam current, straight section length, and front end.

The results of our analysis take two forms: first, we can state for any given situation which HPM, two-period revolver, or SCU device is best. We can also determine the degree to which, for example, the best SCU exceeds the performance of the best HPM. The easiest way to do this is by showing the ratio of the best SCU or ASCU performance to the best HPM performance. This is seen in Tables 3.4-13, 3.4-14, and 3.4-15 where we show the ratio of the optimized minimum brightness for a two-period revolver or SCU in the given band to the same quantity for a single-period HPM device. We also show the ratio of the optimized minimum brightness for an single-period HPM to the "reference" configuration, which we define as a 2.1-m-long U33 device in a canted straight at 100 mA. To find the improvement from, say, an optimized ASCU relative to the reference, one simply multiplies the appropriate "Bright. Ratio" by the "HPM rel. reference."

Note that because the ratios are formed from the *minimum* brightness values in each band, the table may tend to understate the improvement. For example, it may well be that the brightness at certain regions in the band increases by a significantly larger factor. Careful definition of the photon bands of interest is thus essential to getting a reliable result.

At 100 mA, the SCU and ASCU are little different until we look at the 40-100 keV band. For the other bands, improvements over HPM devices are generally factors of 2 to 4, and then only for long

devices. In the 40-100 keV band, we see improvements of an order of magnitude or more. Two-period revolvers give improvements of less than a factor of two. Section 3.4.3.5 shows additional examples of revolver optimization.

At 150 mA, the current for APS-U, the results for SCUs generally become less impressive unless we invoke the EHHL front-end concept. For all other front end choices, long SCUs lose ground compared to 100 mA. The reason is that, at higher current and with long devices, the wide range of K values available from an SCU is less of an advantage, because the possible tuning range is limited by the front-end power density limit. This conclusion is even more evident for 200 mA, where SCUs are in many cases a liability, presumably due to the shorter magnetic length for the same insertion length. Again, a significant advantage for SCUs is still evident for the 40-100 keV band, particularly when the EHHL concept is invoked.

In conclusion, we find that SCUs and advanced SCUs can provide significant advantages, particularly for high photon energies, but to fully capitalize on this technology requires a new way of thinking about front-end operations.

Table 3.4-13. Results of ID optimization for 100 mA. The "HPM rel. reference" column shows the ratio of the optimized minimum brightness for an HPM to the minimum brightness for a U33 device in a short, canted straight at 100 mA. The "Bright. Ratio" column shows the ratio of the minimum brightness for the optimized revolver, SCU, or ASCU to the minimum brightness for the optimized HPM device. The Length and Period columns list values for HPM, Revolver, SCU, and ASCU, in order.

Band	Front End	LSS	HPM Rel. Reference	Brightness Ratio			Lengths	Periods
				Rev.	SCU	ASCU		
keV							cm	mm
5-15	CFE	0	1.1	1.4	1.2	1.3	210/210/150/150	32/24+30/22/20
5-15	HHL	0	2.8	1.6	1.8	1.8	480/480/420/420	31/24+30/23/23
5-15	VHHL	1	3.7	1.8	1.8	1.8	770/770/710/710	31/24+30/24/24
5-15	EHHL	1	3.7	1.8	2.2	2.5	770/770/710/710	31/24+30/22/18
15-25	CFE	0	1.4	1.3	1.6	2.7	210/210/150/150	30/27+30/21/15
15-25	HHL	0	3.4	1.3	2.0	2.0	480/480/420/420	30/27+30/21/21
15-25	VHHL	1	4.5	1.3	1.9	1.9	770/770/710/710	30/27+30/22/22
15-25	EHHL	1	4.5	1.3	2.1	4.3	770/770/710/710	30/27+30/21/15
25-26	CFE	0	2.1	1.0	1.6	3.0	210/210/150/150	26/26+17/15/13
25-26	HHL	0	5.1	1.0	2.4	3.2	480/480/420/420	26/26+17/15/14
25-26	VHHL	1	6.7	1.0	2.6	3.6	770/770/710/710	26/26+17/15/14
25-26	EHHL	1	6.7	1.0	2.6	4.5	770/770/710/710	26/26+17/15/13
25-40	CFE	0	1.9	1.2	1.9	2.8	210/210/150/150	28/28+23/20/18
25-40	HHL	0	4.4	1.2	2.5	2.5	480/480/420/420	28/28+23/20/20
25-40	VHHL	1	5.8	1.2	2.2	2.2	770/770/710/710	28/28+23/21/21
25-40	EHHL	1	5.8	1.2	2.7	4.4	770/770/710/710	28/28+23/20/17
40-100	CFE	0	250.7	1.2	8.2	18.3	210/210/150/150	25/24+25/18/16
40-100	HHL	0	572.0	1.2	10.3	14.5	480/480/420/420	25/24+25/18/17
40-100	VHHL	1	764.2	1.2	10.7	15.9	770/770/710/325	25/24+25/18/15
40-100	EHHL	1	764.2	1.2	10.7	33.2	770/770/710/710	25/24+25/18/15
75-76	CFE	0	7.9	1.1	5.8	11.0	210/210/150/150	25/26+25/17/13
75-76	HHL	0	18.2	1.1	7.3	7.6	480/480/420/420	25/26+22/17/14
75-76	VHHL	1	24.1	1.1	7.5	8.0	770/770/710/710	25/26+22/17/14
75-76	EHHL	1	24.1	1.1	7.5	14.6	770/770/710/710	25/26+22/17/13

Table 3.4-14. Results of ID optimization for 150 mA. The "HPM rel. reference" column shows the ratio of the optimized minimum brightness for an HPM to the minimum brightness for a U33 device in a short, canted straight at 100 mA. The "Brightness Ratio" column shows the ratio of the minimum brightness for the optimized revolver, SCU, or ASCU to the minimum brightness for the optimized HPM device. The Length and Period columns list values for HPM, Revolver, SCU, and ASCU, in order.

Band	Front End	LSS	HPM Rel. Reference	Brightness Ratio			Lengths	Periods
				Rev.	SCU	ASCU		
keV							cm	mm
5-15	CFE	0	1.6	1.4	1.0	1.0	210/210/150/150	32/24+30/24/24
5-15	HHL	0	4.2	1.6	1.1	1.1	480/480/420/420	31/24+30/26/26
5-15	VHHL	1	5.6	1.8	1.1	1.1	770/770/710/710	31/24+30/28/28
5-15	EHHL	1	5.6	1.8	2.2	2.5	770/770/710/710	31/24+30/22/18
15-25	CFE	0	2.0	1.3	1.3	1.3	210/210/150/150	30/27+30/23/23
15-25	HHL	0	5.1	1.3	1.3	1.4	480/480/420/180	30/27+30/26/15
15-25	VHHL	1	6.8	1.3	1.3	1.8	770/770/710/325	30/27+30/27/15
15-25	EHHL	1	6.8	1.3	2.1	4.3	770/770/710/710	30/27+30/21/15
25-26	CFE	0	3.1	1.0	1.6	2.3	210/210/150/150	26/26+17/15/14
25-26	HHL	0	7.6	1.0	2.4	2.4	480/480/420/420	26/26+17/15/15
25-26	VHHL	1	10.0	1.0	2.6	2.6	770/770/710/710	26/26+17/15/15
25-26	EHHL	1	10.0	1.0	2.6	4.5	770/770/710/710	26/26+17/15/13
25-40	CFE	0	2.8	1.2	1.7	1.7	210/210/150/150	28/28+23/21/21
25-40	HHL	0	6.6	1.2	1.6	1.7	480/480/420/180	28/28+23/23/17
25-40	VHHL	1	8.7	1.2	1.4	1.8	770/770/710/325	28/28+23/24/18
25-40	EHHL	1	8.7	1.2	2.7	4.4	770/770/710/710	28/28+23/20/17
40-100	CFE	0	376.1	1.2	8.2	8.2	210/210/150/150	25/24+25/18/18
40-100	HHL	0	858.0	1.2	4.9	13.9	480/480/420/180	25/24+25/21/15
40-100	VHHL	1	1146.3	1.2	5.1	11.2	770/770/325/325	25/24+25/18/16
40-100	EHHL	1	1146.3	1.2	10.7	33.2	770/770/710/710	25/24+25/18/15
75-76	CFE	0	11.9	1.1	5.8	5.9	210/210/150/150	25/26+25/17/14
75-76	HHL	0	27.2	1.1	3.5	5.8	480/480/420/180	25/26+22/15/13
75-76	VHHL	1	36.2	1.1	3.7	6.9	770/770/710/325	25/26+22/15/13
75-76	EHHL	1	36.2	1.1	7.5	14.6	770/770/710/710	25/26+22/17/13

Table 3.4-15. Results of ID optimization for 200 mA. The "HPM rel. reference" column shows the ratio of the optimized minimum brightness for an HPM to the minimum brightness for a U33 device in a short, canted straight at 200 mA. The "Brightness Ratio" column shows the ratio of the minimum brightness for the optimized revolver, SCU, or ASCU to the minimum brightness for the optimized HPM device. The Length and Period columns list values for HPM, Revolver, SCU, and ASCU, in order.

Band	Front End	LSS	HPM Rel. Reference	Brightness Ratio			Lengths	Periods
				Rev.	SCU	ASCU		
keV							cm	mm
5-15	CFE	0	2.1	1.4	0.8	0.8	210/210/150/150	32/24+30/27/27
5-15	HHL	0	5.4	1.6	1.0	1.0	480/480/420/420	32/31+25/30/30
5-15	VHHL	1	6.8	1.8	1.0	1.0	770/770/710/710	33/31+25/32/32
5-15	EHHL	1	7.4	1.8	2.2	2.5	770/770/710/710	31/24+30/22/18
15-25	CFE	0	2.7	1.3	1.0	1.0	210/210/150/150	30/27+30/26/26
15-25	HHL	0	6.1	1.4	1.1	1.1	480/480/420/420	31/27+30/29/29
15-25	VHHL	1	8.1	1.4	1.0	1.0	770/770/325/710	31/28+31/22/30
15-25	EHHL	1	9.0	1.3	2.1	4.3	770/770/710/710	30/27+30/21/15
25-26	CFE	0	4.1	1.0	1.6	1.6	210/210/150/150	26/26+17/15/15
25-26	HHL	0	10.1	1.0	1.5	1.5	480/480/420/180	26/26+17/16/13
25-26	VHHL	1	12.0	1.0	1.9	1.9	770/770/710/710	27/27+17/16/16
25-26	EHHL	1	13.3	1.0	2.6	4.5	770/770/710/710	26/26+17/15/13
25-40	CFE	0	3.8	1.2	1.2	1.2	210/210/150/150	28/28+23/23/23
25-40	HHL	0	8.9	1.2	1.2	1.2	480/480/420/180	28/28+23/26/19
25-40	VHHL	1	10.7	1.3	1.3	1.3	770/770/325/325	28/24+27/20/20
25-40	EHHL	1	11.6	1.2	2.7	4.4	770/770/710/710	28/28+23/20/17
40-100	CFE	0	501.5	1.2	3.9	3.9	210/210/150/150	25/24+25/21/21
40-100	HHL	0	1144.0	1.2	4.4	8.7	480/480/180/180	25/24+25/18/16
40-100	VHHL	1	1528.4	1.2	5.1	5.4	770/770/325/325	25/24+25/18/17
40-100	EHHL	1	1528.4	1.2	10.7	33.2	770/770/710/710	25/24+25/18/15
75-76	CFE	0	15.8	1.1	2.7	2.7	210/210/150/150	25/26+25/15/15
75-76	HHL	0	36.3	1.1	3.1	5.8	480/480/180/180	25/26+22/17/13
75-76	VHHL	1	48.3	1.0	3.6	3.8	770/770/325/325	25/25+22/17/14
75-76	EHHL	1	48.3	1.1	7.5	14.6	770/770/710/710	25/26+22/17/13

3.4.9 Undulator Instrumentation [CAS]

Undulators, like other in-tunnel components of the APS complex, are subject to damage by ionizing radiation. This radiation originates from beam losses that occur during injection, when the beam is dumped, and when particles are lost from the beam due to the finite lifetime. Although losses are generally well controlled in the APS, there have been issues with undulator damage, particularly in the location of the smallest chamber gaps. Hence, we seek to enhance the instrumentation used to monitor radiation losses at undulators.

The primary goals of the beam loss monitor (BLM) upgrade are: (1) developing detectors suitable for dosimetry measurements at the insertion devices; (2) implementing FPGA-based detector electronics to provide sector-specific loss data to aid optimization of the injection and minimization of losses; and (3) instrumenting several detectors per sector to enable meaningful integration of lost charge during user runs. The secondary goals of the upgrades are to provide: (4) turn-by-turn and bunch-by-bunch loss information after injection; (5) turn-by-turn and bunch-by-bunch loss information during major beam loss events; (6) spatial information on the local losses within an ID chamber in all three dimensions.

The current APS BLM system consists of 36 sets of Cherenkov detectors and VME signal-processor boards built in house [3.4-32]. Both the detectors and signal processor boards are based on the PEP-II B-Factory design by A. Fischer [3.4-33]. In 2008, we started a calibration program for the system. After calibrating all detectors from sector to sector, the absolute loss rate at each ID chamber can be derived by normalizing the count rate with the total charge loss rate deduced from storage ring current monitor readout [3.4-34]. While these studies validated a methodology for dosimetry measurements, they also showed serious limitations of the system: (1) the detector does not respond to electrons lost in the downstream end of the chamber;and (2) steering the electron beam has strong effects on the detector sensitivity to local losses. To mitigate these problems, we are experimentally searching for new locations where the detectors are less sensitive to steering. However, a better solution is to add more detectors per sector to better integrate the losses in all directions, and at both ends of the chamber.

At present, over 90% of the electrons lost in the storage ring during top-up operations are from the stored-beam lifetime losses, which are dominated by post-Touschek scattering processes. The remaining losses are from injections and infrequent beam dumps. Of all the beam losses in the ring, about 40% occur at the narrow-gap chamber ID-4, the limiting aperture of the storage ring. Unlike the steady state loss from the stored beam during user runs, the injection losses vary more widely in direction when hitting the chamber, making it more important to have multiple detectors for proper integration of losses. To handle the case of beam dumps, when we lose the entire stored beam in a very short time, the electronics must have a dynamic range of more than nine orders of magnitude.

The existing Cherenkov signal processing board supports only one photomultiplier tube (PMT) and does not have the dynamic range nor the timing circuit for recording beam dumps. Its components are out of date and a new design is needed. The new design will be based on an FPGA to allow a gradual path to increased processing capabilities through firmware upgrades [3.4-35].

Table 3.4-16 shows a list of proposed beam loss monitors in the storage ring tunnel, covering all installed insertion devices. Due to the larger vertical beam deflection by the deflecting cavities, the beam losses inside the SPX region and downstream sectors are expected to increase. More discussion

on the use of beam loss monitors is found in SPX diagnostics section 3.5.9.

Table 3.4-16. List of Beam Loss Monitors.

Device monitored	Location	Total number	Notes
Undulator	S1 - S4	4	
Deflecting Cavity	S5, S7	2	SPX[a]
Undulator	S6 - S15	10	SPX
Undulator	S16 - S35	19	

[a] Additional BLMs are proposed for monitoring local losses due to SPX operations.

3.4.10 References

[3.4-1] R. Dejus. Power and Power Density of Permanent Magnet Hybrid Undulators and Superconducting Undulators in Support of the APS Upgrade. Technical Report MD-TN-2010-003, ANL, (2010).

[3.4-2] R. Dejus et al. On-Axis Brilliance and Power of In-Vacuum Undulators for the Advanced Photon Source. Technical Report LS-314, Advanced Photon Source, (2009).

[3.4-3] R. Dejus. On-Axis Brilliance and Power of In-Vacuum Undulators for the Advanced Photon Source. Technical Report ANL/APS/LS-314, ANL, (2009).

[3.4-4] J. Chavanne et al. Status of the ESRF Insertion Devices, Proc. of EPAC 2004, pp. 372–374, (2004); http://www.JACoW.org.

[3.4-5] T. Hara et al. Revolver undulator for BL15XU at SPring-8, Nuclear Instruments and Methods A, **467-468**, 161–164, (2001).

[3.4-6] R. Dejus and W.-K. Lee. Undulator Gap Tapering for Manipulation of Radiation Properties. to be published, (2011).

[3.4-7] E. Gluskin et al. An Electromagnet Helical Undulator for Polarized X-rays, P. Pianetta, editor, AIP Conf. Proc., volume 521, pp. 344–347. AIP, (2000); http://www.JACoW.org.

[3.4-8] Y.-C. Chae. How Many IVUs Can We Install without Sacrificing 16-mA Operation? Technical Report LS-318, Advanced Photon Source, (2009).

[3.4-9] R. Dejus et al. On-axis Brilliance and Power of In-Vacuum Undulators for the Advanced Photon Source. Technical Report MD-TN-2009-004, APS, (2009).

[3.4-10] Y. Ivanyushenkov et al. A Concept for a Quasi-Periodic Planar Superconducting Undulator, Proc. for PAC 2009; http://www.JACoW.org.

[3.4-11] L. R. Elias and J. M. Madey. Superconducting Helically Wound Magnet for the Free-Electron Laser, Review of Scientific Instruments, **50**, 11, (1979).

[3.4-12] G. Y. Kezerashvili et al. Colliding Beam Polarization Measurement Using Superconducting Helical Undulator at the VEPP-2M Storage Ring, Nuclear Instruments and Methods, **A314**, 15, (1992).

[3.4-13] J. Rochford. The Superconducting Undulator for the ILC Positron Source, Proc. of PAC 2009; http://www.JACoW.org.

[3.4-14] A. Bernhard et al. Performance of the First Superconducting Cold-Bore Undulator in an Electron Storage Ring, IEEE Transactions on Applied Superconductivity, **17**(2), 1235, (2007).

[3.4-15] C. Boffo et al. Fabrication of the New Superconducting Undulator for the ANKA Synchrotron Light Source, Proc. of IPAC 2010; http://www.JACoW.org.

[3.4-16] J. C. Jan et al. Design and Improvement of a Mini-Pole Superconducting Undulator at NSRRC, IEEE Transactions on Applied Superconductivity, **18**(2), 427, (2008).

[3.4-17] Y. Ivanyushenkov. Magnetic Simulation of a Superconducting Undulator for the Advanced Photon Source, Proc. of PAC 2009, p. 310, (2009); http://www.JACoW.org.

[3.4-18] Y. Ivanyushenkov et al. Status of R&D on a Superconducting Undulator for the Advanced Photon Source, Proc. of PAC 2009, p. 313, (2009); http://www.JACoW.org.

[3.4-19] R. Kustom. ANL, Private communication, (2010).

[3.4-20] V. Sajaev. ANL, Private communication, (2010).

[3.4-21] S. Khruschev et al. Superconducting 63-Pole 2 T Wiggler for Canadian Light Source, Nuclear Instruments and Methods, **A575**, 38, (2007).

[3.4-22] Y. Ivanyushenkov et al. Calibration of Hall Probe at Cryogenic Temperatures, Proc. of IMMW 16th 2009; http://www.JACoW.org.

[3.4-23] I. Vasserman. ANL, Private communication, (2010).

[3.4-24] Y.-C. Chae and G. Decker. Advanced Photon Source Insertion Device Field Quality and Multipole Error Specification, Proc. of PAC 1995, pp. 3409–3411, (1995); http://www.JACoW.org.

[3.4-25] J. Bahrdt et al. Active Shimming of the Dynamic Multipoles of the BESSY UE112 APPLE Undulator, Proceedings of the 2008 European Particle Accelerator Conference, pp. 2222–2224, (2008); http://www.JACoW.org.

[3.4-26] J. Safranek et al. Nonlinear dynamics in a SPEAR wiggler, Phys. Rev. ST Accel. Beams, **5**, 010701, (2002).

[3.4-27] Y. K. Wu et al. Explicit symplectic integrator for s-dependent static magnetic field, Phys. Rev., **E68**, 046502, (2003).

[3.4-28] M. Borland. elegant: A Flexible SDDS-Compliant Code for Accelerator Simulation. Technical Report LS-287, Advanced Photon Source, (2000).

[3.4-29] P. Elleaume. A New Approach to Electron Beam Dynamics in Undulators and Wigglers, Proc. of EPAC 1992, pp. 661–663, (1992); http://www.JACoW.org.

[3.4-30] R. Dejus. ANL, Private communication, (2010).

[3.4-31] K. Deb et al. IEEE TEC, **6**, 182, (2002).

[3.4-32] A. Pietryla et al. A Cerenkov Radiation Detection System for the Advanced Photon Source Source Storage Ring, Proc. of PAC 2001, pp. 1622–1624, (2001); http://www.JACoW.org.

[3.4-33] A. Fischer. Diagnostics Development for the PEP-II B Factory, Proc. of BIW 1996, pp. 248–256, (1996); http://www.JACoW.org.

[3.4-34] B. Yang. APS-SR Cherenkov Detector Pulse Counter Initial Calibration. Technical Report DIAG-TN-2008-012, APS/ASD/DIAG, (2008).

[3.4-35] B. Yang et al. Specification of an FPGA-based Cherenkov Detector Signal Processor. Technical Report DIAG-TN-2008-010, APS/ASD/DIAG, (2008).

3.5 Short-Pulse X-Rays

3.5.1 Introduction

One of the major goals of the APS Upgrade is to address the need for intense, tunable, high-repetition-rate, picosecond x-ray pulses. This is a significant challenge for a storage ring light source, due to the physics governing storage rings. The zero-current rms bunch duration is given by [3.5-1]

$$\sigma_{t,0} = \sigma_\delta \sqrt{\frac{\alpha_c T_r E}{e\dot{V}}}, \tag{3.5-1}$$

where σ_δ is the fractional momentum spread, E is the beam energy, α_c is the momentum compaction factor, T_r is the revolution time, and $\dot{V} = 2\pi(h/T_r)V\cos\phi_s$ is the derivative of the h-harmonic rf voltage V evaluated at the synchronous phase ϕ_s. This gives

$$\sigma_{t,0} = \sigma_\delta T_r \sqrt{\frac{\alpha_c E}{2\pi h e V \cos\phi_s}}. \tag{3.5-2}$$

For the APS, $\sigma_\delta \approx 10^{-3}$, $\alpha_c \approx 2.8 \times 10^{-4}$, $T_r = 3.68\mu$s, $h = 1296$, $V = 9$ MV, and $\phi_s \approx 40°$, giving $\sigma_{t,0} = 20$ ps.

As the current increases, the bunch length also increases due to interaction of the beam with the longitudinal impedance of the vacuum chamber and rf cavities. There are two effects at work. The first is potential well distortion (PWD), which results from the relatively low-frequency part of the impedance (i.e., low frequency compared to the bunch spectrum). As the name suggests, the charge of the electron bunch distorts the potential well created by the rf system. This reduces the effective rf voltage and thus increases the bunch length according to Equation 3.5-1 by, effectively, reducing $\dot{V}$. The PWD has no threshold but lengthens the bunch starting from infinitesimal current. For the APS, measurements [3.5-2] show that

$$\sigma_t \approx 25.1 I^{0.1484+0.0346\log_e I}, \tag{3.5-3}$$

where σ_t is in ps and $I > 0.1$ mA is the bunch current. For the 4.25-mA single-bunch current in 24-bunch mode, this gives about 34 ps. When we double the current, this will increase to 40 ps.

A second important phenomenon affecting the bunch length is the microwave instability, which depends on the higher frequency part of the impedance. It results in increased energy spread σ_δ, which again increases the bunch length according to Equation 3.5-1. At the APS, the microwave instability threshold is about 7 mA [3.5-3]. At present, it only impacts the intense bunch in hybrid mode operation. It will have a small affect on 200-mA operation in 24-bunch mode.

3.5.2 Approaches to Short X-Ray Pulses

In the face of these phenomena, various approaches have been tried to create shorter x-ray pulses. In this section, a number of these approaches are reviewed, indicating the strengths and weaknesses of each.

3.5.2.1 High-Harmonic Cavity

One approach is to use a high-harmonic rf cavity to increase $\dot{V}$. However, it is difficult to get a significant improvement using this method, because of the difficulty of obtaining sufficient voltage. A preliminary study [3.5-4] showed that reducing the bunch length at 4 mA by a mere 50% would require 9 MV at 1.4 GHz. In spite of the marginal benefit, this would take up significant space that could otherwise be used for insertion devices. In addition, it would shorten the Touschek lifetime, which is undesirable given the pressure put on top-up by the shorter lifetime in the upgrade lattices (see section 3.2.2.5).

3.5.2.2 Low-α Operation

A more workable approach [3.5-5] is to reduce the value of α_c in Equation 3.5-1, which can be done by adjustment of the lattice. For example, by reducing α_c by a factor of 100 from the present value of 2.8×10^{-4}, we could reduce the bunch length by an order of magnitude, reaching the few-picosecond regime. However, this causes difficulty in obtaining high bunch current, to the extent that the total stored current is typically reduced significantly. In the first place, single-bunch instabilities are worse for shorter bunches, because the peak current is increased (for fixed-bunch charge) and the frequency spectrum of the bunch is broadened. In addition, as α_c is reduced the synchrotron tune ν_s also decreases according to [3.5-1]

$$\nu_s = \sqrt{\frac{\alpha_c e \dot{V} T_r}{4\pi^2 E}}. \tag{3.5-4}$$

When ν_s is smaller, the particles in the head and tail of the bunch change positions less frequently, which gives instabilities more time to build up.

For example, the threshold for the important transverse mode-coupling instability (TMCI) is proportional to $\sigma_t \nu_s \propto \alpha$ [3.5-6, 3.5-7]. Hence, we'd expect the threshold to drop 100 fold for a 10-fold reduction in bunch length. While TMCI can be defeated to some extent with feedback and positive

chromaticity, these cures have limits. Chromaticity can only be increased so much before other aspects of machine performance like injection efficiency and lifetime suffer. While feedback may be effective in controlling centroid instabilities, beam-size instabilities cannot be controlled.

Another important instability for the APS is microwave instability. In this case, the threshold also goes down as we attempt to shorten the bunch, with a scaling of σ_l^3 [3.5-8]. Although the microwave instability does not result in beam loss, significant increase of the energy spread is problematic in a ring like the APS with nonzero dispersion in the straight sections. Of course, it also fights against the intention to obtain shorter bunch duration.

An additional difficulty with low-alpha operation for a double-bend lattice is that the emittance increases significantly, since the optics needed for minimum emittance do not accommodate the change in the sign of the dispersion required by low-alpha optics. For example, in the APS the emittance for a zero-alpha configure is about 20 nm. For these reasons, the APS has elected not to pursue a low-alpha mode as it could serve only a small segment of our user community. Although the APS operates in several special fill-pattern modes for timing experiments, these modes remain suitable for almost all users because the APS continues to run at 100 mA.

3.5.2.3 Laser Slicing

Another method of obtaining short x-ray pulses from storage rings is using "laser-slicing," in which a laser is used to increase the energy spread of a short slice of the bunch [3.5-9]. This has been successfully used to produce ∼100-fs x-ray pulses with repetition rates of hundreds of kHz at the Advanced Light Source (ALS) [3.5-10]. In this concept, a short laser pulse interacts with a section of the electron beam in a wiggler. In order for this interaction to modulate the energy of the electrons, the resonance condition must be satisfied

$$\lambda_w = \frac{2\lambda_l \gamma^2}{1 + K^2/2}, \tag{3.5-5}$$

where λ_w is the wiggler wavelength, λ_l is the laser wavelength, γ is the relativistic factor of the electron beam (1.37×10^4 for APS), and K is the wiggler strength parameter. One readily apparent difficulty is that λ_w increases as γ^2; however, this can be mitigated by making $K = 93.4B[T]\lambda_w[m] \gg 1$, giving

$$\lambda_w \approx 0.077 \sqrt[3]{\frac{\lambda_l \gamma^2}{B^2}}. \tag{3.5-6}$$

A likely candidate for a laser producing a short pulse is a Ti:sapphire laser operating at the wavelength $\lambda_l = 800$. Operating at the fundamental laser wavelength rather than its harmonic is advantageous in terms of available laser power and laser beam quality, since it avoids the use of frequency doubling crystals, which not only reduce the available laser power but also may distort the laser wavefront [3.5-11]. If B = 1.5 T then λ_w = 31 cm and K = 43. No more than 15 periods of such a device can be accommodated in a standard APS straight section. Assuming a 15-period device is placed in a zero-dispersion straight (which would require special optics), it will produce a slight damping effect on the emittance along with a slight increase in energy spread, as well as 34 kW of radiation power distributed into a rather large K/γ angle.

The modulation amplitude of the electron energy is given by equation (9) in ref. [3.5-12]. The rms fractional energy spread of the APS beam is 0.096%, giving an energy spread of σ_E = 6.7 MeV.

The peak energy modulation due to the laser as a fraction of the energy spread is shown in Figure 3.5-1. Requiring $p = \Delta E/\sigma_E > 5$ gives $A_l > 3.4$ mJ for a 50-fs FWHM laser pulse and $A_l > 6.3$ mJ for a 100-fs FWHM laser pulse. This is the minimum requirement and will be increased by various factors such as the effect of nonzero electron beam size [3.5-10]. In practice at ALS, a measured laser pulse energy of about twice the minimum value is needed [3.5-11], so it should conservatively require about 12 mJ per pulse. Commercially available lasers can provide 1-kHz pulses with an average power of 20 W [3.5-13]. Hence, at present the repetition rate would be about 1 kHz, which is quite low. Advances in laser technology, e.g., cryogenically cooled Yb:YLF, could possibly allow an increase in the repetition rate by several orders or magnitude in the not-too-distant future [3.5-14].

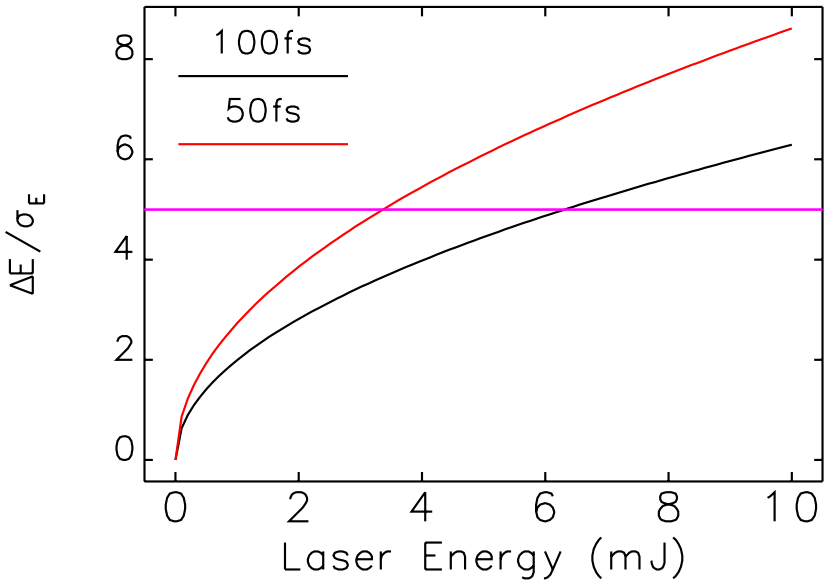

Figure 3.5-1. Energy modulation amplitude normalized to the rms energy spread of the electron beam, for the laser-slicing scheme applied to the APS.

The maximum repetition rate available in this technique when one can alternate electron bunches is determined by the need to limit the beam energy spread increase. To estimate this increase, one first looks at the energy change of an electron during a single turn when the laser hits the bunch. For the i^{th} electron

$$\Delta E_i = (QE)_i + p\sigma_E \sin\omega_l t_i \exp\left\{-\frac{t_i^2}{2\sigma_l^2}\right\}, \tag{3.5-7}$$

where $(QE)_i$ is a random deviate representing quantum excitation, $\omega_l = 2\pi c/\lambda_l$, and σ_l is the laser pulse duration. Averaging this over the electron bunch gives

$$\langle \Delta E^2 \rangle = \mathcal{N}\langle u^2 \rangle T_0 + \frac{p^2\sigma_E^2\sigma_l}{4\sqrt{2}\sigma_t}, \tag{3.5-8}$$

where $\mathcal{N}\langle u^2 \rangle$ is the familiar quantum excitation term [3.5-1], T_0 is the revolution time, and σ_t is the rms electron bunch duration. The effective excitation rate is

$$\frac{d}{dt}\langle \Delta E^2 \rangle = \mathcal{N}\langle u^2 \rangle + \frac{p^2\sigma_E^2\sigma_l}{4\sqrt{2}\sigma_t}\frac{f_l}{n_b}, \tag{3.5-9}$$

where f_l is the laser repetition rate and n_b is the number of bunches. The equation for the equilibrium energy spread is [3.5-1]

$$\sigma_E^2 = \frac{1}{4}\tau_E \frac{d}{dt}\langle \Delta E^2 \rangle \tag{3.5-10}$$

$$= \sigma_{E0}^2 \left(1 + \frac{p^2 \sigma_l f_l \tau_E}{16\sqrt{2}\sigma_t n_b}\right). \tag{3.5-11}$$

If σ_E is allowed to grow by 10%, then we have

$$f_l \leq \frac{16\sqrt{2}\sigma_t n_b}{5p^2 \sigma_l \tau_E}. \tag{3.5-12}$$

For $p = 5$, $\sigma_t = 50$ ps, $n_b = 24$, $\sigma_l = 100/2.35$ fs, and $\tau_E = 4.8$ ms, one has $f_l \leq 1$ MHz. This is much larger than the repetition rate of available lasers and is essentially not a limiting factor.

For purposes of calculation, let us assume that a 1-kW laser delivering 10 mJ pulses will be feasible in the not-to-distant future, giving $f_l = 100$ kHz. Assuming suitable optics between the modulator and the radiator, the effective bunch current for those electrons that contribute to the short pulse is given by [3.5-9]

$$I_b \eta \sigma_l / \sigma_t, \tag{3.5-13}$$

where I_b is the total bunch current and $\eta \approx 0.15$ is the fraction of electrons within the laser pulse that obtain sufficient amplitude to be visible. These parameters (and assuming 200 mA in 24 bunches), yields an effective bunch current of about 1 μA. The flux is reduced by a factor 8×10^3 compared to the full bunch. This low flux may be problematic for many experiments. It could be increased by using a longer, higher-power laser pulse at the expense of a longer x-ray pulse. In addition, on-going improvements in laser technology should allow increasing the pulse energy and/or the repetition rate, making this one of the more promising avenues for producing short-pulse x-rays.

3.5.2.4 Deflecting Cavities

In light of the difficulties associated with these existing methods, a method based on the use of deflecting cavities [3.5-15] has been investigated. In this concept, illustrated in Figure 3.5-2, transverse deflecting rf cavities are used to impose a correlation (“chirp”) between the longitudinal position of an electron within the bunch and its vertical momentum. The x-rays emitted by each electron tend to travel along the path of the electron itself. Hence, by placing an undulator just downstream of the deflecting cavity (for example), one can produce a chirped x-ray beam. At a sufficient distance (e.g., 30 m) from the undulator, this angular chirp will have evolved into a spatial chirp, so that a strong correlation appears in the x-ray pulse between arrival time and vertical coordinate. Use of vertical slits then permits filtering the pulse in the time dimension, allowing production of an x-ray pulse that is shorter than the electron pulse. This scheme is referred to as the SPX (short-pulse x-ray) scheme.

As shown in Figure 3.5-2, two cavities are required, with the purpose of the second cavity being to cancel the effects on the electron beam of the first cavity. This is necessary in order to avoid extremely large vertical emittance growth. The second cavity must be placed at a vertical betatron phase advance $N \times 180^\circ$ downstream of the first, where N is an integer. Because the APS lattice normally

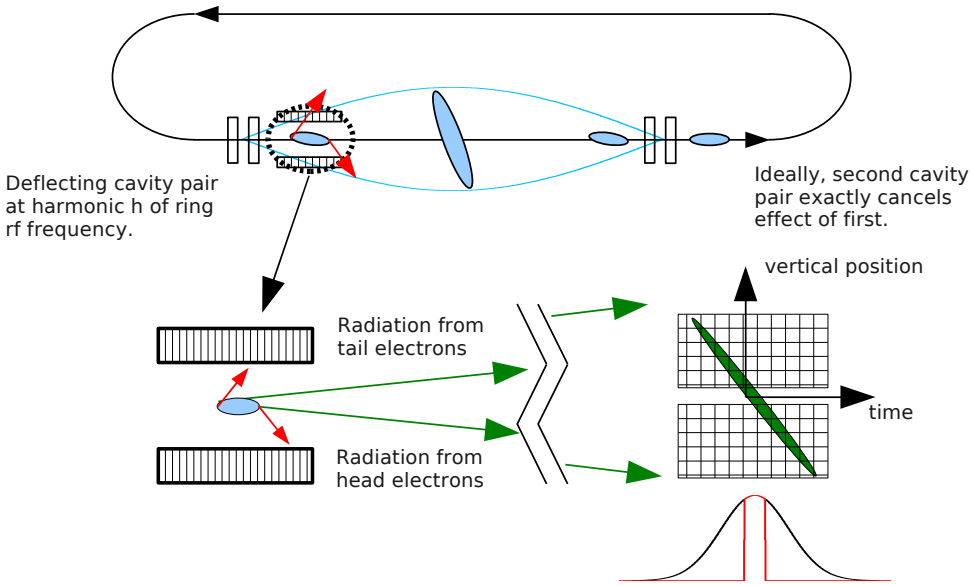

Figure 3.5-2. Illustration of Zholents' scheme for creating short x-ray pulses using deflecting cavities.

has $\nu_y = 19.2$, or $\Delta\nu_y = 0.48$ per cell, this is readily accomplished by having the cavities separated by N sectors and making slight adjustments to the electron beam optics. If $N > 1$, the time-angle chirp of the electron beam will reappear at all intervening straight sections. This allows for providing chirped pulses to a larger number of beamlines. However, N cannot be increased without limit, due to potential issues with storage ring operation [3.5-16].

The cavities must have a deflecting mode frequency that is a harmonic h of the ring rf frequency, 352 MHz. One can characterize the deflecting strength using an effective transverse sinusoidal voltage of amplitude V_t, which can impart a maximum slope change of V_t/E, where E is the electron beam energy. As shown below, $h = 8$ appears to be a workable choice. This corresponds to a deflecting cavity frequency of about 2.8 GHz. This high frequency has implications for the time structure of the x-ray pulses.

As indicated, once the photon beam has drifted a sufficient distance, the pulse can be shortened simply by using vertical slits. This will, of course, discard considerable intensity. Another option [3.5-15] is to use asymmetric-cut crystals to perform pulse compression. Such crystals allow imposing a time-of-flight variation that is proportional to vertical position. In either case, the minimum achievable x-ray pulse duration can be estimated as [3.5-17]

$$\sigma_t \approx \frac{E}{\left(\frac{\partial}{\partial t} V_t \sin\omega_t t\right)_{t=0}} \sqrt{\frac{\beta_{\mathrm{ID}}}{\beta_{\mathrm{rf}}}} \sqrt{\frac{\epsilon_y}{\beta_{\mathrm{ID}}} + \sigma_{y',\mathrm{Rad}}^2} \ , \tag{3.5-14}$$

where β_{ID} and β_{rf} are the vertical beta functions at the ID and deflecting cavities, respectively, ϵ_y is the vertical slice emittance (i.e., the emittance outside the chirp region), ω_t is the angular frequency of the deflecting mode, and $\sigma_{y',\mathrm{Rad}}$ is the intrinsic vertical divergence of the photons. This is given roughly by [3.5-18]

$$\sigma_{y',\mathrm{Rad}} \approx \sqrt{\frac{\lambda_r}{2L_u}}, \tag{3.5-15}$$

where λ_r is the radiation wavelength and L_u is the length of the undulator. Using 2-MV deflecting voltage with $h = 8$, $\beta_{\text{ID}} = \beta_{\text{rf}} = 3$ m, 10-keV x-rays from a 2.4-m-long device, and $\epsilon_y = 35$ pm, we get $\sigma_t \approx 1.2$ ps. As seen below, this is achievable with 1% transmission through the vertical slits.

Because the cavities are operated continuously, in principle every bunch in the ring is chirped identically and hence produces a short x-ray pulse. The most common operating mode, yields a 6.5 MHz bunch rate. Because of the relatively large flux (1% of nominal) and high repetition rate, this scheme outperforms the others that have been considered and has been chosen as the preferred method for meeting the mission requirement of shorter x-ray pulses.

As mentioned above, an option for the deflecting cavity approach is to use asymmetric-cut crystals to perform x-ray pulse compression [3.5-15]. This does not make the x-ray pulse shorter, but rather permits opening the slits to allow a greater fraction of the x-ray pulse through. This should permit increasing the flux by a significant amount, but the x-ray optics has challenges that would need to be addressed and which are outside the scope of APS-U. It provides a possible path forward to allow an order-of-magnitude increase in photons per pulse.

3.5.2.5 Alternative Deflecting Cavity Scheme

In the scheme we propose here, as illustrated in Figure 3.5-2, the insertion device (ID) is located at a vertical phase advance of $n180^\circ$ from the cavities, where $n \geq 0$ is an integer. As a result, the ultimate x-ray pulse length that is achievable in this scheme is limited by the vertical electron beam divergence and the intrinsic opening angle of the radiation, as well as the deflecting voltage slope.

Another configuration [3.5-19] is possible that makes use of a spatial electron beam chirp. This can be implemented by having a four-cavity bump in a very long straight section, or by placing an undulator at a phase advance of $(2n + 1)90^\circ$ from the cavities (where $n \geq 0$). In this case, the relevant comparison is of the size of the chirp to the vertical electron beam size and the intrinsic size of the radiation source. In ID straight sections, the former tends to be small because of the small vertical beta function needed to accommodate the vacuum chamber. The later is given by $\frac{1}{4\pi}\sqrt{2\lambda_r L_u}$. For 1-Å radiation, this is about 10% of the typical vertical beam size at an ID in the APS.

Together, these seem to promise shorter x-ray pulses with less chirp, albeit with lower intensity (since one is still performing slicing). One option for utilization of this scheme requires a long straight section that can accommodate four cavities plus the insertion device. This would have the advantage of eliminating some of the beam dynamics issues described in section 3.5.3. If we implemented this scheme in the APS with a 7.7-m-long straight section, we might be able to fit 6 cavities on either side of a 2.4-m-long ID. The minimum FWHM pulse duration would then be about 3.5 ps with 2% transmission through the slits. As we will see, we expect shorter pulses with similar transmission using the original scheme. In addition, for approximately the same cost, the original scheme allows us to provide chirped pulses to several ID and bending magnet beamlines.

Alternatively, one could modify the optics to achieve 90-degree vertical phase advance between three successive straight sections. However, this requires large vertical beta functions in the middle straight section and is not workable.

3.5.2.6 Conclusion

The major methods of achieving short x-ray pulses in a storage ring have been briefly reviewed. The deflecting-cavity-based method has several advantages over the others discussed. The use of a higher-harmonic accelerating cavity compares very poorly as it cannot reach the few-ps scale. The low-α method suffers from low average beam current, which confines it to use as a special, limited operating mode. The laser slicing method suffers from a relatively low repetition rate and at least 10-fold smaller intensity, although it should improve as laser technology improves. Hence laser slicing is the strongest alternative after the chosen approach of using deflecting cavities.

Subsequent sections go into detail about several aspects of this challenging project. First is a discussion of single-particle dynamics, including controlling the impact of the cavities, determination of tolerances, and detailed predictions of performance. Collective effects of the cavities are examined next, which establishes requirements for damping of cavity modes. Following this are discussions of cavity design, cryogenics, low-level rf, and high-level rf. Next, controls are discussed, as are timing, machine protection, and, finally, diagnostics.

As shown below, creation of the deflecting-cavity-based system is challenging. Success will not only create a new capability for APS users and address a key part of the APS-U science mission, it will also show the way forward for other storage ring light sources that seek to create intense, tunable, picosecond x-ray pulses.

3.5.3 Single-Particle Dynamics

3.5.3.1 Introduction

Soon after starting simulation of the application of the deflecting cavities at the APS, it was found that the cavities make a large impact on the single-particle beam dynamics in many ways. A lot of effort was devoted to studying the effects and mitigating their consequences. Here are described these effects and the ways to control them.

There many ways in which the deflecting cavities can affect the beam and diminish the operational parameters. As mentioned before, the second cavity is introduced to cancel the chirp produced by the first cavity such that the users outside of the two-cavity system ideally would not see any change in the electron beam parameters. However, many things affect perfect cancellation. Errors, inevitably present in the real machine, can lead to emittance increase and orbit change. But even in the perfect machine, there are many effects that could break the cancellation conditions or affect the beam in other ways.

3.5.3.2 Emittance Degradation

There are several effects that result in the emittance degradation in the perfect machine. They are described in details in ref. [3.5-20]; here those effects will be briefly named.

The APS storage ring has 0.1% rms energy spread in the beam. Due to nonzero momentum compaction between the cavities, the energy spread in the beam leads to time-of-flight differences

for different particles. The particles arrive at different rf phases and experience only partial kick cancellation. For a particle arriving with a small time delay of Δt, the additional kick after the second cavity would be approximately

$$\Delta y' = -\frac{eV_t\omega\Delta t}{E}, \tag{3.5-16}$$

which leads to emittance increase in a single turn of

$$\frac{\Delta\varepsilon_y}{\varepsilon_y} = \frac{\sqrt{\sigma_{y'}^2 + \frac{V_t\omega_t\sigma_t}{E}}}{\sigma_{y'}} - 1. \tag{3.5-17}$$

Here V_t and ω_t are transverse (or deflecting) voltage amplitude and angular frequency, E is the beam energy, and $\sigma_{y'}$ and σ_t are the beam divergence and bunch length. Estimations show that this effect is small.

Due to nonzero chromaticity between cavities, the energy spread in the beam leads to different betatron phase advances between the cavities. The closed-bump condition is satisfied only for on-momentum particles. However, if the particle i has an energy deviation of δ_i and the chromaticity between the cavities is ξ_y, then the phase advance of that particle is changed by $2\pi\xi_y\delta_i$. This leads to a particle position change at the second cavity

$$y_2 = \sqrt{\beta_1\beta_2}\; y_1' \sin(2\pi\xi_y\delta_i), \tag{3.5-18}$$

where β_1 and β_2 are vertical beta functions at cavity locations. The rms value of the residual amplitude is

$$\sigma_{y_2} = 2\pi\xi_y\sqrt{\beta_1\beta_2}\;\frac{\omega_t V_t}{E}\sigma_\delta\sigma_t. \tag{3.5-19}$$

Estimations show that in our case for uncorrected chromaticity between cavities the emittance almost doubles. This means that one actually cannot operate without chromaticity correction between the cavities.

To correct the chromaticity between cavities, one needs to install sextupoles. But the sextupoles bring nonlinear fields, betatron phase advance dependence on the kick amplitude, and nonlinear coupling between horizontal and vertical plane. All these effects together lead to vertical emittance degradation, which then increases the minimal achievable bunch length according to Equation 3.5-14. Figure 3.5-3 shows the vertical emittance increase from 25 pm·rad to 600 pm·rad in just a few turns in the presence of nominal APS sextupoles. This would appear to be a show stopper, but, as will be shown, a solution is available.

3.5.3.3 Control of Operational Impact

According to Equation 3.5-14, the minimum achievable pulse length is inversely proportional to the derivative of the deflecting voltage:

$$\left(\frac{\partial V_t \sin\omega_t t}{\partial t}\right)_{t=0} = 2\pi h f_{\text{rf}} V_t, \tag{3.5-20}$$

where f_{rf} is the storage ring rf frequency and h is the harmonic of the deflecting voltage frequency. The choice of h is dictated by the available rf sources, as will be shown later. The maximum possible

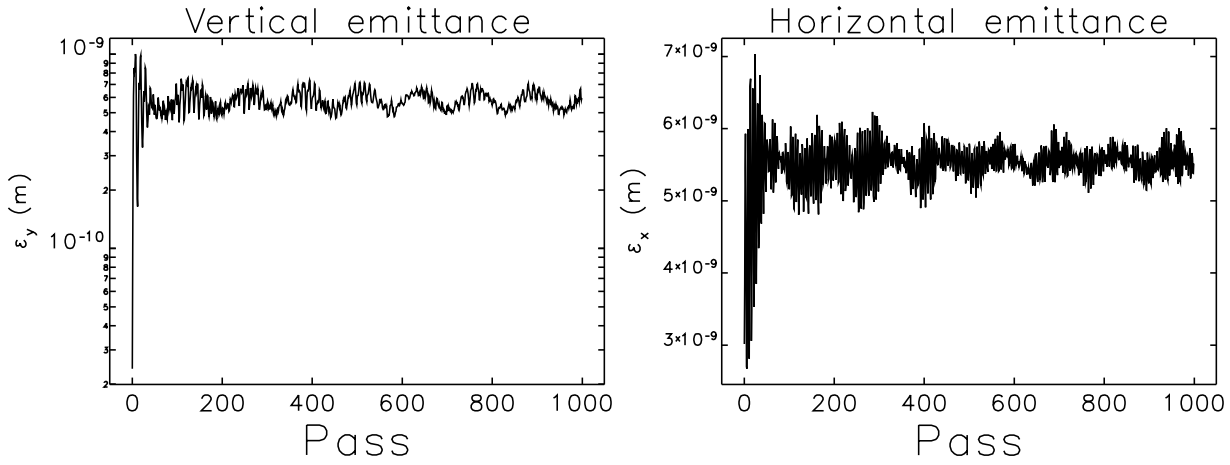

Figure 3.5-3. Emittance blowup with nominal (not optimized) sextupoles. Left plot is vertical emittance, and right plot is horizontal emittance.

deflecting voltage amplitude is defined by the requirement of keeping the beam size smaller than the vacuum chamber. For a 7.5-mm vacuum chamber this gives the following limits: 3.8 MV when the first cavity is placed in the upstream part of the ID straight section and 6.5 MV when the first cavity is located in the downstream end.

High deflecting voltage also leads to vertical emittance increase, and vertical emittance degradation not only undermines the minimal achievable pulse length, it also violates the important requirement of not disturbing the beam for other users that are located outside of the cavity bump. That is why containing the emittance blowup is so important.

In order to understand the processes behind the emittance increase, the effect of an orbit bump produced by a corrector magnet was studied. When an electron is displaced in the sextupole in the vertical direction, it experiences a kick in vertical plane,

$$\Delta y' = b_s(y_0 + y)x, \tag{3.5-21}$$

where b_s is the sextupole strength, y_0 is the orbit displacement, and x and y are betatron coordinates. Following ref. [3.5-21] and assuming $y_0 \gg y$, one can obtain the perturbation to the vertical emittance caused by this kick:

$$\Delta\varepsilon_y \approx 2b_s y_0 \sqrt{\varepsilon_x\varepsilon_y\beta_x\beta_y}\sin\phi_x\cos\phi_y = b_s y_0\sqrt{\varepsilon_x\varepsilon_y\beta_x\beta_y}\sin(\phi_x - \phi_y). \tag{3.5-22}$$

One can also calculate an emittance increase due to such a kick in the case of many sextupoles and also including betatron tune dependence on the particle energy through chromaticity:

$$\Delta\varepsilon_y = \sqrt{\varepsilon_x\varepsilon_y}\; e^{-\frac{\theta^2}{2\tau_y^2}} e^{-\sigma_E^2\frac{(C_x-C_y)^2}{Q_s^2}\sin^2\frac{Qs\theta}{2}}\Im\left[\sum_j b_{sj}y_{0j}\sqrt{\beta_{xj}\beta_{yj}}e^{i\Delta\chi_j}\right]\sin(\Delta Q\;\theta + \psi), \tag{3.5-23}$$

where θ is the longitudinal coordinate, τ_y is decoherence time due to tune shift with amplitude, $C_{x,y}$ is chromaticity, Q_s is synchrotron tune, ΔQ is betatron tune difference, $\Delta\chi$ is betatron phase difference,

and ψ is the initial phase of the emittance oscillation. Note that the expression inside the bracket is proportional to a coupling coefficient for a linear coupling resonance with $b_{sj}\ y_{0j}$ playing the role of a normalized skew quadrupole gradient. Thus one arrives at the well known result that vertical orbit distortion in a storage ring with sextupoles produces coupling. The difference between Equation 3.5-23 and an established result is that Equation 3.5-23 also describes transient oscillations found through simulations [3.5-20].

To compare the above expression with simulations, we can rewrite it in a simpler way:

$$\varepsilon_y(\theta) = \varepsilon_{\text{final}} - (\varepsilon_{\text{final}} - \varepsilon_{\text{initial}})\ \ e^{-\frac{\theta^2}{2\tau_y^2}}\ \ e^{-\sigma_E^2 \frac{(C_x - C_y)^2}{Q_s^2} \sin^2 \frac{Qs\theta}{2}} \sin(\Delta Q\ \theta), \tag{3.5-24}$$

where $\varepsilon_{\text{initial}}$ is the emittance before the kick and $\varepsilon_{\text{final}}$ is the final emittance after the emittance oscillations are damped. Thus the expression 3.5-24 describes the oscillation of the vertical emittance after a sudden coupling change. Figure 3.5-4 compares emittance oscillations found in tracking with Equation 3.5-24 for two different chromaticity settings. The red line shows `elegant` tracking simulations, while the black line shows the fit using Equation 3.5-24 with two fitting parameters, $\varepsilon_{\text{final}}$ and τ_y.

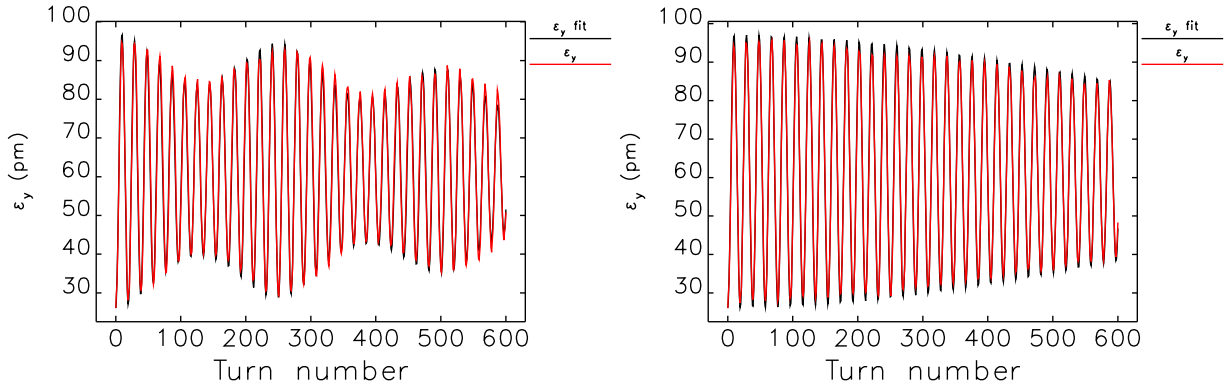

Figure 3.5-4. Comparison of the tracking results (red line) and a fit using Equation 3.5-24 (black curve) due to vertical orbit bump produced by corrector magnets. The left plot is for $C_x = 6$, $C_y = 4$, while the right plot is for $C_x = 6$, $C_y = 6$.

Similar calculations can be done for the horizontal plane. When an electron is displaced vertically in a sextupole, it experiences a kick in the horizontal plane:

$$\Delta x' = \frac{b_s}{2}\ (y_0 + y)^2 \approx b_s\ y\ y_0 + \frac{b_s}{2}\ y_0^2. \tag{3.5-25}$$

This kick creates a perturbation to the horizontal emittance

$$\Delta\varepsilon_x \approx -b_s y_0 \sqrt{\varepsilon_x \varepsilon_y \beta_x \beta_y} \sin(\phi_x - \phi_y) + b_s y_0^2 \sqrt{\varepsilon_x \beta_x} \sin\phi_x. \tag{3.5-26}$$

Here the first term is the same as in Equation 3.5-22, but has the opposite sign. This confirms that the vertical emittance increases at the expense of the horizontal emittance as expected in the case

of coupled motion. Since in the case $y_0 \gg \sqrt{\varepsilon_y \beta_y}$, the second term in Equation 3.5-26 dominates. Keeping just the second term and performing calculations for many sextupoles, one can get the following expression for the horizontal emittance oscillations:

$$\Delta\varepsilon_x = \sqrt{\varepsilon_x}\; e^{-\frac{\theta^2}{2\tau_y^2}} e^{-\sigma_E^2 \frac{C_x^2}{Q_s^2} \sin^2 \frac{Q_s\theta}{2}} \Im\left[\sum_j b_{sj} y_{0j}^2 \sqrt{\beta_{xj}} e^{i\Delta\chi_{xj}}\right] \sin(Q_x\; \theta + \psi_x). \tag{3.5-27}$$

Long enough after a sudden vertical orbit bump, the emittance oscillations will decay and leave just the lattice with a local vertical orbit bump. Equilibrium vertical emittance will be defined by the coupling on the new orbit, and the horizontal emittance will be unchanged (if the orbit bump is reasonably small). What is the source of the horizontal emittance oscillations in the beginning? To understand that, remember that the vertical orbit bump generates a small kick in the horizontal plane that changes the horizontal closed orbit. But the tracking is done on zero orbit; therefore turning the vertical correctors on is equivalent to a sudden kick in horizontal plane, which leads to betatron oscillations and emittance growth due to oscillation decoherence. This means that the horizontal emittance will recover due to synchrotron radiation damping in the case of the vertical bump created by correctors.

The difference between the dipole and the deflecting cavity is that, in the case of a deflecting cavity, the kick strength depends on the longitudinal position of the particle in the beam. The beam can be split in many slices in the longitudinal direction, and every slice will see the constant kick as in the case of the dipole (for a few tens of turns until the synchrotron phase is not changed significantly). The slice-to-slice variation of the kick amplitude changes the way the emittance oscillations decay, as can be seen in Figure 3.5-5. Here again the red line shows tracking simulations and the black line shows the fit using the modified expression

$$\varepsilon_y(\theta) = \varepsilon_{\text{final}} - (\varepsilon_{\text{final}} - \varepsilon_{\text{initial}})\; e^{-\frac{\theta^2}{2\tau_y^2}}\; e^{-\sigma_E^2 \frac{(C_x - C_y)^2}{Q_s^2} \sin^2 \frac{Q_s\theta}{2}} e^{-\sin^2 \frac{Q_s\theta}{2}} \sin(\Delta Q\; \theta), \tag{3.5-28}$$

where the third exponent was added to account for the amplitude variation (the exact derivation of this term is not available). The agreement between the black and red lines is reasonable though not as good as is in Figure 3.5-4.

The emittance oscillations in the cases of dipoles and deflecting cavities may look different, but the final emittances in both cases are close (around 60 pm, compare Figures 3.5-4 and 3.5-5). (Note that the amplitude of the kick in the dipole case corresponds to the cavity kick to a particle at a longitudinal position of one standard deviation.) The exact relation of the emittances for the cases of constant and variable kicks is hard to derive analytically, but simulations were performed for different sets of sextupoles and the equality of the emittances approximately stands. This fact gives a simple way to predict the equilibrium vertical emittance; however one should understand that it works only when the coupling is the dominating effect in the emittance increase.

Now it can be stated that the sextupoles between cavities must satisfy the following requirements:

- Compensate natural chromaticity

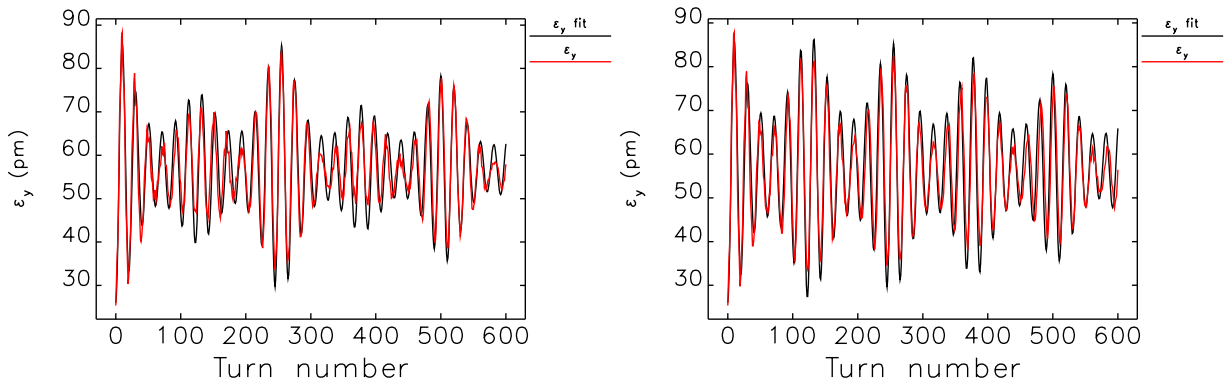

Figure 3.5-5. Comparison of the tracking results (red line) and a fit using equation 3.5-24 (black curve) for a case of orbit bump produced by rf deflectors. The left plot is for $C_x = 6$, $C_y = 4$, while the right plot is for $C_x = 6$, $C_y = 6$.

- Minimize coupling on the vertical bump
- Minimize the total horizontal and vertical kicks that are generated on the vertical trajectory

However, it should be remembered that modern storage-ring based light sources utilize high symmetry to reduce negative nonlinear effects of strong sextupoles. Local optimization of sextupoles between the cavities breaks global sextupole symmetry and can lead to reduction of the lifetime and injection efficiency. Therefore, to the requirements above should be added:

- Maintain satisfactory dynamic aperture (for injection)
- Maintain satisfactory momentum aperture (for lifetime)

Tracking was used to simulate the effect of the deflecting cavities on the beam. We used `elegant` [3.5-22] and its parallel version [3.5-23], which performs tracking in 6D phase space. Given the large bending radius of the APS dipoles ($\rho = 38.9$ m), first-order matrices were utilized for the dipoles. Quadrupoles and sextupoles were modeled as kick elements up to fourth order. Accelerating cavity harmonic and voltage were chosen to reproduce the measured bunch lengthening per Equation (3.5-3) and the nominal rf acceptance of $\pm 2.35\%$.

In a cavity with open beam pipes, the main deflecting mode is a mixture of transverse-magnetic (TM) and transverse-electric (TE) modes, resulting in a radius-independent deflection [3.5-24]. The longitudinal electric field was also included to satisfy Maxwell's equations. According to the present design, each cryomodule contains four single-cell cavities. Each cavity was represented as a uniform deflecting field of length $\lambda_t/2$, where λ_t is the deflecting mode wavelength.

Since there are many different requirements on the sextupoles between the cavities, it is important to perform complex sextupole optimization that takes into account both emittance degradation and nonlinear dynamics consequences. The full optimization process consists of the following steps:

- Linear lattice design that ensures proper phase advance between cavities and allows the setting of other parameters, such as beta functions in the cavities

- Optimization of the sextupoles between the cavities to minimize the emittance growth, which is usually done using single-pass emittance growth
- Optimization of the sextupoles outside of the cavities to improve dynamic and momentum aperture of the resulting lattice

The first two steps of the optimization do not take much time, but the last step is time-consuming and can take up to a week on a multiple-core computer (see section 3.2.2.4). The proper sextupole optimization allows one to limit the emittance growth to very reasonable levels [3.5-16], i.e., to about 10%. Figure 3.5-6 shows the resulting vertical emittance as a function of deflecting voltage for bunches with two different lengths. (The lattice was optimized for extremal values of a 4-MV deflecting kick and a 50-ps-long bunch.) The emittance was obtained by tracking 10,000 particles for 10,000 turns through the optimized lattice. The beam moments were averaged over the last 2000 turns to get equilibrium values. Recall that before the sextupole optimization, the vertical emittance increased to 600 pm (see Figure 3.5-3). For the 41-ps case, thought to be appropriate for 150 mA in 24 bunches (see section 3.5.4.3), one can approximate the emittance dependence on voltage by the following empirical expression:

$$\Delta\varepsilon_y\,[\text{pm}] \approx 0.76 V_t^2\,[\text{MV}]. \tag{3.5-29}$$

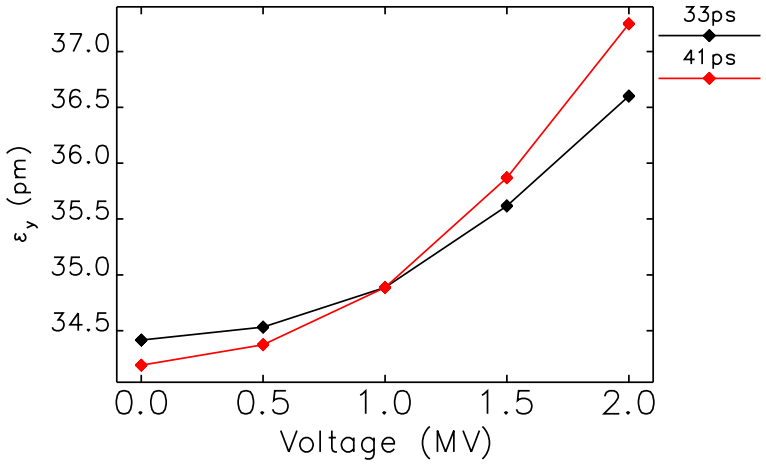

Figure 3.5-6. Dependence of the equilibrium vertical emittance on the deflecting voltage. The 33-ps case is appropriate for 100 mA in 24 bunches, while the 41-ps case is appropriate for 150 mA in 24 bunches (see section 3.5.4.3).

3.5.3.4 Tolerances

In addition to effects present in an ideal machine, the errors existing in the real machine could further degrade the performance. In this section we will look at the effects that arise in the real machine with errors. Simulations were performed for the optimized sextupoles and always included synchrotron radiation effects. Three thousand particles were tracked for 10,000 turns. In case of deflecting cavities, various errors mainly affect vertical emittance and vertical orbit outside of the cavity bump. We set limits to 10% rms emittance variation and rms orbit variation of 10% of the beam size or divergence.

Errors affecting the emittance are unequal cavity voltages, errors in the beta functions, errors in the betatron phase advance between the cavities, cavity rolls, and rolls of magnets between the cavities. Beta function error can be compensated for by changing the relative voltage of the second cavity. Phase advance error can be compensated for by changing the relative voltage of the first and second sets of cells of the second cavity. Magnet rolls can be corrected locally with additional skew quadrupoles. Cavity roll was previously found to have a weak effect [3.5-20]. Hence, all of the emittance budget was assigned to the differential voltage error. Figure 3.5-7 shows the vertical emittance increase as a function of the voltage error. Note that the minimum emittance does not occur at $\Delta V_t = 0$, which results from the fact that even with sextupole optimization, some oscillation amplitude is transferred into the horizontal plane. Hence, the second cavity should be weaker than the first ($\Delta V_t < 0$) in order to minimize the emittance increase.

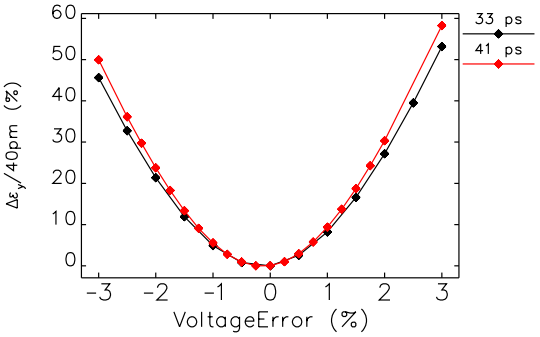

Figure 3.5-7. Variation of vertical emittance with voltage error in the first cavity for $h = 8$ and $V_t = 2$ MV.

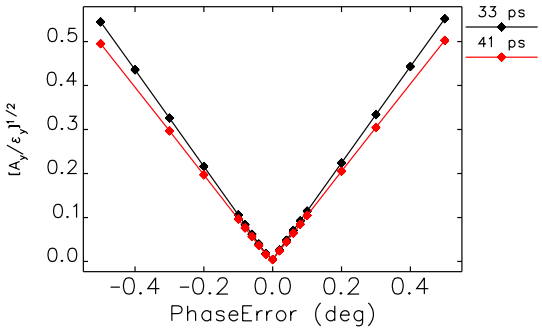

Figure 3.5-8. Beam centroid normalized to beam size as a function of differential phase error between the cavities, assuming $h = 8$ and $V_t = 2$ MV. The assumed vertical emittance is 40 pm.

An rf phase error between the sectors can result in a kick to the beam centroid and therefore an orbit change. If phase errors drift slowly (less than about 100 Hz), the orbit change can be corrected by the orbit feedback system. Otherwise, real beam motion will occur, which must be kept under 10% of the beam size. Common-mode phase errors affect the orbit between the cavities where the beam is already large due to the chirp, so this effect is not important. Differential phase errors affect the orbit everywhere, so all of the orbit error budget is assigned to differential phase error. Figure 3.5-8 shows the beam-centroid shift normalized to the beam size as a function of the differential phase error. Once again, the minimum disturbance occurs for a nonzero error. This appears to result from the fact that deflected particles take longer to arrive at the second set of cavities than undeflected particles. Hence, the phase must be slightly delayed to get the best cancellation.

The discussion of phase and voltage errors in the last two paragraphs describes only the sensitivities. However, we need to set tolerances in terms of allowed rms values of the two types of errors, corresponding to limits on the allowed rms orbit and beam size variation. This was performed using a Monte-Carlo simulation utilizing the response curves shown in Figures 3.5-7 and 3.5-8. To be conservative, we used the 41-ps curve for the voltage tolerance and the 33-ps curve for the phase tolerance. The corresponding tolerances in rms terms are summarized in Table 3.5-1.

A common-mode voltage error changes the chirp seen by the target beamlines and therefore

the pulse duration and intensity. The variation is directly proportional to the voltage variation, so the requirement of 1% stability of intensity leads to the requirement of 1% stability of the common-mode voltage. Using tracking results (i.e., Equation (3.5-29), we can also estimate the change in the emittance due to voltage change: a 1% voltage error at 2 MV translates into 0.2% emittance growth (relative to 40 pm), i.e., a negligible effect compared to differential voltage errors of the same magnitude.

A common-mode phase error changes the portion of the bunch that receives zero kick. That means that the optical slits cut out different parts of the pulse, which leads to arrival time change and to pulse intensity change. It also changes the interior orbit, but that can be ignored due to the large beam size between the cavities. Assuming a Gaussian bunch, the intensity variation can be written as

$$\sqrt{\frac{\Delta I}{I}} \approx \frac{\Delta\phi}{2\sqrt{2}\pi f_t \sigma_t}, \tag{3.5-30}$$

where f_t is the deflecting rf frequency, σ_t is the electron bunch length, and I is the peak intensity. In terms of standard deviations, we have

$$\left(\frac{\Delta I}{I}\right)_{SD} = \frac{\sqrt{2}\phi_{SD}^2}{(2\sqrt{2}\pi f_t \sigma_t)^2}. \tag{3.5-31}$$

Assuming a 33-ps rms bunch duration (the most demanding case), we find that to keep the rms intensity variation below 1%, the rms phase variation has to be below 4.0°.

Table 3.5-1 summarizes the tolerances discussed above.

Table 3.5-1. SPX Tolerance Summary. Tolerances are for a 2 MV SPX system and are determined by beam dynamics and related requirements.

Specification name	**Rms Value**	**Driving requirement**
Common-mode voltage variation	$< 1\%$	Keep intensity and pulse length variation under 1% rms
Common-mode phase variation	$< 4.0^\circ$	Keep intensity variation under 1% rms
Voltage mismatch between sectors	$< 1.1\%$	Keep rms emittance variation under 10% of nominal 40 pm
Phase error between sectors	$< 0.18^\circ$	Keep rms beam motion under 10% of beam size/divergence

The simulations shown above are based on the assumption of static, or slowly varying errors, in that the beam is allowed to find a new equilibrium in the presence of the error. In reality, phase and voltage errors will vary in time. The cavity 3-dB half-bandwidth may be as high as 1.4 kHz if the loaded Q of the rf system is chosen to be as low as 10^6. Significant phase and voltage variation may

appear at several times this frequency. Hence, simulations have been used to explore the frequency dependence of the response to phase and voltage errors in a single cavity.

Before proceeding with the simulations, note that, in the simplest picture, phase error modulation will result in a modulation of a centroid kick. One can approach this analytically, following ref. [3.5-25], section 7.2.1. The beam displacement due to a kick that occurred k turns ago is

$$\Delta y_k = \sqrt{\beta_1 \beta_2}\theta_k e^{-kT_0/\tau} \sin\left(2\pi\nu k + \Delta\psi_{12}\right), \tag{3.5-32}$$

where $\beta_{1,2}$ is the beta function at the observation (kick) point, $\Delta\psi_{12}$ is the phase advance between the two points, θ_k is the kick delivered k turns ago, T_0 is the revolution time, τ is the damping time, and ν is the betatron tune. If θ_k is modulated with frequency f_m, then $\theta_k = \hat{\theta}\cos(2\pi f_\mathrm{m} k T_0 + \phi)$, where $\hat{\theta}$ is the modulation amplitude and ϕ the modulation phase. Since only the frequency dependence is of interest, one can assume the observation point to be the same as the kicker location, so that $\beta_1 = \beta_2 = \beta$ and $\Delta\psi_{12} = 0$. Using some trigonometric identities and Equations 7.13 and 7.14 from ref. [3.5-25], one gets the following expression for the closed orbit:

$$\begin{aligned} y(\phi) &= \sum_{k=0}^{\infty} \Delta y_k \\ &= \frac{\beta\hat{\theta}}{2}\left\{\frac{q\sin A_+\cos\phi}{1-2q\cos A_+ + q^2} + \frac{(1-q\cos A_+)\sin\phi}{1-2q\cos A_+ + q^2} + \right. \\ &\qquad \left. \frac{q\sin A_-\cos\phi}{1-2q\cos A_- + q^2} - \frac{(1-q\cos A_-)\sin\phi}{1-2q\cos A_- + q^2}\right\}, \end{aligned} \tag{3.5-33}$$

where $A_\pm = 2\pi(\nu \pm f T_0)$ and $q = e^{-T_0/\tau}$. The amplitude A of the oscillation is of interest and is given by

$$\begin{aligned} \frac{A^2}{2} &= \frac{1}{2\pi}\int_0^{2\pi} y^2(\phi)d\phi \\ &= \frac{\beta^2\hat{\theta}^2}{4}\frac{q^2\left(1-\cos 4\pi\nu\right)}{\left(1-2q\cos A_+ + q^2\right)\left(1-2q\cos A_- + q^2\right)}. \end{aligned} \tag{3.5-34}$$

The obvious choice for the damping time τ is the radiation damping time. However, we know that the actual damping time is considerably shorter, due to coherent damping that results from high charge and chromaticity. We've used a value of $1/\tau \approx 500 s^{-1}$, based on measurements for the vertical plane with a chromaticity of 7. The result is shown in Figure 3.5-9, where, not unsurprisingly, a resonance behavior at the value of the tune (in this case $\nu = 0.3$) is observed. For the region of interest, up to perhaps 10 kHz, the response is essentially flat.

The effect of phase and voltage modulations was simulated using parallel `elegant`. To do this, sinusoidal modulations were imposed on the phase or voltage error in the first set of cavities. The tracking results were then analyzed to determine the frequency variation of the response. The modulation amplitude was chosen to be relatively large (2% in voltage and 0.2 degrees in phase) to reduce the effects of noise. Although the expected responses to the driving modulations were seen (e.g., vertical centroid oscillation driven by phase modulation), no indication of significant resonance behavior or frequency dependence was observed in the range scanned, which extended from 200 Hz to 4 kHz.

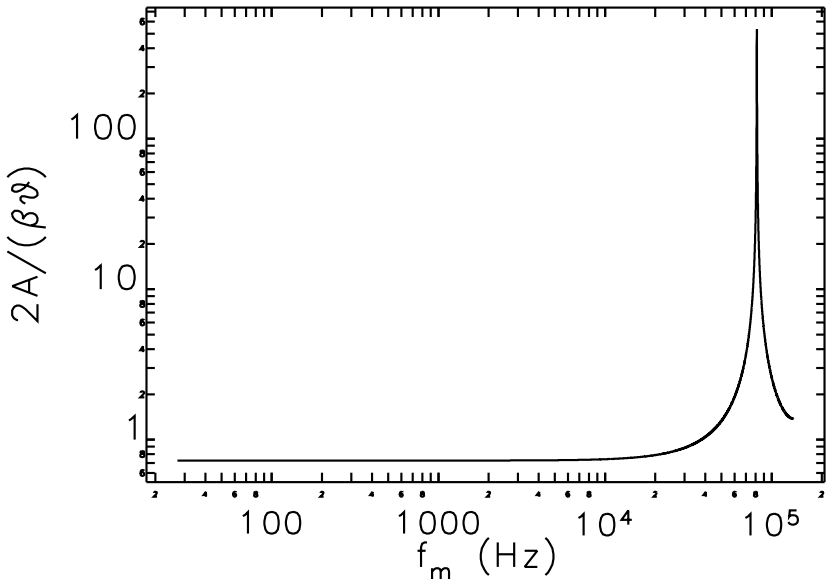

Figure 3.5-9. Frequency dependence of the orbit response to a sinusoidally varying dipole kick.

3.5.3.5 Beam Injection and Aperture Considerations

Vertical aperture limitations play major role in particle losses due to linear and nonlinear coupling. Since vertical beam size between the deflecting cavities is greatly increased, injection efficiency could suffer during SPX operation.

We can perform injection efficiency simulation by tracking a bunch of particles with initial amplitude and beam parameters corresponding to the injected beam from the booster. We used a storage ring model as measured by the response matrix fit for these simulations. The model includes both linear optics distortion and coupling. The injected beam enters the storage ring vacuum chamber with amplitude of -24 mm. After passing through one sector of storage ring optics and two kicker magnets, it experiences free betatron oscillations with the typical residual amplitude of about 6 mm, which also can be changed in the range between 4 and 7 mm depending on the kicker magnet settings. To simplify the simulations, we tracked the beam with the initial amplitude corresponding to the residual injection oscillations. Initial vertical amplitude was set equal to the measured vertical oscillation amplitude during injection. The particles are tracked for a number of turns, and the fraction of survived particles gives the injection efficiency. Figure 3.5-10 shows the results of the simulations. At the deflecting voltage of 2 MV, the injection efficiency is not significantly affected for the 6 to 7 mm initial oscillation level.

3.5.3.6 Effect of Insertion Devices

Next, we looked at the effects of insertion devices on beam properties and injection. First, we repeated the simulations of the equilibrium condition with the addition of kick maps for undulators between the SPX cavities. In Sector 6, which is free of cavities, we placed two 2.4-m-long undulators.

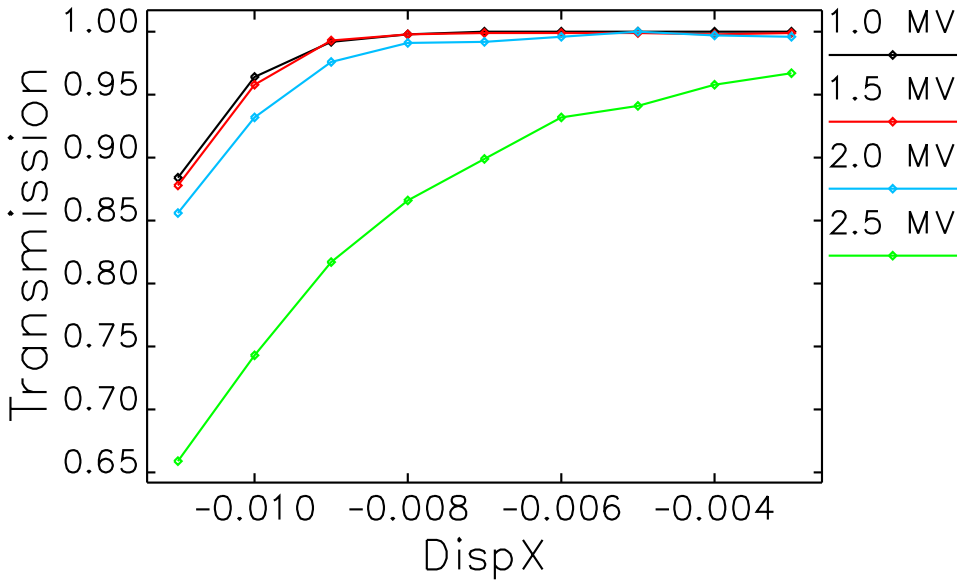

Figure 3.5-10. Particle transmission as a function on initial amplitude for different deflecting voltages. Typical oscillation amplitude is 6 mm. Horizontal emittance of the injected beam is 100 nm·rad and coupling is 5%.

In Sector 7, which has a cryomodule at the downstream end, we placed a single 2.4-m-long undulator. This device was approximately centered in the long straight section. Hence, a total of three 2.4-m-long undulators where placed between the cavities, in agreement with the present plans for the beamlines. Two sets of simulations were performed, the first using three devices with a period of 28 mm, the second using three devices with a period of 30 mm. These are devices in the range of interest to the users. Even with all gaps closed to 11 mm, the only definite effect was an increase of the vertical emittance by less than 0.8 pm. To further test this conclusion, we lengthened the device in Sector 7 to 4.8 m and repeated the simulations for the 30-mm undulator period, which previously showed the largest effect. An increase in the vertical emittance of about 1.3 pm was observed. Hence, we conclude that effects on the equilibrium beam properties are not significant.

We also looked at the effect of the insertion devices on injection efficiency. This involved repeating the analysis of the previous subsection with undulator kick maps. No significant change was seen in the results.

3.5.3.7 Predicted Performance

To simulate what pulse length and what intensity can be achieved, detailed modeling was performed using electron distributions from tracking and photon distributions from `sddsurgent` [3.5-26]. 24-bunch mode was assumed, with a 33-ps or 41-ps rms electron bunch length. After tracking 10000 particles to find the equilibrium for a series of voltages, the particle properties were averaged over 2000 turns. Using these averaged parameters, a single turn was tracked with 1 million particles to get the phase space at the undulator. The undulator was placed 1.2 m from the center of the straight

section, as would be typical. This means that the electron beam phase space has about twice as much spatial chirp as it would if the ID was centered on the straight section.

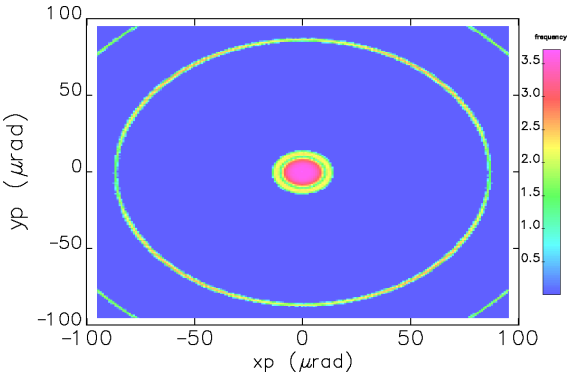

Figure 3.5-11. Angular radiation pattern from 2.4-m-long U33 undulator at 10-keV first harmonic. Relative intensity is shown on a log scale.

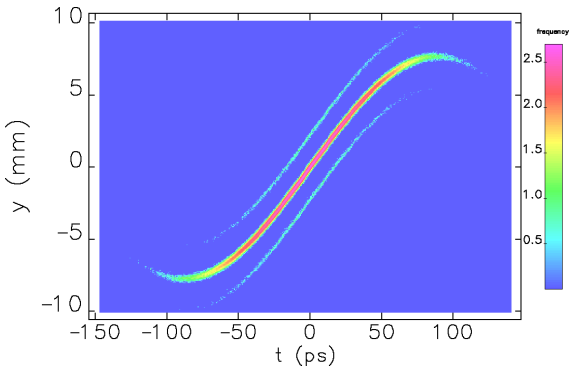

Figure 3.5-12. Radiation phase space at 26.5 m from the source, for 41-ps electron bunch and 2-MV deflection voltage. Relative intensity is shown on a log scale.

`sddsurgent` can calculate the detailed distribution of the central cone radiation and off-axis higher-order harmonics. This distribution was used for convolution with the electron distribution. Photon coordinates generated this way were then read by `elegant`. `elegant` does not specifically recognize these particles as photons, but it can still track them if only drift spaces and slits are used. In modeling the slicing process, an additional ± 0.25 mm horizontal slit at 26.5 m from the source point was used (that slit is used to decrease the intensity of the second harmonic).

Figure 3.5-11 shows the angular flux distribution of the radiation from the Undulator A at 10-keV photon energy. The second harmonic radiation is the large ring at a divergence of about 80 μrad. Use of horizontal slits allows one to attenuate the effect of the second harmonic; however, it cannot be eliminated completely. Figure 3.5-12 shows the radiation distribution at 26.5 m from the source for a 41 ps electron bunch duration. It clearly illustrates the effect of the second harmonic. (For longer bunches, a "back-chirped" portion will also appear.)

Figure 3.5-13 shows the details of time structure of the radiation pulse. The second harmonic presents itself as two pulses around the main pulse with intensity of 1 to 2% of the main pulse at distance of several tens of ps from the main pulse. The exact numbers depend on the undulator parameters. For the 41-ps bunch duration, the back-chirped pulses (which would appear at ± 178 ps) are very weak and are neglected here.

The achievable pulse duration for a particular rf voltage depends on photon energy and undulator length because they change radiation divergence $\sigma_{y',\mathrm{Rad}}$ (Equation 3.5-14). Figure 3.5-14 (left) shows pulse length as a function of the deflecting voltage for 10-keV first harmonic radiation from the 2.4-m-long U33 undulator. Figure 3.5-14 (right) shows the dependence of the pulse length on the photon energy for the same undulator. One can see that the results improve for harder x-rays, as expected from Equation (3.5-14) and (3.5-15).

In addition to the above calculations, we also investigated two additional factors, using the

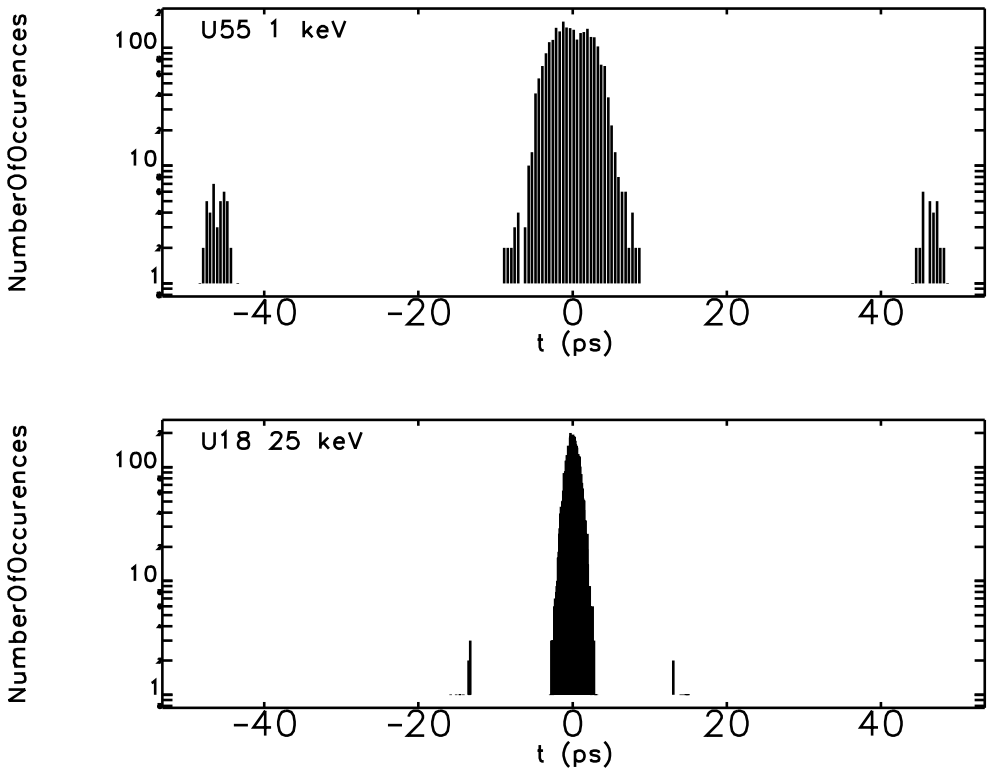

Figure 3.5-13. Time structure of the radiation pulse. The top plot shows 25-keV radiation from undulator U18, while the bottom plot shows 1-keV radiation from undulator U55. The second harmonic presents itself as two pulses around the main pulse with intensity of 1 to 2% of the main pulse at distance of several tens of ps.

program SPECTRA [3.5-27] in place of `sddsurgent`. First, we looked at the effect of beam energy spread on the radiation distribution. `sddsurgent` only includes the effect of the beam energy spread on the beam size, whereas SPECTRA includes the effect on the radiation distribution. Second, we investigated the effect of detuning the monochromator from the exact harmonic. We looked at detuning by $\Delta\lambda/\lambda = -1/N$ and $\Delta\lambda/\lambda = -1/(2N)$, i.e., the nominal undulator linewidth and half the nominal undulator linewidth. Figure 3.5-15 shows the results for a 41-ps rms electron bunch duration as a function of deflecting voltage. Only in the case of "full" detuning, $\Delta\lambda/\lambda = 1/N$, is a significant effect seen.

3.5.3.8 Work Remaining

The beam-dynamics simulations for SPX are highly developed and are believed to give accurate predictions. However, additional tasks suggest themselves, including:

- Perform tolerance estimates with dynamic errors including the effects of orbit feedback and a realistic model of the cavity feedback systems.

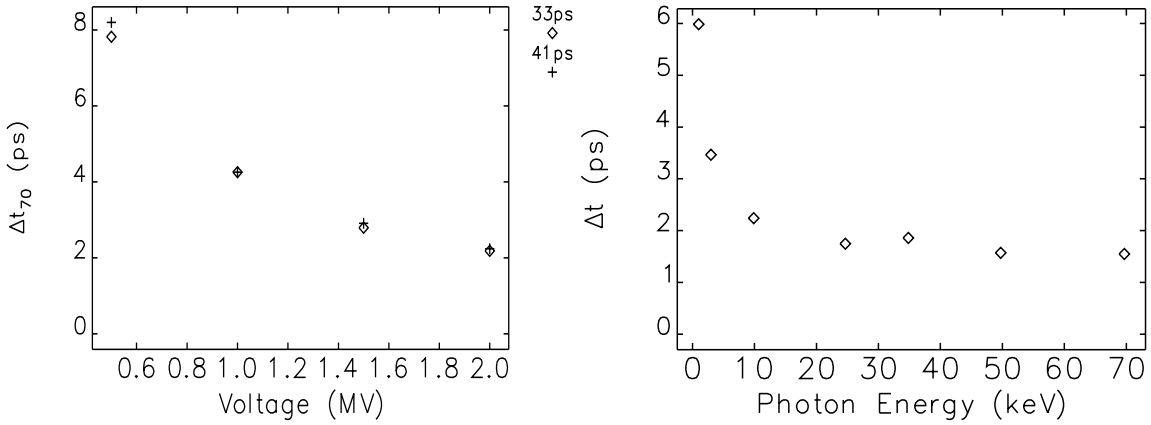

Figure 3.5-14. Predicted pulse duration. Right plot: as a function of deflecting voltage for 10-keV photons and a 41-ps electron bunch duration; left plot: as a function of the photon energy for 2-MV deflection and 41-ps electron bunch duration. The points above 30 keV are for the third harmonic.

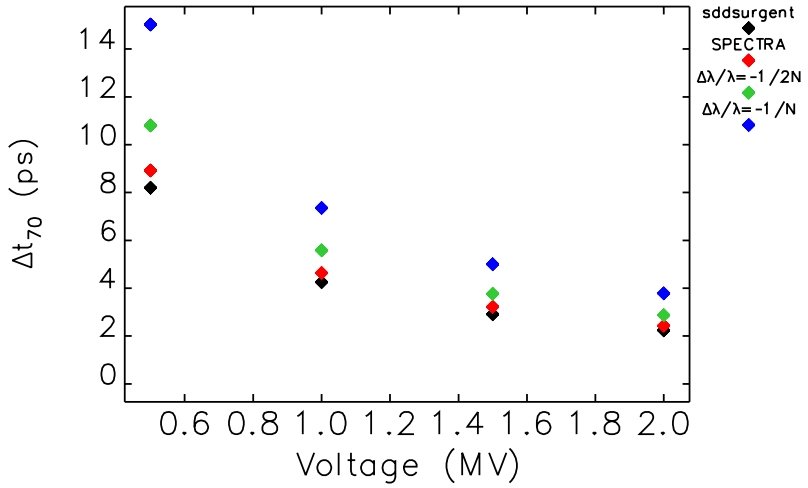

Figure 3.5-15. Predicted pulse duration for 41-ps rms electron bunch duration as a function of deflecting voltage, for four cases: Using `sddsurgent` *to compute the radiation distribution. Using SPECTRA to compute the radiation distribution, which includes broadening due to the beam energy spread. Using SPECTRA with* $\Delta\lambda/\lambda = -1/N$ *and* $\Delta\lambda/\lambda = -1/(2N)$.

- Perform analysis of sensitivity to orbit in interior sextupoles and methods of compensation, including possible additional skew quadrupole elements.

3.5.4 Collective Effects

3.5.4.1 Introduction

Collective effects are the results of those (undesirable) forces produced by the electromagnetic fields of particles of the beam acting back on the beam. These could be an increase of emittance (through, say, intrabunch collisions), a decrease of lifetime (again, through intrabunch scattering), and generation of centroid and head-tail motions (through wakefields).

The collective effects related to the deflecting cavities can be separated into short- and long-range effects. The former act within a single bunch, whereas the latter act over one or more turns.

Depending on the detailed resonant properties (i.e., frequencies and shunt impedance) of the cavities, there may or may not be an undesired beam oscillation known as coupled-bunch motion. Calculation methods can determine the safe range of cavity properties for an arbitrary bunch pattern against this instability. One only needs to specify here the cavity resonant properties required for stability for all desired bunch patterns. This is discussed in section 3.5.4.2.

The single-bunch limit is determined by the sum total of all short-range wakefields produced in the storage ring vacuum-chamber components. The deflecting cavities and the pipes connecting them to the standard chamber thus contribute additional short-range wakefields. The goal is to make an accurate estimation of the impact of the SPX cavities on single-bunch properties, including the single-bunch current limit. This is discussed in section 3.5.4.3.

3.5.4.2 Coupled-Bunch Effects and Requirements

The analysis of multibunch stability consists of determining whether it is possible for an oscillation of a multibunch beam to grow or to be sustained because of the cavity wakefields. This would occur if an HOM[2] frequency happens to be in resonance with one of the beam modes. If that is likely to happen, even for short periods of time, then the cavity design must be modified or rejected. The bunch motion in the longitudinal and two transverse planes must be considered separately as they depend on cavity resonant modes of different symmetries. The inputs to the calculation are essentially the cavity resonator parameters, the bunch pattern, and the total current.

There are three methods of various complexity (and accuracy) to determine the stability of the beam: explicit tracking of the beam with full optical and wakefield effects, normal mode analysis of bunch motion, and simple worst-case calculation from one cavity HOM.

In addition, these methods must somehow include the randomness of the HOM frequency values, as they are not known to sufficient accuracy in advance. The HOM frequencies change from design (and initial measurement) because of construction tolerances, and they also change during operation (changes in tuner position and temperature). In general the calculations are done with an assumed set of HOM frequencies, which are repeatedly randomized from the ideal design values (also known as a Monte Carlo approach). Statistics are done on the results to determine the likelihood of stability (or instability).

[2] In this section we use for simplicity the term HOM for the resonator modes that are not the driving mode of the cavity — thus HOM means any of the Higher Order Modes, Same Order Modes, and Lower Order Modes defined in subsequent subsections.

In superconducting cavities, the quality factor Q of a HOM can be very high, i.e., the resonator response is very sharply peaked in frequency and in general not close to any beam-mode frequency. This appears to be a good thing. However, if the HOM frequency varies due to temperature or operational change, the frequency might coincide with a beam mode frequency and the resulting beam instability would be very strong and cause beam loss. Another situation to consider is several cavity HOMs of much different frequency but resonant with the same beam-mode frequency through aliasing. Thus, a Monte Carlo simulation with sufficient sampling would cover operational conditions in one run.

The bunch pattern affects the type of beam mode that may occur, thus a Monte Carlo simulation has to be done for each operational bunch pattern.

The Monte Carlo method on HOM frequencies was first applied [3.5-28] for a superconducting cavity application at Cornell, then for LEP [3.5-29]. It was used in the design of the APS to determine the required deQing of the HOMs in the original (normal conducting) 352-MHz cavities [3.5-30, 3.5-31]. The method was applied again on the 2.815-GHz normal-conducting cavities in an earlier proposed SPX project [3.5-32, 3.5-33].

The most complex (and time-consuming) calculation method would be an exact multiparticle tracking of all bunches with an assumed set of HOM frequencies, where phases of all HOM wakefields are advanced in time and where wakefield forces are applied at every bunch passage. Such tracking would include helpful damping effects (at least in transverse planes) from chromaticity and short-term wakefields, which, at the APS, can result in at least twice as strong damping than that of synchrotron radiation. Since the tracking run takes some time to complete, repeating this hundreds of times for Monte Carlo sampling would be very time consuming.

For a general parameter investigation the normal-mode analysis approach is preferred because it takes much less time and can be executed in a conservative way. The centroid-motion-only normal-mode approach by Thompson and Ruth is employed [3.5-34] because it allows analysis of arbitrary bunch patterns. While this method won't include the coherent damping that comes from multiparticle effects, one could compare the result with either the synchrotron radiation damping rate (more conservative) or the expected coherent motion damping rate (more realistic), as deemed appropriate. The code `clinchor` [3.5-31, 3.5-35] was written to implement this normal mode analysis.

Before reporting on this normal-mode Monte Carlo simulation, one can make an even simpler estimate of the worst growth rate assuming only one "bad" HOM that is resonant with a beam mode, and where the bunches are equally spaced. Calculations under these strict conditions should only be used as a guide of the possible growth rates.

One assumes N bunches equally spaced and equally charged. An unstable mode would have each bunch follow an oscillation of the same amplitude but with a fixed phase difference between them. For example, in the V-plane the centroid motion of the j^{th} bunch detected at a position monitor would be $y_j = A\exp\{i2\pi jm/N\}\exp\{i\Omega_m t\}$, where A is some complex number constant, m is the mode number (0 to $N-1$), and Ω_m is the coherent frequency of mode m. Successive bunches have $\exp\{i2\pi m/N\}$ phase difference. Ω_m is very close to $\nu_y f_0$ in value for all modes, having small differences in real and imaginary parts proportional to the resonator strengths. The imaginary part gives the growth or damping rate. The resonant condition is $f_{\text{HOM}} = -f_0\nu_y + mf_0$, that is, the HOM frequency must be equal to a harmonic of the beam frequency plus an offset given by the betatron frequency. Obviously one does not want a resonance to occur, but we don't have control over the

HOM frequencies to sufficient accuracy during the design or tuning stage and during operation. To be conservative, one must assume that the frequency has the worst value, the resonant condition.

The instability growth rates depend on three properties of the cavity modes: the resonance frequency, the Q, and the shunt impedance. Before continuing, the definition of the term shunt impedance must be clarified. There are two conventions that differ by a factor of two. One is the "circuit" model, which is used in ring impedance and instability calculations, and the other is the "accelerator" model, which is used in specifying power requirements for driving a cavity. To avoid confusion, Table 3.5-2 gives the definitions of shunt impedance for the circuit model and related quantities.

Table 3.5-2. Definitions for circuit-model shunt impedance. Definitions are given for both monopole and dipole resonators with frequency ω_r and other related quantities.

Quantity	**Longitudinal**	**Transverse**
Voltage integral [a]	$V = \int_{-L/2}^{L/2} E_z(r,z)\ \exp\{-i\omega z/c\}dz$	$V(r) = \int_{-L/2}^{L/2} E_z(r,z)\ \exp\{-i\omega z/c\}dz$
Shunt Impedance[b,c]	$R_s = \frac{\lvert V\rvert^2}{2P_c}$	$R_t = \frac{1}{\kappa_r a^2}\frac{\lvert V(a)\rvert^2}{2P_c}$
Impedance	$Z_\parallel(\omega) = \frac{R_s}{1+jQ(\omega/\omega_r-\omega_r/\omega)}$	$Z_\perp(\omega) = \frac{\omega_r}{\omega}\frac{R_t}{1+jQ(\omega/\omega_r-\omega_r/\omega)}$
Wake coefficient	$W_{\parallel 0} = \omega_r R_s/Q$	$W_{\perp 0} = \omega_r R_t/Q$
Wake function[d]	$W_\parallel(z) = W_{\parallel 0}\exp\left\{-\frac{\kappa_r z}{2Q}\right\}\cos(\kappa_r z)$	$W_\perp(z) = W_{\perp 0}\exp\left\{-\frac{\kappa_r z}{2Q}\right\}\sin(\kappa_r z)$

[a] For dipole modes (transverse plane) the integral is performed with a radial offset $r \neq 0$
[b] P_c is the power needed to maintain the E_z fields, including power dissipated in dampers
[c] κ_r is the wave number ω_r/c of resonator frequency; a is radius of E_z integration.
[d] Used for time-domain calculations, e.g., mode analysis and tracking.

The growth rates for a single HOM resonator with worst-case frequency are

$$\alpha_s = \frac{\alpha_c I_{\text{total}}}{2(E/e)\nu_s}(R_s f_{\text{HOM}})\exp(-\omega_r^2\sigma_t^2), \tag{3.5-35}$$

for the longitudinal plane and

$$\alpha_{x,y} = \frac{f_0 I_{\text{total}}}{2(E/e)}(\beta_{x,y}R_t)\exp(-\omega_r^2\sigma_t^2), \tag{3.5-36}$$

for the transverse planes. A bunch form factor was added, which is sometimes overlooked in the literature. The quantities besides shunt impedance are explained in Table 3.5-3. The table refers to two values of total current. Although the APS-U requirement is 150 mA, the design requirements for stability purposes is 200 mA, for which all stability calculations are done. A design that is stable for 200 mA will certainly be stable at 150 mA.

Each growth rate must be compared with the natural damping time of the centroid of the bunch, which we could take as either the synchrotron radiation damping rate ($1/\tau$) of the given plane or the coherent damping rate in that plane (which includes synchrotron radiation damping effects). As mentioned above, assuming only the synchrotron radiation damping rate in setting stability conditions is more conservative.

Table 3.5-3. Beam and Cavity Parameters

Quantity	Value	Comment
Longitudinal plane ring parameters		
Current I_{total}	200 mA	Design requirement
APS-U Operational Current	150 mA	Not used in stability calculations
Energy E	7 GeV	
Revolution frequency f_0	271.55 kHz	
Synchrotron frequency f_s	2.1 kHz	Incoherent value
Momentum compaction α_c	2.8×10^{-4}	
Longitudinal single-particle damping time τ_s	4.8 ms	
Longitudinal single-particle damping rate $1/\tau_s$	208 s^{-1}	Maximum tolerable growth rate of instability
Transverse plane ring parameters		
Average β_x in cavity	22 m	20 m in standard-length straight section
Average β_y in cavity	7.5 m	Value at end of long straight section.
Transverse single-particle damping time $\tau_{x,y}$	9.6 ms	
Transverse single-particle damping rate $1/\tau_{x,y}$	104 s^{-1}	*Nominal* maximum allowed growth rate of instability
Coherent damping	up to 500 s^{-1}	Charge- and chromaticity-dependent, and includes synchrotron radiation damping rate[a]
Chromaticity	$\geq +6$	Major contributor to coherent damping
Form factor parameters		
rms bunch length σ_t	23 ps	Shortest bunch length in operational bunch patterns (324 bunches)
Form factor for 2.0 GHz and 2.8 GHz	0.92, 0.85	$\exp(-\omega_r^2\sigma_t^2)$

[a] Measurement was done in the vertical plane for 2-mA bunch and y-chromaticity of 7, close to conditions for the hybrid mode bunch train.

The coherent damping rate is determined by other beam dynamics and potentially is much larger in magnitude than the synchrotron radiation damping rate. In some accelerator applications taking credit for this extra damping would make cavities design easier, such as not requiring HOM dampers. In the present case of superconducting cavities, natural Q's are so high that we need HOM dampers whether or not we take credit for the higher coherent damping rate. The benefit of not assuming the coherent damping rate is that we have a fallback for stabilizing new bunch patterns that have higher growth rates than those presently studied (e.g., unexplored variations of the hybrid bunch pattern).

With the ring parameters listed above, the largest allowed resonator impedances are then

determined and are given in Table 3.5-4. The beneficial effect of the bunch form factor is included. These give guidance to the rf cavity designer for target shunt impedances.

Table 3.5-4. Simple Estimates of Largest Allowed Resonator Impedances.

Quantity	Limit on Quantity[a]
$(R_s f_{\mathrm{HOM}})$ for one monopole HOM	0.44 MΩ-GHz [b]
R_s for one monopole HOM at 2 GHz	0.22 MΩ
R_t for one H-plane HOM	1.3 MΩ/m
R_t for one V-plane HOM	3.9 MΩ/m

[a] Estimates include the bunch form factor.
[b] Assumes a conservative bunch form factor for a 2-GHz HOM in all cases.

The next step is to perform the Monte Carlo calculation using resonator parameters from HOMs provided by the rf cavity designer and with the number of cavities desired. The design of the rf cavities is not finalized at this time, so the resonator parameters used here only allow making an estimate of growth rates. A single-cell design with dampers in each cavity will produce very low Qs for all HOMs. Each of the HOMs will almost certainly satisfy Table 3.5-4 by themselves. However the present design calls for a total of eight cavities to be installed eventually, many of which will have overlapping HOM impedance functions. With a statistical model of how the HOM resonant frequencies may vary from cavity to cavity, one may use a Monte Carlo method to estimate the growth rates.

The utility of the Monte Carlo method can be demonstrated with a concrete example of a design reported in section 3.5.6.2 on single-cell superconducting cavities. The V-plane dipole HOMs (Table 3.5-5) are used to calculate the possible transverse instabilities for the 24-bunch fill pattern. Only a few of the HOMs are listed. Others were omitted for brevity because they have much lower R_t.

Table 3.5-5. V-plane HOM Parameters Used for Monte-Carlo Simulation.

Frequency (GHz)	$\mathbf{R_t/Q}$ (Ω/m)	$\mathbf{Q_L}$ [a]
3.02	878	68
3.06	240	797
3.43	449	144

[a] HOM dampers are included.

A calculation for eight cavities was performed with `clinchor`. The modal analysis uses the actual βs at the cavities and a bunch lengthening table (σ_z versus I_b) provided by the user. The frequencies can be randomized uniformly over an interval given by the user. We usually choose the default interval of f_0, giving a chance for any HOM to be centered on a beam frequency. The user can also vary the Qs for a given HOM data set, while maintaining the value of R_t/Q. This feature could be used in other projects, say, to provide a target for HOM damper designs. For the SPX project, the HOM Qs are considered as a given for a particular design, rather than adjustable. One could also

specify a "target" staggering step for any of the HOM frequencies, as was done for the APS 352-MHz cavities for preventing overlap between resonators of different cavities. For now, we don't consider such staggering since the Q are expected to be so low that it would be difficult to avoid overlap.

One may ask whether, for a complete calculation, one should include all resonators in the ring, specifically those of the accelerating 352-MHz cavities. We don't presently have a good model of the HOMs of the as-built 352-MHz cavities that explains the observed lack of multibunch instabilities (up to 245 mA) that were generally expected. (There was one longitudinal HOM observed early on in one of the 16 cavities; this is now damped with an HOM damper.) It is possible that the resonator Qs in general are much smaller than those calculated earlier in the APS development, since the calculations didn't (and couldn't) take into account damping through the coupler and waveguide network. Other factors not included are coherent damping from chromaticity and other de-coherence effects. It is assumed for the moment that the accelerating cavity HOMs do not contribute to multibunch instability when deflecting cavities are added.

The Monte Carlo results are presented as a histogram of the most unstable beam mode for each instance of randomized HOM frequencies in eight cavities. By way of example, Figure 3.5-16 gives such a histogram for the case where only the worst mode is used in the calculation of beam mode growth rates. In addition we plot the cumulative distribution of the most unstable beam mode growth

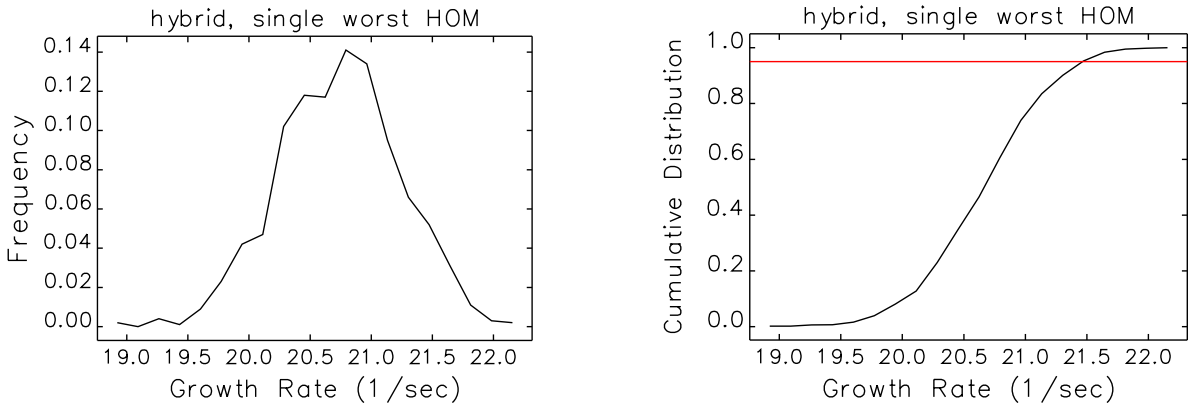

Figure 3.5-16. Distribution of growth rates of instability in the V-plane assuming only the worst dipole HOM. The red line marks the 95th percentile of cases. 1000 samples were calculated.

rate, which is just the integral of the histogram. The cumulative distribution can be used to determine the probability of instability for a given natural damping rate, and thus is more useful to consider.

Note that the distribution in growth rates is quite small. This is due to the low Q values of the resonators and the absence of (large) staggering of frequencies. Randomizing the HOM frequencies for low-Q resonators doesn't have much effect but we performed it anyway to avoid surprises.

The cumulative distribution plot in Figure 3.5-16 also marks the 95th percentile of the distribution, a useful scalar quantity (less noisy than, say, the 100th percentile) that characterizes the distribution when doing scans of parameters.

The simulation with all HOMs is presented in Figure 3.5-17 for the 24-bunch and the hybrid bunch patterns, showing that the growth rates in the hybrid pattern are of the greatest concern.

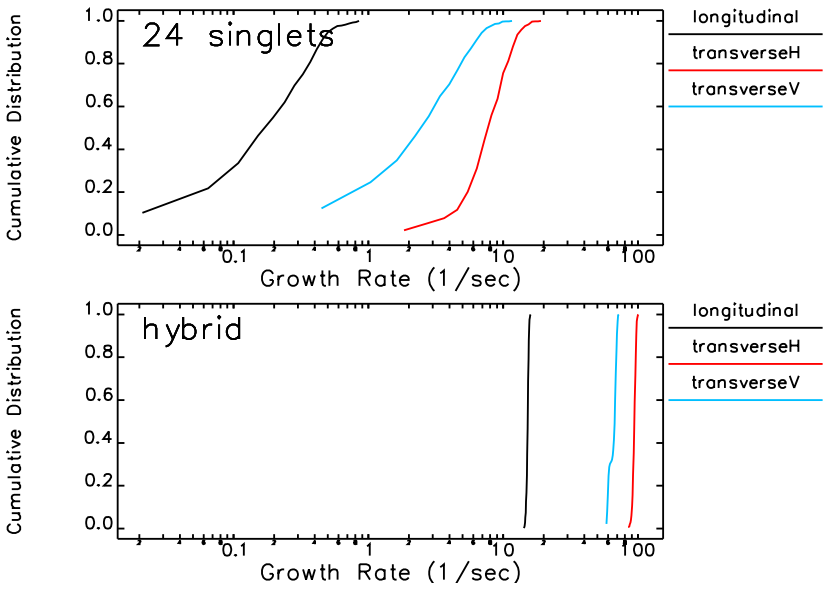

Figure 3.5-17. Distribution of growth rates of instability in the V-plane from an example set of dipole HOMs. The red line marks the 95th percentile of cases. 1000 samples were calculated.

The growth rates must be compared with the natural damping rates of single bunches, which is, at minimum, the synchrotron radiation damping rate, or depending on plane and the optics setting, the coherent damping rate. Table 3.5-6 shows that for all planes and bunch patterns, we predict stability.

Table 3.5-6. Summary of Monte Carlo Simulation of Instability assuming Eight Cavities

Plane	**Growth Rate** s^{-1}	**Synch. Rad. Damping Rate** s^{-1}	**Coherent Damping Rate** s^{-1}	**Comment**
Longitudinal	15	208	Not applicable	Stable
Horizontal	98	104	No recent measurement[a]	Stable
Vertical	70	104	Up to 500	Stable

[a] Values are probably a little less than in vertical plane based on known chromaticity and resistive and broad-band impedance.

It was mentioned earlier that the cavity design has not been finalized and, in addition, that the real Q's will not be known until they are measured on the real cavities. If it turns out that the Q's for the as-built system are a little higher (and if the present accelerating 352 MHz cavities might contribute along with deflecting cavities to multi-bunch instabilities) then we might be transversely unstable if only synchrotron radiation damping was present.

The coherent damping rate, which we nominally do not need to invoke in order to conclude that we are transversely stable, provides margin against such changes. The vertical transverse damping rate was recently measured to be up to 500 s^{-1} for a range of bunch current and chromaticity settings corresponding to what might be used in hybrid "mode," the bunch pattern for which we predict the highest growth rate. If we take the bottom of the range as the minimum coherent damping rate that

we could expect in the future, then our stability margin is a factor of five. Also, other work has demonstrated the possibility of adjusting the hybrid bunch pattern to reduce the estimated worst-case growth rate by an additional factor of two if need be. In conclusion, we have a high level of confidence that we will not have an issue with multi-bunch instabilities.

3.5.4.3 Single-Bunch Effects and Requirements

The SPX system in the storage ring will have a short-range wakefield effect on the beam very much like other impedance sources. The system has two different impedance elements, namely, nonuniform chamber (SPX chamber) and deflecting cavities. Compared to the standard long-straight section (LSS), the SPX chamber[3] will have extra transitions connecting the deflecting cavity pipe to the regular chamber. The detailed 3-D computation by GdfidL shows that the vertical wake of the SPX chamber excited by a bunched beam is almost same as for the LSS chamber, as shown in Figure 3.5-18.

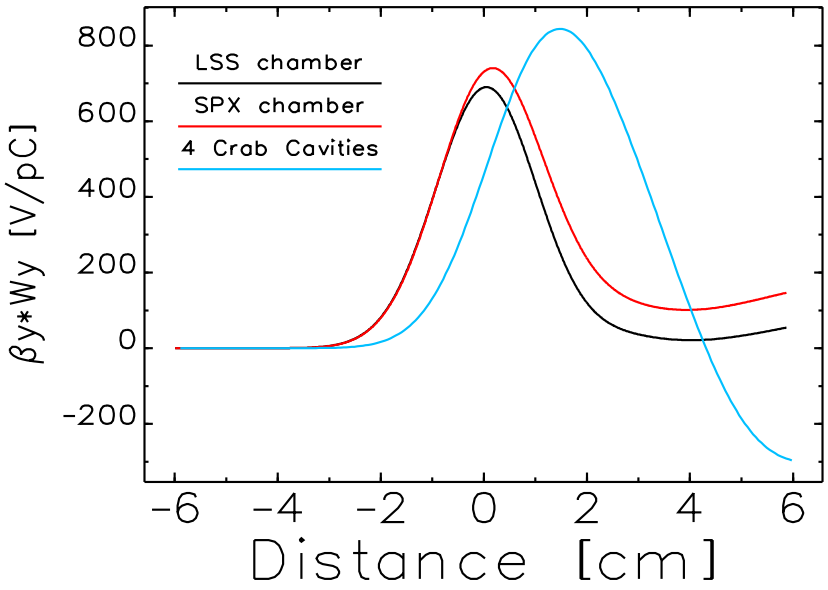

Figure 3.5-18. The vertical wake potential of eight deflecting cavities excited by a bunched beam of σ_z = 1 cm compared with those of the LSS and SPX chambers.

The 3-D model of a cavity used in the wakefield computation is shown in Figure 3.5-19. The cavity aperture is 50 mm, a compromise between the desire to minimize wakefields and maximize the effectiveness of waveguide HOM damping (motivating a larger aperture) and the desire to improve deflecting performance (motivating a smaller aperture). With this aperture choice, four cavities will be needed to generate 2 MV of deflection voltage at each end of the SPX zone, totaling eight cavities.

The vertical wake potential of a set of four cavities is compared with the SPX and LSS chambers in Figure 3.5-18, which shows that the deflecting cavity can significantly impact the vertical kick to the beam in the SPX zone.

[3]When we refer to the "SPX chamber," we do not include the cavities, just the extrusion for IDs, a straight round pipe where the cavities would go and three taper transitions

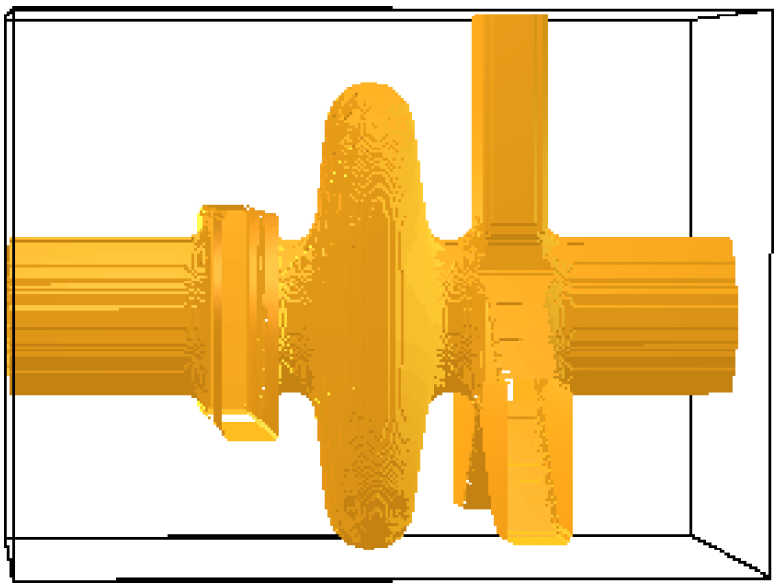

Figure 3.5-19. A model of superconducting deflecting cavity with input/output couplers for the wake potential computation rendered by GdfidL.

Following the same simulation method used in establishing the APS impedance model as described in section 3.2.4, 200,000 macro particles were tracked with the deflecting cavity impedance included. As shown in Figure 3.5-20, with the full 3D impedance, we found that the bunch was lengthened, which reduces the peak current. As a result the transverse mode-coupling instability (TMCI) in the vertical plane was reduced in strength, leading to a small net increase in the single-bunch current. Thus, 16 mA can be delivered in a hybrid fill with the SPX system installed in the ring.

In the low-current regime below 6 mA, the increase in bunch length by deflecting cavities is not significant (Figure 3.5-20). This is compatible with the short-pulse operation of the SPX system in the 24-bunch mode, in which each bunch has 4-6 mA, below the microwave threshold.

Hence, the intensity of short pulses available in 24-bunch mode from SPX will not be affected much by collective effects introduced by the cavities. On the other hand, 16-mA operation in hybrid-fill mode may not be compatible with short-pulse x-ray operation because the coherent motion excited by the microwave instability will make it difficult to produce a precise chirp along the bunch. There are other challenges for SPX operation in hybrid mode, including the phase slew along the 56-bunch train. For these reasons, operation in hybrid mode is not contemplated.

In summary, with up to eight deflecting cavities installed in the ring, more than 16 mA can be stored in a single bunch. Hence, installation of the cavities will not jeopardize hybrid-mode operation. Collective effects with the presence of the cavities should not degrade SPX performance in 24-bunch operation at 150 mA.

Because the deflecting cavities lengthen the bunch, they might be seen as having a helpful effect for other upgrades. For example, we might be able to make other changes in the ring that increase the transverse impedance, without jeopardizing the ability to achieve 16-mA single-bunch current. One obvious possibility would be inclusion of several in-vacuum undulators (IVUs). However,

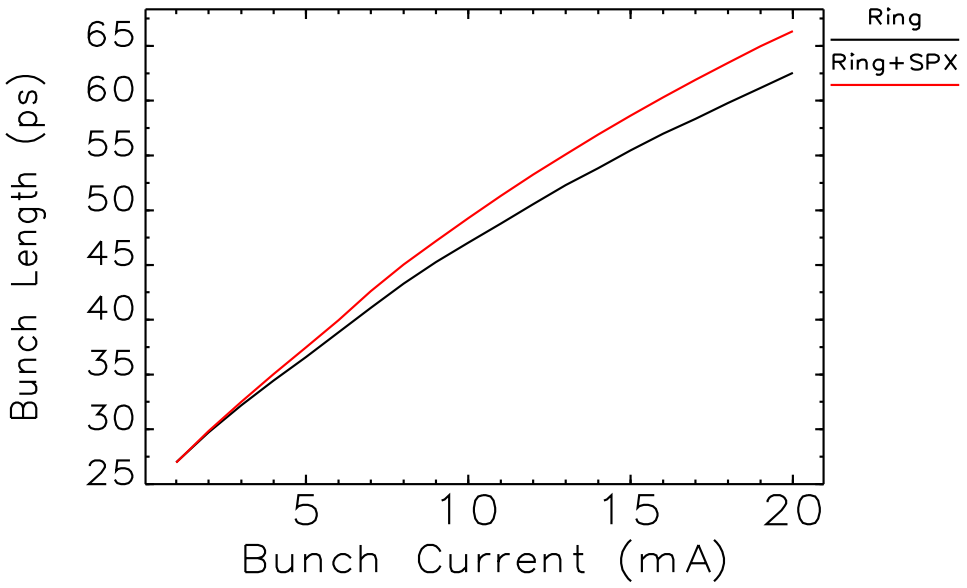

Figure 3.5-20. Bunch lengthening with and without deflecting cavities in the ring, assuming a total of eight deflecting cavities.

we have elected not to pursue this possibility, for four reasons. First, the lengthening is not significant for the eight cavities included in the upgrade. Only with a much larger number of cavities would an appreciable benefit be seen. Second, we do not wish to link the success of one upgrade (insertion devices) to the implementation of another (SPX), since in principle the SPX component of the upgrade could be removed. Third, the potential performance of superconducting undulators, as described in section 3.4.6 is superior to that of IVUs, without the detrimental effect on impedance. Fourth, operation at higher single-bunch current would be a significant benefit to timing experiments, which are emphasized in the mission needs statement. Hence, the upgrade mission would benefit from any improvement resulting from the combination of SPX installation and careful preservation of the transverse impedance.

3.5.4.4 Emittance Degradation Due to Impedance

The performance of deflecting cavities generating short x-ray pulses has been investigated based on the single-particle dynamics. However, collective effects occurring within these two sectors may alter the beam dynamics in all planes in a significant way. The vertical betatron phase, for example, may need to be readjusted because the (small) transverse impedance will detune the phase advance somewhat depending on the charge and shape of bunched beam. Such consideration will make simulations more realistic.

A preliminary simulation of multiparticle dynamics was performed with an emphasis on vertical emittance degradation. The transverse impedances were added to the otherwise magnet-only lattice (the same one used in section 3.5.3) in three stages, and at each stage the effect was assessed:

- Impedance of two sets of SPX cavities, each consisting of four deflecting cavities at Sectors 5

and 7. Each cavity impedance kicks the beam in both the x and y planes.

- In addition, chamber impedance of Sector 6 and Sector 7 between the SPX cavities, where the sector impedance was lumped at S6A:Q1 and S6B:Q1 for Sector 6 and at S7A:Q1 and S7B:Q1 for Sector 7.
- In addition, chamber impedance of remaining sectors outside SPX, where the sector impedance was lumped at the center of each straight section.

Inside the SPX, the bunch will get an impedance kick proportional to the slice offset in the deflecting plane y. Outside the SPX there will be no impedance kick to the beam in an ideal machine because of the cancellation. However, if there will be any residual oscillation in transverse plane, the emittance may be further degraded because of the impedance. In order to see the such effects quantitatively, we tracked 30000 particles over 5000 turns following the same method described in section 3.5.3. We used the same lattice with 2-MV deflecting voltage. The current was 6.25 mA with 41-ps rms bunch length. The result was compared with the reference emittance, which was obtained over the 5000 turns without impedance; any increase in emittance then was attributed to the impedance effect.

The emittance with various impedance elements in the ring is plotted in Figure 3.5-21 together with the one without impedance. For the simulation parameter consistent with the APS Upgrade, we could not resolve any impedance effect on the vertical emittance.

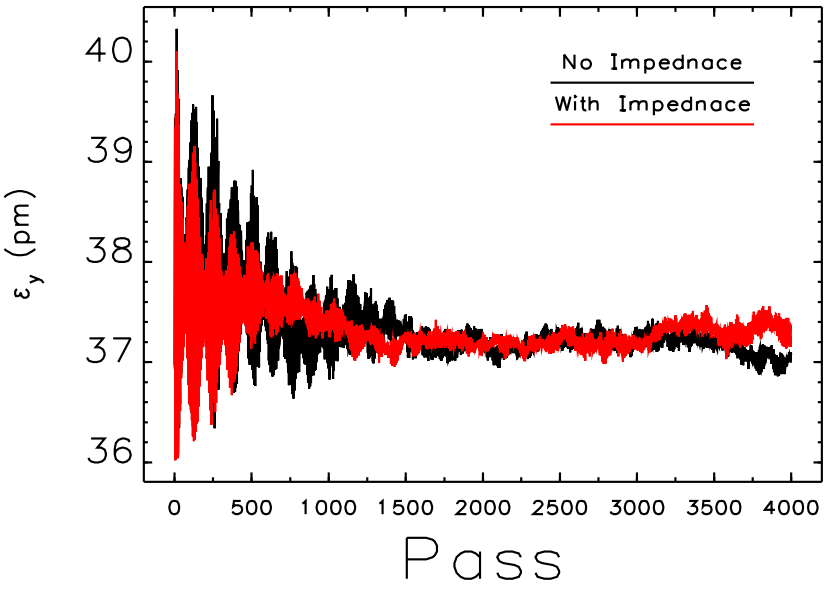

Figure 3.5-21. Vertical emittance with various impedance elements in the ring. See text for explanation.

3.5.4.5 Work Remaining

In the work just reported, we didn't include the effect of longitudinal impedance, which would require a nominal simulation condition of 200000 particles and 10000 turns, taking a week on

a 100-core cluster. However, we believe that the self consistent simulation is important in predicting the SPX performance, so we plan to continue these simulations using larger computing resources. This study will use the lattice with full magnets and impedances, exploring the effect of closed orbit distortion, different injection kicker settings, feedback operation, and SPX cavity errors along with other operational conditions of the ring.

The collective effect simulations for SPX were mainly developed in the context of instability modeling and are believed to give accurate predictions on single- and coupled-bunch effects. Usually, the study of collective effects stops here. However, for unconventional situations, such as the APS-Upgrade with SPX, the performance-related simulation of emittance degradation is an important issue. For this purpose we will need to simulate the ring as closely as possible to that found in realistic operation, which will require large-scale computation on the 1000s of cores.

3.5.5 Conceptual SPX System Design

The tolerances (section 3.5.3.4) and cavity impedance budget (section 3.5.4) for the SPX system will be challenging. Plans to meet the cavity impedance budget are discussed in the cavity design section 3.5.6.2. The differential phase error tolerance of 0.18°rms (see section 3.5.3.4) will present many challenges to the rf system. While the common-mode phase tolerance is much more relaxed at 4.0°rms, storage ring (SR) synchronous phase changes simply due to insertion device (ID) gap changes [3.5-36] and due to main SR rf noise [3.5-37, 3.5-38] must be accounted for.

A conceptual system level design using a beam-based feedback control strategy was developed to address these challenges at a July 2010 SPX Study Meeting by participants from ANL, LBNL, Fermilab, and SLAC [3.5-39], as shown in Figure 3.5-22. In the proposed scheme, beam position monitors outside the SPX zone (section 3.5.9) measure orbit distortions caused by differential phase errors between the SPX cavity sectors and feedback to the phase of the second SPX cavity sector via the real-time feedback system (RTFB) (section 3.3). Residual tilt monitors outside the SPX zone can measure tilt caused by differential amplitude errors and correct the amplitude of the second SPX cavity sector. A beam arrival time monitor can be used to measure and feedback to the phase of the main SR rf to correct for common-mode phase errors introduced by main SR rf noise and synchronous phase changes. Beam position monitors within the SPX zone can be used to refine the common-mode phase errors of the SPX system by feeding back on the first SPX cavity sector. Finally a tilt monitor within the SPX zone can be used to measure and correct for SPX common-mode amplitude errors.

By using beam-based feedback, the inevitable $1/f$ phase noise and long-term drift of the rf system, which ultimately leads to orbit distortions, can be compensated by the RTFB system, at least within its closed loop bandwidth, which is expected to be upgraded from 60Hz to 200Hz (section 3.3.6). If the RTFB system is responsible for correcting SPX system amplitude and phase noise in the frequency range of <200Hz and the low-level rf (LLRF) control system is responsible for regulating noise in the range >10Hz, an overlap between the two systems in principle [3.5-40] can ensure complete spectral coverage for beam-orbit stability.

A signal synchronized to the first SPX sector cavities, which is indicative of the time of short-pulse x-ray production, will be provided to the user lasers via the timing and synchronization system, which also provides all timing fiducials to the rf and beam diagnostics systems (section 3.5.7). Remote

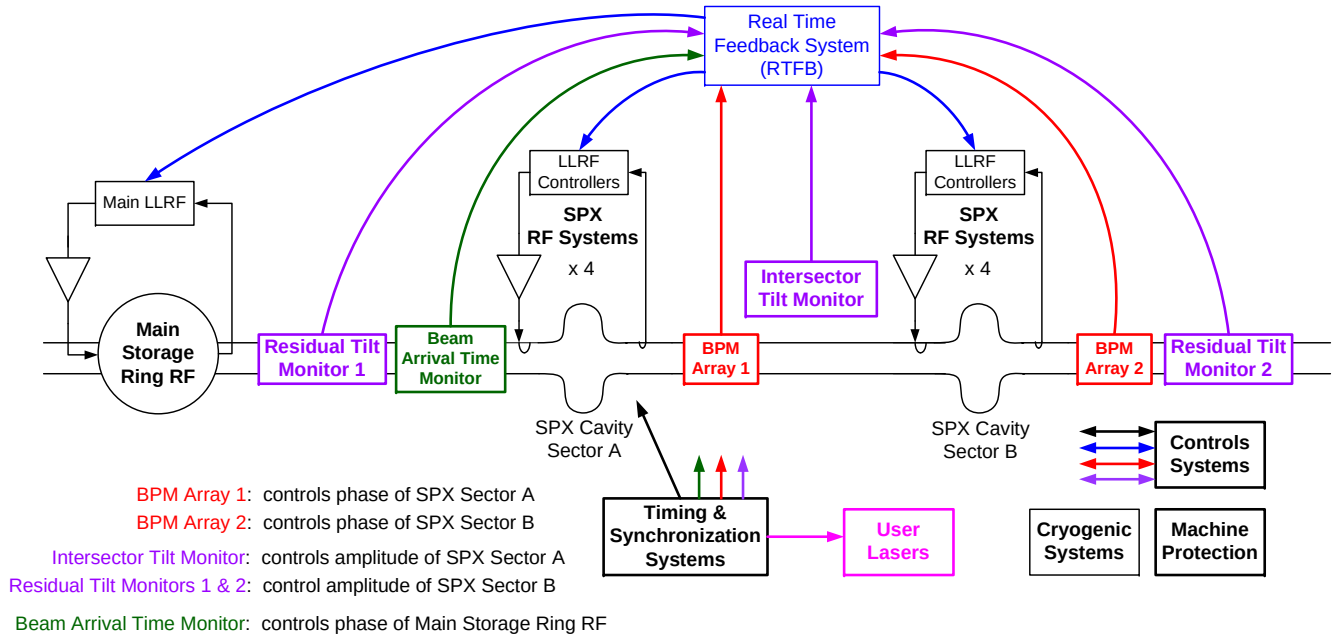

Figure 3.5-22. SPX beam-based feedback control strategy.

control, monitoring, and integration of all SPX subsystems, including within the existing APS storage ring complex, will be provided by the controls systems (section 3.5.7). Details of the individual SPX subsystems, including cavity and cryomodule design, cryogenics, low-level rf, high-level rf, machine protection, and diagnostics are given in subsequent sections.

3.5.5.1 R&D Plan

The proposed SPX system design and its integration into the existing accelerator complex while maintaining beam stability will be challenging. To address these challenges, we plan to install a two-cavity test facility into the APS storage ring. Details of the R&D plans for individual subsystems are included in their respective discussions in subsequent sections. Here, we briefly describe the plans for the two-cavity test.

The two-cavity cryomodule will be delivered by Jefferson Lab fully assembled and under vacuum. Subsequent tests will include a complete module test at the ATLAS facility at ANL's Physics Division, cryogenic system tests in the APS storage ring test area, and in-ring tests.

Initially, the cryomodule will be located at the ATLAS facility, which allows testing down to 2K. We will begin with system checks for mechanical integrity, vacuum condition, and alignment variation. Overall cryomodule tests will include cryogenic performance, rf power distribution and conditioning, tuner verification, cavity performance, low-level RF control and microphonics, low-power rf performance of the dampers, and alignment performance. The tests may also include the evaluation of potential dark current.

Next, the two-cavity cryomodule will be transported to building 400A (APS storage ring test area) for cryogenic system integration. Low-level rf control and microphonics characterization will be tested in the storage ring environment.

Following this, the two-cavity cryomodule will be installed in the storage ring. A slowly ramped electron beam will be introduced with the unpowered, detuned cavities at room temperature, liquid-nitrogen temperature, liquid-helium temperature, and finally sub-λ helium temperature. The performance tests will include assessing beam quality and stability, higher- and lower-order mode (HOM/LOM) power damping efficiency, alignment, and diagnostics under passive conditions.

Next, low power cavity tests will begin, including fast and slow cavity tuning, system timing and synchronization, diagnostics, alignment, and HOM/LOM damper performance. Finally, high-power tests will be conducted, including the beam-deflecting efficiency, rf distribution, HOM/LOM damping performance, alignment, cryogenic performance, and machine protection.

Beam dynamics modeling of the two-cavity test has been performed to assess to what extent it creates an observable chirp and whether it offers a valuable capability for x-ray users. In the modeling, we placed the cavities in the downstream end of Sector 5. Long-term tracking with `elegant` [3.5-22] demonstrated that a steady-state chirp develops that would be visible at all insertion devices. The visibility of the angle chirp is characterized by

$$\alpha_{45} = \frac{\sigma_{45}}{\sqrt{\sigma_{44}\sigma_{55} - \sigma_{45}^2}}, \tag{3.5-37}$$

where $\sigma_{ij} = \langle x_i x_j \rangle$, with the usual number of the phase space coordinates from 1 to 6 (5 is time). This quantity is plotted in Figure 3.5-23. The response is, not surprisingly, reminiscent of a vertical closed-orbit distortion pattern. Based on this analysis, the response at 7-ID is close to the maximum response.

The x-ray pulse duration as a function of transmission through a pair of variable vertical slits is shown in Figure 3.5-24. (See section 3.5.3.7 for a discussion of how these computations are performed.) The minimum FWHM pulse duration for 7-ID is approximately 8 ps. This could be reduced by moving the vertical tune closer to the integer (we used $\nu_y = 19.25$ in this simulation), but the operational workability of that change will need to be investigated.

3.5.6 Superconducting Rf

3.5.6.1 Introduction

Deflecting rf structures (cavities) operate in a mode where the center of the bunch experiences no net Lorentz force while the head and tail of the bunch are deflected in opposite directions. These structures are mainly single-cell or multicell superconducting cavities operating in a polarized TM_{110} mode with electromagnetic fields as shown in Figure 3.5-25. As the dipole mode has two polarizations, the undesired polarization, known as the same order mode (SOM), may cause large deflection to the beam due to its high R/Q. In addition, the fundamental accelerating mode, known as the LOM, strongly couples to the beam and must be damped to avoid any degradation to the beam quality.

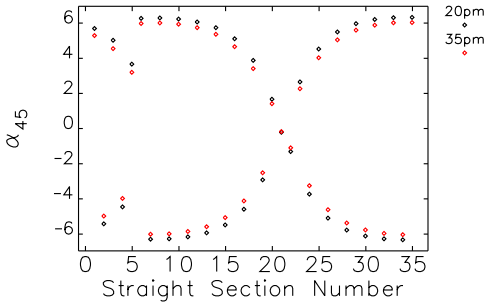

Figure 3.5-23. Chirp visibility function for different ID straight sections when two SPX cavities are placed in the downstream end of Sector 5, for two different electron bunch durations.

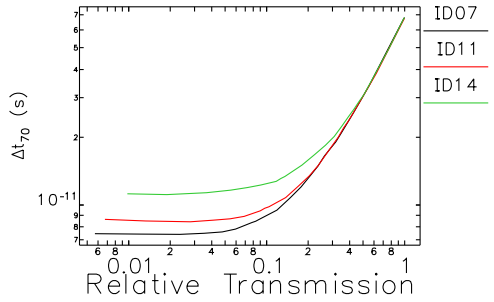

Figure 3.5-24. X-ray pulse duration as a function of transmission through a pair of vertical slits at a distance of 26.5 m from the source at three different beamline locations.

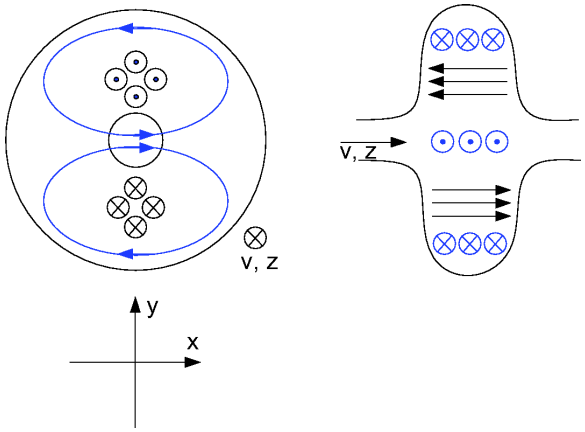

Figure 3.5-25. Polarized TM_{110} mode fields (magnetic [blue], electric [black]) drawn for an electron traveling in the +z-direction receiving a vertical kick up. The magnetic fields lead the electric fields by 90 degrees.

For the APS short pulse x-ray (SPX) project, superconducting rf (SRF) structures are chosen since they are most suited for high repetition rate applications envisioned for time-resolved experiments at the APS. The initial operating deflecting voltage for the APS-SPX deflecting cavities is 2 MV, which will provide x-rays on the order of a few picoseconds. In the long term, additional cavities and rf systems may be added to provide a total deflecting voltage of 4 MV, which will produce shorter x-ray pluses. The APS SPX superconducting rf deflecting cavities are designed to operate at a frequency of 2815 MHz (the eighth harmonic of the APS storage ring rf frequency). It is critical that all HOMs and LOMs are effectively suppressed in the presence of beam in order to meet the APS storage ring beam-stability and vertical-emittance-growth requirements up to the design requirement of 200 mA.

Various design options have been evaluated for the APS deflecting cavities based on existing and proposed cavity designs in the superconducting community. The most recent and successful application of the deflecting cavity is at the KEK-B collider in Japan, where a pair of single-cell

500-MHz SC crab cavities were installed and commissioned at the low-energy and high-energy rings (LER and HER, respectively) for the luminosity upgrade [3.5-41]. The KEK-B crab-cavity design uses a squashed cavity geometry to separate the degenerate dipole modes and a coaxial insertion in the beam pipe to effectively damp the LOMs.

In recent years a new collaboration was formed between Argonne National Laboratory, Jefferson Accelerator Laboratory (JLAB), Lawrence Berkeley National Laboratory, and Tsinghua University in Peking, China, to develop SC-deflecting rf cavities suitable for high-energy light sources. Through extensive numerical and analytical studies, a new optimized squashed geometry deflecting cavity with waveguide damping has been designed.

In the following sections, we discuss the cavity design, cryomodule and mechanical design, the cryogenic system, the low- and high-level rf systems, and the control-system requirements.

3.5.6.2 Cavity Design [1.03.03.07]

The APS deflecting cavities will operate CW at 2815 MHz, using the TM_{110} cavity mode, to produce a head-tail chirp of the beam. A 2-MV deflecting voltage will be applied to achieve 2-ps x-ray pulses. Four single-cell cavities, each supplying 0.5-MV deflection, will be located in a long straight section in Sector 5 to chirp the beam, with another set of four cavities located in Sector 7 to reverse the chirp and return the beam to its nominal orbit. The Mark-I cavity design shown in Figure 3.5-26 represents the original SPX cavity concept and consists of a squashed single-cell cavity with waveguide dampers and input coupler. The Mark-II design shown in Figure 3.5-27 uses a similar cavity shape but relocates the horizontal waveguide damper to the body of the cavity and utilizes a dogbone-shaped coupling iris for enhanced damping; it is the preferred cavity design due to its greater damping and lower beam loss factor. The racetrack cross section of the cavities is similar to the KEK deflecting cavity. It was adopted due to its minimization of the peak surface magnetic fields and frequency relocation of the same-order mode (SOM). The damping features of the KEK design, however, were found to be unsuitable for the SPX cavities, as will be discussed later in this section.

The cavity design was guided by various beam-interaction requirements, including the single-bunch current limit and coupled-bunch instabilities. The single-bunch current limit in the APS must exceed the requirements of the 16-mA intense bunch in hybrid-mode operation by limiting the transverse broad-band impedance of the APS. This limit will be maintained in the deflecting cavities by assigning a minimum beam-pipe radius, as well as designing low-impedance beam-pipe transitions. Coupled-bunch instabilities were addressed by ensuring strong coupling of HOMs and LOMs in the cavity to external damping elements.

The coupled-bunch instability requirements for 200 mA are given, very roughly, by

$$\begin{aligned} R_{\mathrm{s}} \times f_{\mathrm{n}} &< 0.44\ \mathrm{M}\ \Omega\text{-GHz (longitudinal)} \\ R_{\mathrm{t}} &< 1.3\ \mathrm{M}\ \Omega/\mathrm{m}\ \text{(horizontal dipole)} \\ R_{\mathrm{t}} &< 3.9\ \mathrm{M}\ \Omega/\mathrm{m}\ \text{(vertical dipole)} \end{aligned} \tag{3.5-38}$$

where $R_s = V^2/2P_l$, $R_t = \kappa_r V_t^2/2P_l$, $V_t = V/\kappa_r r_{\mathrm{o}}$ is the deflecting voltage, f_n is the LOM / HOM frequency, κ_r is the wave number, P_l is the total loss, and r_{o} is the radial offset of the voltage integration. The limits in Equation 3.5-38 are based purely on synchrotron radiation losses and do not

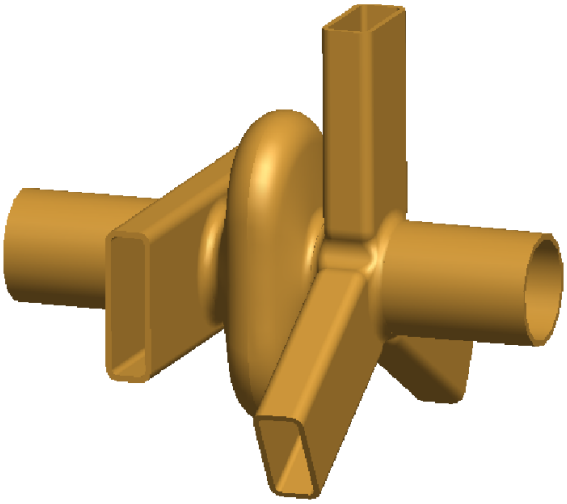

Figure 3.5-26. Mark-I design of the single-cell deflecting cavity with waveguide end groups.

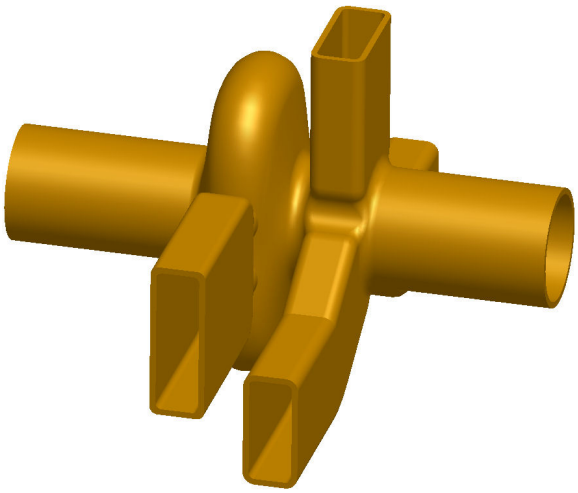

Figure 3.5-27. Mark-II design with on-cell waveguide damping.

consider other damping effects in the storage ring. These limits do not depend on the loaded quality factors explicitly, but the corresponding R is linearly related to the Q of a particular LOM/HOM.

The LOM damping is inherently a more difficult task in a deflecting cavity due to its lower frequency compared with the operating mode and subsequently to the greater containment of its modal fields in the interior of the cavity. Damping methods have been devised to extract the LOM using techniques that are invasive to the cavity fields and interact with both the LOM and the deflecting mode without degrading the deflecting mode. Various options have been proposed for the International Linear Collider (ILC) and Large Hadron Collider (LHC) [3.5-42], but KEK [3.5-43] is the first to successfully demonstrate the operation of superconducting deflecting cavities. An adjustable coaxial insert with a rejection filter is utilized in the KEK design to heavily damp the LOM and ensure minimal effect on the deflecting mode at 500 MHz. Scaling this design to 2815 MHz and applying it to the APS deflecting cavity has been considered, but it was found to be difficult due to manufacturing issues, as well as requiring excessive length. Additionally, the coaxial insert must be included in the cold mass, which has proven to be problematic.

The APS has pursued a design which utilizes selective mode coupling into the LOM waveguide in order to simplify the mechanism for damping. In the Mark-II design, a rectangular waveguide is mounted horizontally off the body of the cavity, which couples to both the deflecting mode and the LOM [3.5-44]. The cavity LOM couples strongly to the waveguide TE_{10} fundamental mode, while the deflecting mode couples as a higher-order TE_{20} mode and is rejected by the natural high-pass filtering of the waveguide, as shown for the LOM waveguide on the beampipe in Figure 3.5-28. The waveguide LOM damper effectively damps the cavity monopole modes, as well as horizontal TM dipole modes (electric fields polarized in the horizontal plane). Vertical dipole mode damping, and additional damping of HOMs, are performed with a Y-end group consisting of three waveguides oriented symmetrically at 120-degree intervals (see Figure 3.5-26).

The level of damping due to the proposed scheme can be seen in Figures 3.5-29 - 3.5-31,

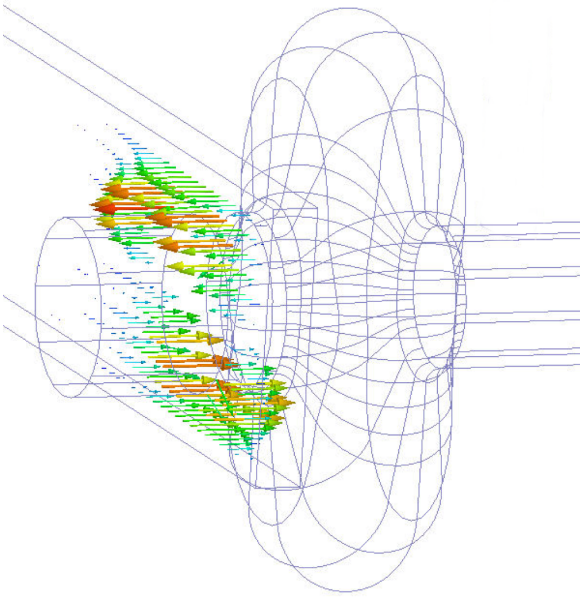

Figure 3.5-28. Field configuration of the deflecting mode coupling to the lower-order mode waveguide.

where the impedance was calculated using the wake potential generated by a beam located on-axis for the longitudinal modes and a beam radially displaced by 10 mm for the transverse modes. Ideal damper ports on each waveguide termination were assumed for extracting the HOM/LOM power. The APS coupled-bunch stability threshold for 200 mA is shown for reference in the figures and is calculated using Equation 3.5-38. Eight cavities have been assumed where the impedance of each mode is assumed to add constructively in each of the cavities since the Q_{ext} of the LOMs / HOMs is on the order of 10s to 1000s.

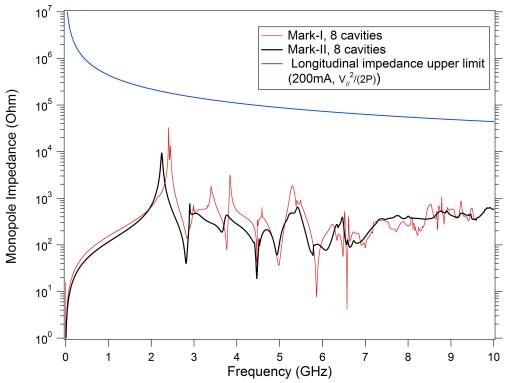

Figure 3.5-29. Longitudinal impedance spectrum of Mark-I and Mark-II deflecting cavity designs with APS beam stability limits for 200-mA beam current.

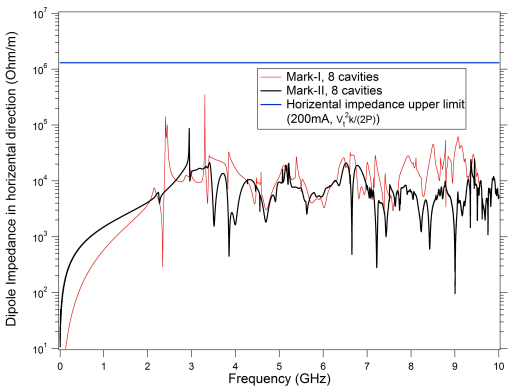

Figure 3.5-30. Horizontal impedance spectrum of Mark-I and Mark-II deflecting cavity designs with APS beam stability limits for 200-mA beam current.

The total power deposited in the dampers due to the beam has been calculated using the cavity

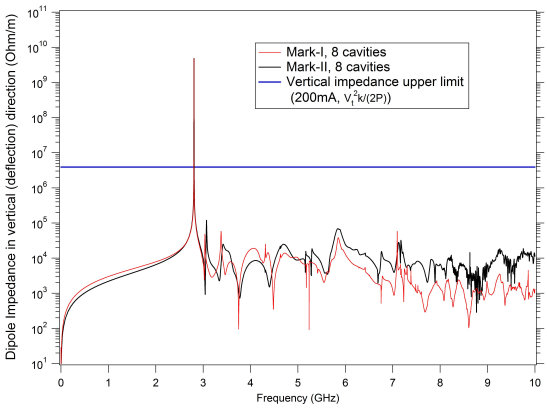

Figure 3.5-31. Vertical impedance spectrum of Mark-I and Mark-II deflecting cavity designs with APS beam stability limits for 200-mA beam current.

loss factor. Additionally, narrowband impedance or resonant buildup of LOM/HOM power has been estimated by utilizing the fundamental theorem of beam loading and tracking the steady-state rise and decay of the cavity voltage due to periodic bunch trains [3.5-45, 3.5-46]. The average power absorbed by the dampers is calculated from the resultant transient voltage in the cavity and is a function of the bunch pattern, the Q_{ext}, and the frequency of the LOM/HOM. Figure 3.5-32 shows the average power, P_b, normalized by the R/Q, for the 324 and 24 uniform bunch fill patterns for Q_{ext}'s of 100 and 1000, where the effects of the bunch form factor have been included. The longitudinal impedance of the SPX cavity is overlaid to show the overlap of the cavity modal structure with the Fourier components produced by the beam. The average power deposited by the beam into the damper is calculated as a sum of $R/Q * P_b$, for all cavity modes. As an example, the lowest-order monopole mode in the Mark-II cavity resonates at approximately 2.3 GHz. For the 24-bunch mode and a LOM Q_{ext} of 100, which is typical for the monopole modes, P_b is 23.2 W/Ohm, as seen in the plot. The damper load is 1.04 kW due to this single mode. The total power loss from the beam in each cavity for all monopole modes is 1.8 kW for the Mark-II cavity and 2.5 kW for the Mark-I cavity, but it is ultimately dependent upon the actual Q_{ext} of the LOMs/HOMs. As seen in the plots, there no predicted resonant enhancement of the LOM power at the expected Q_{ext} values of 100.

While the beam physics design of the deflecting cavity was predicated on fulfilling the cavity/beam-interaction requirements, the rf design optimized various rf performance parameters. Two variations for the SPX cavity design were evaluated consisting of a low-loss (LL) and a low-peak magnetic field (LMF) options. Both designs anticipated improved rf performance from a reduction of the cavity iris diameter; however, in order to meet the single-bunch current requirements, a minimum diameter of 50 mm was chosen.

The LL design was based on optimizing the transverse $(R/Q)'$, which is related to the ohmic cavity losses P_c of the deflecting mode as follows:

$$\begin{aligned} \left(\frac{R}{Q}\right)' &= \frac{V_t^2}{2\omega U} \\ P_{\text{c}} &= \frac{V_t^2}{2\left(\frac{R}{Q}\right)' Q_{\text{u}}} \end{aligned} \tag{3.5-39}$$

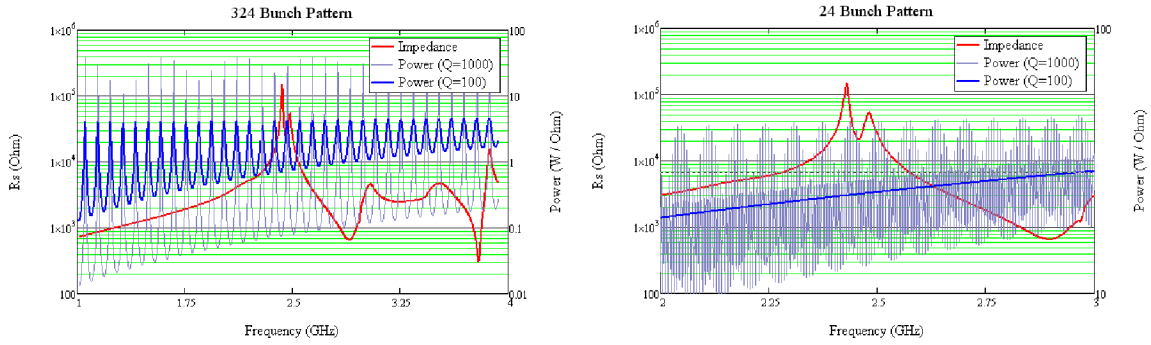

Figure 3.5-32. Longitudinal shunt impedance of the deflecting cavity overlaid on the Fourier spectrum produced by the beam in each of the cavities for the 324 and 24 uniform bunch fill patterns.

where U is the cavity energy and Q_{u} is the unloaded quality factor. Within constraints, the LL design was optimized by increasing the slope of the end walls and creating a cylindrically symmetric cavity geometry, as opposed to the squashed cell. An improvement of approximately 20% for the $(R/Q)'$ was made relative to the LMF variant.

Table 3.5-7. Comparison of Low-Loss and Low-Peak-Magnetic-Field Cavity Designs

Design	**Frequency (GHz)**	$\mathbf{(R/Q)'}$	$\mathbf{P_c}$ **@ 0.5 MV (W)**	$\mathbf{B_p/V_t}$ **(mT/MV)**	$\mathbf{E_p/V_t}$ **(MV/m/M)**
LMF	2.815	17.8	6.9	182	88
LL	2.815	21.25	5.6	208	79

The LMF design was intended to minimize the peak surface magnetic field in order to create a higher operating gradient thereby producing a more compact cryomodule design. The process of optimizing the LMF design resulted in a squashed racetrack shape, similar to KEK's design. Other modifications, such as increasing the radius of the blend in the high magnetic field region on the cavity iris, as well as creating a vertically oriented elliptical iris to distribute the magnetic field over a larger area, were not attractive due either to inadequate mode damping or the reduction of deflecting voltage for a given peak magnetic field.

A comparison of the LL and LMF designs for a cavity iris diameter of 50 mm can be seen in Table 3.5-7. Note that the peak surface electric field is elevated in the LMF design while the peak magnetic field is reduced by 12%. It will be shown that field emission at high gradients, which is a symptom of high-surface electric fields, does not appear to be a significant limiting factor in the single-cell cavity. Since a peak surface magnetic field not exceeding 100 mT has been specified as a design objective and since the cavities will be integrated into limited available space in the APS storage ring, the LMF design offers preferred rf parameters and has been selected over the LL design. The Mark-I and Mark-II cavities are manifestations of the LMF design. Parameters for the Mark-II deflecting cavity are shown in Table 3.5-8.

The damping elements of each of the SPX cavities will be required to cumulatively dissipate up

Table 3.5-8. Mark-II Deflecting Cavity Parameters

Quantity	Value	
Frequency	2815	MHz
Q_{u}	10^9	
V_{t}	0.5	MV
Energy	0.38	J
k_{ll}	0.28	V/pC
σ	40	ps
$(R/Q)'$	18.6	Ohm
E_{peak}	41	1/m
B_{peak}	100	mT/MV
P_{loss} @ $Q_{\mathrm{u}} = 10^9$	7	W
I_{beam}	200	mA
No. Cavities	4×2	

to 2.5 kW of power with the LOM damper receiving the largest percentage due to strong coupling to the cavity monopole modes. The LOM damper design has been rated for 2-kW power loading to handle either the Mark-I or Mark-II designs. As a result, high-power damper designs are being investigated that are capable of dissipating kilowatts of power. The dampers are required to have a good match across a wide bandwidth in order to meet the stability requirements outlined in Figures 3.5-29 - 3.5-31. Based on design work and experimentation for low-power dampers [3.5-47], SiC in-vacuum dampers are shown to be broadband and well-suited for ultrahigh vacuum environments. Preliminary numerical analysis of high-power waveguide dampers using a similar material has been performed [3.5-48], where a network of metal posts brazed to the lossy dielectric has been designed as a possible stress relief for the critical brazing operation.

A four-wedge design has been adopted for the SPX LOM damper based on the 10 kW PEP-II [3.5-49] and 500 W KEK-style [3.5-50] in-vacuum waveguide dampers. The SPX design optimized the distribution of the nearly monochromatic, 2 kW LOM damper load across the volume of the damper [3.5-51]. In this way, the temperature gradient across the damper was reduced and peak stresses were minimized as shown in Figure 3.5-33. An R&D program is underway to reliably braze the damper material to a copper substrate, similar to the approach taken for the PEP-II dampers.

A high-power test facility at 2815 MHz is being outfitted at the APS for testing the damper for performance, reliability, and suitability in a superconducting environment. Low and high-power tests of the damper material will be performed for rf performance and mechanical integrity. Particulate generation tests of the ceramic damper material are planned, as well as outgassing and fatigue tests of the damper-to-copper-brazed assembly. Additional damper design options are being actively investigated including an LOM rf window to permit an out-of-vacuum rf load, and dimensional changes in the damper waveguide assembly, which has been shown to reduce the peak rf loading of the LOM damper by half for a 50% increase in the width of the damper assembly.

The Mark-II cavity design offers improved parasitic mode damping, reduced damper loading, and improved cavity packing factor as compared with the Mark-I design. However, the perturbation on

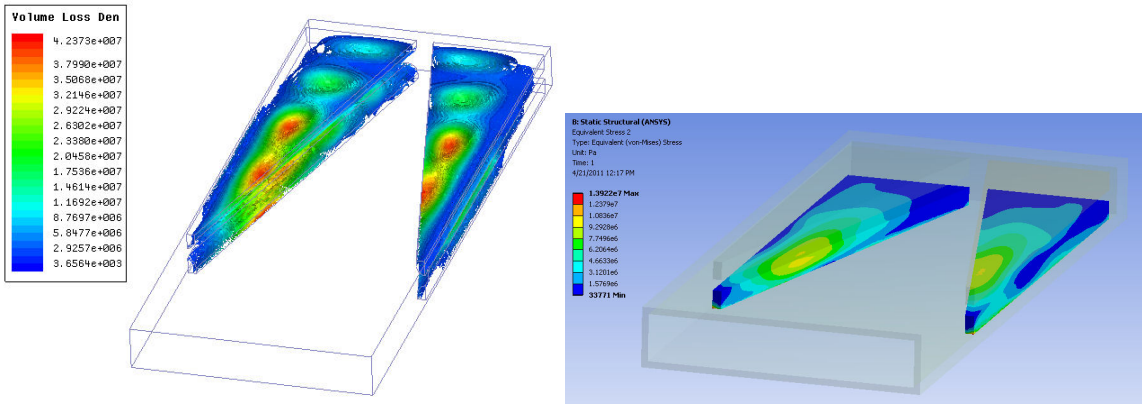

Figure 3.5-33. Four-wedge LOM damper design with power-density distribution and Von Mises stress for solid lossy ceramic wedges.

the surface of the cavity body is not routinely attempted in order to prevent enhancement of the peak surface magnetic field. Due to the magnetic field null on the horizontal center plane of the cavity for the TM_{110} mode, a waveguide damper with a careful design of the coupling iris at this location is not expected to produce a detrimental effect on the cavity rf performance. Since the cavity interior of the alternate design is only slightly modified as compared with the Mark-I design, the rf performance at the operating frequency is not significantly altered.

Although the Mark-II cavity has improved damping, any susceptibility to field enhancement and multipacting has to be carefully considered. The peak surface magnetic field is controlled by adjusting the dimensions of the coupling iris and utilizing the rounded dogbone shape. The potential to suffer from multipacting, on the other hand, is a phenomenon that typically occurs in high magnetic field regions especially near parallel surfaces, conditions which exist near the coupling iris of the LOM waveguides. Multipacting analysis was performed on the Mark-I and Mark-II designs using the parallel 3-D code Omega-3P and Track-3P, where the impact number during 40 rf cycles for electron impact energies between 25 eV and 1.5 keV is shown in Figure 3.5-34. It was found that signs of multipacting occur in both designs along the cavity blend to the end groups with 2^{nd} -order multipacting occurring at a deflecting voltage of approximately 0.3 MV. However, the simulation results do not show any enhancement of multipacting in the Mark-II cavity as compared with the Mark-I design. In fact, experimental results at JLAB of a simplified on-cell damper without end groups has not shown significant signs of multipacting.

Multicell options have also been explored including a two-cell cavity, a novel three-cell cavity with a central damping cell for same-passband modes [3.5-52], a two-cell and a five-cell superstructure [3.5-53]. However, each of these cavities suffer from some combination of peak magnetic surface field enhancement, manufacturing and processing limitations, or insufficient mode damping.

An unloaded quality factor of 10^9 has been assumed for the SPX deflecting cavities based on experimental test data at JLAB as shown in Figure 3.5-35 for a single-cell cavity and for the Mark-I cavity prototype. As a result, the anticipated total cryogenic load at 2K due to static and dynamic losses for eight cavities is approximately 80 W. A modest Q-slope at high gradients can be seen, implying that field emission is not a significant factor. The prototype Mark-II cavity with end groups will be

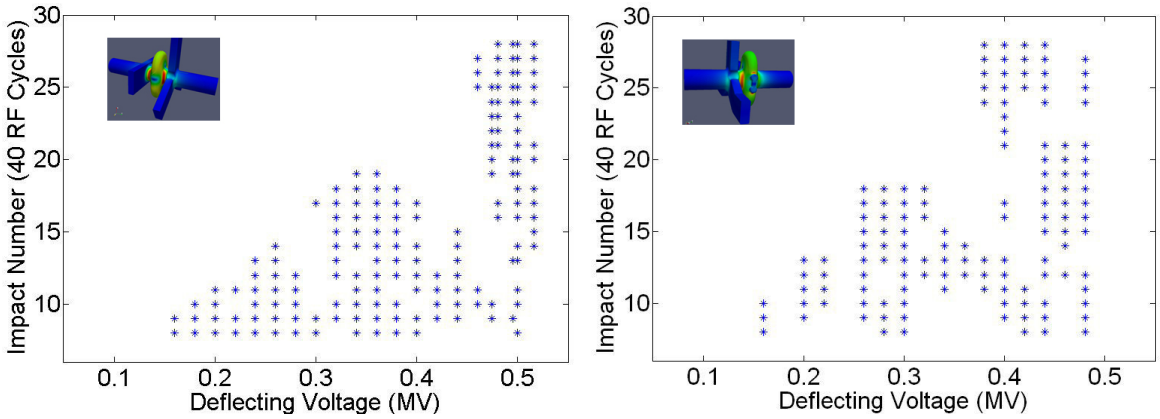

Figure 3.5-34. 3-D multipacting simulation results from SLAC codes Omega3P/Track3P for the Mark-I and Mark-II cavity designs. Forty rf cycles were monitored for resonant electron impacts with energies ranging from 25 eV to 1.5 keV.

constructed at JLAB for evaluation of field emission, peak magnetic field, and unloaded quality factor in July 2011. A final determination of the Mark-I or Mark-II cavity designs will be made in FY2011.

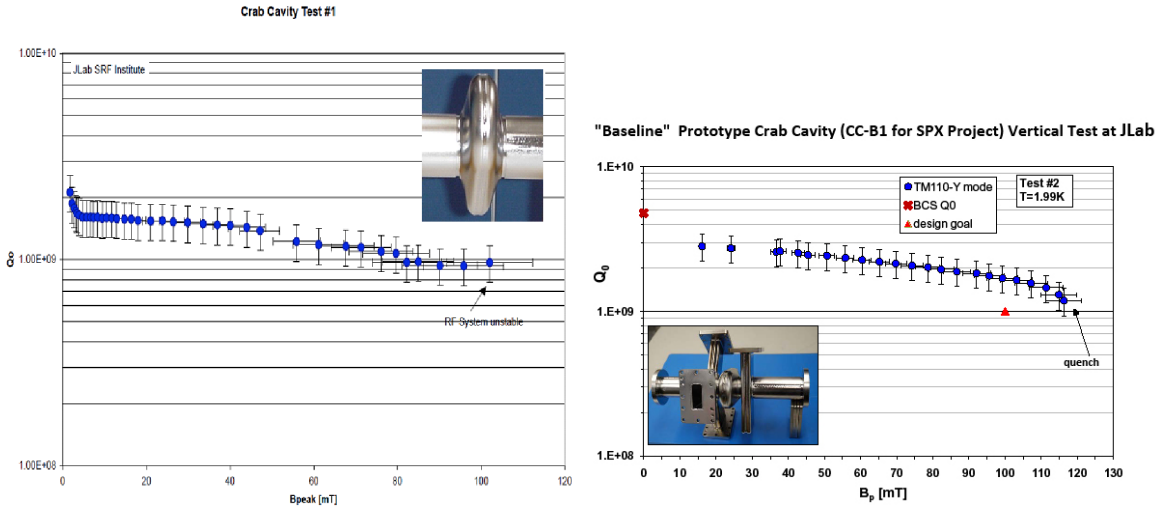

Figure 3.5-35. Experimental data of the Q vs. peak magnetic field for a single-cell cavity without waveguide end groups and for the prototype Mark-I cavity.

Prototype testing of various SPX cavity designs have been performed at JLAB. A single-cell Nb cavity without end groups, shown in Figure 3.5-36, has been constructed and tested. A novel single-cell cavity with on-cell damper shown in Figure 3.5-37 was tested as a proof-of-principle experiment preceding fabrication of the Mark-II cavity. Recently, the Mark-I cavity was fabricated, see Figure 3.5-38, and its performance verified at a gradient in excess of its design goal. Copper models have also been created of a single-cell cavity with the Mark-I beam pipe LOM waveguide damper on the beam pipe, as well as the 3-cell cavity with central damping cell, see Figure 3.5-39. Prototyping has

verified simulation results and assisted in the validation of novel concepts. Various tests will continue to evaluate the unloaded quality factor, multipacting, field emission, effectiveness of the damping scheme, superconducting quenching limits, and Lorentz force detuning (see Figure 3.5-40 and ref. [3.5-53]).

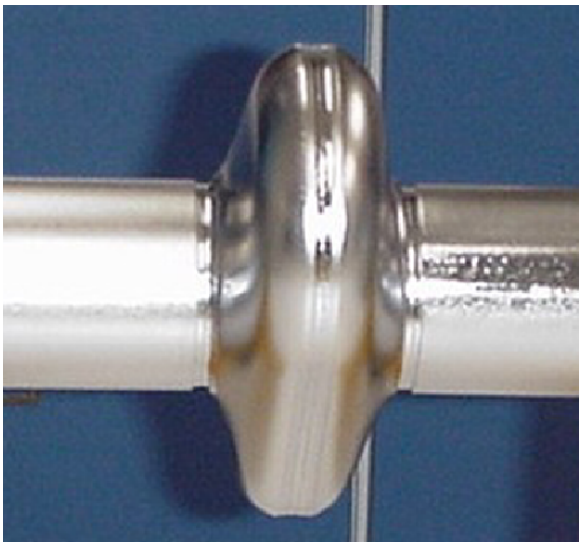

Figure 3.5-36. Single-cell (without end groups) prototype deflecting cavity.

Figure 3.5-37. On-cell damper prototype deflecting cavity.

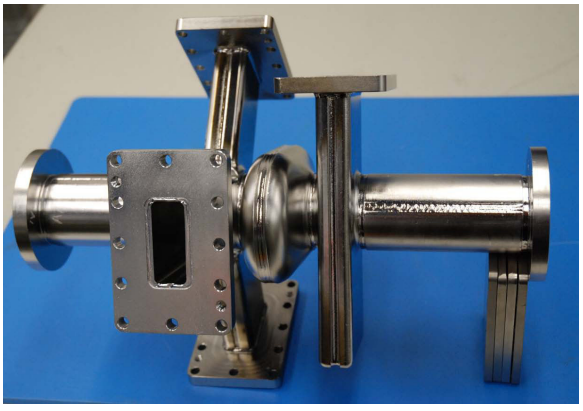

Figure 3.5-38. Mark-I prototype deflecting cavity.

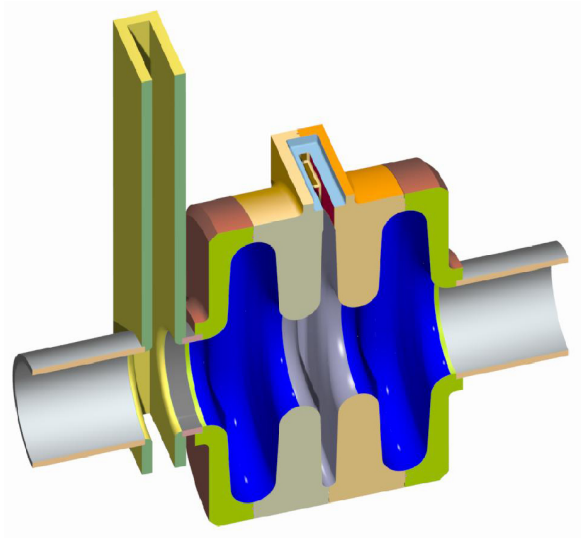

Figure 3.5-39. 3-cell with damping cell model of deflecting cavity.

A vertical cavity test facility is being adapted for the SPX deflecting cavities at Argonne in collaboration with the Argonne Tandem Linear Accelerator System (ATLAS), a heavy-ion superconducting facility. The deflecting cavities manufactured and tested at JLAB will be tested in this facility to benchmark results and to high-power test a fully dressed single-cell cavity in January 2012.

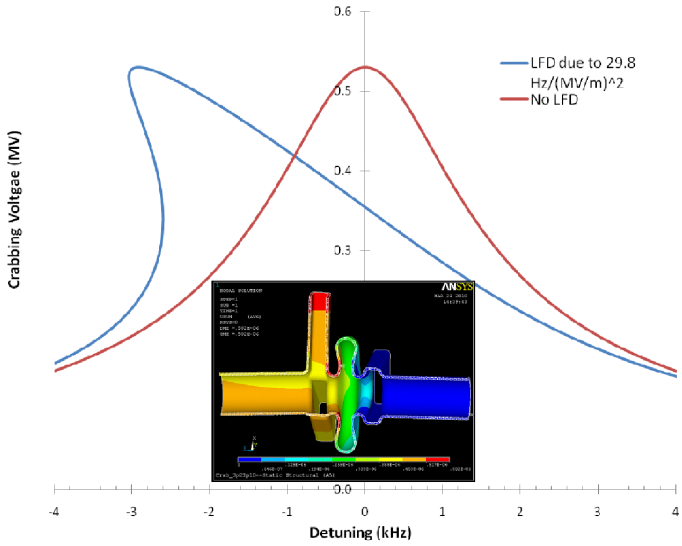

Figure 3.5-40. Lorentz force detuning simulation results in ANSYS, where the resultant frequency shift of the Mark-I cavity is determined up to 0.5 MV deflecting voltage with the cavity supported at a single end.

Additional processing of the cavities may also be performed at ATLAS using the ILC clean room and chemistry facilities.

R&D: Additional R&D work includes (1) Design a compact cavity string with bellows, (2) continue enhancement of LOM/HOM damping, (3) design, prototype, and testing of various damper concepts to produce reliable high-power dampers, (4) evaluate and test the input coupler and rf windows at high power, (5) evaluate the performance of Mark-II cavity with on-cell damping, and (6) perform mechanical analysis of cavity string.

3.5.6.3 Cryomodule and Mechanical Design [1.03.03.05 / 1.03.03.07]

A total of two cryomodules will be utilized for the SPX project. One will be located in Sector 5 to produce a 2-MV beam chirp while the other, located in Sector 7, will reverse the chirp to return the beam to its nominal orbit. Each cryomodule will contain four cavities at 2K operating at 2815 MHz to produce a 0.5-MV deflecting voltage in each cavity. The cryomodule will be required to support a beam current up to 200 mA and, as a result, it must incorporate features to support heavy parasitic mode damping. It will accommodate high cryogenic loads from dynamic losses, as well as from static losses due to numerous waveguide penetrations from the dampers and power couplers. Alignment tolerances are also critical to maintain LLRF tolerances. Parameters for the engineering design of the cryomodule are shown in Table 3.5-9.

The heat load to 2.0K for each of the waveguide penetrations has been estimated to be approximately 0.5 W based on an average loading of the HOM and LOM waveguides and input coupler where dynamic losses have been roughly estimated [3.5-54]. The maximum transmission power through the input coupler will be less than 10 kW, while the LOM and HOM dampers may see a cumulative

Table 3.5-9. Selected SPX Cryomodule Design Parameters

Quantity	Value
Cavity Frequency	2.815 GHz
Operating Mode	TM_{110}
Cavity Iris Radius	25 mm
Cavity Active Gap	53.24 mm
Number of Cells per Cavity	1
Unloaded Q	$> 10^9$
Deflecting Voltage per Cavity	0.5 MV
Coupler Type	Waveguide
External Q	2×10^6
Number of HOM+FPC/LOM Waveguide Coupler	4
Cryogenic Temperature	2.0 K
2K Heat Load due to Waveguide/Tuners per Cavity	2.4 W
2K Dynamic Heat Load Due to Wall Losses per Cavity $@Q_{\mathrm{u}} = 10^9$	7.0 W
2.0K Static Heat Load Due to Miscellaneous Losses per Cryo	2.0 W
Total 2.0K Heat Load $@Q_{\mathrm{u}} = 10^9$	79 W
Slow Tuner Range	$\pm$ 200 KHz
Number of Cavities per Cryomodule	4 (8)
Total Number of Cryomodules	2
Cavity Offset Alignment Tolerance	0.1 mm

load up to 2.5 kW. Additional 2.0K thermal loads of 0.4 W due to the static heat leak of the slow tuner and 2.0 W due to the helium distribution, cryomodule supports, and external beam pipe transitions have been included for a total 2K static heat load of 23 W for two cryomodules. A 1-D model of a waveguide thermal transition from the cryomodule to the warm environment is shown in Figure 3.5-41. A total thermal loss at 2.0 K of 0.26 W was calculated, where 0.21 W loss is attributed to static losses [3.5-53] and where a 15-inch thermal transition and 50 K heat station were assumed. Based on preliminary measurements of prototype deflecting cavities at JLAB, an unloaded quality factor of 10^9 has been assumed for dynamic losses in the cavity per section 3.5.6.2. This corresponds to a dynamic heat load of 7.0 W. As a result, eight cavities situated in two cryomodules produce a cumulative static and dynamic 2.0K heat load of 79 W.

A string of four deflecting cavities will be connected by bellows and supported and aligned using assembly techniques that routinely achieve 500-µm alignment accuracy at JLAB. A cylindrical cryomodule geometry has been chosen for the deflecting cavities due to the availability of proven designs for elliptical cavities [3.5-55–3.5-57] and for the anticipated mechanical advantages in achieving tight alignment tolerances due to the symmetric radial forces during cooldown. The overall diameter of a typical cryomodule at JLAB is 1.0 m and supports a cold mass with transverse dimensions that are comparable with the SPX TM_{110} squashed-cell deflecting cavity.

An R&D effort is being undertaken at JLAB to achieve an alignment of the electrical center of the cavities with the beam axis with a goal of 100 µm when installed and adjusted in the cryomodule. The alignment mechanism will consist of actuators to adjust the vertical offset of each cavity. The final

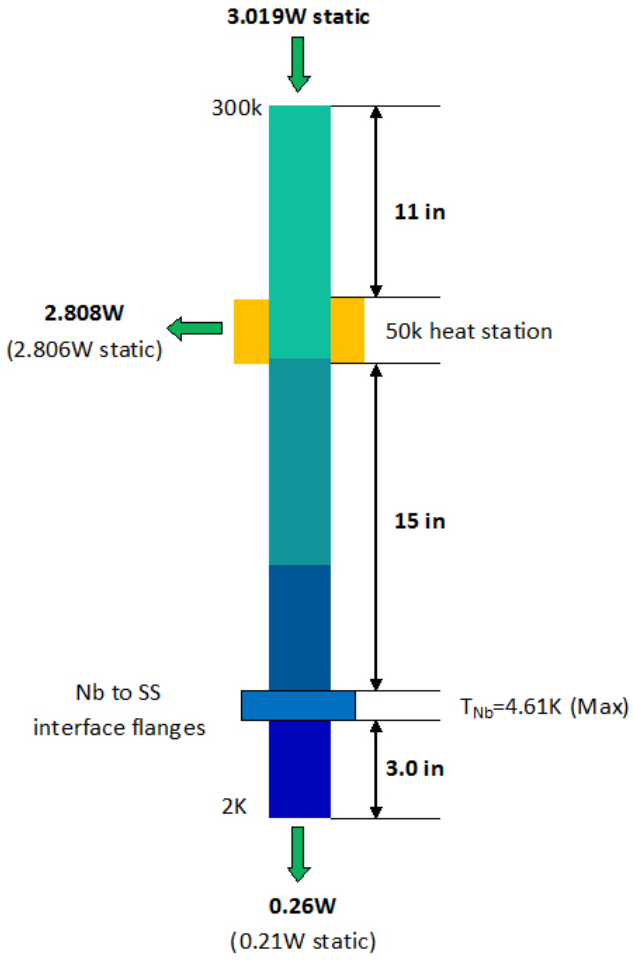

Figure 3.5-41. 1-D thermal model of waveguide transition from 2K to room temperature

alignment will necessarily be beam-based where techniques such as those used by BNL and SLAC will be utilized. The cavity will be adjusted using the TM_{110} dipole mode excitation in the cavity until the signal is nulled, such as during alignment of dipole-mode BPMs. Wire position monitors will be utilized to monitor the alignment during and after cool down. Bellows are required between cavities for individual cavity alignment. Low-impedance bellows, either superconducting or copper, are being evaluated to determine their thermal loading due to beam interaction and the resultant impact on the bellows and the cryogenic environment. Concurrently, KEK-shielded bellows [3.5-58], shown in Figure 3.5-42, are also being evaluated to determine their scalability and suitability for clean-room processing and proximity to a superconducting environment during operation.

A view of the cavity string mounted within a conceptual cryomodule is shown in Figure 3.5-43. Each cavity requires four waveguide penetrations with thermal transitions from the cold mass to room temperature with a flexible waveguide assembly to compensate for thermal contraction.

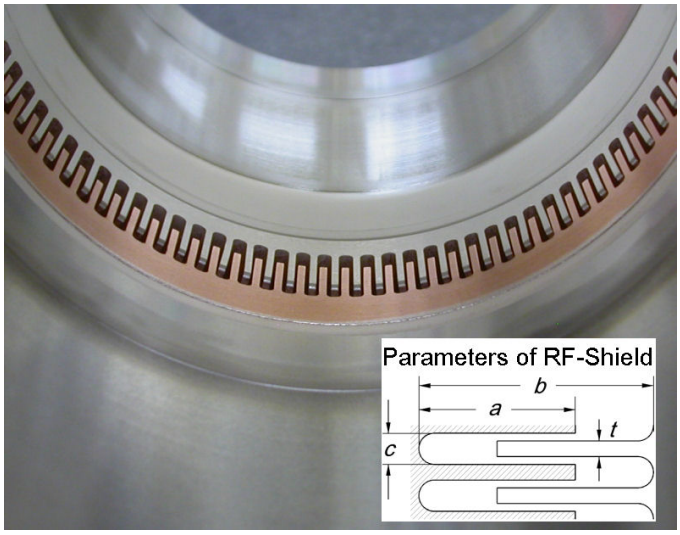

Figure 3.5-42. KEK shielded bellows.

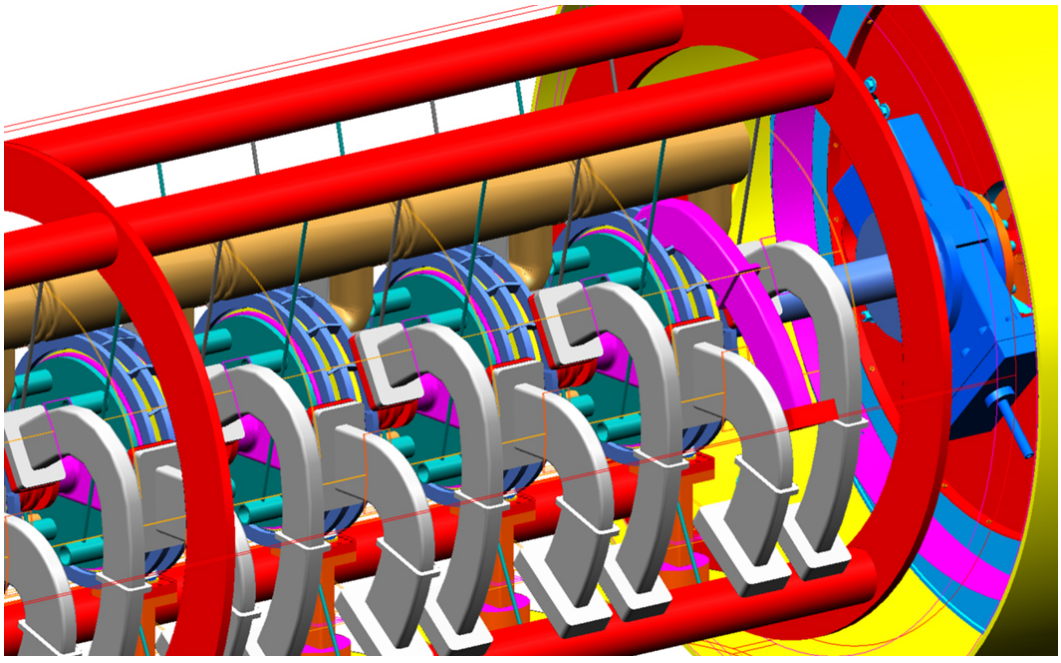

Figure 3.5-43. Deflecting cavity string mounted within a conceptual cryomodule.

The helium vessel shown in Figure 3.5-44 was designed to be compatible with both the Mark-I and Mark-II cavity designs, to optimize the liquid helium volume for stability, and to meet pressure safety standards. A titanium vessel was chosen to minimize effects due to differences in the coefficient

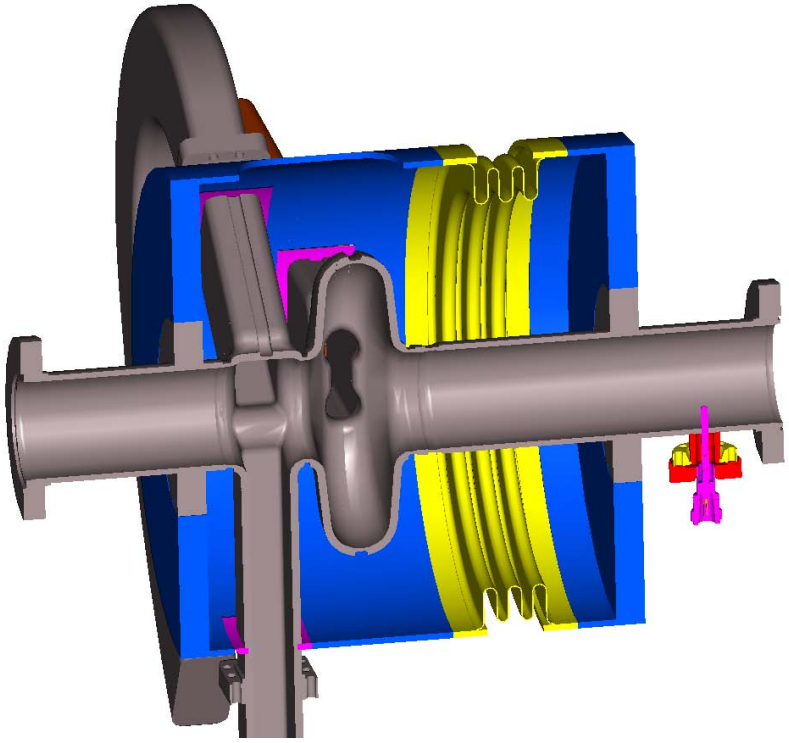

Figure 3.5-44. Mark-II cavity with a generic flat-head helium vessel.

of thermal expansion between the Nb cavity and a stainless steel (SS) helium vessel and to eliminate complicated Nb-to-SS transitions between the helium vessel and the damper waveguides.

The slow tuner will be designed to have at least a $\pm$ 200kHz tuning range. A scissor jack tuner, based on JLAB's 12-GeV upgrade tuner, has been selected as the preferred tuner. A scaled model adapted to the SPX cavities is shown in Figure 3.5-45 where the tuner is modified to accommodate the SPX damping waveguide. The tuner utilizes a warm motor to simplify maintenance and improve reliability. It is side mounted and requires beamline space only for its end plates. The tuner design and adaptation to SPX will benefit from JLAB's operational experience and has demonstrated reliable performance.

The SPX cavities have been shown to have significant frequency sensitivity to cavity deformation. Figure 3.5-46 shows the resultant deformation of the Mark-II cavity due to a 300-kHz frequency shift produced by an 800-N longitudinal force.

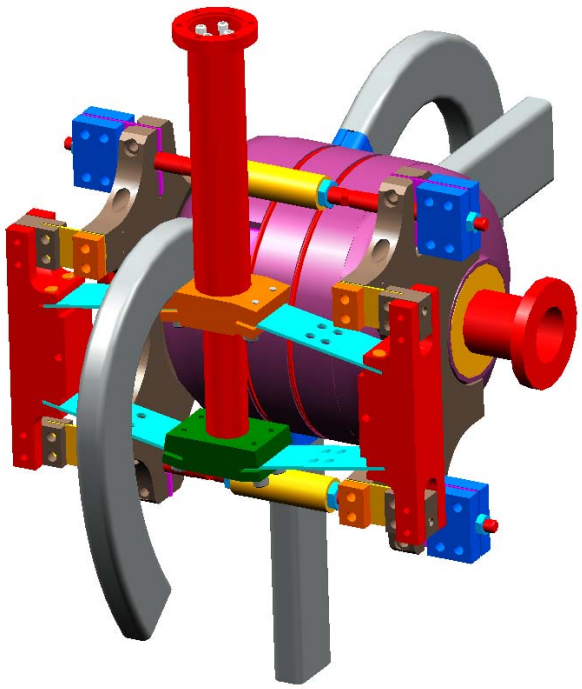

Figure 3.5-45. Scissor tuner adapted to the SPX cavity string.

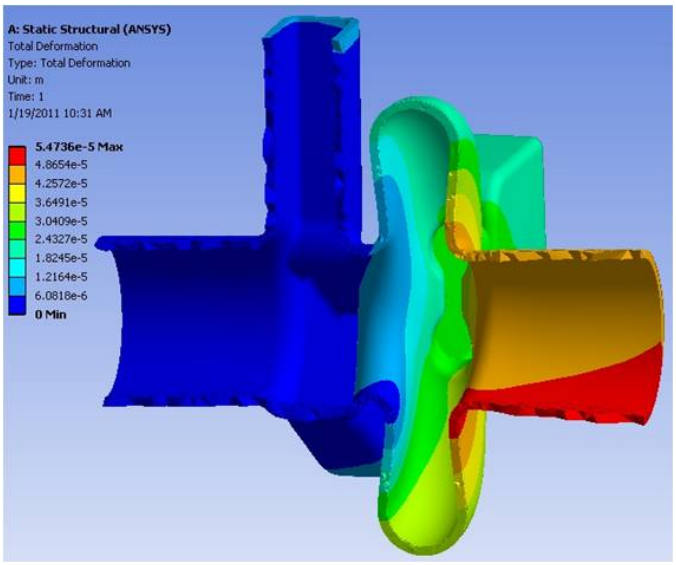

Figure 3.5-46. Displacement of Mark-II cavity to produce a 300 kHz frequency shift

The frequency sensitivity of the cavity has been shown to be approximately 5 Hz/nm. Scaled directly from the JLAB 12 GeV for the SPX cavity, the scissor-jack tuner is estimated to have a frequency resolution of 400 Hz based on the standard step-size of the scissor-jack tuner. Straightforward improvements are being made to the stepper motor and lead screw for an anticipated improved resolution of 40 Hz. Additional modifications, including microstepping, may be implemented to improve the resolution further.

The DESY blade tuner is an alternate design that is being considered due to its successful implementation on numerous superconducting cavities, such as at INFN Milano, Fermilab, and on two-cell cavities for the Cornell ERL injector [3.5-57]. Figure 3.5-47 shows a design of the blade tuner by INFN Milano [3.5-59], which requires no beamline space. The center ring is rotated by a cold stepper motor, and the action of the flexural joints translates the motion into a distributed longitudinal force.

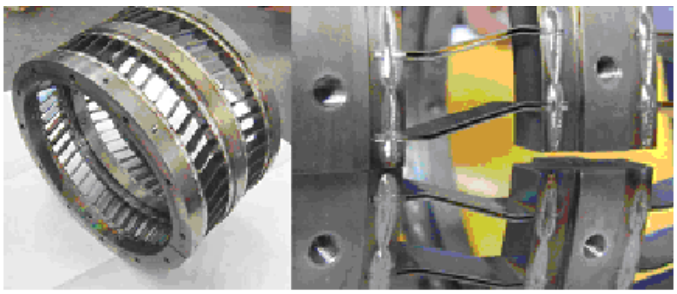

Figure 3.5-47. INFN Milano blade tuner based on DESY design.

R&D: Additional R&D work includes: (1) High-power testing will be performed on the power coupler waveguide, primarily to evaluate multipacting and arcing. The input coupler rf windows will be tested up to 5 kW and should have sufficient bandwidth for possible HOM transmission. (2) The scissor-tuner design will be further investigated to determine its resolution and performance on an SPX cavity. (3) Water cooling of the dampers in the insulating vacuum will be investigated to determine construction and assembly details, as well as issues regarding vibrations and microphonics. (4) The internal cryomodule features will be definitively sized and located including the helium distribution system, vacuum vessel, magnetic and thermal shielding, cavity string, waveguides, cryomodule supports, and alignment components. The cryomodule design and assembly sequence must be compatible with the requirement for clean-cavity rf surfaces. This includes a suitable concept for mounting the cryomodule in the beam line without contaminating the clean-string assembly. (5) A measurement of the ground vibration *in situ* will need to be done in order to determine the driven frequencies in the APS tunnel. Numerical analysis of mechanical modes in the cavity string will be undertaken to ensure there are no issues. (6) Flanges in the cavity string in close proximity to the cavity will be analyzed for losses and compatibility. (7) Evaluation of shielded and low-impedance bellows will be performed to determine beam impedance, bellows durability, and the effect on the cryogenic system. (8) Further simulations of the thermal transitions in the cryomodule will be performed including the waveguide penetrations, beam-pipe transitions, and incidental thermal loads between the cavities in the cavity string.

3.5.6.4 Cryogenics [U1.03.03.06]

The SPX cryogenic refrigeration and distribution system provides cooling to the deflecting cavities sufficient to maintain a stable operating temperature under all operating conditions. The system provides saturated liquid helium at 2.0 K via a low-heat-leak distribution system and must accommodate the static heat loads presented by the cryomodules and distribution system, as well as the dynamic load imposed by cavity operation. Figure 3.5-48 shows a block diagram of the system.

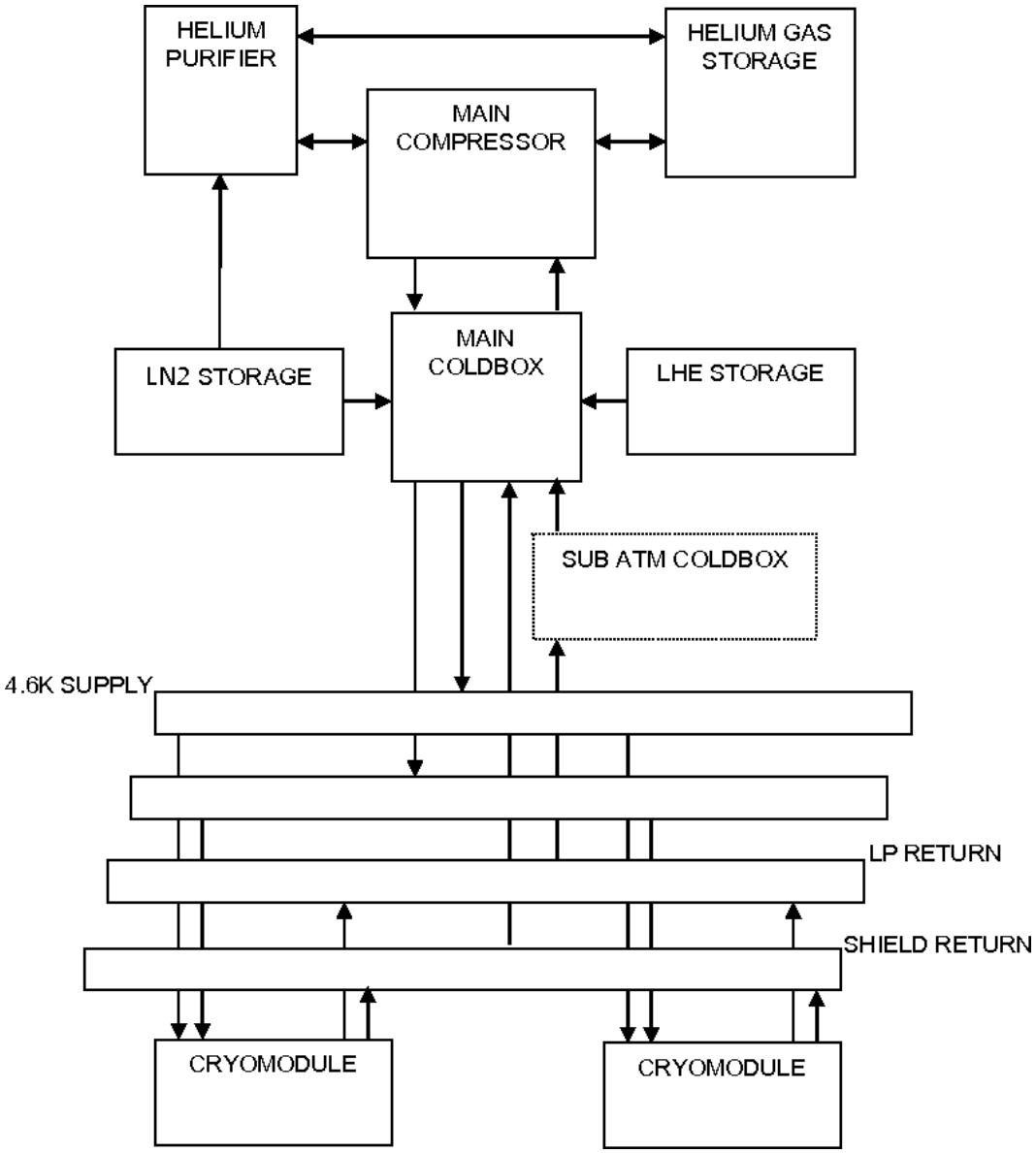

Figure 3.5-48. Cryogenic system block diagram.

The refrigerator provides helium at 300 kPa, 4.6K to the distribution system. Within each

cryomodule the helium is cooled to 2.2K by heat exchange with the 2.0K saturated vapor return stream. The 2.2-K, 300-kPa supply is throttled to 2.0K, 3.13 kPa and supplied to the rf cavities. The vapor space above the cavity bath is maintained at 3.13 kPa (the saturation pressure for LHe at 2.0K) by a hybrid gas pumping system consisting of one or two stages of cold compression and one stage of vacuum screw compression. The cold compressor(s) generate a pressure ratio of about 4, providing a suction pressure of 13 kPa for the vacuum screw compressor bank. Figure 3.5-49 shows a simplified flow schematic of the refrigeration system. The cryoplant also supplies refrigeration at 4.5K and 80K for thermal intercept and thermal shield cooling within the cryomodules and distribution system.

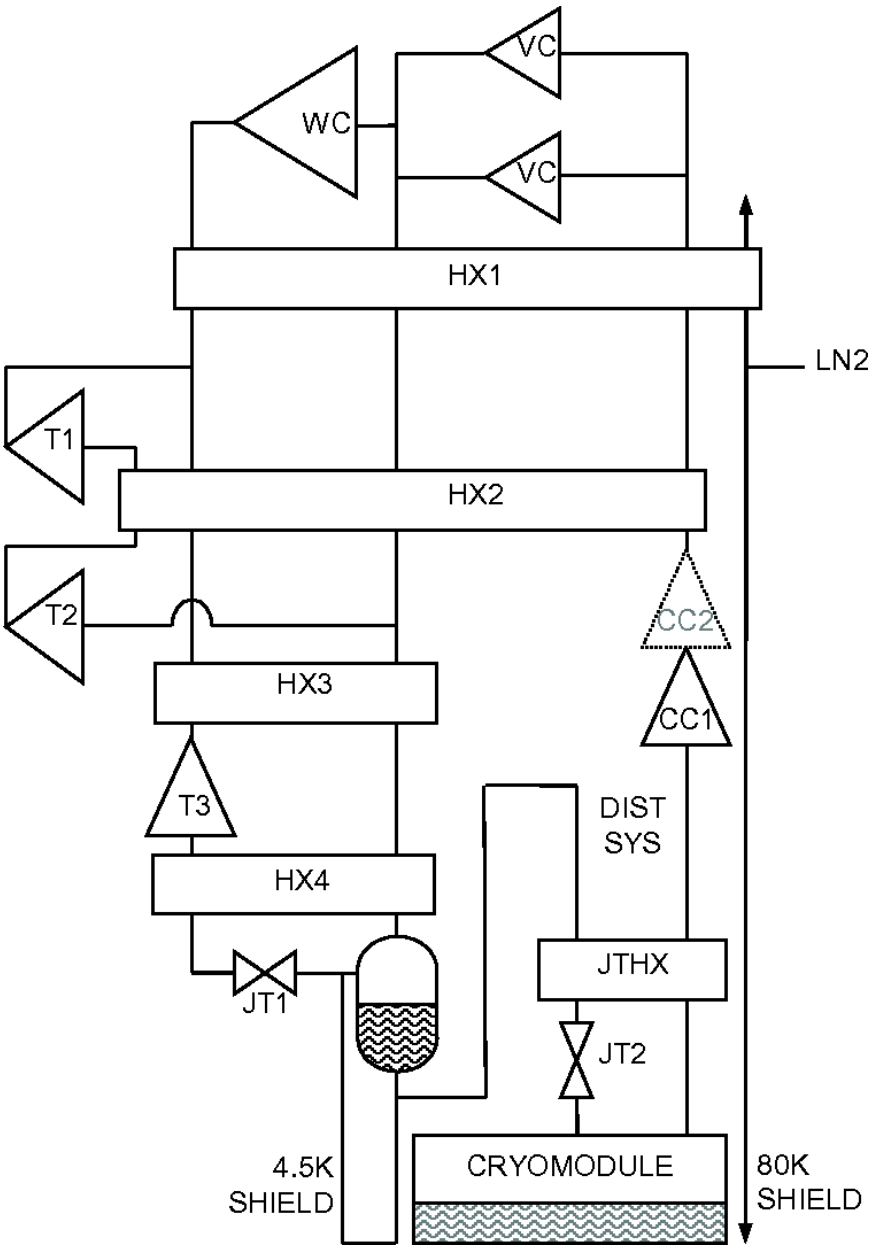

Figure 3.5-49. A simplified flow schematic of the refrigeration system.

Table 3.5-10 provides estimates for the major cryogenic system load parameters.

Table 3.5-10. Nominal Load Parameters

Quantity	Value
Refrigeration at 2.0K (static+dynamic)	79 W
Refrigeration at 4.5K (static)	500 W
Thermal shield cooling at 80-90 K (static)	4 kW (LN2)

Dynamic heat load estimates vary greatly depending on achieved performance. The plant should be designed with a substantial margin in 2.0K capacity and also posses a reasonable upgrade path sufficient to handle unforeseen dynamic and/or static loads, as well as future expansion of the SPX system.

There are many elements that inform the design of a cryogenic system for SRF cavities. These include:

- **Pressure-Stability Criteria:** The 2.0K LHe superfluid bathing the SRF cavities must maintain a stable pressure of 23.5 Torr (3.13 kPa) to keep the cavities on frequency. Considering the performance of typical slow tuners, a pressure stability of $\pm$ 0.5 Torr is adequate and readily achievable with existing cryoplant technology.
- **Vibration Effects on Cavities:** Vibrations from the cryoplant (particularly the warm compressor systems) cannot exceed the LLRF specifications. This likely means isolating the compressor skids from the facility through a combination of remote location, isolated concrete pads, and/or isolation mounts.
- **Off-Design Operation:** The plant must operate efficiently not only at design load but also at reduced load. A thorough understanding of the cavity-operating profile, including time spent at reduced or zero gradient, is necessary to properly specify the off-design operating requirements.
- **System Margin:** Some amount of overcapacity will be designed into the system to mitigate the risks associated with uncertain cavity dynamic heat load and the possibility that the completed plant underperforms. The latter can also be mitigated with an incentive-based procurement contract tied to actual measured capacity during commissioning.
- **Upgradeability:** If the gradients are increased or the cavity performance is well below specification, the cryogenic load may increase beyond that provided by the system margin. In this case, a low-cost, efficient-capacity upgrade will be required. Provision for such an upgrade should be part of the original system design.
- **Safety (Pressure, Cryogenics, Oxygen Deficiency Hazard, System Venting, etc.):** Safety analyses are a fundamental aspect of cryoplant design. Vendors will be held to applicable codes and standards with regard to pressure system safety. Oxygen-deficiency hazard (ODH) analyses will be conducted for all cryoplant enclosures, as well as the regions of the APS tunnel containing cryomodules and distribution-system components.

- **System Reliability:** The cryoplant availability must meet overall APS beam-to-user requirements. This may be achieved via on-line spares, modular design, and system margin. A robust control system is an integral part of this aspect of performance. Any control/monitoring systems supplied by the cryoplant vendor must integrate effectively with the APS control system.
- **Wall-Plug Power Requirements:** Modern hybrid 2.0K cryogenic systems have a load ratio (LR) of about 2.7, where the LR is the ratio of equivalent capacity at 4.5K to actual capacity at 2.0K. It is useful for comparison purposes to normalize the capacity of a cryogenic system containing multiple heat loads at a variety of temperatures to a single refrigeration capacity at 4.5K. In turn, wall-plug-power requirements for modern systems in this size range are typically 240-W-per-watt of refrigeration at 4.5K, plus additional overhead and losses. For the expected capacity range of 160-320 W at 2.0K plus additional shield and static loads, this translates to an estimated wall-plug-power requirement of 0.3-0.5 MW, not including overhead and losses.
- **Similar Systems:** The ELBE facility at TU-Rossendorf shown in Figures 3.5-50 and 3.5-51, operates a cryogenic system capable of 220 W at 1.8K,upgradeable to 380 W with additional compressors and LN2 precooling. Note that the LR for 1.8K refrigeration is more like 3.6 compared to 2.7 for 2.0K. As an example of another similar system, Fermilab has recently purchased a new cryoplant with a design capacity of 500 W at 2.0K, plus shield loads. Both these systems are based on the hybrid concept, which uses both cold compression and warm screw compressors operating in vacuum to generate the subatmospheric pressure required to produce saturated vapor at 2.0K or 1.8K.

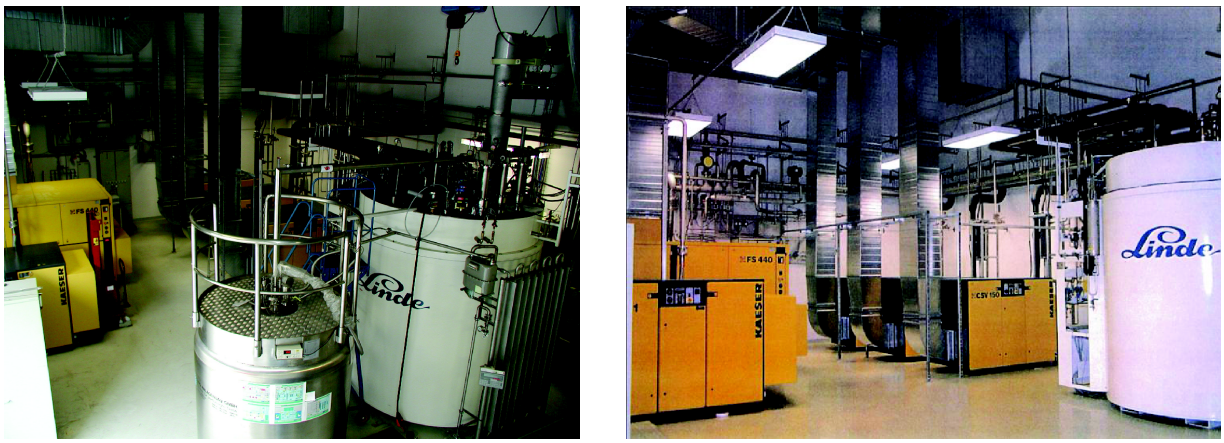

Figure 3.5-50. ELBE 200-W/1.8K cryoplant at FZ-Rossendorf.

- **Delivery Schedule:** Delivery of a cryoplant in this size range is expected to be about 30 months from order to commissioning and final acceptance. The procurement may include on-site start-up, commissioning, and training as part of the deliverables. The plant will be capable of operation using the vendor-supplied control system (independent of the accelerator control system). Acceptance tests are typically performed by making refrigeration into a storage Dewar and measuring capacity via an electric heater.

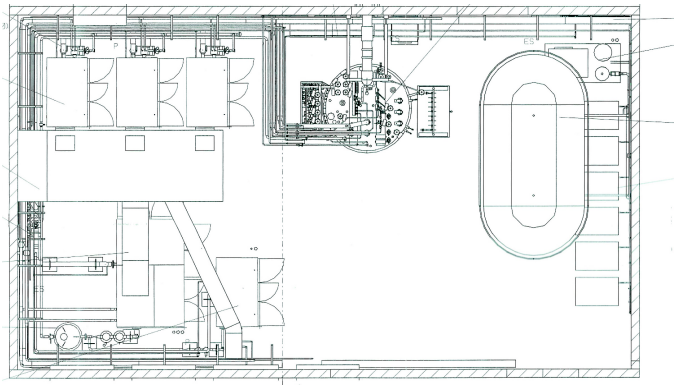

Figure 3.5-51. Plan view of ELBE cryoplant hall — 17 m × 10 m.

3.5.6.5 Low-Level rf [U1.03.03.02]

The primary responsibility of the low-level rf (LLRF) system is to regulate the amplitude and phase of the cavity fields. It must also interface to the machine protection system and the control system's input/output controllers and real-time data processing (section 3.5.7). The beam-based feedback strategy presented in section 3.5.5 requires the LLRF system design to be closely coordinated with beam physics, the rf system, beam diagnostics, and controls in order to meet the SPX tolerances (section 3.5.3.4). The differential phase error tolerance of 0.18° rms will be a challenge even with beam-based feedback. Additionally, deflecting cavities present beam-loading effects not present in conventional accelerating cavities. These issues are discussed and a conceptual rf control architecture is presented to address them.

Beam-Loading Considerations The equivalent circuit [3.5-60] used to represent a single deflecting cavity with multibunch beam loading is shown in Figure 3.5-52. The corresponding phasor diagram is shown in Figure 3.5-53 with the beam-loading phasor, $\hat{I}_B$, expressed as:

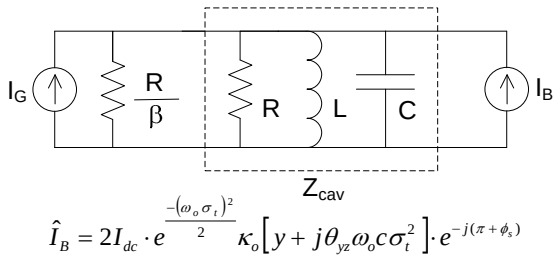

Figure 3.5-52. Single deflecting cavity equivalent circuit.

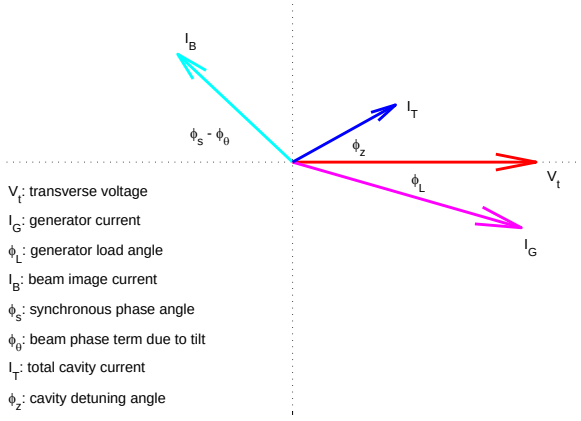

Figure 3.5-53. Cavity phasor diagram.

$$\hat{I}_B = 2I_{dc}\, e^{-\frac{1}{2}(\omega_o\sigma_t)^2}\kappa_o \left[y + j\theta_{yz}\omega_o c\sigma_t^2\right]\, e^{-j(\pi+\phi_s)}, \tag{3.5-40}$$

where I_{dc} is the storage ring dc beam current, ω_o is the rf operating frequency, σ_t is the rms bunch length, κ_o is the wave number, y is the beam vertical offset, θ_{yz} is the beam tilt in the yz plane, c is the speed of light, ϕ_s is the beam synchronous phase angle, and $j = \sqrt{-1}$. The steady-state forward generator power, $P_{\rm g}^{+}$, required to produce a given transverse voltage magnitude, $|V_t|$, can be expressed as

$$P_{\rm g}^{+} \approx \frac{|V_t|^2}{8\beta(R/Q)'Q_{\rm o}}\left[\left(\beta + 1 + \frac{P_B}{P_{cav}}\right)^2 + \left(2Q_o\frac{(\Delta\omega + \delta\omega_m)}{\omega_r} + \frac{|V_t||\hat{I}_B|\sin\phi_B}{2P_{cav}}\right)^2\right], \tag{3.5-41}$$

where $P_B = -\frac{1}{2}|V_t||\hat{I}_B|\cos\phi_B$ is the power delivered to the beam with ϕ_B the phase angle of $\hat{I}_B$, $P_{cav} = \frac{1}{2}\frac{|V_t|^2}{(R/Q)'Q_o}$ is the power dissipated in the cavity walls, $(R/Q)'$ is the circuit definition, $\Delta\omega \equiv \omega_r - \omega_o$ represents controllable static detuning, ω_r is the cavity resonant frequency, $\delta\omega_m$ represents uncontrollable microphonics detuning, and $\beta = Q_o/Q_{\rm ext}$ is the input coupling coefficient with unloaded cavity quality factor $Q_{\rm o}$ and external quality factor $Q_{\rm ext}$.

The required generator power as a function of $Q_{\rm ext}$ for a single SPX deflecting cavity operating at $|V_t|$ = 0.5 MV with $(R/Q)'$ = 17.8 Ω, $Q_{\rm o} = 10^9$, with nominal $\phi_{\rm s}$ = 0, I_{dc} = 200 mA, σ_t = 41 ps, zero static and microphonic detuning, and zero beam tilt is shown in Figures 3.5-54 and 3.5-55. Figure 3.5-54 represents the required power for the first group of deflecting cavities with positive V_t and positive y, as well as the required power for the second group of "undeflecting" cavities with negative V_t and negative y. On the other hand, Figure 3.5-55 represents the required power for the first group of deflecting cavities with positive V_t and negative y, as well as for the "undeflecting" cavities with negative V_t and positive y.

The required power when including 200 Hz peak microphonics and 2 deg of beam tilt is shown in Figures 3.5-56 and 3.5-57. While the level of cavity microphonics that the cavity will experience is unclear at this point, an estimate of 200-Hz peak is reasonable. The largest nominal beam tilt in the last cavity of the first sector and the first cavity of the second sector is expected to be 0.23 deg for a 4-cavity-per-sector system with 2-MV total deflecting voltage.

Disturbances to the SPX rf systems will mainly include cavity microphonics, master oscillator noise, phase reference distribution noise, LLRF transceiver noise, high-level rf (HLRF) system klystron noise, and beam-loading variations. Dynamic beam-loading variations in the SPX deflecting cavities will mainly arise from variations in 3.5-40 due to beam offset, beam tilt, and beam arrival time. Beam arrival time errors from main storage ring rf system noise in combination with beam offset through an SPX cavity can lead to differential phase noise between SPX cavities [3.5-61]. Small-signal noise propagation models for the rf system, such as that developed in ref. [3.5-61] can be used to analyze, develop, and track a system noise budget.

The final design $Q_{\rm ext}$ will be a compromise of the following considerations: beam offset precision, expected worst-case uncontrollable beam offset for cavity protection considerations, required generator power, cavity-to-cavity electrical alignment errors, expected level of microphonics, system noise bandwidth considerations, and the coupling of storage ring main rf noise through the beam-to-SPX noise. For example, choosing a lower $Q_{\rm ext}$ will make the system less susceptible to low-frequency

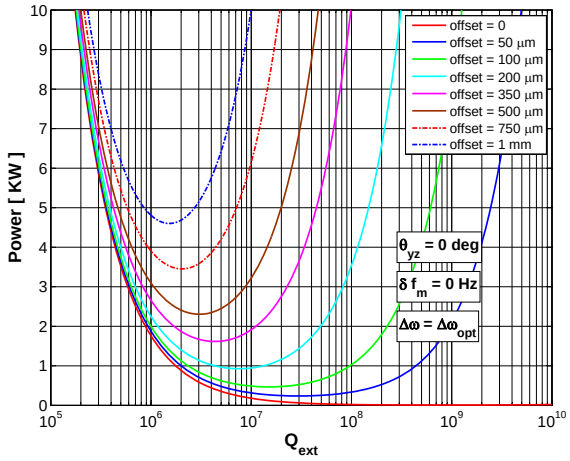

Figure 3.5-54. Minimum required generator power per cavity vs. Q_{ext} for $V_t \times y > 0$.

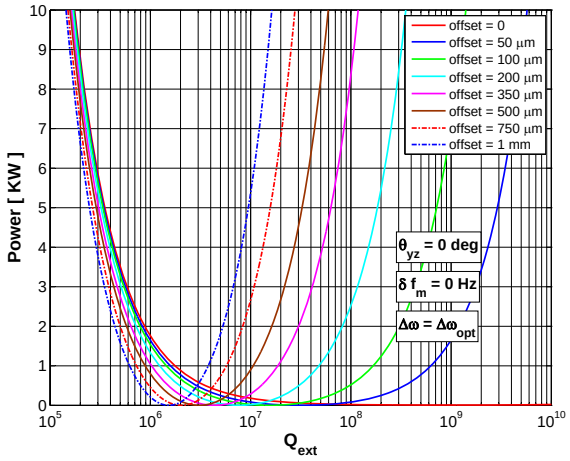

Figure 3.5-55. Minimum required generator power per cavity vs. Q_{ext} for $V_t \times y < 0$.

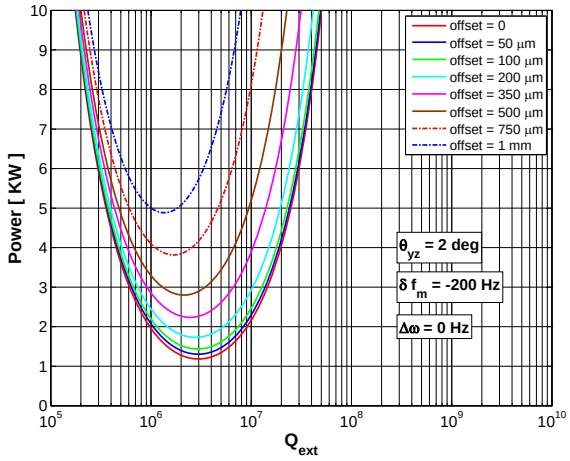

Figure 3.5-56. Required generator power for $V_t \times y > 0$ with microphonics & beam tilt.

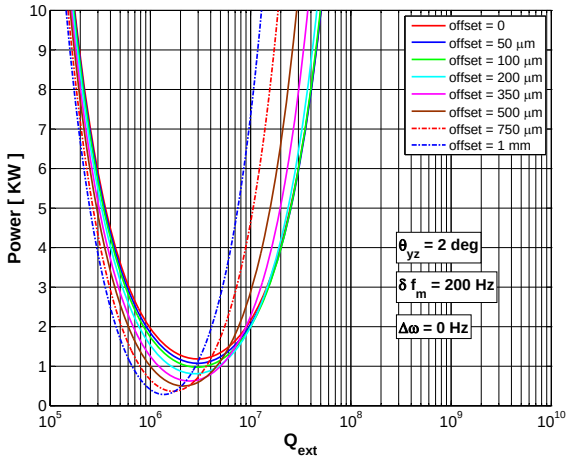

Figure 3.5-57. Required generator power for $V_t \times y < 0$ with microphonics & beam tilt.

microphonics and beam loading variations but increases the system bandwidth and hence reduces the amount of LLRF feedback that can be applied for other noise reduction due to system stability concerns. A lower Q_{ext} also reduces the cavity voltage that can be attained from a large uncontrollable beam offset, thereby relaxing beam vertical offset trip limits for machine protection concerns (section 3.5.8). These system-level tradeoff considerations will be studied during R&D and addressed in the engineering design phase.

Since the beam loading is dependent on both beam offset and beam tilt in deflecting cavities, two cavities within the same sector can see beam loading of opposite polarity simply due to cavity alignment errors causing the beam to appear above or below the cavity electrical center. Beam offset in combination with beam tilt and beam arrival time potentially allows for beam loading in all 4

quadrants of the phasor diagram. Taken together with possible dynamic disturbances to the rf systems, the preferred rf system architecture is to provide the capability for independent LLRF cavity control via a one rf power amplifier per cavity configuration (section 3.5.6.6) in order to be able to compensate for the inevitable differences between individual cavities.

Conceptual Rf Control Block Diagram: A conceptual rf control block diagram is depicted in Figure 3.5-58. The LLRF system includes everything in blue and orange. The master oscillator, timing, and synchronization shown in purple are considered part of the timing and synchronization system (section 3.5.7). The LLRF system is envisioned to consist of the following main components:

- LLRF Controller Assembly

  The LLRF controller assembly is envisioned to be a field-programmable gate array (FPGA)-based controller with analog-to-digital converter (ADC) sampling of the rf signals at an intermediate frequency (IF) via an analog down-converter. The controller will output individual klystron rf drive signals to each cavity via an up-converted IF output from a digital-to-analog converter (DAC). The details of the engineering packaging and hardware platform will be developed during the R&D and engineering phases as the detailed system specifications and interface requirements between systems becomes clearer.

  The LLRF controller assembly will need to provide the following functionality:

  - Individual cavity amplitude, phase, and tuning control
  - Control of intrasector cavity sub-groups to support compensation of betatron phase advance errors (section 3.5.3.4)
  - Control of cavity sectors to support the beam-based feedback strategy (section 3.5.5)
  - Klystron drive and output signal monitoring, as well as klystron amplitude and phase control if klystron noise performance warrants the use of feedback around the klystron.
  - Drift compensation of the LLRF cabling and receivers at the individual cavity level is expected to be needed to control cavity-to-cavity phase errors within an SPX sector as discussed below in the drift compensation hardware item.
  - Interfacing to the controls input/output controllers and the real-time data processing environment (section 3.5.7) for system operations and integration with beam diagnostics for beam-based calibrations and feedback.
  - The LLRF controller must also interface to the machine protection system (section 3.5.8) to allow removal of LLRF drive signals and to provide cavity quench protection.

- LLRF Phase Reference Distribution

  While beam-based feedback (section 3.5.5) is expected to alleviate the need for a LLRF phase reference distribution with ultra-stable long-term stability, the conceptual design includes provisions for both a fiber-based phase reference and a coax-based phase reference. The fiber-based reference has superior long-term stability, while a coax-based reference has superior short-term stability. The fiber-based reference (1) is required to synchronize the user laser to the SPX cavities in Sector 5 (section 3.5.7.3) and (2) relaxes the control effort of the beam-based feedback system. The coax reference ensures lowest possible short-term phase noise. The performance of the two types of references will be studied during the R&D phase.

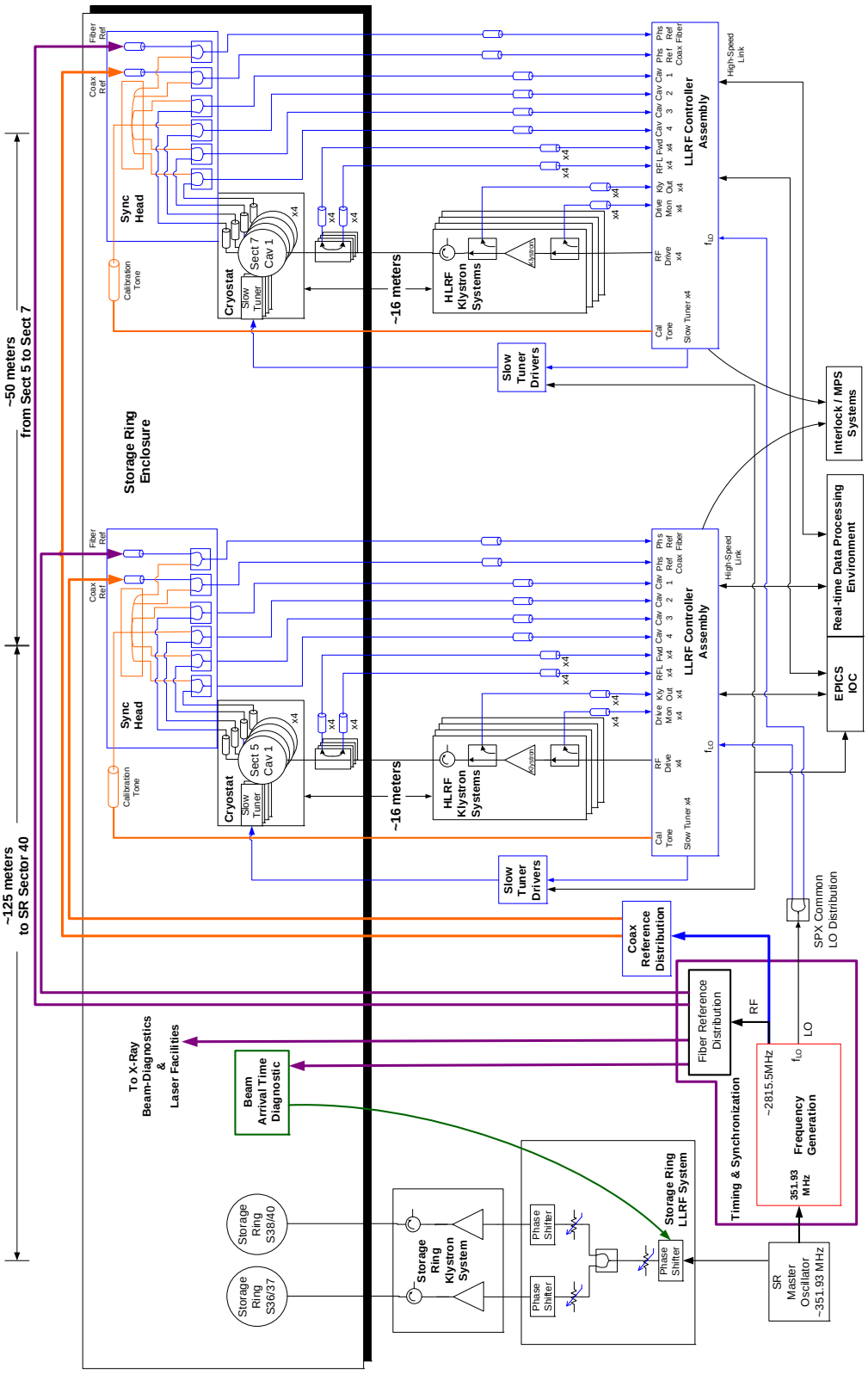

Figure 3.5-58. Conceptual rf control block diagram.

- Drift-Compensation Hardware (“Sync Head”)

  While beam-based feedback is expected to alleviate the need for long-term stability and drift compensation between cavity sectors, phase errors between individual cavities within the same sector may lead to orbit distortions. Thus, drift compensation at the individual cavity level is expected to be needed to compensate for drifts of both the LLRF cables leading from the cavity field probes to the LLRF receiver and the LLRF receiver itself. These drifts can be compensated for by using a calibration tone scheme developed at LBNL for CW applications [3.5-62].

  The scheme relies upon continuously injecting an ideally equal-phased calibration tone, that is offset in frequency, to each cavity field pickup probe, as well as to the phase reference signal that each cavity is compared to, as depicted in Figure 3.5-59. To ensure an equal phase calibration tone to all field probes, the tone is added to the field-probe signals within a temperature-stabilized chassis referred to as the “sync head.” Temperature stabilization is required since the calibration tone scheme cannot compensate for drifts of any components shown in blue or orange. In order to capture as much of the cabling leading off of the cavity field probes, this should be done as close as possible to the cavity pickup probes. Thus, it is envisioned that one “sync head” will be mounted on each cryostat.

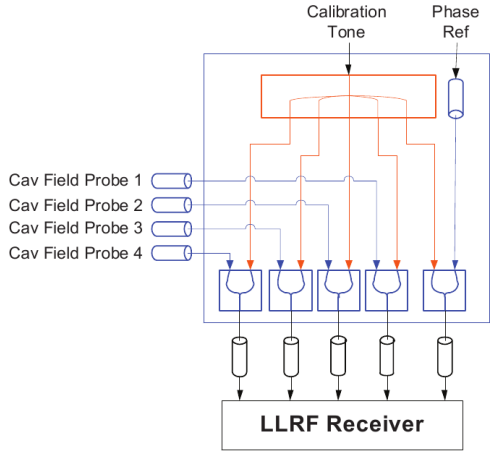

Figure 3.5-59. Concept of calibration tone injection.

- Tuner Driver Electronics

  The slow tuner driver electronics are considered to be part of the LLRF system, thus the driver electronics will need to be compatible with whatever motors are chosen for the cavity slow tuner. The motors and tuners themselves are considered part of the cavity/cryostat system (section 3.5.6.3).

LLRF R&D The biggest question for LLRF control that needs to be addressed through an R&D program is whether the SPX amplitude and phase-stability requirements can be met, especially the differential phase-noise tolerance of 0.18° rms. While beam-based feedback is expected to alleviate long-term stability requirements from the rf system, the LLRF will be on its own above the bandwidth of the orbit feedback system. Furthermore, the amount of rf system noise and drift that orbit feedback

will be expected to suppress needs to be explored. A LLRF R&D plan to address these concerns consists of the following:

- Evaluating rf control and phase stabilization needs for SPX through close coordination with beam physics, the HLRF and cavity systems, beam diagnostics, and controls. The Rf system noise propagation will continue to be explored through the small signal noise model [3.5-61], which can be used to develop system noise budgets.
- A prototype LLRF system for the deflecting cavities will be developed to verify that the rf system can meet the required amplitude and phase stability.

To begin development of a prototype LLRF system a collaboration with Lawrence Berkeley National Lab's (LBNL) Beam Technology Group (BTG) is planned. The LBNL's BTG has been a leader not only in LLRF measurement and control but also in femtosecond-stabilized timing and synchronization. They have extensively developed the LLRF drift-compensation scheme for continuous wave (CW) applications as part of their timing system that is planned for SPX timing and synchronization needs 3.5.7.3. The proposed collaboration is really a two-fold strategy to give the SPX project access to LBNL's expertise and technology in both (a) synchronizing systems to the 10s of femtosecond level, and (b) digital LLRF measurement and control of rf cavities with CW drift compensation capability.

To begin independent LLRF bench-top development, two high-Q cavity emulator circuits, as depicted in Figure 3.5-60, will be built. By mixing the rf input down to the center frequency of a narrow-bandwidth crystal bandpass filter, the effective Q of the circuit is given by the ratio of the rf frequency to the crystal bandwidth. By controlling the frequency of the local oscillator used for downconversion, Lorentz force detuning and microphonics can be simulated on the bench.

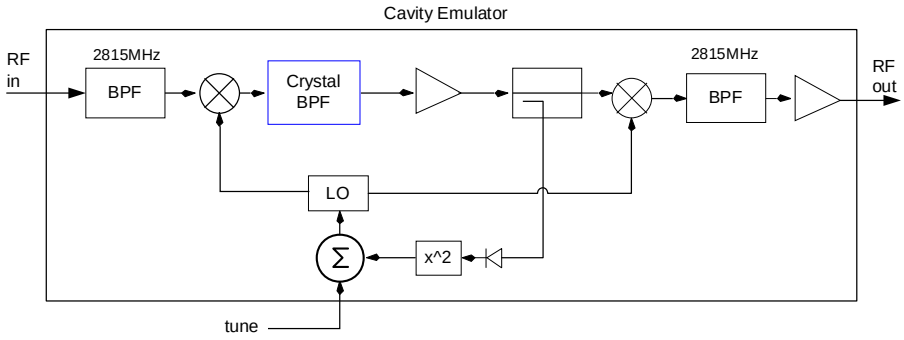

Figure 3.5-60. High-Q cavity emulator concept for LLRF development.

Prototype LLRF controllers will be developed to control the cavity emulators in order to perform benchtop characterization of common-mode and differential-mode amplitude and phase stability between the two emulated cavities, as depicted in Figure 3.5-61. This will allow benchtop development of the LLRF controllers, algorithms, and noise-measurement methods independent of any cavity-development schedule. The initial prototype controllers will be based upon LBNL's LLRF4 boards, which are one of the few LLRF controllers that have actually been characterized in terms of

true residual phase-noise measurements. These measurements have initially been estimated to show promise for SPX tolerance considerations. [3.5-40].

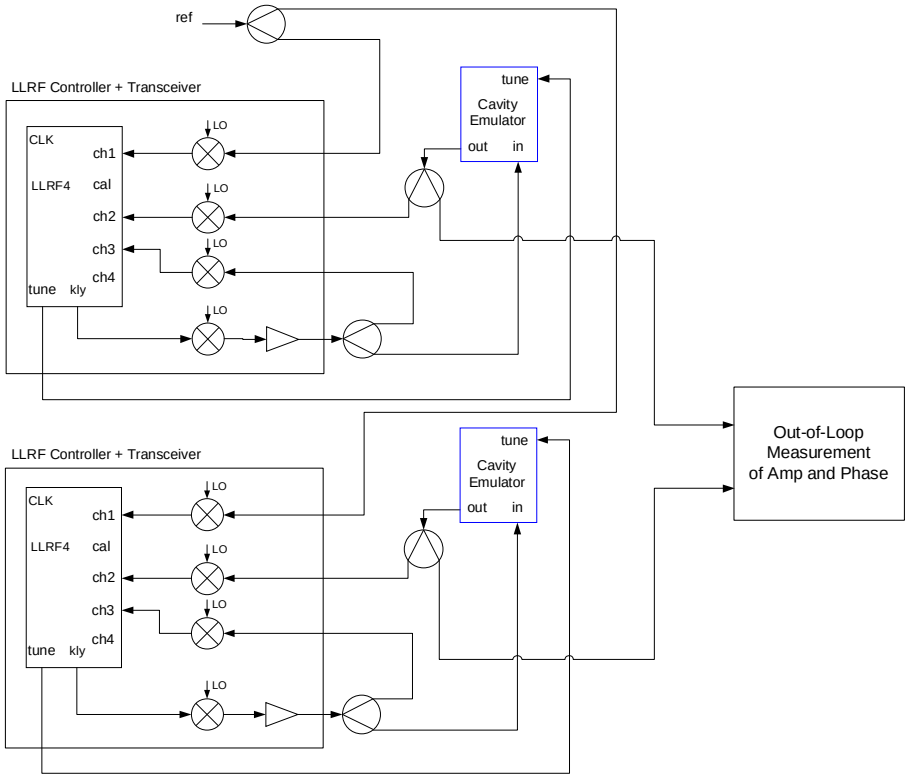

Figure 3.5-61. LLRF Benchtop Test Concept.

Following initial benchtop development, a LLRF prototype control system will then be integrated into a single, dressed-cavity test stand once a fully dressed cavity with tuner becomes available. Next, LLRF control will be tested and evaluated with the two-cavity cryostat that will become available at the rf test stand (section 3.5.5.1). Ultimately, the LLRF control system will be tested under beam-loading conditions as part of the storage ring two-cavity cryostat test (section 3.5.5.1).

3.5.6.6 High-Power RF System [U1.03.03.01]

This section describes the technical requirements and conceptual design of the high-level portion of the SPX deflecting-cavity rf system. The HLRF system encompasses all rf drive-line components and support hardware between the output of the low-level rf control system and the rf input flange of the deflecting cavity cryostat.

HLRF System Specifications The SPX HLRF system is required to produce rf power at a nominal frequency of 2815.44 MHz at the input of the cavity flange sufficient to generate a nominal value of 500-kV-per-cavity deflecting field. It must also provide adequate dynamic range for low-level rf control and adequate power overhead to compensate for waveguide transmission losses, beam loading caused by relative errors in cavity electrical center, and beam-position offsets up to a storage ring current of 200 mA. It is assumed that a maximum cavity detuning of 200 Hz will be required to control cavity microphonic effects, and that the nominal operating point for the rf power amplifier and associated high-voltage power supply will be approximately 80% rated power output during normal short-pulse x-ray operation in order to preserve rf system reliability and lifetime.

Since the rf cavities will be over-coupled, the rf power systems will be required to operate at full rated power into a mismatched load at infinite voltage standing-wave ratio (VSWR) without damage. Due to the rf frequency and power output requirement, conventional klystrons are utilized as rf power-amplifier devices.

HLRF System Topology: Two basic topologies for the HLRF system are proposed. The reference design is shown in Figure 3.5-62.

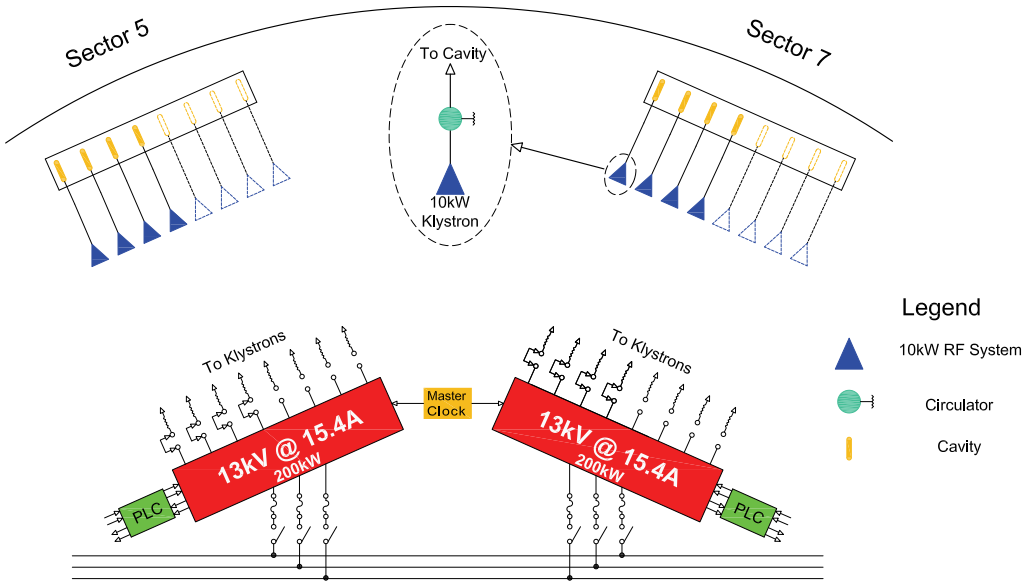

Figure 3.5-62. Reference rf system distribution.

The system consists of four 10-kW HLRF systems per sector, each driving a single rf cavity to produce a total of 2-MV deflecting voltage per sector. This configuration provides the most flexible rf voltage and phase control at the single-cavity level. High-voltage dc power for the klystron rf amplifiers in each sector is provided by a common 13-kV, 200-kW power supply in order to make the power-supply noise contribution between the separate rf systems correlative. The power supply is capable of supplying sufficient dc power for eight klystrons per sector, and will be loaded at approximately 50% capacity for the 2 MV/sector case. High-voltage dc power is distributed to each rf amplifier klystron through a series-limiting resistor to limit fault current and a removable jumper to provide high-voltage

isolation and lockout-tagout of individual klystrons for maintenance. The alternate design, shown in Figure 3.5-63, utilizes a single 20-kW klystron to supply rf power to two cavities and a "magic T" hybrid junction to provide a -3-dB power split of the klystron output to each cavity. Two of these 20-kW/2-cavity rf systems will be used in each sector to generate the required 2-MV deflecting voltage. This design reduces the required number of klystron and circulators to achieve a modest cost savings. In order to achieve individual amplitude and phase control of cavity rf power, a high-level waveguide I/Q modulator is used in the waveguide run to each cavity. As in the reference design, high-voltage dc power for the klystrons is produced by a common 20-kV, 200-kW high-voltage power supply in order to correlate the high-voltage power-supply noise contribution between the four rf systems.

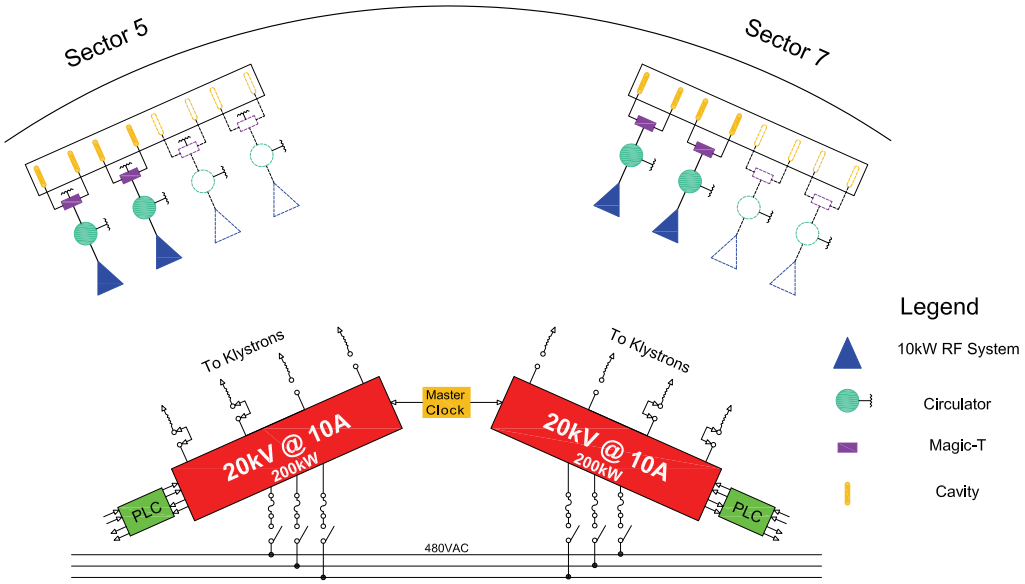

Figure 3.5-63. Alternate rf system distribution.

Waveguide Transmission System: The waveguide transmission system utilizes a standard WR284 aluminum waveguide with a nominal wall thickness of 0.080 inches and air-tight flanges. A typical value for losses in a straight waveguide of this type at S-band frequencies is estimated at approximately 1 dB per 100 feet. Details of the waveguide system are shown in Figures 3.5-64 and 3.5-65.

The waveguide system and circulator will be gas tight and pressurized to approximately 3 psi with dry nitrogen supplied by a standard gas bottle. A pressure regulator and dryer will be used to maintain waveguide nitrogen pressure and humidity. Waveguide system features common to both the reference and alternate topologies include the use of a three-port waveguide switch, klystron harmonic filter, two independent waveguide shutters, output circulator, phase shifter, and directional couplers immediately after the klystron output and immediately before the cavity input flange. The three-port switch is utilized for rapid connection to full-power test load in order to implement klystron testing and maintenance without disassembling waveguide components. The two waveguide shutters are used as personnel safety devices to provide absolute rf isolation between the klystron rf output port and the remainder of the waveguide system in order to allow maintenance of the klystron amplifiers during periods of storage ring operation. The circulator and associated rf loads are required to protect the

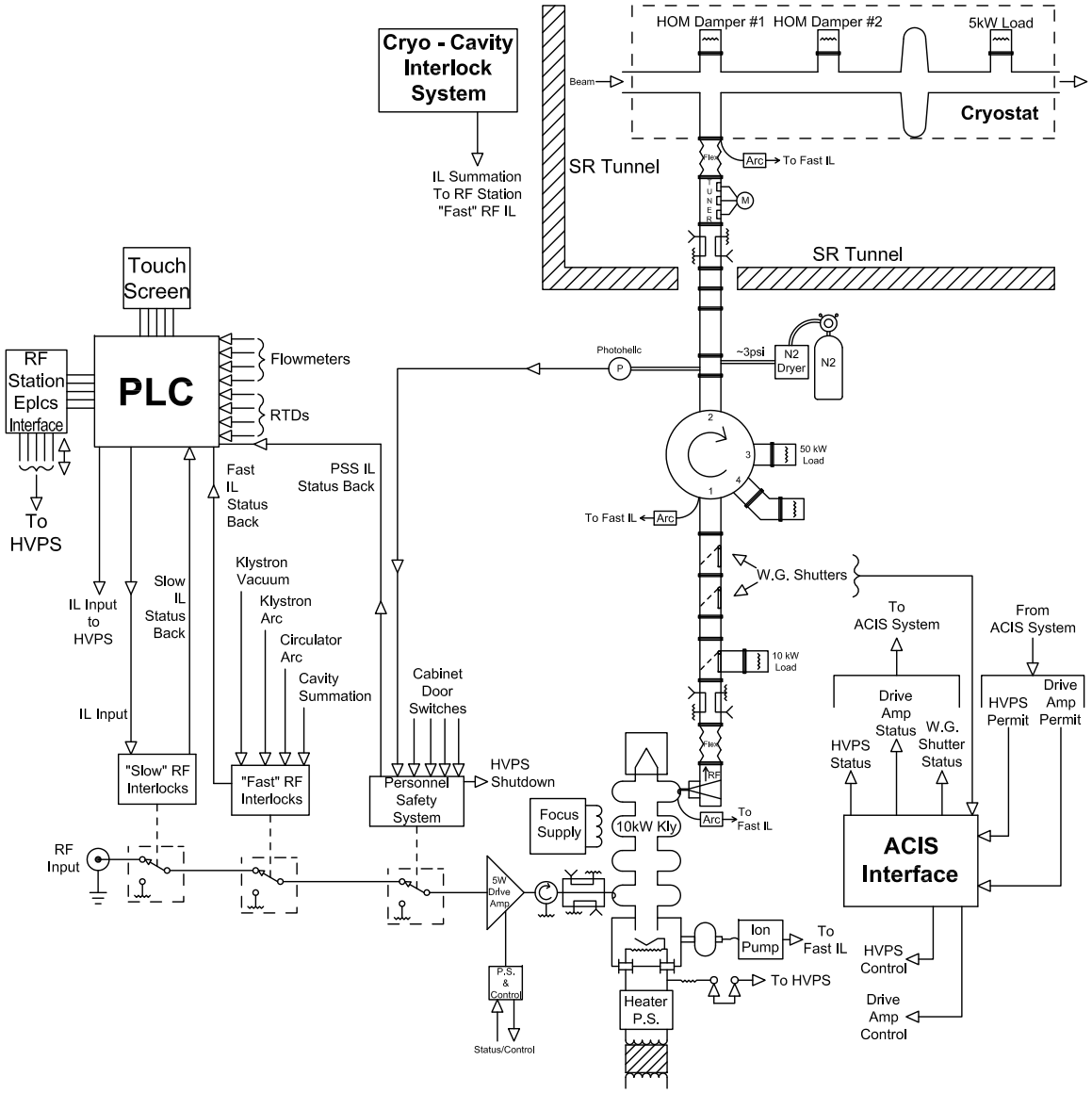

Figure 3.5-64. Reference rf waveguide system layout.

klystron from two expected sources of reverse power: reflected incident power due to over-coupling of the cavity for beam-loading compensation, and rf power generated by the cavity when beam-position errors result in stored beam coupling energy into the cavity.

The total accumulated transmission loss in the waveguide system is calculated from nominal values for losses expected from individual waveguide components, the conceptual waveguide system design, and actual loss measurements taken on a WR284 aluminum waveguide test line at 2.815 GHz. Table 3.5-11 shows estimated component losses. Assuming a total length of 51 feet between the klystron and cavity input flange, the total expected waveguide loss is 0.89 dB, which represents a transmission loss of 18.6% over the path. In the reference design a 10-kW klystron operating a full-

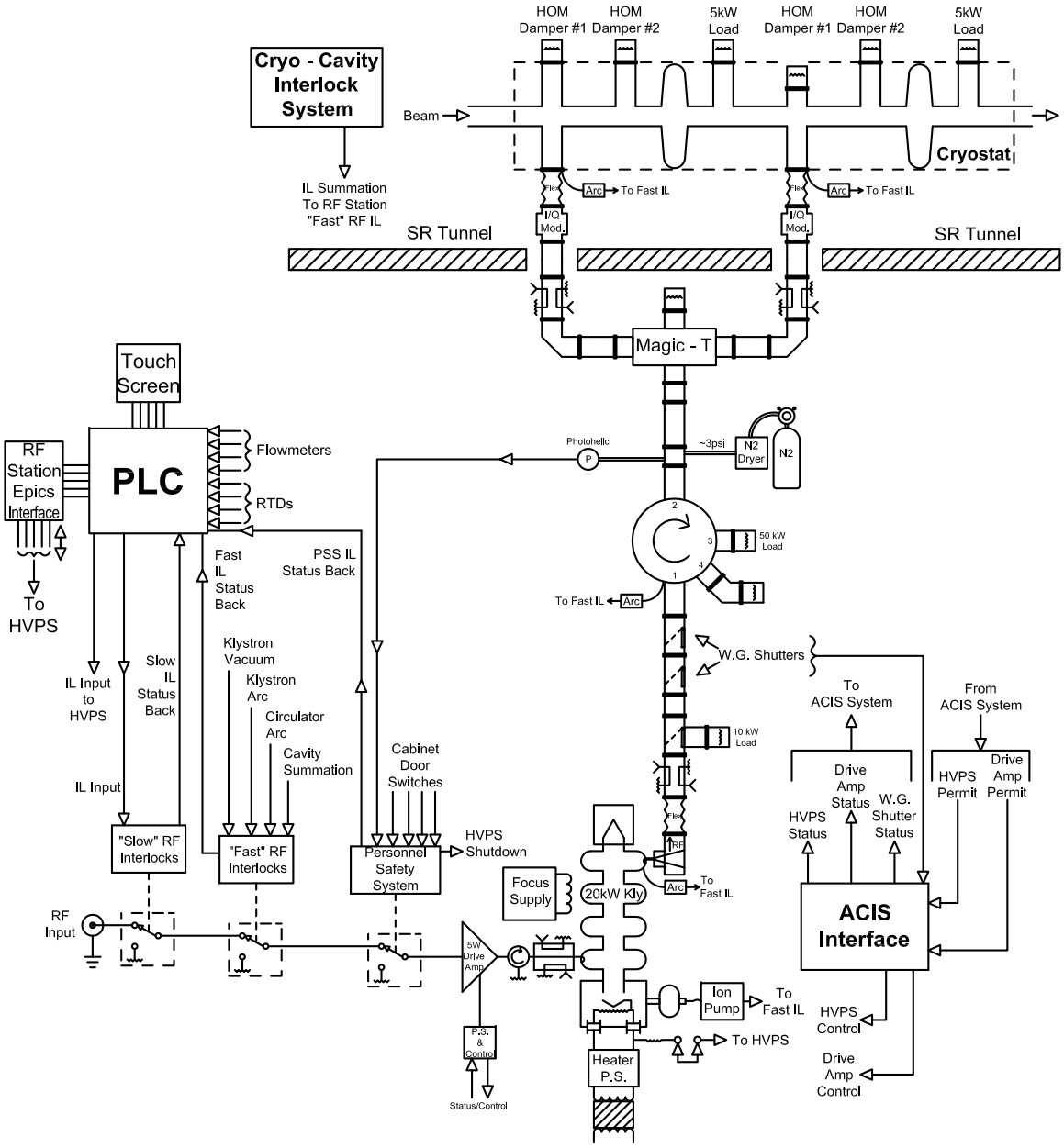

Figure 3.5-65. Alternate rf waveguide system layout.

rated power output would deliver approximately 8.1 kW to the cavity flange under matched conditions.

The alternative design, shown in Figure 3.5-65, utilizes four additional waveguide components to optimize power and load balance between the two cavities. A magic T hybrid junction is used to split the klystron power evenly between the two cavities. A fast I/Q modulator is used in each cavity feedline as a phase shifter and rf attenuator to compensate for static phase and power imbalances between the two cavities. A three-post tuner is used in each cavity feedline to provide adjustment

Table 3.5-11. Estimated Waveguide Component Losses.

Flex section	0.02 dB
Direction coupler	0.02 dB
Waveguide switch	0.01 dB
Waveguide shutter	0.01 dB
Harmonic filter	0.20 dB
Circulator	0.15 dB
Straight aluminum waveguide	1.00 dB / 100 ft
Fast IQ modulator	0.15 dB
"Magic T" hybrid junction	0.1 dB
Waveguide tuner	0.05 dB

range for cavity coupling. The addition of these extra components in the alternative design increases the transmission path loss to each cavity by approximately 0.375 dB, resulting in an additional 8.2% transmission loss to each cavity flange. Factoring in these additional losses, a 20-kW klystron operating at rated power will deliver a maximum of 7.47 kW to each cavity flange under matched conditions.

Klystrons: The reference and alternate designs utilize a conventional klystron capable of 10-kW CW and 20-kW CW output power, respectively. Both klystrons will utilize diode electron guns, waveguide rf output flanges for superior cooling of the output window, and collector designs capable of dissipating full beam power under conditions of zero rf drive. The nominal specifications for the klystrons are shown in Table 3.5-12 and are comparable with that of similar commercially proven CW klystrons designed for CW operation at 2.450 GHz.

Table 3.5-12. Nominal Klystron Specifications.

Parameter	**Value**	**Units**
Operating frequency	2815.44	MHz
Continuous output power	10/20	kW
Saturated power output	12/24	kW
Maximum load VSWR for rated power	$\leq$1.4:1	
Minimum operating efficiency	50	%
Minimum rf gain	40	dB
Rf bandwidth (-1 dB)	5	MHz
Rf output termination	CPRF284 flange	
Water inlet temperature	32.2	°C

Both klystrons will be designed to operate with dc cathode heater power in order to minimize phase and amplitude noise generation at 60 Hz and related harmonics. The heater power supply will utilize a switching regulator operating above 50 kHz and will regulate on output current. The heater power supply will operate from 120 VAC produced by a dc isolation transformer rated for a minimum of 60 kV. Electromagnetic focusing will be utilized, but permanent-magnet focusing will be considered

during the design phase of the klystron procurement as a way to reduce overall system cost and complexity. The klystron design will include sufficient shielding to reduce any emissions of ionizing radiation to less than 0.5 mrem/hr at a distance of 1 m from any part of the klystron under all operating conditions.

High Voltage Power Supplies: To achieve the lowest ripple and distribute residual power-supply noise coherently between all klystrons to the best extent possible, two ultralow-ripple klystron high-voltage power supply (HVPS) units are utilized to provide dc beam power for all klystrons. Both HVPS units are supplied 480 VAC/3-phase primary input power from the same bus and provide single-point LOTO capability at each sector for maintenance and troubleshooting. In the reference design shown in Figure 3.5-62, one 13 kV/15.4 A, 200-kW dc power supply is utilized to supply beam power to a maximum of eight 10 kW klystrons per sector. In the alternate design shown in Figure 3.5-63, two 20 kV/10 A, 200 kW dc power supplies are utilized to supply beam power to a maximum of four 20 kW klystrons per sector. To enhance reliability and service lifetime, both designs load the HVPS units to approximately 80% full-load power when a full complement of klystrons is utilized. Beam power is distributed to each klystron by parallel outputs from the HVPS, with a removable jumper and current-limiting resistor in series with each klystron amplifier to facilitate troubleshooting and limit fault current. The HVPS units utilize paralleled switching regulators and filtering with much less than 20 J of stored energy, thereby eliminating the need for crowbar protection for the klystrons. The paralleled regulators in each HVPS unit are synchronized and switched in order to reduce output ripple at 13 kV and 20 kV to approximately 0.04% and 0.025%, respectively. Feed-forward compensation is utilized to further reduce output ripple to approximately 0.008% and 0.005%, respectively [3.5-63]. Both sector HVPS units are driven by synchronized switching drive signals generated by a master-clock module, resulting in minimum uncorrelated ripple between the sectors. The switching frequency is variable over a 5% range to avoid coincidence with any natural resonance of the stored beam. The switching signals to both sector HVPS units are disabled by an interlock input to the master clock in response to beam-dump commands by the storage ring machine protection system (MPS) or shutdown commands from any of the SPX rf system PSS units. Control and monitoring of the HVPS is achieved by a local PLC interface at each sector HVPS unit. This PLC interfaces with the HVPS control system to provide local and EPICS-based remote control and monitoring of operating parameters and process variables.

Equipment Protection Interlocks: Protection against damage to SPX rf system hardware due to fault conditions, such as rf arcing, vacuum pressure, reduction or loss of cooling water flow, or excessive dissipation, is provided by the equipment protection interlock system. The system consists of two dedicated interlock subsystems, one internal to the rf amplifiers themselves and one at the cryomodule tunnel location. Each interlock system has two main components, a PLC-based portion that provides millisecond response time to fault conditions relating to water flow and temperature-related parameters, and a separate rf interlock module that provides microsecond response time to fault conditions relating to high energy and fast rise time. Upon detection of a fault condition, SPX rf power is muted either by interrupting rf drive power to the amplifier klystrons or shutting down the klystron HVPS, or both. A separate cavity quench detection system is employed to remove SPX and beam-generated rf power from the deflecting cavities in response to detected quench-specific parameters.

SPX Rf Machine Protection System: Protection of SPX rf system hardware from excessive beam-generated rf power is required when the SPX rf equipment protection interlock systems detect a fault condition that cannot be cleared by disabling the SPX rf systems. Under such a scenario, fault conditions, such as cavity or circulator overpower, excessive cavity vacuum pressure, arcing in waveguide windows, LOM dampers or circulator, excessive HOM/LOM damper dissipation, insufficient cooling water flow, or cavity quench in SPX rf hardware will trigger a beam-dump command that will be sent to the storage ring MPS to initiate a rapid dump of storage ring beam.

Personnel Protection Interlocks: Potential hazards to personnel from the SPX rf system hardware include rf radiation leakage from open waveguide flanges, contact with high-voltage conductors, and exposure to ionizing radiation generated by the klystrons. The Personnel Safety System (PSS) controls personnel exposure to these hazards by simultaneously disabling both the LLRF drive to the klystron and the HVPS by dedicated hardware interfaces when unsafe conditions are detected. The PSS interface chassis is designed using simple relay logic for maximum reliability and fail-safe modes.

Gas pressure meters are used to monitor positive nitrogen pressure inside the waveguide in order to detect leaking or open waveguide flanges. Loss of waveguide pressure below a minimum setpoint will constitute a potential hazardous condition and will result in an open contact signal at the PSS main chassis and immediate shutdown of the rf system by two independent and redundant methods. Personnel exposure to high voltage and ionizing radiation is prevented by monitoring klystron amplifier cabinet and HVPS door switches. All access doors and covers on the klystron amplifier cabinet and HVPS must be closed and secured before the PSS system will allow system operation.

Access Control Interlock System Rf Interface and Control: Access Control Interlock System (ACIS) control of the SPX rf systems is implemented by disabling rf output of each rf system individually. Separate control of LLRF drive at each rf station and control of the HVPS at each sector provides independent and redundant interruption of rf power when the storage ring ACIS system is not in beam-permit mode. A separate rf/ACIS interface chassis is utilized at each SPX rf system to provide contact closures to interrupt LLRF drive and HVPS output during conditions when the storage ring tunnel is not in beam permit mode, and to provide status auxiliary contacts back to the ACIS system to verify rf equipment status. The LLRF drive to the klystron is inhibited by interrupting 120 VAC power to the klystron drive amplifier.

The ACIS system also monitors the position of two waveguide shutters located in the output waveguide in order to allow maintenance and testing of the rf system into a load during periods of storage ring authorized access. The waveguide shutters are each rated to block the flow of rf in the waveguide in excess of the rated power of the klystron. The combination of two shutters in series is the accepted protocol for personnel safety credit.

R&D Plan R&D effort will include designing and building two 5-kW, 2.815-GHz klystron-based HLRF systems, complete with all associated interlock hardware, in support of the R&D in-ring test SPX-0.

3.5.7 Controls, Timing, and Synchronization [U1.03.03.03, U1.03.03.04]

The entire SPX system must be thoroughly integrated with existing APS storage ring controls, timing, and diagnostics. Since any instability in the operation of the SPX cavities will impact all APS users, thorough instrumentation and diagnostics will be required to detect any operational abnormalities. Although many details are yet to be determined, it is envisioned that the primary responsibilities for SPX controls are to:

- Provide remote monitoring and control to all SPX subsystems,
- Provide precise timing and synchronization between the APS storage ring rf systems and the SPX rf systems,
- Provide the interfaces to other APS systems to obtain necessary real-time storage ring information,
- Provide a real-time data processing environment where control algorithms can be executed at high speeds to ensure well integrated control with the APS storage ring, and
- Provide thorough diagnostic information and tools to assist in quick determination of performance problems and post-mortem fault analysis.

Figure 3.5-66 illustrates a conceptual block diagram for the SPX controls. The dark gray blocks identify functions typically provided by the control system while the light gray blocks depict the numerous systems and subsystems to which the control system must interface in order to carry out the responsibilities listed above.

3.5.7.1 Input/Output Controllers

EPICS-based input/output controllers (IOCs) provide the primary interface between the SPX subsystems and the APS control system. Considering the number of SPX subsystems, it is envisaged that four IOCs will be required: possibly two dedicated to the rf systems and the other two satisfying the needs of the remainder of the subsystems. It may be advantageous to have some IOCs embedded within the subsystem equipment, which is an increasing trend in the field of controls. If so, the number of IOCs may increase, but the cost of the embedded IOCs would be less and therefore would not significantly impact the cost estimate.

A list of all parameters to be monitored and controlled for each subsystem will be necessary in order to define the process variables for these parameters. The software tools and applications to provide proper control and monitoring of each subsystem will then use these process variables.

3.5.7.2 Real-Time Data Processing

Numerous high-speed control loops will be required for proper operation of the SPX with the APS storage ring. The control system must provide adequate computing and data-processing capacity

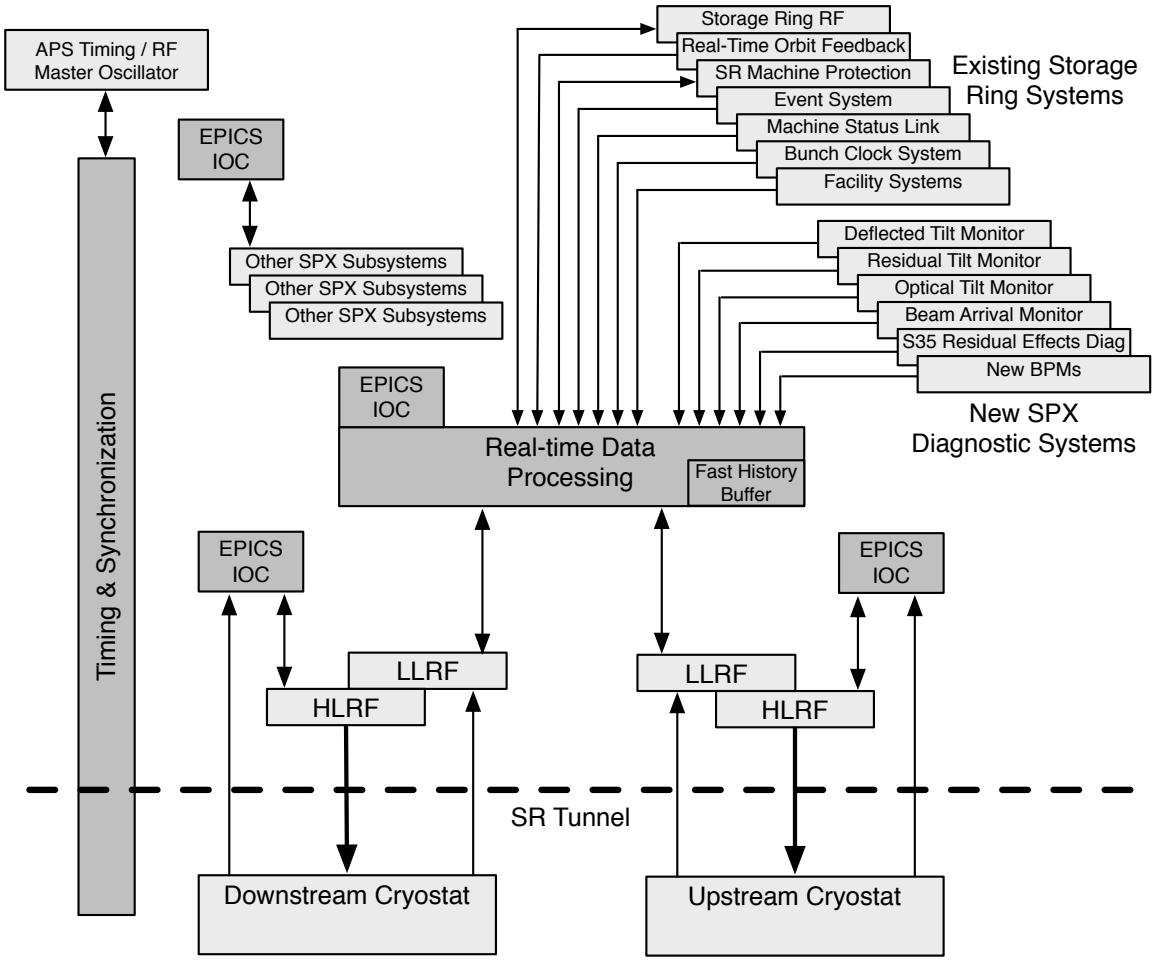

Figure 3.5-66. SPX controls and interfaces to other systems.

to perform these control functions at the necessary speed. Preliminary requirements are discussed in section 3.5.7.6, but significant details will not be known until the design phase of the project. As these control algorithms become better defined, the specifications for the hardware required to perform these algorithms will become increasingly clear. Conceptually, the real-time data processing platform will be highly modular so that several types of processing technologies (FPGAs, DSP CPUs, and fast general-purpose processors) can be accommodated, with the best technology being chosen at design time.

3.5.7.3 Timing and Synchronization

Scope: The timing and synchronization system will provide the information and phase references needed to drive the deflecting cavities and measure the effects on the electron beam within the SPX region and the residual effects outside the SPX region. In addition, phase references will be provided to the beamline lasers for synchronization to the x-ray beam pulses.

Key Specifications: The key specifications driving the timing and synchronization system design are listed in Table 3.5-13.

Table 3.5-13. Key SPX Timing and Synchronization Specifications.

Specification name	Phase error (rms) @ 2815 MHz	Picoseconds (rms)
Cavity Common Phase Variation	<4.0°	<4.0
Phase Error Between Cavities	<0.18°	<0.18

These specifications, in particular the cavity uncorrelated phase specification of 180 femtoseconds, are very demanding and require extraordinary measures to achieve. For example, 1 meter of cable with a temperature coefficient of 7 ppm and a velocity propagation of 67% of the speed of light will experience a 50-fs change in delay per °C change in temperature. Figure 3.5-67 shows the storage ring ambient temperature variation during the last run of 2010. As can been seen from the plot, the temperature can vary by as much as 2.8°C.

A working group for timing and synchronization was formed with representatives from low-level rf, diagnostics, beamline, and controls for SPX. The results of that working group are presented in Table 3.5-14, which lists the stability specifications and the reference for devices associated with the SPX system. Of the devices listed, the beamline lasers have the most demanding specification of 100-femtoseconds variation with respect to the upstream SPX deflecting cavity field zero crossing. This is driven by the requirement that the lasers be synchronized to 10% of the x-ray pulse width. Details are discussed below.

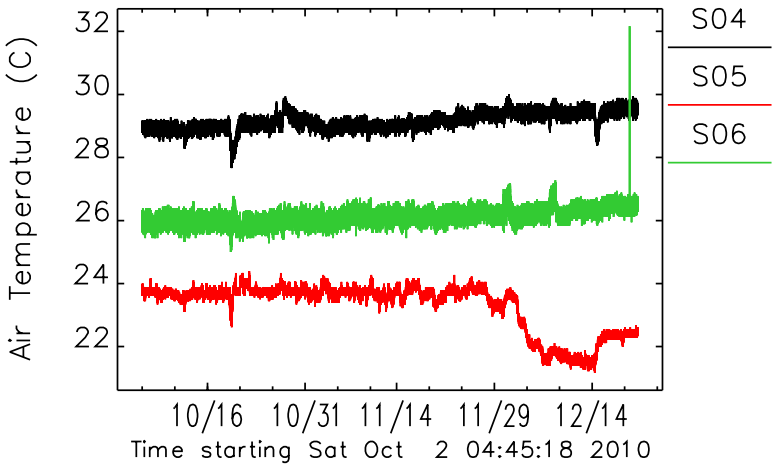

Figure 3.5-67. Example of APS storage ring ambient temperature variation for Sectors 4, 5, and 6.

Approach: Actively-stabilized fiber optic links will be used to distribute a 2815-MHz phase reference to each location. The active phase stabilization will correct for drifts due to environmental effects. John Byrd's group at LBNL has expended a great deal of effort over the years in developing a system capable of delivering a phase reference stable to the 10s of femtosecond level. We plan to

Table 3.5-14. Beamline and Diagnostics Timing/Synchronization Specifications

Specification name	Type	Frequency (MHz)	Reference to	Stability (rms) (>10 Hz)
Beam arrival time monitor[a]	Ref	2815	352 Mo	<1ps
Rf beam tilt monitor (residual)[b]	Ref	11260	352 Mo	<1ps
Rf beam tilt monitor (residual)	ADC clock	TBD	...	TBD
X-ray tilt monitor [c]	Ref	2815	2815 Ref	2ps
X-ray BAT [d]	Ref	2815	2815 Ref 2815 US cavity	250 fs
Laser(s)	Ref	Various	zero crossing + x-ray A.T.	<100 fs
Laser(s)	Rev Clk	272 kHz	...	...
S35	Ref	2815	352 Mo	<4.0 ps
BPMs	Rev Clk	272 KHz	...	...

[a] Short copper (>10 m)
[b] Short copper (<10 m)
[c] ID and BM relative measurement between array elements
[d] ID and BM (BAT monitor uses same sensor as tilt monitor)

Specification name	Interval	Phase Noise (>10Hz)	System Response Bandwidth	P0 (Rev Clock)
Beam arrival time monitor	7 days	TBD	3 kHz	Yes
Rf beam tilt monitor (residual)	7 days	TBD	3 kHz	Yes
Rf beam tilt monitor (residual)	TBD	TBD	TBD	...
X-ray tilt monitor	7 days	TBD	1Hz	...
X-ray BAT	7 days	TBD	1Hz	...
Laser(s)	7 days	TBD	1 Hz	Yes
Laser(s)	...	...	...	...
S35	7 days	TBD	0.1Hz	...
BPMs	...	...	...	Yes

collaborate with the LBNL group and adopt their technology for stable phase-reference distribution. The LBNL scheme precisely measures the optical phase delay through a fiber using a heterodyne interferometer [3.5-64]. The heterodyne process, in which the original optical frequency is mixed with an optical frequency offset by a 110-MHz radio frequency, results in changes in optical phase being translated into identical phase changes in the 110-MHz rf beat note. One degree of phase change in the 1530-nm optical domain, which corresponds to 21 attoseconds, translates to 1 degree of phase change in the rf domain, or 25 picoseconds. This results in approximately a 6 order of magnitude leverage over direct measurement in the rf domain. The phase changes in the 110 MHz beat note are measured and used to correct for changes in fiber-cable delay due to environmental effects such as temperature. Figure 3.5-68 shows a block diagram of the phase reference distribution system. The 2815 MHz reference and local oscillator reference will be generated from a 351.9 MHz reference at the SPX sector upstream sector. A 351.9 MHz reference will be transported from the master oscillator in A014 to the SPX sector via a phase stable coax cable. The fiber-transmitter cw laser output is modulated by the 2815 MHz from the master oscillator. The resulting amplitude-modulated optical signal is fanned out for distribution to the LLRF systems in Sectors 5 and 7, the beamline laser hutches, and sector 35 diagnostics. Each of the optical links is an independent heterodyne interferometer transporting the 2815-MHz reference as an amplitude modulation on the optical carrier. At each receiving end, the receiver measures changes in the optical phase and uses this measurement to correct the phase of the received 2815-MHz signal.

To achieve the high level of phase stabilization relative to the 351.9-MHz master oscillator, one of stabilized links will be used to transport the 2815-MHz signal back to the master oscillator. As shown in Figure 3.5-68, the 2815-MHz phase will be compared to the 351.9-MHz signal multiplied by eight. The resulting error signal will be used to drive a phase shifter in the 2815-MHz reference fed to SPX. This feedback will compensate for environmentally induced drifts in the copper cable transporting the 351.9-MHz reference to SPX.

Master Oscillator: A master oscillator will provide a phase-stable 351.9 MHz for APS operation and a reference for 2815 MHz generation for SPX operation. The 2815 MHz will be generated by multiplying the 351.9 MHz by a factor of eight. The phase noise and frequency stability for the master oscillator are to be determined.

Timing and Synchronization for LLRF and Diagnostics: As shown in Figure 3.5-68, LBNL-type phase-stabilized links will distribute a 2815-MHz reference to SPX LLRF and diagnostics. Each LLRF system will have a separate phase-reference receiver. In addition, separate phase-stable receivers will provide references to the upstream beam arrival time monitor (BAT), the x-ray tilt/BAT diagnostics, and the diagnostic beam line in Sector 35.

Slow drifts (<100 Hz) in cavity phase will be corrected by beam-based feedback from BPMs downstream of each cavity. This feedback will be supplied by a new higher performance real-time feedback system that is part of the APS Upgrade project (see section 3.3.6).

The BAT located upstream of the first SPX deflecting cavity will be based on an rf phase detector and will require an rf phase reference, local oscillator drive, and nanosecond ADC clock. These signals will be derived from the distributed 2815-MHz reference.

The rf residual tilt monitor requires a 352-MHz reference with a variation of less than 1 picosecond with respect to the master oscillator. The 2815-MHz phase reference will be delivered from the receiver to the rf residual tilt-monitor electronics via a phase-stabilized coax cable. This reference will be used to generate the 352-MHz reference.

As shown in Figure 3.5-68, a separate phase-stabilized link and receiver will be used to deliver a 2815-MHz reference to the x-ray beam arrival time monitor/tilt monitor. A separate link is required to achieve a required reference stability of < 250 femtoseconds.

The BPM processors are anticipated to be commercial units. These units will require the storage ring revolution clock and 2-Hz injection trigger. These signals are already available at these locations but need to be distributed to the BPM processors

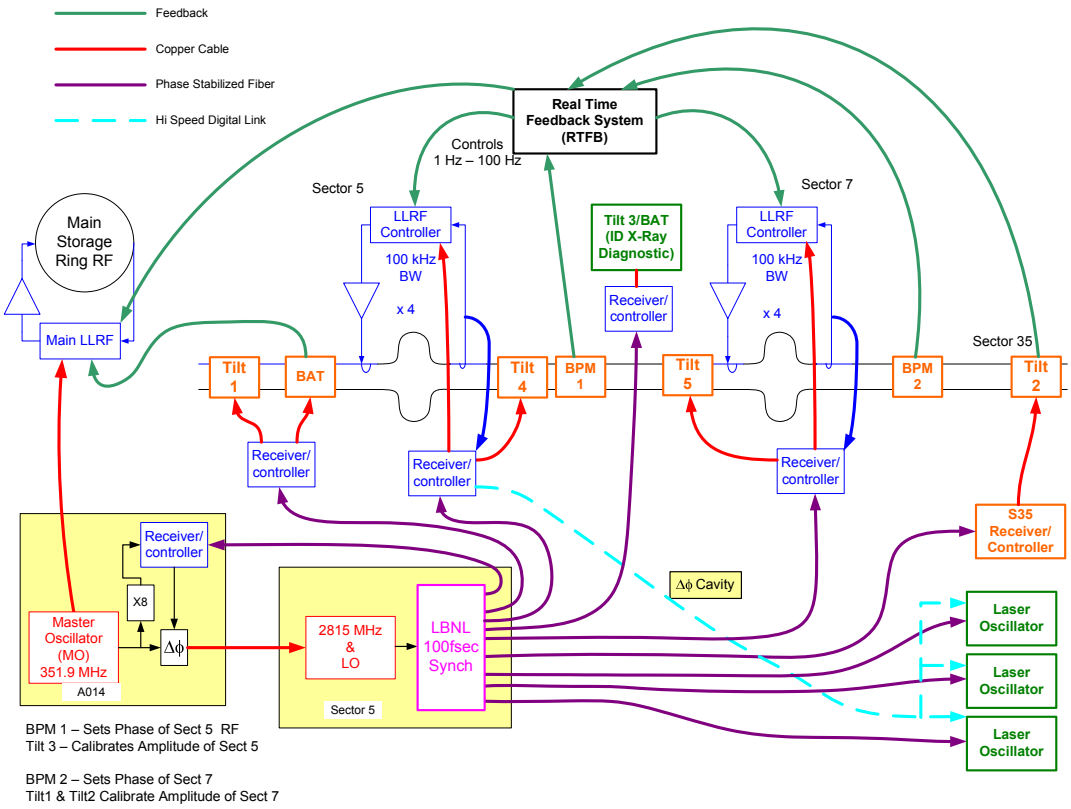

Figure 3.5-68. SPX phase reference distribution.

Timing and Synchronization for S35: Sector 35 requires a phase-stable reference for measurement of residual effects on the beam from the deflecting process in the SPX zone. A 2815-MHz phase-stable reference will be delivered to S35 via a separate phase-stabilized link. Required phase references will be derived from the 2815-MHz reference. A method for making synchronized measurements is a requirement. This will be accomplished by modulating the SPX cavity phase and/or amplitude with a

low-level, low-frequency tone ($\sim$ 200 Hz). The modulation frequency is distributed to S35 and used to synchronously detect the modulation on the electron beam using a lock-in technique. This requires that the modulation frequency be generated and made available both at SPX and S35. Multiple tones may be used to measure multiple residual effects simultaneously. This lock-in technique offers a greatly enhanced measurement signal-to-noise ratio.

Timing and Synchronization for SPX BeamLine: As shown in Figure 3.5-68, each laser hutch will receive a phase-corrected 2815-MHz reference. The required laser reference frequency will be derived from the 2815-MHz reference. Normally the phase reference is used as an input to the laser lock box to lock the laser to the x-ray beam pulses. However, due to the demanding synchronization tolerances required, the lock box may not be adequate. If R&D measurements confirm that the lock box will not be adequate, the optical cavity phase will have to be controlled directly using a picomotor and piezodrive to achieve the required level of synchronization. In addition, a phase-correction signal derived from the measured upstream deflecting cavity phase may be required to be transported digitally from the measured S6 cavity phase to each laser hutch to correct laser synchronization for cavity phase changes. This link will use standard telecom high-speed serial optical technology.

3.5.7.4 Interfaces to SPX Subsystems

Each SPX subsystem must be interfaced to an IOC for supervisory control and monitoring of the technical equipment. Although the exact details of these interfaces will not be know until the design phase, an exhaustive list of the subsystems is provided below to ensure that all requirements are identified.

- Cryogenics
- Cavity/cryomodule instrumentation
- Cavity tuners
- LLRF
- Rf measurements
- Klystron and HVPS systems
- Waveguide instrumentation (pressure, cooling, etc.)
- SPX intersubsystem machine protection interlocks
- SPX facilities (DI water, barometric pressure, etc.)
- SPX timing

3.5.7.5 Interfaces to Other APS Systems

The following list identifies the APS systems that may need to be interfaced to the SPX to provide real-time storage ring information for proper operation:

- SR master oscillator (covered in timing)
- Storage ring rf
- Real-time orbit feedback system (or local beam position monitors)
- SR machine protection system
- Event system
- Machine status link
- Bunch clock system
- Facility systems
- Deflected tilt monitor
- Residual tilt monitor
- Optical tilt monitor
- Beam arrival monitor
- S35 residual effect diagnostics
- BPMs close to cryostats
- Relevant signals from experimental hutch (e.g., I_0 monitor from Sector 7)

3.5.7.6 Control System Software

The control system software responsible for coordinating all of the subsystems listed above is not trivial. There are numerous control loops required to ensure stable operation of the SPX deflecting cavities with respect to the stored beam. This section provides a framework for discussing these requirements while recognizing that detailed algorithms will be a major effort during the design phase of the SPX. Figure 3.5-69 partitions the functions of the control system into hierarchical layers to depict information flow and the relative time criticality of each function. High-level tools are primarily implemented on the main control room (MCR) workstations and are not significantly time critical. Real-time controls will be implemented in the IOC or on special-purpose hardware (FPGAs, DSPs, or multicore processors) and will have definitive real-time constraints.

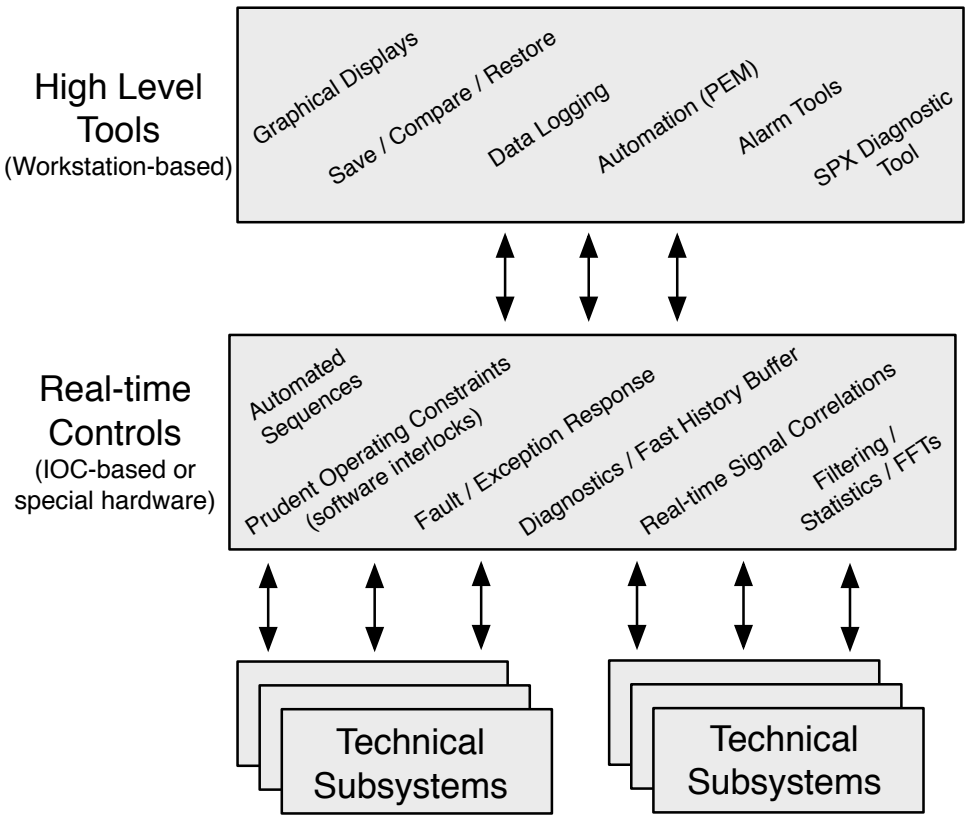

Figure 3.5-69. Hierarchical control functions.

High-Level Tools: These tools are primarily implemented on MCR workstations. Many of the current tools used in the MCR will be sufficient for routine operation of the SPX. Some effort is required for proper configuration of these tools, including the generation of operator displays and alarm/data logging configurations. Tools likely to be used include MEDM (for graphical displays), Save/Restore, Data Loggers, Alarm Tools, and PEM (for Automation). It is likely that a special-purpose or higher-level diagnostic tool will be required to properly convey the operation of the SPX. Possible features of this tool include 10-Hz update of critical waveforms and statistics, replay of recent data capture in slow motion to observe abnormal behaviors, and integrated graphics of beam diagnostics with rf plots and timing measurements.

Real-Time Control & Diagnostics: Numerous algorithms must be performed in a real-time environment to ensure tight control over the operation of the SPX. The list below is an attempt to identify these control algorithms at this early stage, but significant definition must wait until the design phase of the project:

- Deflection control (ensure proper deflection is realized and then properly removed)
- Exception response and automated sequences (e.g., start-up or fault recovery)

- Prudent operating constraints (software interlocks)
- Statistics and preprocessing of data (e.g., mean, standard deviation, minimum, maximum, FFT) for display and acquisition by the APS data loggers for long-term storage and analysis
- Real-time correlation of relevant signals (implies signals to be correlated are acquired by the same system)
- Retain 1 hour of fast monitored data (and some tool to play it back)
- Fault monitor:
  - Define tolerances around critical signals and raise alert when signal exceeds limits (real-time)
  - Capture recent history of vital parameters when an out-of-range tolerance event occurs (including machine synchronous time stamp)

3.5.7.7 R&D Plan

Controls: There are several areas that will require further R&D to ensure the SPX requirements for controls can be met. These tasks are outlined below:

- Provide controls support for the LLRF and timing R&D tasks

  Several of the LLRF and timing R&D efforts will require support from controls staff.

- Evaluate platform options for the real-time processing requirements

  Figure 3.5-66 illustrates the requirement for a high-speed real-time processing subsystem. As the requirements become better understood, several options for this subsystem will be evaluated.

- Demonstrate intersystem communication

  Figure 3.5-66 illustrates the numerous systems that must be interfaced to the SPX control system. R&D effort will be required to evaluate the complexity of these interfaces prior to the design phase.

- Identify additional tools/software required to meet requirements

  An investigation will be made to identify any new software tools or applications that will be required to meet the SPX performance objectives.

Timing & Synchronization: Collaboration will be initiated with LBNL with the goal of evaluating the level of timing reference stability required to achieve the physics specifications. It is planned that at least a two-channel phase stabilization system will be tested at the APS with the goal of supporting the in-ring cavity tests. A major goal is the transfer of this technology to the APS to the extent of enabling receiver production by APS personnel.

Objectives of the R&D plan include:

- Study and report SPX phase-reference stabilization requirements

  Evaluate LBNL's phase-reference-system phase noise relative to requirements

  Investigate methods to reduce phase noise if required

  Investigate beam-based feedback on position data to correct long term drifts

- Perform preliminary testing of the LBNL 2-channel phase-stabilization system at APS
- Transfer LBNL's technology to APS in sufficient detail to reproduce their receiver/synch head
- Procure/develop 2-channel phase-stabilization system to support in-ring cavity testing

  May require loan of LBNL's transmitter

- Evaluate stability of beamline laser lock box

  Investigate methods to improve stability if required including control of laser oscillator phase by phase-stabilization system.

3.5.8 SPX Machine Protection

Operation of the SPX deflecting cavities introduces a number of unique machine protection challenges. We have already discussed on page 3 — 183 the interface between the SPX equipment protection interlocks and the storage ring machine protection system. Here, we discuss requirements for protection of other systems against beam size and centroid-related effects.

3.5.8.1 Vertical Beam Size

Unacceptable amounts of bending magnet (BM) and insertion device (ID) synchrotron radiation heating of vacuum components may result from the large vertical beam size within the SPX zone. Outside the zone, incorrect phasing of the SPX cavities can result in a large vertical beam size for the entire ring; this raises similar concerns, especially for long, high-field ID sources. It is well known that vacuum chambers at ESRF were damaged in the commissioning phase as a result of a vertical beam size blow up caused by a coupled-bunch instability [3.5-65]. Since that time interlocks have been put in place to protect against this eventuality.

Two areas of concern need to be carefully considered in the design of new machine-protection system components associated with increased vertical beam size. First, a large increase in vertical beam size could cause portions of the high-power ID x-ray beam to strike portions of the vacuum chamber that were not designed to accept ID radiation. Presently the beam-position limits detector (BPLD) interlock system is designed to prevent ID beams from striking any vacuum chamber component upstream of the beamline front end. This system assumes a very small beam size (see related discussion in section 3.4.7.2). In addition, BM radiation could strike the vacuum chamber very close to the source since the aluminum extrusion exit slot is only 1 cm high for most of the large-aperture chambers. Generally speaking, heating from ID sources occurs on millisecond time scales, while that from BM radiation requires seconds to heat the chambers to unacceptable temperatures.

Careful ray tracing and thermal analyses along the lines of what was done during the APS design phase [3.5-66] but using modern tools will have to be performed to determine the limits that must be placed on beam size and to help design a beam-size-limiting machine protection interlock, should one be deemed necessary. Inside the SPX zone, the beam size will always be large, so thermal management will need careful study.

The SPX deflecting cavities are sensitive to both beam position and beam tilt, in that offset or tilted beams will deposit potentially large amounts of power into the cavity electromagnetic fields. It is likely that these fields can be easily detected with field probes monitoring reverse power on the input cavity waveguides. This being the case, it may be easiest to use an interlock local to the deflecting cavities to prevent large beam size outside the SPX zone.

3.5.8.2 Beam Centroid Missteering

If the rf system loses control of the cavities (i.e., the loss of a klystron while a cavity is on resonance), and the particle beam is vertically misaligned as it passes through a cavity, the beam generated voltage could result in large field levels inside the cavity and rf power being sent out along the cavity's input waveguides [3.5-60]. The beam offset at which the beam generated voltage equals the expected single SPX cavity operating voltage of 0.5 MV is inversely proportional to the external Q. For example, at a Q_{ext} of 2×10^6, a misalignment up to 1 mm at 150 mA could be tolerated, whereas at a Q_{ext} of 1×10^6 a misalignment could be allowed up to 2 mm. The misalignment tolerance will need to be budgeted with anticipated cavity alignment errors and is among the tradeoffs associated with ultimate choice of Q_{ext} (section 3.5.6.5). A fast interlock, either a BPLD or an rf power detector on the cavity input waveguides, will be required to protect against this eventuality. (See page 3 — 183 for related discussion.)

The short-pulse beamline at 7-ID will always have very large vertical angular divergence during normal SPX operation. Thermal analysis and perhaps a new BPLD interlock system will need to be implemented to assure the safety of downstream vacuum-chamber components. The impact of a tilted beam on the beam position monitors used to detect missteering will need to be assessed.

3.5.8.3 Work Remaining

- Complete thermal analysis of new and existing vacuum-chamber components located inside the SPX zone for normal SPX operation.
- Complete thermal analysis of existing vacuum chamber components located outside the SPX zone for anomalous SPX operation, considering both ID and BM sources.
- Determine the necessity for and specifications of a global vertical-beam-size interlock. Design the interlock if needed.

3.5.9 SPX Beam Diagnostics [U1.03.03.08]

3.5.9.1 Requirements

The short-pulse x-ray source (SPX) presents a new set of beam-diagnostic challenges. Two ensembles of diagnostics are needed, one set inside the SPX zone between the superconducting deflecting cavities, and the other set outside of it to assure that SPX operation does not negatively impact other APS user experiments. As presently envisioned, deflecting cavities will be located within the insertion device straight sections in Sectors 5 and 7, and beamlines 6-ID and 7-ID will be upgraded to take advantage of the short x-ray pulses generated.

The goals of the diagnostics within the SPX zone (Sectors 6 and 7) are to:

- Provide transverse and longitudinal beam-centroid coordinates so the electron bunch can be put through the cryomodules at the right time and at the right place. The rf beam position monitors are to be used for this task.
- Provide beam-position readbacks at both ends of the 6-ID chamber so that the electron beam trajectory through the 6-ID straight section can be stabilized, minimizing timing jitter that orbit changes may cause. Both rf beam position monitors and x-ray beam position monitors (XBPMs) are to be used.
- Quantify the effect of the deflecting cavities by measuring the beam tilt angle at a location downstream of the first cryomodule by odd multiples of $\pi/2$ in vertical betatron phase. Rf tilt monitors and x-ray optical tilt monitors will be used.
- Monitor beam loss patterns associated with SPX operation by expanding our existing beam loss monitor (BLM) system.

The goals of the diagnostics external to the SPX zone are to:

- Measure the beam arrival time with respect to a phase reference and provide this information to a real-time data network for use in the low-level rf controls associated with the deflecting cavities and main rf systems.
- Measure the residual tilt of the electron bunch due to the deflecting cavities. This will require up to two sensitive tilt monitors at two locations outside the SPX, separated by 90 degrees in vertical betatron phase.
- Measure the residual emittance increase, mostly in the vertical plane. This will require several vertical-beam-size monitors around the ring.
- Measure all small residual effects of deflecting cavity operation. This will be accomplished with narrow-band precision measurements in sector 35, where the measurement will be synchronized with the modulations of SPX operation parameters, such as rf deflection cavity voltage and phase. By filtering the measured data in a narrow bandpass filter centered around the modulation frequency, this experimental method is expected to enhance the signal-to-noise ratio of measurements.

Table 3.5-15 lists the beam-diagnostic devices needed to support SPX commissioning and operation.

Table 3.5-15. Diagnostics Supporting the Short-Pulse X-ray Effort.

Location	Parameter	Diagnostic	No. of Units
Diagnostics within the SPX zone	Beam position	Rf BPM	6
	Longitudinal beam tilt	Optical tilt monitor	2 (ID+BM)
	Longitudinal beam tilt	Rf cavity tilt monitor	2
	Particle loss	Cerenkov detectors	TBD
Diagnostics external to the SPX zone	Beam arrival time	Rf BAT monitor	1
	Longitudinal beam tilt	High-res. rf cavity tilt monitor	2
	Particle loss	Cerenkov detectors	TBD
	Vertical emittance	Beam size monitors	3+
	Residual effects	Sector 35 diagnostic beamlines	2 (ID+BM)

3.5.9.2 Beam Position Monitors within the SPX Zone [U1.03.03.08.01]

Three pairs of low-drift rf BPMs are needed within the SPX zone: upstream and downstream of the first cryomodule, upstream and downstream of the 6-ID chamber, and upstream and downstream of the second cryomodule.

Alignment of the particle beam vertically as it passes through the superconducting deflecting cavities must be done with a high degree of absolute accuracy, less than 100 μm peak-to-peak with respect to the electrical center of the cavities. Vertical offsets drive the cavity deflecting modes, potentially resulting in large amounts of beam-driven rf power being coupled back out to the rf generators.

It is expected that space in the straight sections where the cryomodules are located will be at a premium, so it is planned to use standard pickup electrodes that are normally used for APS operation, but with improved electronics. In both Sectors 5 and 7, the cryomodules will be bracketed by an insertion device on one side and a large-aperture standard APS storage ring vacuum chamber on the other. The 4-mm-diameter capacitive button pickup electrodes mounted on the small-aperture insertion device vacuum chambers will provide more than adequate long-term stability to meet the specification, even using existing electronics. For the large-aperture chambers, the geometric position sensitivity is smaller by up to a factor of 7 in comparison to the insertion device chambers. For this reason, improved electronics such as the Libera Brilliance / Brilliance+ boxes from Instrumentation Technologies appear to be a good candidate.

In the 6-ID and 7-ID straight sections, angular jitter in the centroid trajectory through the straight sections will translate directly into timing jitter for the short-pulse experiments being conducted on the beamline. While the beam tilt in the center of this straight section should be zero, there will be detectable tilt at the ends of the straight section where the position monitors likely will be located. Similarly, near the cryomodules the beam tilt should be relatively small; however, the impact of tilt on

beam position monitor performance needs to be carefully evaluated, especially for the small-aperture pickup electrode assemblies.

An objective for the R&D phase is to evaluate the performance of proposed BPM electronics in the presence of beam tilt for different pickup electrode geometries to be used.

3.5.9.3 Beam Arrival Time Monitor [U1.03.03.08.05]

The arrival time of the particle beam with respect to the deflecting cavity fields is an important parameter that must be carefully controlled. For this purpose a phase detector that measures the phase of the particle beam relative to a stable phase reference will be developed. This detector will be located near the upstream cryomodule in sector 5. To prevent beam tilt from impacting the measurement using the technique described here, the detector will have to be located just outside of the SPX zone. It will require access inside the accelerator enclosure to a stable phase reference signal. This beam arrival time (BAT) detector will ultimately be integrated into the SPX low-level rf control system. While the differential phase specification between the cryomodules in Sectors 5 and 7 is extremely tight, on the order of 100s of fs, the BAT detector need only be sensitive to changes in arrival time down to a fraction of the 30-ps bunch length. For this reason, the phase reference stability should be at the level of 1 ps or below.

The BAT monitor development will leverage off of the present APS linac phase detection and stabilization system. The APS linac phase-stabilization system uses phase detectors to measure the S-band accelerating-structure drive phase relative to the beam arrival phase [3.5-67]. The drive phase is measured at a high-power directional coupler located at the furthest upstream accelerating structure and is compared to beam signals from a stripline BPM. Their difference is used in a low-bandwidth feedback loop implemented with EPICS to control input klystron drive phase [3.5-68]. The phase detection system operates at 2856 MHz and has a resolution of 0.1 degree (approx. 100 fs). This diagnostic is used routinely for maintaining optimal performance since it was commissioned in 2005, significantly enhancing system stability and reliability.

The BAT monitor will be arranged in a fashion similar to that shown in Figure 3.5-70, taken from the present linac phase-stabilization system. The phase-detector system will compare the phase of a BPM sum signal to a reference phase signal derived from the deflecting cavity low-level rf control and timing system. The phase detector receiver is composed of a summing network, phase detector, and control and regulation boards. External to the receiver are power supply, data acquisition, digital I/O boards, and input filtering components.

The input signals are first fed into matching networks and then into a summing network front-end board that combines four signals from the BPM button pickup electrodes, summed to minimize position dependence. The sum together with a reference rf phase signal are then sent to an Analog Devices AD8302 RF/IF gain and phase detector chip. The AD8302 integrates two closely matched wideband logarithmic amplifiers, a wideband linear multiplier/phase detector, precision 1.8-V reference, and analog output scaling circuits. The gain and phase video output signals are then filtered and scaled to $\pm$ 1.0 volts. The AC-coupled input signals can range from -60 dBm to 0 dBm in a 50-ohm system, and from low frequencies up to 2.7 GHz. The system is capable of bandwidths up to 30 MHz, which can easily meet our requirements of 1-kHz video output bandwidth.

Data acquisition will be performed with an eye toward integration into a phase-control feedback system. An attractive option is to integrate data from sensors of this type into the fast data-distribution network being developed as part of the real-time closed-orbit feedback system upgrade.

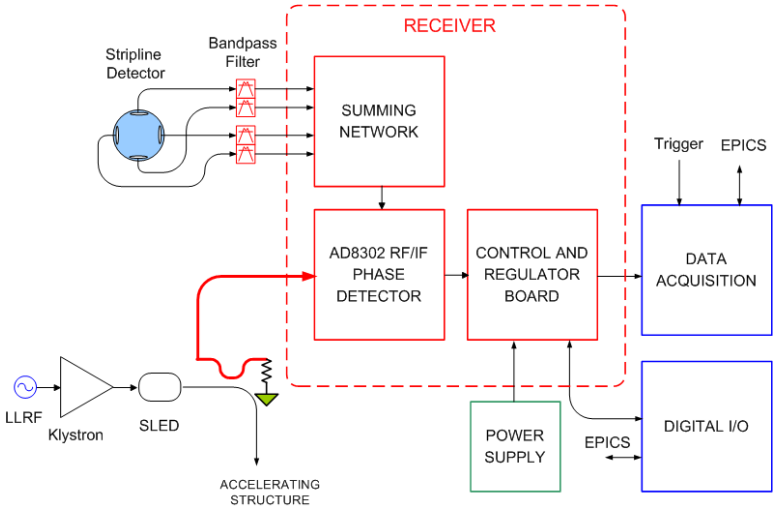

Figure 3.5-70. APS linac beam phase detector block diagram.

3.5.9.4 Rf Beam Tilt Monitor [U1.03.03.08.03]

The rf tilt monitor has several distinct advantages: (1) It has very high sensitivity to both transverse beam position and longitudinal tilt. (2) It requires only a small section of space on the storage ring, which can be fitted as a spool piece between ring vacuum chambers. (3) It can have sufficient bandwidth to resolve individual bunches in 24-bunch fill mode.

A resonant cavity BPM inherently has the capability of detecting both beam position and tilt information with very high sensitivity. The tilt signal component is generated in quadrature with the beam position signal. This signal gives information on the xz or yz correlation within the beam [3.5-69–3.5-71] and is a result of the finite phase extension of the bunch.

For a bunch that is very short compared to the wavelength of the TM_{110} dipole mode, a bunch tilt will not excite the mode when the center of charge passes through the center of the cavity: the effects of the head and tail will exactly cancel. If instead the bunch has a relatively large phase extension, there is no longer cancellation since the fields excited by the head will have evolved before the arrival of the tail.

When used as a BPM, cavity-based monitors of this type have extremely high sensitivity coupled with absolute accuracy at the level of microns. This level of absolute accuracy is due to the ability to very accurately machine surfaces with cylindrical symmetry. Recent experience constructing BPMs of this type for the Stanford Linac Coherent Light Source (LCLS) project have validated this approach.

The detection electronics will be quite similar to what one would use for a cavity BPM, with the addition of in-phase/quadrature (I/Q) detection. Figure 3.5-71 shows the proposed cavities

along with detection electronics presently used for the LCLS cavity BPM system. The first upstream reference cavity, TM_{010} monopole mode cavity delivers a signal proportional to the bunch charge. The second cavity, is the TM_{110} dipole cavity, which produces a signal V_y that is dependent on the beam displacement in addition to beam tilt. After appropriate initial phasing, the dipole cavity's in-phase (I) voltage is proportional to the bunch charge and position offset from the geometric center of the cavity. The quadrature (Q) signal is proportional to bunch charge, tilt angle, and the ratio of bunch length to cavity period. Using rf in-phase/quadrature-phase (I/Q) demodulation of the cavity BPM signal, it is possible to separate position and angle/tilt.

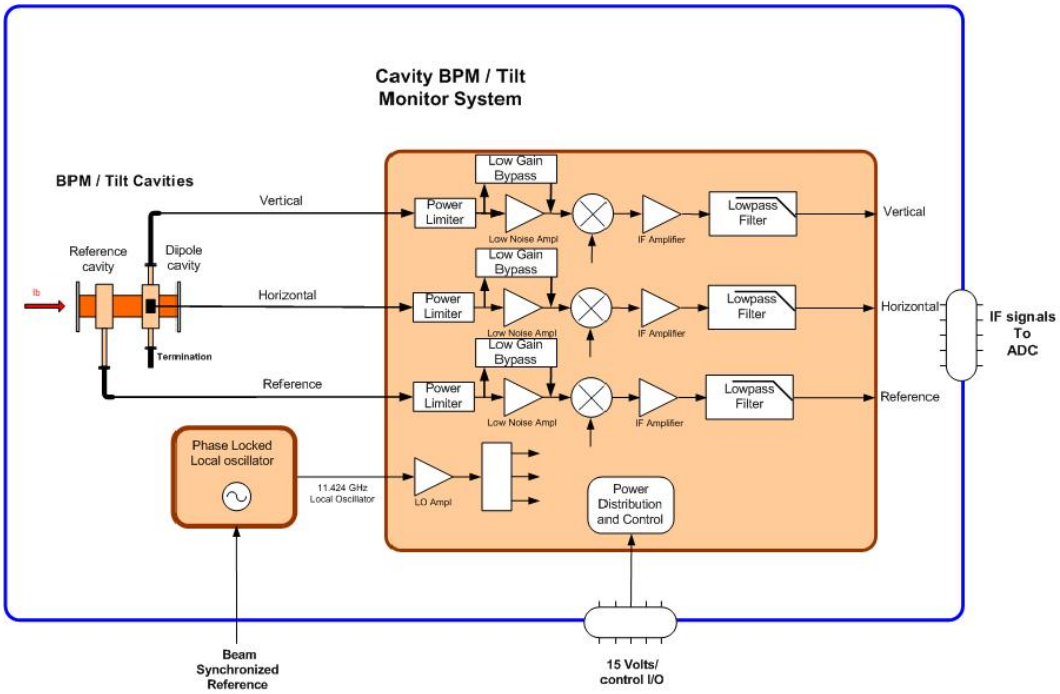

Figure 3.5-71. LCLS rf cavity BPM system diagram.

The receiver topology for the LCLS cavity BPM is a single-stage three-channel heterodyne receiver shown in Figure 3.5-71. The resolution is limited by receiver and data-acquisition electronic noise. The cavity signals are mixed down to an intermediate frequency (IF) in the accelerator tunnel. Cavity signals are first amplified in a low-noise amplification stage and then mixed down to a IF: $f_{\mathrm{IF}} = f_{\mathrm{LO}} - f_{\mathrm{RF}}$. The local oscillator housed in the receiver chassis is phase-locked to the APS timing system and drives all three channels. After the signals are down-converted, they are filtered, amplified, and sent out of the accelerator on shielded coaxial cables.

Altogether two tilt monitors are proposed to be included inside the SPX zone, with two additional monitors outside, located 90 degrees apart in vertical betatron phase. The requirements inside vs. outside are significantly different, since the tilt is very large inside but, by design, needs to be as small as possible outside the zone. Outside the SPX zone, a 40-ps rms bunch (24-bunch mode) with a tilt of 1 mrad (0.3% leakage) has a projected vertical size increase of 12 μm rms, a perceptible beam size change for non-SPX users. Two sensitive tilt monitors with < 1 mrad resolution will be needed to monitor the residual tilt outside of the SPX zone. Readbacks from these detectors will be used to

correctly set the relative phase and amplitude of the deflecting cavities.

It is possible that capacitive button pickup electrodes will have adequate sensitivity to resolve the relatively large beam tilt inside the SPX zone. This is an option to consider to save space, which will be in short supply. The tilt monitor concept using buttons can be investigated using the present machine coupled with a method to excite a beam-tilt transient [3.5-72]. The electronics design will be quite similar to what would be needed for a cavity-based tilt monitor. In any case, cavity-based tilt monitors will be required outside of the SPX zone to achieve the high sensitivity required there.

R&D topics are to develop a computer model of the proposed cavity geometry for sensitivity and wakefield assessments. This will be followed by the design and fabrication of a cold-test cavity for evaluation in the lab and comparison with computer simulations. In parallel, machine studies to use the present APS ring to study tilted beams will be pursued, using existing diagnostics.

3.5.9.5 Optical Beam Tilt Monitor [U1.03.03.08.02]

Figure 3.5-72 shows the proposed electron bunch tilt monitor based on x-ray imaging. It is based on imaging the electron beam at the bend magnet source 7-BM through a vertical slit at the 7-BM source point, about $3\pi/2$ in vertical betatron phase from the first cryomodule [3.5-73].

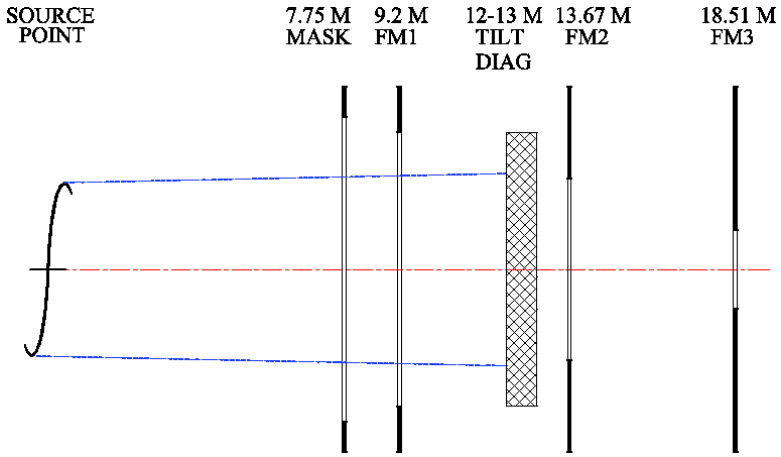

Figure 3.5-72. An x-ray tilt monitor based on measurements of beam height at 7-BM.

This optical tilt monitor has three distinct advantages:

(1) Since no optical components are used to deflect the x-ray beams, a well-calibrated imaging system can be used to measure the absolute tilt angle of the e-bunch from the profile size, and an rf phase shift can be inferred from the asymmetry of the vertical profile. (2) Using time-correlated single-photon counting (TCSPC) techniques, the average phase and tilt can be resolved bunch by bunch. (3) Since the camera acquires the two-dimensional image of the entire bunch, detailed information can be inferred from the acquired image. For example, a strong transverse HOM with horizontal/vertical fields will create modulations on the projected image in the horizontal/vertical direction.

This tilt monitor also has several disadvantages: (1) It takes much more space in the tunnel than the rf tilt monitor. (2) It is more complex to operate and is more costly to build. (3) Unless equipped

with fast cameras, it will be bandwidth-limited by the camera, usually from 10 Hz to 1 kHz.

To improve the detector bandwidth, we will consider other types of optical tilt monitors. Figure 3.5-73 shows one based on an x-ray beam arrival monitor array installed in the 7-ID beamline front end. Fast x-ray detectors are placed above and below the user beam aperture in the upstream undulator front end. Each detector is connected with a beam arrival monitor discussed in a previous section. Analyzing the arrival time as a function of vertical position of the detectors, we may obtain two pieces of information about the x-ray pulse: (1) the on-axis slope of the x-ray pulse is the direct measure of its tilt angle, and (2) the intercept time is the arrival time of the x-ray pulse for on-axis user experiment. While the first part is useful for tuning the deflecting cavity rf voltage to match the user optics, the second could be useful in synchronizing user instruments such as a pump laser or a streak camera.

A crucial part of the R&D program for this tilt monitor design would be finding an appropriate detector or detection scheme: (1) The detector should be able to withstand the intense radiation when the undulator operates at small gaps, although filters may be used to attenuate the beam. (2) The detectors should be fast enough to generate a signal extending to 352 - 2815 MHz. (3) the detectors should be large enough to generate sufficient signal when the undulator operates at a large gap. (4) The detectors should satisfy other engineering requirements, such as vacuum compatibility, thermal stability, etc. (5) The detectors should have a long lifetime to minimize in-tunnel servicing.

Compared to the undulator source, a bend magnet source has more stable intensity and its availability is not affected by undulator gap settings controlled by users. Hence the BM source is better suited for use in machine studies and possibly in SPX cavity feedback controls. For these reasons, we will install x-ray beam arrival time monitor arrays in both the 7-ID and 7-BM front ends, as space allows.

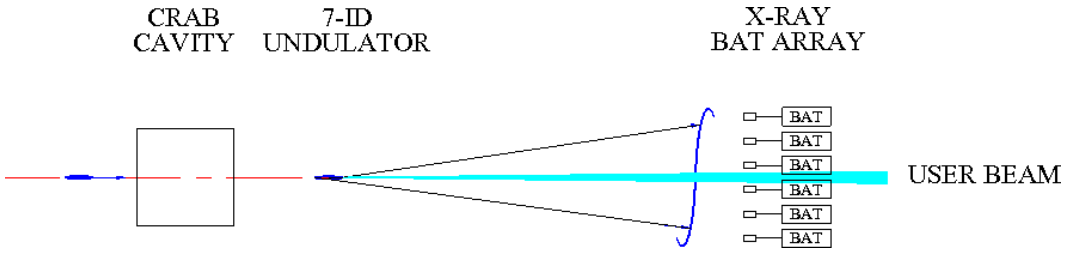

Figure 3.5-73. An x-ray tilt monitor based on beam arrival time monitor array.

3.5.9.6 High-Energy X-ray Vertical Emittance Monitor and Fast X-Ray BPM [U1.03.03.08.06]

During SPX operation, the x-ray pulse length is directly correlated with the vertical emittance of the electron beam. Furthermore, one of the side effects of the SPX deflecting cavity operation is to increase the effective vertical electron beam size outside of the SPX zone. We will implement several vertical beam-emittance measurement stations around ring to improve the efficiency of the minimization of the vertical coupling and to improve the reliability of observing the average residual effect.

These vertical emittance monitors will be located in unused bend magnet front ends, making use of the high-energy radiation penetrating through the water-cooled copper absorbers, which are

approximately 10 mm thick. The photons have a broad energy spectrum with a peak near 100 keV. At this energy, the rms vertical opening angle of the bend magnet radiation is approximately 25 μrad rms, resulting in an x-ray beam size near 100 μm at the end of the bend magnet chamber and 200 μm at the end absorber approximately 8 meters from the source point. Since these x-ray beam sizes are larger than the electron beam size at the source point ($\sim$ 15 μm), and their divergence is higher than that of the electron beam (1.2 μrad rms), a pinhole-camera-like arrangement will be needed to measure the beam size at the source. The imaging slits in this case will be wide open horizontally to increase the usable photon flux. The scintillator and the camera will be at the end of the uninstrumented front-end area, making the optical magnification approximately 1:1. The spatial resolution of the imaging system is expected to be comparable to or slightly less than the vertical beam size at 1% coupling, making the image height a sensitive diagnostic of the vertical beam emittance.

We will also consider instrumenting several fast x-ray beam position monitors with single-bunch single-pass capabilities at 24-bunch fill (6.5 MHz). Two simple approaches can be used: (1) In the ID front end, we can use diamond detectors in the grazing incidence x-ray beam position monitor and instrument them with fast readout electronics. Large-area diamond detectors can take high photon flux and provide sufficient signal for single-bunch single-pass position detection. However, the signal intensity of the XBPM will change by orders of magnitude when beamline users change their undulator gap. (2) An alternative is to make a narrow slits window in the beam stop that blanks off the uninstrumented bend magnet front ends. A thick window using beryllium or diamond would allow substantial x-ray photons below the critical energy to pass while maintaining the vacuum integrity of the ring. A diamond quadrant detector would measure the changes in the horizontal beam position and vertical beam angle in a single-bunch single-pass mode.

These fast XBPMs, while not very linear, would be very sensitive to beam-centroid changes and provide fast signals aiding the tuning up of SPX operations.

3.5.9.7 Beam Loss Monitor Inside and Outside of the SPX Zone [CAS]

The current APS beam loss monitor (BLM) system consists of 36 sets of Cerenkov detectors and VME signal processor boards built in house [3.5-74]. Both the detectors and signal processor boards are based on the PEP-II B-Factory design by A. Fischer [3.5-75]. In 2008, we started a calibration program for the system: All boards were modified and calibrated to improve pulse processing, and all photomultiplier tubes were measured and set individually to maintain identical gains from sector to sector [3.5-76]. Since the detectors are installed in identical geometries in all sectors, the absolute loss rate at each ID chamber can be derived by normalizing the count rate with the total charge loss rate deduced from the storage ring current monitor readout [3.5-77].

During steady-state operation, the injected beams and the Touschek scattered halos have large transverse offsets from the normal orbit. Different beam loss patterns will result when the SPX is turned on. Additional BLMs inside and downstream of the SPX will help characterize the beam loss patterns induced by SPX operation, thus aiding the optimization of the injection process. We plan to add more Cerenkov-detector-based BLMs. Since the existing VME boards for the signal processing need substantial improvement [3.5-78], new electronics will be developed to monitor the beam losses on the cryomodule and nearby downstream insertion devices.

In collaboration with SLAC, we have developed a beam loss monitor system for the LCLS

undulator hall [3.5-79, 3.5-80]. The BLM uses a large Cerenkov detector to cover the entire cross section of the undulator magnet. As part of the LCLS Machine Protection System (MPS), the BLM measures beam losses from each linac beam pulse; the signal is transported to a remotely located MPS link node chassis that performs digital conversion, monitoring, and archiving. A heartbeat light pulse is used to validate the BLM prior to the arrival of each electron bunch up to 120 Hz. During operations, the BLM signal is compared with predetermined MPS thresholds, and the beam delivery is disabled when the setpoint values are exceeded. The loss monitor system was commissioned in the spring of 2009 and to date we continue our collaborative work with SLAC, focusing on data analysis, tracking simulation, and further understanding of system performance [3.5-81–3.5-83]. Experience gained in these collaborations will be highly beneficial when the SPX-BLM is used to protect deflecting cavities or undulators from damage by stored beam losses.

The beam loss monitors in the SPX will use the same electronic controls and detectors to be developed for monitoring APS undulators, described in section 3.4. Due to the complex geometry of the cryogenically cooled deflecting cavities, special beam-loss detectors will need to be developed. Computer simulations of SPX-specific beam-loss scenarios will be used to guide the placement of these detectors inside and downstream of the SPX area. For an overall plan for beam-loss monitors in the storage ring tunnel, see Table 3.4-16.

3.5.9.8 Sector 35 Diagnostics [CAS]

The APS diagnostics beamlines in Sector 35 (S35) consist of one bend magnet beamline and one undulator beamline. They have the following tasks during the SPX development:

- During the R&D phase of the project, S35 will be used to test x-ray-based diagnostics, such as the vertical emittance monitor and the x-ray beam arrival time monitor.
- During the initial commissioning of the deflecting cavities, only one group of deflecting cavities will be installed. Sector 35 will be used to measure the effect of the deflecting cavity on the stored beam.
- During user operations of the SPX, S35 will be used to measure the residual effect of the deflecting cavity outside of the SPX.

Development of electron-bunch tilt diagnostics is a high priority for the SPX project since they are needed for the early test of the deflecting cavities, and the dynamic range of these monitors should cover several decades, well above those used in other facilities. Work on an x-ray-based tilt monitor will commence as soon as funding and manpower becomes available. We will test fast x-ray detectors made of silicon, indium gallium arsenide, silicon carbide, and diamond. Once the appropriate candidate is identified, 35-ID will be used to perform lifetime tests of the detectors. If a custom configuration is needed, it will be designed with vendor participation, and further tests of the assembly will be performed at 35-ID. Concurrent with the detector development, beam arrival monitor electronics will be developed and tested at S35, along with the complete suite of engineering solutions from selection and transport of reference timing signals, transport of detector signals, signal processing in FPGA, output signal delivery, etc.

During the initial commissioning of the deflecting cavities, only one group of deflecting cavities will be installed. Minimally, a single bunch in the ring can be used, and the effect of the deflecting cavity measured on a single-turn basis at 271 kHz. If 24-bunch fill is used, the deflecting cavity effect needs to be measured at 6.5 MHz. For large bunch tilt, a visible-light streak camera will be used to visualize the tilt in y-z space, but its spatial resolution will be limited due to diffraction of visible light. The x-ray streak camera is not sensitive enough to record an image from a single bunch in a single pass. Hence it will be used to visualize the average y-z space electron distribution over many turns, at an improved spatial resolution. The x-ray BAT array will be installed in S35 to support the deflecting cavity test. We will use the data from the R&D phase to determine whether to install the detector permanently at 35-BM or 35-ID. We note that the bandwidth requirement for the BAT array is higher during this test than during normal SPX operations. Additional effort will be needed in developing the detectors and their electronics.

A less difficult alternative would be to measure the projected vertical beam sizes alone, at the bunch rate of 6.5 MHz, or averaged over many turns. Fast digital cameras will be used to provide beam sizes in the vertical direction. Both 35-ID and 35-BM will be used: 35-ID monochromatic beam for its sensitivity and 35-BM for its robustness.

During normal operation of the SPX, S35 will be used to measure residual effects of the deflecting cavity operations. Since 35-ID is also used for x-ray beam position monitor development, which will be ongoing as different types of insertion devices are brought online, and 35-BM is used for routine emittance measurement for the user operations, S35 beamlines may not be conveniently dedicated to SPX feedback control. However, the beamlines should have the ability to switch into SPX diagnostics mode quickly when required. These diagnostics include the following capabilities:

- Fast vertical emittance measurements, preferably single-bunch single-pass. Higher sensitivity is more important than better linearity. We will need to evaluate both ID and BM lines for this application. At this time, the 35-ID monochromatic beam has the best vertical resolution for emittance measurements, but the 35-BM white-light slits could be more robust with thin filters.
- Fast centroid measurements at a single-bunch single-pass rate of 6.5 MHz. In the event that a clean vertical size measurement cannot be made, the centroid measurement will help determine whether the increase of effective vertical beam size is due to fast centroid oscillations.
- Narrow-band measurements of beam centroid and sizes synchronized with modulations of the SPX operating settings, such as deflecting cavity rf voltages and phases, or their combinations. The narrow-band lock-in technique has been widely used to improve signal-to-noise ratio in many fields of engineering and experimental sciences. Potentially, they can be performed with small perturbations during user operations and remain almost invisible to user experiments. Furthermore, several measurements can be performed concurrently using different frequencies to improve measurement efficiency. If coupling between these frequencies occurs, it yields information regarding the nonlinearity of the system.

3.5.9.9 Research and Development Tasks

Several important questions related to SPX diagnostics need to be addressed by an R&D program:

- What is the impact of the tilt on beam position monitor performance, especially those near the cryomodules and the 6-ID source point?
- Is it possible to measure beam tilt using conventional button pickup electrodes, and if so, what are the limits of this technique?
- What is the sensitivity of different cavity BPM designs to beam tilt, and how much does such a cavity contribute to ring impedance?
- What is the most appropriate detector for use as an optical/x-ray tilt monitor, taking into consideration radiation hardness, sensitivity, speed, vacuum compatibility, thermal stability, etc.
- What are the trade-offs in the design of a distributed vertical beam-size monitoring system, considering their use for SPX tuning vs. a beam-abort interlock application. Spatial resolution, reliability, speed, and cost need to be considered.

Many of these items can be addressed during machine studies, for example using the method of Guo et al. [3.5-72] to induce tilted bunches in a transient fashion. Existing turn-by-turn BPM diagnostics should address questions of their sensitivity to tilted beams. It should also be possible to study the application of button pickups to the detection of tilt, using modified versions of in-house electronics together with other test equipment.

Development of a cavity-BPM-type tilt monitor will require developing an rf model design and the construction of a cold test model for testing in the lab, together with the generation of prototype detection electronics suited for this purpose. Collaboration with accelerator physicists will be needed to assess the impact of cavity impedances on beam stability.

Almost all areas including beam position monitoring, tilt monitoring, phase detection, and loss monitoring, could benefit from the application of field programmable gate array (FPGA) technology. Development of general-purpose data acquisition and processing solutions employing FPGAs will play an important role in not only SPX diagnostics but also in low-level rf control and feedback, as well as beam stability.

Sector 35 is a valuable resource for testing different types of x-ray and optical detectors and electronics and will be used extensively to support our R&D goals. In general, the availability of the APS ring throughout the course of the upgrade should allow relatively rapid turnaround in addressing technical questions regarding diagnostic detectors and techniques as they arise.

3.5.10 References

[3.5-1] M. Sands. The Physics of Electron Storage Rings: An Introduction. SLAC Report SLAC-121, SLAC, (1979).

[3.5-2] V. Sajaev. Longitudinal bunch profile. APS web site, (2008). http://www.aps.anl.gov/asd/oag/SRparameters/node6.html.

[3.5-3] Y.-C. Chae et al. Measurement of the Longitudinal Microwave Instability in the APS Storage Ring, Proceedings of the 2001 Particle Accelerator Conference, pp. 1817–1819, (2001); http://www.JACoW.org.

[3.5-4] M. Borland. A Very Preliminary Analysis of Using a Harmonic Cavity in the APS. Technical Report OAG-TN-2004-003, APS, (2004).

[3.5-5] J. Feikes et al. Sub-picosecond electron bunches in the BESSY storage ring, Proceedings of the 2004 European Accelerator Conference, pp. 1954–1956, (2004); http://www.JACoW.org.

[3.5-6] K. Satoh and Y. Chin. Transverse mode coupling in a bunched beam, Nuclear Instruments and Methods in Physics Research A, **207**, 309–320, (1983).

[3.5-7] M. Bei et al. The Potential of an Ultimate Storage Ring, Nuclear Instruments and Methods in Physics Research A, **622**, 518, (2010).

[3.5-8] C. Limborg. *Ultimate brilliance of storage ring based synchrotron facilities of the* 3^{rd} *generation*. PhD thesis, University Joseph Fourier, Genoble, France, (1996).

[3.5-9] A. A. Zholents and M. S. Zolotorev. Femtosecond X-Ray Pulses of Synchrotron Radiation, Phys. Rev. Lett., **76**(6), 912–915, (1996).

[3.5-10] R. W. Schoenlein et al. Generation of Femtosecond Pulses of Synchrotron Radiation, Science, **287**(5461), 2237–2240, (2000).

[3.5-11] A. A. Zholents, ANL, (2010). Private communication.

[3.5-12] A. Zholents and K. Holdack. Energy Modulation of the Electrons by the Laser Field in the Wiggler Magnet, Proceedings of the 2006 Free Electron Laser Conference, pp. 725–727, (2006); http://www.JACoW.org.

[3.5-13] Y. Li, ANL, (2010). Private communication.

[3.5-14] T. Y. Fan, (2009). Private communication.

[3.5-15] A. Zholents et al. Generation of subpicosecond X-ray pulses using RF orbit deflection, Nuclear Instruments and Methods in Physics Research A, **425**, 385, (1999).

[3.5-16] M. Borland and V. Sajaev. Simulations of x-ray slicing and compression using crab cavities in the Advanced Photon Source, Proceedings of the 2005 Particle Accelerator Conference, pp. 3886–3888, (2005); http://www.JACoW.org.

[3.5-17] M. Borland. Effect of Increased Beta Functions for Closed Chirp Bump. Technical Report OAG-TN-2005-026, APS, (2005).

[3.5-18] K. J. Kim. Characteristics of Synchrotron Radiation. M. Month and M. Dienes, editors, AIP Conference Proceedings 184. AIP, (1989).

[3.5-19] T. Fujita et al. Overview of Short-Pulse X-ray Generation Using Crab Cavities at SPRING-8, Proc. of ICAP 2010, pp. 39–41, (2010); http://www.JACoW.org.

[3.5-20] M. Borland. Simulation and analysis of using deflecting cavities to produce short x-ray pulses with the Advanced Photon Source, Phys. Rev. ST Accel. Beams, **8**(7), 074001, (2005).

[3.5-21] A. Piwinski. Synchrotron sidebands of betatron coupling resonances. Technical Report DESY 93-189, DESY, (1993).

[3.5-22] M. Borland. elegant: A Flexible SDDS-Compliant Code for Accelerator Simulation. Technical Report LS-287, Advanced Photon Source, (2000).

[3.5-23] Y. Wang et al. Recent Progress on Parallel ELEGANT, Proc. of ICAP 2009, (2009); http://www.JACoW.org.

[3.5-24] M. Borland et al. Beam Dynamics, Performance, and Tolerances for Pulsed Crab Cavities at the Advanced Photon Source for Short X-Ray Pulse Generation, Proc. of PAC 2007, pp. 3429–3431, (2007); http://www.JACoW.org.

[3.5-25] H. Wiedemann. *Particle Accelertor Physics*, 2nd ed., volume I. Springer, (1998).

[3.5-26] H. Shang. sddsurgent software based on US by R. Dejus and URGENT by R. Walker, http://www.aps.anl.gov/Accelerator_Systems_Division/Operations_Analysis/manuals/elegant_latest/node89.html.

[3.5-27] T. Tanaka and H. Kitamura. J. Synch. Rad., **8**, 1221–1228, (2001).

[3.5-28] R. Siemann. Instability Growth Rate Calculations for High Energy Storage Rings, IEEE Transactions on Nuclear Science, volume NS-28, pp. 2437–2439, (1981); http://www.JACoW.org.

[3.5-29] J. Hagel and B. Zotter. PC-BBI, A Program to Compute Bunch Beam Instabilities on a PC. CERN SL-AP 90-62, CERN, (1990).

[3.5-30] L. Emery. Coupled-Bunch Instabilities in the APS Ring, Proc. of PAC 1991, p. 1713, (1991); http://www.JACoW.org.

[3.5-31] L. Emery. Required Cavity HOM DeQing Calculated from Probability Estimates of Coupled Bunch Instabilities in the APS Ring, Proc. of PAC'93, p. 3360, Washington DC, (1993); http://www.JACoW.org.

[3.5-32] L. Emery. Instability Estimates for Three-Cell Deflecting Mode Cavities. Technical Report OAG-TN-2007-023, APS, (2007).

[3.5-33] L. Emery. Monte Carlo Instability Calculations for Three-Cell Deflecting Mode Cavities. Technical Report OAG-TN-2007-024, APS, (2007).

[3.5-34] K. Thompson and R. D. Ruth. Transverse coupled bunch instabilities in damping rings of high-energy linear colliders, Phys. Rev., **D43**, 3049–3062, (1991).

[3.5-35] L. Emery. User's Guide to Program clinchor. http://www.aps.anl.gov/Accelerator_Systems_Division/Operations_Analysis/manuals/clinchor_V1.0/clinchor.html.

[3.5-36] M. Borland. SPX phase variation due to changes in ID gaps. Technical Report AOP-TN-2010-010, APS, (2010).

[3.5-37] T. Berenc. Storage Ring RF System Phase Noise Studies. Technical Report ICMS-APS-1414611, APS, (2010).

[3.5-38] T. Berenc. Storage Ring RF System AM & PM Noise Studies Report. Technical Report ICMS-APS-1416636, APS, (2010).

[3.5-39] SPX Study Meeting. APS web site, (2010). http://www.aps.anl.gov/Accelerator_Systems_Division/SPX_Meeting.

[3.5-40] T. Berenc. Introduction to RF System Noise Propagation for SPX. Technical Report ICMS-APS-1412274, APS, (2010).

[3.5-41] T. Abe et al. Beam Operation with Crab Cavities at KEKB, Proceedings for the 1997 Particle Accelerator Conference, pp. 1487–1489, (2007); http://www.JACoW.org.

[3.5-42] G. Burt. New Cavity Shape Developments for Crabbing Applications. Technical report, European Coordination for Accelerator Research and Development, (2010).

[3.5-43] K. Hosoyama et al. Development of the KEK-B Superconducting Crab Cavity, Proc. of EPAC 2008, (2008); http://www.JACoW.org.

[3.5-44] G. Waldschmidt. SC Deflecting Cavity LOM/HOM Dampers. Technical Report RF-TN-2008-001, APS/ASD/RF, (2008).

[3.5-45] S. Kim et al. Higher-order-mode (HOM) Power in Elliptical Superconducting Cavities for Intense Pulsed Proton Accelerators, NIM, **492**, 1–10, (1991).

[3.5-46] H. Padamsee. *RF Superconductivity for Accelerators*. John Wiley & Sons, Inc., (1998).

[3.5-47] F. Marhauser. Investigations on Absorber Materials at Cryogenic Temperatures, Proc. of PAC 2009, (2009); http://www.JACoW.org.

[3.5-48] B. Brajuskovic et al. Thermomechanical Design of Normal-Conducting Deflecting Cavities at the Advanced Photon Source for Short X-ray Pulse Generation, Proc. of PAC 2007, (2007); http://www.JACoW.org.

[3.5-49] R. Pendleton et al. Broadband, Multi-Kilowatt, Vacuum, HOM Waveguide Loads for the PEP-II RF Cavity, Proc. of PAC 1995, (1996); http://www.JACoW.org.

[3.5-50] S. Sakanaka. Development of a Broadband HOM Load for the 714-MHz HOM-Damped Cavity, Proc. of PAC 1997, (1998); http://www.JACoW.org.

[3.5-51] G. Waldschmidt et al. Superconducting Cavity Design for Short-Pulse X-Rays at the Advanced Photon Source, Proc. of PAC 2011, (2011); http://www.JACoW.org.

[3.5-52] G. Waldschmidt. Variations of the Three-Cell SC Deflecting Cavity With a Comparison of a Single-Cell Cavity Design. Technical Report RF-TN-2008-002, APS/ASD/RF, (2008).

[3.5-53] H. Wang et al. Progress Toward the Design and Prototype of a Superconducting Crab Cavity Cryomodule for the APS, Proc. of PAC 2010, (2010); http://www.JACoW.org.

[3.5-54] T. Hiatt et al. Cryogenic Testing of the RF Input Waveguide for the CEBAF Upgrade Cryomodule, Proc. of PAC 2001, (2001); http://www.JACoW.org.

[3.5-55] N. Ohuchi et al. Plan of the S1-Global Cryomodules for ILC, Proc. of PAC 2009, (2009); http://www.JACoW.org.

[3.5-56] B. Rimmer et al. JLAB CW Cryomodules for 4th Generation Light Sources, Proc. of SRF 2007, (2007); http://www.JACoW.org.

[3.5-57] M. Liepe et al. The Cornell High-Current ERL Injector Cryomodule, Proc. of SRF 2009, (2009); http://www.JACoW.org.

[3.5-58] Y. Suetsugu et al. Development of a Bellows Chamber with a Comb-Type RF Shield for High Current Accelerators, Nuclear Instruments and Methods in Physics Research A, **531**, 367–374, (2004).

[3.5-59] C. Pagani. SRF Activities at INFN Milano-Lasa, 10th Workshop of RF Superconductivity, (2001); http://www.JACoW.org.

[3.5-60] T. Berenc. An Equivalent Circuit Model and Power Calculations for the APS SPX Crab Cavities. Technical Report ICMS-APS-1405978, APS, (2011).

[3.5-61] T. Berenc. SPX Crab Cavity Noise Propagation Modeling & the Effects of Common Mode Synchronous Phase Noise. Technical Report ICMS-APS-1417419, APS, (2011).

[3.5-62] G. Huang et al. Signal Processing for High Precision Phase Measurements, Proc. of BIW10, pp. 3447–3449, (2010); http://www.JACoW.org.

[3.5-63] G. Bees et al. A Precision 75KW, 25KV Power System for a Klystron Amplifier, Proc. of PAC 2007, pp. 593–595, (2007); http://www.JACoW.org.

[3.5-64] R. Wilcox et al. Stable transmission of radio frequency signals on fiber links using inteferometric delay sensing, Optics Letters, **34(20)**, 3050–3052, (2009).

[3.5-65] A. Ropert. Challenging Issues during ESRF Storage Ring Commissioning, Proceedings of the 1993 Particle Accelerator Conference, pp. 1512–1514, (1993); http://www.JACoW.org.

[3.5-66] I. Sheng et al. Thermal Analysis of the Beam Missteering in APS Storage Ring, Proceedings of the 1993 Particle Accelerator Conference, pp. 1500–1502, (1993); http://www.JACoW.org.

[3.5-67] S. J. Pasky et al. LINAC Automated Beam Phase Control System, Proceedings of LINAC 2006, pp. 241–243, (2006); http://www.JACoW.org.

[3.5-68] N. S. Sereno et al. Automated correction of phase errors in the Advanced Photon Source linac, Phys. Rev. ST Accel. Beams, **11**(7), 072801, (2008).

[3.5-69] W. Wuensch. Measurements for Adjusting BNS Damping in CLIC. Technical Report CLIC-244, CLIC, (1994).

[3.5-70] M. Ross et al. RF Cavity BPMs as Beam Angle and Beam Correlation Monitors, Proceedings of PAC 2003, pp. 2548–2550, (2003); http://www.JACoW.org.

[3.5-71] P. Tenenbaum et al. Beam Tilt Signals as Emittance Diagnostic in the Next Linear Cillider Main Linac, Proceedings of EPAC 2002, pp. 512–514, (2002); http://www.JACoW.org.

[3.5-72] W. Guo et al. Generating Picosecond X-ray Pulses with Beam Manipulation in Synchrotron Light Sources, Proc. PAC 2005, pp. 3898–3900, (2005); http://www.JACoW.org.

[3.5-73] B. Yang et al. A Design Study for Photon Diagnostics for the APS Storage Ring Short-Pulse X-Ray Source, Proceedings of the 2007 Particle Accelerator Conference, pp. 1156–1159, (2007); http://www.JACoW.org.

[3.5-74] A. Pietryla et al. A Cerenkov Radiation Detection System for the Advanced Photon Source Source Storage Ring, Proceedings of the 2001 Particle Accelerator Conference, pp. 1622–1624, (2001); http://www.JACoW.org.

[3.5-75] A. Fischer. Diagnostics Development for the PEP-II B Factory, Proceedings of the 1996 Beam Instrumentation Workshop, pp. 248–256, (1996); http://www.JACoW.org.

[3.5-76] B. Yang et al. Bench Calibration of the APS Cherenkov Detector Photomultiplier Tubes. Technical Report DIAG-TN-2009-008, APS/ASD/DIAG, (2009).

[3.5-77] B. Yang. APS-SR Cherenkov Detector Pulse Counter Initial Calibration. Technical Report DIAG-TN-2008-012, APS/ASD/DIAG, (2008).

[3.5-78] B. Yang et al. APS-SR Cherenkov Detector Electronics: Summary of Mod-0807. Technical Report DIAG-TN-2008-013, APS/ASD/DIAG, (2008).

[3.5-79] W. Berg et al. Development a Beam Loss Monitor System for the LCLS Undulator Beamline, Proceedings of the 2008 Linear Accelerator Conference, (2008); http://www.JACoW.org.

[3.5-80] B. Yang et al. Beam Measurements of a Large Solid-Angle Beam Loss Monitor in the APS, Proceedings of the 2010 Beam Instrumentation Workshop, (2010); http://www.JACoW.org.

[3.5-81] J. Dooling et al. Modeling the Optical Coupling Efficiency of the Linac Coherent Light Source Beam Loss Monitor Radiator, Proceedings of the 2010 Beam Instrumentation Workshop, (2010); http://www.JACoW.org.

[3.5-82] J. C. Dooling et al. Simulations of the Beam Loss Monitor System for the LCLS Undulator Beamline, Proceedings of the 2009 Particle Accelerator Conference, (2009); http://www.JACoW.org.

[3.5-83] M. Santana-Leitner. Study of the Optical Coupling of the LCLS Beam Loss Monitors. Technical Report RP-10-02, SLAC Radiation Physics, (2010).

3.6 Higher-Current Operation

3.6.1 Introduction

The nominal APS operating current is 100 mA. The brightness and flux are directly proportional to the beam current, which provides a clear path to delivering higher-brightness hard x-rays, an important component of the mission.

The planned operating current after the upgrade is 150 mA. The high-current threshold in the ring has been explored, and it was determined that no accelerator upgrades are required for 150-mA operation. To establish the performance margin above 150 mA, storage ring components have been

identified that either drive collective instabilities through the interaction of wakefields with the beam, or are subjected to excessive beam-driven wakefield heating. Two components, the higher-order mode (HOM) dampers and the vertical diagnostic scraper chambers, presently limit higher-current operation above 150 mA, especially in 24-bunch mode.

The accelerator could operate today at 150 mA, but the front ends (FEs) and x-ray beamlines must be upgraded to overcome present thermal limitations. New front ends will be 200-mA capable, but existing FEs will be upgraded to a 150-mA level. Details on the FEs are discussed in Chapter 5.

In this section, we review the safety envelope, present accelerator capabilities, relevant past work, and related on-going operations-funded efforts. The performance margins are also discussed for the different standard user operating modes.

3.6.2 Safety Envelope

Operation at 150 mA is within the operating envelope, which is itself within the safety envelope, as defined in the APS Safety Assessment Document (SAD) [3.6-1]. The SAD operating envelope gives a maximum stored beam current of 300 mA at 7.0 GeV and a maximum top-up injection charge per cycle of 10 nC. Presently, the top-up injection charge is 3 nC. It is expected that in the upgraded lattice, 3 nC will be sufficient to maintain the stored current with top-up injection. As mentioned in section 3.2.5, top-up safety tracking will be repeated per the SAD and Accelerator Systems Division procedures.

3.6.3 Present Capabilities and Configuration

First we describe the present capabilities and configuration of the APS systems. We also give background on how the present capabilities were developed. This helps to set the stage for discussion of the accelerator performance margin in the various user operating modes above 150 mA.

For nominal, 100-mA operation, we require two 1.1-MW, 351.93-MHz klystrons to drive the 16 radio-frequency (rf) cavities, with each klystron delivering approximately 650-kW rf output power. Operation at 150 mA can be achieved with two klystrons operating at nearly full-rated power output, approximately 800 kW to 1 MW each depending on the total gap voltage required. Alternatively, up to four klystrons can be used at lower power when operated in a parallel configuration [3.6-2]. The average individual klystron output power and average cavity input power were measured for high current with ID gaps open; these data are shown in Fig. 3.6-1. For user operation, the rf power is higher due to the additional ID radiation energy loss; the amount depends on the ID gaps. The ID reference gaps are a standardized set of ID gaps that are used regularly to reproduce user beam alignment. The average klystron and cavity power with the ID reference gaps are shown with a gray bar on the figure. The ID power increment was scaled by 50 percent to estimate the power at 150 mA, shown with a broken gray bar.

The rf system is expected to handle 150-mA operation within the design limits of 1.1-MW klystron power and 180-kW coupler power (based on the original LEP design [3.6-3]). The overall reliability of the rf systems will be reduced to some degree when operating at greater than 100-mA stored beam. Reasons for this reduced reliability include operation of the cavity input couplers closer

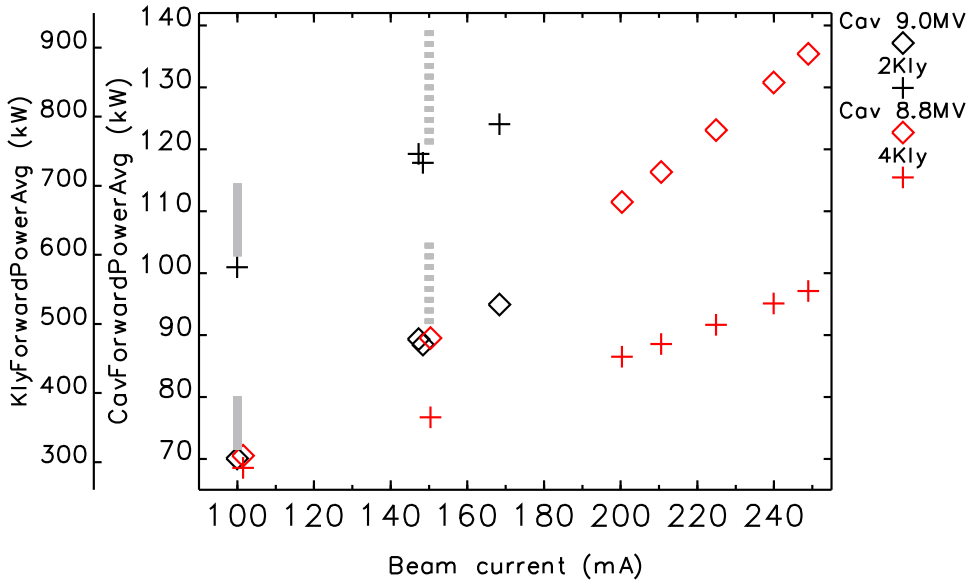

Figure 3.6-1. Average cavity input power (with 16 cavities) and average klystron output power (with 2 or 4 klystrons) for high current and ID gaps open. The 4-klystron data shown were with 324 bunches, and the 2-klystron data were with 24 bunches or hybrid mode. The rf power with ID reference gaps is shown with the gray bar; the estimated rf power at 150 mA with ID reference gaps is shown with the broken gray bar.

to their design power rating and operation of the klystrons at or near their maximum rf power output. Alternately, more than two klystrons can be operated in a parallel configuration with partial or total loss of rf system redundancy, but this is not required for 150 mA. Ongoing or planned programmatic efforts to address rf system reliability are discussed later.

Higher-current operation has been tested using four klystrons with beam stored in the 24-bunch and 324-bunch user operating modes, both of which have uniform bunch current and bunch spacing. Top-up injection was operated for a short time with 24 bunches. Higher-current operation has also been tested for the hybrid bunch mode using only two klystrons. In all these tests, the ID gaps were open, the chromaticity was high (i.e., 10 units in each plane) and the bunch-by-bunch feedback system was off. The maximum current and the reason for the limitation at maximum current is summarized in Table 3.6-1. For a complete description of the operating modes, see [3.6-4].

The high-current thresholds are dominated by longitudinal effects, either rf-cavity longitudinal HOM-driven coupled-bunch instabilities (CBIs) or heating by longitudinal wakefields in various accelerator components, e.g., the vertical scraper chamber. With 324 bunches, the CBI threshold is 245 mA. With 24 bunches, several components are approaching temperature limits above 160 mA, including the rf couplers and the HOM dampers themselves. CBIs were not observed at the current limit with 24 bunches but could occur at higher current. Higher current was limited by klystron power in the hybrid mode in two-klystron operation. The performance margin of <15 mA is smallest for 24-bunches and is >20 mA for hybrid mode. The margin is highest for 324 bunches, at 95 mA. The heating issues are discussed later in more detail.

Transverse multibunch instabilities are driven by the resistive wall impedance. Presently,

Table 3.6-1. Maximum Stable Total Current for All Operating Modes. These results are with high chromaticity and HOM dampers installed, using four klystrons in parallel, unless noted.

Operating mode (no. bunches)	Current limit (mA)	Performance margin (mA)	Limitation at maximum current
24	164	< 15	Heating[a]
324	245	95	CBI (longitudinal)
hybrid	170[b]	> 20	–[c]

[a] Rf coupler, vertical scraper chamber, and rf cavity HOM damper (1 of 4).
[b] Tested with two klystrons only near maximum output power.
[c] To be determined using all four klystrons.

high positive chromaticity is used to stabilize the transverse multibunch instabilities. A transverse bunch-by-bunch feedback system is used with 100 mA in the 24-bunch mode to further stabilize the beam, reducing the chromaticity required for stability by two units in each plane [3.6-5]. Tests show that the chromaticity can be reduced by at least two units when operating the feedback system with 150 mA in 24 bunches.

A number of improvements have already been implemented to address heating and/or impedance issues, namely, redesign of the ceramic injection kicker magnet chambers [3.6-6] and installation of HOM dampers in the rf cavities [3.6-7]. After a brief summary of these past improvements, the present high-current limits are discussed with these improvements in place.

3.6.3.1 Past Improvements

Ceramic Kicker Vacuum Chambers: The four pulsed-injection kickers are mounted over ceramic vacuum chambers. With high-bunch currents like the 24-bunch mode, elevated temperatures were measured on the flanges, vacuum chambers, and attached bellows. The original resistive paste coating was found to be inadequate or damaged, resulting in heating effects that are proportional to the square of the bunch current [3.6-8]. Improvements in the design included improving the rf finger contact and metalizing the inner surface with moly-manganese to a thickness of about 10 microns [3.6-6]. The improvement can be seen in Figure 3.6-2, showing 324-bunch non-top-up operation followed by 24-bunch top-up operation before and after the redesign. The plot on the left includes blowers and water cooling of the flanges.

HOM Dampers: rf cavity HOMs have long been known to potentially drive longitudinal CBIs in the APS storage ring [3.6-9–3.6-11]. To reduce the effects of the HOMs, the physical lengths of each of the rf cavities were staggered by 0.3 mm during initial construction.

Operationally, the instability threshold was found to be strongly bunch-pattern dependent [3.6-12, 3.6-13]. In 24-bunch operation, the lowest monopole HOM near 538 MHz was found to drive a CBI with a threshold of about 85 mA. This threshold is consistent with a predicted threshold of 80 mA for this HOM for a uniformly filled ring [3.6-9]. Initially, the beam was stabilized for 100-mA

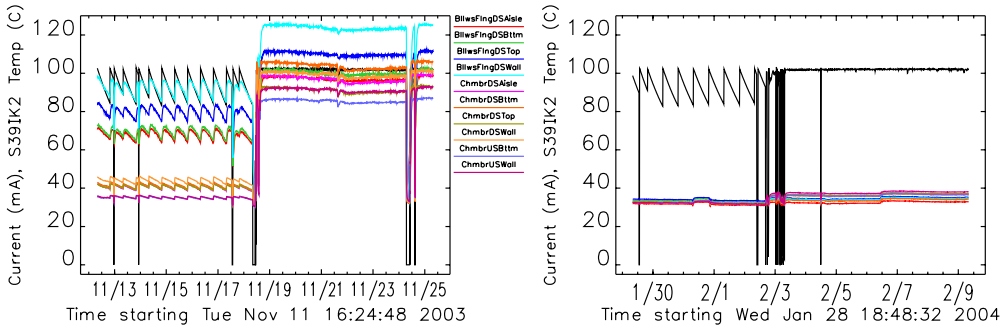

Figure 3.6-2. Kicker chamber temperatures before (left) and after (right) redesign, each showing a one-week period of non-top-up, 324-bunch operation followed by a one-week period of top-up, 24-bunch operation (nominal 100 mA). The black curve is the beam current.

operation through a combination of adjusting the cavity cooling water temperature (regulated in sets of four cavities) and, if necessary, detuning the offending cavities. These are standard methods to shift the HOM frequency by changing the cavity volume, which can shift the HOM out of resonance with the beam.

A program (1999 - 2005) to move storage ring straight-section girders inboard in order to minimize bending magnet radiation pollution of the insertion device x-ray BPMs [3.6-14] had an unanticipated effect on CBI mitigation. The girder displacements were accompanied by an rf frequency evolution to compensate for the circumference change. As a greater number of girders were displaced, it became more and more difficult to mitigate the CBIs using the standard methods. The total frequency shift was almost 10 kHz, which is many times the synchrotron frequency. It was also found that in some bunch patterns, e.g., the 324-bunch mode, instabilities were observed at certain values of the rf voltage, which is typically set to a value between 8.5 MV to 9.5 MV to optimize the momentum aperture and lifetime.

The situation led to the design and installation of HOM dampers on four of the 16 cavities to damp the 538-MHz mode. Design and manufacturing considerations for the rf cavity HOM dampers are discussed in refs. [3.6-15, 3.6-16], and details of the damper testing and installation can be found in ref. [3.6-7]. The 538-MHz HOM has a strong electric field component along the equatorial plane of the cavity, and a standard coaxial electric-probe damper with a ceramic lossy load was chosen for the design, shown schematically in Figure 3.6-3, left. Since the radial component of the fundamental accelerating mode is zero along the mid-plane, no rejection filter was needed to prevent excessive deQing of the fundamental. The ceramic load is made of AlN with 40% SiC.

Low-power testing of the dampers agreed well with the simulation models. High-power testing of the dampers, as well as conditioning of the damper ceramic load, were performed at the APS 352-MHz rf test stand. During the conditioning process, multipacting was detected on the surface of the damper probe and occurred along the length of the probe that passed through the cavity port (see Figure 3.6-3, right). This multipacting issue was resolved by coating the probes with approximately 10 nm of titanium.

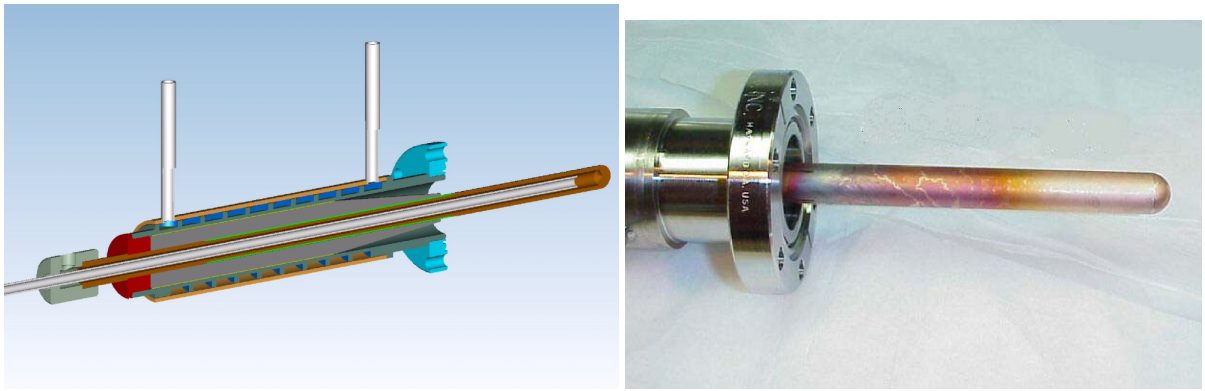

Figure 3.6-3. (Left) Mechanical design of present damper. (Right) Coaxial damper with probe discoloration due to multipacting during high-power conditioning.

Separate flow meters and resistive thermal devices (RTDs) were attached to each water circuit for each of the dampers to monitor the heat load. The flow rates, RTD temperature readings, and the calculated power absorption levels are continuously monitored by a Kyoto programmable logic controller (PLC) that is remotely accessed by EPICS [3.6-17].

Once installed, the dampers performed as expected. With 100-kW fundamental input power, there was no detectable power loss in the damper ceramic. The damper center probe dissipated 240 W, which compares closely with the calculated values [3.6-7]. Since the installation of the dampers, instabilities resulting from the 536-MHz HOM have rarely been observed up to 100 mA with the nominal bunch patterns (exceptions are generally for nonstandard machine conditions). However, due to the frequency shift of the HOM by the insertion of the damper, the operating conditions that previously produced the instability cannot be recreated and directly compared.

Many studies have been performed, and it is believed that the dampers have increased the storage ring CBI threshold current by at least 60% over undamped cavities for nominal machine conditions, at which point either other HOMs dominate, or the 538-MHz HOMs in other cavities contribute to driving the beam. The HOM dampers have enabled stable 100-mA operation with greater flexibility (i.e., over a range of rf voltages and without cavity detuning) for the standard bunch patterns for the nominal operating conditions.

There are a number of issues with the present HOM damper configuration. Instabilities are sometimes observed when operating at 100 mA with fewer than the nominal 16 cavities, or with 324 bunches at lower values of the rf voltage. Some nonstandard bunch patterns, such as 14 bunches, have a CBI driven by a HOM near 920 MHz, which is not damped. Exploration of high beam current or other nonstandard bunch patterns has shown that the HOM dampers themselves can be subjected to excessive heating.

3.6.3.2 Longitudinal Limits

A total current of 164 mA can be stored stably in 24 bunches. CBIs are not observed up to this current; the HOM dampers appear to have raised the threshold by at least 60 percent compared to

undamped cavities. However, several storage ring components approach their temperature or absorbed-power limits above about 160 mA (see Table 3.6-1 and Figure 3.6-4). In the figure, 324 bunches were stored in the period up to 8:00 hours (h) and between 15:45 h and 17:15 h; otherwise 24 bunches were stored. Beam stability was monitored as were the temperatures of hundreds of accelerator components as higher current was stored. The highest-temperature components are included in the figure. The vertical diagnostic scraper temperature is shown in red. The green and blue curves show the power absorbed by the Sector 38 cavity 3 and cavity 4 HOM dampers, respectively.

The vertical scraper chamber reached high temperatures with high current in 24 bunches. The cavity 4 damper absorbed higher power with 24 bunches, whereas the cavity 3 damper absorbed higher power with 324 bunches. The Sector 37 cavity 4 rf power input coupler downstream/upstream temperatures (turquoise/magenta) showed a large differential of almost 50 C in high-current 24-bunch operation; it is expected that the coupler heating can be mitigated with rf conditioning. Note that the ceramic kicker chambers did not reach high temperatures during this test.

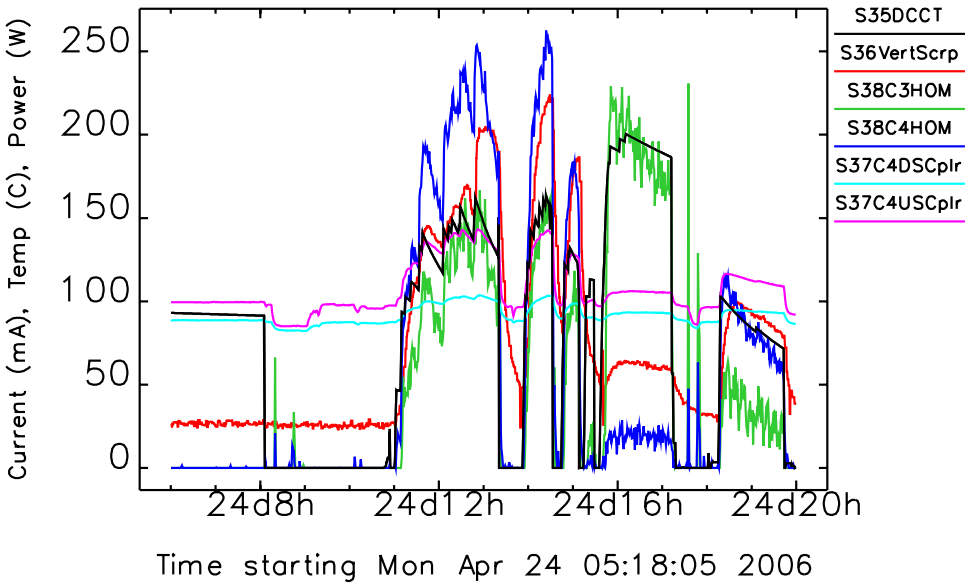

Figure 3.6-4. Temperature excursions for high-current studies. The beam current is shown in black, and the operating modes are described in the text.

With 324 bunches, the beam is stable up to about 245 mA. Above the instability threshold, the beam spectrum clearly shows a CBI signature. The CBI can also be induced with nonstandard operating conditions even at lower current: for example, at 100 mA and reduced rf voltage of 8.5 MV.

For the latter case, an analysis of the CBI modes can determine which cavity HOMs are responsible for driving the beam. Since the bunch spacing is four rf buckets, the beam spectrum has a four-fold degeneracy, as if the rf frequency were $f_{\rm rf}/4$. Thus the frequency range of any spectrum measurement only needs to be $f_{\rm rf}/4$ (or $f_{\rm rf}/8$ since the upper half of the $f_{\rm rf}/4$ spectrum is a reflection of the lower half). The coupled-bunch mode numbers are determined by dividing the rf frequency span by four, and renormalizing each reduced frequency span to $N_b = 324$. The longitudinal spectrum for unstable beam as a function of mode number n is shown in Figure 3.6-5. The actual spectrum displayed is the rms average of the measured spectra minus the stable beam spectra to retain the

phase-modulation signal (coupled-bunch motion) and remove the amplitude-modulation signal (from uneven bunch population).

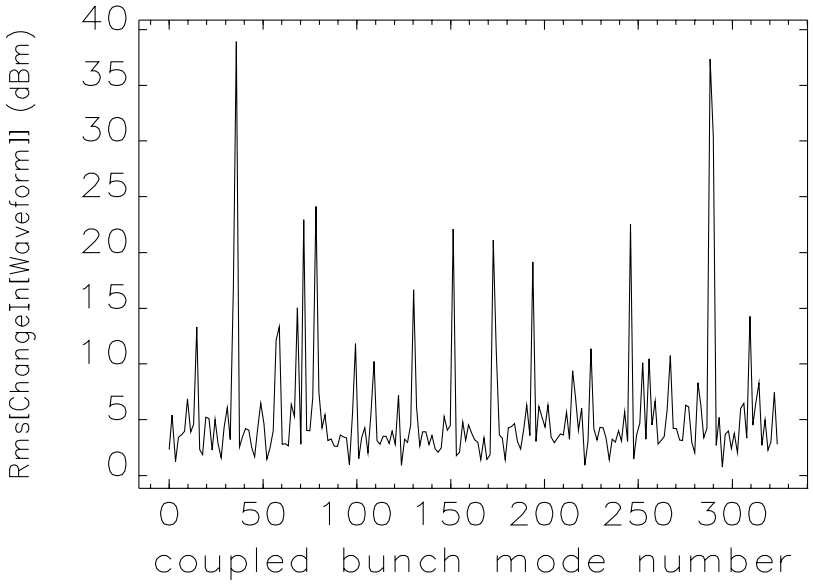

Figure 3.6-5. Dominant longitudinal CBI modes for unstable beam, 324 bunches, 100 mA, 8.5 MV rf voltage (nonstandard conditions), corresponding to monopole HOMs near 538 MHz, 915 MHz, and 1211 MHz.

The dominant mode numbers n, in decreasing strength, are 36, 78, 151, and 130 (and the mirror-symmetric mode numbers $(324 - n)$). The phase shift between oscillations of adjacent bunches is given by $2\pi n/N_B$. To drive the beam at mode n, the HOM frequency must be equal to

$$f_{\text{HOM}} = \frac{f_{\text{rf}}}{h}(N_b p + n + m\nu_s), \tag{3.6-1}$$

where $h = 1296$ is the harmonic number, p and m are positive indices, and ν_s is the synchrotron tune. Using $f_{\text{rf}} = 351.936$ MHz, the computed CBI mode frequencies are closest to the measured monopole cavity HOMs 538 MHz, 1211 MHz, and 915 MHz. When the beam is unstable, the cavities in Sectors 38 and 36 show relatively strong HOM signals, and thus make good candidates for future HOM dampers.

3.6.3.3 Transverse Limits

The transverse multibunch instabilities are driven by long-range wakefields such as the resistive-wall (RW) impedance. There is little evidence that the main rf cavity dipole HOMs contribute to the instabilities observed in the APS [3.6-18], despite predictions of low transverse CBI thresholds [3.6-9, 3.6-11]. Similar observations are reported at the European Synchrotron Radiation Facility [3.6-19].

Presently, positive chromaticity is used to stabilize the transverse multibunch instabilities at 100 mA [3.6-18]. The transverse bunch-by-bunch feedback system is used in the 100-mA, 24-bunch mode

to further stabilize the beam, reducing the chromaticity required for stability by at least two units in each plane [3.6-5].

At the stability threshold in the horizontal plane, we observe the onset of a steady-state instability, characterized by emittance growth, a self-excited betatron tune signal, and bunch centroid oscillations with constant amplitude. The bunch phases are coupled with a bunch-to-bunch phase corresponding to a transverse mode number of 0.8, which is consistent with an RW-driven transverse CBI. At lower chromaticity, the onset of a bursting instability is observed, characterized by a semi-periodic variation in the bunch centroid oscillation amplitude. The multibunch bursting phenomenon is qualitatively similar to the single-bunch instability observed in the APS.

At the instability threshold in the vertical plane, x-y coupling growth is typically observed before a self-excited vertical tune or centroid oscillations can be seen. The bunch phases do not appear to be coupled, at least for the standard 24-bunch operating mode; rather, individual bunches become unstable — this might be a coincidental occurrence of single-bunch and multibunch instability for this bunch pattern. Also, vertical bursting is often but not always observed. For reference, the single-bunch TMCI threshold is about 4 mA in the horizontal plane and 2 mA in the vertical plane [3.6-20].

Figure 3.6-6 shows the chromaticities corresponding to the instability onset and the bursting instability threshold in both planes for 100 mA total beam current. These measurements are without the bunch-by-bunch feedback system.

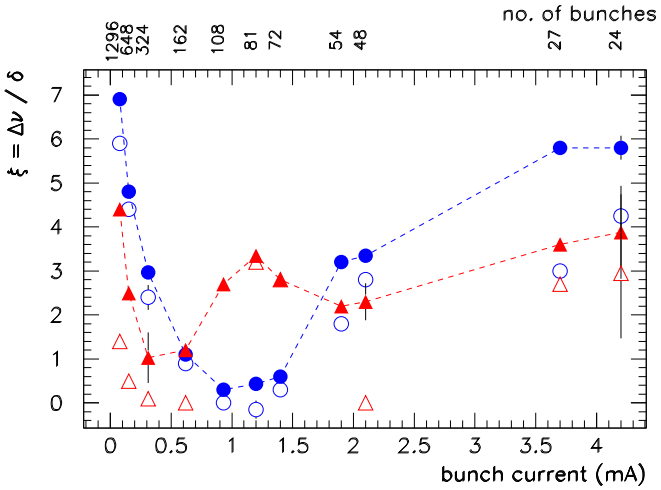

Figure 3.6-6. Horizontal (circles) and vertical (triangles) chromaticity thresholds as a function of uniformly spaced bunch number and bunch current (100 mA total). The closed symbols give the instability onset and the open symbols the bursting threshold.

By convention, the instability threshold is given as the current at which the onset of collective motion is observed. In practice, however, it is difficult to determine the current threshold for transverse instabilities because the injection process mixes linear and nonlinear single-particle beam dynamics with impedance (collective) effects. Instead, we determine the threshold by filling the ring starting with high chromaticities (stable conditions), then slowly lower the chromaticity in each plane separately until collective motion is observed.

The relationship between the chromaticity and the current threshold is not strictly linear, but the threshold expressed as a chromaticity can be useful for relative comparisons. In the range of 324 to 1296 bunches, the threshold in both planes is inversely proportional to the bunch current. This is consistent with the increased head-tail damping for higher bunch current. In the 24- to 54-bunches range, the threshold appears to be dominated by another mechanism, likely single-bunch effects. The horizontal onset is consistently 1-2 units above the vertical. There is a curious deviation from these trends for 72-162 bunches. The reason for this behavior is not understood.

The impact of high chromaticity on beam lifetime is most important for 24 bunches. For 150 mA in 24-bunch mode, the chromaticity thresholds were measured to be about 9.5 units in each plane (this is not shown in Fig. 3.6-6). Preliminary tests at 150 mA with the transverse feedback system show that the chromaticity can be reduced by at least two units in both planes while maintaining a stable beam. This result is consistent with the assumptions and requirements discussed in section 3.2.2.5.

Measurement of the betatron tune shift as a function of current is used to estimate the transverse impedance. The tune shift as a function of single-bunch current was measured for different uniform bunch patterns. For each bunch pattern, the current was scanned from 100 mA down to 10 mA except for two- and one-bunch fills where current was limited by a single-bunch limit. The results are presented in Figure 3.6-7.

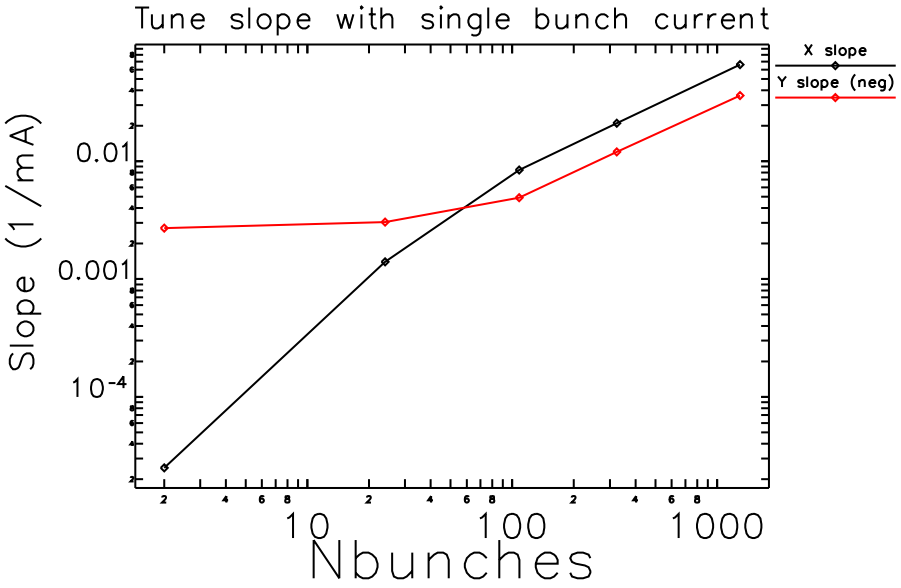

Figure 3.6-7. Tune slope with single-bunch-current dependence on the number of equally spaced bunches (or bunch spacing). Black curve shows horizontal tune slope, red curve shows vertical tune slope multiplied by -1 *to present in log scale.*

One can see that the horizontal tune slope is positive. This was recently observed at several rings [3.6-19, 3.6-21] and is explained by a quadrupolar wakefield of asymmetric vacuum chambers.

The APS has a large number of small-gap insertion device vacuum chambers that are essentially open on one side in the horizontal plane. In the APS, the insertion device chambers dominate the transverse impedance. One might assume that the vertical RW impedance is orders of

magnitude larger than the horizontal due to the 1:2 to 1:5 aspect ratio and inverse cubic dependence on the chamber radius. However, the horizontal and vertical multibunch instability thresholds are comparable (horizontal is actually slightly higher), which implies that the impedance is also comparable. Thus the chamber asymmetry is highly suspected to be the source of a significant impedance in the horizontal case.

An alternative solution to high chromaticity or multibunch feedback for high current may be reducing the beta functions in the IDs. To study the latter, an all-ID reduced-horizontal beta lattice was tested. The horizontal multibunch instability threshold was increased roughly in proportion to the betatron function reduction factor, as expected [3.6-22]. This solution may be limited in practice by other lattice constraints.

3.6.4 Performance Margin

For 150-mA operation, the performance margin in the 24-bunch mode is relatively small. The margin is higher in the other user modes. The accelerator limitations at the maximum current are understood, and we are confident that 150-mA operation can be achieved in all user modes without the need for upgrades. In this section, we discuss the accelerator limitations and programmatically funded effort and improvements that are related to reliable 150-mA operation.

Rf Coupler: The storage ring rf cavity input couplers have been a significant contributor to rf system downtime since the start of APS operation [3.6-23, 3.6-24]. On-going improvements have been implemented and further improvements are planned under programmatic funding that are expected to meet the reliability goals for 150-mA operation.

In the past, coupler failures caused by arcing, excessive ceramic heating, and the sudden appearance of pinhole vacuum leaks in ceramics have been analyzed in order to improve coupler performance. Improved fabrication methods, minor design changes, and improvements in the coupler conditioning process have been utilized to reduce coupler failures for operation up to 100 mA. New couplers are routinely conditioned up to 100-kW input power [3.6-23]. In the ring, the rf couplers are conditioned with 115 mA beam at the beginning of every run and operated at 80-90 kW for 100 mA, depending on the ID gaps and rf voltage.

It is expected that operation at beam currents greater than 100 mA will place additional stress on the existing input couplers by operating them closer to their original rf power design limit of 180 kW [3.6-3]. In studies, the measured cavity input power for 200 mA was about 110 kW (ID gaps open, Fig. 3.6-1). This power is similar to what is estimated at 150 mA with ID reference gaps (gray broken bar in figure). Heating of the coupler ceramics (due to HOM power, which is dependent on the HOM frequency and power level) places additional stress on the input couplers. The additional stress can result in an increased risk of coupler failures. Several design changes and the implementation of an automated conditioning script show promise in improving the power-handling capability and operational lifetime of the couplers. Details are discussed in ref. [3.6-23].

Parallel-Klystron Operation: Presently, APS operates at 100 mA with two of the four klystrons delivering power to the cavities. Two klystrons are sufficient for 150-mA operation. The klystron

power can be reduced by operating three or four klystrons in an alternate mode known as "parallel mode," albeit with a loss of redundancy. Some LLRF changes and software development are needed to improve this mode for use in routine operation. It is expected that these improvements will be funded programmatically.

The present parallel-klystron scheme utilizes one existing phase-control loop at two of the four rf storage ring stations for parallel-klystron phase control, which results in an increase in AC power line-related phase-noise sideband levels of approximately 10 dB over the existing single-ended rf system performance. The existing low-level rf systems will require some level of modification to maintain 60-Hz power-line-related phase-noise sidebands at a level of -50 dBc or better, thereby matching the existing rf system performance when operating in single-ended mode. Also, due to the more complex operator involvement required for the parallel-klystron configuration, automation scripts will need to be developed to assist machine operators in consistent and rapid rf system start-up and reset.

Scraper Chamber: Two double-bladed vertical scrapers and three single-bladed horizontal scrapers are installed in the APS. During operation, one horizontal scraper is inserted to help localize beam losses [3.6-25]. The blades of all the other scrapers are retracted to the full-out position. In high-current operation, a temperature rise to greater than 200°C is observed in the sector 36 vertical scraper tube (red curve in Figure 3.6-4) and is considered serious. Machine studies suggest that the heating is sensitive to local beam steering. Optimizing the local beam steering through the scraper may reduce the heating effects and increase the performance margin as far as the scraper is concerned.

Simulations show that the transverse force exerted on the beam by wakefields induced by the vertical scraper is small compared to other components, but the energy lost by the beam due to the longitudinal wake could result in a serious heat-load problem [3.6-26]. The longitudinal loss factor k_{z0} is computed to be 1.2 V/pC, assuming a zero-current rms bunch length σ_{z0} of 5 mm, and the loss factor scales approximately with bunch length as $(\sigma_z/\sigma_{z0})^{-1.5}$. The power dissipated by the beam can be estimated using $I^2 k_z/(N_b f_{\text{rev}})$, where I is the total beam current, N_b is the number of bunches, k_z is scaled to the bunch length, and $f_{\text{rev}} = f_{\text{rf}}/h$ is the revolution frequency [3.6-27].

An estimated power scaling can be carried out for 24-bunches. From Figure 3.5-20 the rms bunch length for 100 mA is 35 ps (10.5 mm), which gives a loss factor of 0.33 V/pC. For the high-current test, the current was 160 mA with an rms bunch length of 40 ps (12 mm), giving a loss factor of 0.27 V/pC. The dissipated power is about 570 W for 100 mA and would be expected to be about 1.1 kW for 160 mA. If this power is dissipated in the small volume between the scraper and the housing, undesired heating can result. The scraper tube temperature rise due to this beam power has not been simulated, but from Figure 3.6-4, the temperature rise is about a factor of two from 100 mA to 160 mA in 24 bunches. This appears to be consistent with the rough estimate of the beam-induced power.

Preliminary work has been carried out on a new conceptual design that mitigates the heating effects. Simulations show that a reduction of k_z by a factor of six can be achieved [3.6-27]. No further work is planned at this time to develop a mechanical design.

It would be valuable to directly measure the HOM spectrum in the vertical scraper chambers where heating is critical. As an illustration of the usefulness of such diagnostics, we designed and installed a collimating horizontal scraper chamber with built-in electric-field pickups. We can observe beam-driven HOMs in the pickup spectrum as a function of scraper position, shown in Figure 3.6-8.

The HOM spectra show about five peaks with moderately high quality factors. In contrast to the vertical scrapers, the horizontal scrapers do not exhibit excessive heating.

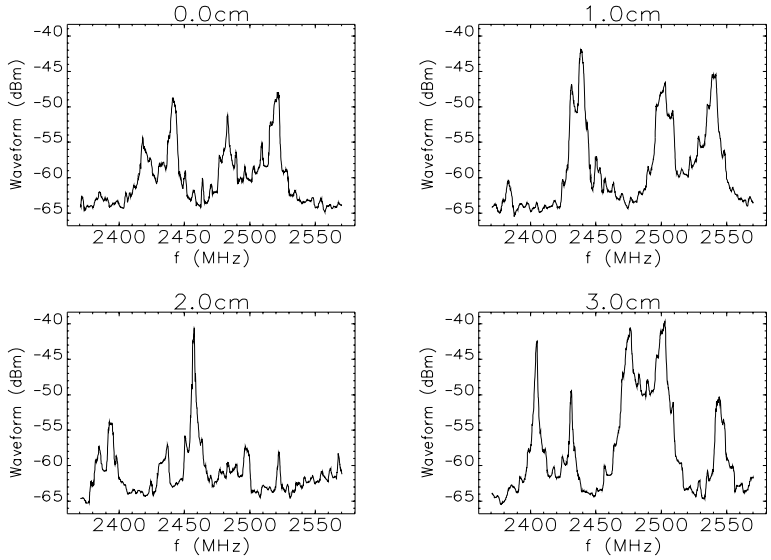

Figure 3.6-8. Horizontal scraper HOMs vs. inserted position.

HOM Damper Power Dissipation: New HOM dampers are not needed for 150-mA operation. However, the present design exhibits beam-induced heating in one of the four dampers above about 164 mA in 24-bunch mode. There are no heating issues for the 324-bunch or hybrid user operating modes at 150 mA.

Since the coaxial damper is inherently a broadband device and its power measurements are made using calorimetry, it is difficult to evaluate the frequencies of the modes that are being absorbed or to measure their power levels to a precision greater than tens of watts. During typical operation with a 24-bunch fill pattern, the damper ceramic dissipates roughly 100 W of power. In the high-current studies, the damper ceramic dissipated over 250 W of power, which has been designated as the limit to protect the damper.

The HOM damper power dissipation is reproducible over time, as shown in two sets of data acquired several years apart (see Figure 3.6-9). We are confident that 150-mA operation will keep the HOM damper power below their limits under otherwise normal machine conditions.

Preliminary work on a new HOM damper design has been carried out under programmatic funding that addresses the heating issues, and its design goal would be to enable beam operation up to 200 mA. The new damper designs are inductively coupled and include a detachable rf load that enables mode spectral data to be extracted to address the rf diagnostics limitations of the present HOM dampers. A full discussion is beyond the scope of the APS Upgrade; details on the new HOM damper design can be found in ref. [3.6-28].

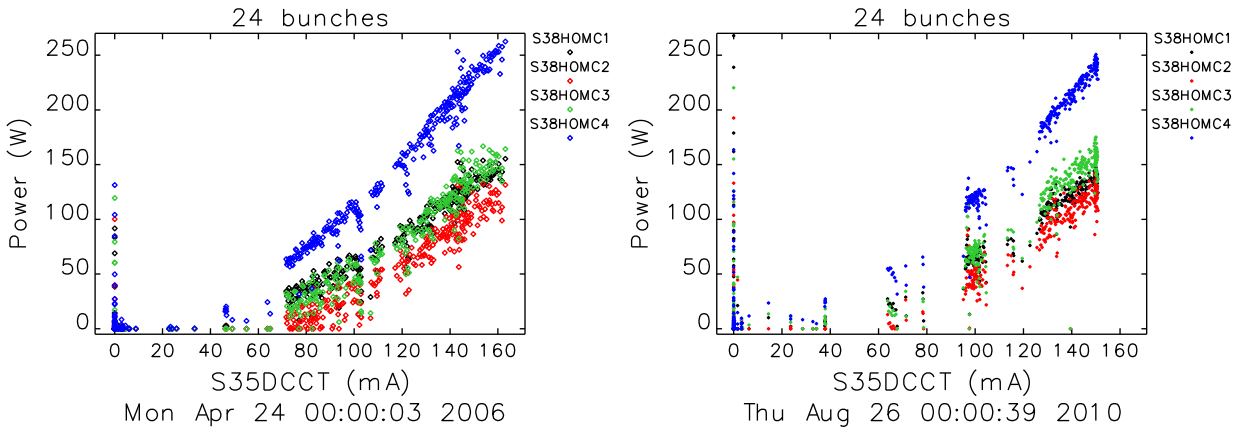

Figure 3.6-9. Power dissipated in HOM damper ceramic body for 24-bunch-mode as a function of current. The data are reproducible, as acquired on different dates, four years apart.

Other Considerations The HOM dampers are expected to stabilize the beam against longitudinal coupled-bunch instabilities at 150 mA in all user modes. Wakefield heating is possible in other, non-rf system components. Long periods of storing 150 mA with top-up injection are planned in order to monitor wakefield heating at longer times scales, to condition the rf system, and to study overall accelerator reliability. This effort will carried out under programmatic funding.

Higher chromaticity is needed for transverse stability with 150 mA. Optimization of the transverse feedback system can potentially further reduce the chromaticity and improve the beam lifetime; this can also simplify upgrade lattice development. This effort will be carried out under programmatic funding. Shorter beam lifetimes will increase beam losses and potentially impact operation of the undulators. An improved collimation system is planned under programmatic funding.

3.6.5 References

[3.6-1] Advanced Photon Source Safety Assessment Document. Technical Report APS-3.1.2.1.0, Rev. 3, APS, (2006).

[3.6-2] D. Horan and E. Cherbak. Parallel Klystron Operation at the Advanced Photon Source Storage Ring, Proc. of PAC 2001, p. 990, (2001); http://www.JACoW.org.

[3.6-3] P. Brown et al. Status of the LEP Accelerating Structure, Proc. of PAC 1989, p. 1128, (1989); http://www.JACoW.org.

[3.6-4] http://www.aps.anl.gov/Facility/Storage_Ring_Parameters.

[3.6-5] C.-Y. Yao et al. Recent Progress of the Bunch-by-Bunch Feedback System at the Advanced Photon Source, Proc. of IPAC 2010, p. 2803, (2010); http://www.JACoW.org.

[3.6-6] L. Morrison et al. Proc. of MEDSI 2002, p. 34, (2002); http://www.JACoW.org.

[3.6-7] G. Waldschmidt et al. Proc.of PAC 2005, p. 2443, (2005); http://www.JACoW.org.

[3.6-8] C. Doose et al. Proc.of PAC 1997, p. 3577, (1998); http://www.JACoW.org.

[3.6-9] L. Emery. Proc. of PAC 1991, p. 1713, (1991); http://www.JACoW.org.

[3.6-10] T. Smith. Mode Identification and Cavity Stretching for the Prototype Storage Ring Cavity. Technical Report LS-194, ANL, (1992).

[3.6-11] L. Emery. Proc. of PAC 1993, p. 3360, (1993); http://www.JACoW.org.

[3.6-12] K. Harkay. Proc.of PAC 1997, p. 1575, (1998); http://www.JACoW.org.

[3.6-13] K. Harkay et al. Recent measurements of coupled-bunch instabilities and higher-order modes (HOMs) in the APS storage ring. Technical Report ASD/APG/2005-13, Argonne Accelerator Systems Division, (August 11, 2005).

[3.6-14] G. Decker and O. Singh. Method for Reducing X-ray Background Signals from Insertion Device X-ray Beam Position Monitors, Phys. Rev. ST Accel. Beams, **2 (11)**, 112801, (1999).

[3.6-15] P. Matthews et al. Storage Ring Cavity Higher-Order Mode Dampers for the Advanced Photon Source, Proc. of PAC 1995, p. 1684, (1995); http://www.JACoW.org.

[3.6-16] Y. Kang. Damping with Coaxial Dampers in the Storage Ring Cavities of the Advanced Photon Source, Proc. of EPAC 1994, p. 2149, (1994); http://www.JACoW.org.

[3.6-17] Experimental Physics and Industrial Control System, http://www.aps.anl.gov/epics.

[3.6-18] K. Harkay et al. Transverse Multibunch Bursting Instability inthe APS Storage Ring, Proc.of PAC 2007, p. 4360, (2007); http://www.JACoW.org.

[3.6-19] R. Nagaoka et al. Observation, Analysis, and Cure of Transverse Multibunch Instabilities at the ESRF, Proc. of EPAC 2000, p. 1158, (2000); http://www.JACoW.org.

[3.6-20] K. Harkay et al. Impedance and the Single-Bunch Limit in the APS Storage Ring, Proc. of PAC 1999, p. 1644, (1999); http://www.JACoW.org.

[3.6-21] A. Chao et al. Phys. Rev. ST Accel. Beams, **5**, 111001, (2002).

[3.6-22] K. Harkay and V. Sajaev. Transverse Instability Thresholds for the All-ID RHB Lattice and Its Relation to Tune Slope. Technical Report AOP-TN-2008-058, ANL, (2008).

[3.6-23] D. Horan et al. Improvements to the Rf Cavity Input Couplers at the Advanced Photon Source, Proc. of PAC 2009, p. 1005, (2010); http://www.JACoW.org.

[3.6-24] D. Horan and D. Bromberek. Technical Report RFTN-2008-10-13, ANL, (2008).

[3.6-25] M. Borland and L. Emery. Touschek Lifetime and Undulator Damage in the Advanced Photon Source, Proc. of PAC 2005, pp. 3835–3837, (2005); http://www.JACoW.org.

[3.6-26] Y.-C. Chae. The Impedance Database and its Application to the APS Storage Ring, Proc. of PAC 2003, p. 3017, (2003); http://www.JACoW.org.

[3.6-27] Y.-C. Chae. Wakefield consideration on the design of new vertical scraper. Technical Report ASD/APG/2004-02, ANL, (June 30, 2004).

[3.6-28] G. J. Waldschmidt et al. Inductively Coupled, Compact HOM Damper for the Advanced Photon Source, Proc. of 2011 PAC, (to be published); http://www.JACoW.org.

Chapter 4

Experimental Facility Upgrades

4.1 Overview

The experimental facilities section of the APS-U project Conceptual Design Report deals with the new beamlines included in the project, upgrades to existing beamlines, optics and component upgrades that will be required to assure continued operations with enhanced APS operating parameters, and x-ray detector development capabilities required to meet the scientific objectives of the new and upgraded beamlines. The new beamlines and beamline upgrades address new scientific opportunities provided by the enhanced characteristics of an upgraded APS accelerator and are grouped according to the science areas:

- Ultrafast dynamics
- Imaging and coherence
- High-resolution spectroscopy
- Extreme conditions
- Interfaces in complex systems

The APS-U CD-0 document and prior versions of this document had an additional theme, “Proteins to Organisms” that was section 4.7 of the CDR. Beamlines in this area are not being funded through the APS-U because of their life-science-oriented mission, so 4.7 section has been removed. We hope to develop them in partnership with the APS-U and will help to seek funding for them from the appropriate sources.

4.2 Ultrafast Dynamics

4.2.1 Introduction

One frontier for x-ray science in the 21st century is to combine atomic-level *spatial* and *temporal* information in a quest to understand and control the behavior of complex chemical, materials, and biological systems at a molecular level. This quest is being approached by a variety of methods and facilities, but perhaps no probe is as incisive and versatile as tunable, short-pulse x-rays. Tunable short-pulse x-rays provide access to elemental, chemical, orientational, and electronic orbital information for atoms in complex environments on time scales ranging from a few femtoseconds to many seconds.

Worldwide realization of the enormous potential of short-pulse x-rays has led to a flurry of construction of ultrafast x-ray facilities over the past decade [4.2.1-1], culminating in the highly successful turn-on of the world's first hard x-ray FEL, the LCLS at SLAC, in 2009 [4.2.1-2]. These accelerator-based ultrafast x-ray sources fall into two classes: FELs [4.2.1-3] and synchrotron-based laser-slicing sources [4.2.1-4]. FELs and laser-slicing sources differ substantially in their capabilities and specifications. FELs provide ~10^{12}-10^{13} x-rays/pulse, whereas laser-slicing sources provide ~10-100 x-rays/pulse for pulse durations of ~100 fs. The many-fold difference in fluence means that the FEL has the potential to explore x-ray nonlinear phenomena and take single-shot images on a femtosecond time scale, whereas laser-slicing sources will remain a traditional linear x-ray probe for dynamics. Indeed, the remarkable peak brightness of FELs (more than a billion times greater than a synchrotron) may enable single biomolecule imaging at atomic resolution without resorting to crystallization [4.2.1-5] by acquiring a diffraction pattern in a few femtoseconds prior to sample destruction [4.2.1-6]. Interpretation of such scattering patterns remains a significant challenge and sample damage can limit the effective use of the available flux from FELs. The first experiment at LCLS has demonstrated that multiphoton absorption can strip all electrons from a neon atom within a single ~100-fs x-ray pulse—indicating that the target is continually changing during the course of a single x-ray pulse [4.2.1-7]. On the other end of the intensity scale are the slicing sources [4.2.1-8], which have come on-line within the last few years to provide dynamical information on molecular [4.2.1-9], electronic [4.2.1-10], and crystal [4.2.1-11] motions. Due to their severely limited flux, only the most elementary of x-ray methods, x-ray absorption by transmission [4.2.1-7, 4.2.1-9] and diffraction [4.2.1-10], have been used at laser-slicing sources.

Enter the APS-U project, which offers an intermediate and complementary path: tunable, short x-ray pulses of few picoseconds duration containing ~10^{4}-10^{6} x-rays/pulse at a repetition rate (6.5 MHz) ~10^{4}-10^{5} times greater than the laser-slicing or FEL sources. As a result, the average x-ray flux available for ultrafast x-ray experiments at an upgraded APS is roughly equivalent to that at an x-ray FEL, and exceeds greatly that available from laser-slicing sources. This point is illustrated in Figure 4.2.1-1, which shows a comparison of the average flux from the existing ultrafast x-ray facilities in the United States (LCLS and the ALS laser-slicing beamline) with the SPX facility at the APS. Two advantageous features of the SPX are that the relatively modest per-pulse fluence places the APS squarely in the perturbative regime, thus allowing more straightforward interpretation of experimental data, and the high average flux encourages the use of more advanced x-ray methodologies, such as fluorescence detection of absorption, microscopy, and imaging on the nanoscale. While phenomena on the femtosecond timescale are best studied at an FEL, multiple time scales are important in describing complex systems. The APS-U project featuring picosecond, tunable, polarized x-ray pulses via the SPX facility is poised to investigate many interesting phenomena, as discussed in section 4.2.2.

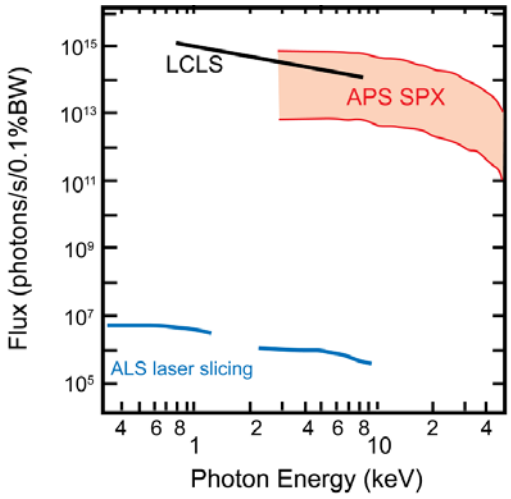

Figure 4.2.1-1. Average x-ray flux at U.S. light source facilities dedicated to ultrafast x-ray science. The projected values for the APS SPX assume Undulator A, 3.3-cm period, 2.4-m length, 100-mA ring current. The SPX upper bound represents a 100 ps pulse and the lower bound a 1 ps pulse at 4MV deflection.

The SPX facility of the APS-U project is based on the innovative method of rf deflection of the stored electron bunches to allow efficient temporal slicing of the relatively long (~100 ps) x-ray pulses at the full repetition rate of the storage ring. This method was originally proposed by Zholents et al. [4.2.1-12] and simulated for the APS storage ring lattice by Borland [4.2.1-13]. Two rf-deflection cavities are used: first to induce a correlation between the longitudinal position of an electron within the bunch and its vertical momentum, i.e., a chirp, and second to undo the chirp, such that the electron trajectory around the remainder of the storage ring is unaffected. Between the two cavities, variable duration x-ray pulses can be selected by slitting the x-ray beam and/or adjusting the rf-deflection voltage to provide, e.g., 1-, 10-, and 100-ps pulses. Many APS users are excited about the possibility of increasing the time-resolution 100-fold in order to visualize molecular and nanoscale motions that are currently blurred on the 100-ps time scale.

The APS can truly be a center for ultrafast x-ray studies on the picosecond and longer time scales due to the resident community, distributed activities, and the SPX facility. A large and diverse user community has been built up over the years, fostered by the advantageous timing structure of the APS storage ring, where the standard 24-bunch operation mode leaves ~150 ns between x-ray pulses. This relatively long period between x-ray pulses, has allowed the development of specialized high-speed chopper systems that isolate a single x-ray bunch in addition to the use of gated commercial detectors to isolate the x-ray pulse of interest. The overall availability of beam time for timing studies at the APS (28 weeks/year) far exceeds that available at other synchrotron sources, e.g., ESRF (~4 weeks/year). The advantageous timing structure is, and will remain, unique in the U.S. for the foreseeable future (standard operating mode at NSLS-II will be 2 ns between pulses). Recent investments over the past few years from the APS and APS partner users have significantly enhanced the capabilities for 100-ps-time-scale x-ray studies, producing upgrades to Sectors 11 and 14 that include dual-undulator sources, new laser systems, and at Sector 7, incorporation of a versatile, high-repetition-rate laser system. The APS time-resolved research community includes leading groups interested in observing dynamical processes on the 100-ps time scale with atomic resolution in biological, chemical, condensed matter, materials, and atomic/molecular systems.

In section 4.2.2 the SPX facility and the associated advanced laser excitation facilities are described. Section 4.2.4 describes enhancements for time-resolved Laue diffraction studies with 10^{10} x-rays/pulse at Sector 14.

4.2.1.1 References

[4.2.1-1] T. Tanaka and T. Shintake, "SCSS X-FEL Conceptual Design Report," Riken, Japan, May (2005).

[4.2.1-2] P. Emma et al., Nature Photonics (2010). Online 1 August 2010; DOI:10.1038/NPHOTON.2010.176

[4.2.1-3] J. Madey, J. Appl. Phys. 42, 1906 (1971).

[4.2.1-4] A.A. Zholents and M.S. Zolotorev, Phys. Rev. Lett. **76**, 912 (1996).

[4.2.1-5] R. Neutze et al., Nature **406**, 752 (2000).

[4.2.1-6] H. N. Chapman et al., Nat. Phys. **2**, 839 (2006).

[4.2.1-7] L. Young et al., Nature **466**, 56 (2010).

[4.2.1-8] P. Beaud et al., Phys. Rev. Lett. **99**, 174801 (2007).

[4.2.1-9] C. Bressler et al., Science **323**, 489 (2009).

[4.2.1-10] T. E. Glover et al., Nat. Phys. **6**, 69 (2010).

[4.2.1-11] S.L. Johnson et al., Phys. Rev. Lett. **103**, 205501 (2009).

[4.2.1-12] A. A. Zholents et al., Nucl. Instrum. Methods A **425**, 385 (1999).

[4.2.1-13] M. Borland, Phys. Rev. ST Accel. Beams **8**, 074001 (2005).

4.2.2 Short-Pulse X-ray Facility [U1.04.02.02]

The principal goal of the SPX facility is to provide picosecond-duration, high-repetition-rate pulses of tunable, polarized x-ray radiation for experiments in chemical dynamics, condensed matter physics, materials science, and atomic physics. The picosecond time scale has unique importance because it is an excellent match for structural dynamics in nanoscale systems and for conformational changes in molecular and supramolecular systems. These areas are of technological relevance, as well as fundamental interest. The experimental facilities associated with the short-pulse x-ray source will combine picosecond temporal resolution with atomic-scale spatial resolution, elemental specificity, and nanoprobe capabilities, to enable an understanding of the relationship between structure and function in complex systems.

The SPX facility is designed to take advantage of the unique features of the SPX source, the most important of which is that the SPX produces short-duration x-ray pulses at the full 6.5-MHz repetition rate of the APS. The high average x-ray flux is conveniently parceled in bunches of 10^4-10^6 x-rays/ps pulses to provide a gentle, linear x-ray probe for viewing dynamics on an atomic-length scale. The additional features of variable x-ray pulse duration (controlled by the magnitude of the rf deflection) and straightforward tunability of photon energy, polarization, bandwidth, and spot size make this source of short-pulse x-rays very versatile. The advantageous timing structure of the storage ring makes it straightforward to select variable repetition rate as required for different systems. The maximum repetition rate is ideal for flowing gas and liquid phase samples and for emerging nanoscale devices operating in the terahertz domain.

The SPX facility will potentially provide five independent beamlines (three hard x-ray insertion device and two bending magnet beamlines) feeding seven independent end stations to provide time-resolved diffraction, microscopy, spectroscopy, and novel time-dispersed diffraction capabilities. Dynamics are typically initiated with optical laser pulses, which can be used to generate radiation from the terahertz through the extreme ultraviolet for excitation of electronic, vibrational, and rotational degrees of freedom. The time scale for implementation of the SPX source overlaps well with emerging high-repetition-rate optical laser sources that can already produce *sub-picosecond* 10-μJ pulses at repetition rates up to ~80 MHz, as described in section 4.2.2.6.2. Indeed, research and development can be carried out on high-repetition-rate excitation and detection schemes prior to SPX implementation because a high-repetition-rate, 10-ps laser system (50 kHz – 6.5 MHz), synchronized (~250 fs) to the x-ray pulses, is already installed at APS Sector 7.

Figure 4.2.2-1 shows a potential layout for the SPX facility with beamlines, end stations, laser laboratories, and experimental control rooms. This layout assumes a site for the facility in Sectors 6 and 7 on the APS experimental floor with the rf cavities placed in the downstream ends of long straight sections at Sectors 5 and 7. Both of the straight sections as well as both of the bending magnets of Sectors 6 and 7 will have the chirped electron beam and produce short-duration x-ray pulses. Since both Sectors 5 and 7 are planned to have 7.7-m-long straight sections, the siting of the rf cavities in these sectors should still allow standard 2.4-m-long undulators to be used. The engineering consequences of chirping the electron beam on the downstream ID and BM front-end components are under study. The accelerator considerations that dictate the optimal location of the rf cavities are still being determined. At present, a configuration that includes two sectors within the rf cavities is thought to be optimum. The progress of rf cavity R&D within the context of the APS-U project is discussed in Chapter 3.3.

Sectors 6 and 7 are well suited as a location for the SPX beamlines because costs are substantially reduced by the use of existing co-located infrastructure, namely the current suite of x-ray hutches providing front ends and seven independent end stations, advanced timing and laser technology, an adjacent 600-ft^2 laser development laboratory (not shown), and a dedicated rf-power building on the APS

infield (not shown). An alternate site would require rebuilding the entirety of the infrastructure at a minimal additional cost of $6M. The present plans for the facility would use two of the three possible undulator beamlines with the third for future expansion, instrument the 6-BM beamline for soft-x-ray experiments (CAS) and initially use 7-BM for SPX x-ray diagnostics with similar future expansion possibilities. The conceptual design presented here is based on present estimates of the parameters of the SPX source and will be further developed as rf R&D and development of engineering requirements progress.

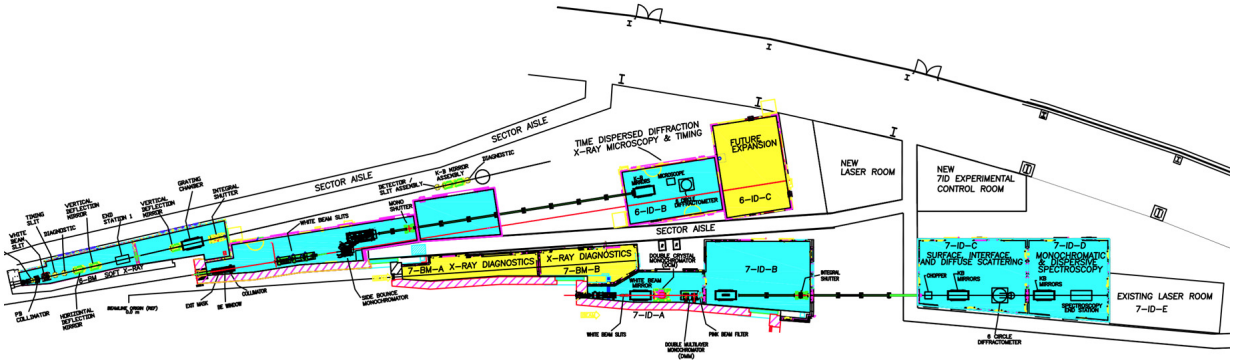

Figure 4.2.2-1. Layout for the SPX facility. Seven independent end stations for short-pulse x-ray studies are planned in the full build-out. Canted undulators in the Sector 6 straight section will provide independent sources for the 6-ID-B beamline and a future 6-ID-C beamline. The Sector 7 long straight section will be the source for the 7-ID-C/D beamline The Sector 6 bending magnet in contingent additional scope (CAS) will deliver soft x-rays while 7-BM is planned for future SPX x-ray diagnostics. Experiments with 100-ps pulses will continue on other APS sectors.

4.2.2.1 Scientific Scope

The SPX will enable researchers to address key challenges in physics, chemistry, materials science, and electronics. The 1-ps time scale has unique importance because it is an excellent match for the dynamics of systems with nanometer-scale lengths and because it bridges the time scales of ultrafast, localized electronic, and atomic motions with those of thermally equilibrated, longer-range dynamics in molecular and supramolecular systems. Examples are shown in Figure 4.2.2-2. Nanometer-scale systems include molecules as well as nanostructures created by both top-down and bottom-up processes. Understanding photoabsorption and subsequent energy transfer and dissipation, as well as electron transport in complex systems will lead to a deeper insight into the structure-function relationship in molecules relevant to efficient solar energy conversion, storage, and utilization. In condensed matter physics and materials science, emerging nanoscale devices operate in the terahertz domain, and the SPX source enables the study of structural, magnetic, and electronic aspects of these devices in real time.

In condensed matter physics and materials science, the responses of materials to applied fields, including mechanical stresses and magnetic and electric fields, provides both useful functionality and a key to understanding the fundamental origin of their functional properties (Figure 4.2.2-3). Materials respond to applied fields by developing strain, electric, or magnetic polarization or dramatic phase changes. The dynamics of the relationships among structure, magnetism, polarization, and applied fields in solids extends from very long times to times as short as 1 ps or less. Applications of the SPX to condensed matter systems are greatly enhanced by an x-ray nanofocusing instrument with simultaneous picosecond time resolution and spatial resolution of tens of nanometers. This unique microscopy capability is not available at any light source; a nanofocused x-ray beam with picosecond resolution will be a unique capability of the SPX. Focused x-ray beams are particularly important because many of the most scientifically and technologically relevant phenomena occur in nanoscale systems.

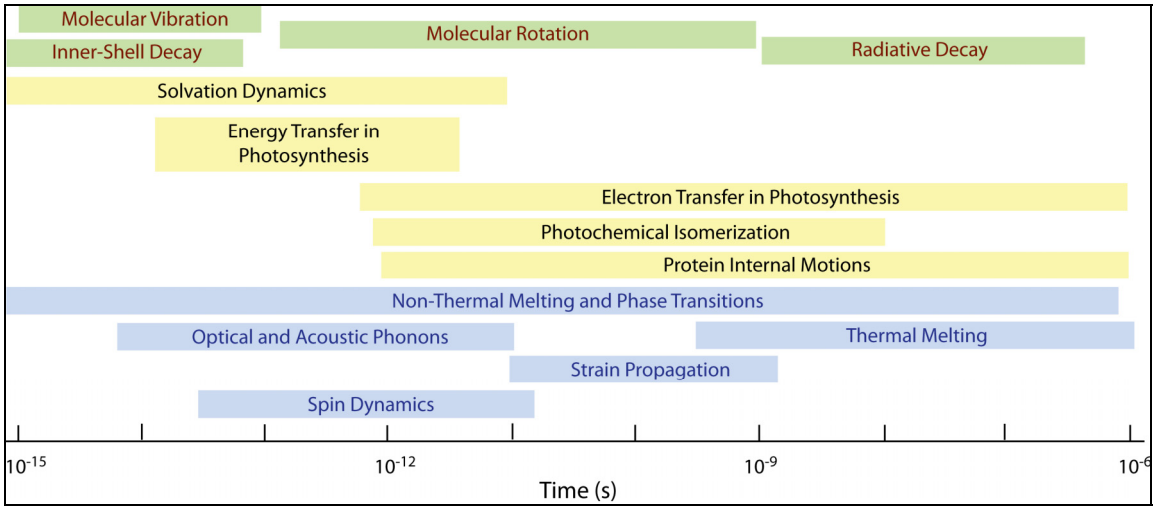

Figure 4.2.2-2. Fundamental time scales for atomic, molecular, and condensed matter processes. Adapted from [4.2.2-1].

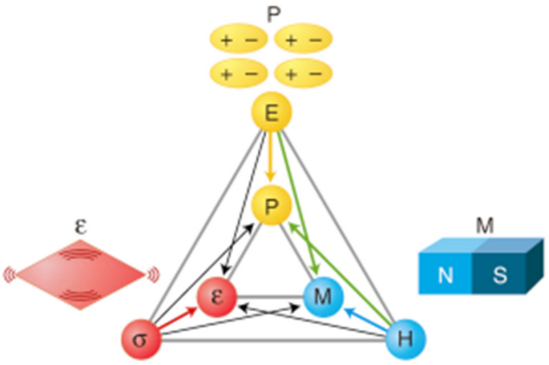

Figure 4.2.2-3. Coupling of magnetic, electronic, and structural degrees of freedom. From [4.2.2-2]

The relationships between applied fields and responses are central to the phenomena underpinning nanomagnetism, nonlinear optical materials, ferroelectric devices, and metamaterials. The responses to applied fields are also the keys to understanding correlated electron systems such as sliding charge density wave conductors, emerging superconductors, and colossal magnetoresistive oxides. Although quantitative tools for probing the magnetism and structure of the ground states of materials are highly advanced, few probes are capable of looking at structures driven into transient states that are far from equilibrium. The SPX facility can address these questions by providing the opportunity to perform time-resolved x-ray-diffraction and scattering-studies of short-lived transient states.

Phenomena associated with domain dynamics and the conventional linear constitutive relations such as elasticity or polarizability all have characteristic time and length scales. The time resolution of structural measurements at the SPX facility will be comparable to the fundamental time scales associated with these phenomena. Electronic and magnetic phenomena can be driven at the high repetition rates available at the SPX and benefit from the inherent versatility of the high-repetition-rate approach. X-rays couple to these phenomena with a wide range of quantitative scattering mechanisms including resonant- and non-resonant magnetic scattering, diffuse scattering, and coherent scattering. Strong coupling

between applied fields and magnetic or electronic response may enable new composite devices on the nanoscale [4.2.2-2]. The additional coupling to strain allows x-ray diffraction to probe dynamical phenomena such as polarization switching. The time scale for polarization switching and lateral domain growth is thought to be set by the speed of sound, typically 1-nm/ps. Picosecond microscopy can probe these dynamics in nanoscale systems.

Spin dynamics in solids occur across a wide range of time scales, with many important processes in the range of 10 ps and below. These phenomena, in many materials, offer potential for creating exotic spin-electronic devices. In semiconductors and metallic systems, the phenomena of interest include spin accumulation, spin injection and propagation, the influence of ultrafast modulation or gating fields on spin populations, and thermal demagnetization processes [4.2.2-3]. Structurally driven magnetic-phase transitions also occur in the 1- to 10-ps regime, and offer insight into the interaction between strain, symmetry, and magnetic order [4.2.2-4]. In many oxide materials, a balance between spin, charge, and lattice degrees of freedom produces a set of interdependent electronic and magnetic phenomena, such as metal-insulator transitions and multiferroic behavior. Optically induced magnetic-phase transitions and spin dynamics may also involve direct coupling of laser fields to the spin-dependent band structure and offer non-thermal control of magnetization at speeds that are unattainable with field- and current-driven approaches [4.2.2-5]. All of these phenomena are ideally suited to x-ray techniques, as they often involve multiple magnetic elements with small moments. A soft x-ray facility with a pulse duration of 1 to 5 ps and polarization control offers the ability to probe these new phenomena with high sensitivity, element selectivity, and at time scales important for understanding their dynamics. Due to the strong interaction of soft x-rays with the unoccupied states in solids, picosecond time-resolved absorption spectroscopy in this energy regime can resolve transient electronic states during structural, chemical, and magnetic phase transitions. Such transient states may be manifested in spin-dependent or spin-integrated spectroscopies.

Continuing to sub-nanoscale molecular systems, the SPX also provides unique opportunities. A long-held dream of chemists is to “see” a chemical reaction take place [4.2.2-1]. X-ray spectroscopy and scattering on the picosecond time scale enables one to capture transient states stroboscopically following photoexcitation. The few-picosecond time scale is particularly suitable for monitoring photoinduced electron transfer and structural reorganization in natural and artificial photosynthetic systems. In solution-phase systems, combining the high-repetition-rate methodology with micron-scale focusing allows a vastly more efficient use of x-ray flux. Simultaneously increasing the repetition rates of the laser and x-ray pulses results in an increase in data rate by a factor of up to 6,500 in comparison with present 1-kHz-scale repetition rates, and thus, a significant gain in statistical quality in a given experiment time.

Achieving control of dynamical processes at the atomic or molecular level is a fundamental and enduring challenge [4.2.2-6]. The 2006 National Academy Report, *Controlling the Quantum World*, poses the scientific issues surrounding molecular-scale control as one of the BES Grand Challenges. Exemplary opportunities arising from quantum control are the potential to steer molecular processes to a desired outcome, and to modify electron dynamics in solid-state systems, e.g., to reduce non-radiative processes in semiconductors and thus enhance solar conversion efficiency. Phenomena arising from quantum control that can be probed using picosecond-duration x-ray diffraction and spectroscopy include laser-dressed, molecular, potential-energy surfaces; the field-free alignment of molecules; molecular alignment in the liquid phase; strategies for controlling and probing molecular vibrational and electronic motion; and gas-phase photoexcitation of photosynthetic molecular systems.

For laser-based control, the combination of ultrashort x-ray pulses from the SPX with excitation in the terahertz frequency regime opens new scientific opportunities. Terahertz radiation directly enables transitions with characteristic energies of several to tens of milli-eV. In contrast to IR/visible excitation, it selectively couples to low-energy transitions without exciting undesired physical and chemical processes. This long-desired excitation scheme yields clean resonant excitation of interesting processes in a wide variety of systems, such as phonons in strongly correlated materials, electron response in quantum

structures and nanomaterials, pair-breaking in superconductors, and chemical reactions in molecular systems [4.2.2-7]. It is possible to excite such low-energy transitions with visible light, but the mismatch in energy scales also fundamentally leads to the possibility of exciting undesired physical and chemical processes. Recently, a mode-selective vibrational excitation at 17 THz was used to control the electronic phase of the manganite $Pr_{0.7}Ca_{0.3}MnO_3$, and to induce a transition between insulating and conducting electronic phases [4.2.2-8], highlighting potential opportunities with terahertz pump/x-ray probe experiments.

In addition to resonant excitation, the intense ultrafast electric field of terahertz radiation on the order of 1-MV/cm represents a novel route to the control of materials and devices. Unlike conventional multicycle laser fields in the visible/IR regime, sub-cycle high-field terahertz pulses can transfer net momentum to charged particles on ultrafast time scales, initiating field-driven dynamics in nanomagnets, nonlinear optical materials, ferroelectric devices, and metamaterials. Excitation in this case inherently occurs across a broad frequency range, and it can lead to structural phase transitions, such as the switching of ferroelectric or ferromagnetic domains, the production of metastable structures, or pair breaking in superconductors. These effects are driven quite rapidly, on the picosecond time scale of the pulse, and as a result, the path of the sample through its phase space can be quite different than with longer-duration excitation. In ferroelectric materials, for example, the coupling between field and strain already allows x-ray diffraction to monitor dynamical phenomena such as polarization switching [4.2.2-9]. Pumping with terahertz radiation presents the possibility to coherently switch ferroelectric materials between structural states by directly exciting the dipole moment of the material at times that can be faster than the relevant phonon modes [4.2.2-10].

The scientific program's x-ray requirements at the hard and soft x-ray end stations are shown in Table 4.2.2-1 and Table 4.2.2-2.

Table 4.2.2-1. Hard X-Ray Performance Requirements for SPX End Stations

Hard X-ray End Station	**Value**	**Comments**
X-ray energy range	4-35 keV	Encompass K-edges of Ti through 2nd row transition metals
Energy resolution, $\Delta E/E$	10^{-4}	Match natural linewidth of 1s-hole states
	10^{-2}	High resolution diffraction Low resolution scattering, dispersive spectroscopy
Pulse duration	1, 10, 100 ps	Variable pulse duration allows optimization for phenomena at different time scales
Spot size	50 nm-50 μm	Variable spot size allows optimization for samples
Flux	10^{11}, 10^{12}, 10^{13} /s	For bandwidth of 10^{-4}

Table 4.2.2-2. Soft X-Ray Bending Magnet Performance Requirements for SPX End Stations

Soft X-ray End Station	Value	Comments
X-ray energy range	250-2000 eV	Encompass C, N, O, S. K-edges: 250-2000 eV Transition metal L-edges: 550-1000 eV Ga, Ge, As L-edges: 1100-1400 eV Rare earth M-edges: 1000-1600 eV
Energy resolution, ΔE/E	0.2-0.5 × 10^{-3}	Matches natural linewidths
Pulse duration	1, 10, 100 ps	Variable pulse duration allows optimization
Spot size	10 × 10 μm	For emission spectroscopies of spin-dependent phenomena
Flux	10^{9}-10^{10}/s	Depending on bandwidth
Polarization	Linear, circular	For spin-dependent phenomena, circular off axis

4.2.2.2 Source Requirements

The scientific scope of the SPX insertion device beamline to be built in 7-ID requires tunable radiation over a photon-energy range of 4 to 35 keV with high photon flux and with no tuning gaps, while the energy range for the 6-ID-B SPX beamline is 7 to 14 keV. For both SPX ID beamlines a permanent-magnet undulator with a period = 3.0 cm meets these energy range requirements, providing a continuous tuning curve with an 11-mm gap. In both sectors revolver undulator periods of 3.0 and 2.7 will provide enhanced brilliance for experiments at energies from 8-14 keV The tuning curves for these undulator periods on a rotator device are shown in Figure 4.2.2-4.

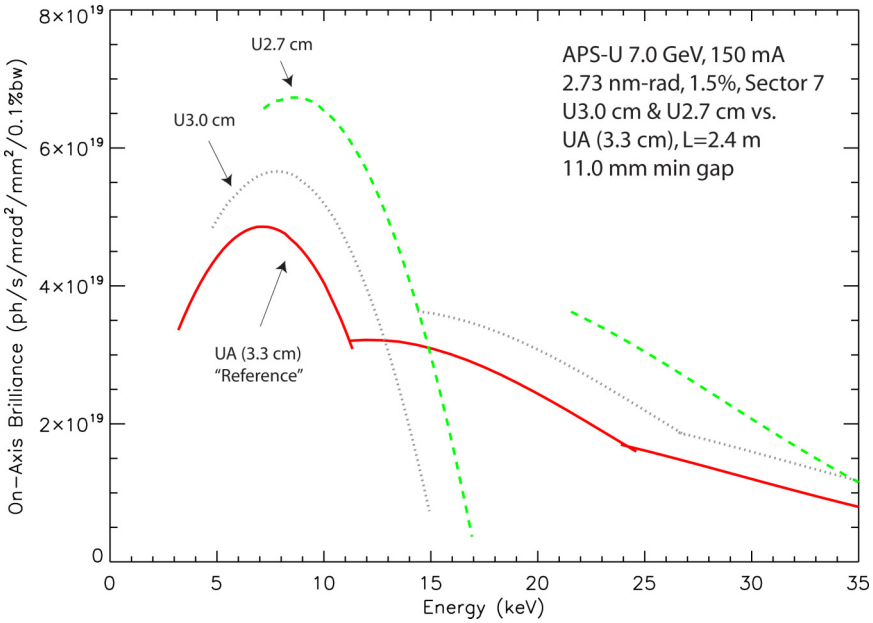

Figure 4.2.2-4. Tuning curves for U3.0 and U2.7 undulators for a revolver undulator device for the two SPX beamlines. The tuning curve for an Undulator A (3.3 cm period) is shown for comparison.

Soft x-ray experiments at the SPX facility could be conducted using a bending magnet source presently in contingent project scope. With the bending magnet source, the 1-ps x-ray pulse duration

through a vertical slit of 0.016 mrad [4.2.2.12] is shorter than that obtained for SPX undulator radiation in the soft x-ray range [4.2.2-13]. Figure 4.2.2-5 shows flux tuning curves for the APS bending magnets in the 100- to 2000-eV range. Across the soft x-ray range of interest, from 100-1000 eV, the flux from an APS bending magnet is approximately equal to that of the flux from bending magnet sources at the ALS.

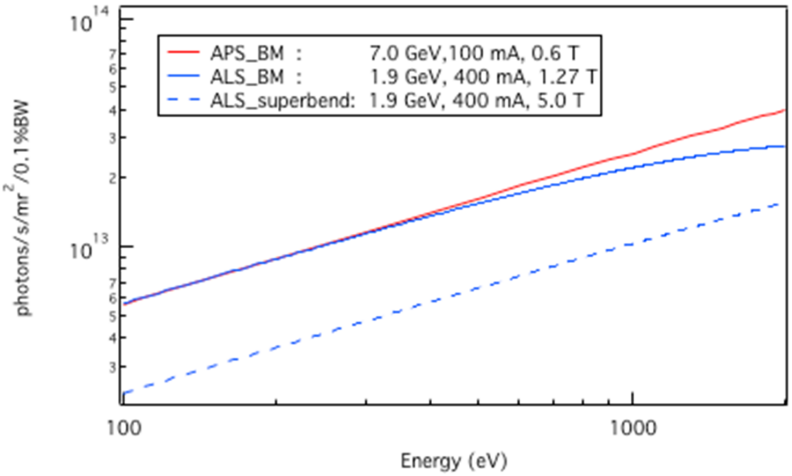

Figure 4.2.2-5. Soft x-ray tuning curves for APS bending magnets vs. ALS bending magnets. From [4.2.2-12].

4.2.2.3 Beamline Description

Picosecond-duration x-ray pulses will be available at the beamlines and experimental stations shown in Figure 4.2.2-1. The SPX uses the existing Sector 6 and 7 experimental hutches. The rf cavities will be placed at the downstream end of the 5-ID straight section and the downstream end of the 7-ID straight section. Two undulators in a canted configuration are possible in the 6-ID straight section but at this point only one of the two canted beamlines will be constructed with the remaining beamline reserved for future expansion based on user demand or future proposed beamlines. The siting of the second cavity in the 7-ID long straight section leaves enough space upstream for a 2.4-m-long undulator providing x-rays to a single beamline at 7-ID.

The two SPX facility ID beamlines provide opportunities to exploit specific features of the SPX source. First, short x-ray pulses are used in the 7-ID-C and D experimental stations with a vertical slit selecting a specific time window out of the radiation fan from the chirped-electron bunches. A front-end vertical slit of 0.5 mm will capture 1% of the radiation and produce x-ray pulses with a duration of 2 ps. The use of slits allows the pulse duration to be varied easily via changes to the rf-deflection voltage. In addition to the strategy based on selecting a portion of the beam using slits, it will also be possible to use a larger fraction of the vertical fan of radiation and to use the correlation of time and space, or angle and time, to capture the time-dependence of the experiment. Transporting the larger vertical fan of radiation is somewhat challenging; an rf-deflection voltage of 2 MV results in a vertical divergence of 0.6 mrad producing a beam height of 16 mm at the beamline window. The conceptual design, however, allows for transport of a portion of the vertical fan through the standard canted undulator front-end mask; a 2-mm vertical aperture at the ratchet wall. Mirror optics provides a focused beam in the 7-ID-C/D experimental station for optimum overlap of laser and x-ray pulses.

In addition to the selection of a segment of radiation using slits, the 6-ID-B beamline provides an alternative strategy to exploit the chirp induced by the rf cavities. The time-dispersed strategy described

below and in section 4.2.2.3.2 takes advantage of a large-offset horizontal-bounce monochromator on the 7-ID-B beamline, which can accept more than a mrad of vertical divergence. A variable-focal-length vertical-focusing second crystal will introduce a time-angle correlation at the focal point of the optics at the sample position of a diffractometer. The large vertical beam required for the 6-ID-B branch beamline will require modifications to the 6-ID front end. The vertical aperture that can be achieved will depend on the details of the canted-undulator front-end and requirements for operations with both the chirped and unchirped beam at the 6-ID beamlines.

4.2.2.3.1 7-ID-C/D Beamline

The 7-ID-C/D beamline will provide picosecond x-ray pulses to the 7-ID-C and -D experiment stations with an energy range of 4.7 keV to 35 keV and a 1-μm spot size. The key components of the 7-ID-C/D beamline are shown in Figure 4.2.2-6 and are listed with their locations and descriptions in Table 4.2.2-3. The standard 0.5-mm-thick Be window seriously affects the beamline performance at energies below 6 keV, transmitting only about 60% of the beam at the low-energy limit of the monochromator (4.7 keV) and might be replaced with a differentially pumped or low-energy-compatible window. Placement of the focusing mirror and multilayer monochromator will depend on the results of ongoing ray-tracing calculations.

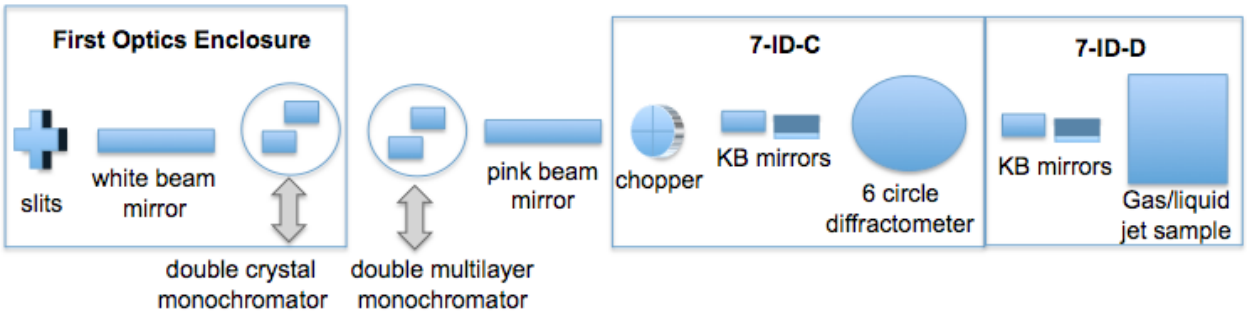

Figure 4.2.2-6. Optics and instrumentation for the 7-ID-C/D beamline.

Table 4.2.2-3. Beamline Components in the 7-ID-C/D Beamline

Component	Distance to Center of Straight (m)	Notes
White-Beam Slits	27	Maximum beam size 2 mm (V) × 3 mm (H)
White-Beam Mirror	28	Collimating, vertically deflecting (up bounce), water cooled, 1.2-m Si substrate, Pt, Ni and Si coatings, 2-mrad incident angle, dynamic bender (4-point), 2-Å surface roughness, and 1-μrad slope error
Double-Crystal Monochromator	30	Kohzu, Diamond 111 crystals, 24-mm vertical offset, water-cooled
Double Multilayer Monochromator	32	24-mm vertical offset, water-cooled Multilayer d-spacing and bandwidth TBD
Filters	33	Diamond, Be, Al, thickness TBD
Pink-Beam Mirror	34	Focusing, vertically deflecting (down bounce), 1.2-m Si substrate, Pt, Ni and Si coatings, 2-mrad incident angle, dynamic bender (4-point), 2-Å surface roughness, and 1-μrad slope error; final mirror position TBD
Vacuum Pipe	35-41	Vacuum through 7-ID-B experimental station
Integral Shutter	40	Shutter/beamstop for mono and multilayer beams
Chopper	49	Isolates single pulses in 24-bunch mode, at up to P0 repetition rate (271 kHz), 10-W power
KB Mirrors	51	Long (0.5 m) KB pair Si substrate, 2-Å roughness, 1-μrad slope error
6-Circle Diffractometer	55	See section 4.2.2.6 Instrumentation (refuburished).
Pink Stop	56.5	
KB Mirror Pair	58	Long (0.5 m) KB pair Si substrate, 2-Å roughness, 1-μrad slope error
Spectroscopy End Station	61	See section 4.2.2.6 Instrumentation (refuburished).
Pink Stop	63	

4.2.2.3.2 6-ID-B Beamline

A diagram of the components of the 6-ID-B beamline is shown in Figure 4.2.2-7 and a listing of the components, their locations, and their descriptions is given in Table 4.2.2-4. The 6-ID-B beamline will provide two capabilities. First, a time-slice of the x-ray bunch can be selected using slits in the first optics enclosure. In a second mode of operation, the complete chirped x-ray pulse will be delivered to the 6-ID-B hutch and focused to produce an x-ray beam in which the arrival time of each photon is correlated with its vertical angle. The correlation of time and angle provides the novel capability for *time-dispersed* diffraction experiments yielding time-dependent structural information via the angular dispersion of the beam.

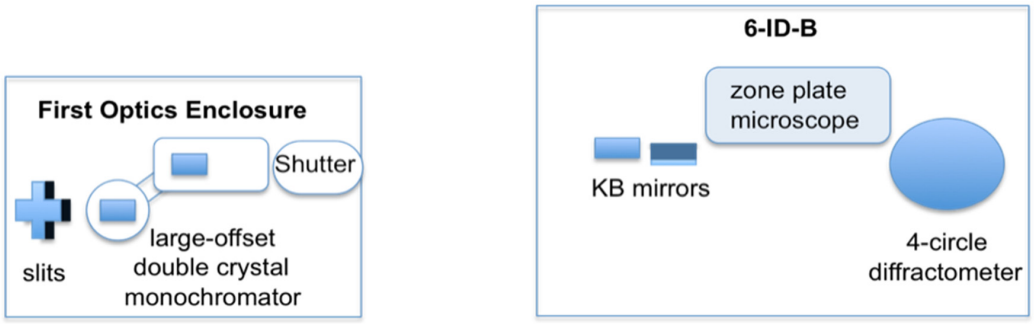

Figure 4.2.2-7. Optics and instrumentation for the 6-ID-B beamline.

Table 4.2.2-4. Beamline Components in the 6-ID-B Beamline

Component	Distance to Center of Straight (m)	Notes
White-Beam Slits	32	Maximum beam size TBD (V) × 3 mm (H)
Side-Bounce Monochromator	37	Large-offset, Si 220 crystals, optional Si 111, 1st crystal water cooled for SPX operation only or liquid N_2 cooled for non-SPX operations, 2nd crystal vertical focusing similar to ESRF design. Si 111 energy range: 4.5-8.3 keV, Si 220: 7.2-14 keV.
Monochromatic Shutter	40	Accommodates full vertical fan
KB Mirrors	57	Long (0.5 m) KB pair Si substrate, 2-Å roughness, and 1-mrad slope error; final mirror position TBD
Zone-Plate Microscopy	60	See section 4.2.2.6 Instrumentation
6-Circle Diffractometer	61	See section 4.2.2.6 Instrumentation

The side-bounce monochromator will have an energy range of 7.2 keV to 14 keV. Standard 0.5-mm-thick Be windows are sufficient at these energies. The placement of the components downstream of the large-offset double-crystal monochromator is still to be determined, depending upon both the vertical aperture and the results of detailed ray-tracing studies.

4.2.2.3.3 Short Pulse Soft X-ray Spectroscopy Beamline [CAS]

The 6-BM beamline will be used to conduct picosecond transient absorption spectroscopy in the soft x-ray range (250-2000 eV), a spectral range where important chemical and material systems have prominent absorption resonances. The bending magnet source has an extended, smooth-tuning profile that is ideal for time-resolved dispersive spectroscopy. Absorption cross sections in the soft x-ray range are large, and as a result, the photon flux required for soft x-ray spectroscopy is modest in comparison with hard x-ray experiments. The spectrograph will be designed with an area detector interchangeable with an exit slit, such that it may also be used as a monochromator at a second experimental station. Components of the 6-BM beamline are shown in Figure 4.2.2-8 and listed in Table 4.2.2-5.

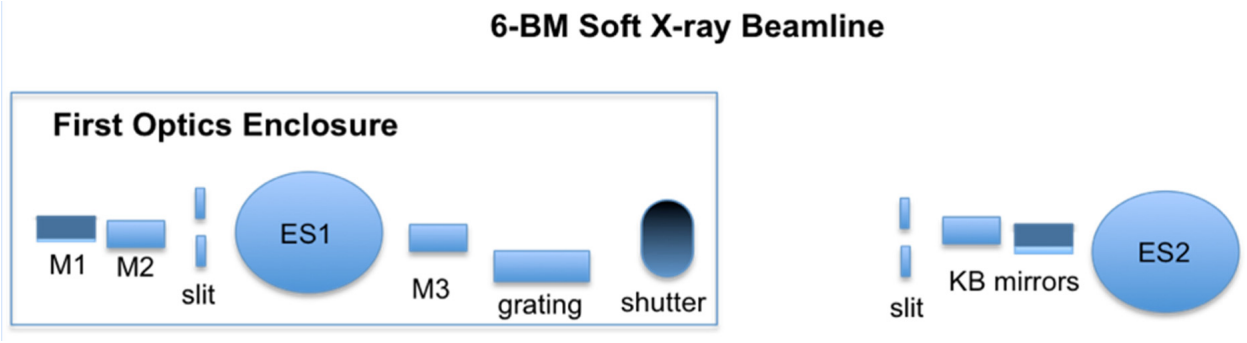

Figure 4.2.2-8. Optics and instrumentation for 6-BM-B.

Table 4.2.2-5. Beamline Components in the 6-BM-B Beamline

Component	Distance to Source (m)	Notes
White-Beam Slits	23	Maximum beam size TBD (V) × 3 mm (H) Polarization defining
M1 Mirror	23.5	Horizontal deflection, focus at ES2, 1.0 deg. incidence, 1-mrad acceptance, 1.5 m, Au coating
M2 Mirror	24.5	Vertical deflection, focus at Timing Slit, 0.7 deg. incidence, 0.5-mrad acceptance, Au coating (>80% reflectivity over 250-2000 eV)
Timing Slit	25.5	Horizontal, defines time slice of chirped beam
Diagnostic 1	26	Au mesh, I_0 monitor
End Station 1 (ES1)	26.5	Sample motion to 10 µm. For example: user-supplied Liq. He cryostat (4.2-350K, 5T horizontal split-coil magnet)
M3 Mirror	27.5	Vertical, 1.25 deg. incidence, figure TBD, Au coating
VLS-PGM	29	Grating chamber (3-4 interchangeable plane gratings, varied line spacing, 400-2400 l/mm)
Integral Shutter	30.5	
6-BM-B Hutch Wall	31.3	
Detector/Slit Assembly	31.5	Area detector, interchangeable with monochromator exit slit assembly
M4,5 KB Mirrors	33	Vertical and Horizontal refocusing mirrors (bendable, for adjustable focal point, 10-µm spot size)
Diagnostic 2	34	Au mesh, I_0 monitor
End Station 2 (ES2)	37	Sample motion to 10 µm. For example: Liq. He cryostat (4.2-350 K, horizontal magnetic field)

4.2.2.4 Optics

4.2.2.4.1 7-ID-C/D Beamline Optics

The primary optical elements in the 7-ID-C/D beamline, as listed above in Table 4.2.2-3, are:

A *collimating white-beam mirror,* which provides a nearly parallel beam of x-rays to the monochromators and other optical components that follow. Coatings (Pt, Ni, and Si) and incident angle (2 mrad) are chosen to allow the mirror to match the energy range of the beamline, 4.5-35 keV, and to discriminate against higher harmonics. Water-cooled, white-beam mirrors using single-crystal Si substrates with dimensions of 10 cm × 10 cm × 1.2 m are already used in a horizontal reflecting geometry at beamlines 2-ID and 12-ID of the APS. Similar mirror systems are employed in a vertical geometry at the APS, at beamline 11-BM and as part of a long KB mirror pair (up to 1 m) at 13-ID.

A *double-crystal monochromator* with diamond 111 crystals, such as the Kohzu monochromator currently in use at 7-ID, will provide monochromatic x-rays with a $\Delta E/E$ energy resolution of 5×10^{-5}. The maximum monochromator angle of 40° gives a minimum energy of 4.7 keV.

A 24-mm offset provides a maximum energy of 35 keV. Diamond crystals presently in use at the APS will diffract only about 40% of the full 2 mm of vertical beam at 35 keV because the beam footprint will be larger than the crystal at this photon energy. Recent reports of larger crystals promise to make higher energies more efficient than is presently available. Diamond crystals with a length of 25 mm are required for the maximum proposed beam height.

A *double multilayer monochromator* with a 24-mm vertical offset will provide x-rays with a larger $\Delta E/E$ of $\sim 1 \times 10^{-2}$. The design of the monochromator and multilayer will take into consideration the energy range required for experiments and the details of the mechanical design.

An uncooled *focusing mirror***,** similar to the collimating white-beam mirror above, but in bounce-down geometry, will follow either the crystal monochromator or second-multilayer monochromator. The placement of the mirror and monochromator will require detailed ray-tracing calculations to determine the beam parameters at the chopper located at the upstream end of 7-ID-C. Two K B mirror systems will be located in 7-ID-C and 7-ID-D. Placement of the monochromators before the focusing mirror simplifies the motions required because no large vertical translation will be required.

4.2.2.4.2 6-ID-B Beamline Optics

X-rays will be delivered to the 6-ID-B beamline by a large-offset double-crystal monochromator. The monochromator is similar in design to the monchromator at beamline 12-ID of the APS, which has a 750-mm horizontal offset and provides energies from 4.5 to 8.3 keV with Si (111) monochromator crystals and from 7.2 to 14 keV at $\Delta E/E$ of 10^{-4} with Si (220) crystals. Lower energies may be accessed by modifying the current monochromator design to allow switching to Si (111) monochromator crystals. A modified monochromator design with a smaller offset or longer second crystal travel range would allow somewhat higher maximum energy operations. The 6-ID-B beamline will employ a modified version of this design that includes a vertical-focusing second crystal. A flexure design in use at the ESRF and a number of APS beamline provides confidence that this change can be made. The beam at the time-dispersed diffraction experiment will be further focused with a KB mirror pair. Specifications of the mirrors, placement of the mirror system, and determining the focal spot size obtainable with this optics design require detailed ray tracing in progress.

4.2.2.4.3 Short-Pulse Soft X-ray Spectroscopy Beamline [CAS]

The beamline design for 6-BM is based upon a variable-line-spacing-plane grating and is similar to that of 29-ID, which is being constructed [4.2.2-14]. Here, an additional experiment station (ES1) is

included before the monochromator to allow the beamline to be used in both dispersive and monochromatic spectroscopic modes. The first horizontal mirror (M1) will accept a 1-mrad fan and focus it at the second end station (ES2). The first vertical mirror (M2) will focus the beam to a time-selecting slit with a demagnification of 10, allowing slicing of the chirped pulse to 2 ps. This approach allows a greater portion of the fan to be collected, while providing high time resolution [4.2.2-15]. This mirror/slit combination, in conjunction with a collimating slit upstream of M1, will allow selection of either on- or off-axis parts of the fan, enabling polarization control. The mirror M3, downstream of the first sample station, will image the timing slit at the monchromator exit slit at unit magnification. The use of a spherical mirror here will allow for converging light at the gratings, resulting in a shorter grating-to-exit-slit distance [4.2.2-16]. The spectrograph/monochromator will have a series of interchangeable plane gratings to cover an energy range of 250-2000 eV. Variable-focus KB mirrors (M4,5) will provide a small beam size (10 μm × 10 μm) at ES2, to maximize flux density. The design goal for the spectrograph/monochromator will be a moderate resolving power of 2000-5000.

4.2.2.5 Anticipated Performance

The anticipated performance of the 7-ID-C/D beamline can be extrapolated from the performance of similar beamlines at the APS and other sources. Although there are, of course, no short-pulse sources in the class of the SPX, many beamlines with similar x-ray optics use standard, unchirped APS undulator sources. At 7-ID-C/D, the diamond 111 monochromator and mirror system will provide a flux of 1×10^{13} photons/s at 10 keV with the full-duration, unchirped, 100-ps x-ray pulses. Beamline mirrors will focus this flux source into a chopper with a 10-μm (V) × 1-mm (H) aperture located 50 m from the source. The chopper will isolate a single pulse in 24-bunch mode where pulses are spaced by 153 ns. Selective exposure of the sample to x-ray radiation will mitigate x-ray-induced sample damage. A picoseconds-duration x-ray pulse, produced by operating the rf cavities at their design field of 4 MV/m and using a 0.5-mm time-resolving slit, will provide a flux of 1×10^{11} photons/s and a similar focus at the chopper.

At 6-ID-B, the large-offset monochromator with Si 220 crystals will have a flux equal to the 7-ID-C/D beamline, with slightly lower photon energy resolution. The larger flux, due to the relatively large angular width of the Si 220 rocking curve compared to diamond 111, is balanced by the inherent polarization-dependent losses of the horizontal monochromator geometry. The total flux transmitted to experiments in 6-ID-B will depend on the vertical opening obtainable in the front end. A large opening to accommodate the large beam produced by the SPX source will not decrease the flux transmitted to experiments in 6-ID-B because the efficiency of the monochromator is nearly independent of the vertical-beam size.

In the 6-BM-A hutch (CAS) it is expected that the flux shown in Figure 4.2.2-4 will be reduced by the angular acceptance of the vertical and horizontal mirrors, the mirror reflectivities, and the timing-slit acceptance. At 1000 eV for 100-mA storage ring current this will be (2×10^{13} photons/s/mrad^2/0.1% BW) × 1 (H) mrad × 0.5 (V) mrad × $(0.8)^2 = 6.4 \times 10^{11}$ ph/s/0.1% BW. For operation at 2 ps the timing slit will reduce the flux by a factor of 100, and for operation with off-axis, circularly polarized radiation, a further cut of a factor of 10, or 6.4×10^8 ph/s/0.1% BW at ES1 is expected.

In the 6-BM-B hutch (CAS) the flux at the second end station will be reduced by the mirror reflectivities and grating efficiencies, and will depend strongly on the line density used. According to the IEX CDR, grating efficiencies of 20 – 35% can be expected with an rms roughness of 3 nm. This results in (6.4×10^8 ph/s/0.1% BW) × (0.2) × $(0.8)^3 = 6.5 \times 10^9$ ph/s/0.1% BW. For operation of the mono-chromator at a moderate resolving power of 2000, the expected incident flux is therefore ~3×10^7 ph/s at ES2. In comparison with the typical signal levels at undulator beamlines (1–100 nA in electron yield, and 10^7-10^8 photons/s in reflectivity), one can expect 1-100 pA in electron yield and 10^4-10^7 photons/s in reflectivity. These levels are challenging, but can be accommodated with careful low-noise data

acquisition designs. Recently, it was shown that XMCD spectra of sufficient quality for quantitative analysis of spin and orbital moments can be obtained in transmission with a laser-bunch slicer with a repeat rate of only 1.5 kHz [4.2.2-17]. In this experiment at BESSY-II, the dynamics of the spin and orbital moments were mapped separately, even using a bunch-slicing technique that only provides $\sim 10^4$ photons/s incident flux. The approach taken here, therefore, offers significantly-higher average-flux ($\times 1000$) while providing high-time resolution.

4.2.2.6 Instrumentation

4.2.2.6.1 Advanced Laser Systems for the SPX Facility

The scientific program for the SPX has several parallels to the challenges articulated in the BES Basic Research Needs reports, which highlight the need for increased understanding and control of matter at the level of atoms, electrons, and electronic spins. Short-duration x-ray pulses have an important role because x-rays provide elemental, chemical, orientation, and electronic information for atoms in complex environments. The ability to obtain such information from x-ray studies on time scales commensurate with atomic motion will be transformational. One versatile means to achieve control of complex processes, or excite the system into non-equilibrium states, is through laser-based control. Laser-based excitation sources will perform two key functions with respect to studies at the SPX: excitation of matter from its equilibrium state, and control of the time evolution of molecular and materials systems using either radiation of specific wavelengths or coherent electromagnetic pulses. While excitation mechanisms using relatively energetic ultraviolet and visible photons have been widely used in laser-pump/x-ray probe experiments, two other excitation strategies, pumping via terahertz radiation and coherent control, are just emerging in conjunction with x-ray probes.

In order to meet the aforementioned scientific challenges, a suite of versatile laser sources is specified. The laser systems are: (1) a high-peak-power, broadband, ultrafast (pulse duration < 50 fs) Ti:Sapphire laser system; (2) high-intensity terahertz sources pumped by the Ti:sapphire system; (3) a tunable ultraviolet-mid-infrared source pumped by the Ti:sapphire system; and (4) a high-repetition-rate, high-average power, sub-picosecond fiber laser. All of these optical sources will be synchronized to the x-ray pulses produced by the SPX with a timing jitter of less than 250 fs using the timing system discussed in Chapter 3.3. Their properties are summarized in Table 4.2.2-6 and a more complete description of these sources and the instrumentation for laser pulse engineering follows the table.

These laser sources will be located in the existing laser enclosure behind 7-ID-D, in a new laser room located between 7-ID-B and 7-ID-C, in a new laser enclosure at the downstream end of 6-ID, or in the case of extreme portability, in the x-ray hutch itself. Optical transports for efficient, safe, and versatile delivery of these pump sources to the desired experiment stations will be designed and installed. Remote controls and diagnostics will be implemented following the example of the existing 7-ID laser system with an improved transport infrastructure. The terahertz and ultraviolet-mid-infrared pump source will be generated close to the experiment site with mobile instrumentation. Some of the fiber-laser systems can also be located in an experiment hutch, due to their compact sizes, eliminating the need for beam transport.

Table 4.2.2-6. Advanced Laser Systems for the SPX Facility

	Wavelength	Duration	Repetition Rate	Power Energy Per Pulse	Remarks
High-Intensity kHz laser	800 nm and harmonics	50 fs	1-10 kHz	> 100 W 10-100 mJ	Some R&D required to push the average power and pulse duration limit
THz source	~100 μm	<1 ps	1-10 kHz	100 μJ per pulse	Pumped by line 1, needs R&D effort
UV-mid IR source	0.2-20 μm	<100 fs	1-10 kHz	Varied	Pumped by line 1
High-power, high-repetition-rate laser	1 μm	<0.2 ps	0.1-88 MHz	>1 kW ~ 0.1-1 mJ	Current state of the art is within a factor of 4 in average power

Multi-kHz, 100-W, high-peak-power ultrafast laser system: This system will serve as a standalone system for direct excitation of samples for high-field and coherent control experiments, as well as the driver for the terahertz and tunable sources discussed above. Technology for all solid state Ti:Sapphire-based chirped-pulse amplification laser systems is evolving rapidly. Such lasers deliver sub-50-fs pulses centered at 800 nm. Ti:Sapphire remains the most versatile system for phase tailoring and frequency conversion via harmonic generation or optical parametric amplification due to its superb broad bandwidth.

Technology and engineering of Ti:Sapphire laser systems are mature. Several commercial laser systems are examined and can serve as a basis for extrapolation. One of them is the Coherent Legend-HE-Cryo [4.2.2-18], which runs at 5 kHz with an average power of 25 W. It requires a cryogenic cooling system to maintain the beam quality. A system without cryogenic cooling running at 10 kHz is also being marketed, delivering 10-W average power. The pulse duration is 40 fs from those systems. The company also makes the RegA system that operates at 250 kHz, with 3 μJ per pulse and 50-fs pulse duration.

The second example is the Thales Alpha kHz system [4.2.2-19]. The options included are 1 kHz/20 W, 5 kHz/40 W, or 10 kHz/30 W, with pulse duration of the order of 25 fs. Focusing to a spot size of 50 μm, the peak intensity is above 10^{15} W/cm^2. These are all diode-pumped, solid state laser systems that demonstrate excellent energy stability and reliability.

High-power, sub-cycle Terahertz source: Development of intense, sub-cycle terahertz sources remains an active R&D endeavor. Although it is, in general, straightforward to generate terahertz radiation using an array of different techniques, for many of the applications envisioned for the SPX, a peak field of over 1 MV/cm is needed. Terahertz sources at this intensity are not yet available.

At present, the most energetic terahertz pulse (100 μJ per pulse, 1 ps, focusing field ~ 1 MV/cm) is measured using a high-power electron beam in an accelerator installation at BNL [4.2.2-20]. Compact devices, based on an electron bunch train, have also been proposed [4.2.2-21]. However, the electron-beam-generated terahertz radiation is normally difficult to access, especially in combination with an x-ray synchrotron radiation facility.

For tabletop terahertz sources that can be readily integrated into the SPX, several techniques can be considered, including photoconductive antennas, and two-color laser-induced plasmas in air and optical rectification. Photoconductive antennas are commercially available with per pulse energy at the pJ to nJ level. The scalability of energy and power is limited by the damage threshold of the antenna material [4.2.2-22]. Laser driven plasmas in air, especially the two-color laser scheme, are an attractive source of terahertz radiation [4.2.2-23, 4.2.2-24]. As recently demonstrated, this technique has generated 2-μJ terahertz radiation using a total pump energy of 30 mJ [4.2.2-23]. One of the major advantages is the

broader bandwidth, up to tens of terahertz over other generation methods [4.2.2-23]. In addition, there is no damage problem with the active medium and the sources can easily be focused (Figure 4.2.2-9 (a)). So far, the most efficient way of converting laser power into terahertz radiation is phase-matched optical rectification [4.2.2-25]. It improves upon the optical rectification scheme by matching the phase velocity of the terahertz radiation and the group velocity of the drive laser pulses. This has led to the generation of 30 μJ of 0.5 THz radiation with a per pulse pump energy of 28 mJ from a kHz Ti:Sapphire laser, a conversion efficiency of about 0.1% [4.2.2-26] (Figure 4.2.2-9 (b)).

Ultraviolet to mid-infrared source: Optical parametric amplification is a mature technique for generating continuously tunable radiation sources and it is fully commercialized. Devices to generate radiation with wavelengths ranging from 200 nm to 20 μm that are tailored for pump sources with different pulse durations and energy are available off-the-shelf from many laser companies. As an example, the tuning curve of the Quantronix Palitra-FS [4.2.2-27] is shown in Figure 4.2.2-10. The system takes up to 20 mJ of pump energy with 130 fs or 5 mJ at 25 fs. For 20-mJ pump pulse at 1 kHz, this will generate 60-μJ pulses at a wavelength of 20 μm with an average power of 60 mW. With proper focus, this is already enough to resonantly excite phonon modes in many materials.

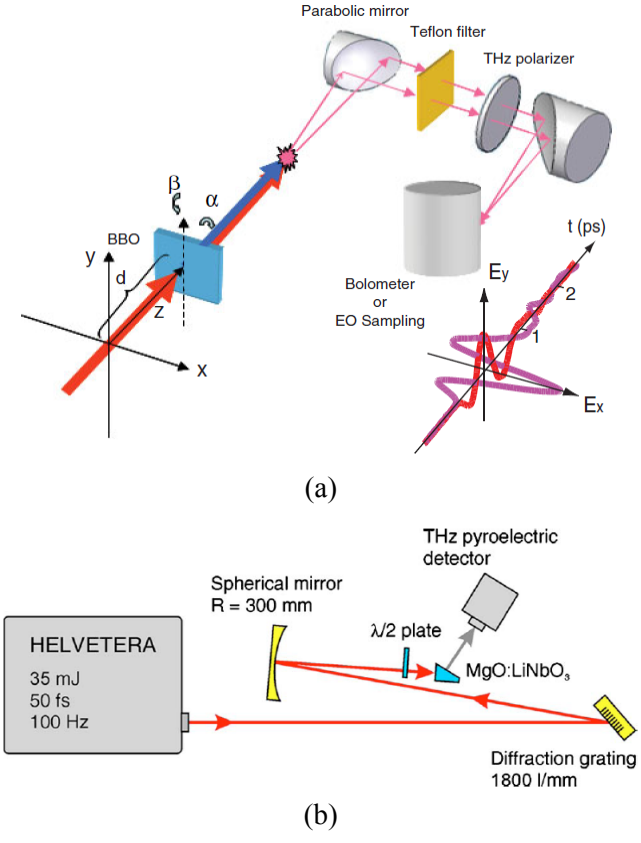

Figure 4.2.2-9. Diagram of generation of high-intensity single- or half-cycle pulses of THz radiation using (a) two-color laser filamentation and (b) phase-matched optical rectification techniques, adapted from [4.2.2-23] and [4.2.2-25], respectively.

High-repetition-rate, femtosecond, MHz, kW fiber laser system: For higher repetition rates that still require relatively large per-pulse energy, but may not require the shortest pulses that Ti:Sapphire produces, fiber lasers are an attractive solution. Fiber-laser systems provide the best stability and normally are very compact devices. The technology has been evolving rapidly in the past few years. In a recent publication [4.2.2-28], a 1.040-μm, femtosecond, chirped-pulse amplification fiber-laser system was

shown to deliver an average power of 830 W at 78 MHz with a pulse duration of 0.6 ps. The per-pulse energy was 10 μJ and the peak power was 12 MW. The authors (Jena University) expect that they can develop a system with over a kilowatt, with a per-pulse energy of 1 mJ.

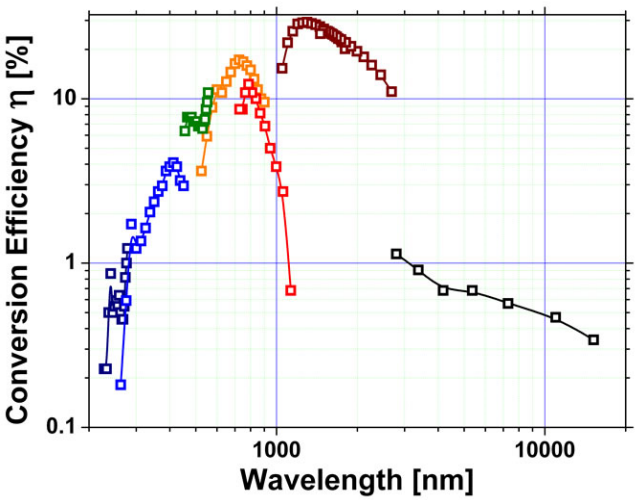

Figure 4.2.2-10. Tuning curve of the Quantronix Palitra-FS optical parametric amplifier, Quantronix, Inc.

There are also commercially available laser systems from several companies. One example is the Tangerine-fs by Amplitude Systems [4.2.2-29]. In very compact formats, the Tangerine emits pulses of 0.7-ps duration, with energy up to 10 μJ per pulse and a pulse rate up to 2 MHz. Another company, Clark MXR, has an Impulse system that delivers the equivalent of 20-W average power, with pulse duration of 0.2 ps [4.2.2-30]. A spin-off company from the Jena group is also marketing custom systems with 50 W of average power [4.2.2-31]. It is noticeable that these systems give the same or higher peak power performance (14 MW and 50 MW for Tangerine and Impulse, respectively) compared with the research system discussed above. It should also be mentioned that both Amplitude Systems and Clark MXR are developing a system with 50-W average power, making it feasible to have a 10-μJ, 6.5-MHz system available for the SPX source.

Two areas of research may significantly improve performance on the time scale of SPX development. They are higher-average power and shorter-pulse length. Scaling the power beyond the kilowatt level and the realization of higher-pulse energies is possible by using appropriate fiber designs with larger cores and reduced higher-order mode contents, including gain and/or loss control. Using these high-average-power large-mode-area fibers will enable ultrashort-pulse fiber systems combining output powers beyond 1 kW and pulse energies in the millijoule range [4.2.2-28]. The technology is already there, and the engineering challenge can be met with R&D, e.g., via SBIR funds from DOE. In addition to the increase in per-pulse energy, it will be very desirable to develop shorter pulses, ~ 100 fs, for these compact and reliable fiber-based systems. The limiting factor here is the limited bandwidth of the fiber-laser material in combination with the gain-narrowing and nonlinear-phase (B-integral) effects in the system.

Laser pulse engineering: For pulse engineering to implement strategies for coherent control of samples, the commercialized acousto-optic programmable dispersive filter (AOPDF) DAZZLER, which uses the transient Bragg effect in a crystal induced by an acoustic wave to manipulate the phase and amplitude of a laser pulse [4.2.2-32] will be used. The technique has proven to be robust in many applications related to laser-pulse shaping and phase control, and is available for lasers with different

wavelengths and bandwidths [4.2.2-33]. In comparison with the liquid-crystal-based spatial light modulator, an AOPDF is advantageous because it has a large tuning range in time and phase.

4.2.2.6.2 End-Station Instrumentation for the SPX Facility

Specialized instrumentation is required for spectroscopy, scattering, diffraction, and nanofocused beam experiments. At the 7-ID-C/D beamlines, spectroscopy and scattering end stations will be developed, primarily using the existing experimental facilities at Sector 7, which have undergone continual development. In 7-ID-C the existing six-circle diffractometer, with refurbishment, will be used in conjunction with advanced-area detectors described below. In 7-ID-D, user-provided liquid and gas-phase jets will be used for spectroscopy and scattering, again in conjunction with advanced-area detectors. Facility-provided instrumentation will include sample positioning to one-micron precision and advanced detectors.

6-ID-B: The development of the 6-ID-B beamline will require the development of two new experimental capabilities. An x-ray nanodiffraction and imaging experiment will provide simultaneous resolution in time and space, with diffraction and imaging modes of operation. The nanofocusing will use zone-plate optics illuminated by a parallel beam from the second crystal of the large-offset monochromator, as in Figure 4.2.2-11. It is important to note that although the vertical divergence of the source is increased by the rf deflection, the source size of the SPX is unchanged to allow nanofocusing. A zone-plate focal length of 5 cm at 10 keV at 39 m from the source will have a demagnification of 650, sufficient to provide a focal spot size limited only by the outer-zone width of the zone plate. The cm-scale focal length of the zone plate will provide suitable sample volumes near the sample for optical or electrical excitation. Provisions will be made for image formation using the transmitted beam and for detection of diffracted beams. A fluorescence-detection capability will be provided to allow detection of time-resolved fluorescence spectra from 50-nm-scale samples.

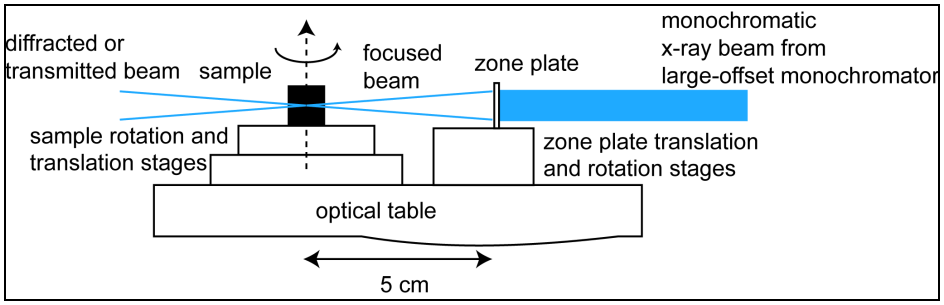

Figure 4.2.2-11. Components of the 6-ID-B nanofocusing experiment.

A second experiment station on the 6-ID-B beamline will be developed to provide time-dispersed diffraction capabilities using the unique correlation between incidence angle and time afforded by the SPX source. The time-dispersed diffraction instrument will include full 6-circle diffraction capabilities coupled with sample excitation, and the required area detector.

6-BM horizontal split-coil superconducting magnet end station (CAS): The first 6-BM experiment station will require horizontal magnetic fields of up to 5 T for biasing of samples during laser-pumped ultrafast transmission XMCD experiments. For this purpose a split-coil cryogen-free superconducting electromagnet will be implemented, with the horizontal field along the beam direction. For these experiments, a wide variety of sample environments and absorption geometries are envisioned, so the system will be designed with maximum flexibility in mind. The instrument will be equipped with a sample cryostat capable of 4.2-350K, polar-angle variability, sample interchange, and access for electrical connections to samples. Axial ports with ±10° acceptance will provide access for the x-ray beam and pulsed laser inputs. Radial ports with ±5° acceptance will also be provided for optical access to the

sample. Fluorescence detection will be provided in one radial port to allow correlation of surface-sensitive information with the bulk-sensitive transmission data.

Detectors: State-of-the-art detection and excitation schemes will be necessary for experiments at the SPX facilities. For SPX operation at the full-repetition rate of 6.5-MHz, or at lower-repetition rates selected by the chopper, standard detectors are suitable. Advanced pixelated *photon counting* detectors, e.g., Pilatus, are required at both 7-ID-C/D and 6-ID-B for detection of fluorescence and scattering from dilute samples. For these pixelated photon-counting detectors, two additional features are desirable: an upper- and lower-level discriminator; and multiple, independently-gateable count registers. Complementary, advanced pixelated *integrating* detectors with large dynamic range and fast readout are desirable for diffraction studies, especially for time-dispersed diffraction. High-repetition-rate time-resolved experiments require lasers for sample excitation with high repetition rates, tunable wavelength, fluence on the order of 1 μJ/1000 μm^2, and synchronization of better than 200 fs with respect to the x-ray pulse arrival.

4.2.2.7 References

[4.2.2-1] M. Chergui and A. Zewail, Chem. Phys. Chem. **10**, 28 (2009).

[4.2.2-2] N.A. Spaldin and M. Fiebig, Science **309**, 391 (2005).

[4.2.2-3] J.M. Kikkawa and D.D. Awschalom, Phys. Rev. Lett. **80**, 4313 (1998).

[4.2.2-4] B. Bergman et al., Phys. Rev. B **73**, 060407 (2006), and references therein.

[4.2.2-5] A.V. Kimel et al., Nature **435** 685 (2005).

[4.2.2-6] H. Rabitz, Science **314**, 264 (2006).

[4.2.2-7] DOE-NSF-NIH Workshop on Opportunities in THz Science, February 12-14, 2004, http://www.er.doe.gov/bes/reports/files/THz_rpt.pdf.

[4.2.2-8] M. Rini et al., Nature **449**, 72 (2007).

[4.2.2-9] A. Grigoriev et al., Phys. Rev. Lett. **96**, 187601 (2006); A. Grigoriev et al., Phys. Rev. Lett. **100**, 027604 (2008).

[4.2.2-10] T.T. Qi et al., Phys. Rev. Lett. **102**, 247603 (2009).

[4.2.2-11] R. Dejus, private communication, 2010.

[4.2.2-12] http://henke.lbl.gov/optical_constants/bend2.html.

[4.2.2-13] M. Borland, Phys. Rev. ST Accel. Beams **8**, 074001 (2005).

[4.2.2-14] B.X. Yang, A.H. Lumpkin, E.C. Landahl et al., Proc. of PAC07, Albuquerque, NM, p 1156 (2007); http://www.JACoW.org.

[4.2.2-15] Conceptual Design Report for IEX.

[4.2.2-16] B. Yang, private communication, 2010.

[4.2.2-17] P. Nachimuthu et al., AIP Conf. Proc. **705**, 454 (2004).

[4.2.2-18] Legend Elite Cryo PA, http://www.coherent.com/Lasers/index.cfm?fuseaction=show.page&id=1019&loc=834.

[4.2.2-19] Alpha kHz Ultrafast Ti:sa series, http://thales.nuxit.net/pdf/Alpha%20kHz%20_%20August%202009%20_%20BF.pdf.

[4.2.2-20] Y. Shen et al., Phys. Rev. Lett. **99**, 043901 (2007).

[4.2.2-21] Y. Li et al., Phys. Rev. ST Accel. Beams **11**, 080701 (2008).

[4.2.2-22] H. Roehle et al., Opt. Express **18**, 2296 (2010).

[4.2.2-23] K. Y. Kim et al., Nature Photonics **2**, 605 (2008); T.-J. Wang et al., Appl. Phys. Lett. **95**, 131108 (2009).

[4.2.2-24] H. Wen and A.M. Lindenberg, Phys. Rev. Lett. **103**, 023902 (2009).

[4.2.2-25] J. Hebling et al., Opt. Express **10**, 1161 (2002); J. Hebling et al., Appl. Phys. Lett., **90**, 171121 (2007).

[4.2.2-26] A.G. Stepanov et al., Opt. Lett. **33**, 2497 (2008).

[4.2.2-27] Quantronix, http://www.quantron.com/products/products.asp?Prd1=PRD-10022&pcat=CAT-10013&Scode=profl.

[4.2.2-28] T. Eidam et. al., Opt. Lett. **35**, 94 (2010).

[4.2.2-29] Amplitude Systems, http://www.amplitude-systems.com.

[4.2.2-30] Clark-MXR, Inc., http://www.cmxr.com/fiberlasers.html#impulse.

[4.2.2-31] Active Fiber systems, http://www.afs-jena.de/Sci-Series.

[4.2.2-32] Dazzler Products for Insertion Before or Inside Amplifiers, http://www.fastlite.com/en/pag13-Dazzlers-for-amplifiers.html.

[4.2.2-33] P. Tournois, Opt. Commun. **140**, 245 (1997); F. Verluise et al., Opt. Lett. **25**, 575 (2000).

4.2.3 *section deleted*

4.2.4 High-Flux Pump-Probe Upgrade (14-ID) [U1.04.02.04]

The 14-ID beamline is part of BioCARS, a national user facility for synchrotron-based macromolecular crystallography and an integral part of the multi-disciplinary Center for Advanced Radiation Sources (CARS) at the University of Chicago. With the ability to isolate a high-flux single x-ray pulse, the 14-ID beamline provides unique capabilities at the APS and in the U.S., and is one of three synchrotron beamlines with similar capabilities around the world (ID09 at the ESRF [4.2.4-1] in France and NW14 at the Photon Factory in Japan [4.2.4-2] being the other two). We are actively broadening our scientific scope to include both physical science and biological time-resolved research, and are currently seeking additional funding elsewhere to support operation of our newly developed physical sciences program. BioCARS has sought and received supplemental funding from the APS in the past. For example, during a recent 14-ID upgrade the APS contributed substantial funds to BioCARS for the design and purchase of two specialized in-line undulators that allow continuous first harmonic coverage over a spectral range of 7-18 keV. We hope to build on this very successful collaboration and to this end we outline modifications to the sector's infrastructure and additional equipment we hope to acquire through the APS-U initiative that will enhance our capabilities to deliver new cutting-edge time-resolved science.

The current 14-ID end station was designed and built in the mid-1990s. The station is small by present beamline standards, which limits the ability to easily accommodate specialized user apparatus such as vacuum chambers and associated equipment. Varied sample environments are critical to the study of real materials under real conditions. Moreover, we seek to increase the sample-to-detector distance for WAXS/SAXS experiments that require high q resolution. We therefore propose to enlarge the 14-ID end station. In addition, we are also requesting an analog pixel array detector (APAD) (if such a detector is not available at the time of the APS upgrade, the second choice is the fastest commercially available large-area CCD detector), secondary focusing, and additional instrumentation often required for complex time-resolved experiments. The present Mar165 CCD detector at 14-ID imposes significant experimental limitations. Its active area is relatively small and limits our crystallographic resolution. With a slow readout frame rate of 0.2 frames/s, this detector is also completely inadequate to address a wide class of important, irreversible systems especially in measurements where the sample is destroyed in a single shot. For such systems, a time-slicing detector is needed to allow a sequence of probe x-ray pulses to interrogate the reaction following a single reaction initiation with a pump laser pulse. This is not possible for reactions faster than 5-10 seconds due to the very slow detector readout and low frame rate of the Mar165. We are therefore restricted to a single pump - single probe sequence, which requires a new sample (or sample volume) for each pump-probe event. The most appropriate is the future, large-area APAD detector, which promises to enhance the frame rate to above 100 frames/s. A fastest-frame rate CCD detector, at the time of the upgrade is our second choice.

BioCARS presented scientific cases to the APS Scientific Advisory Committee for both physical sciences and life sciences. Both proposals referred to the same project described above and each was rated in the top A1 tier of APS-U projects. APS management has decided to split the cost of the project between APS-U funding and future life sciences funding. Rather than partition the costs for the entire project evenly, we have identified those parts of the project that will most benefit the physical sciences and those that benefit primarily life sciences. The enlarged 14-ID-B station and secondary focusing K-B mirror system will be funded directly from APS-U while the APAD detector and x-ray chopper will be funded from life sciences. In this way, the subprojects are decoupled. The following CDR sections describe these upgrades.

4.2.4.1 Scientific Scope

A central theme of the DOE-BES Grand Challenges [4.2.4-3] is to develop methods and tools to characterize and control matter under conditions far from equilibrium. Chemical and material processes,

such as photosynthesis and photovoltaic conversion of sunlight, that involve charge transfer are two such examples of non-equilibrium processes in which photons are converted into chemical energy stored in molecular bonds or directly converted to electrical current. A more recent DOE-BES report, *Next-Generation Photon Sources for Grand Challenges in Science and Energy* [4.2.4-4], identified ultrafast femtosecond x-ray sources as a critical tool for the investigation of the temporal development of systems far from equilibrium. However, the time evolution of many systems including, for example, structural rearrangement and solvent responses during a chemical reaction, can span many decades in time as the reaction proceeds through several intermediate states. Relatively new, laser-based x-ray sources such as the Linac Coherent Light Source (LCLS) allow sub-ps investigations of non-equilibrium processes for the first time and offer ultra-bright x-ray beams. But, as mentioned above, not all such processes require sub-ps time resolution or the highest x-ray brightness. Third-generation synchrotron sources such as the APS remain ideally suited to study materials in the time domain from 100 ps to seconds or even longer. Moreover, third generation, storage ring sources offer high stability in pulse-to-pulse intensity, x-ray energy spectrum and spatial profile of the source. This stands in marked contrast to x-ray-laser-based sources in which the intensity and spectrum can vary markedly from shot to shot, due to the noise amplification characteristics inherent in SASE sources. Our 100-ps time-resolution, single-pulse, high-flux x-ray source at BioCARS Sector 14 is fully operational, and potential projects are abundant in both the physical and biological sciences. Several ongoing projects that illustrate the broad range of experiments in the physical sciences being carried out at BioCARS are described below. All these projects would benefit from the proposed beamline enhancements described in the following sections, particularly the larger 14-ID end station and a faster frame-rate detector.

Nonequilibrium phonon dynamics, David Reis and Mariano Trigo (Stanford University): Recently, the Reis group studied the time dependence of non-equilibrium phonons in InP and InSb after laser irradiation, using an x-ray diffuse scattering technique to image lattice vibrations [4.2.4-5]. In these studies both InP and InSb exhibit strong and complex non-equilibrium redistributions of scattered intensity that persist for several hundred picoseconds after excitation. Using singular value decomposition (SVD), a delayed increase in the transverse-acoustic (TA) phonon population in InP is clearly shown, along with a decrease in the longitudinal-acoustic phonons. This population increase is most significant along the high-symmetry <111> and <010> directions. However, in InSb the TA phonon population is less directional and is distributed more isotropically within the Brillouin zone.

Time-resolved studies of molecular excited states and chemical reactions, Philip Coppens (State University of New York at Buffalo): Small-molecule chemical crystallography studies by the Coppens group aimed at extracting excited state structures [4.2.4-6, 4.2.4-7] have been carried out on $Cu_4I_4(pip)_4$ (pip = piperidine, $C_5H_{10}NH$). These experimentally structures are compared to those derived by calculation and provide direct feedback for improvement of modeling techniques. Small-molecule crystals typically diffract much more strongly than macromolecular crystals and therefore require only a single pump/probe cycle to record an excellent x-ray diffraction pattern on a single CCD frame. For these atomic resolution measurements of chemical processes, the accuracy and repeatability to which a diffraction spot intensity is measured is critical. Kaminski et al. [4.2.4-6] show that the beamline stability is excellent and Bragg intensities can be reproduced to within 2-3%.

Synchrotron Mössbauer spectroscopy using high-speed shutters, Gopal Shenoy (Argonne National Laboratory): A highly novel approach to Mössbauer spectroscopy with synchrotron radiation has been carried out [4.2.4-8] by Shenoy and his team. Mössbauer spectroscopy is normally performed with a four-bounce, ultra-high-energy-resolution x-ray monochromator to reduce the bandwidth of the exciting x-ray beam and allow discrimination in time between the weak decay radiation and the prompt exciting beam, without saturating the detector. Such monochromators are limited to a relatively small range of x-ray energies and therefore restrict the number of Mössbauer-active elements that can be studied. A new method for performing this experiment in which the Jülich chopper is used to block the prompt radiation has been demonstrated using the 14-ID pulse-isolating system. This method is based on mechanically

separating the exciting and decay radiation using the Jülich chopper and notably, will allow the use of standard x-ray monochromators. This opens the possibility of conducting Mössbauer spectroscopy over the full range of Mössbauer-active elements.

Structural dynamics in phase transition of molecular crystals, Lin X. Chen (Northwestern University): Using pump-probe time-resolved single-crystal x-ray diffraction (TR-XRD) techniques at 14-ID, this work investigates the structural origins of a group of photo-switchable organic ferroelectric materials made of small aromatic organic electron donors (D) and acceptors (A) self-assembled into alternating three dimensional DADA… arrays. These arrays are held through hydrogen bonding or electrostatic and van der Waals interactions, resulting in new charge transfer (CT) states. The CT states can be switched on and off by light pulses that shift electron density in the DA arrays, suggesting important applications of these materials in information storage.

Time-resolved x-ray diffraction studies of photoinduced phase transitions in molecular crystals, Eric Collet (University Rennes 1, France): Collet's group aims at understanding the mechanism by which control of a material's physical properties (e.g., magnetic, optical, conduction, ferroelectric, structural) can be achieved using a light pulse [4.2.4-9]. This research is in close connection with the field of ultrafast photoinduced phase transitions and requires an understanding of how electronic excitation relaxes via transient states by coupling to structural degrees of freedom. An example is spin-crossover systems where structural analysis shows that photoswitching dynamics span a wide time range, from molecular transitions (sub-picosecond) to volume expansion (nanosecond) to thermo-switching (microsecond).

X-ray ultrafast many-body physics, Steve Durbin (Purdue University): The Durbin group is studying time-dependent processes in semiconductors using a novel spectroscopic technique that reverses the usual pump-probe order: he utilizes the x-ray pulse as the pump and the laser pulse as the probe by measuring optical absorption in the material as a function of delay time after the x-ray pump pulse. The ultimate time resolution in this technique is limited by the 1.2-ps laser pulse. A manuscript describing x-ray-generated band-tail states in GaAs using this technique is close to completion.

Materials under extreme conditions, Anthony van Buuren (Lawrence Livermore National Laboratory): van Buuren's team from LLNL pursues characterization of the morphology of carbon nano-foams under dynamic loading conditions, with the goal of validating models of void evolution in these important materials. Since the dynamics of the material's collapse upon implosion plays an essential role in achieving inertial confinement fusion, characterizing the performance of low-density materials under these extreme conditions will provide crucial feedback to target designers and fabricators at the National Ignition Facility at LLNL. Recent experiments clearly showed the temporal evolution of this collapse; a manuscript is being prepared.

X-ray diffraction imaging of laser-aligned molecules, Linda Young (Argonne National Laboratory): The quest to image a single biomolecule with atomic-scale spatial resolution has served as a principal motivation for x-ray free-electron laser research, for example, at the LCLS. Orienting each molecule using a strong laser field will remove one degree of freedom thereby simplifying subsequent data analysis. The Young group from Argonne seeks to develop a robust method to orient and determine structures of isolated complex molecules with Ångstrom-level resolution, and are developing this technique at 14-ID.

4.2.4.2 Description of the Existing Beamline

The 14-ID beamline has recently undergone a major upgrade of its x-ray optics and experimental infrastructure [4.2.4-10]. The addition of a K-B mirror system increased the x-ray flux density by a factor of 100 compared to the old setup. A minimum focal spot size of 90(H) × 20(V) μm^2 achieved by the new

mirrors also reduced the minimum opening time of the chopper system, thus allowing the beamline to operate with 100-ps time resolution for nearly 80% of the APS run cycle, taking advantage of both 24-bunch and hybrid modes. For most experiments, the critical parameter is the number of photons per 100-ps pulse impinging on the sample. The 14-ID beamline delivers as many as ~$4 \cdot 10^{10}$ ph/pulse in a bandwidth of ΔE/E~4% at a maximum repetition rate of 1 kHz. By comparison, the LCLS operating in 10-fs mode has a maximum flux of 10^{11} ph/pulse in a bandwidth of 0.5% at a repetition rate of 120 Hz. The near identity of time average flux and photons per pulse in 14-ID and LCLS makes BioCARS a suitable precursor for LCLS experiments that use samples where interesting, slow dynamics occur on time scales >100 ps. Additionally, a broadly tunable picosecond laser system was installed at BioCARS, which makes the temporal width of the storage ring electron bunch the factor that limits the overall time resolution. Each laser pump pulse is synchronized to the time of arrival of the x-ray bunch to within a 10-ps rms jitter and can be delayed relative to the x-ray pulse over a time range from picoseconds to seconds.

Figure 4.2.4-1 shows a schematic of a typical time-resolved, pump-probe experiment at sector 14-ID. Moving from right to left, a high-heat-load chopper reduces power on downstream components to less than 1% of the original power in the x-ray beam. This chopper typically produces a 22-µs burst of x-rays at a repetition rate of 82.3 Hz. Single-pulse isolation is achieved using the fast Jülich chopper, which has a minimum opening time of ~200 ns and can isolate a single pulse from the initial synchrotron pulse train at 1 kHz. Since this chopper is continuously rotating, a second shutter with a millisecond open time acts like the shutter on a photographic camera, exposing the CCD detector on demand to the x-rays scattered by the sample. The laser beam is oriented orthogonal to the x-ray beam and intersects the crystal at the center of the goniometer rotation. Two APS storage-ring modes are used (Figure 4.2.4-1 upper left) for ~100 ps time-resolved experiments at BioCARS. The standard APS operating mode has 24 bunches circulating with 4.25 mA/bunch and 153.4-ns separation between bunches. The bunch length

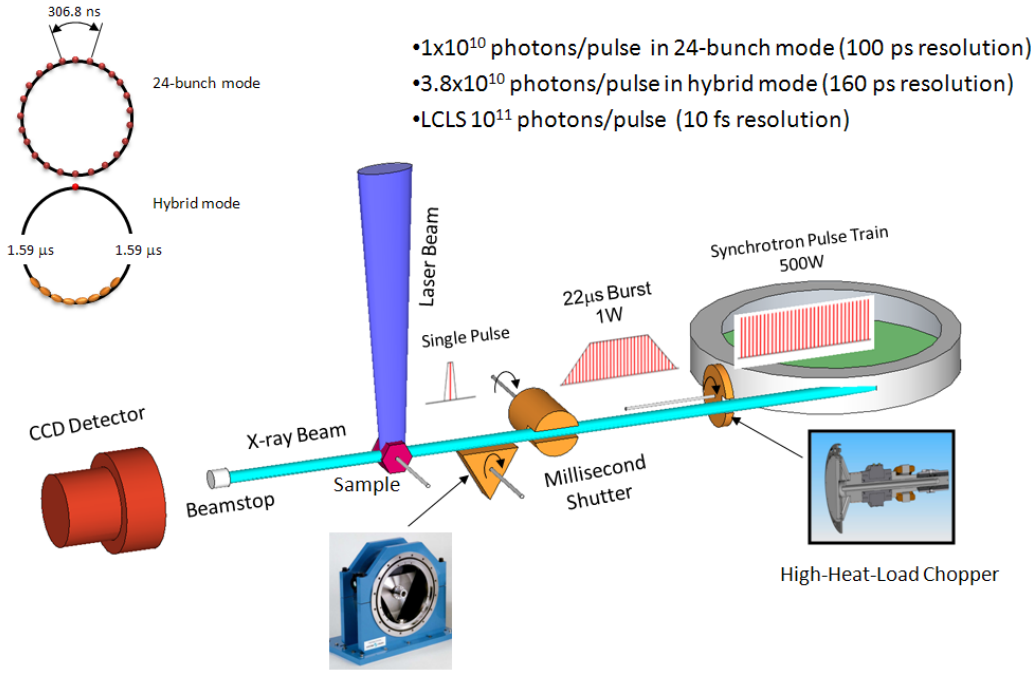

Figure 4.2.4-1. Schematic layout for a typical pump-probe experiment. A chopper/shutter system isolates a single x-ray pulse that is synchronized with the time of arrival of a laser pulse at the sample. The laser pulse can be delayed relative to the x-ray pulse so that the time course of a reaction can be mapped out. Experiments can be performed with 100-ps resolution in either 24-bunch mode or hybrid mode.

in this mode is 79 ps (FWHM). Hybrid mode has a 16-mA bunch separated from adjacent septuplets by 1.59 µs with a bunch length of 118 ps (FWHM). There are three 12-week runs per year at the APS, with hybrid mode accounting for ~19% of the total run cycle and 24-bunch mode accounting for ~65%. In both modes, periodic top-up of the individual bunches maintains the total ring current at 102 mA.

4.2.4.3 Source Enhancements

Not applicable.

4.2.4.4 Beamline Enhancements

Designed and built in mid-1990s, the current 14-ID-B end station is rather small (3×4.5 m^2). Considering the expanding scope of the time-resolved experiments conducted at 14-ID that require additional customized equipment to be located in the end station, the proposed new detector (section 4.2.4.7), and secondary focusing (section 4.2.4.5), a larger end station is clearly necessary. The new station must be large enough to accommodate the additional infrastructure necessary to host complicated sample environments and house a large-area detector system, a laser light delivery system, and secondary focusing to afford focused pink and mono beams with ~10-µm diameter. Time-resolved SAXS/WAXS measurements will also benefit from an expanded q-range made possible by the larger sample-to-detector distances. The proposed size of the new end station is roughly 4×8 m^2. Figure 4.3.2-2 shows the layout of the proposed station with the current station footprint superimposed.

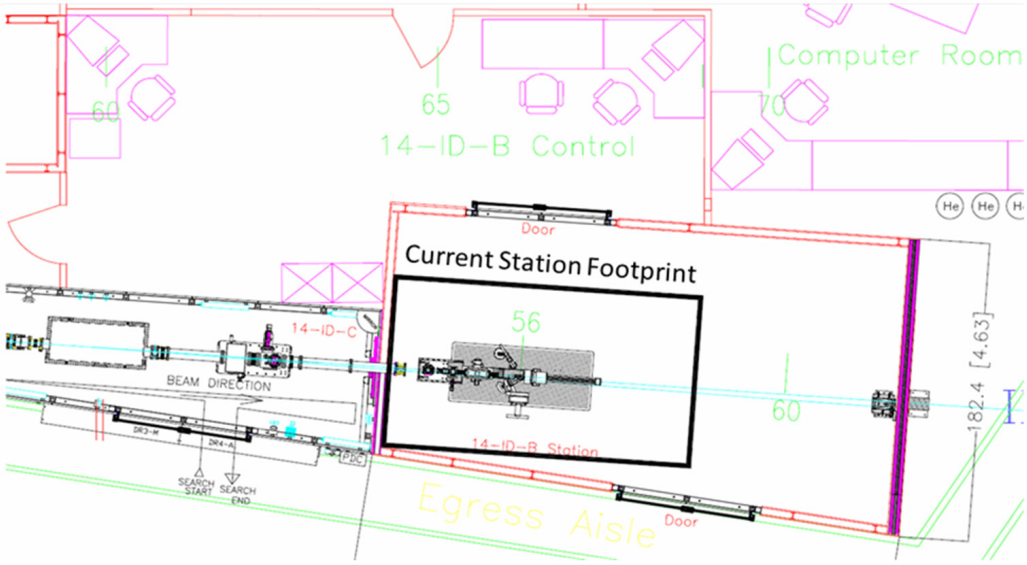

Figure 4.3.2-2. The current station footprint with a bold black outline. The new station will allow the use of an overhead crane and will have two sets of double doors. The current maximum sample-to-detector distance is 0.5 m. The new station will allow distances as large as 4.5 m, greatly expanding the accessible q-range for SAXS/WAXS measurements.

4.2.4.5 Optics

We request a small K-B mirror system for secondary focusing that images the virtual source created by our large K-B mirror system, thereby further demagnifying the source. A smaller x-ray spot size could be achieved by placing an aperture in the x-ray beam. However, this would significantly reduce the flux at the sample position, and high flux is essential for time-resolved measurements. A second K-B

mirror system will allow us to reduce the spot size and increase the flux density at the sample by a factor of ~10.

The ability to provide a smaller x-ray focus is very beneficial to many experiments. For example, the Young experiment (section 4.2.4.1) requires very high peak laser intensity (~10^{12} W/cm^2) to achieve molecular alignment in a gas. This is realized in part by creating a smaller laser focal spot than would normally be used at 14-ID. In order to maximize the signal to noise, the x-ray spot must be as small or smaller that the laser spot in order to only probe the laser-aligned volume of gas. Crystallography will also benefit from a small x-ray spot size. "Standard" crystal size continues to get smaller; therefore, having a small x-ray spot that matches the crystal size will increase the signal to noise in this case as well. Also, large crystals that have poor crystallinity can be composed of near perfect microdomains. Probing the microdomains of larger crystals will be beneficial to time-resolved crystallography, particularly for irreversible reactions.

4.2.4.6 Anticipated Optics Performance

To measure the performance of secondary focusing at 14-ID a small K-B-mirror system was borrowed from ChemMat CARS for testing purposes and was used in an experimental run for the Young group (section 4.2.4.1). The virtual source was demagnified by a factor of 2 in the vertical and 5 in the horizontal and had a measured throughput with pink beam of ~ 0.75 ($flux_{in}/flux_{out}$), effectively increasing the flux density at the sample by a factor of 7.5. This setup was not optimal and could not be used for crystallography given the current component layout in the station. With a larger 14-ID-B station and a reconfiguration of our component layout, this performance could be improved. Figure 4.3.2-3 shows an image of the secondary focus measured by imaging the fluorescence from a YAG crystal with a microscope camera. The focal-spot size was 10(V) × 20(H) μm^2 FWHM.

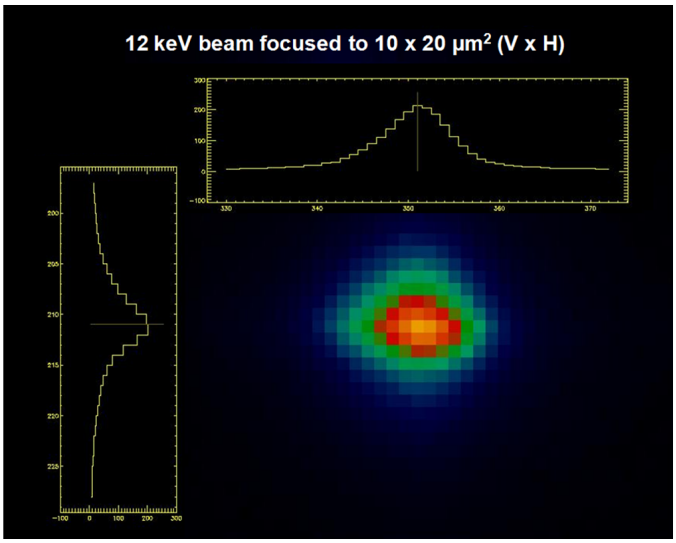

Figure 4.3.2-3. An image of the secondary focus obtained by imaging the virtual source created by the large K-B mirror system.

4.2.4.7 Instrument Enhancements

An ideal x-ray area detector for time-resolved measurements should include the following important characteristics (among others). First, it must have a large area, on the order of 300 × 300 mm^2, to enable high-resolution data to be collected at a large sample-to-detector distance. For crystallography, this effectively minimizes the background and maximizes the mean spot separation. Also, good spatial

resolution is crucial for crystals with large unit cells where many diffraction spots on a single frame may overlap. This leads to the requirement of ~100-μm pixel size. Finally, it must be possible to take multiple consecutive frames with an inter-frame rate as high as possible. As described in the introduction to this section, such time-slicing capability is essential for studies of irreversible reactions. Ideally, the inter-frame rate would be matched to the x-ray pulse frequency of 6.5 MHz in the standard 24-bunch fill pattern of the APS (153.4-ns pulse spacing). This would allow one laser pump pulse to be followed by many probe x-ray pulses, with each generating an x-ray scattering pattern that could be separately recorded and stored. Although such a detector would be capable of isolating data from single x-ray pulses electronically, a mechanical chopper is necessary in some cases to protect the sample from radiation damage due to prolonged x-ray exposure. These characteristics are challenging, but each has been realized technologically, though only in separate detectors. As yet, they have not been combined in a single detector.

Pixel array detectors (PADs), in which each pixel has its own signal processing and readout electronics to enable the pixels to be read out in parallel, are being developed as an alternative to CCD detectors. As a result of their quite different design, PADs are capable of much higher time resolution and faster readout compared with currently available CCD detectors. Recently, the promise of PADs has led to the commercialization of this exciting technology by the group at the Paul Scherrer Institute that developed the PILATUS detector [4.2.4-11]. In groundbreaking work, Sol Gruner's group at Cornell University is developing an analog-integrating PAD, or APAD [4.2.4-12]. The European XFEL project is developing a similar detector for use at the European Free Electron Laser Facility [4.2.4-13]. Although the PILATUS detector and the APAD are conceptually similar and both have analog and digital circuitry, there is a crucial difference between them. The PILATUS is essentially a photon-counting detector, in which absorption of each individual photon produces an electrical pulse that is discriminated by a comparator and counted. The maximum instantaneous count rate of this detector is limited by the temporal width of the electrical pulse to 1 MHz for the PILATUS. In other words, two photons that arrive at a single pixel within 1 μs of each other will be counted, erroneously, as one. This detector is therefore unsuited for the ultrafast time-resolved Laue measurements at 14-ID, where instantaneous count rates can be as high as 100 THz. In contrast, an APAD stores the charge produced by each photon in a capacitor and thus effectively integrates the x-ray flux. An APAD is limited by the well depth (well capacity), or the total amount of charge that can be stored per pixel (proportional to the number of photons absorbed and to the photon energy), and not by the rate at which photons arrive. This version of the PAD is in principle ideal for the time-resolved experiments at 14-ID, where ~5×10^4 photons can arrive at a single pixel within a single x-ray pulse.

Currently, several prototype APADs are being developed and tested: the Gruner/Cornell detector for LCLS use, the ADSC MMPAD, and the European Adaptive Gain Integrating Pixel Detector (AGIPD). Unfortunately, none of these detectors have exactly the specifications required for the ultrafast time-resolved science described above. However, the key elements of the technology are in place and, with sufficient funding, an APAD suitable for time-resolved crystallography experiments can be developed and manufactured.

As mentioned previously, PADs require an appropriate mechanical chopper to protect the sample from radiation damage for the studies of irreversible reactions (Figure 4.2.4-4). The BioCARS ultrafast Jülich chopper is not suitable for these applications, since the minimum time between the chopper openings is 1 ms. The current 14-ID heat-load chopper also has a maximum opening frequency of 1 kHz. A rotating-disk chopper design in which the x-ray beam is perpendicular to the surface of the disk is ideal (Figure 4.2.4-5). For example, a chopper that rotates at 31,822.81 rpm, with a 100-μm slot width and 280-mm disk diameter, would result in an opening time of 223 ns and would enable isolation of a single x-ray pulse at 14-ID in the APS 24-bunch mode. Such isolation is possible because of the vertically and tightly focused x-ray beam at 14-ID (20-μm vertical beam size). Similarly, a slightly slower mechanical chopper was produced by the Professional Instruments Corporation for time-resolved measurement by

Philip Coppens' group (University of Buffalo-NY) at Sector 15 [4.2.4-14]. Many slot configurations are possible, and one is depicted schematically in Figure 4.2.4-5. This particular configuration would produce an x-ray pulse train in which 8 x-ray pulses are logarithmically spaced in time by powers of 2. At the maximum chopper rotation speed, each of the 8 openings would transmit a single x-ray pulse, with pulse spacing of 1 μs, 2 μs, 4 μs, 8 μs, and so forth. If the rotational speed of the chopper is lowered, for example by a factor of 10, the time periods between the x-ray pulses would increase by the same factor, and 10 times slower reactions could be probed.

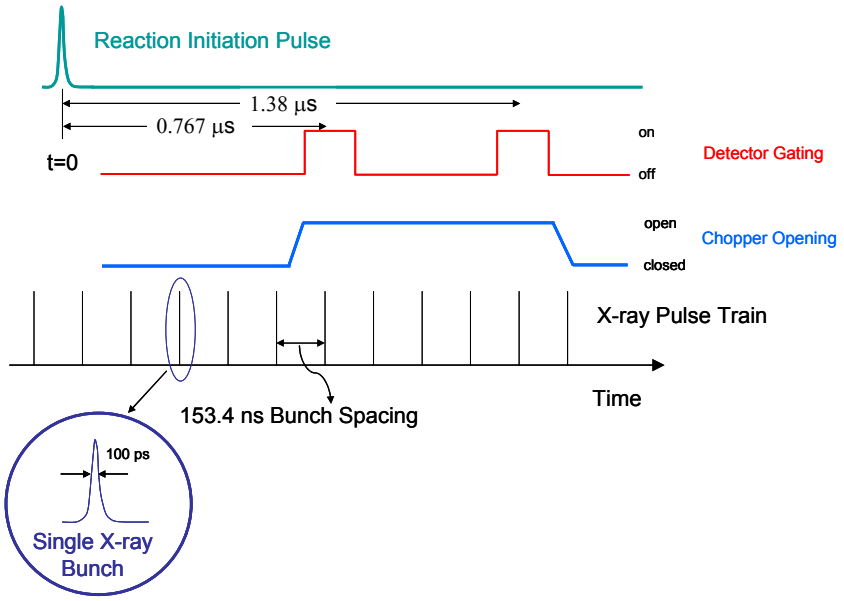

Figure 4.2.4-4. Schematic timing diagram of the 24-bunch mode of the APS storage ring. The image at the foot (black) represents an x-ray pulse train in 24-bunch mode with a 153.4-ns interpulse spacing. The top curve (green) represents the reaction initiation pulse at time t = 0. Two frames of data are recorded at 0.767 μs and 1.38 μs, which are multiples of the interbunch spacing. The detector is synchronized with the storage ring (detector gating curve, red), so that it is recording sometime before the x-ray pulse arrives and is turned off sometime later. In order to protect the sample from x-ray radiation damage, a mechanical x-ray beam chopper is opened during this period (chopper opening, blue).

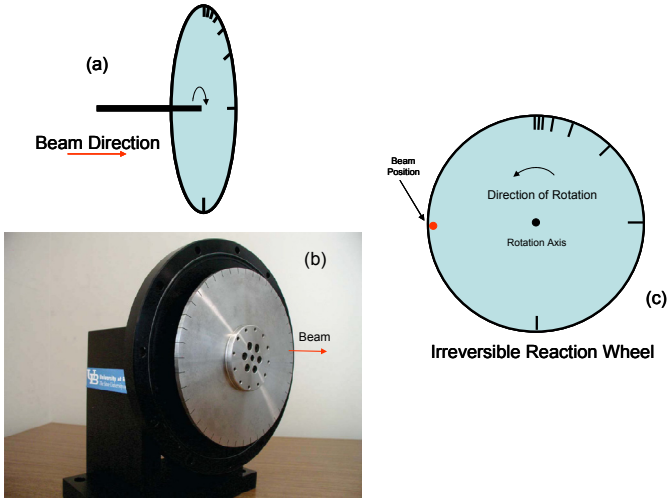

Figure 4.2.4-5. (a) Design of a rotating disk x-ray chopper. (b) Photo of a similar chopper fabricated for experiments by Philip Coppens (University of Buffalo-NY) at Sector 15, with 45 equally spaced radial slots. (c) Possible disk configuration with desirable logarithmically spaced radial slots, each 0.1 mm wide and 2 mm long, starting from the 12 o'clock position.

4.2.4.8 References

[4.2.4-1] M. Wulff et al., Faraday Discuss. **122**, 13 (2002)**.**

[4.2.4-2] S. Nozawa et al., J. Synchrotron Rad. **14**, 313 (2007).

[4.2.4-3] Directing Matter and Energy: Five Challenges for Science and the Imagination, U.S. Department of Energy, December 20, 2007; http://www.sc.doe.gov/bes/reports/files/GC_rpt.pdf.

[4.2.4-4] Next-Generation Photon Sources for Grand Challenges in Science and Energy, U.S. Department of Energy, October 27-28, 2008; http://www.sc.doe.gov/bes/reports/files/NGPS_rpt.pdf.

[4.2.4-5] M. Trigo et al., Phys. Rev. B, **82**(23), 235205 (2010).

[4.2.4-6] P. Coppens et al., Acta Cryst. A **66**, 179 (2010).

[4.2.4-7] R. Kaminski et al., J. Synchrotron Rad. **17**, 479 (2010).

[4.2.4-8] T.S. Toellner et al., J. Synchrotron Rad. **18**, 183 (2011).

[4.2.4-9] L. Guérin et al., Phys. Rev. Lett. **105**, 246101 (2010).

[4.2.4-10] T. Graber et al., J. Synchrotron Rad. **18**, 2011 (in press).

[4.2.4-11] Ch. Broennimann et al., J. Synchrotron Rad. **13**, 120 (2006).

[4.2.4-12] A. Ercan et al., J. Synchrotron Rad. **13**, 110 (2006).

[4.2.4-13] B. Henrich et al., Nucl. Instrum. Methods A, 2011 (in press).

[4.2.4-14] M. Gembicky et al., J. Synchrotron Rad. **12**, 665 (2005).

4.3 Imaging and Coherence

4.3.1 Introduction

When the APS was conceived 25 years ago, there were only a handful of research efforts worldwide that were exploiting the coherence of synchrotron radiation, and only a few research teams that were developing x-ray imaging methods. The situation today is dramatically different: Coherence is routinely exploited for delivering statistical measures of material rearrangement via photon correlation spectroscopy and for producing nanofocus beams, and a variety of imaging methods are now finding regular use across the full spectrum of scientific and engineering research carried out at the APS. The APS-U project will allow us to exploit the improved brightness of the machine, and to develop optimized beamlines and end stations for techniques that were barely even on the horizon when the APS was built.

Kondratenko and Skrinsky [4.3-1] first pointed out that electron storage rings are bright sources of radiation, although x-ray holograms recorded by Aoki et al. [4.3-2] had effectively demonstrated this a few years before. A useful modern picture is to describe spatially coherent modes with an *x-y* phase space area of about λ^2, so that the number of coherent modes can be described by the horizontal and vertical source emittance divided by λ^2, and the spatially coherent flux is described by the source brightness multiplied by λ^2. The original beam parameters of the APS meant that Undulator A emitted into 60×6 modes and a coherent flux of 3×10^{10} photons/second at 10 keV, whereas after the APS-U project, a 3.3-cm superconducting undulator will emit into 27×1 modes with a coherent flux of 1×10^{12} photons/second. The upgraded APS allows for these improved source characteristics to be transferred into high-impact science.

This chapter describes three beamlines that are part of the APS-U project; they fit into two distinct categories.

- The first category involves improved nanoprobe instruments that exploit the short wavelength of hard x-rays for sub-100-nm resolution imaging. Section 4.3.8 describes the *In Situ* Nanprobe, a beamline that uses Kirkpatrick-Baez mirror optics for high flux at 50 nm or better spatial resolution, and zone plate or multilayer Laue lenses for sub-20-nm resolution. This instrument will allow one to work with *in situ* specimen environments such as variable temperature or pressure, or the presence of liquids, for studies of real materials under real conditions.
- The second category involves improved beamlines that exploit the penetrating power of x rays, and the unique electron bunch structure of the hybrid mode in the APS ring, to study large-scale structures and to image processes at time scales as fast as 100 picoseconds. In section 4.3.2 of this CDR, a wide-field imaging beamline is described that will use phase contrast to image phenomena such as crack propagation in energy-saving lightweight materials with a field of view of 1 cm. In section 4.3.4, a high-energy-tomography beamline is described that will provide 3-D views of large, high-density specimens for applications including the study of failure in nuclear fuel rod materials.

Together, these beamlines will make it possible for researchers to use the APS to study length scales ranging from nanometers to centimeters, as is required to gain a complete picture of the hierarchical structure of real materials.

The APS currently has an even broader spectrum of research in imaging and coherence. The GSECARS Collaborative Access Team has been pioneering x-ray tomography and microprobe studies of complex geophysical systems. The CNM/XSD at beamline 26-ID operates a recently-commissioned

nanoprobe aimed at 30-nm-resolution imaging and diffraction studies of nanoscience materials. The Proteins to Organisms program for the APS upgrade (not described in this CDR, because it is not part of the Basic Energy Sciences portfolio) includes a second-generation bionanoprobe that will allow these capabilities to be extended to radiation-sensitive soft materials including biological specimens. These and other APS beamlines will benefit from the cryo-sample preparation facility that is also part of the Proteins to Organisms program.

High-resolution optics are key to many imaging techniques. The APS has pioneered the development of multilayer Laue lenses, which offer a path toward <10 nanometer beams; this is discussed in section 4.8.3. Advances in imaging methods are only possible with new detectors, and these detectors are described in section 4.9.2. Synchrotron x-ray science is entering a new era of complexity in imaging studies, where computational analysis methods must be brought into play so that researchers can pick out the key details from vast datasets; this will rely on the computational resources described in section 5.3.7. These advances, plus developments in specimen environmental chambers described in connection with particular beamlines, mean that the APS will be a leader in using imaging and coherence to study real materials in real time under real operating conditions.

4.3.1.1 References

[4.3-1] A.M. Kondratenko and A.N. Skrinsky, Opt. Spectrosc. **42**, 189 (1977).

[4.3-2] S. Aoki, Y. Ichihara, and S. Kikuta, Jpn. J. Appl. Phys. **11**, 1857 (1972).

4.3.2 Wide-Field Imaging Beamline [U1.04.02.05]

Full-field imaging is an extremely versatile technique that is broadly applicable over almost all scientific and engineering disciplines. Its versatility is reflected by the fact that every major synchrotron facility in the world has a dedicated full-field imaging facility. In many cases, full-field imaging is the keystone linking the sample to other x-ray techniques such as transmission x-ray microscopy, coherent x-ray diffraction, and a host of x-ray scanning techniques such as microfluorescence and microdiffraction.

The new wide-field imaging (WFI) beamline will enable x-ray imaging of cm-sized samples, with a spatial resolution in the 1-10-μm range and exposure times down to 100 ps (APS single electron bunch length) using white beam or 10-60-keV monochromatic x-rays. This beanmline expands the current full-field imaging capabilities at the APS in three crucial aspects: (1) increases the beam size from the millimeter to centimeter scale, (2) increases the sensitivity for phase-contrast imaging, and (3) reduces the source size blurring to the spatial resolution. The scientific research program will focus on the following areas: (a) materials dynamics, including processing and failure mechanisms, (b) transient fluid dynamics and (c) real-time imaging of biological function in organisms. Currently, such a wide-field x-ray imaging facility does not exist in the U.S.

The beam size available will span three orders of magnitude, from the few mm^2 to ~ 1000 mm^2; with the corresponding change in the photon density. The ability to cover such a broad parameter space is important, not just from the perspective of different sample sizes. In many experiments, it is crucial to be able to image a small region with high speeds, while at the same time, having the ability to do tomography over a much larger region; or, high spatial resolution in a small region and a lower spatial resolution over a larger region. One example of this is crack tracking experiments, where, for the dynamics, one needs to image a local region at high speeds using phase-contrast radiography, but, at the end of the experiment, obtaining a 3D CT scan of the entire sample to look at the final crack morphology is useful. Another example is in small animal physiology, where one might want to focus on the dynamics a specific region of the organ (e.g., heart valve), but, at the end of the measurement, a full 3D CT scan of the entire animal (or organ) is needed. The ability to perform both these measurements within a short time frame is crucial to many fields, because, in many cases, the sample cannot be reliably “frozen” for a subsequent visit to another beamline or facility.

The scientific scope reflects the two major themes of the APS-U project: Mastering hierarchical structures through imaging and real materials in real conditions in real time. The science encompasses both basic and applied research, with emphasis on dynamics of “real” systems, such as actual fuel-injector systems and living organisms.

4.3.2.1 Scientific Scope

Time-resolved *in situ* studies of materials

Understanding material dynamics is critical for improving many engineered products with applications in defense and industry. Examples of important material dynamics are those that occur during material processing (e.g., synthesis of metallic foams, coating of surfaces) to those that occur during material failure (e.g., crack propagation in anti-explosive shields or airplane wings). While there has been theoretical and/or computer simulation studies in these fields, there is a dearth of direct experimental data to support or refute these studies. For example, since the materials of industrial importance are mostly opaque to visible light, most experimental work on crack propagation has been limited to surface investigation or measurements by indirect methods [4.3.2-1, 4.3.2-2]. In many of these dynamic systems, x-ray imaging is proving to be the only technique capable of direct visualization at the μm and sub-ms level. However, the small field of view currently available at the APS limits the sizes of

samples and length-scales that can be studied. This limitation is significant because in many of these systems, the length scales of the problem span several orders of magnitude. Furthermore, in most realistic material failure systems, it is not possible to know in advance to the millimeter scale where the material will fail. The proposed WFI beamline will extend the ability to handle larger samples and probe dynamic changes over much larger length-scales. As an example, a University of Michigan group has begun to study *in situ* fatigue damage in single-crystal nickel-based superalloys, which are used in high-duty cycle, high-temperature environments such as in turbines, using WFI [4.3.2-3]. In order to track the initiation and propagation of the fatigue-induced crack, the sample is pre-notched using a laser beam to localize the crack initiation (Figure 4.3.2-1). This requirement cannot always be fulfilled (for example in cases of damage due to ballistic impact) and the laser pulse used for pre-notching can affect the material properties around the notch. A WFI facility will greatly increase the size of the sample that can be imaged and more importantly, will allow investigation of more realistic experimental conditions for material damage.

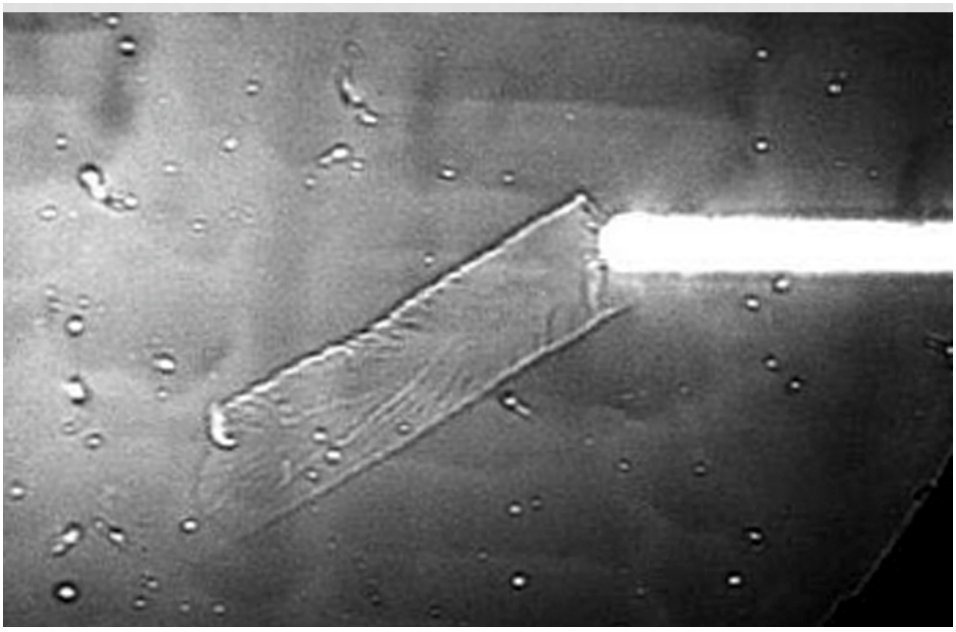

Figure 4.3.2-1. A 23-keV x-ray phase-contrast image of a fatigue crack in a Ni-based superalloy. A notch is required to localize where the crack will start. Image courtesy of Wayne Jones, University of Michigan. The x-ray image allows one to track the internal crack propagation dynamics. Here, one line of the crack front is arrested by a carbide inclusion (arrow). Subsequent tomography of the sample will yield the 3D crack structure. The WFI facility will enable this type of studies to be performed on a realistic sample without the need for the notch.

Dynamics of complex fluid systems

Fluid dynamics is a broad field that is relevant to a wide variety of natural phenomena (e.g., water or oil seepage and flow, physiology, geology) and technological systems (e.g., sprays, fluid transport, mixing). For the investigation of sprays, the majority of experimental measurements have been performed using visible light techniques. Visible light techniques, however, suffer from several major problems. Large refraction and reflection effects make it extremely difficult to visualize fluid surfaces at μm and better resolution. Multiple scattering prevents probing of systems with a large number of free fluid surfaces, such as two-phase (gas and liquid) flow systems. As a result, there is a dearth of experimental data (at the μm and μs scales) in many important phenomena, such as the structure and dynamics of

optically opaque sprays and the impact of liquids on structured surfaces. X-ray imaging has been demonstrated to be a powerful tool for the quantitative measurements of sprays [4.3.2-4]. However, the limited field of view means that in order to characterize the spray, one has to rely on the shot-to-shot reproducibility of the spray system to create a spatial-temporal montage of the spray. The proposed WFI beamline will greatly enhance this capability by its larger beam size and better spatial coherence, enabling sharper images with better contrast and the ability to look at a substantial portion of the spray instantaneously. In many systems of interest, such as automobile fuel injection systems or where the fluid is trapped in a porous geological structure, the fluid is part of a complex system. A particular example is in the case of diesel fuel injectors, where the dynamics of the injector itself is critical to the combustion efficiency and the subsequent amount of pollutants in the discharge. Because the injectors are made of steel and the entire injection cycle is only ~ 1 ms, during which the injector pintle only moves by ~ 200 um, there has not been any direct measurement of the injector dynamics until now (Figure 4.3.2-2). The current field of view is insufficient to track the complete initiation and trajectory of the cavitation bubbles, which directly affects the subsequent spray structure. A wide-field phase contrast x-ray imaging facility will greatly enhance the capability to: (i) Image the internal dynamics from larger spray nozzles, such as those used in gas turbine, furnaces, or automotive electrostatic bell paint sprayer; (ii) probe multiple-stream sprays at once to focus on stream-to-stream variability rather than focusing on single-hole laboratory type injector, which is the current limit; and (iii) characterize the spray further downstream of the nozzle and spray-wall interactions, where aerodynamic breakup and multiple droplets interaction processes are more important.

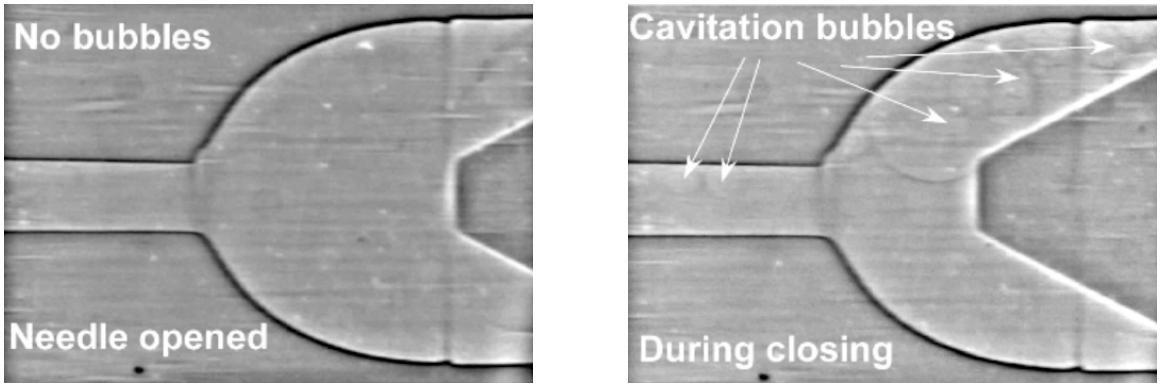

Figure 4.3.2-2. High-speed, phase-contrast images through a 3-mm-thick high-pressure steel diesel injection nozzle. The size of the exit hole (left) is ~200 μm. During the closing phase, cavitation can be seen. The exposure time in these images is 10 μs, and the entire injection cycle is ~1 ms. The current field of view is insufficient to track the initiation and dynamics of the bubbles within the injector. Images taken with filtered white beam; the average energy of the detected photons is ~ 70 keV.

Geoscience is another field that involves complex fluid systems. These systems affect geological phenomena (mudslides, earthquakes) [4.3.2-5, 4.3.2-6], the oil industry (oil extraction), and the environment (methane sequestration and contaminant pathways) [4.3.2-7]. In these types of measurements, there are two key pieces of information that are desired: the 3D structure of the porous solids and the 3D connectivity of the pores or interstitial fluid. Since most geological materials are opaque, hard x-ray imaging is the only non-destructive technique that can obtain such information. However, the present 1-2-mm-sized field of view available at 32-ID is not sufficient because in many cases, the imaged area would not be a good physical representation of the system as only a few grains would be in view. In addition, it is a challenge to obtain pore or fluid connectivity due to insufficient

spatial resolution and contrast. The proposed WFI beamline will greatly benefit this broad field because in addition to the increased beamsize, it will have the best phase-contrast sensitivity in the U.S. This will lead to significantly better phase-contrast imaging and higher spatial resolutions, which are crucial for obtaining micron-level pore or fluid connectivity. Furthermore, the high beam intensity at the WFI compared to other facilities will enable 3D flow dynamics to be measured in real time. Based on the current photon flux estimates, it is expected that complete 3D tomography data at micron-level resolution should be feasible at 10-100 Hz.

Real-time imaging of physiology and biological function in small animals and tissues

Every living organism is the outward physical manifestation (phenotypes such as structure, function or behavior) of the internally coded heritable information (genotype). Today, in biology and biomedicine, some of the most fundamental problems are in understanding the links between genotype and phenotype. Advances in molecular biology have created an avalanche of data on genetic diversity and expression. We remain far from being able to reliably link this new genetic information to the major problems in biology, ranging from basic research questions on biological diversity to applied concerns, such as why one individual but not another becomes ill in response to the same stress. Resolving these genotype-to-phenotype questions requires techniques that bridge the scale of molecular biology with that of organisms. Associated with the biomedical interest in these biological systems is the rapidly growing field of biomimetics and designs [4.3.2-8]. Nature has the great advantage of millions of years of evolution, and, in many cases, has developed materials and designs that are profoundly better than what can currently be manufactured.

Real-time phase-contrast x-ray imaging has been shown to be an excellent technique for studying small animal physiology (Figure 4.3.2-3). However, many samples of biological interest cannot be well-visualized with the current 1 × 2-mm imaging window; increases to cm-sized windows will exponentially increase the type of organisms and structures that can be studied. In addition, most biomedical systems require phase-contrast imaging techniques. The WFI beamline, with its significantly better beam coherence, will enable higher sensitivity and higher spatial resolutions. This type of research has the potential to answer critical questions in a variety of scientific questions, e.g., fundamental metabolic scaling relationships of small animals, environmental and ecological responses of the internal structures of organisms, why some plants/animals survive freezing or extreme heat while others do not, structural effects of disease and real-time effect of medicines in small animals, and *in vivo* dynamic interaction of artificial biomaterials, e.g., how artificial scaffolds interact with bone formation. The new WFI beamline will enable study of the physiology and biological function of small animals, leading to breakthrough results in basic and applied biology, biomedical science, and, via biomimetics, materials science, and engineering.

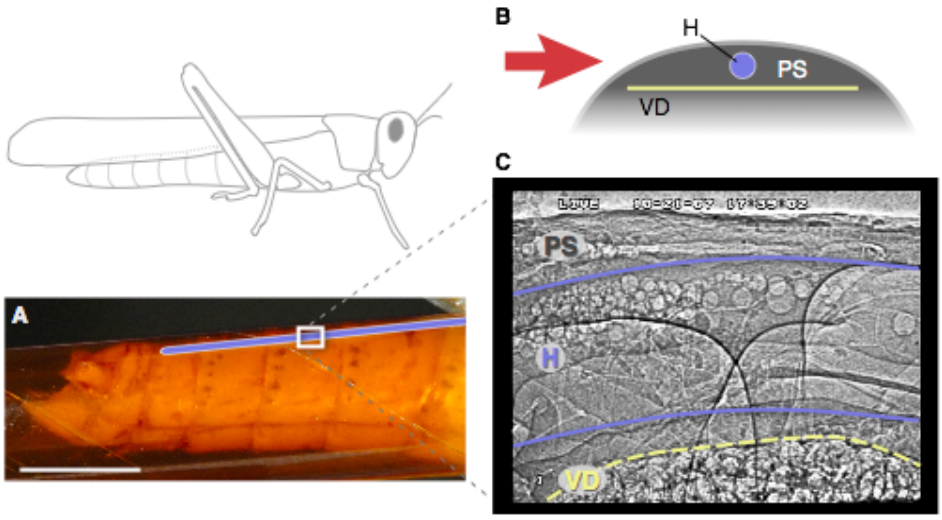

Figure 4.3.2-3. Flow visualization in the heart of a grasshopper (Schistocerca americana) using 25-keV x-rays. (a) Side view of the grasshopper abdomen showing the approximate location of the heart (blue) and the relative size of the imaging window (white rectangle, 1.3 × 0.9 mm). The abdomen is encapsulated in an x-ray transparent Kapton tube. Scale bar, 5 mm. (b), Cross-sectional schematic of the dorsal abdomen showing the relative sizes and locations of the heart (H), dorsal diaphragm (DD), and pericardial sinus (PS). The red arrow indicates the orientation of the x-ray beam. (c) X-ray video still of a region in the dorsal 3rd abdominal segment in lateral view. Round structures are air bubbles used to visualize patterns of heartbeat and hemolymph flow.The current small field of view limits the ability to understand the dynamic relationships between different parts of the heart. The proposed WFI beamline will enable the entire heart structure to be imaged in real time, which will directly answer the question of how the heart functions. Image from [4.3.2-9].

4.3.2.2 Source Requirements

Many of the scientific applications described above require phase-contrast imaging with ~ 1 m sample-detector distances and beam sizes that are in the few cm range. Thus, the two design requirements on the beamline are: (1) a beam size that is ~ 25-50 mm horizontally and 10-20 mm vertically at the end station and (2) a projected source size (Figure 4.3.2-4) at 1 m behind the sample that is no more than ~ 1 μm. In the reduced-horizontal-beta (RHB) mode, the horizontal source size is ~ 120 μm (1-σ value). Thus, to achieve the projected source size requirement, one must go far from the source. At 250 m, the projected horizontal source size in RHB mode at 1 m behind the sample is ~ 1 μm (FWHM). Recent measurements and simulations have shown that at 250 m from the source, the required beam sizes can be reached by tapering the undulators (section 4.3.2.5). The advantage of the undulator over the wiggler is that the photon density is higher for the undulator. Also, the ability to simply increase the beam size by tapering gives great flexibility during operation, enabling the user to choose between a smaller beam but higher photon density (e.g., single shot imaging) vs a larger beam but lower photon density (e.g., small animal imaging). The scientific focus of the beamline is dynamics, and as high a photon flux as possible is needed. Therefore, the current design calls for either a single 5-m-long undulator or two 2.4-m-long undulators. White beam will be available in all the stations. The monochromatic energy range will be 10-60 keV.

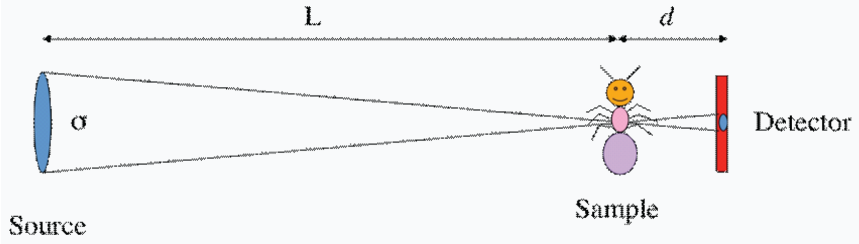

Figure 4.3.2-4. The blurring effect due to a finite source size. For a source-sample distance L and sample-detector distance d, the blur due to the source penumbral angle is σd/L.

4.3.2.3 Beamline Description

The layout of the beamline is shown in Figure 4.3.2-5. It consists of 5 stations, two of which are for optics. The three experimental stations will cover experiments requiring the highest temporal resolutions to those that require less temporal resolution but require a larger beam.

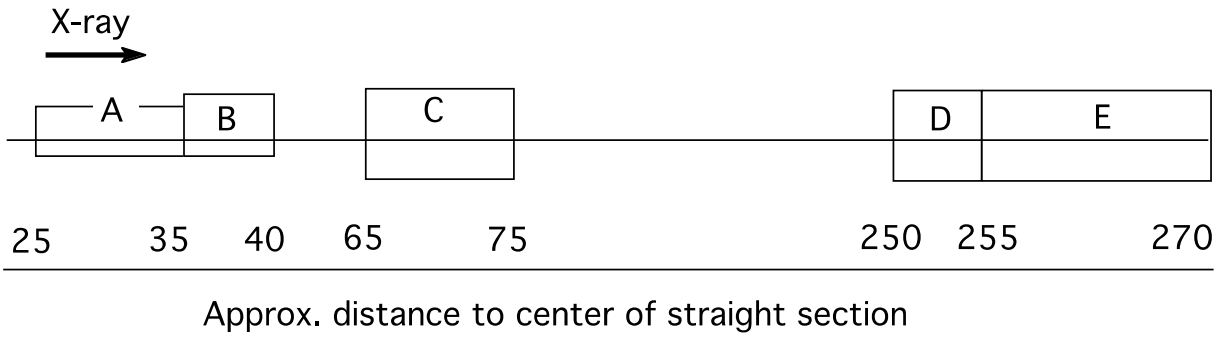

Station	Location	Function
A	25-35 m; 2 m wide	FOE
B	35-40 m; 2.5 m wide	Highest time resolution work
C	65-75 m; 5 m wide	Medium time resolution work
D	250-255 m; 5 m wide	Second optical station
E	255-270 m; 5 m wide	Slow time resolution work

Figure 4.3.2-5. Schematic and description of beamline stations.

The B station will host the single-shot white-beam imaging experiments and serve as a second station for the single-shot (100 ps) imaging program (the other being at the upgraded 32-ID, see Section 4.3.6). Single-shot experiments can currently only be done during the singlet-hybrid mode, where there is sufficient charge in the singlet bunch. As a result, only 2 weeks per run are currently available. Thus, to accommodate more users of this technique, single-shot imaging must be available at more than one beamline. Because it is nearer to the source, the experiments in the B station will not be as good as the E station in terms of spatial resolution for phase-contrast imaging. The E station will serve experiments that require a large beam (25-50 mm H × 10-20 mm V) but less stringent time resolution, such as the majority of biomedical applications. Biomedical applications are usually also the ones that require a larger sample-detector distance for phase contrast, where the long sample-source distance is advantageous. The E station will also serve experiments that require the highest spatial resolution.

Because it is closer to the source, the C station will serve experiments that are in-between. The C station will have a beam size that is ~ 10× smaller than the E station, but will have a corresponding advantage in photon density.

4.3.2.4 Optics

Both white beam and monochromatic (10-60 keV) beam capabilities are required at all the stations. In-line phase contrast does not require a narrow bandwidth. Fabricating perfect multilayers that do not impart unwanted structures in the beam is extremely challenging. Due to the phase-contrast formation mechanism, beam intensity fluctuations in the beam from optics cannot be easily removed. As such, the silicon monochromators will be available, while R&D is being done to fabricate good multilayers. There is place reserved in the optics' stations to add the multilayer monochromator. The E station is far away, and there is a general concern about the possible vibrations from the monochromator in the A station. The D station thus serves as an optics station for the experiments in the E station, if necessary. Having a secondary optics station near the E station is similar to the long beamlines (ID-19 and ID-17) at the ESRF.

4.3.2.5 Anticipated Performance

The anticipated performance of the beamline is shown in Figure 4.3.2-6, assuming the RHB mode, where the horizontal source size decreases from 270 µm to 120 µm, with a corresponding increase in electron horizontal angular divergence from 10 µrad to 26 µrad. For the current 32-ID and BM source, the plot assumes experimental stations at 35 m and 70 m from the source. For the WFI, two in-line 3.0-cm-period, 2.4-m undulators are assumed. The undulator beam size can be increased by tapering the device. The plot includes both untapered and a 1 mm taper over the 2.4 m length of each device. Without tapering, the beam size at 70 m at 20 keV is only 5 mm^2, while tapering increases the beam size to 48 mm^2. For the BM, a 1-mrad horizontal acceptance and 100-mA operation is assumed; while the beamsize

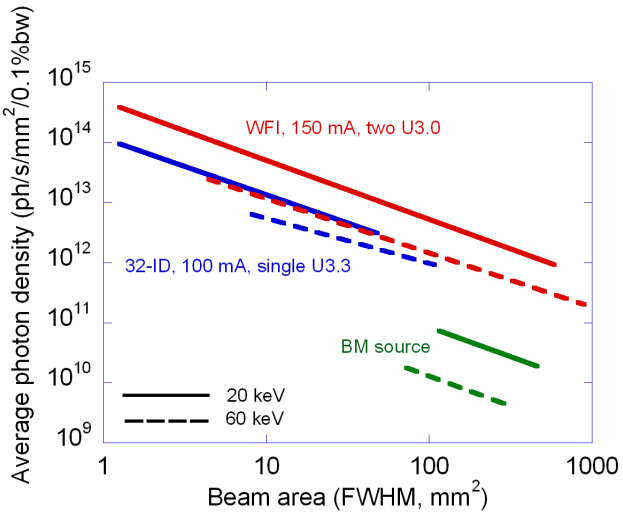

Figure 4.3.2-6. Beam size and photon density (averaged over the FWHM beam size) for the current full-field imaging beamline (32-ID, blue), a typical BM source (green) and the WFI beamline (red). RHB operation is assumed. The solid lines are for 20 keV, while the dashed lines are for 60 keV. The beam size for the BM source assumes a 1-mrad horizontal acceptance. For 32-ID and BM, the plot assumes experimental stations at 35 m and 70 m from the source and 100 mA operation. The WFI beamline includes an experimental station at 250 m from the source and assumes 150 mA operation with two in-line U3.0 undulators.

can be larger, it does not affect the photon density. The solid lines in the figure are for 20 keV, and the dashed lines are for 60 keV. For the proposed WFI, in the 20-keV case, the undulator gap was 13.11 mm (K=1.63, 3rd harmonic), and, in the 60-keV case, the undulator gap was 11.7 mm (K=1.92, 11th harmonic). One key feature of the beamline is that, by using tapering, one has the option of selecting either a larger beam size or a higher photon density, changing each by up to 10×. The WFI beamline will have the highest beamsize/photon-density combination in the world for hard x-rays, making it the best facility for imaging dynamics in cm-sized samples. For cm-sized beams, the photon density will be >10× higher than the ESRF ID19 imaging beamline across the 10- to 60-keV energy spectrum.

An alternative to achieving a larger beamsize on a regular length beamline is the use of a bending magnet or wiggler as the radiation source. In both cases, the projected angular source size requirement would not be satisfied; at 70 m the horizontal source projection angle would be ~ 3× larger for the bending magnet than in the proposed WFI, while for the wiggler, it would be even worse due to the additional source size contribution from the projected wiggler length in the off-axis direction.

Another alternative to achieving the larger beamsize and/or a smaller effective source size is to use x-ray optics to create a secondary source using K-B mirrors. However, this approach was not pursued because it is not compatible with the high-energy and white beam requirements of the proposed beamline.

4.3.2.6 References

[4.3.2-1] J. Fineberg, Nature **426**, 131 (2003).

[4.3.2-2] M.J. Buehler, F.F. Abraham, and H. Gao, Nature **426**, 141 (2003).

[4.3.2-3] N.S. Liu et al., J. Engr. Mater. Techn. **130**, 021008 (2008).

[4.3.2-4] Y. Wang et al., Nat. Phys. **4**, 305 (2008).

[4.3.2-5] M. Scheel et al., Nat. Mater. 7, 189 (2008)

[4.3.2-6] F. Fusseis et al., Nature **459**, 974 (2009).

[4.3.2-7] J. Han, Y. Jin and C. S. Willson, Environ. Sci. Technol. 40, 1547-1555 (2006)

[4.3.2-8] C. Ortiz and M. C. Boyce, Science 319, 1053 (2008)

[4.3.2-9] W-K. Lee and J. Socha, BMC Physiology **9**, 2 (2009).

4.3.3 *section deleted*

4.3.4 High-Energy Tomography Beamline [U1.02.04.06]

The high-throughput microtomography system currently installed at beamline 2-BM provides a reliable and easy to use instrument able to determine the distribution of physical quantities (density, porosity distribution, crack size etc.) in 3D on a large population of samples [4.3.4-1, 4.3.4-2]. Recently developed environment control cells allow monitoring of creep/fatigue interaction [4.3.4-3], crack formation and sample expansion during temperature cycles, the evolution of defects during loading as shown in Figure 4.3.4-1 [4.3.4-4, 4.3.4-5], and ***in situ*** material corrosion [4.3.4-6].

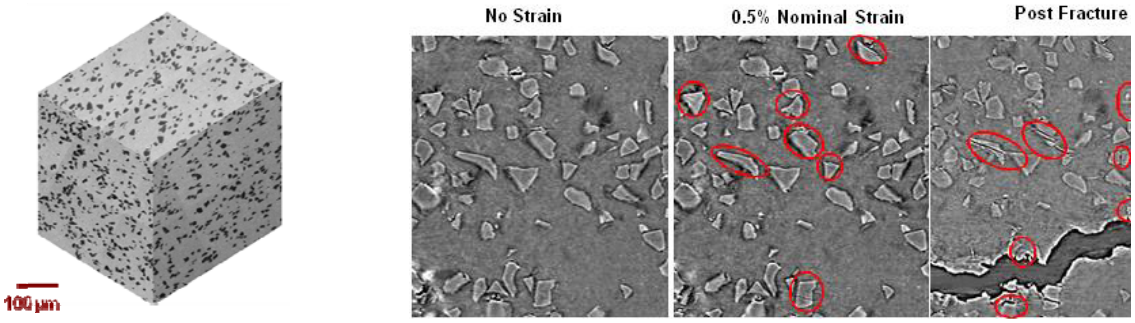

Figure 4.3.4-1. Evolution of damage to SiC particles as a function of applied strain. Note the increase in the number of particles fractured and the increase in crack opening displacement with increasing strain. Courtesy of Nikhilesh Chawla, images taken at 2-BM with 1.3-µm voxels.

Microtomography has proven to be very successful in new materials properties characterization, engineering material structural imaging [4.3.4-7, 4.3.4-8], biology and highly mineralized biological tissues [4.3.4-9–4.3.4-11], and industrial applications. However, the highest x-ray energy available at 2-BM is 30 keV. At this energy, x-rays can penetrate less than 3-mm mid-crustal shear zone rock [4.3.4-2] or 0.3-mm steel. To look at highly absorbing samples using lower energies requires reducing the size of the sample, which is often not possible without compromising the experiment.

Many man-years of effort have been spent developing tomography instrumentation and analysis infrastructure at 2-BM. Currently, high-energy tomography has been conducted at the APS only on an *ad hoc* basis. Beamline 10-BM, for example, has high-energy white-beam tomography ability, but tomography is not the main mission of 10-BM; moreover, the space in the 10-BM white-beam hutch is very limited and is not suitable for phase-contrast high-energy tomography. High-energy ID x-ray beamlines like 1-ID and 11-ID are capable of tomography experiments, but both are heavily oversubscribed and tomography/radiography is only implemented as a supplementary technique to their scattering experiments. Moreover at these ID beamlines, the beam size is much smaller than the samples that a dedicated high-energy tomography will be able to handle. To cover important applications such as those listed below, a tomography beamline with a higher energy range than 2-BM and larger beam than the ID high-energy beamlines is needed.

4.3.4.1 Scientific Scope

The ability to perform 3D tomography on real samples in real conditions often requires high energies to provide sufficient penetration length. This new facility will provide the United States industrial and scientific communities with a unique tool. The areas that will directly benefit from this new capability include transportation and engine technology, battery technology, electronic circuit analysis, medical implant technology, geosciences, and paleontology.

Transportation Technology

Metal-matrix composites (MMCs) are used in a variety of automotive and other ground transportation applications. The main attractions of MMCs are: high strength-to-weight ratio, enhanced mechanical and thermal properties over conventional materials, improved fatigue and creep characteristics, better wear resistance, and general tailorability of properties. Because the transportation industry is extremely cost sensitive, understanding the mechanical property and reducing the manufacturing costs of MMC components will increase their use, and lower the vehicle weight leading to better fuel economy.

The design and development of high-performance materials requires a thorough understanding of the microstructure and its effect on properties. It is well known that damage in MMCs takes place by a combination of particle fracture, particle/matrix interface debonding, and matrix void growth. Traditionally, the characterization of damage in materials is determined by mechanical testing followed by cross sectioning. This approach is laborious and limited by the two-dimensional nature of the analysis and is inherently destructive.

High-energy x-ray tomography with *in situ* load cell capability would provide a powerful tool to nondestructively characterize damage in real size material samples (Figure 4.3.4-2). This methodology will allow understanding of the critical link between microstructure and deformation.

(a) (b)

Figure 4.3.4-2. (a) Three-dimensional reconstructions of the microstructure of particle SiC-reinforced Al alloy matrix composite after fracture. (b) Digital analysis showing particles, cracks in the particles, and voids in the matrix. Courtesy of Nikhilesh Chawla, images taken at 2-BM with 1.3-µm voxels.

Engine Technology

Advanced engine components is one area of manufacturing where fast and detailed non-destructive analysis can substantially improve the quality and performance of engines. X-ray CT can be applied in the development and design phases, as well as in quality control and failure analysis. In the design phase, 3D tomographic reconstructions can validate manufacturing processes, while in failure analysis, tomography can be used as a primary evaluation tool or to select volumes of interest for more extensive analysis using destructive techniques.

An example microtomogram of a cast turbine blade is shown in Figure 4.3.4-3. This blade is made of a very dense nickel superalloy; the density and size prohibit high-quality reconstructions on tube sources or at low-energy synchrotron sources. For this measurement, a filtered white beam with peak detected energy of 175 keV was used. Even with this high energy, the sample was nearly 6 absorption lengths thick in the projections with the greatest absorption.

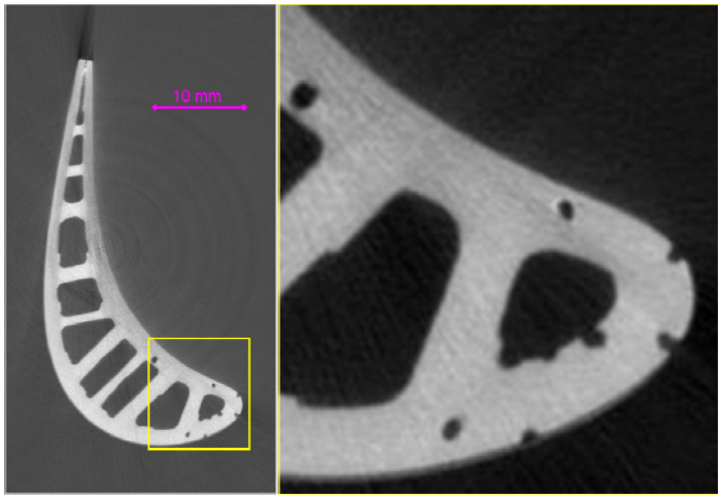

Figure 4.3.4-3. Cast turbine blade made of a nickel superalloy. The interior features are both for strength and for air flow (cooling). This sample is an example of a blade that is too complicated to analyze for quality control using 2D radiography. Critical dimensions are the wall thicknesses and the size and penetration of the laser-drilled cooling holes (cross sections of several are seen in the zoomed region). Data courtesy of Jeremy Kropf, images taken at 10-BM in white-beam mode.

Other Applications

High-energy tomography in the 80- to 100-keV range allows the study of new materials with higher densities like high-temperature and multifunctional Ti lattice-load supporting structures [4.3.4-12], as well as leadless ceramic chip carriers. Electronic packaging is a critical part of products, such as computers, cellular phones, automotive components, and other electronic devices. The package must be designed to incorporate as many input/output interconnects as possible in a limited amount of space. Until recently, most solder balls were made of a eutectic Pb-Sn alloy, because of its low melting point, excellent wetting characteristics, and adequate creep and thermal fatigue strength. The potential health hazards associated with the toxicity of lead are significant. Given the widespread use of Pb-Sn solder in the manufacture and assembly of circuit boards, the development and reliability of new Pb-free solders is crucial for the successful substitution of these materials in the electronics industry [4.3.4-13].

Lead-free solder alloys are complex materials with various important microstructural attributes. These include the nanoscale precipitates of Ag_3Sn in Sn-Ag-Cu or Sn-Ag alloys, as well as Cu_6Sn_5 intermetallics formed at the interface between the solder and Cu metallization. The mechanical behavior of solder alloys is extremely important because solder joints must retain their mechanical integrity under a myriad of conditions such as creep, thermal fatigue, and mechanical shock and drop resistance. Because of the relatively high density of Sn, higher energy tomography capability will be required to study and visualize the morphology, size, and distribution of the precipitates in these materials. Preliminary results showing cross sections of multifunctional Ti lattice structures and of a ceramic chip carrier are shown in Figure 4.3.4-4.

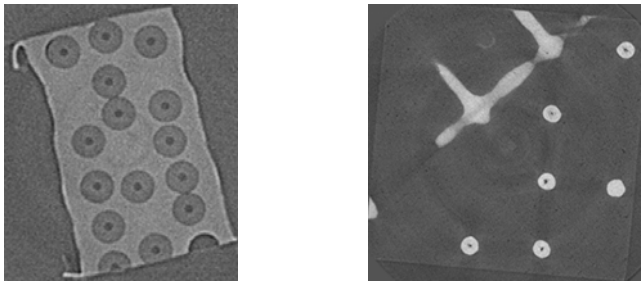

(a) (b)

Figure 4.3.4-4. (a) Small section of a metal matrix composite: Ti matrix with aligned ceramic monofilaments (SiC) sheaths around a C core), (b) ceramic chip carrier. Al_2O_3 matrix surrounding 3-D Mo circuitry. Unpublished data courtesy of Stuart Stock, images taken at 1-ID at 80 keV with 1.45-µm voxels.

4.3.4.2 Source Enhancements

In x-ray projection-based tomography, the match between x-ray penetration length and the beam size is important. The deep penetration of high-energy x-rays allows for the use of larger samples (for a given material), which is often of great utility. A bending magnet (BM) source, with an inherently large horizontal spread, is preferable to an undulator for this purpose. Figure 4.3.4-5(a) shows the source flux spectrum of an APS-U BM.

Some years ago, a "strong bend" was explored as a possible higher energy source of bending magnet x-rays [4.3.4-15]. This is a very interesting source for a high-energy tomography beamline. Figure 4.3.4-5(a) shows the significant increase in flux at higher energies. Also of importance for tomography, the vertical beam size increases with the higher magnetic fields of the strong bend and is approximately doubled with the strong bend option, see Figure 4.3.4-5(b). Due to the obvious benefits of the strong bend for high-energy tomography, having this source would be a considerable enhancement to the beamline.

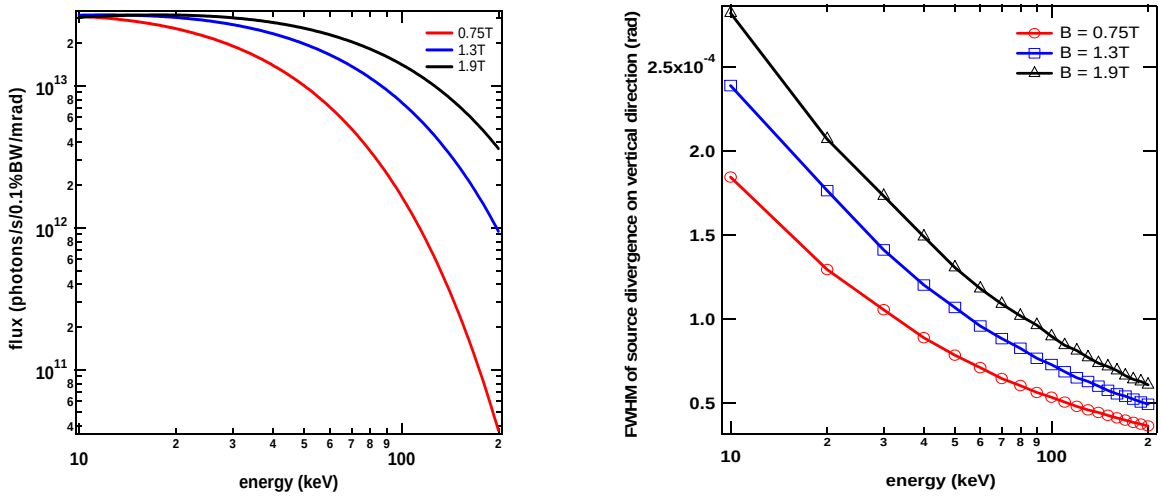

(a) (b)

Figure 4.3.4-5. (a) Flux integrated in vertical direction from bending sources of 0.75 T, 1.3 T, and 1.9 T, (b) vertical source divergence as a function of x-ray energy.

4.3.4.3 Beamline Enhancements

The new beamline will include three stations. A standard BM FOE, BM-A, 9 m in length, located right behind the rachet wall. This station will house white-beam aperture, filters, slits, DCM, DMM, and a P6-type shutter stop. A white-beam station BM-B is immediately downstream of the FOE, covering the rachet wall door, approximately 7 m in length. This station will house an ultrafast tomography setup and an experimental table. A downstream station BM-C (white-beam capable) will be as far downstream as possible on the experiment hall floor and be 5 m × 12 m in size. This station will house a tomography setup optimized for high-speed high-sensitivity tomography and a second setup optimized for high-resolution high-throughput, see section 4.4.6, and a white-beam stop (Figure 4.3.4-6).

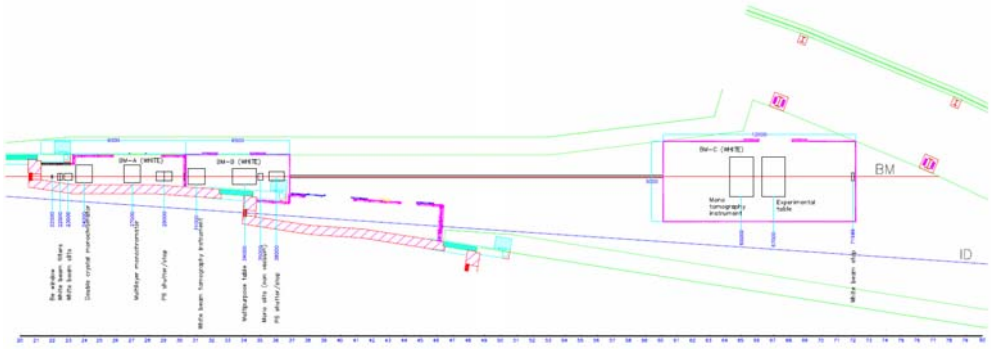

Figure 4.3.4-6. High-energy tomography layout.

Table 4.3.4-1. High-Energy Tomography Beamline Component List

Approx. Distance from Source (m)	Component Name
22	Window (100 mm H × 10 mm V)
22.5	White-beam filters
23	White-beam slits
24	Double-crystal monochromator
27	Multilayer monochromator
29	Shutter/Stop (P6)
31	Ultrafast tomography instrument
34	Multipurpose table
37	Shutter/Stop (P6)
59	Mono slits
61	Tomography instrument compatible to high-speed tomography and high-resolution tomography
62	Experimental table
72	White-beam stop

At 2-BM, microtomography experiments are highly automated, both in the sample handling and in data analysis. The existing computing infrastructure is also being used by other microtomography systems cloned from the one at 2-BM to provide 3D imaging capability as a complementary technique at 1-ID and 32-ID. The capacity of the computing infrastructure will be increased to integrate the new high-energy tomography facility.

4.3.4.4 Optics

The new beamline will operate in three modes: white beam, monochromatic beam with double-crystal monochromator with an operating range of 50-100 keV, and monochromatic beam with double-multilayer monochromator with an operating range of 30-50 keV. The BM-A hutch houses the white-beam-filter bank system, a Laue double-crystal monochromator system, and a double-multilayer monochromator system. The Laue double-crystal monochromator system will be similar to that used at 1-ID with appropriate modifications for the wider bending magnet beam and with water cooling. The double multilayer monochromator system will be similar to that used at 2-BM but with a multilayer coating optimized to work in 30-50 keV range. Such a multilayer system is commercially available and used at other synchrotron facilities (ESRF ID19, SLS tomocat beamline).

Synchrotron x-ray radiation is partially coherent and therefore allows phase-contrast-based imaging. Since phase contrast is much stronger than absorption contrast in the high-energy regime, obtaining high-resolution results with the aid of phase contrast is essential. Currently, grating interferometry working at about 35 keV is commercially available. Preliminary experiment of high-energy grating interferometry (> 80 keV) has been recently conducted at the ESRF. At Sring8, grating interferometry with white beam has also been demonstrated. Grating interferometry is expected to have broad applications in high-energy tomography. For the APS high-energy tomography beamline, gratings for high-energy x-rays (> 40 keV) will be developed in collaboration with the XSD Metrology Group. To obtain experience with grating interferometry, a grating interferometer working at 35 keV that is commercially available from the Paul Scherrer Institute will be acquired.

4.3.4.5 Anticipated Performance

Currently both monochromatic beam mode and pink-beam mode are available at 2-BM. With monochromatic beam from a double-multilayer monochromator, high-resolution (~1 μm), high-sensitivity tomography (soft tissue imaging) experiments can be performed. With pink beam from a mirror, fast-tomography (2 Hz) capability has also been developed.

The high-energy tomography beamline is similar to the 2-BM configuration but without the energy limitation. With monochromatic beam, thanks to the partial coherence of the synchrotron beam, high sensitivity and therefore high resolution can be expected. With white beam, fast tomography suitable for real size materials in real time, can be conducted. Figure 4.3.4-7 shows the flux density of the illumination beam at different distances from different sources. At the BM-B position, the flux density from a 1.9-T bending source is about 4 times of that from a regular 0.75-T bending source. To achieve 10-Hz tomography, a strong-bend source is necessary (see Table 4.3.4-1).

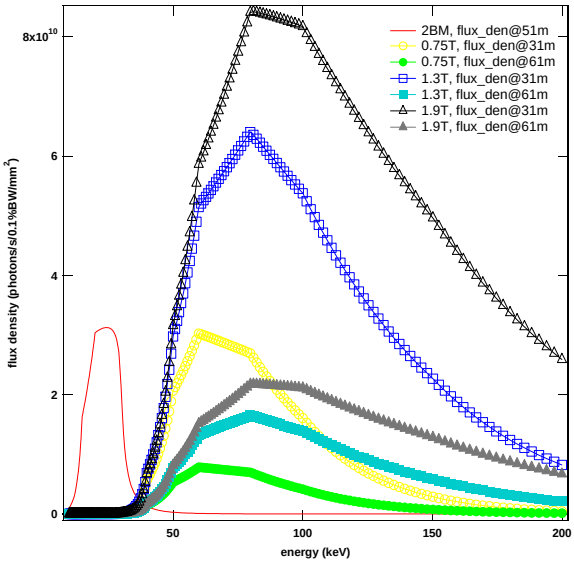

Figure 4.3.4-7. Flux density at different positions from different sources. The 2-BM flux is determined using the standard 2-BM configuration (0.15° Pt-coated mirror and a 0.6-mm Al foil). In all other cases a 0.8-mm Cu filter was used to shift the x-ray peak energy above 60 keV.

4.3.4.6 Instrument Enhancements

The high-energy microtomography instrument will include four experimental setups. Two setups, one located in B and another in C, will be optimized for ultrafast and fast white-beam tomography (UF-WT and F-WT). The C station will also have a fast monochromatic tomography (F-MT) and a phase-contrast-enhanced tomography (PT) system. The four systems will use different detectors to assure all measurements are x-ray flux limited and not detector limited. All detectors will be coupled-scintillator-screen optimized for higher efficiency at high energies, and used in a 90-degree geometry to protect the detector from the x-rays. (See Figures 4.3.4-8 and 4.3.4-9 for the instrumentation layouts for these stations.)

Table 4.3.4-1. Flux Density at Different Positions from Different Sources

BM (T)	**Integrated Flux (ph/s/mm^2) at 61 m from the source**
0.75	6.2×10^{12}
1.3	1.5×10^{13}
1.9	2.3×10^{13}
BM (T)	**Integrated Flux (ph/s/mm^2) at 31 m from the source**
0.75	2.4×10^{13}
1.3	6.0×10^{13}
1.9	8.7×10^{13}

The UF-WT system in the B station will be able to handle samples up to 100 mm horizontal and 10 kg in weight and will allow testing real engineering components under real operating conditions while their 3D internal morphology is monitored. The UF-WT system will use an ultrafast camera, like the Photron SA2 or the PCO.dmax, and be able to routinely perform tomography in 100-200 ms. The current detector technology allows for the UF-WT to take the 100-200 ms 3D snapshot of a sample at a 3D

volume rate of ~ 10 minutes. This is currently limited by the data transfer from the detector internal memory to the hard disk, but a faster 3D volume rate is expected in the next 1-2 years.

The C station will focus on high-resolution and high-sensitivity measurements but will also be suitable for large-size specimens and slow dynamics. In this station, an F-WT system will be installed that is able to handle the largest samples, up to 200 mm horizontal and 20 kg in weight to test real engineering components under real operating conditions in slow dynamics. This system will monitor the 3D internal morphology in a few seconds to one minute 3D frame rate. The PT system, in line with the F-WT system, will provide high-sensitivity imaging and will be based on grating interferometry.

The F-MT system will be optimized for high resolution, will operate in monochromatic beam ranging from 30 to 50 keV, and be able to handle samples up to 1 cm in diameter. This system will use a more sensitive/slower camera, like the PCO Edge sCMOS high-performance digital camera, and be able to collect a full tomography data set in ~ 1 minute.

The current detector technology allows for the F-MT to operate in a sustained mode, i.e., with a 3D volume rate of one minute. For this system, full automation for sample alignment will be added, loading and unloading achieving a maximum throughput of over 1000 samples per day.

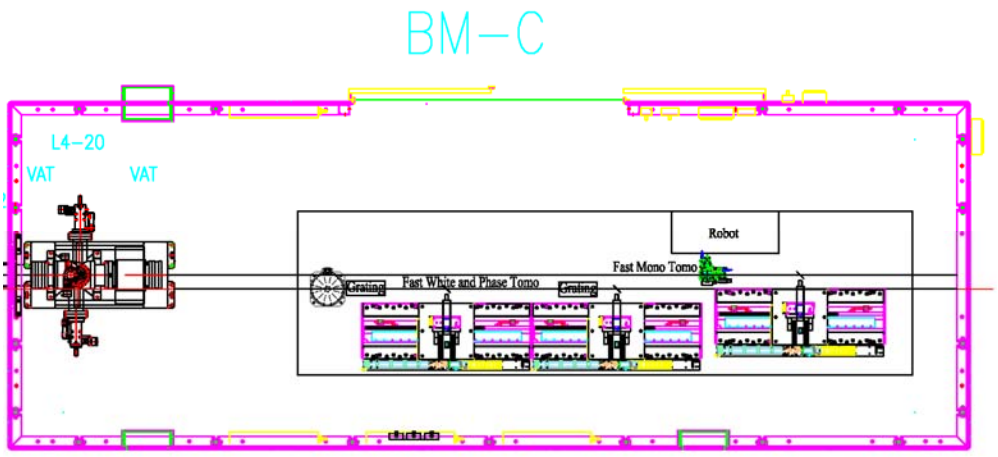

Figure 4.3.4-8. C Station instrumentation layout. This station will focus on high-resolution and high-sensitivity measurements but also will be suitable for large-size specimens and slow dynamics.

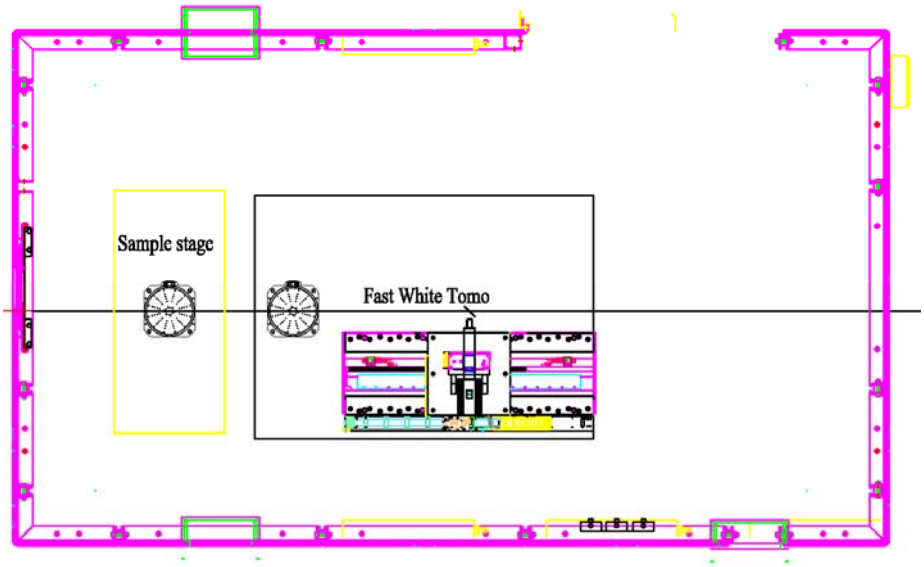

Figure 4.3.4-9. B Station instrumentation layout. This station will focus on ultrafast dynamics.

4.3.4.7 References

[4.3.4-1] F. De Carlo et al., SPIE **4503**, 1 (2002).

[4.3.4-2] F. Fusseis et al. Nature **459**, 974 (2009).

[4.3.4-3] J.L. Drummond, J. Dent. Res. **87**(8), 710 (2008).

[4.3.4-4] N. Chawla and K.K. Chawla, *Metal Matrix Composites*, (Springer, New York, 2006).

[4.3.4-5] H. Liu et al., Proc. Nat. Acad. Sci. USA. **105**(36), 13229 (2008).

[4.3.4-6] F. Eckermann, Corrosion Sci. **50,** 3455 (2008).

[4.3.4-7] Z.W. Hu and F. De Carlo, Scripta Materialia **59,** 1127 (2008).

[4.3.4-8] T. E. Wilkes et al., Philosophical Magazine **89**(17), 1373 (2009), DOI: 10.1080/14786430902956457.

[4.3.4-9] J.J. Socha and F. De Carlo, Proc. SPIE **7078, 7078A**, 0277-786 (2008), DOI: 10.1117/12.795210.

[4.3.4-10] S.R. Stock et al., J. Struct. Bio. **161**(2), 162 (2008).

[4.3.4-11] E. R. Bandstra, M.J. Pecaut, E.R. Anderson, Radiat. Res. **169**, 607 (2008).

[4.3.4-12] P. Moongkhamklang et al., Composites: Part A **39,** 176 (2008).

[4.3.4-13] N. Chawla, Int. Mater. Rev. **54**, 368 (2009).

4.3.5 X-ray Photon Correlation Spectroscopy Upgrade (8-ID) [CAS]

X-ray photon correlation spectroscopy is the x-ray analogue of dynamic light scattering. It permits characterization of the equilibrium or steady-state dynamics of condensed matter on length scales shorter than can be achieved with optical techniques and on longer time scales than can be achieved via neutron scattering. Even on optically accessible length scales, opaque and metallic samples are readily studied, presenting new opportunities for studies of colloidal and other soft matter systems. The overall thrust of these XPCS upgrades is to enable pioneering time-resolved and coherence-based scientific work by extending state-of-the-art multispeckle XPCS-accessible time scales from 10s of milliseconds to 100s of microseconds. The key idea underlying these XPCS upgrades is that the signal-to-noise ratio (SNR) in an XPCS experiment is proportional to product of the source brightness and the square root of the fastest measurable time scales [4.3.5-1]. Thus, increasing the source brightness by more than a factor of 10 with long, tandem insertion devices (IDs) in a fully populated long, straight section (LSS) and higher storage ring current, increases accessible time scales by approximately two decades.

Grazing-incidence x-ray scattering (GIXS) applies the power and utility of small-angle x-ray scattering (SAXS) and wide-angle x-ray scattering (WAXS) to study the static, kinetic and dynamic structural properties of surfaces and buried interfaces; GIXS is currently capable of measuring structure and kinetics corresponding to wave vector transfers in the range 10^{-3}–1 nm^{-1} and time scales ≈ 10–1,000 s. Here changes to the GIXS capabilities at the APS will extend accessible time scales from several seconds to milliseconds and, importantly, provide the capability to apply coherent x-rays in the grazing-incidence geometry to study intriguing kinetic and dynamic phenomena at surfaces and interfaces. As described in more detail below, these major improvements to the XPCS and GIXS science capabilities at the APS can only be realized using x-rays provided by optimized ID's fully populating a long straight section.

4.3.5.1 Scientific Scope

The upgrade will enable advances in knowledge in a wide range of systems that are currently difficult or impossible to study today. Below, several examples are highlighted that fully demonstrate the unique new capabilities that are envisioned.

Self-assembly is the approach with the highest potential for the design and fabrication of materials with enhanced or new combinations of properties for use in energy applications and related technologies, such as photovoltaic and energy-storage devices. To gain full control of the design and creation of such materials, a complete understanding of the structures and interactions in these assemblies, especially those proximate to the surface and within thin films, is needed. As an example, diblock copolymers have been shown to self-assemble on patterned substrates into two-dimensional ordered microscopic domains having a density of 10 terabits per square inch (Tb/in^2) [4.3.5-2]. The structure in such systems varies from nm's to μm's. Because of the wide span of relevant length scales, GIXS is the best tool for characterizing the degree of ordering (Figure 4.3.5-1). However, as the extent of ordering is improved towards even larger length scales, highly collimated x-rays of a high coherence will be required. The upgraded instrument described later in this section will be essential to perform such characterizations.

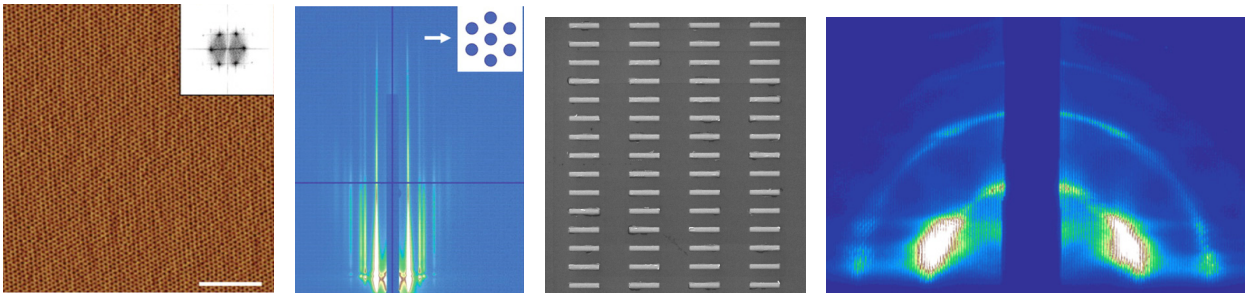

(a) (b) (c) (d)

Figure 4.3.5-1. (a) An AFM phase image and (b) a GIXS image of a PS-b-PEO thin film with highly ordered PEO cylindrical domains [4.3.5-2]. The scale bar is 100 nm. (c) A SEM image and (d) a GIXS image of 300 nm × 2 μm gold nanolines [4.3.5-3]. The GIXS image shows interference between the gratings and the nanoline form factor.

Bio-interfacial processes at the cell membrane level are critical to cell function and interaction with the extracellular matrix. The wide range of time scales (μs–sec) and length scales (nm-μm) over which these processes occur makes *in situ* measurements of their kinetics and dynamics challenging. Figure 4.3.5-2 shows recently measured correlation functions from Langmuir lipid monolayers measured in the GIXS geometry at beamline 8-ID. The measurements show the key role that surface pressure has on fluctuations of the membrane. The upgraded instruments will enable measurements of the fluctuations of two-dimensional lipid membranes, not only at liquid/vapor interfaces but also under fully hydrated conditions at liquid/liquid or liquid/solid interfaces

Measurements of the diffusion and surface fluctuations in free-floating vesicles and Brownian motion within concentrated protein solutions can provide crucial insight into the central role of thermal fluctuations in biological activity at the cellular scale. In principle, XPCS is well suited to such measurements, but, in practice, there is insufficient coherent flux especially at higher x-ray energies where sample radiation damage issues can be mitigated. As a specific example, consider the recent (and first) application of XPCS to study the dynamics of concentrated suspensions of alpha and gamma crystallin proteins extracted from bovine eye lenses [4.3.5-4]. The autocorrelation decay in Figure 4.3.5-3 shows the interdiffusion of alpha crystalline suspended in a concentrated matrix of gamma crystallin on a length scale corresponding to the protein diameter. The results from such studies could have impact on our understanding of cataract formation and presbyopia. Upgraded APS XPCS capabilities will facilitate such measurements via higher coherent flux at higher x-ray energies and will be a unique XPCS capability of the APS.

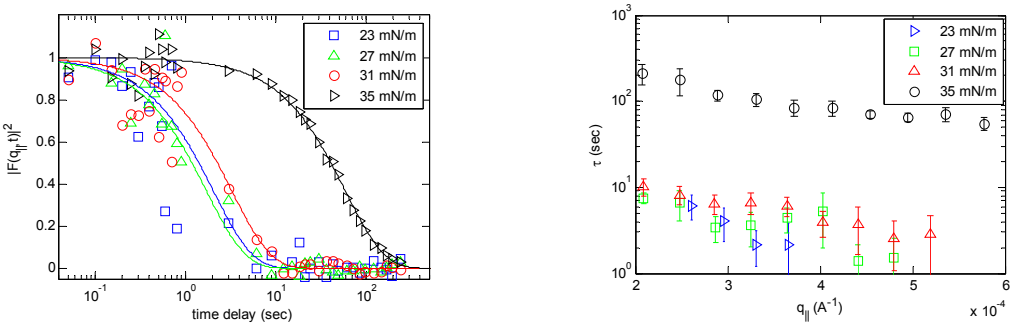

(a) (b)

Figure 4.3.5-2. XPCS in the GIXS geometry from a Langmuir lipid monolayer of DPPC on water measured at 8-ID [4.3.5-5]. (a) Autocorrelation functions at various surface pressures. (b) Relaxation time constants as a function of the in-plane wave vector transfer.

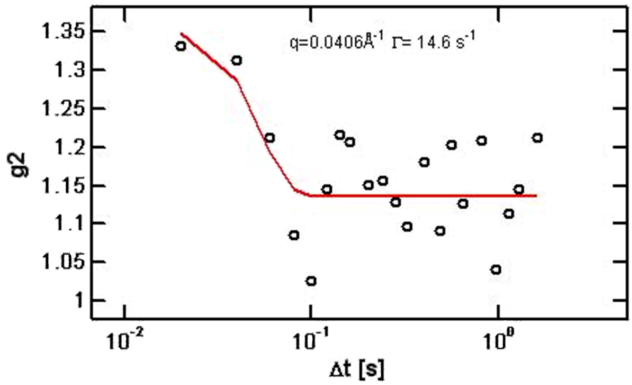

Figure 4.3.5-3. Time autocorrelation function measured at beamline 8-ID for the diffusion of eye-lens alpha crystallin within a matrix of gamma crystallin.

All the emerging science cases require high coherent flux in the hard-energy region (10–25 keV for higher sample penetration) and extremely stable x-ray beams. More specifically, unique to the APS, the higher x-ray-energy operations that will be enabled by the upgrade described below will facilitate measurements of the dynamics of biologically relevant materials by allowing x-rays to penetrate aqueous solutions and by minimizing beam damage.

4.3.5.2 Source Enhancements

Because of relatively low signal levels, a crucial aspect of any XPCS experiment is the SNR. For XPCS, the SNR is proportional to the number of photons per correlation time (Bτ), where B is the on-axis source brilliance and τ is the correlation decay time, multiplied by the √(number of correlation times) [√(1/τ)]. Thus the source must be as brilliant as possible, because the XPCS SNR is linearly proportional to the source brilliance [unlike the square root dependence on brightness seen in many conventional (non XPCS) scattering experiments]. Many of the same considerations apply to GIXS when the power of the technique is extended via the use of coherent beams. Accordingly, to achieve the scientific aims described above, the source brilliance must be maximized. A sector with a fully populated LSS is required.

The LSS should have tandem IDs with an energy range of ≈ 10–24 keV. Assuming a LSS of 7.7 m, each ID should be 7.7/2 = 3.85 m long. We are considering two choices for the IDs. Simplest and most flexible are a triplet tandem of APS Undulator A's phased at ≈ 8 keV. Operation on the third harmonics provides high brilliance beams up to 30 keV with peak brilliance above 20 keV in the range 20–24 keV. The triplet also provides considerable flexibility by allowing operation, for example, of 2 devices at one energy (for XPCS) and the third at another energy for GIXS. Alternatively, a second option for both IDs is 3.0-cm-period APPLE-II helical undulators set to produce circularly polarized radiation. These devices have limited tunability and would limit higher-energy operations but have the virtue of minimizing the power load on the front-end and downstream optics. A final decision on appropriate IDs will depend on input from the user community and more careful engineering studies of power loads and the performance of beamline components under such power loads. Figure 4.3.5-4 shows the expected on-axis brilliance from phased 3.0-cm-period APPLE-II helical IDs at 100 mA of storage ring current compared to other possible or existing IDs. Scaled to 150 mA or 200 mA of storage ring current, the upgraded ID provides ≈10× more brilliance than available at 8-ID today with the promise of accessing time scales more than 100× faster than today. Importantly, this takes us from the regime of slow dynamics exhibited by glassy materials or long chain polymers to dynamics exhibited in aqueous environments, such as model cell membranes.

The long straight section will require an upgraded front end capable of handling the power generated by the tandem insertion devices. It is estimated that the existing APS high-heat-load front-end (FE) design will suffice with possible restrictions on gap settings. The beam will exit the FE via a 3 mm exit-diameter differential pump.

Finally, a potentially brighter class of IDs, namely superconducting undulators (SCUs), are in the early research and development phase within the Magnetic Devices Group at the APS. Per unit length, the SCU promises significantly increased brightness and tunability (but increased power and power density) as compared to a normal device. For example, at 10 keV and scaled to 150 mA of ring current, a 2.0-cm-period SCU provides 4× more brilliance than Undulator A [4.3.5-6]. The 2.0-cm-period SCU, when it becomes available, will be carefully evaluated as the potential first or upgraded choice for an ID.

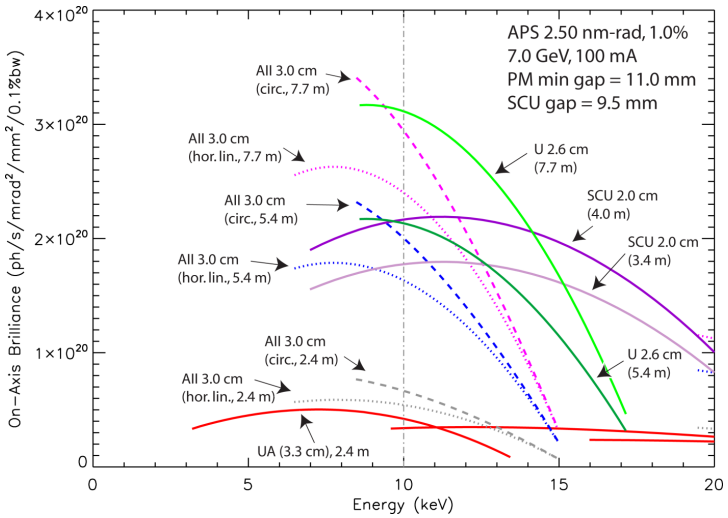

Figure 4.3.5-4. Comparison of brilliance delivered by Undulator A to possible insertion devices for the upgraded XPCS and GIXS beamline. The 3.0-cm-period APPLE-II helical ID delivers high brilliance at ≈ 12 keV with relatively modest power loads compared to the other ID options.

4.3.5.3 Beamline Enhancements

Based on our current knowledge of adding SPX capabilities to Sectors 6 and 7 via adding rf deflection cavities to Sectors 5 and 7, we believe the upgrade to XPCS and GIXS capabilities can best be achieved via an in-place upgrade to Sector 8-ID. A schematic plan view of the modified beamline is provided in Figure 4.3.5-5 while a 3-D schematic is provided in Figure 4.3.5-6. In brief, existing and expanded shielded enclosures 8-ID-A and 8-ID-D, respectively, will house beam-shaping and beam-conditioning optics. Enclosure 8-ID-E will house the GIXS and large-Q XPCS programs and extended enclosure 8-ID-I will host the small-angle XPCS experiment program. Details of the new layout, from upstream to downstream, are described below.

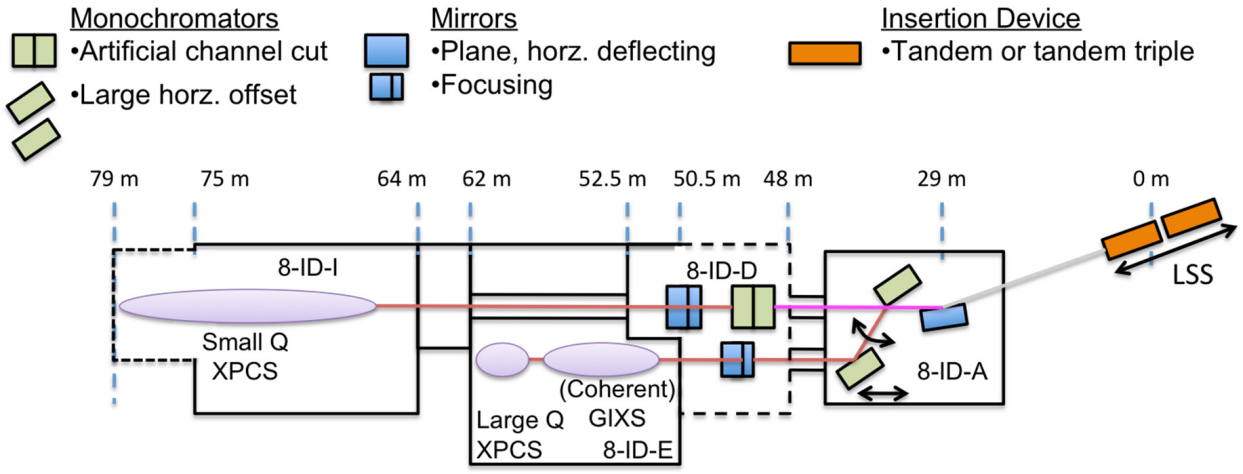

Figure 4.3.5-5. Schematic plan view of the upgrade to the XPCS and coherent GIXS scientific programs at 8-ID. Approximate distances from the center of the straight section are indicated. Existing shielded enclosures are shown with solid black outlines while modified enclosures are outlined with dashed lines. A key feature of the current XPCS and GISAXS programs hosted at 8-ID, which is retained in the upgrade, is simultaneous operation of the small-Q XPCS program and the large-Q XPCS/GIXS program.

A tapered pinhole at the entrance of the beamline (26 m from the source) with an exit diameter of 0.6 mm. The pinhole's main function is to reduce the power on the downstream optics for increased stability while not limiting the coherent flux available from the IDs.

White-beam slits at 27 m from the source capable of withstanding the power load provided by tandem IDs and 200-mA storage ring operation. The primary purpose of the slits is to aperture the horizontal source for selected experiments.

A diffraction-limited horizontally deflecting (0.3° inboard deflection angle) plane mirror fully illuminated in the horizontal by the ≈ 0.6-mm beam (26.5 cm). More details on the optics requirements are provided below in the optics section. The mirror will require constant-pressure and constant-flow vibration-free gravity-fed side cooling by either by water or liquid nitrogen. The mirror is 29 m from the source.

A large horizontal-offset (≈ 0.86-m outboard offset) side-bounce monochromator providing energy tunability in the range 8–14 keV using lower order reflections. The monochromator crystals will be cooled by a constant-pressure and -flow vibration-free gravity-fed cooling system using either water or liquid nitrogen. The monochromator crystals will be Si(220) or C*(111) or C*(004). The first crystal of the monochromator is ≈ 31 m from the source. The monochromator requires a precision horizontal translation so that it can intercept half the beam provided by mirror M0. The monochromator should closely follow the design adopted by 12-ID during their recent upgrade [4.3.5-7].

A compound refractive lens (CRL) assembly providing low demagnification focused beam for the GIXS and large Q XPCS set-ups when required for experiments limited by flux density. The CRL is an in-line optic so it can easily be added to or removed from the beam without requiring re-alignment of the downstream optics and experiments.

Separate pink (inboard) and monochromatic (outboard) beam shutters for the secondary optics enclosure (SOE) 8-ID-D. Both shutters are ≈ 35 m from the source.

Parallel shielded transport lines to take the inboard pink and outboard monochromatic beams to SOE 8-ID-D. SOE 8-ID-D is a significantly enlarged version of existing shielded enclosure 8-ID-D. It

will contain general-purpose monochromatic-beam-conditioning elements for the GIXS and large Q experiments in 8-ID-E (item 1 below) and monochromatizing and focusing optics for the small-Q XPCS program in 8-ID-I (items 2 and 3 below).

Monochromatic beam elements in 8-ID-D for GIXS and large-Q XPCS experiments in 8-ID-E include in-vacuum collimating and guard slits, experiment shutters (non-PSS shutters), and filters.

The existing 8-ID-I artificial channel cut monochromator [4.3.5-8] will be moved to 8-ID-D and located 49 m from the source. The compatibility of this monochromator with increased power loads needs to be verified. The monochromator crystals will be cooled by a constant-pressure and -flow vibration-free gravity-fed cooling system using either water or liquid nitrogen. The monochromator requires and currently has a pink-beam mode that allows the incident pink beam to pass through unperturbed.

A small vertical offset vertically focusing monochromatic beam two-mirror system will be located 51.5 m from the source with a demagnification ratio of 3:1. The mirror should be capable of collecting either the entire vertical extent of the monochromatic beam or letting either the pink or monochromatic beam pass unperturbed. Note that the coherent scattering beamlines at PETRA -III [4.3.5-9] and NSLS-II [4.3.5-10] have specified one-dimensional beryllium compound refractive lenses (CRLs) as their main vertical focusing optical elements. Because CRLs are in-line optics, they offer several simplifying advantages over mirror systems. Their ability to preserve brilliance is, however, not known. Nevertheless, the experience of these beamlines, especially the PETRA-III beamline that has just begun commissioning, will be closely monitored, and plans will be revisited based on their experience.

Downstream of the SOE, will be pink-beam compatible shielded transport for the though beam to 8-ID-I followed by a pink-beam shutter for shielded enclosure 8-ID-I. The shutter will be located in existing shielded enclosure 8-ID-MH-1 and will be 62.5 m from the source.

Existing enclosure 8-ID-I will be modified to make it nearly 4 m longer than it is today. This, combined with relocation of the artificial channel cut monochromator to the enlarged SOE, will allow larger exit flight paths that provide a match to anticipated fast XPCS-suitable detectors. The need for extended exit flight paths and extending 8-ID-I can be understood as follows. The current FWHM vertical source size is ≈ 30 μm and is not expected to change significantly as a result of the upgrade. With 3:1 demagnification, the effective FWHM source size will be ≈ 10 μm. Upstream of the sample, approximately 4 m of space is required for miscellaneous optics and to ensure that the sample is in the far field. The coherence length at the sample depends on x-ray energy, distance from the source, and the source sizes, but a reasonable estimate is 10 μm. If we assume 2 m of space between the virtual source and the sample, and a detector pixel size of ≈ 75 μm (see section 4.3.5.6), then with 12– to 15–keV x-rays, the required sample to detector distance is ≈ 10 m. Adding 1–2 m for personnel access, we require a station length of ≈ 15 m.

The GIXS and large- and small-Q XPCS setups will also be improved as part of the upgrade. Details of the required modifications are described in section 4.3.5.6.

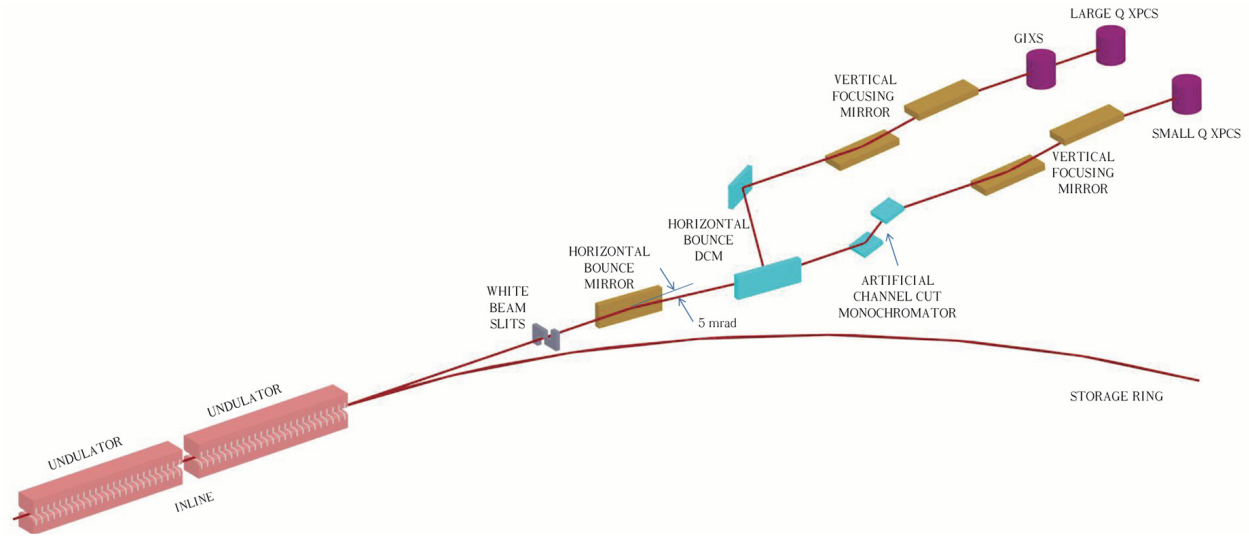

Figure 4.3.5-6. Schematic 3-D solid model showing the main features of the upgrade for the XPCS and coherent GIXS scientific programs.

Finally, among the changes listed above, the compatibility of all the existing 8-ID radiation safety shielding (RSS) components will have to be evaluated with respect to the increased power delivered by the tandem IDs. These include the V1-90 differential pump and mask, the M9-30 white-beam stop, the P9-30 8-ID-D shutter, and the P9-50 8-ID-I shutter. It is possible that some of these components may need to be upgraded or replaced as well.

4.3.5.4 Optics

Experiments using XPCS and coherent GIXS are particularly sensitive to the quality of the optics in the beamline, so the philosophy is to minimize the number of and power load on the optics and to maximize their quality. The following is a list of brilliance-preserving optics that will be required as part of the upgrade:

- Single-bounce horizontally deflecting plane mirror 29 m from the source (see Table 4.3.5-1 and accompanying text).
- Vertically focusing, vertical-offset monochromatic beam double-mirror system with ≈ 3:1 demagnification (small-Q XPCS) (see Table 4.3.5-2 and accompanying text).
- Multilayer monochromator crystals with relative energy bandwidth of $\Delta E/E \approx 0.1–0.3\%$. These items are currently under development for the CHX beamline at NSLS-II and should development prove successful, we will employ such crystals and a small offset horizontal-bounce monochromator inside the SOE 8-ID-D. Because of current uncertainty about the performance of these optics, however, we have not included the multilayer in our conceptual design.
- High-demagnification general-purpose 1-D and 2-D monochromatic-beam focusing optics, such as Kirkpatrick-Baez (KB) mirrors or CRLs.

The specifications for the single-bounce horizontally deflecting mirror are critical as it produces a low-pass filtered beam shared by the XPCS and coherent GIXS experiment programs. Preliminary specifications for this optic are summarized in Table 4.3.5-1.

Table 4.3.5-1. Horizontally Deflecting Plane Mirror Specifications

Item	Specification
Optical length	265 mm
Figure	Flat with |R| > 200 km (tangential) and |R| > 100 km (radial)
Surface roughness	< 1 Å rms over a wavelength band from 5 to 2000 μm
Slope errors	< 0.15 μrad root-mean-square (rms) over a wavelength band from 2 mm to the clear aperture and < 0.4 μrad peak-to-valley (PTV) with no curvature removed (tangential)
	< 0.15 μrad rms over a wavelength band from 2 mm to the clear aperture and < 0.4 μrad PTV with no curvature removed (sagittal)
Incidence angle	0.15º, horizontal
Source	Tandem (helical) undulators per section 4.5.3.2
Distance from source	≈ 29 m
Substrate	Silicon
Surface coating	Three stripes: Si (bare), Rh and Pt
Cooling	Constant pressure and flow gravity-fed water or liquid nitrogen (LN_2)

The second beamline optic required is a pair of multilayer crystals for a possible multilayer monochromator. Multilayer crystals provide monochromatic beams with wider energy bandpasses than single-crystal optics. Because the longitudinal coherence requirements for an XPCS experiment are more forgiving in the small-angle geometry [4.3.5-11] because of small-path-length differences across the span of the illuminated sample area, multilayer optics can be used to deliver increased flux to very small-angle XPCS experiments. Specifically, the optical path length difference (δ_D) should be less than or equal to a few times the longitudinal coherence length (Λ) of the x-ray beam. The longitudinal coherence length is given by $\Lambda = \lambda E/(\Delta E)$, where E is the x-ray energy and ΔE is the energy bandwidth. In the small-angle regime, the optical path length difference is given by $\delta_D \approx 2DQ/k$, where D is the size of the beam illuminating the sample (D is typically 20 μm), Q is the wave-vector transfer and k is the wave vector. At E ≈ 10 keV, a multilayer with $\Delta E/E = 0.25\%$ will yield acceptable contrast to $Q \approx 0.05$ nm^{-1}, which is sufficient Q for many systems of interest. Accordingly, in cooperation with Ray Conley of NSLS-II [4.3.5-12], multilayer crystal specifications have been developed and are summarized in Table 4.3.5-2.

Table 4.3.5-2. Multilayer Crystal Specifications

Item	Specification
Material	$MoSi_2$/Si
Reflectivity	75% (single multilayer)
Number of bilayers	2,000
Interfacial roughness	0.25 nm
$\Delta E/E$ at 10 keV	0.248%
Period	1.7 nm
Ratio of layer thicknesses	0.5
Substrate	Silicon with 0.1 μrad flatness and < 0.4 Å rms roughness after annealing

The vertically focusing double-mirror system is another vital aspect of this upgrade. The large asymmetry in coherence lengths means that the beam must be focused vertically at the sample so that the entire coherent flux delivered by the undulators is used for XPCS experiments. The focusing mirror system will only be used with monochromatic x-rays. A small fixed vertical offset of 4.8 mm after the two mirrors is required so that the downstream experiment does not have to move too far when the beam is either focused by the mirror system or bypasses the mirror system. Table 4.3.5-3 summarizes the requirements for the double-bounce vertically focusing mirror system.

Table 4.3.5-3. Vertically Focusing Mirror System Specifications

Item	First Mirror	Second Mirror
Optical length	300 mm	300 mm
Figure	Bendable plane	Flat with |R| > 200 km (tangential) and |R| > 100 km (radial)
Surface roughness	< 1 Å rms over a wavelength band from 5 to 2000 μm	< 1 Å rms over a wavelength band from 5 to 2000 μm
Slope errors	< 0.15 μrad rms over a wavelength band from 2 mm to the clear aperture and < 0.4 μrad PTV with no curvature removed (tangential)	< 0.15 μrad rms over a wavelength band from 2 mm to the clear aperture and < 0.4 μrad PTV with no curvature removed (tangential)
	< 0.15 μrad rms over a wavelength band from 2 mm to the clear aperture and < 0.4 μrad PTV with no curvature removed (sagittal)	< 0.15 μrad rms over a wavelength band from 2 mm to the clear aperture and < 0.4 μrad PTV with no curvature removed (sagittal)
Incidence angle	0.15º, vertical	0.15º, vertical
Source	Monochromatic beam	Monochromatic beam
Distance from source	≈ 51.5 m	
Source demagnification	3:1 (small-Q XPCS) or 6:1 (GIXS and large-Q XPCS)	N/A
Substrate	Silicon	Silicon
Surface coating	Three stripes: Si, Rh and Pt	Three stripes: Si, Rh and Pt
Cooling	None	None

4.3.5.5 Anticipated Performance

Table 4.3.5-4 summarizes the anticipated performance of the upgrades to the GIXS and XPCS experiment programs currently hosted at 8-ID.

Table 4.3.5-4. Anticipated Performance at 12 keV Resulting from the Upgrades to the XPCS and GIXS Programs

Upgrade	XPCS	Coherent GIXS	Comment
I_{ring} = 200 mA	2× coherent flux	2× coherent flux	
7.7 m straight section			LSS
2× 3.7-m 3.0-cm-period helical ID or 3× 2.4-m Undulator A	7× coherent flux	7× coherent flux	At phased x-ray energy
Front end upgrade			HHL to support increased power
First optics enclosure optics	Diffraction limited side-bounce mirror	Diffraction limited side-bounce mirror	
Large horizontal offset mono	N/A	Energy tunable from 8-14 keV	Energy fixed at 7.35 keV today
End station vertical focusing	10× coherent flux	N/A	
Total estimated enhancement factors	140× increased coherent flux Minimum delay times 1,000× faster	10× increased tunable flux Minimum delay times 100× faster Kinetic time resolution 1,000× faster Energy tunability	Excludes additional gains from horizontal (XPCS) and 2-D (GISAXS) focusing and wide bandpass (XPCS) multilayer mono operation

4.3.5.6 Instrument Enhancements

Several instrument enhancements are required to complete the upgrade process and take full advantage of the increased brightness and flexibility provided by the tandem IDs:

- On-axis viewing is required for locating increasingly small samples.
- A kappa diffractometer will facilitate novel sample environments for wide angle XPCS experiments but the stability and load capacity of such a device needs to be carefully evaluated before it is included as part of the upgrade plan.
- Extended exit flight path and exit flight path translations are required to maximize the range of accessible small-angle wave vector transfers. In this regard, designs from inelastic scattering beamlines at the APS and XPCS beamlines at LCLS and NSLS-II should be leveraged.
- New sample environments such as shear cells, pressure cells, compact high temperature ovens, flow cells, and the ability to apply electric and magnetic fields are required to support general user demands.
- The ability to rapidly and reliably switch between appropriate detectors for a particular set of measurements.
- For selected samples, high de-magnification 2-D focusing (i.e., zone plates) is required to better match coherence lengths to characteristic domain sizes.

As well as source brilliance, the other critical component assuring continued success of the XPCS program is a fast, small-pixel high-efficiency and high-gain or counting area detector. Table 4.3.5-5 summarizes the requirements for XPCS-suitable detectors.

Table 4.3.5-5. Requirements for XPCS-Suitable Area Detectors

Item	Requirement
Pixel size	≈ 75 μm or less
Number of pixels	≈ 1,000 × 1,000
Counting mode	Photon counting or high-gain integrating
Efficiency	100% for E < 20 keV
Frame rate	≥ 10^4 frames per second (fps)
Controls and firmware	On-the-fly compression and possibly on-board correlation

By late 2011 or early 2012, the above requirements, to a frame rate of 100 fps, will be satisfied by the second-generation ANL-LBL Fast CCD [4.3.5-13]. Faster frame rates from such a CCD await the development of the third-generation ANL-LBL Fast CCD featuring fully column-parallel readout [4.3.5-14]. Alternatively, Dectris and the Paul Scherrer Institute are in the midst of developing the Eiger detector, which promises 75-μm pixels, 24,000 fps, and photon counting. When released (~ 2013 or 2014), the Eiger detector promises to be an extremely powerful detector for XPCS. We also note that detector developments currently underway for the CHX beamline at NSLS-II [4.3.5-15] are very relevant and will be monitored. Specifically, design and development work is proceeding on the VIPIC and VIPIC-2 detectors that promise 80-μm pixels and even faster readout than the Eiger detector. We also note in passing that detector developments for LCLS tend to be somewhat less relevant because of the low repetition rate (120 Hz) of LCLS.

Having just completed a major upgrade, including the recent installation and commissioning of a high-speed version of the Pilatus 1M detector, namely the Pilatus 1MF, the GIXS setup will remain largely intact. Additional required features will facilitate measurements of lateral ordering and especially fluctuations at liquid surfaces and interfaces. The first requirement for such measurements is a single-bounce downward-deflecting x-ray mirror. The mirror should be 300-400 mm before the sample, have an incidence-angle range of 0-0.3˚ (providing a 0-0.6˚ incident angle on liquid), and be made with silicon with a rhodium stripe. The mirror-positioning assembly requires precision vertical (y) and horizontal (x) translations, and pitch and roll rotations. The second requirement for such measurements is a liquid-surface sample holder with various environmental options, such as surface pressure adjustment, temperature control, and solvent control, and is crucial in order to carry out *in situ* liquid-surface GIXS experiments, for example, floating lipid membrane phase separation and fluctuations. An additional upgrade to the GIXS set-up is the need for a gantry-like support and positioning assembly for the Pilatus 1MF detector similar to those used at macromolecular crystallography beamlines. Such an assembly will facilitate rapid changes in the sample-to-detector distance. It will also enable rapid and repeatable repositioning of the detector orthogonal to the beam direction so that overlap exposures can be obtained to eliminate "dark" regions in the collected scattering patterns resulting from the physical separation of the Pilatus's detection modules. A final upgrade requirement is a wide-field Pilatus detector that would permit simultaneous collection of wide-angle and small-angle scattering data.

4.3.5.7 References

[4.3.5-1] D. Lumma et al., Rev. Sci. Instrum. **71**, 3274 (2009).

[4.3.5-2] S. Park et al., Science **323**, 1030 (2009).

[4.3.5-3] T. Sun et al., private communication, 2010.

[4.3.5-4] J. DeBartolo et al., private communication, 2010.
[4.3.5-5] Z. Jiang and M. Mukhopadhyay, private communication, 2010.
[4.3.5-6] R. Dejus, private communication, 2010.
[4.3.5-7] S.-H. Lee and O. Schmidt, private communication, 2009.
[4.3.5-8] S. Narayanan et al., J. Synchrotron Rad. **15**, 12 (2008).
[4.3.5-9] M. Sprung, private communication, 2009.
[4.3.5-10] A. Fleurasu, private communication, 2009.
[4.3.5-11] D.L. Abernathy, G. Grübel, S. Brauer et al., J. Synchrotron Rad. **5**, 37 (1998).
[4.3.5-12] R. Conley, private communication, 2010.
[4.3.5-13] J. Weizeorick, private communication, 2010.
[4.3.5-14] P. Denes, private communication, 2010.
[4.3.5-15] A. Fleurasu, private communication, 2010.

4.3.6 *section deleted*

4.3.7 Fluid Dynamics Imaging Upgrade [CAS]

High-pressure, high-speed sprays are an essential technology in many industrial and consumer applications, including fuel-injection systems, inkjet printers, liquid-jet cutting tools, and liquid-jet cleaning systems. High-pressure sprays are optically dense, or the liquid droplets generated by the sprays scatter light so strongly that the detailed structure of the sprays can be difficult to study by conventional optical means. Other challenges arise from the transient nature of features of the jet sprays, such as frequently requiring imaging on microsecond or faster time scales. The importance of detailed gasoline and diesel fuel-spray analysis is well recognized as vital information that is needed to increase the combustion efficiency and reduce the emission of pollutants of internal-combustion engines.

Understanding the liquid-breakup processes in the region close to the nozzle has a significant bearing on the design of the nozzle geometry and is a key to realistic computational modeling. These interests have spurred considerable activity in the development of optical techniques to characterize fuel sprays. Despite significant advances in diagnostics over the last 20 years, the region close to the nozzle has not satisfactorily yielded to experiments designed to acquire quantitative information due to its optical opacity.

X-rays are highly penetrative in materials composed of extremely dense droplets of low-Z materials due to the intrinsically low interaction cross section. This makes x-rays a suitable tool for fuel-spray studies designed to overcome the limitations of visible light as shown in Figure 4.3.7.1. With the advent of synchrotron radiation sources, brilliant monochromatic x-ray beams are now available. These sources have paved the way for fast experiments of this type using monochromatic beams and achieving time resolution of 1 μs or better. At the APS, a dedicated fuel spray beamline was built at 7-BM-B based on a fast (μs) and quantitative radiography imaging technique. The data collected at the beamline have already started to make enormous scientific and engineering impacts on the transportation engine R&D community. The thrust of the upgrade of the beamline is to significantly improve the data throughput and the imaging quality by taking advantage of a more intense x-ray beam and longer source to sample distance as proposed in this section.

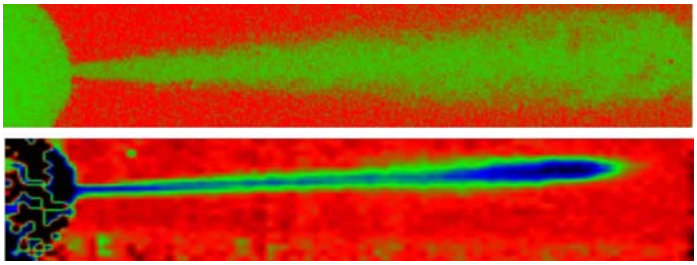

Figure 4.3.7.1. Comparison of optical (top) and x-ray (bottom) images of diesel sprays injected at a pressure of ~30 MPa and 10 μsec after the start of injection. The imaged area is 13 mm (horizontal) × 2.5 mm (vertical).

4.3.7.1 Scientific Scope

High-speed liquid injection is responsible for numerous scientific and technological applications such as fuel injection in internal-combustion engines, where fuel-jet breakup is a crucial precombustion step determining combustion efficiency and emission production. In an advanced internal combustion engine, the evolution of fuel sprays plays a defining role in controlling the efficacy of ignition and the uniformity of combustion. To enable high combustion efficiency, i.e., low NOx and soot emission, the

control of the fuel-air mixture ratio can be extremely crucial, as shown in Figure 4.3.7.2. Such control can be achieved by advanced and smart injection systems, to ensure combustion at optimal conditions. Therefore, key processes such as the physical breakup of fuel sprays are particularly critical in the design of new engines that will run on emerging fuels, such as biofuels.

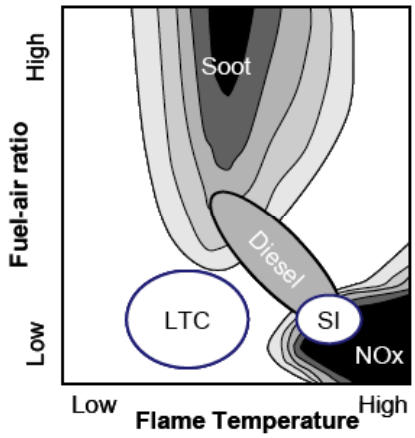

Figure 4.3.7.2. Combustion phase diagram: Traditional spark-ignited gasoline engines and diesel engines have to operate at unfavorable combinations of temperature and fuel-air ratios for the formation of NOx, and in the case of diesels, soot. Novel low-temperature combustion devices aim at creating conditions where the formation of soot and nitrogen oxides is avoided.

With time-resolved quantitative x-ray radiography, a significant amount of new knowledge has been learned in the past few years. The future success of this innovative research lies in proving the practicality of the technique and in demonstrating the accessibility of the technique to Argonne's industrial partners. That is the overall goal of this component of the APS-U project. By way of analogy, the structures of the sprays from different nozzles, different injection systems, and under different injection conditions bear the same relationships to one another as the structure of different proteins. They can be completely different objects, although probed by similar x-ray techniques. By using x-ray spray diagnostics, investigating the effects of nozzle geometry and injection parameters on near-nozzle spray characteristics becomes more feasible, which has significant bearing on the design of the nozzle geometry and the entire injection system. Prior to the new "x-ray vision" technique, the portion of fuel sprays nearest to the injector nozzle had been usually too opaque for visible light to penetrate, leaving engine designers and manufacturers to guess about conditions inside the fuel spray. Therefore, engine manufacturers and designers of combustion devices will directly benefit from acquiring the knowledge of fuel sprays by using this upgraded beamline. The scientific and engineering scope can be extended to test fuel sprays in the entire combustion phase diagram shown in Figure 4.3.7.2.

With the beamline afforded by the partner user program, Argonne will tackle the following scientific areas by answering the following critical questions:

- How do injection nozzles affect fuel breakup and atomization? The experiments will allow testing of the effects of many proposed breakup mechanisms, including turbulences of internal flows, spatial gradient and temporal pulsation of the internal pressure of the nozzle, internal cavitation due to the nozzle's physical geometry, and the change of the velocity profile at the nozzle exit.
- How do the physical properties of fuel affect the breakup? The breakup and the spray morphology are sensitive to viscosity, i.e., the surface tension of the fuel, especially at ambient temperatures that mimic the cold-start conditions of an engine with new types of

fuels, such as biodiesel from feedstocks. The relationship between the spray evolution and the physical properties of the fuel will be revealed in a quantitative manner.

- How do injection conditions affect the spray and breakup? With no doubt, the fuel breakup and atomization of fuels depend on the injection conditions such as injection pressure, timing, and cylinder pressure. In the future, this will be an effective method for Argonne to use to actively control the spray properties in real time.
- How do transient conditions affect the spray breakup? The use of conventional and alternative fuels for future advanced-combustion transportation engines has brought great impetus to the understanding of the fluid dynamics of fuel inside the nozzle orifice as well as the fuel spray outside, and their dependence on transient dynamics during opening and closing of the orifices. During transient conditions, the majority of harmful emissions are generated and this effect has been difficult to predict by any existing simulation models. The experimental evaluation of sprays in the transient situation is extremely desirable, if the spray morphology can be visualized and the fundamental breakup mechanism can be understood in a time-resolved manner.

4.3.7.2 Source Enhancements

Since the time-resolved radiography technique requires x-ray flux density to be as high as possible at the sample position, this will take full advantage of the 150-mA proposed higher-beam current in this Upgrade. With the double-intensity of the x-ray beam alone, the new beamline will have twice the throughput. In addition, the proposal is to have two types of operations: a pink beam in the first experiment station, and a monochromatic beam in the second downstream station.

4.3.7.3 Beamline Enhancements

Due to the physical limitations imposed by the existing FOE and experiment station at 7-BM, preserving the full beam flux while achieving a micrometer-sized beam was compromised. In the APS Upgrade, full use will be made of a normal-sized bending magnet beamline, where experimental stations are properly designed in the planning stage. Also, two normal-sized stations will accommodate the use of industrial-scale injection equipment.

The Upgrade includes three stations: an FOE and two experiment stations. The enhancements to the current 7-BM beamline are itemized as follows.

First optic enclosure (FOE):

- A water-cooled sagittal-focusing multilayer monochromator will be the main component in the FOE at 26 m from the source. A new bending mechanism will be designed to intercept the 3.5-mrad BM radiation cone. The larger bender can collect 70% more radiation than the current MLM does and it will have significantly less beam aberration due to anticlastic bending so that a theoretically predicated vertical focusing limit can be achieved.
- The second major optics in the FOE will be an x-ray mirror to allow 10-keV photons to pass through to the first experiment station for the pink beam operation.
- The third component in the FOE is a water-cooled filter bank that houses two to three edge filters to condition the pink x-ray beam with a desirable low-energy limit.

First experiment station – pink beam station:

- For low-spatial-resolution imaging (> 75 μm resolution), an unfocused pink x-ray beam can be used to image the sprays with a pixel array detector (see section 4.3.6).

- For higher-spatial-resolution imaging (10-μm resolution), a pink x-ray beam will be focused with a pair of high-quality K-B mirrors intercepting 2 mm (H) × 2 mm (V) of the unfocused pink beam. In-line magnification of 1:15 will be used to achieve this spatial resolution with the pixel array detector with a pixel size of 150 μm × 150 μm.
- A combination of a ms-chopper and a μs-chopper will be installed in the station. The former should be in front of the K-B mirrors and the latter should be immediately after the mirrors and near the focal point. The purpose of the choppers is to reduce the radiation damage to the detector and the mirrors.

Second experiment station – mono-beam station:

- The wide-bandpass monochromatic beam will be used for the radiography measurement when precise mass density information is needed. While the multilayer monochromator provides sagittal focusing in the horizontal direction, a 300-mm-long K-B mirror will be used to focus the x-ray in the vertical direction to achieve a focused beam size to 200 μm (H) × 10 μm (V) at the sample position.
- In this station, the focal point can be set at a very upstream location so the in-line magnification will be possible to take advantage of the high efficiency of the 2D pixel array detector (see section 4.3.7.6).
- A combination of a ms-chopper and a μs-chopper will be installed in the station. Both can be placed in front of the K-B mirror. The purpose of the choppers is to reduce the radiation damage to the detector and the mirror.

4.3.7.4 Optics

The radiography imaging experiments are sensitive to the quality of the optics in the beamline. The experiments will be performed between 6 keV and 10 keV, in most cases. All mirrors can be coated with Au to maximize the critical angles.

4.3.7.5 Anticipated Performance

The upgraded beamline performance is summarized in Table 4.3.7-1.

Table 4.3.7-1. Beamline Specifications

Parameter	Target Specification
Beam energy	6 keV to 10 keV
Pink Beam intensity	5×10^{13} photons/s at beam focal point
Pink Beam focal size	10 μm (H) × 10 μm (V)
Pink Beam bandwidth	High-energy cutoff 10 keV, low-energy cutoff adjustable between 6 to 8 keV
Mono Beam intensity	5×10^{12} photons/s at beam focal point at 10 keV
Mono Beam focal size	200 μm (H) × 10 μm (V)

4.3.7.6 Instrument Enhancements

Thus far, the most advanced, time-resolved radiography detector for fuel spray study has been the analog PAD. Collaborating with Professor Sol Gruner at Cornell University, Argonne has proposed the development of a PAD, specifically for successive bunch imaging. The proposed specifications are given in Table 4.3.7-2. It will be built with a 0.25-μm CMOS process with a proven radiation-hardening by layout design. The signal will be analog integrated onto storage capacitors, as with the prototype PAD. There will be design modifications to allow the signal to be added into capacitors in steps prior to readout,

to integrate successive cycles of a repetitive process. The CMOS process allows a maximum chip area of about 21 mm on a side. The minimum size of the pixel depends on the functionality that is required within the pixel and cannot be specified exactly before a full layout has been designed. It is expected to be 150 μm on a side, corresponding to a format in the range of 140 × 140 pixels per chip. It is proposed that the chip will have all wire bonds only on one edge, making chips "buttable" next to one another on three sides. The format of the proposed detector is 2 × 4 chips. Again, depending on the size of the pixel, this corresponds to detectors of 280 × 560 pixels over an active area of 42 mm × 84 mm. The goal is to be able to do 8-bit imaging at successive frame rates of 150 ns (to accommodate the APS bunch structure), and full-well imaging at 1-μs frame rates.

Table 4.3.7-2. Proposed PAD Specifications

Parameter	Target Specification
Minimum exposure time	150 ns for 8-bit imaging 1 μs for full-well imaging
Capacitor well depth	2000-4000 x-rays
Nonlinearity (% full well)	< 0.2%
Diode conversion layer	500-μm-thick Si
Number of capacitor wells/pixel	5 - 8
Full chip frame time	4 ms/frame, e.g., 20 ms for 5 capacitors
Pixel size	150 μm on a side
Detector chip format	2 × 4 chips

4.3.8 *In Situ* Nanoprobe Beamline [U1.04.02.07]

X-ray fluorescence microprobes and nanoprobes at APS Sectors 2-ID and 26 ID have been used for novel studies in materials, environmental, earth and planetary science, biomedical and life science, and nanoscience. The world-class performance of these instruments has led to many ground-breaking scientific studies and technical developments over the last decade, as is evidenced by the publication record and ever increasing user demand. Driven by new scientific inquiries, however, the user community has expressed a critical need for significantly improved spatial resolution, much higher throughput, better detection schemes, additional contrast modalities, and sample environments adapted for specific inquires that are currently not available. Many of these requirements have been documented in several recent workshops [4.3.8-1]. To address these needs, we have proposed development of an *in situ* Nanoprobe (INP) beamline, which is in the APS-U project scope, and the upgrade of the existing Sector 2 capabilities into a Micro/Nanoprobe (MNP) branch, which is in the APS-U contingent additional scope. This design report presents the design for the INP, sited as a canted beamline in APS Sector 2.

The INP beamline will operate with a spatial resolution of 20-50 nm and provide various *in situ* environments, such as cooling to well below 70 K, heating to ~1000°C, flow of gases and fluids, and application of electric fields. The beamline will be designed with the future possibility to host, in addition, a nanoprobe instrument capable of characterizing samples with a highest spatial resolution approaching 5 nm, thus providing powerful capabilities for the study of advanced materials systems and devices. We outline here a concept that sites the INP as a canted beamline in Sector 2, next to the current microprobe programs. Such a combined facility, dubbed "Next Generation Nanoprobes," would consist of two hard x-ray branch lines, one branch supporting the *in situ* Nanoprobe and the second branch supporting the Micro/Nanoprobe. The MNP branch would continue to support the existing 2-ID-D and -E microprobes. An alternative to siting the INP at Sector 2 that we have considered would be construction of a new beamline at a different sector. This option would allow us to select and optimize a site for highest resolution capabilities, and would reduce construction impact on Sector 2.

The INP will use mirror optics to achieve a spatial resolution of 50 nm, to allow high-throughput fluorescence imaging, fluorescence tomography, and nanospectroscopy. A spatial resolution of 20 nm will be achieved by use of advanced diffractive optics such as zone plates (ZP) or multilayer Laue lenses (MLL). The INP will be optimized for fluorescence detection. In addition, it will provide coherent diffraction capabilities to allow mapping of low-Z matrices using hard x-rays [4.3.8-2]. The design provides significantly higher focused flux (10-100×) relative to current nanoprobes, due to higher focusing efficiency and wider bandpass of mirror optics. The INP takes advantage of the large penetration depth of hard x-rays for imaging of thick, complex systems, such as energy harvesting, storage and conversion systems, nanoelectronic devices, and advanced building materials, to analyze and quantify their constituent trace components as well as their chemical state. It will allow 2D and 3D imaging of hierarchical systems at different length scales, thereby avoiding sectioning of specimens or other preparation techniques. By being optimized for fluorescence detection, the INP instruments will provide very high elemental sensitivity, allowing e.g., the detection of individual nanoparticles in thick, complex environments. Imaging of the sample at cryogenic temperatures will reduce structural damage from high radiation dose and thus allow the study of, for example, trace element contamination in polymeric solar cells and other non-hydrated material systems based on organic matrices and scaffolds at very high spatial resolution [4.3.8-3–4.3.8-5]. Imaging at high temperature will allow, for example, understanding phase separation in inorganic solar cells. To optimize characterization of hierarchically organized systems, the INP will be designed to allow "zooming", i.e., switching between a high-flux configuration that uses partially coherent x-rays with large bandwidth to image structure and composition at large scale with 50-nm resolution and above, and a high-resolution configuration with a focal spot size of 20 nm that uses coherent x-rays and a small bandwidth. We will deploy fly scanning techniques in fluorescence mode to

acquire high-resolution maps with a large number of pixels in 2D and 3D, and utilize advanced detectors for transmission imaging to simultaneously correlate structure of low-Z matrices with fluorescence of other elemental constituents.

The x-ray source and beamline will be designed to optimize the performance of the proposed instruments. The beamline will be canted, with the MNP branch optimized for the MNP instruments in the energy range from 5 keV to 25 keV, and the INP branch optimized for the INP instrument in the energy range between 4 and 30 keV. We desire to use revolver-type undulators to maximize the brilliance of the source in particular in the high-energy range. For proper operation of scanning nanoprobes at the nanometer scale, beam stability and optics stability are of primary importance. To achieve high beam stability over days, and to allow nanospectroscopy of small sample areas, a beam-defining aperture will be used as the last optical component of each branch beamline. In addition, we will use beam position monitors to monitor the beam position in the beamline and close to the end station.

If the INP is added as a canted beamline to the existing Sector 2 program, impact of construction on the existing operation has to be minimized. We will carefully plan the beamline upgrade and installation schedule to accommodate ongoing operations. Since new optical components and new stations are required to accommodate an additional canted branch at Sector 2, an alternative to upgrading 2-ID that we consider is to build out a new sector with a canted front end at the Advanced Photon Source (green field option).

4.3.8.1 Scientific Scope

The scientific scope for the INP encompasses energy harvesting, energy conversion and storage systems, approaches to sustainable energy, and nanoelectronics. The instrument will also allow advances in environmental and planetary science and help provide a better understanding of biological and biomimetic systems.

Energy Materials and Applications: Efficient, affordable and scalable systems for energy harvesting, energy conversion and energy storage are major components of a secure energy future for the United States and the world. Concurrently, it is vital to minimize the environmental impact of energy technologies around the globe, providing sustainability for energy production and usage. For instance the rise of data centers and personal computing has continued to increase the fraction of energy usage dedicated to computing and related infrastructure, and makes increase of efficiency of electronics, with the dual purpose of improving energy efficiency and enabling future supercomputing capabilities, an important goal. The INP encompasses the study of advanced energy harvesting, conversion and storage systems, approaches to sustainable energy, platforms for advanced electronics and of materials and systems aimed at sustainable construction and carbon capture. All these systems have in common complex, hierarchical structures with nanoscale features in often nonplanar geometries, where small quantities of inhomogeneously distributed dopants, precipitates, contaminants, and second-phase particles play an increasingly important role in system performance. In many cases, we seek to understand and control material properties that determine system performance, system efficiency and environmental impact. Examples of materials systems and devices to be studied are solar cells, fuel cell components, and advanced battery concepts [4.3.8-6–4.3.8-7]. The science of nanoelectronics will include the study of complimentary metal-oxide semiconductor (CMOS) devices designed for 22-nm node technologies and below, with a view to increase performance, speed and power efficiency. Approaches to sustainable energy will include the study of advanced building materials that reduce CO_2 emissions, research on understanding natural carbon sinks and development of artificial carbon sinks, and biogeochemical cycling of metal contaminants [4.3.8-8–4.3.8-9]. In most cases, high spatial resolution, imaging at trace-level sensitivities in complex 2D or 3D geometries, and imaging under real operation conditions are required. Additional challenges need to be addressed to allow imaging of these systems: many systems,

such as organic solar cells or batteries fabricated ”bottom up” are based on organic matrices, making cryogenic protection during high-resolution imaging vital for minimizing radiation-induced changes.

Environmental Science and Planetary Science: Bioremediation is a powerful method to immobilize or remove contaminants, such as toxins and radioactive materials, from the environment. Bioremediation takes advantage of the capability of bacteria and biofilms to change the chemical state of metals in their environment. This allows the formation of chemical compounds that might be more stable than their precursors, reduces or prevents their dispersal in the environment, and permits easier removal of contaminated soil systems. These processes often take place in hydrated environments, which can affect both the chemical process as well as the dispersion of contaminants. Understanding the process of the uptake of metals by bacteria and the change of the chemical state of contaminants in interaction with bacteria and biofilms requires both high spatial resolution and high sensitivity to trace elements. The NGN facility will also be well suited to study interstellar grains collected, for example, by NASA’s Stardust mission or other missions aimed at collecting interplanetary dust particles from asteroids and comets. These particles are often less than 1 micron in size, thus requiring very high resolution for elemental imaging and chemical state study. Analysis of these particles will lead to better understanding of, for instance, the conditions in the dust clouds in interstellar and circumstellar space, and their formation in the solar nebula.

Biological and Biomimetic Systems: With current developments in genomics and proteomics, our knowledge of the enormous number of pathways in which metals and trace elements are necessary for life is ever increasing. However, this knowledge is largely static, as we still do not have appropriately sensitive approaches to follow the fluctuations in normal metal homeostasis that accompany processes of development, differentiation, senescence, stress responses, and so forth. Likewise, our knowledge about the redistribution of metals and trace elements that accompany the development of different diseases is equally lacking. Elemental fluctuations in cellular homeostasis involve dynamic changes in the concentrations and localization of metals, and an ever-increasing body of biological literature is showing the importance of metals in health and disease [4.3.8-10–4.3.8-13]. Metals are essential to most biological functions, and their dysregulation contributes to many degenerative diseases. Also, their uptake is important for many pathogenic diseases, including cancer growth. Metals and metal chelators represent an increasingly important class of drugs used to treat a diverse variety of diseases [4.3.8-14–4.3.8-18].

4.3.8.2 Source Enhancements

Each branch of the canted beamline will have a dedicated undulator. Each nanoprobe will cover a relatively broad energy range, to allow spectroscopy at and imaging close to the binding energies of elemental constituents in questions. As diffraction-limited resolution only uses the coherent flux provided by the source, it is of particular importance to maximize the brilliance of the insertion devices for high energies, where the coherent flux F_{coh} is relatively small due to its dependence on the energy, $F_{coh} \sim B*\lambda^2$. Figure 4.3.8-1 shows an example of the revolver-type devices, with a combination of periods of e.g., 3.3 cm for lower energies and 2.7 cm for higher energies. The 3.3-cm-period undulator will provide continuous energy coverage and good brilliance for lower photon energies, where coherent flux is large, while a 2.7-cm-period undulator can provide higher brilliance at selected high-energy regimes.

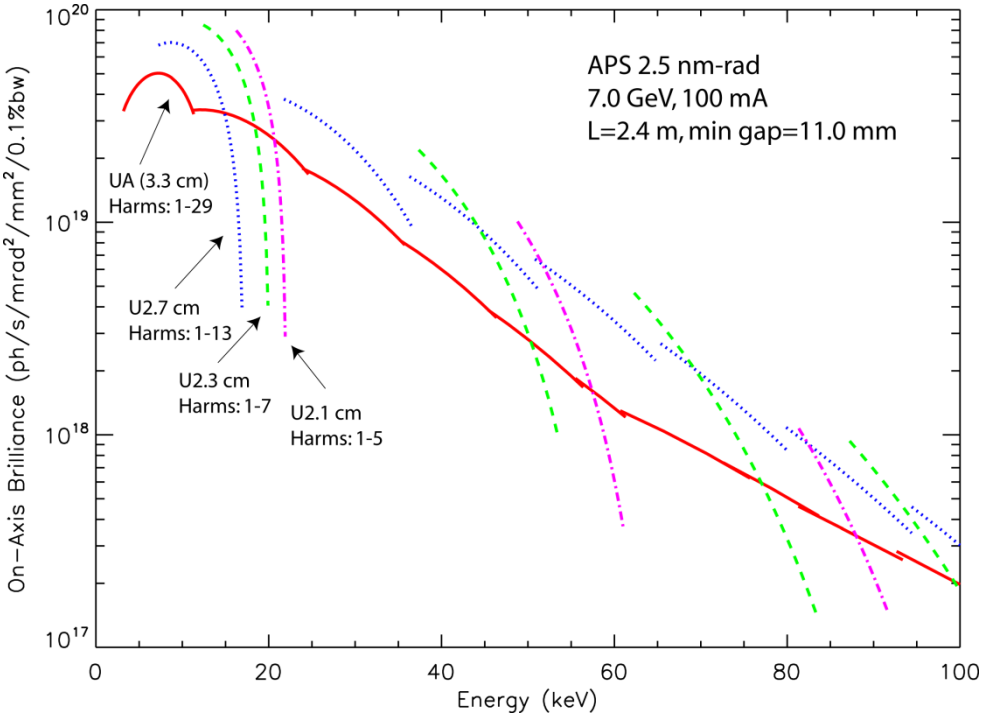

Figure 4.3.8-1. Brilliance of revolver-type IDs. The NGN facility would benefit from 3.3-cm-period ID for continuous coverage in the 4- to 30-keV range, and from 2.7-cm-period ID for higher brilliance at the 7- to 15-keV and the 22- to 30-keV energy regime (courtesy R. Dejus).

4.3.8.3 Beamline Description

We describe here the option of siting the INP beamline on a new canted branch in APS Sector 2. In addition to the beamline optics required for the INP, this option requires both installation of additional optical components for the existing Sector 2 program and lengthening of the existing first optics enclosure 2-ID-A to accommodate optics for both branch lines.

The beamline layout is based on using diffraction-limited focusing to achieve high spatial resolution, and manipulation of a spatial filter to allow easy switch to higher flux at lower spatial resolution. Diffraction-limited imaging requires coherence preservation and matching of the lateral coherence length of the incident beam to the acceptance of the focusing optics. To achieve diffraction-limited imaging, the focusing optic must accept the spatially coherent part of the incident beam. We will match the acceptance D of the focusing optic to the vertically coherent part s_v of the x-ray source, $D = 0.5 \lambda/s_v$. Since the source is much larger horizontally than vertically, a beam-defining aperture (BDA) will be used to define a secondary source. This scheme allows extraction of the full coherent fraction of the undulator beam, while providing significant flexibility in operation of the nanoprobe instrument. In particular, by changing the size of the BDA, the (horizontal) spatial coherence can be changed to allow a trade of flux vs. spatial resolution in the horizontal direction (see Figure 4.3.8-2).

To allow operation of two branch beamlines with full undulator control in parallel, several steps will be taken: the MNP branch, with energies between 5 and 25 keV, will employ a horizontally deflecting double-mirror system M2, which will steer the beam outboard by 12 mrad using two consecutive reflections in the same direction. The INP branch, with energies from 4 to 30 keV, will employ a single mirror system M1 that will steer the beam inboard by 5 mrad. Together, this will produce an angular separation ~ 16-18 mrad between the two branch lines, which results in a separation of 600-

700 mm at the end stations. Each branch will have two interchangeable monochromators. Horizontally diffracting double-crystal monochromators, H-DCM, will be used to provide a stable beam at high spectral resolution, as required for spectroscopy and focusing with diffractive optics. Double-multilayer monochromators, H-DMM, will be used to provide high flux for imaging applications with reflective optics. The final beamline optics for each branch is the BDA at a position of approximately 40 m from the source. The BDA will provide fixed source position in the horizontal direction and thereby minimize the effect of potential drifts of mirror and monochromators on the position of the beam focus in the nanoprobes.

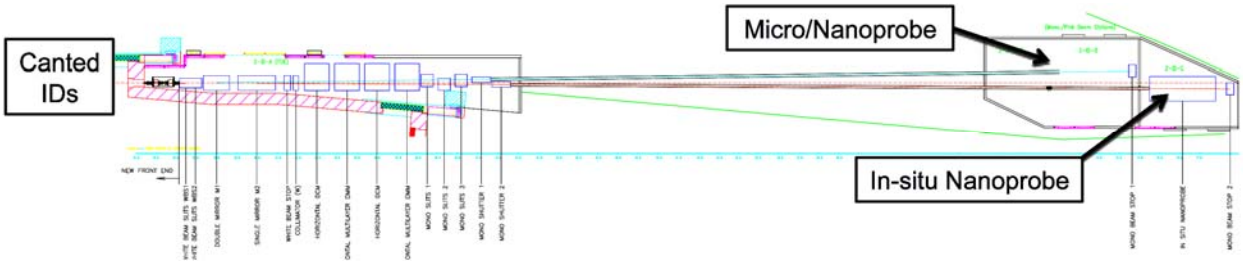

Figure 4.3.8-2. Layout of the NGN beamline with stations and major beamline components.

For all monochromators, a horizontally deflecting geometry will be utilized. This has the significant advantage that an imprecision in energy scans results only in a displacement of the beam on the BDA, and does *not* translate into motions of the focal spot. In addition, most monochromator vibrations in this geometry will lead only to a horizontal source vibration across the BDA, and therefore not in an apparent source vibration (which is defined by the position and stability of the BDA) and corresponding movement of the focal spot position. This setup leads to some loss due to reduced reflectance caused by the mismatch between the horizontally polarized x-ray beam and the horizontally reflecting crystal plans. The loss amounts to 67% for a Si <111> monochromator at 4 keV, and lessens with increasing photon energy to 2% at 10 keV and 0.3% at 30 keV. The loss amounts to 16% at photon energy of 5 keV for the diamond <111> monochromator used for the MNP branch. Since coherent flux is largest at low energies, $F_{coh} \sim B*\lambda^2$, the reduction of reflectivity at low energy will have little effect on the overall instrument performance. For the multilayer monochromators, the Bragg angles are much shallower than for the crystal monochromator, and, consequently, the polarization-related losses are much lower.

The canted front end will be designed for windowless operation and will be capable of handling the heat load from the two 2.4-m devices at relevant synchrotron current. The exit mask will have two apertures of 2 mm × 2 mm each, which will limit the total power that enters the first optics enclosure. The exit mask will be followed by white beam slits WBS1 and WBS2, each with tungsten blades for effectively aperturing of the canted beams to limit the total power incident on the first optical component.

For the INP branch, a single water-cooled mirror system M1 will be used to deflect the beam inboard, providing higher harmonic rejection and reducing significantly the heat load on downstream monochromators. The mirror will have a substrate length of ~ 800 mm with Si, Rh, and Pt coatings and a fixed grazing incident angle of ~2.6 mrad. The mirror will be illuminated along its full length, thereby avoiding thermal bumps. Mirror M1 will be located at ~ 28 m from the source and will include beam diagnostics components. This will be followed by a horizontally diffracting double-crystal monochromator H-DCM, using LN2-sidecooled Si crystals with small offset (5-10 mm) to provide high angular stability and a monochromaticity $\Delta E/E$ of 10^{-4}. For high flux measurement, the H-DCM can be interchanged with a horizontal diffracting double-multilayer monochromator H-DMM, which uses narrow bandwidth multilayers ($<10^{-2}$) with offset to match the H-DCM. These two monochromators will be

located at 36-38 m and will contain beam diagnostics components. For experiments that permit a large bandpass, both monochromators can be retracted. They will be followed by a beam-defining aperture BDA3 mounted on a stable granite support at ~ 40 m. The BDA enables spatial filtering by adjusting its width to select the spatially coherent beam size for illumination of the zone plate. The BDA is adjustable from approximately 10 μm to 2 mm. Typically, the BDA will be closed to a size $d = 0.5 \cdot L'\lambda/D$, to form a spatially coherent x-ray source for the zone plate. By opening the BDA in a controlled fashion, the x-ray flux on the specimen can be increased, for example, to perform fast low-statistics scans of large specimen areas. The INP end station with the nanoprobe instrument is positioned roughly 75 m from the source.

4.3.8.4 Optics

The canted beamline is designed to achieve, with the INP instrument, a spatial resolution of 20 nm with maximum flux in the diffraction-limited focal spot. This requires extraction of the coherent flux from the x-ray source, best possible coherence preservation during low-pass filtering and monochromatization in the branch lines, and optimum focusing efficiency for the high-resolution optics.

Focusing Optics

The INP will deploy an advanced mirror system to achieve a 2D spot size as small as 50 nm, and diffractive optics, such as stacks of zone plates or multilayer Laue lenses, for further focusing to 20 nm. A wide bandpass of 1% can be used with focusing mirrors for elemental mapping, yielding very high focused flux particularly at high photon energies. Table 4.3.8-1 provides an estimate of the photon flux focused on the sample for different energy ranges and optics. The combination of very high focused flux with high spatial resolution and optimized fluorescence geometry makes feasible the detection of around ten metal atoms in low-Z matrices with an exposure time on the order of one minute (see Table 4.3.8-3).

Table 4.3.8-1. Estimate of Focused Photon Flux in the *in situ* Nanoprobe for Different Photon Energies. An efficiency of 20% for diffractive optics (zone plates or "flat" MLLs) is assumed across the full energy range between 4 and 30 keV. A reflectivity of 80% for the focusing mirror is assumed. A bandwidth of 1% is used for focusing with the mirror system using the double-multilayer monochromator; a bandwidth of 0.01% is used for focusing with diffractive optics using the double-crystal monochromator.

Energy [keV]	**4**	**6**	**10**	**15**	**20**	**30**
Brilliance [photons/s/mm/mrad/0.1% BW]	$4 \cdot 10^{19}$	$5 \cdot 10^{19}$	$7 \cdot 10^{19}$	$2 \cdot 10^{19}$	$1 \cdot 10^{19}$	$2 \cdot 10^{19}$
Photon flux in mirror focus with spot size of 50 nm, $\Delta E/E = 10^{-2}$						
Coherent flux [photons/s/1% BW]	$3.9 \cdot 10^{12}$	$2.2 \cdot 10^{12}$	$1.1 \cdot 10^{12}$	$1.4 \cdot 10^{11}$	$5.8 \cdot 10^{10}$	$3.4 \cdot 10^{10}$
Focused flux [photons/s]	$3.1 \cdot 10^{12}$	$1.7 \cdot 10^{12}$	$8.7 \cdot 10^{11}$	$1.1 \cdot 10^{11}$	$4.6 \cdot 10^{10}$	$2.7 \cdot 10^{10}$
Focused flux density [photons/s/μm^2]	$1.2 \cdot 10^{15}$	$6.9 \cdot 10^{14}$	$3.4 \cdot 10^{14}$	$4.4 \cdot 10^{13}$	$1.8 \cdot 10^{13}$	$1.1 \cdot 10^{13}$
Photon flux in zone plate focus with spot size of 20 nm, $\Delta E/E = 10^{-4}$						
Coherent flux [photons/s/0.01% BW]	$3.8 \cdot 10^{10}$	$2.2 \cdot 10^{10}$	$1.1 \cdot 10^{10}$	$1.4 \cdot 10^{9}$	$5.8 \cdot 10^{8}$	$3.5 \cdot 10^{8}$
Focused flux [photons/s]	$7.8 \cdot 10^{9}$	$4.3 \cdot 10^{9}$	$2.2 \cdot 10^{9}$	$2.8 \cdot 10^{8}$	$5.8 \cdot 10^{7}$	$3.4 \cdot 10^{7}$
Focused flux density [photons/s/μm^2]	$1.9 \cdot 10^{13}$	$1.1 \cdot 10^{13}$	$5.4 \cdot 10^{12}$	$6.9 \cdot 10^{11}$	$1.4 \cdot 10^{11}$	$8.6 \cdot 10^{10}$

Focusing mirrors have seen very significant development over the last 10 years, with a demonstrated spatial resolution of below 10 nm in one dimension at a beamline with a length of 1 km, and a spatial resolution of around 100 nm at beamlines with typical length of 50-80 m. Based on novel

mirror geometries, in particular the Montel design, the APS optics group is pursing an R&D path that makes focusing to 50 nm feasible over the next 5 years.

Diffractive optics combine ease of alignment with compactness and intrinsic capability to focus x-rays to very small spot size. At the same time, the focusing efficiency of high-resolution zone plates has been very low in the hard x-ray range, and multilayer Laue lenses still require multidimensional alignment. Several of these issues can be addressed by employing advanced nano-engineering approaches, in particular microelectromechanical systems (MEMS) techniques. For example, we are currently developing MEMS-based approaches for both stacking up to four zone plates within the optical near-field and to achieve quasi-monolithic MLLs devices. However, continued improvement in existing fabrication technologies and novel approaches, such as deployment of atomic layer deposition (ALD) approaches, is required to achieve the potential of diffractive optics for the hard x-ray range.

4.3.8.5 Anticipated Performance

The main criteria for instrument performance are spatial resolution, elemental sensitivity, throughput and range of *in situ* parameters. The spatial resolution is determined by coherence preservation in the beamline optics, beamline stability, and the performance of the focusing optics. The elemental sensitivity is determined by background levels and photon statistics. The throughput is determined by the focused photon flux and detection efficiency. We will use advanced mirror optics with a focusing efficiency of 80% for focusing to 50 nm. Mirrors can accept a bandwidth of $\Delta E/E$ of 1% for imaging, while a bandwidth of better than 0.1% is required for nanospectroscopy. Advanced diffractive optics systems, either multiple zone plates or MLLs in MEMS-manipulators, are expected to provide a focusing efficiency of 10-20% across the full energy range of 4 – 30 keV. These optics require a bandwidth of 0.1% or below. We will use these parameters in estimating the sensitivity below.

A critical aspect of the INP instruments is the expected elemental sensitivity. Generally speaking, two effects have an influence on the sensitivity. The signal-to-background level plays a significant role, in that, even with nearly ideal photon statistics, the characteristic fluorescence from an element must rise above the background level (e.g., due to incomplete charge collection in the detector or bremsstrahlung from the ionized electrons), particularly for thick samples. For example, for an incident flux of (0.5-9)*10^8 photons/sec and a detected solid angle of 0.001, Sparks estimates a sensitivity for Zn of ~0.5 µg/g/sec in a matrix of similar atomic numbers [4.3.8-19]. For NGN configuration with diffractive optics, a focused flux on the order of 10^{10} photons/sec and a detected solid angle of 0.25 is expected, so this would correspond to a sensitivity of 0.08 ppm/sec in a matrix of similar Z. In a matrix of low Z, a better signal-to-background ratio is anticipated, yielding a sensitivity exceeding 80 pM for Zn. However, the main purpose of the instrument will not be to investigate an infinitively thick specimen. Since the thickness of the sample plays a significant role in quoting the elemental sensitivity as a concentration, elemental sensitivity as a minimum number of atoms that can be detected in a given time will be estimated. Table 4.3.8-2 shows the minimum detection limits (MDLs), as measured at the hard x-ray microprobe 2-ID-D at the APS [4.3.8-20].

Table 4.3.8-2 Measured MDLs for Selected Elements of Interest in the Hard X-Ray Microprobe Installed at 2-ID-D (in a focused spot size of 200 × 200 nm^2, for a dwell time of 1 s at 10-keV incident energy, at a solid-angle coverage of the fluorescence detector of ~ 5%)

Element	Ca	Fe	Zn
Grams	$3.5E^{-17}$	$1.0E^{-17}$	$2.2E^{-18}$
Atoms	$5.3E^{+5}$	$1.1E^{+5}$	$2.0E^{+4}$

Three different modes are envisioned for the main instrument, resulting from using two different sets of optics (a high-resolution zone plate or "flat" MLL objective with a spatial resolution of ~20 nm, and a mirror optic with a spatial resolution of ~50 nm) and two different sets of monochromators (a DCM with a bandwidth of 10^{-4}, for nano-XANES and chemical-state mapping applications, and a DMM with a bandwidth of 10^{-2}). (1) Highest resolution is obtained by using diffractive optics coupled with a DCM. (2) Highest flux with 50 nm resolution is obtained by use of mirror optics coupled with a DMM. (3) Nanospectroscopy with 50 nm resolution is performed by use of mirror optics coupled with a DCM. In these configurations, we obtain, based on the above measurements, the MDLs listed in Table 4.3.8-3. The sensitivity for Zn is highest since the photon energy of the incident x-rays is closed to the absorption edge of Zn. By tuning the incident energy to be close to the absorption edges of other materials (e.g., Ca and Fe in the example in the table), the sensitivity will be significantly higher than listed.

Table 4.3.8-3 Estimated MDLs in Atoms for the *in situ* Nanoprobe for Excitation with X-rays with a Photon Energy of 10 keV, and with an Exposure Time of 1 second

	# of Ca atoms	**# of Fe atoms**	**# of Zn atoms**
nano-XANES, δ = 50 nm, $\Delta E/E = 10^{-4}$	15000	3000	560
Elemental mapping, δ = 20 nm, $\Delta E/E = 10^{-4}$	2500	500	90
Elemental mapping, δ = 50 nm, $\Delta E/E = 10^{-2}$	1500	300	60

For these estimates, a twice increased incident flux (compared with APS beamline 2-ID-D) is assumed, based on higher storage ring current and more optimized undulator, as well as an increased detector acceptance by factor 5, using an optimized multi-element detector geometry. The experiment-based MDL correlates well with simulations we performed. It should be noted that the estimates for MDLs in micro-XANES mode for the above table reflect only the detection limit. They do *not* include radiation damage that might alter the chemical state during the measurement [4.3.8-21–4.3.8-22].

Table 4.3.8-4 Molar Concentrations for 100 Atoms of Trace Element in Water within the Probed Volumes

	Volume	**Molarity**
100 atoms in	$0.02 \times 0.02 \times 1\ \mu m^3$	$4e^{-4}$ mol/l
100 atoms in	$0.02 \times 0.02 \times 10\ \mu m^3$	$4e^{-5}$ mol/l
100 atoms in	$0.05 \times 0.05 \times 1\ \mu m^3$	$7e^{-5}$ mol/l
100 atoms in	$0.05 \times 0.05 \times 10\ \mu m^3$	$7e^{-6}$ mol/l

To put the above estimates into perspective, Table 4.3.8-4 shows the calculated elemental concentrations in water for 100 atoms in volumes that would typically be probed. To show how these concentrations compare with the metal content of biological cells, Table 4.3.8-5 lists some of the elemental content of yeast cells grown in a metal-depleted minimum medium, as measured by Outten and O'Halloran (2001) [4.3.8-23]. It should be noted that these metal concentrations represent the average over the whole cell, so local concentrations could be much higher when the elements are not homogenously distributed.

Table 4.3.8-5 Elemental Content of Yeast Cells Grown in a Metal-Depleted Medium (derived from [4.3.8-23])

Element	K	Ca	Cr	Mn	Fe	Ni	Cu	Zn	Se
[Metal] mol/l	$1e^{-1}$	$1e^{-4}$	$1e^{-6}$	$1e^{-6}$	$1e^{-4}$	$<2e^{-6}$	$5e^{-6}$	$1e^{-4}$	$1e^{-6}$

4.3.8.6 Instrument Enhancements

To study the materials and systems proposed, it is necessary to provide adjustable temperature, flow of different gases and fluids, and application of electric fields. The main focus in the design of the INP will be to provide a temperature range from 90K and below to 1000°C and above, with a temperature accuracy of 0.1 K. Imaging at cryogenic temperature will allow study of (non-hydrated) soft matter samples; imaging at elevated temperature will allow study of, e.g., formation of precipitates, or changes of dopant distrubutions under annealing. We will provide flow of gases and fluids to the sample if needed, in order to simulate real processing conditions. We will also install feedthroughs that allow application of electrical fields to the sample, to record, e.g., current voltage characteristics of devices.

The INP end station will provide an environmentally controlled specimen area as outlined above. To achieve diffraction-limited resolution, vibration isolation of the experimental system will be crucial, along with an encoder-based positioning system. We will use laser interferometers to accurately measure the position of the sample and the optic. In addition, we will measure the sample temperature, and implement advanced controls approaches to correct the specimen position in response to drifts [4.3.8-24–4.3.8-25]. The supported experimental techniques will include x-ray fluorescence (for elemental mapping, chemical state mapping, and nano-XANES), absorption and phase contrast, as well as coherent diffraction in small-angle geometry to allow mapping of low-Z matrices at very high spatial resolution. Energy-dispersive detectors will be used to detect x-ray fluorescence radiation; dedicated transmission detectors will be used for absorption and (differential) phase contrast. A pixel array detector will detect scattered radiation at high dynamic range to allow data reconstruction using ptychography. The focused flux and throughput of a scanning x-ray microprobe or nanoprobe is intrinsically limited by the brilliance of the x-ray source (i.e., the coherent flux provided by the x-ray source). Therefore, it is mandatory to make use of as much the fluorescence radiation emitted by the specimen as possible. In addition, radiation damage degrades biological samples or soft materials at high resolution. In particular, the chemical state of elements can be changed at even lower radiation dose, making effective collection of emitted signal essential. A multielement energy-dispersive detector system, which can collect large solid angles, is therefore required. In particular, a setup is envisioned where a multielement detector is positioned to the side of the specimen to take advantage of the minimized scattering at 90 degrees (in plane) to the incident x-rays. This will be complemented by a multielement silicon drift diode either in front of or behind the specimen. A circular hole in the detector center will allow the direct beam to pass through, and the detector can be moved very close to the specimen to maximize the detected x-ray fluorescence, while preserving the capability to mount and scan relatively large specimens. Simultaneous data acquisition also brings the advantage that certain effects (e.g., sample absorption) can be accounted for by cross comparison.

For accurate positioning of sample and focusing optics, the INP will have laser interferometer encoders and temperature sensors with related feedback controls to achieve high positioning accuracy. A state-of-the-art off-line optical microscope will be used for sample prealignment. Telescopes with high-resolution cameras will be used for *in situ* monitoring of the sample. Kinematic specimen mounts will be designed to allow as much compatibility as possible with other instruments, such as electron microscopes, and visible light microscopes. In particular, we plan to coordinate our efforts with other instruments that can provide complementary information, such as infrared microscopy, soft x-ray microscopy, light microscopy (including confocal laser scanning microscopy), and analytical electron microscopy.

4.3.8.7 Micro/Nanoprobe Beamline [CAS]

The current Sector 2 fluorescence microprobes support a strong program that focuses on environmental science, biology, and materials science. Systems studied include bacteria/soil systems relevant to environmental sciences, cells and tissues with an impact on understanding biological processes and life sciences, and metal impurities that impact the performance of inorganic solar cells. The microprobes currently achieve a spatial resolution of 150-300 nm with zone plate optics.

We plan to upgrade the existing Sector 2-ID-D/E microprobe beamline to a Micro/Nanoprobe branch optimized for fluorescence imaging of static samples in 2D and 3D. We will use mirror-based focusing optics to provide a spatial resolution down to 50-70 nm for the 2-ID-D nanoprobe at ambient or cryogenic temperature, and 200 nm for the 2-ID-E microprobe at ambient temperature. Significantly higher focused flux (10-100×) relative to current microprobes is expected, due to higher focusing efficiency, larger beam acceptance, and wider bandwidth of mirror optics. This will enable the Micro/Nanoprobe to further enhance the very successful program and the large user community already developed at 2-ID.

The beamline layout for the MNP branch in the Sector 2 siting option is similar to the INP branch. Two consecutive water-cooled mirrors M2 will be used to deflect the beam outboard. The substrate length of each mirror is ~ 700 mm with Si, Rh, and Pt coatings for higher harmonics rejection and a fixed incident angle of ~3 mrad. Mirror M2 will significantly reduce the heat load on the downstream monochromators by absorbing most photons with energy above the cutoff-energy of the mirror. M2 will be located ~ 30 m from the source and will include beam diagnostics components. This will be followed by a horizontally diffracting double-crystal monochromator (H-DCM), using diamond crystals with small offset (~ 10 mm) to provide an x-ray beam with high angular stability and a monochromaticity $\Delta E/E$ of 10^{-4} for the 2-ID-D nanoprobe. Thin diamond (~ 100 μm) will be employed as the first crystal, such that undiffracted x-rays above 6 keV will be transmitted and available for use by the 2-ID-E microprobe. For high-flux measurements, the H-DCM can be interchanged with a horizontally diffracting double-multilayer monochromator (H-DMM), which uses multilayers with a narrow bandwidth of $\Delta E/E = 10^{-2}$ or smaller, with an offset to match the H-DCM. The monochromators will be located at ~ 33-35 m, and will contain beam diagnostics components. They will be followed by two beam-defining apertures BDA1 and BDA2 (for the MNP instruments) mounted on a stable granite support at ~ 38 m. The MNP instruments are located in the end station at ~ 68 and 71 m, respectively.

4.3.8.8 Summary of Siting Options for the INP

Option 1: Siting of the INP at APS Sector 2

We have presented here an option for siting the INP beamline as a canted beamline in Sector 2. This option involves construction of a canted front end with an angular separation between undulator beamlines of 1 mrad, and beamline optics that further separate the x-ray beams (600-700 mm) to allow operation in separate and independent hutches. Additional resources, as requested in the contingent MN section (see above), are:

- Two mirror systems, to deflect the beam for the existing Sector 2 beamline outboard to provide sufficient separation of the endstation instruments.
- One crystal monochromator and one multilayer monochromator capable of passing beam to the ISN branch line while allowing independent selection of energy for the existing Sector 2 MN.
- Extend the 2-ID-A hutch to accommodate beamline optics for both ISN and MN branches.
- Construction must be scheduled such that interruptions to the ongoing scientific programs at Sector 2 are minimized.

Option 2: Siting as a canted beamline at a new location

The INP could alternatively be located as a canted beamline at a separate APS sector. Advantages would be:

- A site with optimized vibration background could be chosen. This would be of particular relevance for the future possibility of hosting an instrument with a spatial resolution limit approaching 5 nm.
- Nanoprobes require positioning as far from the source as possible, to maximize the working distance at diffraction-limited resolution. As such, it could be advantageous to site the ISN beamline at an ID port that supports instrumentation that does not use the full length available on the floor, and where a transport pipe for the ISN would be compatible with the exsiting instrument.

4.3.8.9 References

[4.3.8-1] T. Paunesku, S. Vogt, T. C. Irving et al., Int. J. Radiat. Biol. **85**(8), 710 (2009); DOI: 10.1080/09553000903009514

[4.3.8-2] B. Abbey, K.A Nugent, G.J Williams et al., Nature Physics **4**(5), 394 (2008).

[4.3.8-3] M.R. Howells et al., J. Electron Spectrosc. **170**(1-3), 4 (2009).

[4.3.8-4] J. Maser et al., J. Microsc.-Oxford **197**, 68 (2000).

[4.3.8-5] T. Beetz and C. Jacobsen, J. Synch. Radiat. **10**, 280 (2003).

[4.3.8-6] M Armand and J.M. Tarascon, Nature **451**(7179), 652 (2008).

[4.3.8-7] B Dunn, J.W. Long, D.R. Rolison, Electrochem. Soc. Interface **17**(3), 49 (2008).

[4.3.8-8] F.M. Morel and N.M. Price, Science **300**(5621), 944 (2003).

[4.3.8-9] R.S. Oremland and J.F. Stolz, Science **300**(5621), 939 (2003).

[4.3.8-10] L.A. Finney and T.V. O'Halloran, Science **300**(5621), 931-936 (2003).

[4.3.8-11] B. Desoize, In Vivo **17**(6), 529 (2003).

[4.3.8-12] J.F. Mercer, Trends Mol. Med. **7**(2), 64 (2001).

[4.3.8-13] P.M. Doraiswamy and A.E. Finefrock, Lancet Neurol. **3**(7), 431 (2004).

[4.3.8-14] K.H. Thompson and C. Orvig, Science **300**(5621), 936 (2003).

[4.3.8-15] N. Farrell, Coordin. Chem. Rev. **232**(1-2), 1 (2002).

[4.3.8-16] Z.J. Guo and P.J. Sadler, Angew. Chem. Int. Edit. **38**(11), 1513 (1999).

[4.3.8-17] J. Reedijk, Curr. Opin. Chem. Biol. **3**(2), 236 (1999).

[4.3.8-18] C.X. Zhang and S.J. Lippard, Curr. Opin. Chem. Biol. **7**(4), 481 (2003).

[4.3.8-19] C. J. Sparks, "X-ray fluorescence microprobe for chemical analysis," in *Synchrotron Radiation Research*, H.Winick and S. Doniach, Eds., pp. 459-512, Plenum Press: New York, 1980.

[4.3.8-20] B. Lai, Personal communication.

[4.3.8-21] J.M. Holton, J. Synchrotron Radiat. **14**, 51 (2007).

[4.3.8-22] J. Yano et al., Proc. Natl. Acad. Sci. USA **102**(34), 12047 (2005).

[4.3.8-23] C.E. Outten and T.V. O'Halloran, Science **292**(5526), 2488 (2001).

[4.3.8-24] A. H. Koevoets et al., Proc. of 13th International Workshop on THERMal INvestigation of ICs and Systems, THERMINIC 2007, September 17-19, 2007, Budapest, Hungary, 2007, pp. 208-213.

[4.3.8-25] B. Mokaberi and A. A. G. Requicha, IEEE T. Autom. Sci. Eng. **3**, 199 (2006).

4.3.9 Transmission X-ray Microscopy Upgrade (32-ID) [CAS]

High-resolution x-ray microscopy (TXM) is a full-field direct imaging method with 15-nm resolution in 2D and 3D and better than 10 Hz exposure rate. Combined with tunable synchrotron x-ray sources, the elemental and chemical compositions can also be mapped dynamically in 3D. This makes TXM a unique tool for dynamic *in situ* studies with not only the 3D morphology of nano-structures, but also their physical and chemical reactions in real time. Since its introduction, the TXM system has proven to be the most effective method to study 3D mesoscale devices and their functions in real operational conditions. In particular, the TXM system at 32IDC has been applied to investigate a wide range of applications in energy production, energy storage, material science, electrochemistry, biology, and infrastructure materials. The TXM has been a critical tool for these studies for the very reason that the function of these devices is largely determined by the morphology and chemical reactions of these nano-structures. As these applications have become critically important for the mission of DOE as well as our national interest, we expect the TXM will become an increasingly important tool for the future of scientific research.

The TXM system at 32IDC currently leads the world's hard x-ray TXM facilities in resolution, speed, and *in situ* imaging capabilities. However, many facilities around the world have realized the potential of the TXM technique and are actively developing indigenous instruments or purchasing commercial systems. Major high-resolution TXM facilities have been planned for Beijing Synchrotron, Shanghai Synchrotron, SRRC at Taiwan, ANKA, NSLS/NSLS2, etc., some with multiple beamlines dedicated to this technique. This proposal describes a plan to significantly expand the capabilities of the TXM technique at APS, particularly its ability to map a greater range of elemental composition and chemical states at nanometer scale. Its *in situ* 3D imaging capabilities, as well as the ability to synthesize the TXM data with information from other analysis techniques includes x-ray fluorescence microscopy, x-ray micro-CT, x-ray diffraction, small-angle scattering, and electron microscopy techniques. Our strategy is to exploit the significant high-energy advantage of APS to place the TXM at 32IDC significantly ahead of other synchrotron radiation facilities in resolution, automation, *in situ* imaging, and material analysis capabilities. The capability improvements planning for the upgrade are summarized in Table 4.3.9-1 in section 4.3.9.4. Successful implementation of the upgrade will make APS the premier facility for TXM and nano-CT imaging in the world for scientific and industrial research.

4.3.9.1 Scientific Scope

The proposed upgrade will bring significant benefits to our user base, particularly those in the field of energy production and storage, and many with direct DOE funding. In this section, we will describe three examples of the TXM's scientific program in energy production, energy storage, and electrochemistry.

Energy Production – Fuel Cell Development

Although there are many advantages of using a solid oxide fuel cell (SOFC) for efficient energy conversion, significant technical challenges remain before this technology can be commercialized and used on a large scale. Substantial power and electrical efficiency losses can arise in a SOFC due to the changes in the composition and microstructure of cell components during standard operation. These losses, which are known as degradation, can generally reduce the SOFC's electrochemical potential achieved at constant current by up to ~40% depending on the cell design and operation [4.3.9-1]. To develop a more efficient and power dense SOFC, degradation needs to be better understood and minimized. The mitigation of SOFC degradation can be enabled by proper materials selection with respect to thermal expansion and chemical stability. However, materials that satisfy these criteria can also

exhibit microstructural changes that contribute to decreased performance [4.3.9-1, 4.3.9-2]. A reliable SOFC design requires sustained ion and electron conduction pathways to the electrochemically active three-phase boundary (TPB), sufficient diffusion pathways for the transport of fuel and oxidant, and a structure robust enough to support the chemical environment and thermal and mechanical stresses that are applied. Due to the complexity of these relationships and the component microstructures, it is difficult to optimize a particular aspect of a SOFC design without directly impacting other aspects of the cell performance.

The performance degradation of SOFC can result from several phenomena including: (1) microstructural changes in the electrode; (2) teactions between functional materials to form new phases; and (3) contamination of active interfaces. The TXM technique is the only non-destructive and non-invasive technique that holds the promise to extract these data from an operating fuel cell, thereby providing the most direct information on the degradation mechanism. During extended operation, the materials composing a SOFC can be reorganized, leading to a decrease in active transport pathways and reaction sites. Factors that affect this reorganization and the associated degradation include (1) electrode microstructure, especially composition with respect to percolation thresholds; (2) operating conditions such as cell temperature and current density; (3) micro-scale crack growth; and (4) the design and properties of cell components. Changes in SOFC electrode microstructure have been observed after thermal cycling [4.3.9-3–4.3.9-5] and due to the introduction of fuel stream contaminants [4.3.9-6, 4.3.9-7]. Microstructural changes have been related to residual stresses and degradation in SOFC electrodes [4.3.9-1, 4.3.9-2, 4.3.9-8]. Excellent papers describing issues and challenges have been published [4.3.9-9–4.3.9-11], and it is quite clear from the literature that in order to understand the degradation of SOFC electrodes, the influence of the evolving SOFC microstructure on transport and electrochemical processes must be thoroughly understood at the pore scale. Modeling of SOFC is an invaluable tool in this respect. The coupling between various transport phenomena in the SOFC has been modeled at the macroscopic scale [4.3.9-12–4.3.9-14], but there are very limited studies at the microstructural level (~ 1 μm) where the processes driving performance degradation originate.

The importance of SOFC performance degradation has been recognized for quite some time. But only recently has there been effort directed at a detailed understanding of the role microstructural changes take in degradation using SEM [4.3.9-1], dual-beam focused ion beam (FIB)/SEM [4.3.9-15], and TXM [4.3.9-16]. However, the main difficulty for analyzing degradation is the lack of knowledge about the fuel cell's 3D structure at the pore scale and uncertainties about the phenomenon occurring in the cell itself. There is a need for developing a comprehensive pore-scale approach that considers the actual geometrical structure of SOFC electrodes and the appropriate phenomena (charge transfer, mass transfer, reformation, electrochemical reactions).

The acquisition of 3D map of elemental composition and chemical state with sub-50-nm 3D spatial resolution or better will be critical in identifying reactions between functional materials to form new phases and contamination of active interfaces. *Ex situ* fuel cell samples can be studied to determine if operation will create new interfaces or contaminated regions in the tens of nm range spatial scale that deactivate the fuel cell. For example, sulfur, phosphorus, and chromium from the fuel stream and the stack are known contaminants. However, little is known about how the intermediate species form their role in deactivating the triple phase boundaries, and mediation schemes. The fuel cell is also known to undergo chemical changes under prolonged operation, resulting in deactivation of phases and reduction in triple-phase boundaries. Three-dimentional maps obtained *in situ* will be able to aid researchers in identifying the chemical and spatial origin of this phenomena, thereby increasing the fuel cell durability. Current TXM allow mapping of Ni and its chemical compounds, but other elements, such as yittrium-stabilized zirconium (YSZ), is outside its energy range. Extending the energy range to 30 keV will be extremely valuable for mapping the exact composition of a SOFC sample as well as the chemical state of each constituent. Furthermore, the ability to combine the TXM data with x-ray fluorescence images will

further supplement the 3D TXM data with more detailed information on the low-concentration elements in the sample; and the ability to simultaneously acquire x-ray diffraction or micro-diffraction data during the *in situ* TXM imaging process will provide information on the strain and structural information in the sample. These *in situ* measurements will provide extremely valuable insights into the fuel cell operation that cannot be obtained with other techniques.

Energy Storage – Next-Generation Battery Research and Development

In the portable electronics industry, the recent trend has been toward smaller and more powerful devices. This requires batteries made from materials with very high energy densities. Because of its very high energy density, the battery of choice for both portable electronics and electric vehicles is currently the Li-ion battery, which typically consists of a graphite negative electrode and a $LiCoO_2$ positive electrode. However, to meet the ever-increasing energy demands of modern devices, researchers are seeking new materials that will lead to smaller, lighter, and longer-lasting batteries [4.3.9-17]. For the negative electrode, some of the most promising materials include silicon, tin, and alloys containing these elements [4.3.9-18–4.3.9-22]. Silicon in particular has a theoretical specific capacity of nearly 4200 mAh/g (~9800 mAh/mL), which corresponds to a fully lithiated state of $Li_{22}Si_5$ (~4.4 Li per Si). This value is very favorable when compared to the specific capacity of graphite, which is only 372 mAh/g (LiC_6) [4.3.9-17].

A critical hurdle for commercialization for these materials is the capacity loss over a large number of cycles [4.3.9-22]. Some may fall below 50% of their initial capacity after less than five cycles. The capacity loss in these alloy materials can occur for several reasons. In crystalline materials, new intermetallic phases are formed on lithium insertion [4.3.9-22]. This leads to inhomogeneous volume expansions in the two-phase regions, which can cause cracking and pulverization of the material. Following these defects, the particles may lose electrical contact with the electrode and result in capacity loss.

In amorphous alloys, the capacity loss occurs for a different reason. Beaulieu et al. [4.3.9-23–4.3.9-26] have shown that in amorphous alloys of Si and Sn, the expansion on lithium insertion is homogeneous and that 10- to 30-μm pieces of thin films expand and contract reversibly without further pulverization. It appears that in these amorphous films, the capacity loss results from contact loss due to expanding and contracting particles undergoing large volume changes rather than the pulverization that occurs in crystalline films [4.3.9-17].

To take advantage of the capacity available from silicon and to overcome the problems with cycling, it is necessary to study it in detail. Previous studies in this area are largely been based on the x-ray diffraction technique [4.3.9-17] and electron microscopy, so that direct *in situ* observation has not been possible. TXM techniques, however, provide a direct way to image all components of a battery including the electrodes and electrolytes. Nano-structures within these components can be monitored with up to 30 nm in 3D while the battery undergoes multiple charge/discharge cycles. Electrical performance, such as charge current, voltage, and capacity can be correlated to the dynamic evolution of nano-structures precisely in real time. The failure mechanisms discovered in previous work and postulated in the community can then be observed directly in the experiment.

In our current experiment design, a specialized battery cell with thin chamber walls needs to be used because of the relatively low energy of x-rays. The upgrade to the TXM to higher energy operation will be highly beneficial to our *in situ* experiments by allowing a far wider range of battery geometry as well as different electrode and electrolyte materials to be studied. This is significant because of the wide range of materials being studied. A highly automated *in situ* TXM system will be instrumental in understanding their electrochemical performance in real operating conditions without the need of specialized battery cells. This capability has the potential to make TXM a significant tool in battery research and development in the near future.

Electrochemistry

The metallic porous materials are of great interest [4.3.9-27–4.3.9-32] for electronic, catalytic, and sensor applications because of their large surface-to-volume ratios. Materials with multimodal porosity or hierarchical porous materials are particularly interesting because larger pores in the structure facilitate mass transport while smaller pores increase the surface area. Although porous metal materials have been used extensively in catalytic, electrochemical, and purification processes, synthesis of hierarchical porous metal materials is challenging and the process is poorly understood despite significant progress in preparing other types of multimodal porous materials. In addition, metal nanofoams are potentially useful as voltage-tunable microelectronic devices, such as actuators, magnets, and resistors, because of their electronically tunable physical properties. Finally, the effects of scaling from macro to nano on the mechanical behavior of nanofoam materials have been a subject of intensive studies and discussion. Structural imaging at sub-50-nm resolutions on nanoporous materials will provide the essential information on why these nanofoam materials behave differently from their homogeneous bulk counterparts. In addition, *in situ* x-ray imaging will allow direct observations of the nanofoam formation process with the aim to better control the nanostrutures and thus their properties.

The TXM has been used extensively in the study of a process of fabricating porous metal with controlled porosity [4.3.9-33]. This process contains two steps: de-alloying, where an alloy of two types of metals are immersed in a chemical bath to dissolve and remove the less noble metal, thus leaving porous noble metal, followed by annealing, where the porous metal is heat treated in controlled time intervals to adjust porosity. In the de-alloying process of our experiment, an Au-Ag alloy was placed in HNO_3 to remove Ag and obtain porous Au. This process was monitored *in operando* with a nano-CT system. Quantitative measurements, such as de-alloying speed, can be measured directly from both the 2D images and 3D data. The annealing process can also be monitored *in situ* with the TXM at up to 900°C. Quantitative measurements on the sample, such as porosity change as a function of annealing time, can be measured directly from the 3D data.

An upgraded TXM with higher energy, full automation, and better elemental/chemical mapping would further provide the community with unique capabilities to study these advanced materials, including nanoporous metal, from various critical means:

- **Higher Energy - Studying structural evolution under real synthesis processing and functioning environments.** The ability to perform experiments *in situ* is essential to studying the continuous evolution of the functional materials. A higher operative energy will provide a larger penetration depth and therefore the materials enclosed in an environmental cell or devices under real operating conditions (*in operando*) can be directly imaged. A sufficient penetration depth will also allow us to image a larger volume of materials, which represents the true behavior. For instance, a heterogeneous catalysis usually involves a solid-phase catalyst with the reactions happening in liquid or gas phases.
- **Full Automation - Revealing the structure in full three dimensions (3D).** The complex structures of functional materials must be revealed in 3D [4.3.9-34]. A full automation TXM with tomography capability will dramatically increase the 3D data output from the precious limited beam time. Therefore, continuous 3D structural evolution can be imaged in a more efficient way. Any synthesis processes or functions that depend on diffusion or transport will require 3D instead of 2D analysis. For instance, in a fuel cell, the porous connectivity determines the performance of the cell. However, a pore in a 2D slice looks isolated but might be connected in 3D [4.3.9-34]. On the other hand, with advanced computational power, 3D experimental microstructures can be used as input in 3D modeling for guidance of the future materials design.

- **Improved resolution.** During the dealloying process the porosity is below the resolution of the TXM system so that we can only monitor the de-alloying front resulting from the loss of Ag in the alloy. Improving the resolution to below 20 nm during the upgrade will allow us to resolve these pores during the very early stage of formation (as well as beginning of the annealing process).
- **Elemental/chemical mapping -** Detecting multi-phases functional materials. Functional materials can be composites including ceramics, metals, and polymers phases, or can have different oxidation states during operation. While different phases can carry different functionalities, being able to image different types of materials becomes critical. For instance, the nanoporous metal can be fabricated via a so-called dealloying process that involves the use of a corrosive agent to selectively dissolve the less noble metal from a binary alloy system. Being able to distinguish the less noble element from the nobler element is essential for understanding the pore formation mechanism underlying this unique material. Increasing the energy range to include the Ag absorption edge will provide a significant ability to better monitor the flow of Ag atoms. The elemental information combined with the higher resolution will be extremely valuable for gaining a fundamental understanding of chemical and fluid mechanical interactions in the dealloying process.

4.3.9.2 Source Requirement

The TXM system provides unique high-resolution elemental mapping and chemical speciation capabilities. Therefore, it requires a continuous spectral coverage from 6 to 30 keV. The existing U3.3 undulator, in service in 32IDC, or the U3.0 undulator are the best options.

4.3.9.3 Beamline Description

The exiting 32-ID-C beamline is a relatively simple design that delivers roughly a 1-mm beam to the end station with 1/10,000 monochromaticity with possible energy range between 6-30 keV. This setup is ideal for TXM operation. We propose to maintain this beamline configuration for the upgraded TXM system.

Because of the need to extend to higher-energy operation, the current optical table will be replaced with a larger 9-m-long × 2-m-wide table. The existing 32-ID-C hutch is ideally suited for the new TXM system operation. If the wide-field imaging proposal is implemented, the TXM will occupy the 32-ID-C hutch and share Sector 32 operation with the high-speed imaging program. Otherwise, the upgraded TXM will be developed to share the operation with the phase-contrast imaging program in 32-ID-C.

TXM Instrumentation

The transmission x-ray microscope (TXM) is a direct analog of the transmission electron microscope (TEM) or light microscope for x-ray radiation. As shown in Figure 4.3.9-1 in its simplest form, it consists of a condenser to project x-ray source to the sample plane and an objective lens to project a magnified image to the detector. When in focus, the image represents a map of transmitted x-rays through the sample. The energy dependency of x-ray absorption can be used to map the elemental composition and furthermore, x-ray absorption near-edge spectroscopy (XANES) and extended x-ray absorption fine structure (XAFS) spectra can be used to map chemical composition. These techniques are fully compatible with computed tomography (CT) 3D imaging techniques.

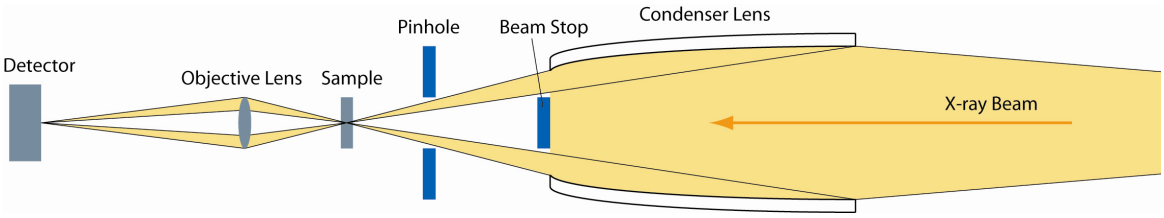

Figure 4.3.9-1. Schematic illustration of a transmission x-ray microscope.

The key improvements are in the significant increase in x-ray energy coverage and automation of the most complex spectral data acquisition and analysis sequences. Current TXM allows many important industrial metals in the fourth and sixth rows of the periodic table to be mapped, as shown in green in Figure 4.3.9-2. This will will be expanded in the upgraded system to cover nearly all elements above Mn (shown in orange). The one to two orders of magnitude increase in attenuation length allows larger and more complex samples to be imaged in their native state and more flexible *in situ* imaging. The TXM at 32-ID-C currently has a large number of *in situ* sample chambers compatible with full 3D nano-CT imaging at low temperate to -160˚C, high temperature up to 1500˚C, pressure up to 100 GPa, electrical testing, and chemical reactions, including aggressive chemicals. These capabilities have become invaluable for the user community and will be enhanced with better integration and automation control during the upgrade.

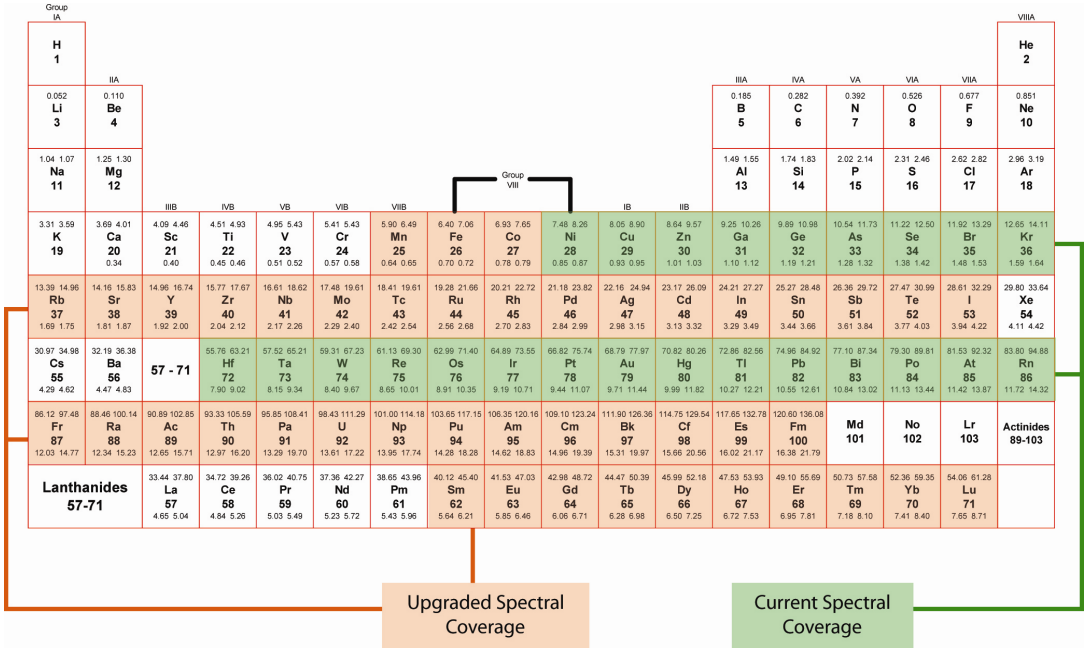

Figure 4.3.9- 2. Energy coverage of current TXM (green) and proposed upgrade (orange).

As illustrated in Figure 4.3.9-3, the goal of the upgrade of the TXM program is to produce the world's most advanced 3D nano-CT system with highly integrated and highly automated multi-modality imaging system capable of:

1. obtaining 3D morphology of nano-structures with up to 20-nm resolution,
2. mapping nearly all elements above Mn by differential absorption imaging,
3. mapping chemical composition with the XANES or XAFS spectral imaging techniques, and

4. mapping phase and strain with the micro-diffraction technique.

These imaging techniques will be fully compatible with a specialized environmental chamber for high-temperature, low-temperature, high-pressure, and chemical reactions, so that samples can be studied *in situ* at a high speed of over 100 Hz at full resolution and over 1 kHz at reduced resolution.

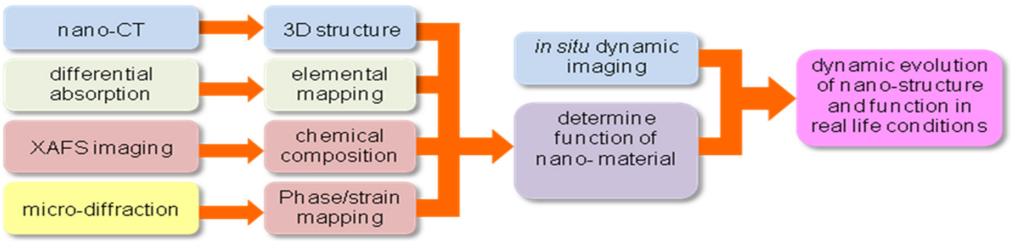

Figure 4.3.9-3. Capability summary of the TXM at 32-ID-C.

Technical Improvements

Using primarily the existing 32-ID-C beamline components, the majority of technical improvements are made in the end-station subsystems. The x-ray optics to be used in the upgraded TXM system are being developed in an LDRD project. The pathway to achieving the proposed upgraded resolution has been developed.

A new sample stage system, shown in Figure 4.3.9-4, is being developed to provide a better extreme low rotation runout error of less than 20 nm, comparable to the imaging resolution. It also integrates a rotary union and slip ring assembly to provide fluid and electrical power. This new system will allow fully automated 3D nano-tomography imaging with a wide range of *in situ* experiments. Further integration with beamline control system will provide fully automated material analysis capability in 3D with XANES and XAFS techniques at up to 10-nm voxel resolution.

The upgrade throughput is achieved by a combination of efficiency improvements with x-ray optics and scintillators. During our LDRD project, we expect to be able to improve the optics efficiency by a factor of 5-10 from current optics, and current scintillator development efforts at APS will improve the efficiency by a factor of 5 from the current level while maintaining the same resolution. The combination of these improvements will lead to over an order of magnitude improvement in throughput and push the exposure rate to kHz scale with relaxed resolution.

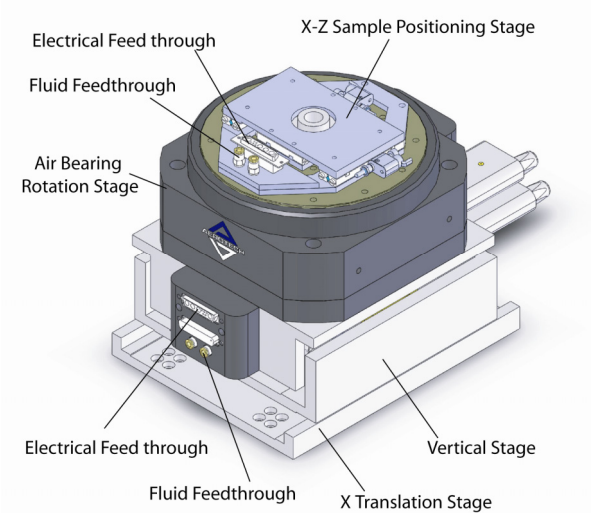

Figure 4.3.9-4. Sample stage system being developed for the upgraded TXM system.

4.3.9.4 Anticipated Performance

Anticipated performance improvements from the upgrade are summarized in Table 4.3.9-1.

Table 4.3.9-1. Current Capabilities of the TXM at 32-ID-C Compared with those Proposed for the Upgrade

	Current TXM at 32-ID-C	**Proposed Upgrade**
Energy Range	8-15 keV (0.01% resolution)	6-30 keV (0.01% resolution)
Maximum 2D Spatial Resolution	25 nm	10 nm between 6-12 keV 30 nm between 12-20 keV 50 nm between 20-30 keV
Working Distance	nominal 25 mm	> 20 mm at all energies
3D Spatial Resolution	70 nm	match 2D resolution above
Photons Recorded at Sample (per second per pixel)	~1,000 photons (12 nm pixel at 10 keV)	~10,000 photons
Field of View	Variable with energy: 25 μm at 8 keV 40 μm at 12 keV	Constant at all energies: 20 μm in High-Resolution Mode 100 μm in Wide-Field Mode
3D Imaging and Analysis	Semi-automatic	Fully Automated
Spectral Imaging Sequence	Manual Control	Fully Automated
Imaging Modalities	Abs/Ph/XRD	Abs/Ph/XRD/μXRD/μFluo
Sample Temperature Range	-160°C – 900°C, manual control	-160°C – 1,200°C, computerized control
Sample Pressure Range	0 – 100 GPa, manual control	0 – 100 GPa, computerized control
Other Sample Environments	Electrical connection. Chemical feed/bath.	Integrated electrical feedthrough to 5A. Integrated chemical feedthrough.

4.3.9.5 References

[4.3.9-1] A. Faes et al., Fuel Cells **9**(6), 841 (2009).

[4.3.9-2] P. Tanasini et al., Fuel Cells **9**(5), 740 (2009).

[4.3.9-3] C.-H. Lee et al., Solid State Ionics **98**, 39 (1997).

[4.3.9-4] Y. C. Hsiao, J. R. Selman, Solid State Ionics **98**, 33 (1997).

[4.3.9-5] H. Tu, U. Stimming, J. Power Sources **127**, 284 (2004).

[4.3.9-6] M. Gong, D. Bierschenk, J. Haag, K.R. Poeppelmeier, S.A. Barnett, C. Xu, J.W. Zondlo, X. Liu, J. Power Sources, In Press, 2010.

[4.3.9-7] F. Zhao and A.V. Virkar, J. Power Sources **141**, 79 (2005).

[4.3.9-8] D. Quinn, S.M. Spearing, B.L. Wardle, "Residual Stress and Microstructural Evolution in Thin Film Materials for a Micro Solid Oxide Fuel Cell (SOFC)," Materials Research Society (MRS) Annual Fall Conference, Boston, MA, December 2004 (2004).

[4.3.9-9] J. Fleig, Annu. Rev. Mater. Res. **33**, 361(2003).

[4.3.9-10] T. Klemenso et al., J. Electrochem. Soc. **152**(11), A2186 (2005).

[4.3.9-11] N.M. Tikekar et al., J. Electrochem. Soc. **153**(4), A654 (2006).

[4.3.9-12] M.A. Khaleel et al., J. Power Sources **130**, 136 (2004).

[4.3.9-13] B. Morel et al., J. Electrochem. Soc. **152**(7), A1382 (2005).

[4.3.9-14] V.M. Janardhanan, O. Deutschmann, J. Power Sources **162**, 1192 (2006).

[4.3.9-15] J.R. Wilson et al.,Nat. Mater. **5**, 541 (2006).

[4.3.9-16] J.R. Izzo et al., J. Electrochem. Soc. **155**, B504 (2008).

[4.3.9-17] T. D. Hatchard and J. R. Dahn, J. Electrochem. Soc. **151**(6), A838 (2004).

[4.3.9-18] C. J. Wen and R. A. Huggins, J. Electrochem. Soc. **128**, 1636 (1981).

[4.3.9-19] J. Wang et al., J. Electrochem. Soc. **133**, 457 (1986).

[4.3.9-20] J. Yang et al., Electrochem. Solid-State Lett. **2**, 161 (1999).

[4.3.9-21] I. A. Courtney et al., Phys. Rev. B **58**, 15583 (1998).

[4.3.9-22] M. Winter and J. O. Besenhard, Electrochim. Acta **45**, 31 (1999);

[4.3.9-23] L. Y. Beaulieu et al., Electrochem. Solid-State Lett. **4**, A137 (2001).

[4.3.9-24] L. Y. Beaulieu et al., J. Electrochem. Soc. **150**, A149 (2003).

[4.3.9-25] L. Y. Beaulieu, T. D. Hatchard, and J. R. Dahn, poster presented at the 11th International Meeting on Lithium Batteries, Monterey, CA, 2002.

[4.3.9-26] L. Y. Beaulieu et al., J. Electrochem. Soc. **150**, A1457 (2003).

[4.3.9-27] R. Li and K. Sieradzki, Phys. Rev. Lett. **68**, 1168 (1992).

[4.3.9-28] O. V. Shulga et al., Chem. Mater. **19**(16), 3902 (2007).

[4.3.9-29] H.-J. Jin, D. Kramer et al., Adv. Eng. Mater. **9**(10), 849 (2007).

[4.3.9-30] G. W. Nyce et al., Chem. Mater. **19**(3), 344 (2007).

[4.3.9-31] J. Erlebacher., Nature **410**, 450 (22 March 2001); doi: 10/1038/35068529.

[4.3.9-32] F. U. Renner, Thin Solid Films **515**(14), 5574 (23 May 2007).

[4.3.9-33] Y. K. Chen et al., Appl. Phys. Lett. **96**, 1 (2010).

[4.3.9-34] K. Thornton and H.F. Poulsen, MRS Bulletin **33**, 6 (2008).

4.4 High-Resolution Spectroscopy

4.4.1 Introduction

The APS has a history of strong and successful programs in high-resolution spectroscopy. Current capabilities include spectrometers and monochromators optimized for the full range of energy resolution, from nuclear resonant scattering at nano-electron-volt resolution, to a full suite of inelastic x-ray spectrometers, with resolutions from milli-electron-volt to electron volt. There are also strong and growing programs utilizing emission spectroscopy, and more traditional tools such as XAFS and micro-XAFS.

Sections 4.4.2 and 4.4.3 describe the possible enhancements for Sector 20. Currently 20-ID supports a number of experiments including the LERIX spectrometer (0.8- to 1.3-eV resolution), an x-ray microprobe that also supports emission spectroscopy using miniXS spectrometers, time-resolved XAFS, and two UHV chambers supporting surface XAFS and diffraction. Dual canted undulators will be used to provide two independent beamlines to support most of these efforts. The Advanced Spectroscopy Sector described in section 4.4.2 will provide an enhanced microprobe station optimized for microspectroscopy, in both absorption and emission modes, with high flux and resolution down to a few microns. In contrast to other microprobes at the APS, the emphasis is on high flux and dilute detection limits rather than on achieving the smallest spot size. It will feature an adjustable beam size to minimize radiation damage and to match the sample features. It also includes the option for a wide-band-pass multilayer monochromator for the highest possible flux when needed.

The second branch line at 20-ID is described in section 4.4.3. It is primarily dedicated to an enhanced version of the LERIX spectrometer, LERIX-2, and it will also support operation of the UHV chambers. The time-resolved program at 20-ID will be phased out and folded into the other time-resolved efforts at the APS. The beamline will be optimized for supporting the LERIX-2 spectrometer, providing improved energy resolution (down to 0.3 eV), and more optimized focusing options (down to 10-20 microns). The LERIX-2 spectrometer will be a major enhancement, incorporating a number of improvements based on lessons learned from operating LERIX and the interim LERIX-1B upgrade. These include improved support for *in situ* sample environments, improved analyzer performance, improved net energy resolution, and up to 10 times the collection solid angle. This beamline will also incorporate the UHV chambers in a separate hutch. These will be refurbished by the Canadian partners at Sector 20 to better support *in situ* emission spectroscopy and surface XAFS. While their programs are more aligned with the Advanced Spectroscopy line, they require an end station. Combining these programs in one sector will allow this sharing of capabilities with minimal inefficiency.

The upgrade and consolidation of a dedicated resonant inelastic x-ray scattering (RIXS) facility, envisioned to be implemented on beamline 9-ID or another equivalent insertion device beamline, is described in section 4.4.4. Currently, RIXS activities at the APS are spread over two different beamlines, using an older first-generation instrument and a newer state-of-the-art instrument at 50% level each. Within the APS-U project, 9-ID will be rebuilt in terms of the front-end and shielding enclosures. It will be outfitted with a powerful tunable, multiple-undulator source and dedicated to RIXS entirely. The newer RIXS instrument together with its supporting instrumentation will be moved there and will be further augmented with multiple-analyzer assemblies, polarization control and analysis, and enhanced compound micro-focusing. Critical for an advancement of the RIXS technique is the improvement of energy resolution from the current level of ~100 meV to the 20- to 30-meV regime. An aggressive R&D program to develop the technology for fabricating diced-spherical sapphire and quartz analyzers will be implemented and, based on existing prototype experiences, is expected to yield the desired increase in resolution.

4.4.2 Advanced Spectroscopy Upgrade (20-ID) [CAS]

The Advanced Spectroscopy Beamline is part of a canted undulator expansion to Sector 20. It will share the sector with the LERIX-2 beamline described in section 4.4.3. The Advanced Spectroscopy Beamline expands on the capabilities of the current Sector 20 microprobe station to optimize it for additional spectroscopy applications based on variable resolution analysis of the sample fluorescence. The resolution will be optimized to the application. High-resolution methods, based on diffracting analyzers, will achieve 0.5- to 1.0-eV resolution with large-collection solid angles, suitable for rapid measurement of resonant and non-resonant x-ray emission spectra for determination of valence, spin, and some aspects of local electronic environment in a complementary method to usual XANES analysis. Lower-resolution fluorescence detection with extremely large-collection solid angle and detector efficiency will enable detection and analysis of parts per billion concentrations, thus opening new venues, especially in biological, environmental, and surface sciences.

Many synchrotron facilities including the APS have microprobe stations with varying resolutions and capabilities. This is a result of growing user demand for these capabilities, and the growing number of third generation sources that can support such experiments. In spite of the growing number of microprobe beamlines we have not seen a significant reduction in demand for our microprobe over its 10 years of operation. In developing our proposal we have decided to emphasize high flux and newer spectroscopy applications, but want to continue to support the traditional microprobe needs of our current user base. These goals are largely compatible requiring beam size in the 2- to 20-micron range with the smaller sizes supporting the traditional microprobe applications and the larger sizes useful for fluorescence spectroscopy by providing higher flux. The larger beam sizes also have been requested by our microprobe users for rapid initial scanning of large samples. Many of the newer microprobe beamlines have this rapidly variable beamsize capability. For the ultimate in flux we are also proposing a multilayer monochromator option for non-resonant fluorescence spectroscopy studies. When combined with miniXS spectrometers, this will open unique possibilities for rapid valence or chemically sensitive imaging.

In contrast to the microprobe capabilities, the fluorescence spectroscopy capabilities will have much less competition. The proposed X-ray Emission Spectroscopy (XES) capabilites at the microprobe end station would surpass any existing facility in the range of applications. It also is compatible with, and generally surpasses, any traditional multi-SBCA system in throughput. The new 0.5-meter dispersive instrument being developed by Glatzel at ESRF is the current competitor to the miniXS approach. The relative performances and ranges of applications of the two different approaches may converge over the next few years, but the extreme convenience of the miniXS paradigm for rapid implementation in new environments (i.e., at beamlines not previously performing XES) and the ability to custom design miniXS for special environment with scattering geometry constraints will remain.

In the future, the SRX demonstration beamline under development at NSLS-II will put $\sim 10^{13}$ photons/sec/eV onto a 50- to 70-nm spot. This beamline team hopes to eventually have a diverse suite of spectroscopic capabilities, likely including XES by miniXS or a small SBCA array with many options for analyzer crystals. However, the very small distance from the optic to the sample spot (~1.5 cm) at SRX will put some barriers to applications, especially in extreme environments. Larger working distances allowing compatibility with extreme environments is an important design goal of the Advanced Spectroscopy Beamline.

4.4.2.1 Scientific Scope

Samples of real-world interest in environmental, biological, geophysical, and energy sciences are frequently, and predominantly, spatially heterogeneous. Naturally heterogeneous environmental samples have been a natural focus of microprobe work. However, micron scale studies of energy related systems are of growing importance. Examples include metallic impurities in solar cells, complex fuel cell electrodes, and heterogeneous catalysts. This is the over-arching motivation for the development of microfocused x-ray sources at synchrotron light sources, and also for the development of suites of experimental techniques associated with these end stations. However, while the exceptionally fine focus presented by the most precise optics open unique scientific opportunities, it is important to note that optimum experimental throughput follows when using a spot size that is not too much smaller than the length scale of the compositional or structural variation in a given sample. Use of an overly focused beam strongly decreases the incident flux due to the finite brilliance of the insertion device source.

This beamline will support three classes of experiments: micron scale x-ray microprobe, XAFS requiring the high flux and brilliance of an undulator source (i.e., very dilute systems, high pressure cells or glancing angle measurements of thin films), and fluorescence spectroscopy using miniXS or other high resolution spectrometers. The first two categories include most of the applications at the current microprobe station. The current station has a diverse and active set of users averaging about 20 publications/year while using about 50% of the available beamtime at 20-ID. The enhanced capabilities should attract additional users for the current applications, and bring in a new community of users interested in fluorescence spectroscopy.

It is a particular goal of the upgraded Advanced Spectroscopy Beamline to be able to detect parts per billion levels of trace elements. Such capabilities are of particular importance in environmental or biological systems, where environmental contaminants or biologically important trace elements are present at very high dilution. The beamline should provide focused monochromatic photons with flux close to 1013 Hz. A sample containing 100 ppb of a heavy element in a lighter matrix (i.e., Fe in a silicate matrix) will have approximately 107 photons/sec absorbed by the element of interest. Assuming 30% fluorescence efficiency and a 1% detection efficiency, 3×10^4 fluorescence photons/sec will be detected. This is more than enough for rapid XANES studies and even EXAFS is possible in a few hours. However, these photons will be accompanied by a large background of scattering and fluorescence from other components in the sample. Such backgrounds can easily be greater than 1% of the incident flux or 10^9 photons/s in the collection solid angle of the 1% efficient detector. This can overwhelm standard solid-state detectors. Even for detectors with high-multiplicity capable of high-total count rates, the finite peak-to-background ratio (typically less than 104) of solid-state detectors makes the detection of very weak peaks impractical. A better approach is to reject the background using a crystal spectrometer. Some possible detection schemes are discussed in section 4.4.2.6.

As the detection resolution is improved, fundamentally distinct variants of spectroscopic information now become accessible. These include lifetime-broadening suppression which occurs when selecting regions of individual emission channels, magnetic-state or valence-specific XAS when selecting emission channels which couple directly to the spin- or charge-state of a metal ion, and the possibility of performing nonresonant and resonant x-ray emission spectroscopy (XES and RXES, respectively).

Nonresonant XES (or simply “XES”) is the spectral emission from the target species when the incident photon energy is at least ~100 eV above the binding energy, so that quantum mechanical coupling between the absorption and emission processes is only weakly relevant for the emitted spectrum. That means a core hole has been formed and some electrons from a less-tightly-bound shell will decay to fill the core-level vacancy. For hard x-ray applications, with ~30 to 70% probability, this will result in the emission of a fluorescence x-ray. This process is manifestly atomic in nature, with a weak, but still

sometimes useful, influence of the nearest neighbor species. Most critically, it is important to note that XES characterizes the *occupied* density of states – without the complications of final state effects – while XANES is instead sensitive to the *unoccupied* density of states. For example, the many K□ features for 3*d* transition metals often provide unique insight into spin, valence, ligand species, and ligand bonding. Such information could be of critical importance for studies of bulk and nanophase transition metal oxides compounds used in numerous energy science applications. Unfortunately, comparatively few XANES studies at hard x-ray energies are accompanied by XES measurements with resolution comparable to the core-hole lifetimes (e.g., 0.5 - 2 eV for 3*d* transition metals) – even though many such studies will vastly benefit from the complementary information provided by XES. This is due to the complexity, cost, and sheer physical scale of high throughput x-ray spectrometers based on arrays of spherically-bent crystal analyzers. As described below, recent work at the APS has successfully demonstrated a new type of "miniature" x-ray spectrometer (miniXS), which overcomes many of these issues, while also providing better than order of magnitude improvement in measurement times compared to existing APS apparatus. Using either the miniXS approach or a traditional SBCA-based system, as needed, x-ray emission spectrometers will be developed for operation from 3 to 10 keV. This energy range is of high scientific importance, as it spans the K-emission for 3d transition metals, the L-emission for lanthanides, and the *M*-emission for actinides.

By means of context, a technically relevant example from a recent study at 20-ID is presented in Figure 4.4.2-1 (a). In the figure, the nonresonant 3*p*→1s XES is shown for somewhat dilute Co species in two different states of a commercial Co-Mo catalyst used to produce ultra-low sulfur gasoline. The performance of this catalyst is positively correlated to the cobalt sulfidation, such that mapping the location of the sulfided versus unsulfided (calcined) Co within an extrudate is of primary importance. For Co, as with all of the heavier 3d transition metals, the position of the main peak (spectroscopically designated Kβ1,3) is much more sensitive to the degree of covalency of the metal-ligand bond than to the nominal valence of the metal ion. The position of this peak then gives an unambiguously atomic fingerprint of the evolution from calcinated to sulfided Co species upon catalytic processing. Using the high-flux option at the microprobe beamline (via a wide-bandpass monochromator) and new developments in highly efficient x-ray spectrometers, such spectra could be collected in less than 1 sec for the catalyst samples, and even more quickly for concentrated systems. Such capabilities will enable rapid 2-D raster-imaging of entire XES spectra, a capability never before achieved at any hard x-ray light source. This will allow spatial imaging of information that is often very complementary to that obtained by 2-D imaging of specific XANES features, or even when collecting entire XANES spectra.

These considerations are further diversified when moving to resonant XES (RXES). Here, the APS convention is used and a study is designated to be "RXES" when the energy resolution is ~0.5 eV or poorer, as opposed to calling it resonant IXS or RIXS, a designation reserved for significantly higher resolution studies of the same coupling of absorption and emission channels. The results of a recent, spectroscopically complete RXES study at 20-ID are presented in Figure 4.4.2-1 (b). In this example, the splitting of the *f*-orbital final states (accessible by quadrupolar transition channels) at ~5719-eV incident energy gives a clean fingerprint of the *f*-electron ground state properties.

The final capability in this upgrade is the ability to combine these methods with *in situ* UHV sample preparation. Electron techniques can be used to study exposed surfaces or low coverage films, but multi-electron excitations can complicate interpretation. It would be difficult, or impossible, for electron methods to study a buried interface, but *ex situ* methods with hard x-rays could penetrate capping layers to reach a buried interface. This enables, then, studying the start and end points, but the main advantage of using hard x-rays for *in situ* studies is the ability to gain knowledge of the growth process in going from start to finish. Process knowledge obtained through *in situ* studies, using advanced spectroscopic techniques will aid in understanding film growth and the development of new thin film materials and applications. Presently, at the APS, there is no capability to prepare and measure *in situ* under ultra-high-

vacuum conditions, films, and interfaces using the techniques being advocated for the Advanced Spectroscopy sector in the APS-U. Because of space and operational constraints this end station will actually use the LERIX-2 x-ray source.

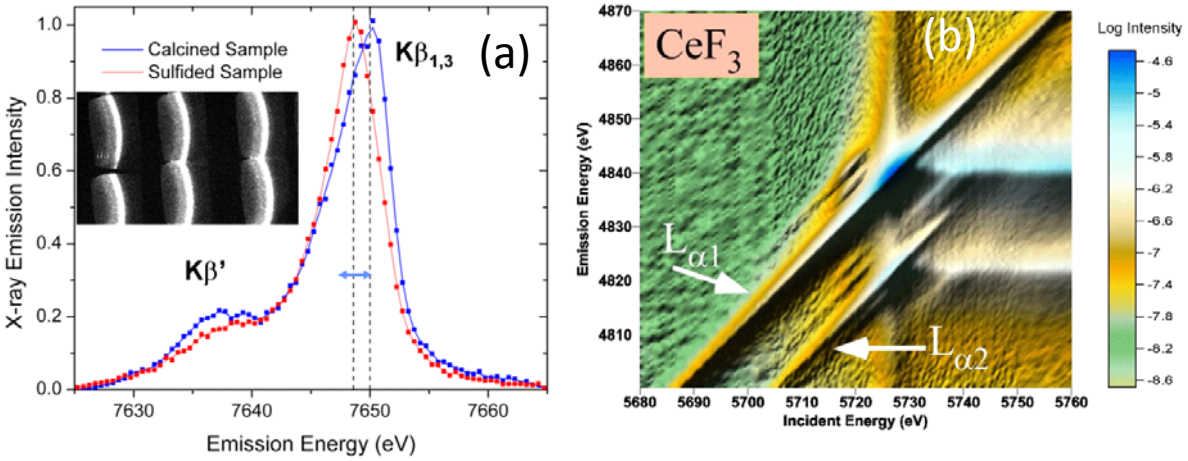

Figure 4.4.2-1. Some recent minXS results. ***(a)*** *Non-resonant x-ray emission spectra showing the shift in the $K\beta_{1,3}$ maximum x-ray emission energy depending on the sulfided or oxidized Co bonding environment. The inset shows the XES spectrum collected from a single snapshot from the miniXS for one of the samples. The reflection from six crystals is shown.* ***(b)*** *A spectroscopically complete RXES study for the Ce Lα emission of CeF_3 using the miniXS instrument installed at 20-ID of the APS. Note the strong splitting of the pre-edge resonance at ~5719-eV incident photon energy.*

4.4.2.2 Source Requirements

Since it requires microfocusing, the performance of this beamline is directly related to the brilliance of the source. To allow spectroscopy on either the K, L, or M edges of all elements heavier than Ar, the necessary energy range is 3.5-27 keV. To cover this range, a standard Undulator A is most appropriate. If smaller gap undulators become available, then it might be possible to cover this range with a shorter period device, yielding a gain in brilliance. Ideally, this would be on a long straight section, since the canted configuration on a regular straight requires a shorter undulator than the current Undulator A. However, if neither of these options becomes available, then the increased current of the APS-U will help provide a modest overall increase in brilliance over the current 20-ID beamline.

4.4.2.3 Beamline Description

This beamline will share a sector with the LERIX-2 beamline. A general layout is shown in Figure 4.4.2-2. In a canted configuration, one of the beamlines must be a side station with limited clearance. The large LERIX-2 spectrometer requires the clearance available at an end station. The Advanced Spectroscopy station is well suited to a side station configuration. The miniXS spectrometers are relatively compact, and the other fluorescence spectrometers will be located on the open side of the sample. The only potential loss as a side station is the possibility of placing detectors on the back side of the samples. For most samples this is not a practical option. The layout in Figure 4.4.2-2 assumes the lines are built as an upgrade to the existing Sector 20 beamline. There is also the possibility that Sector 20 will be needed for a long beamline. A case that is being considered is building these beamlines in an empty sector. In that case, the layout will be substantially the same. The hutch sizes and locations of the end stations would likely change by a few meters, but it is not expected that this would significantly

change the performance. The budget would be similar with the exception of the need to replace the existing hutches and utilities.

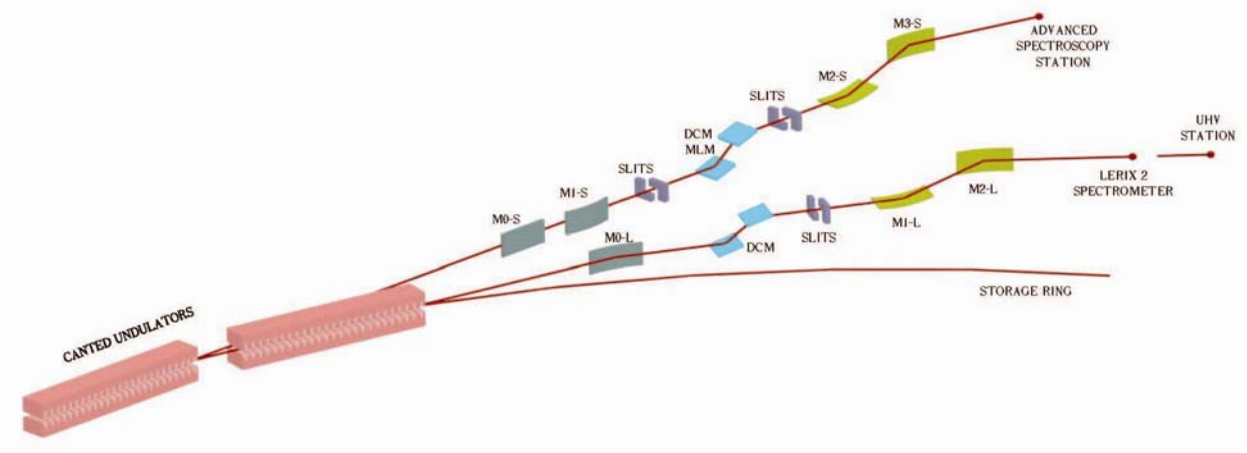

Figure 4.4.2-2. Schematic of the beamline layout for the Sector 20 APS-U project option showing the relationship of the LERIX-2 and the advanced spectroscopy beamlines.

The canted undulator beams are only separated by 1 mrad, and need to be further separated to be useful. This is accomplished by having two consecutive horizontally-deflecting mirrors giving a total additional deflection of about 12 mrad. One of the mirrors will be bent to focus the beam horizontally at the intermediate focal point. The next major component is the monochromator. This will have Si (111) crystals. These have proven to give the necessary energy resolution over the desired energy range. In addition, the monochromator will have multilayers to provide an increased bandpass of about 0.5%. To facilitate the use of multilayers, the monochromator will have a small beam offset. This is possible since the large horizontal deflection of the beam by the mirrors will provide the offset needed for bremsstrahlung shielding.

The final focusing will be done using KB mirrors. These will be large enough to collect the full undulator beam, and have sufficient working distance (15 cm) to allow the mounting of complex sample cells and detectors. The beampipe for the LERIX-2 beamline will be passing by. The expected beam separation is about 300 mm. For the relatively compact microprobe station, this should not be a major problem, but will require careful engineering.

The KB mirrors and end station will be located on a stable granite base. High-precision heavy-duty stages will be needed to align and scan the sample and spectrometer components. The miniXS spectrometers will be mounted as an integrated system with the sample mounts. Other detectors such as multi-element Si drift detectors, crystal-based WDX detectors, and area detectors for micro-diffraction will be mounted on a secondary table with independent motions. This will allow these detectors to be moved or exchanged without disturbing the alignment of the mirrors or sample.

The UHV chambers will be housed in the last hutch, which is formally part of the LERIX-2 beamline described in section 4.4.3. Although primarily to be used for XES and surface XAFS studies, they need the space of an end station. A separate hutch is also desirable, to allow setup and bakeouts to proceed while experiments are underway in the other hutches. Therefore, they have been placed at the end of the LERIX-2 branch. When in use, the beam will be passed through the LERIX-2 spectrometer into the last hutch. The Canadian staff will provide the instrumentation to accomplish this research. This includes UHV chambers, pumps, gauges, deposition sources, RHEED and Auger capabilities, x-ray windows, and positioning and other hardware totaling over $1M in externally funded equipment. All of this is available

for general users working with the external staff that designed, built, maintained, and operated the UHV systems. Of the two systems currently in use at Sector 20, the one which had emphasized both XAFS and SXRD (the other is optimized for polarization-dependent surface XAFS) is being re-commissioned by the Canadian partners to permit *in situ* RIXS/RXES using the analyzer technology being developed for this beamline. This modified end station will enable detailed, orientation-dependent studies of the electronic structure down to the submonolayer (i.e., ultra-dilute) regime. It is anticipated that this end station upgrade will be completed well in advance (in 2012) of the APS-U and it will be in a position to benefit from the improvements accompanying the Advanced Spectroscopy sector.

4.4.2.4 Optics

The optics need to provide a variable beam size. For imaging and microspectroscopy, small beams are required in the order of a few microns. At these beam sizes, the flux will be limited by the source brilliance, as long as reasonable working distance is maintained. For applications not requiring the smallest beam sizes, larger beams will allow for maximum flux. Large beams can also be used to mitigate radiation damage. The crystal spectrometers typically require beam sizes of ~50 microns or less to achieve their ultimate resolution. Therefore, a configuration has been adopted that allows for variable beam sizes. An intermediate focal point serves as the horizontal source point for the horizontally focusing KB mirror. This will allow the size of the horizontal focus to be controlled with a slit placed at the intermediate focus. The vertically focusing KB mirror will directly image the source. Typically, the vertical focus will be maintained at its best value (~2 μm) and vertical scanning of the sample will be done in a quick scanning mode. Thus, the vertical resolution will be controlled by the readout interval used during quick scanning. For imaging applications this means that the effective beam size can be easily varied between 2 to 20 μm. For static measurements where radiation damage is a concern, the bend of the vertical and horizontal mirrors will need to be varied to defocus the beam. Therefore, these mirrors will need to be bimorphs or equipped with mechanical benders.

The first optical components are dual horizontally-deflecting mirrors. These will be set at approximately 3 mrad incident angles, giving a total horizontal deflection of about 12 mrad. The first mirror will absorb most of the heat load and it will be flat. The second mirror will be bent to focus at the intermediate source point at about 46 m from the source. For harmonic rejection and to minimize the influence of the absorption edges in the mirror coating, the mirrors will have three reflecting stripes, Si, Rh, and Pt. The Si stripe will provide good harmonic rejection when operating below 10 keV, the Rh stripe will cover the intermediate energy range, and Pt will allow operation to 27 keV. To change between stripes, the mirrors will need to have a vertical translation capability. The use of dual mirrors increases their slope error requirements. However, since the intermediate focus that determines the final horizontal focal spot size is controlled by a slit, the slope errors of these mirrors affect the intensity, but not the minimum spot size at the sample. A requirement of 2-μrad slope error for each mirror should be sufficient, and should be easily achievable.

As mentioned earlier, the monochromator can be a standard Si (111) fixed exit type. It is desirable to have the option of switching to a multilayer set for applications that would benefit from a broader bandwidth with higher flux. It will be located in the FOE, which means that it needs to be designed to allow the pink beam of the LERIX-2 beamline to pass by. At this location, the expected horizontal separation is only about 50 mm. This means that it will be difficult to have these crystals side-by-side and provide adequate size for liquid nitrogen cooling. If the beam offset is small (10 mm), then the first and second crystals of the multilayer pair could be mounted upstream and downstream of the first and second Si (111) crystals respectively. Switching to the multilayer pair would then be a matter of moving to small-incident angles combined with a small-vertical shift of the monochromator. Since the dual mirrors will intercept close to half of the heat load, there should be no problem cooling these crystals using the highly-stable, indirectly-cooled mounts that are currently in use at 20-ID.

The specifications for the KB mirrors are also within current manufacturing capabilities. Use of an intermediate focus significantly reduces the length needed for the horizontal focusing mirror. To collect the full beam, these mirrors will need to have an active length of 300 to 400 mm. If a working distance of 300 mm from the end of the last mirror is allowed, then the horizontal focusing mirror center will need to be about 500 mm from the focus and the vertical mirror needs to be about 900 mm from the focus. To achieve a 2-μm focus, the horizontally-focusing mirror can have a slope error of 1 μrad, while the vertically focusing mirror will need a slightly better slope error. While challenging, sub-microradian slope errors have been achieved for mirrors of similar lengths.

4.4.2.5 Anticipated Performance

The performance of the end station will be significantly enhanced over the current microprobe station. The full undulator central cone that currently provides about 1×10^{13} ph/s when using Si (111) monochromator crystals will be collected. With a canted Undulator A and 150 ma, similar flux is expected, even after accounting for reflection losses in the mirrors. This can be focused to about 2 μm vertically. The horizontal focus for full beam will be about 20 μm. To achieve a symmetrical 2 μm beam, the intermediate slit will need to be closed to approximately 40 μm. At this size, the flux is estimated to be about 9% of the full beam or 9×10^{11} ph/s. This is approximately twice the flux of the current microprobe for the same beam size.

The use of the multilayer monochromator crystals will further enhance the flux. It seems reasonable to expect a multilayer with 0.5% bandwidth to have about 70% reflectivity. Combining two such multilayers in the monochromator will give about a 20 times flux increase.

4.4.2.6 Instrumentation

The end station will require several types of detectors. The detectors include the miniXS spectrometers for rapid parallel detection of the emission spectrum, high-efficiency high-resolution fluorescence detectors for dilute concentrations, general purpose Si drift detectors for full spectrum analysis of the total fluorescence signal, and an area detector for simultaneous microdiffraction. In principle, the miniXS spectrometers could also serve as detectors for dilute concentrations. However, with non-focusing optics and using an area detector, it is difficult to minimize the backgrounds. In the future, the development of pixel array detectors with individual mca capabilities might change this. Then the residual background in the miniXS spectrometer could be rejected at the detector.

As the miniXS spectrometers are a recent development at the APS and they have not yet been fully documented in published reports, it is useful to review their principles of operation and performance to date. Professor Gerald Seidler's research group at the University of Washington has led this effort. The key idea behind these instruments is that the modern availability of microfocused x-ray beams and zero-noise photon-counting area detectors has subtly undermined the historical conditions which have, since the 1930's, led to the overwhelming reliance on bent-crystal optics for high-resolution x-ray spectroscopy [4.4.2-1]. Specifically, assemblies of few-mm- to 1-cm-sized flat Bragg analyzers placed 1 to 10 cm away from the sample can serve as highly efficient dispersive optics for x-ray emission spectroscopy at ~0.5 to 1.0 eV resolution when using a modestly focused beam and presently available area detectors (i.e., the Pilatus100k with pixel dimensions of 170×170 μm^2). In the resulting spectrometers, the energy resolution is effectively limited by the angular sizes of the camera's pixel dimensions and of the beam spot on the sample. The total collection efficiency is set by the solid angle subtended by the camera active area, and is typically comparable to 4 to 10 "typical" spherically bent crystal analyzers (i.e., 10-cm diameter at 1-m working distance), i.e., often as much as 1% of 4π sr. This collection solid angle can be improved with larger area detectors, or (equivalently) with detectors having

a larger number of pixels, even if the size of the pixels decreases. Cameras with smaller pixels could instead be used to improve the energy resolution until it was limited by the beam-spot size on the sample.

After several iterations in the two years since the beginning of the miniXS project, a final, dedicated miniXS spectrometer system is nearing the end of commissioning at the existing 20-ID microprobe end station. A photograph of this instrument is presented in Figure 4.4.2.3, and data collected with this exact configuration has been presented in Figure 4.4.2-1(b). For the final instrument, the emission energy range can be rapidly selected by simply selecting the appropriate crystal mount, the white plastic optical component visible in the photograph. This component is fabricated on-site by the APS engineering division using rapid prototype machining (i.e., 3-D plastic "printing") and the needed flat-crystal diffracting elements are fabricated in the APS optics shop. This optic is essentially a discrete-element generalization of the famous, but seldom used, Johannson optic which perfectly satisfies the Rowland circle criterion. Elastic scattering from the sample is used for an *in situ* calibration of the energy response function of each pixel on the area detector by scanning the incident photon energy through the relevant detection-energy bandwidth of the spectrometer. Based on experience with these instruments, no difficulties are foreseen with their entry into general user operations for the 3- to 10-keV energy range; substantial additional experience will accrue, especially in the next year when numerous additional miniXS studies will be performed at the existing microprobe end station. At substantially higher energies, however, it often becomes impossible to find a suitable Bragg reflector which will not also have a second, spurious reflection, capable of illuminating the detector and providing uncontrolled background, usually from the Compton scattering from the sample. For work at higher energies spherically bent analyzers will be provided as needed. A GUI-driven, user-friendly software package for spectrometer calibration and data processing is in beta testing. In addition to the detector-driven issues indicated above, it would also be useful to investigate the use of weakly-strained crystals to improve the integrated reflectivity of these instruments above 5 keV.

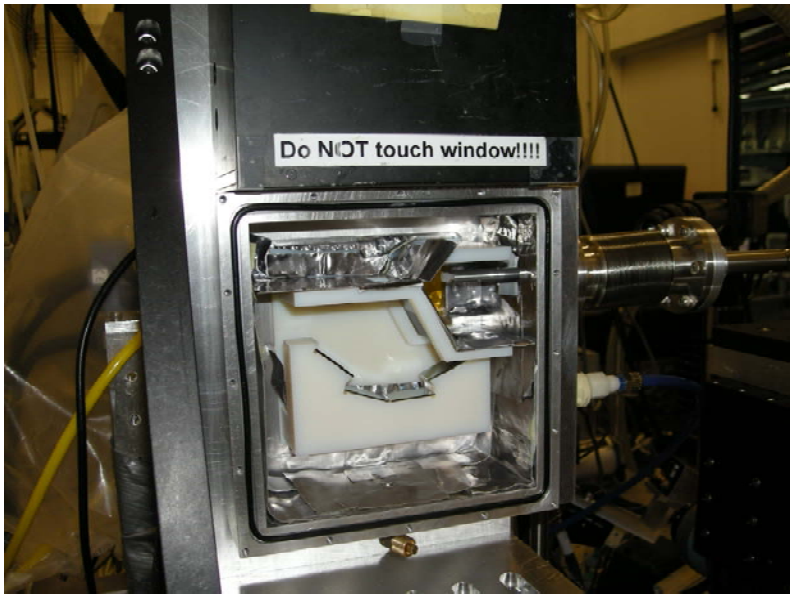

Figure 4.4.2-3. The "modular miniXS" instrument at beamline 20-ID of the APS. The white plastic part is manufactured by rapid prototype machining ("3D-printing") and can be rapidly changed to select the detected-energy range for an XES experiment. The instrument has ~0.8-eV energy resolution and a collection solid angle comparable to ~10 "usual" spherically bent crystal analyzers. For scale, the square He box is 6 inches on edge. (From G.T. Seidler et al., in preparation, 2010.)

The simple construction, small scale, and excellent performance of miniXS instruments all suggest that miniXS spectrometers may play an important role in accelerating the use of XES and RXES methods to complement XAS studies at spectroscopy beamlines. However, some key limitations exist when compared to traditional spectrometers based on spherically bent crystal analyzers. First, as miniXS systems are dispersive, they actually achieve large gains in throughput compared to SBCA-based systems, only when the user is actually interested in a broad spectral range (i.e., several tens of eV). When the intent is instead, for example, to perform a partial fluorescence yield XANES study exactly at some nonresonant emission line energy, then SBCA systems (whose entire response function is concentrated at one energy) outperform miniXS. For very-low concentration systems, the much superior rejection of stray scattering for the SBCA-based instruments may also be a critical consideration. In the future, the development of pixel array detectors with individual mca capabilities might change this, allowing the residual background in the miniXS spectrometer to be rejected at the detector.

There are several approaches for constructing the high-resolution spectrometers for detection of fluorescence from dilute species. These need to offer improvements on the energy resolution (150 to 250 eV) and background rejection (typical peak to background ratio $<10^4$) of solid-state detectors. Currently, WDX spectrometers are used, that were originally developed for electron microscopy. These are Rowland circle designs with Johannson crystals. They have energy resolution of 5 to 20 eV, and are easily tunable over a wide energy range. However, their collection efficiency is only 10^{-3} to 10^{-4} of 4π. In practice, it is found that they provide peak to background ratios of about 10^5, better than solid-state detectors, but still not sufficient for the lowest concentrations. However, since they are focusing optics, it should be possible to add an energy-discriminating detector at the focus, to further reduce the background. They are rather bulky and it would be impractical to have more than four to five operating simultaneously.

Two other possibilities are purpose-built Rowland circle spectrometers, based on large, spherically-bent crystals [4.4.2-2] and polycapillary-collimating optics combined with flat-analyzer crystals [4.4.2-3]. As for the WDX, a Rowland circle device can be combined with an energy-resolving detector for the ultimate background rejection. There are some significant engineering challenges to push these designs to many crystals while maintaining a reasonable energy range for a particular set of crystals.

The polycapillary-based analyzer is very simple, using a collimating-capillary bundle to feed a flat-crystal spectrometer. Being non-focusing, the background rejection is lower, but again, an appropriate energy resolving detector on the output should give adequate total background rejection. An advantage of this approach is the compact nature of the polycapillary bundles, allowing several to be placed around the sample. Once the beam is collimated, it can be passed some distance to the spectrometer hardware, providing adequate space for the analyzer crystals and detectors. A disadvantage of this approach is the rather poor collimation provided, and the lower efficiency at higher energies. These can be mitigated somewhat by matching the crystals to the analyzer output, but at this point, it is not clear that this approach will be superior to the spherical analyzer approach. An initial test experiment using a polycapillary based spectrometer is promising. Figure 4.4.2-4 shows the output of a test spectrometer measured by a vortex Si-drift detector. For a silicate sample with 9% Fe and 110 ppm of Ni, the Fe fluorescence and scattering background are nearly eliminated by the graphite analyzer. When the analyzer rejection ratio is combined with the energy resolution of the vortex, the total rejection ratio is greater than 10^6, approaching the level needed for ppb work.

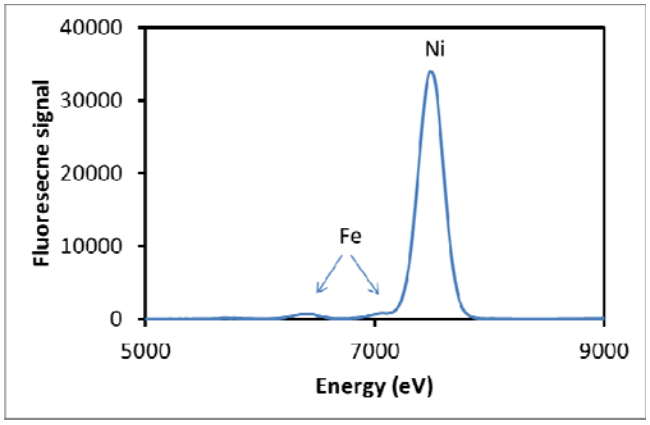

Figure 4.4.2-4. Spectrum obtained from a polycapillary collimator and a HOPG graphite crystal analyzer using a Vortex detector. The sample was a silicate standard with 9% Fe and 110 ppm Ni.

4.4.2.7 References

[4.4.2-1] B. Dickinson et al., Rev. Sci. Instrum. **79**, 123112-1 (2008).

[4.4.2-2] P. Glatzel, F.M.F. de Groot , U. Bergmann, Synchrotron Radiat. News **22**(2)**,** 12 (2009).

[4.4.2-3] J. Szlachetko et al., J. Synchrotron Rad. **17**, 400 (2010).

4.4.3 LERIX Upgrade [CAS]

The LERIX-2 beamline will support the new LERIX-2 spectrometer and the UHV component of the advanced spectroscopy techniques described in Section 4.4.2. The LERIX-2 spectrometer will be a significant upgrade from the current LERIX-1 system and the ongoing upgrade of LERIX-1 to the LERIX-1B system. LERIX-1 was the first spectrometer optimized for high throughput non-resonant inelastic x-ray scattering. It has the notable and unique feature of collecting a wide range of scattering angles simultaneously. Somewhat surprisingly the q-dependence of the scattering has proven to be a rich source of information in many systems, and the LERIX-2 spectrometer will maintain this unique capability with upgraded detectors and beamline optics.

To put the beamline into context note that NIXS spectrometers for the study of semi-core and core initial states (NXRS) fall into three catgeories:

Those optimized to have energy resolution truly comparable to the core-hole lifetimes, i.e., 0.1-0.2 eV, for XANES (and q dependent XANES) studies which can be certain to lose no information with respect to soft x-ray XANES. This requires high-resolution monochromators and also the use of dispersion compensation. The only multianalyzer XRS system which accomplishes this goal is presently at ESRF ID-16, where nine analyzers share one PSD.

Those optimized for high throughput, while sacrificing some energy resolution. These further split into two categories: Those which retain q-dependent information and those which pack detectors as tightly as possible in a low-q region (for nearly dipole-limit information) and/or a high-q region (for best study of edges with binding energies of ~500 eV or higher). LERIX-1 is presently the premier instrument for q-dependent XRS, with 19 analyzers spanning the vertical scattering plane, but with energy resolution of ~1 eV. The LERIX-2 upgrade, together with the use of improved optics, will reliably reach a net 0.5 eV energy resolution with ~200 analyzers. In the future, a damping wiggler beamline proposed for NSLS-2 might also have a LERIX-2 type instrument, and would target 0.5 eV resolution at 10^{14}/s. However, spot sizes below ~0.3 mm would result in a steady (and rapid) loss of flux. An example of the second case is the new SSRL IXS spectrometer that has ~100 analyzers, positioned only at low-q and high-q, and reflecting onto a small number of solid-state detectors. The planned ESRF ID-16 upgrade may supplement the main, vertical scattering plane instrument with a few modules in the horizontal plane at either low or high q.

Those optimized specifically for operation with diamond anvil cells (DAC). XRS measurements from DAC have two special constraints: (i) the geometric constraints on scattering imposed by the DAC itself and the sample geometry; (ii) the extreme issues posed by the background from the scattered radiation from the gasket or diamond. The LERIX-2 design will have sufficient coverage in scattering space to be compatible, and likely near optimal, for many of the common DAC scattering geometries.

The second component of the LERIX-2 beamline is a separate station to house the *in situ* UHV spectroscopy capabilities at Sector 20. This capability will be maintained because it is essential that it remain associated with a spectroscopy sector. The existing surface XAFS capabilities will be upgraded to support the high-resolution fluorescence spectroscopy (miniXS) of the advanced spectroscopy beamline. Of the numerous capabilities for studying surfaces and interfaces under UHV at synchrotron facilities, few have the ability to use spectroscopic methods like XAFS and only one other, so far, plans to apply high resolution spectroscopic techniques to interfaces and buried layers. The Galaxies beamline at Soleil will have similar UHV capabilities to the advanced spectroscopy sector, including high resolution XAS and *in situ* chemical analysis.

4.4.3.1 Scientific Scope

X-ray Raman scattering, from semi-core and relatively low-lying electronic core levels, is an emergent branch of synchrotron-based science. XRS is a subset of nonresonant, inelastic x-ray scattering, which more broadly also includes the scattering from valence levels. In XRS or NIXS, a fixed-energy spectrometer and a scanning monochromator work in unison to generate energy loss spectra which, at given momentum transfer Q, provide a direct probe of the electronic excitations in the system. This technique has gone from being a curiosity, with only a handful of studies that incorporated it completed prior to 1995, to being a central part of the plans of all third-generation light sources in 2010, with dozens of papers (if not soon as many as 100), published each year using XRS/NIXS.

X-ray Raman spectroscopy is a very powerful tool for examining the chemical structure and environment in light elements embedded in thick or absorbing objects [4.4.3-1]. It combines the power of soft x-ray spectroscopy with the in situ capabilities of hard x-rays. This technique has been widely used in high-pressure research to examine light elements, including hydrogen. Recent work at the APS has demonstrated that XRS is applicable to working on Li-ion batteries, providing important information about the redox chemistry through measurement of all low-energy edges in the system (i.e., the oxygen K-edge, transition metal L- and M-edges, and, in some cases, the Li K-edge). In addition, it is possible to explore the momentum transfer (Q) dependence of the scattering, move beyond the dipole approximation, and access a unique combination of $S(Q,\omega)$,which cannot be observed with longer-wavelength, electromagnetic radiation [4.4.3-2–4.4.3-6].

The LERIX instrument at XSD/PNC (20-ID), commissioned in 2006, holds a special role as the first instrument designed to optimize experimental throughput for many NIXS measurements, while also retaining good versatility to explore new applications. To date, LERIX has been responsible for:

- The discovery of strongly dipole-forbidden excitations from semi-core levels in f-electron systems; these resonances give a new window into chemical bonding in such systems.
- The first gas-phase measurements of NIXS from valence orbitals of N2 [4.4.3-6].
- The first demonstration of in situ XRS studies of electrochemical cells (i.e., Li-ion batteries). These studies have important consequences both for their importance in addressing the central issue of charge transfer and also as a path-finder in experimental methodology.
- The first demonstration of the TRIXS technique holds special promise for surface-sensitive studies of low-energy edges for thin films during film growth or when special gas environments are necessary, such as during *in situ* studies of catalysis.
- The demonstration of a protocol for quantitatively reliable measurement of O K-edge XAS/XRS in actinide compounds, such as the UO_{2+x} oxides relevant for fission fuels [4.4.3-7].

When looking to the future, it is important to seek experimental capabilities which further enable the ongoing transition of NIXS to a truly standard synchrotron radiation technique. The optimized beamline for NIXS capabilities and an improved LERIX (LERIX-2) spectrometer will have substantially improved capabilities, as follows:

- Beamline capabilities under “typical” experimental conditions include an incident flux of 4×10^{12}/s; incident energy resolution of ~0.3 eV; and appropriate long-working-distance focusing optics for a 10–20 micron spot size at the sample.
- Spectrometer (LERIX-2) capabilities will include a significant increase in the number of analyzer modules; improved detectors (against both count-rate saturation and for fluorescence-rejection); options for imaging mode operation; improved He-containment for

substantial improvement in throughput, especially for lower-energy operation; and greatly improved convenience for use of furnaces and cryostats.

These improvements will instantly enable and make standard a broad range of important studies that are generally impossible, or at least prohibitively difficult, to conduct with existing facilities at the APS or elsewhere. The most obvious of these fall into several quite distinct categories:

1. Truly high-quality and reliable measurements of the O K-edge near-edge structure with bulk sensitivity, even for samples in extreme experimental environments that are incompatible with soft x-ray techniques or EELS.

2. Truly high-quality and reliable measurements of the $L_{2,3}$ edges of transition metal compounds. Obtaining such measurements can be quite difficult with soft x-ray spectroscopies (see, for example, the continuing debate about $LaCoO_3$), but the process is straightforward with NIXS. The improved facility will be able to resolve a dramatically enlarged range of effects, while also enabling q-dependent studies and improving measurement times by at least an order of magnitude (see Section 4.4.3.5).

3. Expansion of 20-ID capabilities to include high-throughput measurements of NIXS in diamond anvil cells. A strong case can be made that the most important NIXS studies to date have often been DAC studies of phase transitions under very high pressures. While researchers using HP-CAT and GEO-CARS have published numerous such papers, LERIX has been absent from this rich field because of the large spot size at the sample location for the present beamline. The upgrade will immediately make 20-ID the premier facility for performing such measurements, with more than order-of-magnitude improved measurement throughput and also significantly improved energy resolution. Further improvement in throughput may accrue from three additional developments: (a) a new internal-slit (micro-machined) system under development that aims to completely eliminate the NIXS background from the Be gasket, providing up to another factor of 10 in improvement in measurement times for the same final NIXS signal-to-Poisson-noise ratios, (b) diamond anvil cells with thinned sections for the incident and scattered beams, greatly reducing the background scattering; and (c) the known capability to use the “imaged” analyzed radiation on an area detector to further reject scattering from the gasket [4.4.3-8].

4. The expansion of NIXS to surface and interface systems. Recently, it has been shown that LERIX can also be used at grazing incidence, providing both surface- and bulk-sensitive capabilities. With the upgrades in beam size and flux, LERIX-2 will provide a unique user facility for TRIXS.

The second major capability of the beamline is the UHV station. In addition, to continuing to allow UHV surface XAFS studies, it will be upgraded to allow the fluorescence spectroscopy described in section 4.4.2, and to allow use of the advanced detectors being developed for ultra-dilute detection. This upgrade will be carried out by Canadian collaborators, and will likely be complete prior to the beamline upgrades. They have also agreed to support its use by general users subject to possible restrictions on what will be allowed in the chamber. There will always be a subset of samples that will require in-situ UHV conditions. These include kinetic studies of growing films and interfaces, the initial bonding as interfaces are formed, and air sensitive thin films that are not amenable to capping layers.

4.4.3.2 Source Requirements

Inelastic scattering experiments like x-ray Raman are intrinsically flux limited. The canted option on a regular straight section will result in a source slightly shorter than the standard Undulator A. Thus, a long, straight section has been requested to allow the use of two longer undulators. However, if a long straight is not possible, some improvement is still possible resulting from the higher current and the use of an undulator more optimized to the needs of LERIX. The energy range of operation will be from

5–23 keV. This range means a 3-cm-period undulator can be utilized. As shown in Figure 4.4.3-1, even at a 100-mA beam current, the usable flux is equal to or better than a standard-length Undulator A, except for an energy region not often used by LERIX (12–13 keV).

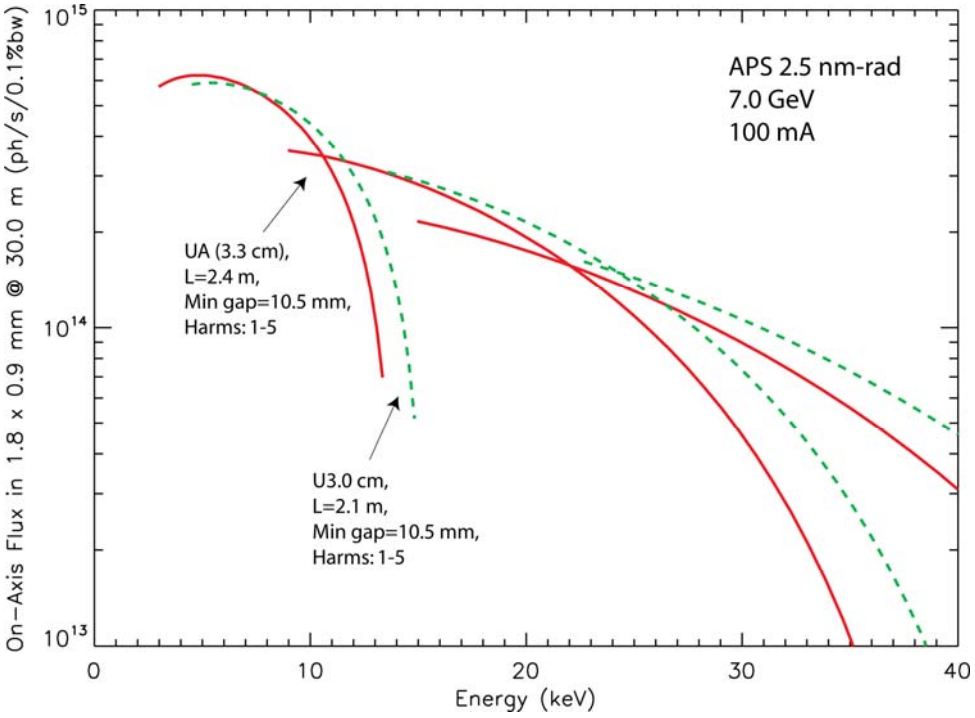

Figure 4.4.3-1. Comparison of the flux through a typical aperture for a U3.0 undulator in the canted configuration (green dashed line) with the current Undulator A (red line) at 20-ID.

4.4.3.3 Beamline Description

The sector layout is shown in Figure 4.4.2-1 (in the previous section). The LERIX-2 beamline will be on the inboard end-station branch, with the AS microprobe situated as a side station. Dual-side deflecting mirrors on the AS beamline will give an approximately 300-mm beam separation at the microprobe station. This separation should be adequate for the relatively compact microprobe station that has most of its detectors on the outboard side. The assumption in the figure is that the beamlines are located at Sector 20 using existing hutches. If Sector 20 is selected as a location for a long beamline, then the beamlines will need to be moved to an unoccupied sector. In this case, the hutch sizes and locations might be changed slightly. However, the layout will remain approximately the same, and the beamline performance will be essentially the same.

To support the UHV chambers that are being upgraded for advanced spectroscopy applications, a third experimental hutch will be added. The separate hutch will allow sample preparation and chamber bakeout while experiments are ongoing. The large KB optics can be refocused onto this station to provide the necessary small focal spots. Additional information about the UHV station can be found in section 4.4.2.

4.4.3.4 Optics

The optics for new beamline will be significantly enhanced. The current LERIX experiment has a toroidal focusing mirror in approximately the 1:1 focusing condition. It is fed by a fixed-exit

monochromator that uses Si (111) or Si (311) crystals. The new optics will be based on long KB mirrors located close to the spectrometer. This positioning will allow focusing of the entire beam to approximately 10–20 μm. The separate horizontal and vertical focusing will also give researchers the flexibility to provide expanded beams in the horizontal and/or vertical directions. The beam size can be varied from millimeters to microns and optimized for the experiment. For radiation-sensitive samples, larger beams will be desired, whereas for high-pressure work in diamond anvil cells, the smallest beam size will be needed. An intermediate case is use of glancing angles in surface studies. In this case, the smallest possible vertical beam size is needed, although the horizontal size could be large to reduce beam damage. These mirrors can also be refocused further downstream to provide a focused beam for the UHV station. At this position, the spot size will be approximately 50 × 15 microns.

For the monochromator, an upgraded version of the current 20-ID monochromator will be used. The upgrade will replace the vacuum chamber with another that is capable of transmitting the second beam from the advanced spectroscopy branch. The chamber replacement also affords us the opportunity to replace some kapton wiring damaged by radiation, improve the Compton shielding, and install an improved encoder. This monochromator has worked well over the past 12 years, has been optimized for spectroscopy applications, and allows for quick interchange between crystal sets by a horizontal translation. Si (111) crystals provide adequate resolution with the maximum flux, while Si (311) crystals provide better energy resolution with a loss of about 5× in flux.

There will also be a collimating mirror in front of the monochromator. This mirror will serve two purposes. It will filter out about half of the power, allowing operation up to 200 mA without any moncochroator heat-load problems. The collimation will also provide improved energy resolution when using the Si (311) monochromator crystals. Currently, the Si (311) resolution is degraded by more than 50% by the vertical divergence of the undulator beam. Ideally, this mirror will operate in the horizontal deflection mode to provide additional separation of the two beams. However, this operation requires a nonstandard conical mirror shape. While manufacturers have indicated that such mirrors are possible, more study is needed to determine whether executing this design is feasible with the necessary slope errors. A more standard, vertically deflecting mirror would also work.

4.4.3.5 Anticipated Performance

The improvements in the source and optics, combined with the increased number of detectors, will result in a dramatic improvement in data rates. Table 4.4.3-1 shows a comparison of the current LERIX spectrometer with the estimated performance of LERIX-2 on the new beamline, assuming 200 mA of beam current and a normal-length straight section. This comparison is for Si (311) monochromator crystals. For these crystals, the collimating mirror provides a significant improvement in the energy resolution. For Si (111) crystals, the comparison is similar with the flux numbers about 5 times higher. In this case, there is little improvement in the energy resolution from the collimating mirror.

Table 4.4.3-1. Comparison of the Current LERIX Performance with the Expected Performance for LERIX-2 (both cases are for the Si (311) monochromator crystals.)

	Energy Range (keV)	**ΔE/E**	**Spot Size (μm)**	**Flux at 10 keV (ph/sec)**	**Number of Analyzers**
APS 20-ID - LERIX	7–50	4×10^{-5}	400 H × 100 V	2×10^{12}	19
APS-U project LERIX-2	5–23	3×10^{-5}	20 × 10	4×10^{12}	~200

To better illustrate the improvement in performance, Figure 4.4.3-2 shows some simulations for various cases. This estimate is based on the observed count rates from similar samples. With the current

LERIX, there is always a trade-off in count rate and resolution. The new beamline and spectrometer will allow collection of high-quality data within reasonable times.

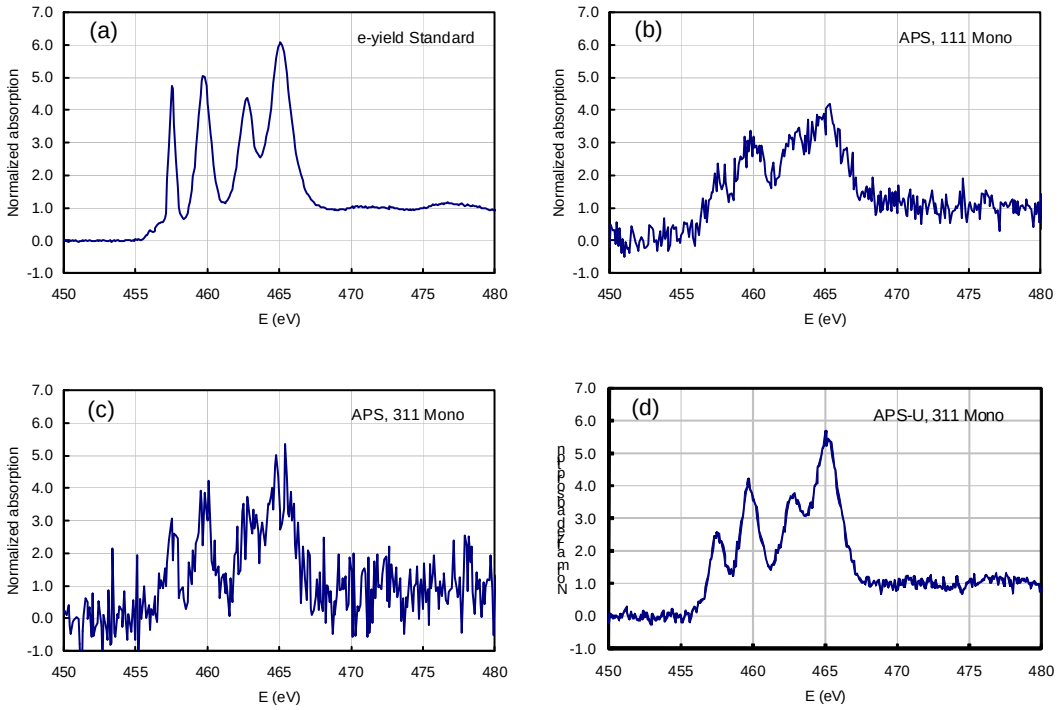

Figure 4.4.3-2. The expected performance improvement at the Ti $L_{2,3}$ edge for LERIX-2 and the upgraded beamline: (a) high-resolution spectrum for Ti in $CaTiO_3$; (b) simulated data from the current LERIX using Si (111) monochromator crystals and assuming a 20-minute scan; (c) same as (b), except with Si (311) monochromator; (d) expected performance for the upgraded beamline and LERIX-2 using an Si (311) monochromator.

4.4.3.6 Instrumentation

For reasons concerning both throughput and improved and enlarged scientific opportunities, LERIX-2 will be designed and constructed as a substantially upgraded, LERIX-style spectrometer. The instrument will be designed by Prof. G. Seidler's group at the University of Washington, in close collaboration with APS staff and other experts in IXS spectrometer design, and the existing LERIX user base. It will be important to have a beamline scientist transition into a leading role during the subsequent construction and especially commissioning of LERIX-2.

It is useful to briefly review the capabilities of the present LERIX-1 spectrometer and the final transition in capabilities to LERIX-2. To begin, a photograph of the LERIX-1 instrument is presented in Figure 4.4.3-3. The incident beam comes from the right, in the plane of the circular geometry of the instrument, to strike the sample, as shown. Radiation scattering into the vertical plane then strikes the 19 spherically bent crystal analyzers (each mounted on an "analyzer module"). Such radiation is Bragg scattered out of the plane of the figure by a few degrees (with subsequent energy selectivity) back to 19 matching scintillation detectors. Each detection channel thus samples a different scattering angle and hence a different momentum transfer, q — recall that the beam is in the plane of the spectrometer. IXS energy-loss spectra are generated by scanning the incident photon energy with the spectrometer elements held fixed at one detection energy. This "inverse scanning" mode is the most convenient and cost-effective strategy for NIXS measurements by multi-analyzer systems.

While LERIX-1 has been a scientific success for the APS, some design and performance characteristics of LERIX-1 have begun to inhibit desired XRS applications and also need to be addressed as part of the design path toward LERIX-2. Consequently, in the spring of 2010, the APS has allocated funds to upgrade to the LERIX-1B configuration. There are three goals to this upgrade that are relevant to the development of the LERIX-2 spectrometer.

First, the LERIX-1 superstructure and He box will be replaced with one providing maximum and flexible clearance for environmental chambers and x-ray optics (i.e., KB mirrors). This dramatically improved compatibility with apparatus needed for studies of samples in extreme environments will help to further increase the APS's user base in XRS studies, laying important scientific and organizational groundwork for LERIX-2. In particular, it will immediately enable studies in cryostats, furnaces, thin-film fabrication vacuum chambers, and diamond anvil cells.

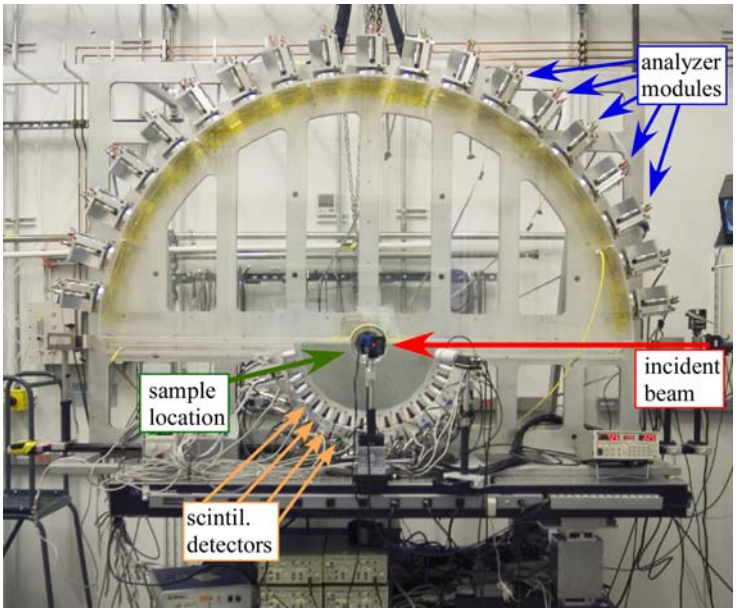

Figure 4.4.3-3. The LERIX-1 spectrometer at the Advanced Photon Source, Sector 20-ID XSD/PNC (the various components are discussed in the text).

Second, an analyzer module design will be adopted in which all three axes of the tilt stages are motorized (i.e., allowing for tuning of both tilt angles and the distance to the beam-spot on the sample). This step is needed for LERIX-2, where several analyzers at similar q will share a common detection channel; if the analyzers are not tuned with sufficient precision to the same energy, a loss in energy resolution will occur.

Third, the LERIX-1B configuration will allow easy modification of the detector assembly. This will allow us experiment with the transition from individual scintillation detectors to shared area detectors. The transition is important for the final design of LERIX-2, which will use two to three large x-ray-sensitive area detectors as the detection mechanism for all 200 analyzer channels.

3D CAD rendering for one possible configuration of analyzers for LERIX-2 is presented in Figure 4.4.3-4. Investigations of ray-tracing and design considerations are already well under way by Prof. G. Seidler's group. LERIX-2 will have approximately 20 times the collection solid angle of the present instrument, in addition to much superior compatibility with environmental chambers for studies of samples in extreme environments and much improved energy resolution in usual operation. This apparatus will have a suite of dedicated sample-control apparatus (automated sample exchange, cryostat,

furnace, miniature 2-circle goniometer, hermetically sealed sample holders for battery or actinide studies, liquid flow cells, gas pressure cells, etc.).

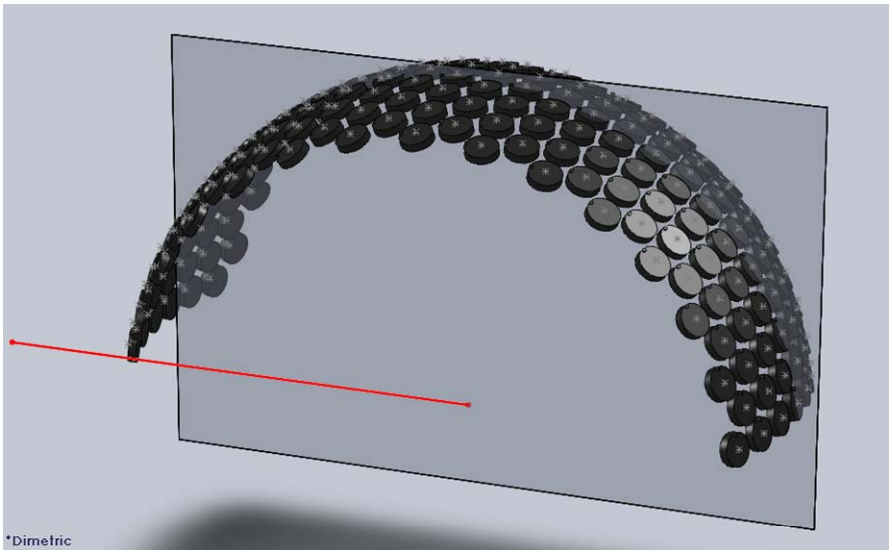

Figure 4.4.3-4. A 3D CAD rendering of one possible configuration of spherically-bent crystal analyzers for the LERIX-2 spectrometer. This example covers 20% of the upper 2π sr and nearly 40% of the 'useful' solid angle, given the polarization dependence of NRIXS.

It is useful to itemize some key targeted design criteria for LERIX-2 that will be relevant to the majority of anticipated science projects that will be studied with this new instrument:

- A total collection solid angle of 20% of the upper 2π sr of the scattering geometry, positioned symmetrically in the vertical scattering plane. This will entail, for example, ~200 spherically bent crystal analyzers with 10-cm diameters at the typical 1-m working distance. Given the polarization dependence of XRS (from the Thomson differential cross-section), this 20% coverage of the upper 2π sr actually subtends a much larger fraction, ~40%, of the useful collection solid angle for this scattering process.
- Net energy resolution not significantly degraded from the anticipated ~0.3 eV resolution of the double Si-311 monochromator. This criterion requires, for example, analyzer energy resolution of similar order when illuminating a single pixel detector.
- Independent control of detector position, off-circle location, and two-axis tilts for each analyzer.
- Provision for imaging mode operation by combining the imaging properties of the analyzers with area detectors [4.4.3-9].
- Retention of the ability to study q-dependent XRS by being able to group detection channels by q, not by local clustering of analyzers.
- Easily maintained He spaces to reduce losses from air scatter.
- The possible use of energy-resolving area detectors both to allow maximum flexibility in analyzer placement (i.e., for optimum collection solid angle) and also to provide rejection of stray fluorescence or of scattering from undesired harmonics on the spherically bent crystal analyzers.

This combination of characteristics will provide revolutionary capabilities for the users of the Advanced Photon Source.

4.4.3.7 References

[4.4.3-1] U. Bergman, P. Glatzel, and S. Cramer, Microchem. J. **71**, 221 (2002).

[4.4.3-2] J.A. Soininen, A.L. Ankudinov, and J.J. Rehr, Phys. Rev. B **72**, 045136 (2005).

[4.4.3-3] J.A. Bradley et al., Phys. Rev. Lett. **105**, 053202 (2010).

[4.4.3-4] T. Gog et al., Synchrotron Radiat. News **22-6**, 12 (2009).

[4.4.3-5] T.T. Fister et al., J. Am. Chem. Soc., **130**, 925 (2008).

[4.4.3-6] R.A. Gordon et al., Europhys. Lett. **81**, 26004 (2008).

[4.4.3-7] J.A. Bradley et al., J. Am. Chem. Soc. (accepted).

[4.4.3-8] R. Verbeni et al., J. Synchrotron Radiat. **16**, 469 (2009).

[4.4.3.9] S. Huotari, T. Pylkkanen, R. Verbeni, G. Monaco, and K. Hamalainen, submitted (2010).

4.4.4 Resonant Inelastic X-ray Scattering Upgrade [U1.04.02.08]

The emergence of IXS as a mainstream experimental technique has been one of the most significant developments in x-ray instrumentation at synchrotron radiation facilities in the past decade. IXS has been successfully employed to study electronic and vibrational excitations in real materials of fundamental and technological importance, spanning a broad spectrum of scientific disciplines that reaches from fundamental physics to materials science, biophysics and geophysics.

Resonant inelastic x-ray scattering (RIXS), one variety of IXS with a medium-energy resolution of currently 80 meV to 300 meV, is particularly well suited to study elementary electronic excitations in complex materials by measuring their dependence on energy, momentum, and polarization. A vast body of important information has been accumulated by this unique technique in the past decade, especially with regard to correlated electron systems in transition metal compounds. These materials are the hosts of such technologically important phenomena as high-Tc superconductivity and colossal magneto-resistance [4.4.4-1].

The RIXS program at the APS, consisting of dedicated instruments on beamlines 9-ID (50% of beam time) and 30-ID (MERIX) (50% of beam time) is currently the world's leading program of its kind [4.4.4-2]. Its sophisticated in-house capabilities have produced the largest selection of high-resolution, diced spherical analyzers of any facility, making accessible most pertinent x-ray absorption edges in the range of 6.5 keV to 13 keV. Due to its high-quality analyzers in connection with position-sensitive detection, the highest energy resolutions are available. At 30-ID, beam sizes at the sample position as small as 20 μm × 30 μm (v × h) can accommodate extreme sample environments, such as diamond anvil cells, for high-pressure work. A choice of vertical or horizontal scattering geometries enables polarization-dependent measurements and reduction of the elastic line for extracting low-amplitude signals at small energy transfers. Tandem 30-mm insertion devices at 30-ID currently provide the highest flux while preserving a tuning range that covers the required spectrum of absorption edges of interest.

Competing programs at other facilities are inferior in one or more aspects, but upgrade plans at these facilities are underway that will diminish the current APS advantage very soon.

At SPring-8's BL11XU beamline approximately 25% of the beam time is used for RIXS. Spherical analyzers are non-diced, delivering inferior resolution than their diced counterparts; however, collaboration is underway to transfer analyzer fabrication experience from the APS to SPring-8 staff. Beamline BL12XU has limited RIXS capabilities but does not use them on a regular basis.

At the ESRF beamline ID-16 has RIXS capabilities; however, in its present state, this beamline is used almost entirely for partial yield fluorescence measurements. Its advantages over the APS program are a large angular 2Θ range (0 to 170 degrees) and an extended incident-energy range (5-15 keV). Its capabilities are inferior to the APS program in energy resolution (nominally 0.1 eV to 1.5 eV, but publication seems to hover near 1 eV) and beam focus of (100 μm × 50 μm). The ESRF renewal contains plans for corrections to these deficiencies and further improvements, including improvements in resolution, smaller beam sizes, polarization analysis, and multi-analyzer arrays.

At the NSLS II at Brookhaven National Laboratory, Diamond, and Soleil, RIXS capabilities are in the planning stage but not yet close to operation.

The APS upgrade will greatly enhance existing local RIXS capabilities by:

Consolidating the two existing RIXS instruments on one dedicated insertion device beamline: This will replace 50% of the present beam time on a rather outdated first-generation instrument with beam time on a state-of-the-art instrument. Also, experimental overhead will be

eliminated because the beamline will not have to be converted back and forth between two different techniques, as is currently the case on both 9-ID and 30-ID.

Increasing the incident flux: Measurement times necessary to acquire publishable data sets for these flux-starved, long-counting-time experiments are decreased proportional to the increase in particle current and extended length of available insertion devices. Currently it takes approximately 2 to 3 one-week visits for a user group to obtain a complete set of data for a publication. By increasing the current to 150 mA or eventually to 200 mA and adding a third insertion device in an extended straight-section, a one-week measurement cycle could result in a publishable set of data.

Continuing analyzer development and improving the energy-resolution: This item has been declared critical for a successful advancement of the RIXS technique. It appears feasible at this time to improve the energy resolution of RIXS to the 10- to 20-meV range for many specific cases. This improvement will require R&D into alternative crystal materials such as quartz and sapphire, together with new, appropriate fabrication techniques.

Enhancing the MERIX instrument: Fully integrated vertical and horizontal scattering geometries, polarization selection on the incident beam and polarization analysis on the scattered beam, and improved efficiency through better detectors and detection schemes will greatly broaden the spectrum of materials and phenomena that can be successfully studied.

Developing extreme sample environments: Integrating sample environments for high pressure, high and low temperatures, external electric and magnetic fields, and many more enables the study of real materials under real condition in their native (e.g., geophysics, biology) or technical application environment.

The APS-RIXS program started at the former CMC-CAT beamline 9-ID in 2001, driven largely by a research group from Brookhaven National Laboratory. Over time, through significant efforts toward training, instrument development, and publicizing the RIXS capabilities, as well as the addition of the second-generation instrument (MERIX) in 2007 on a brand-new, optimized insertion device beamline 30-ID, the user base of RIXS facilities on 9-ID and 30-ID has broadened to 18 distinct research groups with more than 70 researchers and collaborators.

The RIXS technique thrives on the availability of hard x-rays in the 4-keV to 15-keV range. The resonant enhancements of the inelastic signal for electronic excitations has made possible studies of technologically relevant transition metal compounds, shining light on novel phenomena such as high-Tc superconductivity and colossal magneto-resistance. The availability of incident x-ray energies in the vicinity of the absorption edges of these materials is thus crucial for the continued success of this technique and can only be found at hard x-ray sources such as the APS.

This section describes the upgrade of the RIXS program, which at its core consists of relocating the MERIX instrument from 30-ID to 9-ID and transforming 9-ID into a dedicated state-of-the-art RIXS facility. At the same time, beamline 30-ID will be optimized for high-resolution IXS.

It should be noted that as an alternative to 9-ID, the RIXS program could be moved to any unassigned insertion device beamline where the RIXS instrument and associated shielding enclosures as described below can be accommodated.

4.4.4.1 Scientific Scope

The upgrade of the RIXS program will greatly increase its scientific productivity and enable research into subjects currently not accessible. A few examples shall serve to illustrate this.

The recent discovery of high-temperature superconductivity in Fe-pnictides [4.4.4-3–4.4.4-5] has drawn enormous interest as a new class of superconducting materials and its practical implications for

energy research. In a short period of time, a quite complete phenomenology has emerged. Resonant IXS experiments have already made significant contributions to the understanding of these compounds.

One prominent theoretical explanation for superconductivity in Fe-pnictides [4.4.4-6, 4.4.4-7] is based on interband Cooper pairs. Therefore, probing interband excitations and their momentum dependence, indeed, trying to understand the full electronic structure of these materials is enormously important for elucidating the mechanism of their superconductivity. Resonant IXS is an ideal probe to provide the required bulk-sensitive, momentum-dependent information; however, the current energy resolution of the instrument at the Fe K-edge (~250 meV) is insufficient. The upgrade of the RIXS program at the APS is designed to meet these requirements at 30- to 50-meV resolution for this particular case. The major goal of the improved energy resolution is to increase access to the low-energy loss region separated from the elastic line, probing excitations of smaller energies. Obviously, a narrower elastic line is one ingredient, but a better spectrometer design (fully integrated horizontal scattering) is an invaluable contribution since the polarization dependence of Thomson scattering, which is the primary contribution to the elastic line intensity, can be reduced or eliminated in horizontal scattering.

Multiferroic materials exhibit multiple functional properties, such as ferromagnetism and ferroelectricity [4.4.4-8–4.4.4-10]. Due to the coupling between the magnetic and charge degrees of freedom, the magnetic polarization can be switched by applying an electric field; likewise the electric polarization can be switched by applying a magnetic field. Potential applications of such multifunctional material range from electromechanical actuators to multiple-state memory devices, in which data can be stored in both electrical and magnetic polarization states. Again, resonant IXS is a suitable probe to study the effects of applied fields on the magnetic and charge order, as well as the overall electronic structure, if a fitting sample environment is provided, together with a sufficient photon flux and focusing capabilities.

The study of pressure-induced changes in electronic structure is very useful for these and many other compounds [4.4.4-11, 4.4.4-12]. For example, superconductivity can be induced by chemical doping, but this naturally introduces positional disorder, as well as charge carriers. The application of pressure directly modifies the electronic structure providing a clean way to investigate the emergence of superconductivity. In order to conduct studies of materials under high pressure, a suitable sample environment is necessary, such as diamond anvil cells, in situ pressure regulation, etc. Additionally, extreme sample environments require focusing of the incident x-ray beam to μm-size with high efficiency, a condition to be achieved by means of the upgrade. Increased momentum resolution is also very desirable, and instrumental upgrades will make this possible.

Another important area is the study of photoinduced effects in complex correlated systems, such as the manganite Pr0.7Ca0.3MnO3, where a metal-insulator transition, accompanied by an 8-order of magnitude drop in resistance, can be driven in the presence of an electric field by illuminating with an optical laser [4.4.4-13–4.4.4-15]. As part of the upgrade, instrumentation will be developed and implemented to carry out resonant inelastic x-ray scattering measurements of the electron dynamics under photo-illumination.

The recent discovery that 5d-transition metal compounds, such as the Iridates, exhibit a large new class of correlated electron phenomena has generated much excitement in the scientific community and raised hopes for new and important technological applications. RIXS is the only technique that can measure the excitation spectrum of these materials in the relevant energy and momentum regime. With feasible energy resolutions in the 10- to 20-meV range, the upgrade of the RIXS program will make a substantial contribution to this field of research.

Both current resonant IXS instruments are occasionally used for nonresonant, medium-resolution IXS [4.4.4-16–4.4.4-18]. Nonresonant results are easier to interpret than resonant results, although signals are typically much weaker. It is believed that nonresonant medium-energy IXS will become an

increasingly important technique as the incident flux is increased (through, for example, higher ring current) and other advances make the available beam time more efficient.

4.4.4.2 Source

The source requirements for RIXS are chiefly determined by the need to tune the incident photon energy to all pertinent absorption edges. Three types of permanent magnet undulators currently in use at the APS with period lengths of 33 mm, 30 mm, and 27 mm deliver a suitable energy spectrum between ~5 keV and ~12 keV in the first harmonic. The 30-mm-period-type device is currently in use and has performed very well in the past. It is the preferred device for the upgraded RIXS facility, also. All IXS techniques are chronically flux starved. A long straight section in Sector 9, accommodating three instead of two undulators, would increase the available incident x-ray intensity by 50% and would linearly benefit these long-counting-time measurements directly.

4.4.4.3 Beamline Enhancements

The construction of beamline 9-ID began in 1996. It is one of the older beamlines on the floor of the APS and is somewhat outdated in various regards. The APS-U provides an opportunity to return and enhance this beamline to a state-of-the-art facility for resonant inelastic scattering.

One major instrumental requirement for such a facility is a microfocusing capability for the incident x-ray beam with a demagnification ratio resulting in a beam size of approximately 10 μm horizontally and vertically at the sample position. Given the natural divergence of the synchrotron radiation beam and restrictions in the maximum length of complex focusing mirrors, the spectrometer has to be located at a rather short distance from the undulator source, approximately 40 m in the case of the RIXS instrument. The current structure of shielding enclosures on 9-ID is not conducive for microfocusing. Therefore, the major effort in terms of beamline enhancement is the replacement of the existing shielding enclosures with new ones. Figure 4.4.4-1 shows an overview of Sector 9 with current and future enclosures and the optimal location for the RIXS spectrometer. Enclosures 9-ID-A and 9-ID-B are largely new construction, except for the very upstream portion of 9-ID-A. Their overall configuration is very similar to the equivalent enclosures on beamline 30-ID, and the design is directly transferable. Downstream of 9-ID-B, an enclosed operations area will be constructed that will provide experimenters with a suitable place to prepare and conduct their scientific experiments. Existing enclosures near the downstream end of the current beamline will be retired.

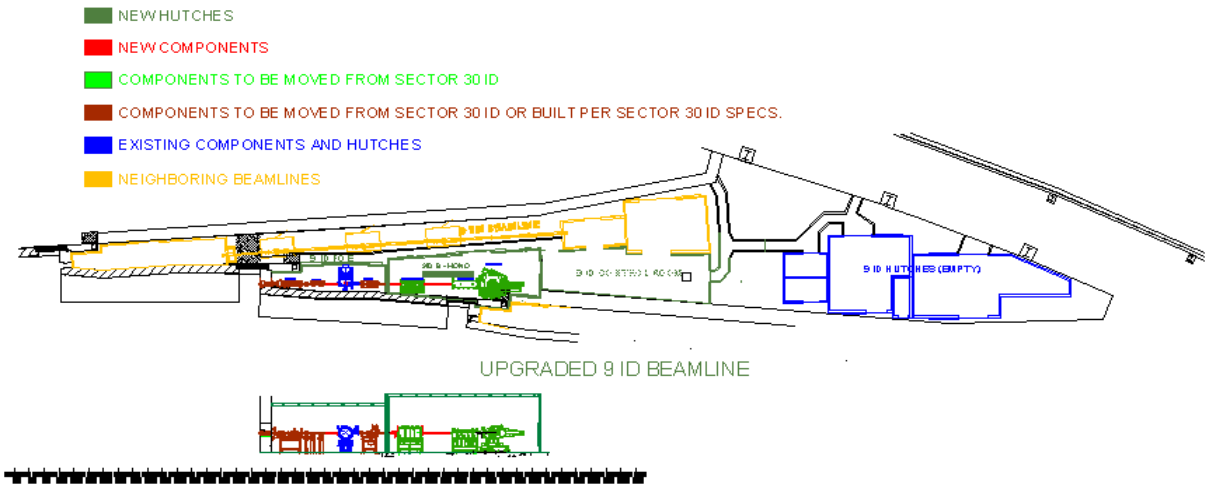

Figure 4.4.4-1. Overview of the reconfigured insertion device beamline 9-ID in Sector 9.

4.4.4.4 Optics

The most important consideration regarding the beamline optics for 9-ID is the dramatic increase in x-ray power that needs to be accommodated after the APS upgrade.

Front Ends: One viable option for 9-ID is to re-use the front end from 30-ID. However, with an ultimate particle current of 200 mA and a possible third in-line undulator in case of an extended straight section in Sector 9, the power loading would increase by up to a factor of 3, possibly requiring appropriate modifications to this front end.

9-ID Beamline Optics: Based on previous operational experiences with RIXS in Sector 9 and Sector 30, the following optics is presented for 9-ID:

1. Tandem or preferably triple 30-mm period, permanent magnet undulators as the x-ray source.
2. Windowless transition between front end and beamline based on existing differential pump.
3. Entrance aperture and variable white-beam slit, standard APS components.
4. High-heat-load monochromator based on existing Kohzu device, to be equipped with cryogenically cooled diamond(111) crystals.
5. Integrated white beam absorber and photon shutter, standard APS component, to be housed in the experimental station (9-ID-A).
6. High-resolution secondary monochromator with exchangeable sets of crystals.
7. Convertible phase plate assembly to control the incident polarization.
8. Compound focusing mirror system.
9. RIXS spectrometer.

The current Kohzu-type high-heat load double-crystal monochromator (4) located in 9-ID-A will be re-used. However, due to the increased heat load, the cryogenically cooled silicon crystals will be replaced by diamond. Although at current power levels water cooling is sufficient for diamond monochromators, after the upgrade, cryogenic cooling might be necessary or desirable.

A suitable high-resolution secondary monochromator is currently in operation in Sector 30 and will be moved to 9-ID. However, to be able to rapidly match the monochromator resolution and throughput with the requirements of a particular measurement and the resolution of the analyzer being used, the secondary monochromator needs to be augmented by multiple crystal stages for alternate channel-cut crystals and diamond phase retarders for control of the incident polarization.

A vertical and horizontal system of bimorph Kirkpatrick-Baez (K-B) mirrors is currently used in Sector 30 and will be moved to 9-ID. It is capable of generating beam sizes in the 10-to 30-μm range. In order to further reduce the beam size for sample environments, such as diamond anvil cells, an additional set of small elliptical KB mirror will be added to form a compound system with the main mirrors.

The RIXS spectrometer currently operating in Sector 30 will be moved to beamline 9-ID. In order to provide full Euler-geometries in the horizontal and vertical scattering plane, it will be augmented by additional motion stages as described further below.

4.4.4.5 Anticipated Performance

Currently, a typical incident intensity at the sample position, at an incident energy of 9 keV and a monochromator band pass of 70 meV, is approximately 7×10^{11} photons per second. This intensity will

increase by a factor of 1.5 due to the initial increase in particle current to 150 mA and may be increased by a factor of 3 if a long straight section in Sector 9 and a 200-mA current in the accelerator are achieved.

Count rates at the detector may increase proportionally to the number of analyzers in a multi-analyzer system as shown schematically in Figure 4.4.4-2. However, they will decrease as the resolution and the incident band pass are tightened. Beam sizes at the sample will be reduced to μm size, enabling specialty sample cells and aiding in improving the energy resolution.

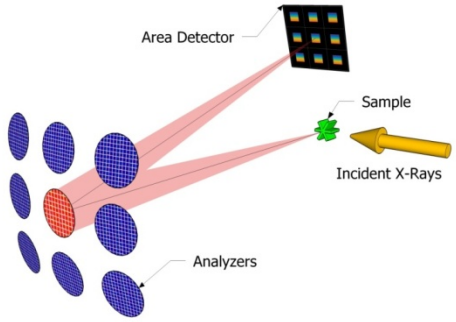

Figure 4.4.4-2. Sketch of a multi-analyzer instrument. Many configurations are possible, in the one shown here each spherically bent diced analyzer is focused on a different part of an area detector in a horizontal scattering geometry. The scattered and reflected x-rays are shown in red for one analyzer only for clarity. Each focal spot represents a different part of momentum space, with the corresponding energy-dispersed spectrum is shown as a color gradient.

4.4.4.6 Instrument Enhancements

Energy Resolution, Development of High-Resolution Spherical Analyzers: Improving the current energy resolution in RIXS from the 80- to 300-meV range to the 10- to 20-meV range for many particular scientific cases has been identified as one of the most important requirements for a successful upgrade of the RIXS facility. A schematic RIXS experiment is shown in Figure 4.4.4-3. A micro-focused, monochromatic x-ray beam of energy E_i and band pass ΔE_i are incident on the sample. Scattered radiation is collected by a diced, spherical analyzer, which disperses the captured spectrum of energies onto a position-sensitive (strip-) detector with pixel-size p. Sample, analyzer, and detector are arranged in

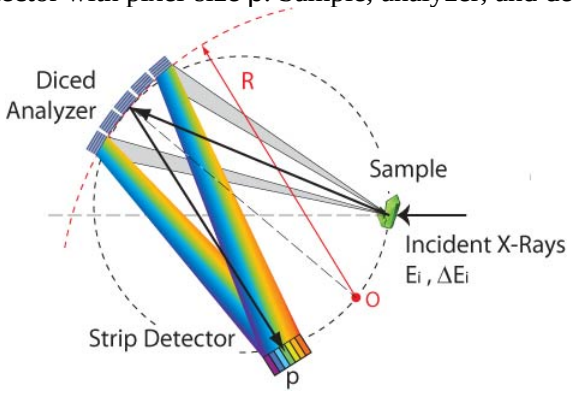

Figure 4.4.4-3. Schematic RIXS experiment and detection system.

Rowland geometry, the radius R being typically 1–2 m. The basic energy-resolution of this set-up can be approximated by

$$\Delta E_{tot} = \sqrt{\Delta E_i^2 + \Delta E_{ana}^2 + \Delta E_{beam}^2 + \Delta E_{det}^2} \ ,$$

where the four contributions arise from the monochromator, the intrinsic resolution of the analyzer, the beam size at the sample, and the spatial resolution of the detector. Highly efficient monochromators can be designed to suit any need. With state-of-the-art micro-focusing and with spatial resolutions for current strip detectors, the associated contributions to the overall energy resolution are very small. The remaining bottleneck is the intrinsic analyzer resolution, where reflections of lattice spacings in the immediate vicinity of $d = hc / 2E_\alpha$, E_α being the resonance energy, are necessary, and the crystal quality needs to be nearly perfect. In the past, silicon and germanium were the preferred choices; however, with advances in crystal growth, other materials that offer more choices and better resolution are becoming very viable. Sapphire, quartz and silicon carbide are being prototyped; however, an aggressive R&D program has to be implemented to ascertain that suitable spherical analyzers made from these materials are routinely available. This R&D program will be funded on an operational basis, and will be carried out in collaboration with the APS Optics group.

Momentum Resolution: The current dispersive setup with a 4” analyzer at the end of a 1-m arm has provided adequate momentum resolution for the majority of RIXS experiments so far. The ability to measure multiple positions in reciprocal space will be very advantageous and will speed up the data collection immensely. Indeed, the ability to measure a greater range in reciprocal space will be of greater benefit to most experiments than to simply provide better momentum resolution.

The upgraded instrument will have multiple analyzers that can be used together for a higher throughput at the expense of momentum resolution or independently to measure multiple points in reciprocal space. This high flexibility can be achieved with independent dispersive detectors or, more practically, with different sections of a single strip (or area) detector. Additionally, the analyzers can each be masked (or manufactured) to an arbitrary shape to provide the desired reciprocal space resolution.

These changes will result in a large increase in performance and flexibility, since no two experiments have the same optimal setup requirements. Both survey and detailed-scan strategies can more easily be pursued in the same instrument, by either combining the signal from all analyzers or by analyzing the data collected by each analyzer, each at a different momentum transfer, separately.

Horizontal / Vertical Scattering Geometries: Implementation of full (Euler-) geometries for horizontal and vertical scattering planes will greatly enhance the capabilities of the MERIX instrument. Scattering in the horizontal plane is generally preferred for resonant IXS measurements because the elastically scattered signal is minimized, allowing investigations of electronic excitations with very small energy loss. Vertical scattering is usually preferred for nonresonant IXS experiments, because it maximizes the elastic signal. In addition to providing both horizontal and vertical scattering capabilities, good sample manipulation is also desirable because it allows various sample axes to be aligned with the polarization of the incident light, permitting incident polarization dependence studies of electronic excitations. Currently, the existing RIXS instrument as shown schematically in Figure 4.4.4-4 does not feature an independent “horizontal-theta” rotation stage, which will be implemented as part of the APS-U project.

Polarization Analysis

Incident polarization (Phase Plates): In order to study the polarization behavior of an electronic excitation with resonant IXS, the polarization of the scattered beam needs to be analyzed as a function of incident polarization [4.4.4-19, 4.4.4-20]. A diamond phase retarder placed in the incident beam is a

practical and efficient means to convert the natural linear horizontal polarization ("σ") of a synchrotron radiation beam to vertical ("π") or even circular polarization [4.4.4-21, 4.4.4-22]. This phase retarder is shown schematically in Figure 4.4.4-5. Its operation is based on the principle that, for dynamical crystals, in-plane and perpendicular polarization components are diffracted differently, thus generating a relative phase shift between them. For a phase shift of π, vertical linear polarization is generated; at π/2, circular polarization is achieved.

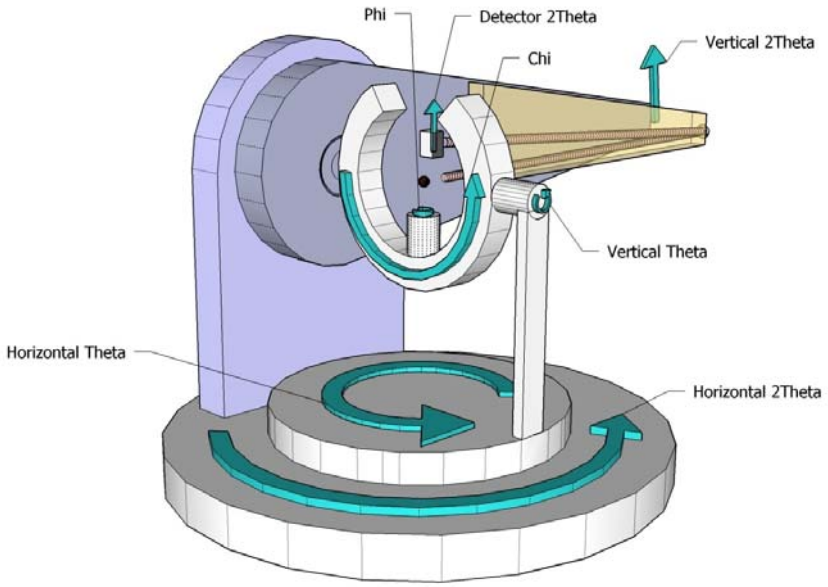

Figure 4.4.4-4. Schematic setup of the MERIX spectrometer. The instrument will be optimized for IXS by modifying the 2-theta arm and by adding a split Euler circle with the opening on the top, to allow the detector to approach backscattering geometry.

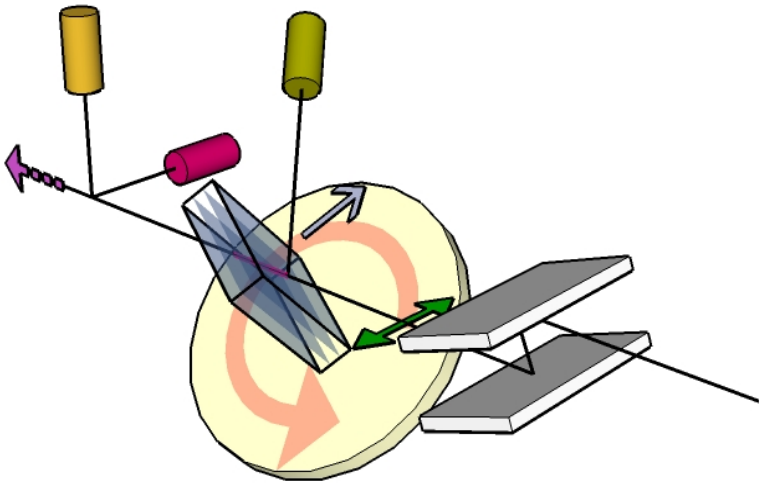

Figure 4.4.4-5. Single transmission-type diamond phase retarder.

Owing to its small absorption coefficient, diamond is an ideal material for transmission-type phase retarders. Inclining the diffraction plane of the diamond by 45° with respect to the incident beam, the natural σ polarization is split into two equal perpendicular components. In the vicinity of a diamond Bragg reflection and as a function of incident angle, the two polarization components in the transmitted beam are recombined after being individually phase shifted, resulting in the new desired polarization state. Single-phase retarders suffer from aberrations due to the limited collimation and monochromaticity of the incident beam. These aberrations can be largely compensated by placing two or four diamond stages in sequence along the beam, on rotation axes spaced 90° apart. If the combined thickness of these diamonds is equal to the thickness of the original single phase plate, no additional absorption losses are incurred, however, the phase purity is greatly enhanced.

For beamline 9-ID such a diamond phase-retarder assembly is currently being developed and tested and will be installed downstream of the secondary monochromator to deliver full incident polarization control to the IXS experiment.

Scattered beam polarization analysis: Up to now RIXS instruments measure the outgoing photon energy and momentum but completely omit measuring its polarization due to significant practical challenges, even though such a measurement would provide very important information on the excitation symmetry.

Given the great technological advances in optics and detectors, modern instrument performance and throughput make the addition of polarization analysis feasible. There is a current effort in Sector 30 as part of a PUP to develop and test such instrument extension.

In an upgraded RIXS facility, this polarization analysis capability will be built in. As shown in Figure 4.4.4-6, a small concave reflector at right angle, to be placed after the main analyzer, will retain the primary energy and momentum analysis capabilities of a modern dispersive setup. This optic will be matched to the energy of each edge, like the main analyzer.

The reflector material will be a thin Si (or maybe Ge) foil pressed onto a revolution logarithmic spiral. The sigma or pi polarization components of the scattered beam are accessed by rotating the reflector/detector arm by 90°.

Sample Environments: For RIXS studies of relevant material under “real” conditions, various occasionally extreme sample environments have to be made available. These include high-pressure cells, high- and low-temperature cryostats, and facilities for applying external electric and magnetic fields. R&D is already underway to develop and refine these facilities.

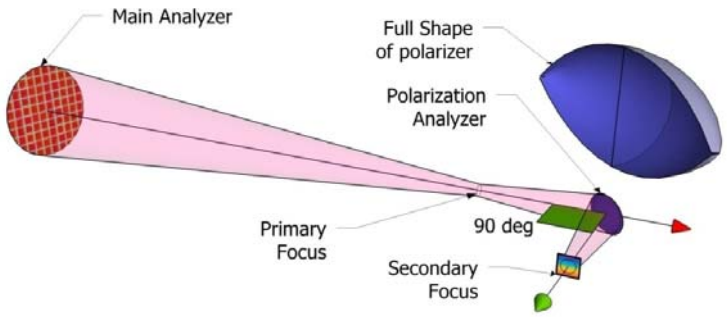

Figure 4.4.4-6. Sketch of the polarization analysis setup. The radiation collected by the main analyzer goes past the primary focus where the detector will be in a conventional setup. It is then reflected at a right angle by the concave polarizer and refocused at the secondary focus, with its energy gradient preserved (color gradient). The full shape of the polarizer (“half-football”) is shown separately for illustration purposes, the actual optic will extend only to a small area near the center.

4.4.4.7 References

[4.4.4-1] L.J.P. Ament et al., arXiv:1009.3630v2 and accepted by *Rev. Mod. Phys.*

[4.4.4-2] T. Gog et al., *Synchrotron Radiation News* **22**, 12 - 20 (2009).

[4.4.4-3] S. H. Pan et al., *Nature* **413**, 282 (2001).

[4.4.4-4] J. M. Tranquada, in *Handbook of High-temperature Superconductivity*, J. R. Schrieffer, J. S. Brooks, Eds. (Springer, New York, 2007).

[4.4.4-5] S. Wakimoto et al., *Phys. Rev. Lett.* **102**, 157001 (2009).

[4.4.4-6] M. Norman, *Physics* **1**, 21 (2008).

[4.4.4-7] C.-C. Lee et al., *Phys. Rev. Lett.* **103**, 267001 (2009).

[4.4.4-8] S.-W. Cheong et al., *Nat. Mater*. **6**, 13 (2007).

[4.4.4-9] D. Khomskii, *Physics 2* **2**, 20 (2009).

[4.4.4-10] R. Ramesh et al., *Nat. Mater.* **6**, 21 (2007).

[4.4.4-11] B. J. Kim et al., *Science* **323**, 1329 (2009).

[4.4.4-12] B. J. Kim et al., *Phys. Rev. Lett.* **101**, 076402 (2008).

[4.4.4-13] K. Miyano et al., *Phys. Rev. Lett.* **78**, 4257 (1997).

[4.4.4-14] V. Kiryukhin et al., *Nature* **386**, 813 (1997).

[4.4.4-15] D. Casa et al., *Europhys. Lett.* **47**, 90 (1999).

[4.4.4-16] J. P. Reed et al., *Science* **330**, 805 (2010).

[4.4.4-17] P. Abbamonte et al., *Advanced Materials* **22**, 1141 (2010).

[4.4.4-18] B. C. Larson et al., *Phys. Rev. Lett.* **99**, 026401 (2007).

[4.4.4-19] P. Kuiper et al., *Phys. Rev. Lett.* **80**, 5204 (1998).

[4.4.4-20] P. Abbamonte et al., *http://arxiv.org/abs/cond-mat/9911215v1*.

[4.4.4-21] J.C. Lang et al., *Rev. Sci. Instrum.* **66**, 1540 (1995)

[4.4.4-22] K. Okitsu et al., *J. Synchrotron Rad*. **8**, 33 (2001)

4.4.5 *section deleted*

4.4.6 *section deleted*

4.4.7 *section deleted*

4.5 Extreme Conditions

4.5.1 Introduction

Materials subjected to the extremes of pressure, temperature, and electromagnetic fields often display novel electronic, magnetic, and structural properties. Discovering and understanding these phases of matter can provide key insight for designing new materials and improving their properties. The most extreme sample conditions, however, can typically be realized only over relatively small volumes. With its intrinsic brilliance, high-penetrating power, and sub-micron spatial resolution, synchrotron radiation provides an ideal probe for revealing the structure, correlations, and dynamics of materials in extreme environments. An exciting frontier for synchrotron radiation research is offered by the simultaneous application of multiple extreme conditions. Using current technology, for example, it is possible to include a compact high-pressure cell inside a high-field magnet and cool it to below 300mK. Such ultralow temperature combined with high pressures and fields can be used to tune in order parameters that are observable only under multiple stimuli.

The following sections describe the new and upgraded beamlines focused on enhancing the capabilities at the APS for probing materials under extreme conditions. This includes one new beamline (1-ID cant) and upgrades to three other existing beamlines (1-ID current, 4-ID-C, and 4-ID-D) within the current baseline scope, while a second new beamline for high-magnetic field scattering (port not finalized) and an upgraded beamline for high-pressure studies (16-ID) are included within contingent additional scope. The new canted beamline on 1-ID will provide additional high-energy scattering capabilities for *in situ* studies of materials under realistic processing conditions. Such processing frequently involves extreme temperatures and/or pressure that require containments, which can result in strong x-ray beam attenuation and limited angular access to the sample. The penetrating x-rays generated at high-energy storage rings help mitigate both these problems. Upgrades to the optics and end stations are also envisioned for the existing high-energy stress/strain and 3D micro-diffraction instruments on 1-ID. Similarly, the optics and sample environments for both the soft (4-ID-C) and hard (4-ID-D) x-ray magnetic spectroscopy beamlines will be upgraded in order to both increase the detection sensitivity and expand the high magnetic field and pressure capabilities. Within the contingent scope, a new dedicated beamline is planned for high-magnetic field scattering studies at the APS. This beamline will be equipped with both continuous field (~20 T) and much higher pulsed field (~30 T to 60 Tesla with 1- to 30-ms pulse width) magnets. Also being considered within contingent scope is the installation of new optics on beamline16-ID for sub-micron focusing for high-pressure experiments. The use of ~0.1 μm beams should extend pressure studies at the APS to the TPa range and permit high-resolution imaging of samples inside diamond anvil cells.

4.5.2 High Magnetic Field Scattering Beamline [CAS]

The application of magnetic fields provides a contact-free experimental "knob" for tuning and manipulating novel states of electronic matter. Understanding the origin and nature of these states is not only of fundamental interest, but also critical towards developing new functionalities in next-generation materials. The diversity of magnetic-field-induced phenomena in condensed matter systems [4.5.2-1] includes competing order in high-T_c superconductors, fundamental physics of Bose-Einstein condensation in spin-gap compounds, multipolar order and quantum criticality in rare-earth magnets, multiferroicity in complex oxides, and magnetic frustration. The magnetic field not only affects the arrangement of spins (*magnetic* order), but also frequently alters the *orbital* and *structural* ordering as well.

There are over 30 laboratories world-wide dedicated to studying field-induced states of matter. However, nearly all of the measurements performed at these magnet laboratories involve macroscopic measurements on the sample, because they lack the necessary tools to determine the microscopic arrangements of structural, spin, and orbital degrees of freedom in underlying field-induced phases. This inadequacy of research tools led to a fundamental knowledge gap in our understanding of a diversity of materials. The proposed X-ray High-Field (XHF) facility at the APS will close this gap by integrating a number of pulsed and continuous field magnets on a single beamline offering precision tools capable of probing all of these various degrees of freedom. High-resolution x-ray diffraction, for example, can be used to examine a wide range of structural effects such as magnetostriction, crystallographic phase transitions, formation of superlattices, and field-induced texture. Resonant techniques, on the other hand, can be employed to enhance the signal from particular elements akin to taking "atomic fingerprints," thereby probing either the magnetic and multipolar-ordered moments. Furthermore, polarization dependence of nonresonant and high-energy magnetic scattering can directly reveal spin and orbital composition of magnetic moments. The conceptual design of the XHF beamline described below will offer a comprehensive set of instruments and techniques in order to precisely determine the varying interplay between spin, orbital, and structural ordering phenomena.

4.5.2.1 Scientific Scope

The XHF beamline will employ a number of pulsed and continuous field magnets to subject materials to extreme fields, as well as a broad energy range in order to accommodate both low-energy resonant techniques and high-energy structural scattering measurements with variable focusing. This combination of complementary magnet geometries and a wide range of available techniques will provide APS users with flexible tools for probing materials subjected to extreme magnetic fields.

Magnetostriction (MS), i.e., macroscopic and intra-unit-cell distortions of the crystal structure, is one of the most ubiquitous field-induced effects. High-resolution measurements of anisotropy, temperature, and field dependence of MS effects yield a wealth of information about the spin-lattice coupling and symmetry of the underlying order parameter. For example, the magnetoelastic behavior of a spin-liquid system, $Tb_2Ti_2O_7$, has recently been studied using a 30-T pulsed magnet [4.5.2-2]. This material manifests a number of structural effects under the application of magnetic fields including a structural phase transition (Figure 4.5.2-1) revealing a strong role of the lattice in spin-liquid physics [4.5.3-3]. Another example is vortices in superconductors, which provide insight into the symmetry of the superconducting order parameter and a window into competing ground states. They can form complicated phases, which include ordered vortex lattices, glassy phases, and liquid states, appearing at high magnetic fields (Figure 4.5.2-1) [4.5.2-4]. Formation of these phases and transition between them, as well as inherent anisotropy of vortices, give rise to structural effects [4.5.2-5] that can be studied with x-ray diffraction.

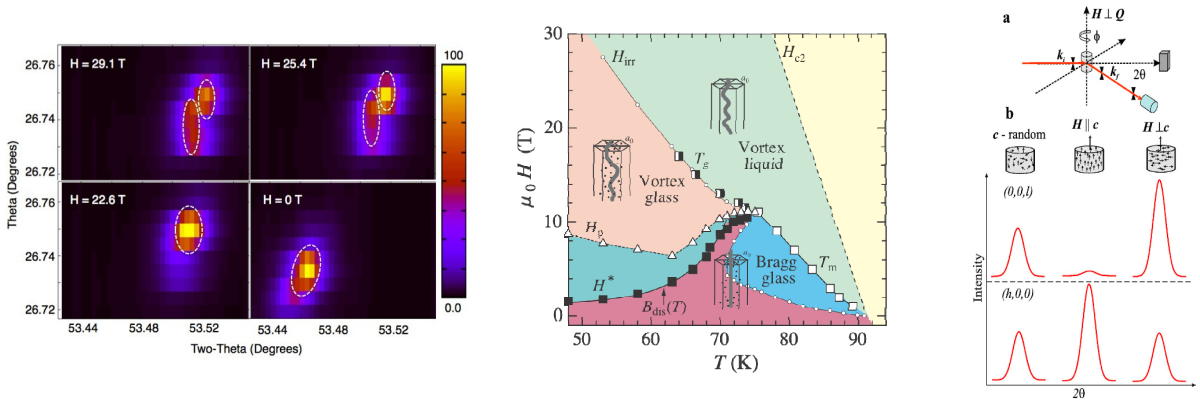

Figure 4.5.2-1. Left: Two-dimensional scans of a Bragg peak in $Tb_2Ti_2O_7$ at low temperature, demonstrating MS below and a structural transition above 25 T [4.5.2-3]. Center: Vortex phase diagram in a high-temperature superconductor [4.5.2-4]. Right: Field-induced texture measurements in MgB_2 [4.5.2-7].

Structural studies using powder diffraction have shown great potential in pulsed magnetic fields when magnetic anisotropy is not an issue. This is because integrated intensities can be collected efficiently on an area detector by an appropriate timing scheme with x-ray shutters or electronic gating synchronized with peak pulsed field. Such a technique has recently been successfully used in the study of field suppression of Jahn-Teller phase transition [4.5.2-6]. Powder diffraction can also be applied to study magnetic-field-induced texturing or preferred orientation of micron-size single-crystal grains of superconductors below the superconducting transition temperature (Figure 4.5.2-1). Such measurements can provide a powerful means for determining the interplay between critical field anisotropies and London penetration depths [4.5.2-7].

While measurements of structural effects will form a core component of the research on the XHF beamline, studies of magnetic and orbital effects, such as spin waves and multipolar order, will be an equally important part of the research at the beamline. Novel phases can arise from competing energy scales associated with spin and orbital degrees of freedom. Resonant x-ray scattering is ideally suited for the study of multipolar order in 4*f* and 5*f* electron systems. This is because very large resonant enhancements (4*f* L edges and 5*f* M edges) and polarization-sensitive cross section provide a direct coupling to such order parameters. Recent x-ray resonant-scattering studies at the Np edge in NpO_2 have revealed novel octupolar orbital ordering [4.5.2-8]. Such phenomena may be related to various field-induced phases in materials like URu_2Si_2 (Figure 4.5.2-2, left), where fields as high as 40 T are required to manifest them [4.5.2-9].

Scattering measurements can also be applied to help elucidate the nature of high-temperature superconductivity, which continues to remain one of the most compelling problems in contemporary condensed matter physics. There has been much discussion about different types of order that may compete with superconductivity. Many of the proposed models can be experimentally tested using novel scattering techniques. A continuous-field magnet will enable studies of small-amplitude spin- and charge-ordered phases in copper-oxide superconductors with x-ray scattering. While fields well beyond 30 T are required to access the full range of phenomena, studies in 16- to 20-T fields will reveal crucial information about the underlying mechanisms in these compounds. Elastic neutron scattering experiments have recently demonstrated that spin-density wave (SDW) order is enhanced by application of modest magnetic fields [4.5.2-10]. It should be possible to measure this field-enhanced SDW order using x-ray techniques [4.5.2-11]. Although the presence of charge-density wave (CDW) in the cuprate super-

conductors is controversial, a series of high-energy diffuse scattering experiments (Figure 4.5.2-2, right) on YBCO compounds in zero-field have clearly demonstrated short-range-ordered super-lattices throughout the phase diagram. They act as nucleation centers for CDWs associated with electronic instabilities, which appear as "shoulders" of super-lattice peaks [4.5.2-12]. Diffuse scattering measurements of such modulations [4.5.2-13] in the presence of large magnetic fields will provide better insight into competing phases to superconducting ground state.

Novel Order and Resonant Diffraction

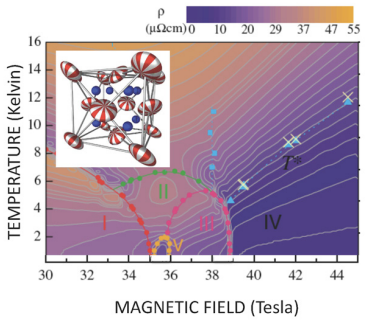

Competing Order and Diffuse Scattering

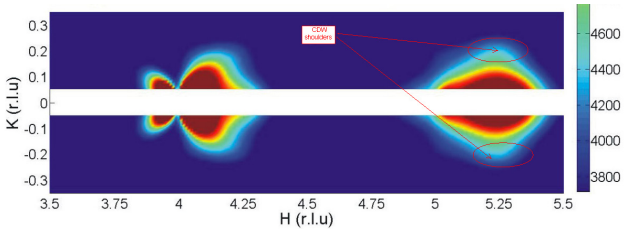

Figure 4.5.2-2. Left: Phase diagram in 5f-element compound URu_2Si_2 [4.5.2-9] deduced from resistivity measurements. Inset shows the model of related multi-polar order in NpO_2 [4.5.2-8]. Right: Diffuse scattering pattern showing short-range ordered superlattice peak and CDW "shoulders" [4.5.2-12].

4.5.2.2 Source Enhancements

The experiments envisioned for the XHF beamline necessitate a broad spectrum of energies (3.2 to 100 keV) in order to access resonances of interest and mitigate optical access limitations imposed by magnets. To provide the optimum flux at both ends of the energy spectrum, the beamline at a new sector will have two in-line insertion devices, a fully tunable ~3.0 cm device and a second short-period (~1.6 cm) superconducting undulator optimized for high energies. In the case of the 6-ID option (4.5.2.7), the short-period undulator can be used as the source both for the magnet stations (6-ID-B and 6-ID-C) and the high-energy scattering program located in the 6-ID-D station. These stations currently use a single insertion device, which results in diminished flux in 6-ID-D during some resonant scattering experiments on the primary beamline. The addition of a short-period device will not only provide high-energy x-rays for the magnet stations but also greatly enhance the high-energy flux for 6-ID-D, permitting this station to operate fully independent of the other beamline.

Siting selection of the SPX (see section 4.2.2), may restrict the use of the full 6-ID straight section, and the source request for 6-ID will be appropriately modified. Other alternative locations for the high-magnetic-field scattering program are being considered. One scenario is the location of the XHF beamline in APS sector 11. The required changes to the source and optics in this scenario are discussed in section 4.5.2.7.

4.5.2.3 Beamline Enhancements

The XHF beamline (Figure 4.5.2-3) will consist of four major stations: (1) a first-optics enclosure with the monochromators; (2) an optics station; (3) a station optimized for single-crystal diffraction and pulsed field scattering experiments; and (4) a continuous-field superconducting magnet station. In addition, there will be a special enclosure for a large capacitor bank (1.6 MJ) and a primary experiment control cabin. Details on the magnets are presented in sections 4.5.2.5 and 4.5.2.6.

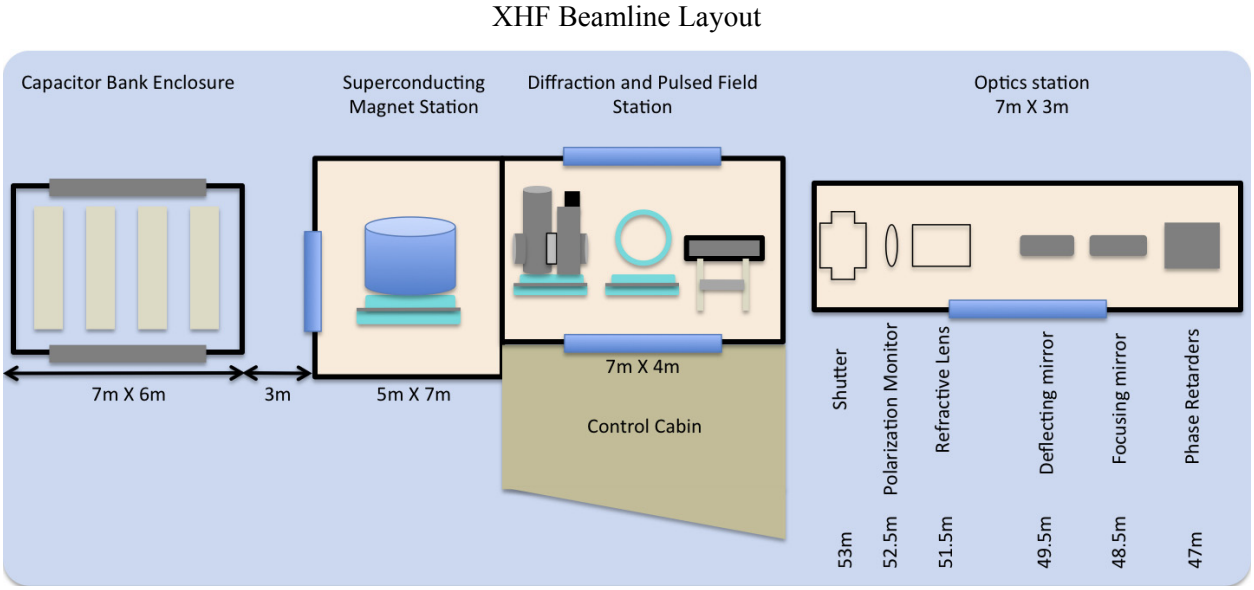

Figure 4.5.2-3. Schematic showing the XHF facility. Two magnet experimental stations, an optics station, capacitor-bank enclosure, and control cabin are shown.

Diffraction and pulsed-field station: This is the primary station for scattering studies in pulsed fields with two diffractometers and an optical table. An existing high-resolution ψ-diffractometer will continue to be used for experiments not involving magnetic fields, particularly low-temperature studies. In addition, this diffractometer will accommodate a 40-T "hour-glass" pulsed magnet described below for diffraction studies with the field applied along momentum transfer, **Q**. A second diffractometer will be placed downstream of the first for horizontal scattering experiments involving a 50-T split-pair and a 60-T solenoid magnet. The mount for these magnets and sample cryostats will incorporate means to minimize vibration propagation to sample during field pulses. Both diffractometers will have fixtures so that either 2D pixel-array detectors or analyzers with point detectors can be mounted.

Superconducting magnet station: This station will accommodate 16-T and 20-T superconducting magnets (SCM) with complementary field orientations for continuous field diffraction studies, using a new heavy-load diffractometer. The diffractometer will have a large 2θ circle for a detector mounted on a 0°-15° arc for off-horizontal-plane scattering and an Eulerian cradle with a θ circle and a ±5° arc (χ). The magnet will be mounted on a translation stage with x, y, and z, degrees of freedom, which is attached to the cradle, allowing a precise centering of the magnet and the sample in the x-ray beam. Both magnets will be installed inside the station, so they can be interchanged as needed.

4.5.2.4 Optics

Monochromators: To efficiently deliver monochromatic x-ray beams into the magnet stations with energies from 3.2 to 100 keV will require the use of two separate monochromators. Installation of two monochromators at a new sector beamline is straightforward. A high-energy monochromator (Laue-Laue) and a double-crystal Bragg-type monochromator will be installed in a separate white-beam station (not shown in Fig. 4.5.2-3) upstream of the optics station.

Polarization manipulation: Manipulation of the x-ray beam polarization is essential for many resonant scattering experiments. Varying the incident polarization allows an experimenter to measure the polarization dependence at a given momentum transfer without rotating the samples inside high-field

magnets [4.5.2-14, 4.5.2-15]. In order to enable such analyses, two in-vacuum diamond (111) phase retarders (PR) similar to those currently installed on APS beamline 4-ID-D will be included [4.5.2-16]. The 4-ID-D design will be modified, however, to incorporate independent rotation about the incident beam on each PR crystal. This will both enhance the linear polarization rate and enable the rotation of the incident linear polarization. A schematic of such an instrument recently tested at ESRF is shown in Figure 4.5.2-4.

Polarization Manipulation

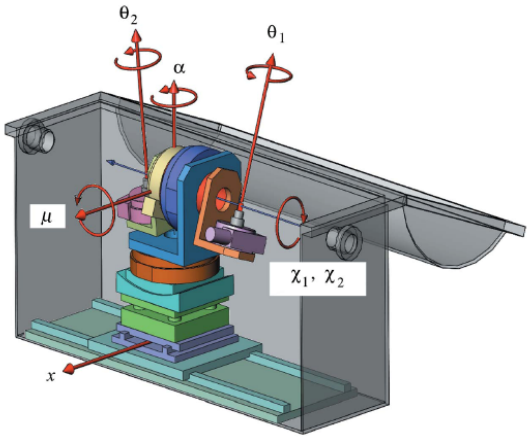

Figure 4.5.2-4. Schematic of an in-vacuum double-phase-retarder diffractometer for changing incoming polarization for magnetic scattering studies [4.5.2-14].

Focusing optics: A toroidal mirror with two stripes with different sagittal radii will be used for focusing of x-rays for energies below 30 keV. The differing stripes will permit focusing at two different incidence angles for optimizing harmonic suppression and provide the flexibility to focus in either experimental magnet station. Design options with either vertical or horizontal deflection for this mirror are being considered. A vertical deflection design has been successfully used on beamline 4-ID-D for several years, while a horizontal-scattering mirror could provide improved stability and result in less structure in the beam. The focal distance for either geometry is fairly short at 6 m, but ray tracings demonstrated a well-formed 100 × 50 μm^2 focal spot at the diffractometer and 200 × 100 μm^2 at the SCM station. A second flat mirror will provide improved harmonic rejection and keep the beam parallel to incident radiation. At higher energies (~50-100 keV), compound refractive lenses will be used to focus the beam. This optic will be similar to the modular design recently installed on the high-resolution scattering beamline at PETRA-III or a modified saw-tooth-type design developed on APS 1-ID (see section 4.5.4). A list of the key performance parameters for the optics is given in Table 4.5.2-1.

4.5.2.5 Anticipated Performance

Table 4.5.2-1. XHF Beamline

Feature	Expected Values
Energy	3.2-100 keV
Resolution	10^{-4} (<30 keV); 10^{-3} (50-100 keV)
Beam size	100 × 50 μm^2 (@10 and 100 keV)
Flux	10^{13} photons/s at 10 keV; 10^{12} photons/s at 100 keV
Polarization	linear (any direction); circular (<15 keV)

Table 4.5.2-2. High-Field Magnets

Quantity	Magnet type	B_{Peak}	Direction	Angles	Temperature
Superconducting magnets					
1	Cryogen-free solenoid magnet	20 T	B ∠ Q	~30°	~1.4-1000 K
1	Cryogen-free split-pair magnet	16 T	B ⊥ Q	180°	~0.3-500 K
Pulsed field magnets					
1	Cryogenically cooled solenoid	60 T	B ∠ Q	~25°	~1.4-350 K
1	Cryogenically cooled split-pair	50 T	B ⊥ Q	>60°	~1.4-350 K
1	Cryogenically cooled hour-glass	40 T	B ∥ Q	>50°	~1.4-350 K

4.5.2.6 Instrument Enhancements

The primary instrument enhancements needed are state-of-the-art high-field magnets and fast detectors. High-field pulsed magnets provide economical solutions for x-ray scattering studies that require magnetic fields beyond 16 T. However, for weak-order parameters as in high-temperature superconductors for which scattering intensity is small, continuous field superconducting magnets are necessary. Furthermore, in-field x-ray scattering experiments require a large optical access combined with the ability to apply magnetic fields along specific crystallographic axis for inducing certain phases while allowing specific relative orientation of **B** and **Q** for measurements. Magnets, by design, impose geometric restrictions on photon-in photon-out experiments, which become more stringent for high-field magnets, as illustrated in Figure 4.5.2-5. With these considerations in mind, two complementary sets of superconducting (SC) and pulsed field (PF) magnets are specified (see Table 4.5.2-2).

Magnet Geometries for In-Field Scattering Studies

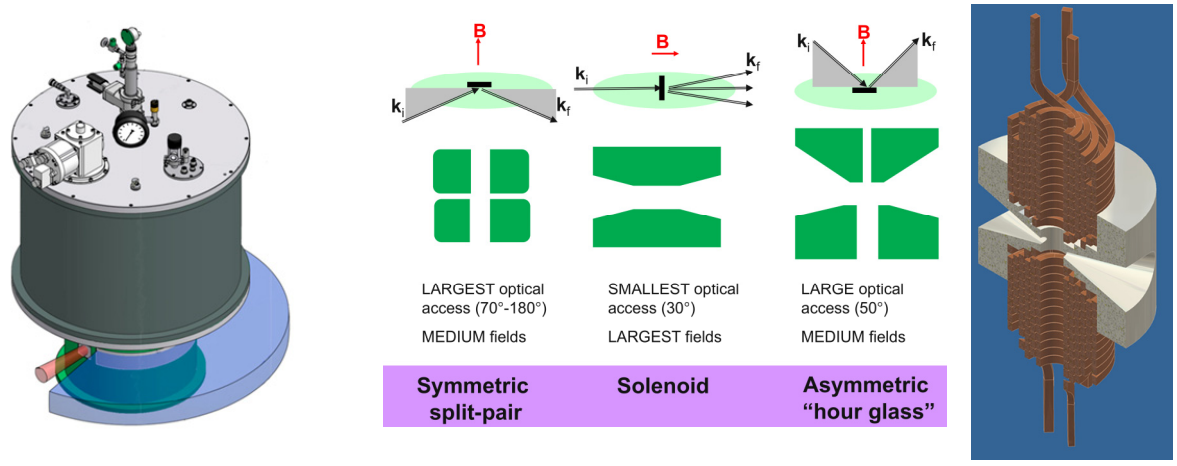

Figure 4.5.2-5. Left: Schematic of a split-pair SC magnet. Center: Three magnet geometries with relative orientation of incident photon and **B** *indicated with arrows. Right: Conceptual design of an "hour-glass" pulsed magnet.*

Superconducting magnets: Two SC magnets, one split-pair and one solenoid geometry, available from commercial vendors are specified. The primary purpose of the split-pair magnet is to enable single-crystal scattering experiments, while the solenoid geometry will enable powder-sample techniques. Both magnets are cryogen-free in that they are cooled down to their operating temperatures of

~4K using closed-cycle cryostats. Since SC magnets have a large dipole moment, we will investigate the incorporation of active shielding to reduce stray fields to below 5 Gauss within 1.5 m from the magnet center in order to minimize shielding requirements on detectors and electronics. A 16-T active-shielding magnet has been manufactured by Bruker for the Spallation Neutron Source at Oak Ridge. The inner bores and overall diameter of the split-pair magnet are 50 mm and ~900 mm, respectively, with a vertical aperture of ±5°. For a 20-T solenoid the inner bore and overall diameters are ~25 mm and ~1000 mm, respectively. For both magnets cryogen-free variable-temperature inserts will allow sample cooling down to 0.3-1.4 K. By utilizing small pressure cells in the bore of the SC magnets, materials subject to combined stimuli of high fields and moderate pressures (5 GPa) can be studied. A high-temperature stage in the solenoid magnet will facilitate *in situ* metallurgical studies of microstructures and their control with magnetic fields using high-energy x-ray scattering techniques.

Pulsed-field magnets: In collaboration with National High Magnetic Field Laboratory's Pulsed Field Facility (NHMFL-PFF) we have developed preliminary specifications of three types of user magnets for the XHF. An initial design of a novel "hour-glass"-type pulsed magnet capable of generating fields up to 40 T has already been done. Total pulse duration will be of the order of 3-5 ms in order to keep a repetition rate on the order of a few minutes. The "hour-glass" geometry incorporates a novel polyhelix design. The use of a pair of polyhelix sets within a single-block structure makes the system mechanically robust with scattering angles as large as 50° and 30° in the vertical and horizontal directions, respectively. This novel design will not only allow dominant magnetic and structural effects to be determined but also provide access for azimuthal scans necessary for investigating orbital effects. Preliminary design specifications are 6 mm bore with a ~100 mm outer diameter and an overall length of ~150 mm. Such dimensions are compatible with standard Huber 512 Eulerian cradles. Independent magnet and sample cooling with some rotational freedom of the sample about the field axis can be incorporated into a standard diffractometer [4.5.2-2].

A dual-cryostat system for high-field single-solenoid pulsed magnets (Figure 4.5.2-6) has been conceived that will facilitate diffraction techniques with magnetic fields applied in the scattering plane [4.5.2-17]. The 60-T solenoid proposed herein will have a conical bore in order to increase optical access. This instrument also incorporates independent cooling for the magnet coil (using LN_2) and the sample (using a closed-cycle refrigerator). Liquid-nitrogen cooling along with vents incorporated into coils may allow a fast repetition rate for peak fields of 60 T. Figure 4.5.2-6 shows how such a "quick cool" technology can cool a large-bore long-pulse solenoid within a few minutes [4.5.2-18]. The system is unique in that the LN_2 cryostat uses a double-funnel vacuum tube passing through the solenoid's conical bore in order to preserve the entire angular range allowed by the magnet bore for scattering studies. Second, the use of a separate refrigerator for the sample allows precise positioning of samples in the bore, while minimizing magnet vibrations propagating to the sample during pulsed-field generation.

The third magnet is a split-pair magnet with a peak field of 50 T and pulse duration of ~25 ms. Since the peak field is substantially higher than in the hour-glass design, a much stronger support structure is needed to keep the two coils apart. As a result, the maximum scattering angle is probably not higher than 70° compared to 180° in the SC split-pair magnet. Like in the hour-glass design, the inner bore is 6 mm with a repetition rate comparable to that for the 60-T magnet.

Design of 60-T Pulsed Magnet

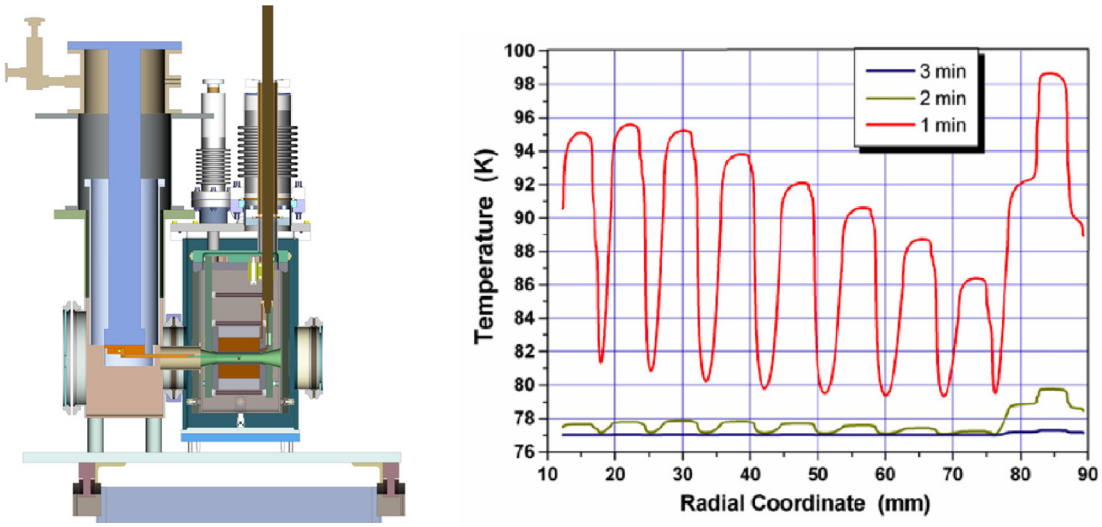

Figure 4.5.2-6. Left: Dual-cryostat instrument implementing a double-funnel scheme [4.5.2-17]. Right: Quick cool simulation of 55-T large-bore long-duration pulsed magnet.

All of the high-field pulsed magnets described above will be powered by capacitive discharge. A crowbar circuit will be used to generate half sine with an extended decay pulse shape. In order to generate fields in the range of 40-60 T with pulse duration as large as ~25 milliseconds, a large energy capacitor bank is necessary (the1.6-MJ capacitor bank located at the NHMFL-PFF at Los Alamos is shown in Figure 4.5.2-7). Preliminary estimates indicate that a 10-kV capacitor bank capable of providing 1.6 MJ of energy would provide sufficient energy and flexibility to power all three types of pulsed magnets. Magnets will be designed to operate at peak fields with 20-30% less than the full charge of the capacitors to extend the lifetime of the bank and to eliminate any capacitor failures.

An Example of a Rack of Capacitors

Figure 4.5.2-7. Picture of one of the four 400-kJ racks of capacitors (gray and white cases) at NHMFL-PFF. Switching circuits including SCR, diode stacks, and snubber network are on the back of the rack. Two cylinders containing the blue $CuSO_4$ solution serve as dump resistors.

Detectors: Pulsed-field studies require time-resolved data collection (~μs to ~ms) for both single-crystal and powder diffraction measurements. Using a fast 1D (Si strip) detector, the field dependence of an entire line in reciprocal space using a single field pulse has been observed [4.5.2-2]. A 2D pixel-array detector with a full-frame readout time of less than 1 ms will enable the entire field dependence of an area in reciprocal space and the entire powder pattern in a single pulse of total duration ~25 ms with excellent field resolution. Development of fast 2D detectors is underway at various facilities and vendors world-wide. For example, a fast 2D detector made of 150-μm CMOS silicon sensors with CsI:Ti scintillator is being manufactured in England. This detector has a full-frame readout of 0.5 kHz and can be configured to operate over the entire energy range available at the XHF beamline. A 2D pixel-array detector operating at ~1 kHz will be developed in partnership with a commercial vendor.

Global context: There are currently comparable high-field (>10 T) x-ray scattering facilities employing super-conducting (SC) magnets at the ESRF, SPring-8, NSLS, and PETRA-III. In addition, both the ESRF and SPring-8 have active research programs using pulsed field magnets (up to 40 T) for both scattering and spectroscopy measurements. The considerable cost and time-consuming efforts involved in operating liquid-helium cooled SC magnets have constrained their use at these other facilities. The proposed XHF beamline will provide at least one 16-T SC split-pair magnet as well as a novel 40-T "hour-glass" and a 60-T solenoid for pulsed fields. The SC magnet at the APS will be cryogen-free, which will facilitate more efficient use [4.5.2-7, 4.5.2-19, 4.5.2-20] at substantially reduced costs. In the case of pulsed magnets, APS will implement a "quick cool" technology [4.5.2-18] developed at the NHMFL-PFF, to improve repetition rates (see below) and make more efficient use of the incident photons. The "hour-glass" magnet design will enable powerful resonant-diffraction techniques in pulsed fields, which has not been attempted at any other beamline. Therefore, the XHF beamline will move well beyond these other comparable facilities by providing both higher fields and magnets with complementary scattering geometries.

4.5.2.7 Alternate Scenarios

As mentioned above, the location for the XHF beamline has not been determined yet. In this section two scenarios to upgrade existing beamlines 6-ID and 11-ID-D, respectively, are discussed.

The layout for the 6-ID is the same as shown in Fig. 4.5.2-3. In this case, an additional high-energy monochromator (Laue-Laue) can be installed after the current double-crystal Bragg-type monochromator and Laue monochromator used by station 6-ID-D (see Figure 4.5.2-8). The Bragg-type monochromator for beamline 6-ID-B,C uses a thin-web-design primary crystal, which permits higher energy x-rays to pass through with relatively little attenuation. Currently a Laue monochromator with a large (600 mm) offset is used to deliver x-rays (50-130 keV) into the 6-ID-D station for high-energy scattering experiments. Since this monochromator uses a thin (~3-mm-thick) Laue crystal, a third monochromator with a small horizontal offset will be added to deliver high energies to the magnet stations. Similar monochromators have been successfully installed on beamline 1-ID at the APS and ID-11 at the ESRF [4.5.2-21, 4.5.2-22]. This monochromator would be used when energies above 50 keV are required for magnet experiments.

Monochromator Layout (6-ID)

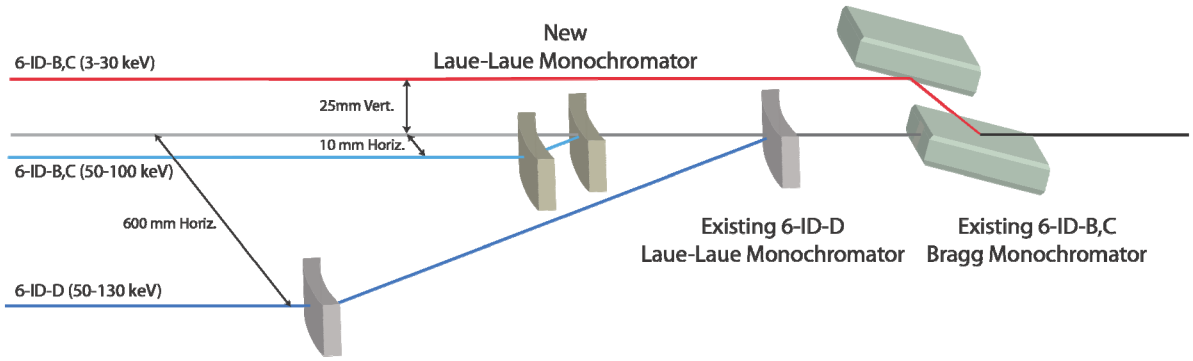

Figure 4.5.2-8. Schematic showing monochromator layout for 6-ID option.

An alternate scenario for the XHF facility involves upgrading 11-ID-D (Figure 4.5.2-9). Given the configuration of this sector, such an upgrade involves major changes. A new optics station can be constructed within the limited space adjacent to 11-ID-B and 11-ID-C. However, in order to accommodate a double-phase-retarder tank for changing polarization state of the incoming x-ray beam, the upstream end of the hutch has to extend outboard. Compared to an upgrade of 6-ID, a new double-crystal monochromator, a new magnet station, a second door on 11-ID-D, and a second tier for the capacitor bank enclosure must be built. The new magnet station has to be large enough to accommodate a heavy-load diffractometer for SCMs and a second diffractometer for the 50-T and 60-T pulsed magnets as 11-ID-D can fit only one diffractometer. Since each rack of the capacitor bank may weigh as much as 7000-8000 lbs. the second tier of the enclosure needs to be built to carry that load with an access bridge from the new hutch roof.

XHF Beamline Layout (11-ID-D)

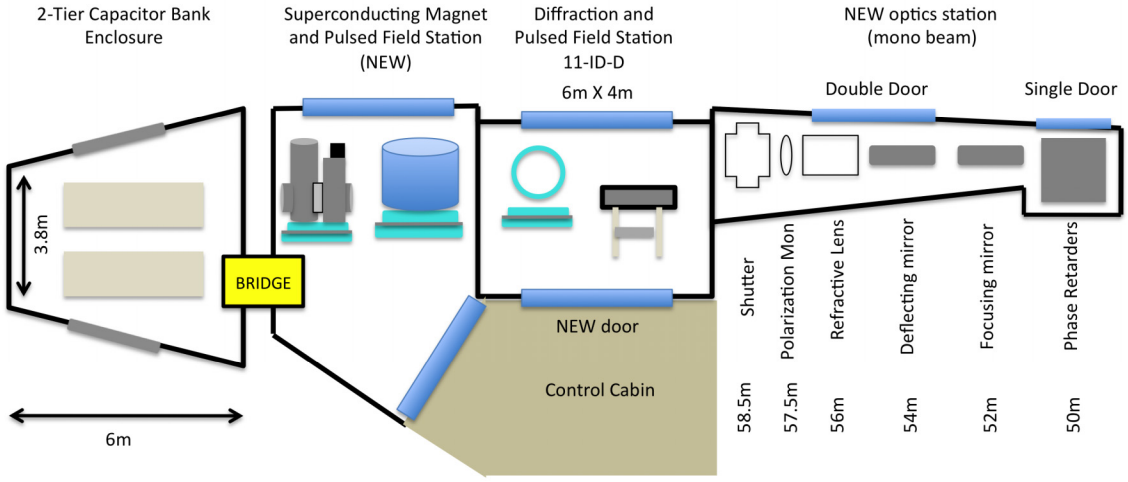

Figure 4.5.2-9. Schematic showing the XHF facility on 11-ID-D. A new optics station, a new SCM station, and a two-tier capacitor-bank enclosure need to be added.

4.5.2.8 References

[4.5.2-1] F. Herlach and N. Miura, *High Magnetic Fields: Science and Technology*, 1st ed. (World Scientific, Singapore, 2003).

[4.5.2-2] Z. Islam et al., Rev. Sci. Instrum. **80**, 113902 (2009).

[4.5.2-3] J. P. C. Ruff et al., Phys. Rev. Lett. **105**, 077203 (2010).

[4.5.2-4] T. Nishizaki and N. Kobayashi, Supercond. Sci. Technol. **13**, 1 (2000).

[4.5.2-5] R. Lortz et al. Phys. Rev. Lett. **90**, 237002 (2003).

[4.5.2-6] C. Detlefs et al., Phys. Rev. Lett. **100**, 056405 (2008).

[4.5.2-7] J. Li, D. Vaknin et al., Phys. Rev. B **74**, 064502 (2006).

[4.5.2-8] J. A. Paixão et al., Phys. Rev. Lett. **89**, 187202 (2002).

[4.5.2-9] K. H. Kim et al., Phys. Rev. Lett. **91**, 256401 (2003).

[4.5.2-10] B. Khaykovich et al., Phys. Rev. B **66**, 014528 (2002).

[4.5.2-11] Z. Islam et al., Phys. Rev. B **71**, 212506 (2005).

[4.5.2-12] X. Liu et al., Phys. Rev. B **93**, 157008 (2004).

[4.5.2-13] J. Kim et al. Phys. Rev. B **77**, 180513(R) (2008).

[4.5.2-14] V. Scagnoli et al., J. Sync. Rad. **16**, 778 (2009).

[4.5.2-15] P. D. Hatton et al., J. Magn Mag. Mater. **321**, 810 (2009).

[4.5.2-16] J. W. Freeland et al., Rev. Sci. Instrm. **73**, 1408 (2002).

[4.5.2-17] D. Capatina et al., Diamond Light Source Proc. MEDSI-6, 1, e42 (2010).

[4.5.2-18] C. A. Swenson et al., NHMFL Research Report (2004).

[4.5.2-19] L. Tan et al., Phys. Rev. B **77**, 064425 (2008).

[4.5.2-20] X. S. Xu et al., Phys. Rev. Lett. **101**, 227602 (2008).

[4.5.2-21] S. D. Shartri et al., J. Sync. Rad. **9**, 317 (2002).

[4.5.2-22] R. Baruzzo et al., MEDSI Conf. Proc. (2008).

4.5.3 High Pressure Diffraction Upgrade (16-ID) [CAS]

It took nearly three decades to reduce the x-ray beam size from 50 μm to the current 5 μm in high pressure (HP) research. This one-order-of-magnitude reduction has been responsible for many recent breakthroughs in HP science using synchrotron radiation (SR). Currently there are approximately 15 beamlines world-wide specialized for HP measurements, and the beamsize at nearly all these facilities is presently limited to ~5 μm limiting the maximum accessible pressure to ~300-400 GPa. Optics technology has advanced to a point, however, that at least another order-of-magnitude improvement in focal spot size is feasible. Beam sizes of a few tens of nanometers have been reached on specialized beamlines [4.5.3-1, 4.5.3-2], yet a size of approximately 5 μm is still typical at all leading HP synchrotron beamlines around the world [4.5.3-3–4.5.3-5]. After the upgrade, 16-ID will be the only beamline with dedicated sub-micron focusing capabilities. Sub-μm beam sizes will enable the study of more complex and smaller samples at increasingly broader pressures and more extreme temperatures. Further measurements can be performed with higher accuracy for characterization of the structural, electronic, and phonon properties using HP x-ray diffraction and spectroscopy (emission, absorption) techniques. The upgrade will facilitate new types of HP-SR measurements, such as probing sample at pressures in the TPa region; investigating grain-to-grain interactions with sub-μm resolution in all three dimensions; evaluating local stress/strain and structure evolution within the individual grain; combinatorial studies of a large array of samples; and isolation of a μm-size single crystal from a polycrystalline aggregate. These capabilities coupled with the higher x-ray energies available at the APS will place this beamline as the leading facility for conducting high-pressure research in the world.

Beamline 16-ID currently serves a broad spectrum of the users requiring high-pressure x-ray measurements to address problems in physics, chemistry, earth and planetary sciences. The primary users of the beamline are drawn from the contributing CAT institutions, Carnegie Institution of Washington, Lawrence Livermore National Laboratory, Carnegie-DOE Alliance Center (CDAC), and University of Nevada- Las Vegas. Over the last three years the beamline has produced over 200 publications, with over 20% in journals with an impact factor above 7 (i.e., Nature, Science, Proc. Natl. Acad. Sci., Phys. Rev. Lett.). The enhancements will place this beamline at the forefront of high-pressure research and ensure that it continues to have the maximum scientific impact. The access to the significantly higher pressures provided by the upgrade has the potential to attract a significant number of new users particularly those interested in accessing pressures into the TPa regime and relevant to planetary interiors.

4.5.3.1 Scientific Scope

The application of pressure can directly alter the chemical, structural, mechanical, electronic, magnetic, and phonon properties of materials. A state of increased pressure can reveal intriguing behaviors across boundaries between insulators and metals, ferromagnets and superconductors, ordered and disordered states, and vigorously reactive and inert compounds. In Earth and planetary sciences, research from experiments at high pressure and high temperature provides key information in understanding processes, dynamics, and formation of the deep interiors. For materials applications, such as the search for new energy materials and superhard materials, the study of extreme conditions remains a vast, unexplored field. Because HP conditions are achieved at the expense of diminishing sample volumes, the high-brilliance, high-energy, low-emittance SR sources provide powerful small-sampling probes for the minute samples and resolve weak sample signals from the background signals of massive surrounding vessel materials.

Submicron beams for maximum P: The maximum attainable and sustainable pressures define the ultimate scope of HP research. Pressure is defined as force per unit area; therefore, the most extreme conditions are achieved at the cost of reduced sample volume. The current maximum achievable pressures

have remained at a plateau of 300-400 GPa [4.5.3-6, 4.5.3-7] partly because of the ~5-μm limitation on probe size. Furthermore, recent studies have shown that there is a large strain gradient across diamond anvil tips. This gradient results in approximately a 10% drop in pressure over only a 1-μm spatial extent at 280-GPa central pressure [4.5.3-8] (Figure 4.5.3-1). The enabling of sub-μm probes optimized for HP research will allow for further reducing the sample volumes and will help break the pressure barrier. The fine probes can also be used for analyzing 3D deformation and strain of the anvils and the pressure gradients and distribution within the sample and gasket. Finite-element calculations [4.5.3-9] based on quantitative measurements of the pressure vessel could be used to optimize the shape of diamond anvils and vessel geometry. The drive to "megabar" (100 GPa) static pressures in the 1970s and the achievement of 300-400 GPa led to the subsequent boom in HP sciences that is being experiencing today. The drive toward achieving TPa pressures will redefine the scope of HP research, challenging new and longstanding quests, such as the study of metallic hydrogen, the pressure effect on core electrons in free electron gas, room-temperature superconductivity, complexity of "simple metals" (e.g., Li, Na), and interiors of giant planets, etc.

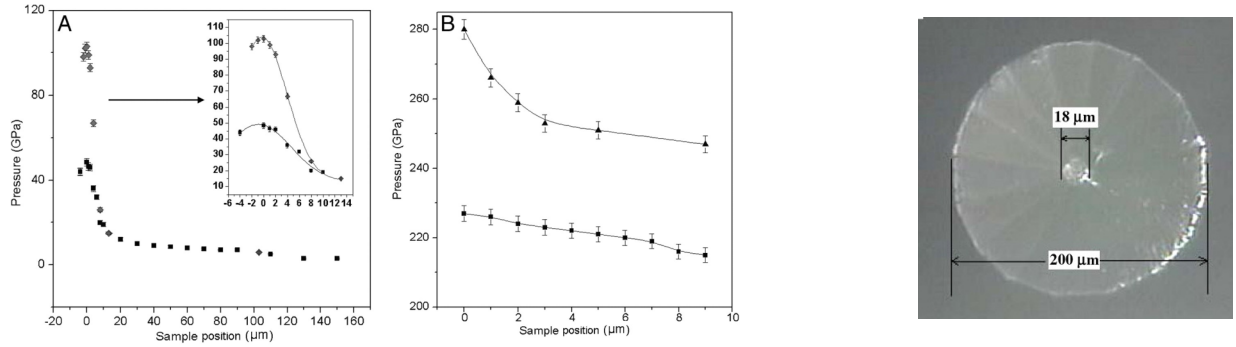

Figure 4.5.3-1. The pressure distribution as a function of sample position (radial distance from the center of anvil) determined by a 5-μm (black square) and 0.6-μm (diamonds and triangles) x-ray beams at peak pressure of 105 GPa (A) and 282 GPa (B) [4.5.3-8].

Sub-μm single-crystal diffraction: Single-crystal x-ray diffraction experiments are unique and important sources of structural information that is crucial to understanding the microscopic mechanisms of HP phenomena. With sub-μm spatial resolution, individual grains in many powder samples may be treated as single crystals. This approach will open tremendous opportunities to study single crystals at extreme conditions. Structural information of new HP phases at megabar pressures can be accurately obtained. Many identified HP phases may be revisited with the sub-μm single crystal diffraction. For example, an experiment conducted on the μ-diffraction 34-ID beamline demonstrated that a recently discovered, post-perovskite structure may have a different space group than previously reported [4.5.3-9]. Moreover, sub-μm probes will provide strain information of individual crystalline grains and will make major contributions to the high P-T rheology.

Earth and planetary science: Reducing the probing beam size to sub-μm will not only allow for extending the P-T ranges currently available but also will provide better spatial resolution, such as in determining element partitioning, anisotropy, and phase separation. The sub-μm probe will play an important role in deep earth mineralogy and in studying interiors of super-earth and giant planets where the interior pressures are in the TPa regime (Figure 4.5.3-2). Nanoscale tomography could also play an important part in rheological studies of liquids and partial melts under HP and HT conditions.

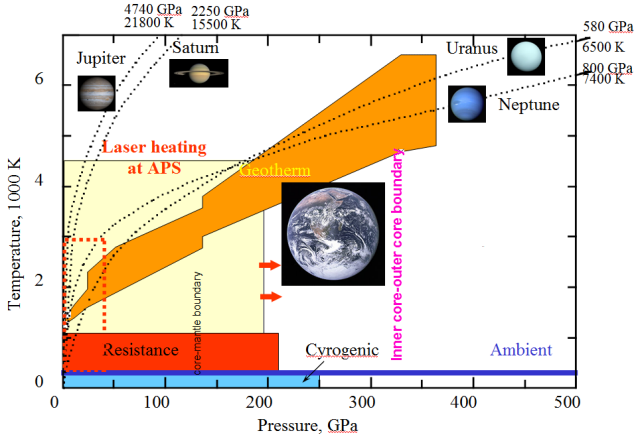

Figure 4.5.3-2. Advances in maximum static pressures achieved in the laboratory and the corresponding pressures at depths within the Earth, together with the approximate P-T ranges currently accessible. The estimated temperature profiles for the geotherm of the Earth and other planets are indicated.

4.5.3.2 Source Enhancements

High-pressure experiments are flux-demanding and require maximum brilliance of hard x-rays. Because of the multiple techniques developed, energy coverage is also an important factor in selecting insertion devices. A long straight section (~8 m) is specified for the 16-ID with two canted undulators. The outboard branch of 16-ID will be dedicated to HP spectroscopy using sub-μm probes, which require an energy range of 4.5-45 keV, with the first harmonic of the undulator peaked at 10-12 keV. The inboard branch will be for micro-XRD in an energy range of between 10–50 keV, with optimum flux at 30-40 keV. Revolver-type undulators U2.6cm - U3.1cm and U2.5cm – U3.0cm are proposed for the outboard branch and inboard branch, respectively, both with 3.4m long and 11.0mm minimum gaps. Brilliance gain of 2.5 times at 10 keV and 4.0 times at 30 keV is expected using the proposed undulators, as compared with the current U3.3-cm undulator. Considering the higher current operation (to 200 mA) in the APS-U project, the gain in brilliance with the proposed insertion device will be about 5 and 8 times current values for outboard and inboard branches, respectively, as compared to the present status.

4.5.3.3 Beamline Enhancements

The current undulator line 16-ID contains two branches operating in two separate energy ranges. A double crystal diamond monochromator with a 35-mm vertical offset is used to provide beam into stations 16-ID-C, -D, and -E. The high-energy portion of the beam, which passes through the first diamond crystal of the DCM, is incident upon a branching double crystal monochromator (BDCM) located downstream with a 1-m horizontal offset. The BCDM provides 25- to 36-keV x-rays for station 16-ID-B. Because both branches use the same undulator source, the energies used by each branch of the beamline are coupled. To permit *independent* operation, 16-ID is scheduled for canting the straight section and installing an additional undulator in 2011. This canted beamline layout is consistent with the upgrade to 16-ID in the APS-U project (Figure 4.5.3-3). The canted geometry will separate the beams by 1 mrad and allow independent undulator control, thereby providing optimal operation of both branches (16-ID-B and 16-ID-C,D,E) and increasing the usable ID beam time. The upgrade will mainly involve extending the first optics enclosure (16-ID-A) in order to accommodate additional high heat-load optics and a virtual source for sub-μm focus in the horizontal direction.

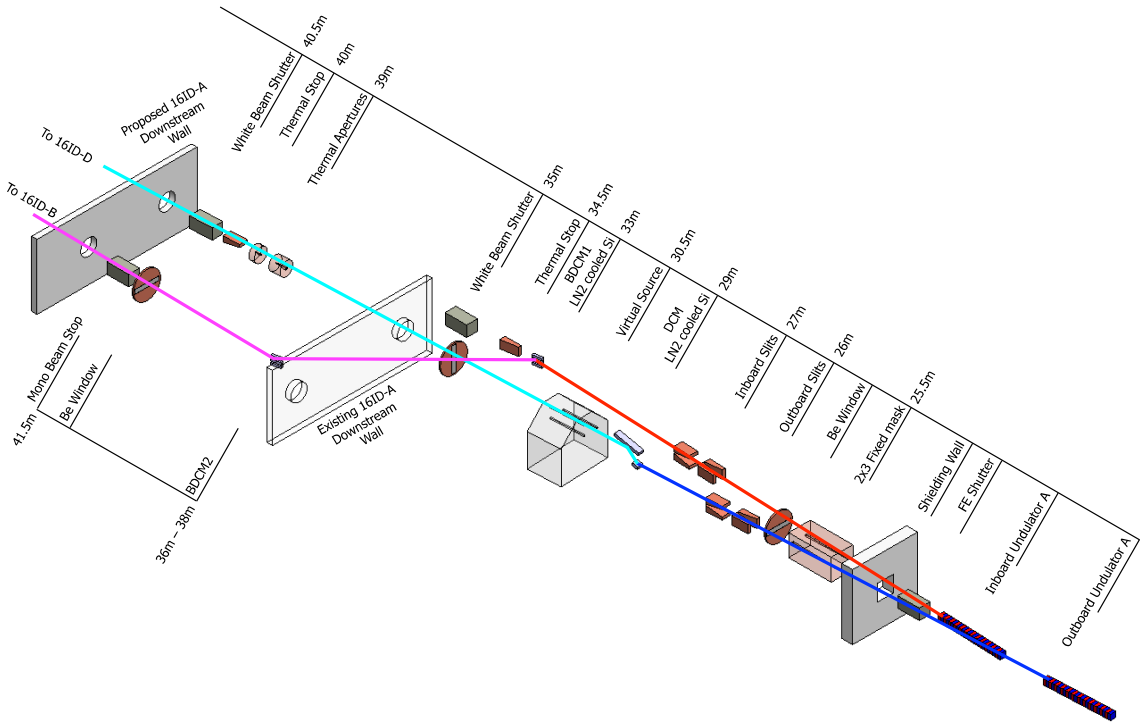

Figure 4.5.3-3. Layout of the optical components on 16-ID: Canted undulator sources with 1-mrad separation provide beams for two fully independent beamlines. The outboard branch will be used for 16-ID-D-E and for enabling submicron probes.

4.5.3.4 Optics

Two canted beams from the undulators will first go through the primary slits, and then will encounter the DCM, the virtual source unit, the BDCM, thermal apertures, and thermal beam stops, as shown in Figure 4.5.3-4. Two new monochromators (i.e., the DCM and BDCM) matching the canted geometry will be installed at 16-ID-A in 2011, with funds supported by HP-CAT members. The DCM will be a Bruker-Accel monochromator with liquid-nitrogen–cooled crystal assembly. Switchable crystals will provide a large energy range covering 4.5-35 keV with Si (111) and to 45 keV with Si (220) or (311). The monochromatic beam from the outboard branch will be vertically offset by +25 mm and will deliver the beam to the 16-ID-C,D,E branch. The specified sub-μm focusing optics will be located in this branch. The BDCM will be a specially designed unit by Bruker-Accel. It will diffract the inboard branch horizontally by an offset of 1 m. The monochromatic beam will have an energy range of 10-50 keV and deliver to 16-ID-B for micro-diffraction experiments. Although both the DCM and the BDCM will be compatible with the upgrade in terms of geometry, the higher heat load from the higher operation current in the APS-U project will require redesign of the crystal assemblies of both monochromators.

All high heat-load optics will accommodate the maximum heat load for the fully upgraded APS source. They include: front-end, high heat-load optics; primary slits; thermal apertures; and beam shutters and stops. It is clear that the first optical enclosure (16-ID-A) needs to be extended by 6-7 m in order to accommodate all of the heat-load optics (Figure 4.5.3-4).

The size of the APS undulator source in vertical direction (~25 μm) is small enough for sub-μm focus. In the horizontal direction, however, the source size (~600 μm) needs to be redefined by a virtual source. INVAR materials will be utilized to maximize its thermal stability and a stable granite table to

provide long-term stability better than 1 μm. The mechanical design will be similar to the one installed at 26-ID. The virtual source system will be installed right at the downstream of the DCM (~30 m from the source; Figure 4.5.3-4).

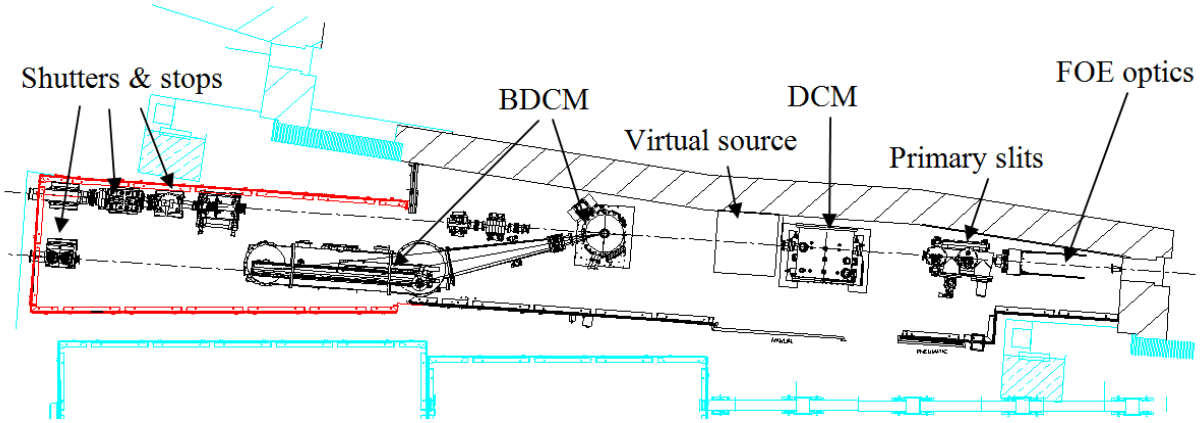

Figure 4.5.3-4. Layout of the optics in 16-ID-A. The lines in red denote the required hutch extension.

4.5.3.5 Instrument Enhancements

The sub-mm probing capability will be enabled at the 16-ID-E station that will be dedicated to HP XRD and HP x-ray spectroscopy studies. High pressure applications require a relatively long working distance (>75 mm) and high deliverable x-ray energies (up to 35 keV) with relatively low divergence (<1 mrad). The setup will consist of four major components: focusing optics, sample stages, detectors, and a stable base table. Achromatic K-B mirrors are specified as the focusing device (Figure 4.5.3-5) for a wide energy range. Considering the HP vessels, the K-B mirror system will have a relatively large working distance of 75 mm. With the mirror lengths of 100 mm and 400 mm, the geometrical demagnification ratios will be 360 and 200 in horizontal and vertical directions, respectively, which corresponds to a theoretical focus size of 0.2-0.5 μm in the horizontal and 0.12 μm in the vertical. The size of the virtual source in horizontal direction may be adjusted for balancing between the focus size and flux for specific experimental needs. Commercial products will be used for the KB mirrors. For example, the JTEC Company provides quality mirrors (e.g., 0.1-nm rms roughness and 0.1-μrad rms slope errors) and precise control systems.

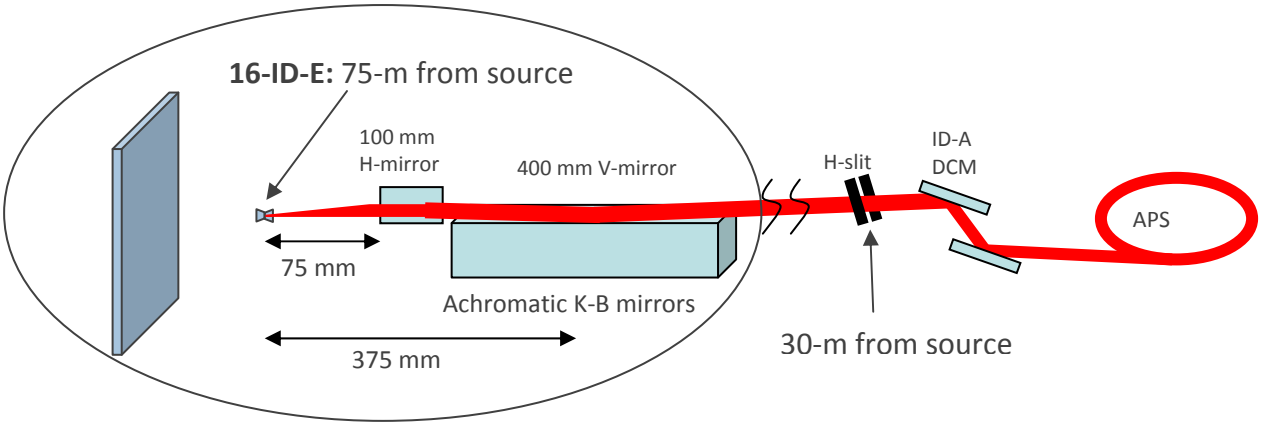

Figure 4.5.3-5. Schematic of the sub-μm focus system to be enabled in 16-ID-E.

High-performance sample stages are specified to have < 50-nm accuracy with 25-mm travel distance. In addition to X-Y-Z stages, a rotary stage with < 1-μm concentricity is required for HP experiments. A state-of-the-art large area and high-speed detector are essential parts of this instrument. Among the most promising types of detectors are novel flat-panel detectors and Pilatus pixel array detectors. PAD detectors offer several advantages compared to current state-of-the-art CCD and IP detectors: they eliminate readout noise and provide superior signal-to-noise ratio, a read-out time of 5 ms, a dynamic range of 20 bit, high detective quantum efficiency, and the possibility to suppress fluorescence by setting an energy threshold individually for each pixel. Currently, Pilatus is optimized for an energy range of 5-15 keV only. For HP diffraction experiments, the energy range used most often is around 30 keV. Contacts with the vendor have indicated that higher-energy Pilatus detectors (30-40 keV) will be available by 2012. A set of apertures, slits, and ion chambers will also be incorporated in the system. The entire setup will be enclosed and set on a stable optical table, which has a mechanical and thermal stability of < 100 nm.

4.5.3.6 Anticipated Performance

Table 4.5.3-1. Highlights of the Relevant Features and their Expected Performance at 16-ID

Feature	Expected Values of 16-ID-E
Energy	4.5-45 keV
Resolution	10^{-4} (at 10 keV)
Beam Size	100-500 nm at sample position
Flux	$\geq 10^{12}$ photons/s at sample position
Enabled techniques	HP sub-μm x-ray diffraction HP sub-μm x-ray absorption HP sub-μm x-ray emission HP sub-μm nuclear forward scattering HP scanning x-ray microscopy
Supporting HP techniques	On-line pressure calibration, on-line laser heating, cryostat, computer pressure controls

4.5.3.7 References

[4.5.3-1] W.J. Liu et al., Rev. Sci. Instrum **76**, 113701 (2005).

[4.5.3-2] H. Mimura et al., Nat Phys **6**, 122 (2010).

[4.5.3-3] G. Shen et al., High Pressure Res. **28**, 145 (2008).

[4.5.3-4] G. Shen et al., J. Synchrotron Radiat. **12**, 642 (2005)

[4.5.3-5] M. Mezouar et al., J. Synchrotron Radiat. **12**, 659 (2005).

[4.5.3-6] H.K. Mao et al., J. Geophys. Res. **95**, 21737 (1990).

[4.5.3-7] Y. Akahama, H. Kawamura, J. Phys. **215**, 012195 (2010).

[4.5.3-8] L. Wang et al., P. Natl. Acad. Sci. **107**, 6140 (April 6, 2010).

[4.5.3-9] S. Merkel, R.J. Hemley, H.K. Mao, Appl. Phys. Lett. **74**, 656 (1999).

4.5.4 High Energy X-ray Diffraction Upgrade (1-ID) [U1.04.02.10]

High-energy x-rays from third-generation synchrotron sources including the APS possess a unique combination of high penetration power with high spatial, reciprocal space, and temporal resolution. These characteristics can be exploited nondestructively to measure phase, texture, and strain distributions under extreme environments, including thermo-mechanical loading [4.5.4-1], high-pressure, irradiation, and supercritical environments [4.5.4-2]. Over the past several years, the 1-ID beamline has developed a number of programs for these purposes, namely (1) high-energy diffraction microscopy (HEDM), in which grain and subgrain volumes are mapped in polycrystalline aggregates, and (2) combined SAXS and WAXS techniques, which permit information over a broad range of length scales to be collected from the same (micron-level) volume. These programs have been increasingly used to test and extend predictive simulations of materials' behaviors over scales ranging from nanometers to millimeters in size. In addition, it is becoming recognized that the only way to achieve new insight into processes such as fatigue crack initiation will be through a closely coupled approach of experiments and simulations.

As part of the APS-U project, the capacity and breadth of these and related studies at 1-ID will be increased by canting the beamline; installing specialized undulators and optics; developing experimental stations optimized to produce stable, micro-focused beams; and installing new detector arrays to permit simultaneous near- and far-field imaging for both HEDM and SAXS/WAXS. The increased capacity will allow programs currently sharing beamline space to develop specialized instruments and will allow for the development of an *in situ* experimental program to exploit the properties of high-energy x-rays to study the evolution of materials under the extreme conditions often imposed during processing.

4.5.4.1 Scientific Scope

The enhanced high-energy beamlines will open new windows to observe dynamic processes on subsecond timescales with submicron spatial resolution. The experimental techniques will often employ different measurement modes on the same specimen to reveal microstructural and strain information over a wide range of size scales. Through the increased development and use of diffracted beam apertures and reconstruction algorithms, this information will be mapped in three dimensions. An important aspect that applies to all of the techniques described herein is the ability to use special environments. With high-energy x-rays, the environmental chambers (i.e., furnaces, cryostats, shear cells, diamond anvil cells) can have thicker walls and be made of heavier materials than are possible for lower-energy x-rays. The low absorption of high-energy x-rays means that a chemical-reaction vessel can be made of stainless steel with no need of beryllium windows. It is possible to make very high-quality furnaces that have both high-temperature capability and very small thermal gradients. The penetration capability of high-energy x-rays enables the use of large, polycrystalline test samples that closely approximate the actual conditions experienced by an engineering component. These combined features will enable the study of many important and technologically relevant processes, including the stamping of alloys, welding, battery stability, and the thermomechanical response of turbine blades. The creation of dedicated beamlines also presents the opportunity to create a tightly intertwined network of high-fidelity experiments and simulations, which will benefit energy-related materials implementation through enhanced material selection and design.

The planned upgrades for high-energy scattering within the APS-U project will also address novel "extreme" samples such as irradiated materials. High energies are particularly relevant for such studies due to their ability to penetrate through needed encapsulations and measure bulk behavior/response in the (often) high-Z materials. Among a number of scientific and technological challenges associated with nuclear materials, two prominent issues can be highlighted. First is the development of more radiation-tolerant materials, for which nanostructured materials containing a large

volume fraction of interfaces are prime candidates due to their high defect-sink densities. A fundamental understanding of the controlling processes that determine the trapping effects of interfaces under irradiation, in which material swelling/voiding can occur, is needed to develop nanostructure-tailored, damage-tolerant materials. Unique understanding can be gleaned from simultaneous WAXS-diffraction (which is sensitive to the both matrix and nanoscale precipitates) and SAXS (sensitive to electron density, thus primarily void/bubbles relative to the matrix) under thermo-mechanical processing [4.5.4-3]. The second is gaining an understanding of deformation and fracture mechanisms in irradiated materials, which is of critical importance to structural integrity and lifetime prediction of nuclear reactor components. Characterization of thick specimens (several millimeters to centimeters) is critical to ensure proper materials constraint conditions, as often required by testing standards. Through full-field imaging, internal cracks can be visualized and then "zoomed in" on with microbeam WAXS to characterize the stress/strain state, grain orientation, and local chemistry to provide a fundamental understanding of the cracking mechanisms in irradiated materials. Similar efforts are needed to understand degradation in Zr-based alloys (hydride formation and cracking) used for structural and cladding applications [4.5.4-4], and for development of next-generation reactor materials based on ceramic composite materials (e.g., SiC fiber reinforced SiC matrix). The high-brilliance beamlines can also be utilized to study irradiated (and non-irradiated) materials under high-pressure conditions. Taken together, this data will stringently test and refine the extensive computational models of materials behavior in these extreme environments.

The ability to microfocus high-energy x-rays provides a unique tool to study buried interfaces in a variety of natural and technologically relevant systems including fuel cell batteries and functionally-graded coatings. The performance of these systems is tied to their complex microstructures, each of which evolves during operation. In the case of fuel cells and batteries, the chemical and phase stability throughout the (nanoporous) electrode layers, as well as at the electrode/electrolyte interfaces is of particular interest. Such information can be gathered over the relevant and broad range of size scales through microfocused, SAXS/WAXS, using beam sizes (and corresponding spatial resolutions) on the micron-level [4.5.4-5]. For even higher spatial resolution and interface sensitivity, a relatively new technique of high-energy surface scattering will be employed. In addition to the solid-solid interfaces described above, this tool will also enable the structural study of solid-liquid, and liquid-liquid interfaces, while penetrating through cm of material and minimizing the background signal to accentuating the interface of interest.

Polycrystals are hierarchically structured and consist of grains which are often subdivided by a distribution of correlated lattice defects. Modeling the performance of polycrystalline components is therefore a complex multiple length scale problem. Grains are characterized by their crystallographic orientation and boundary topology. Individual grains and boundaries have anisotropic properties but are constrained by their neighborhood until damage occurs. It is therefore crucial to observe the individual states of grains and boundaries before macroscopic averaging to reveal underlying physical principles. Utilizing orientation contrast, HEDM provides the unique opportunity to probe a statistically representative number of grains during thermomechanical processing. An example of the current capability in this area is shown in Figure 4.5.4-1. The grain-boundary topology and stress tensors of several thousands of grains have recently been mapped. High–resolution, reciprocal space mapping is sensitive down to the nanometer-length scale and has been demonstrated to be a powerful probe of evolving dislocation structure [4.5.4-6]. Furthermore, it has been shown that postmortem sectioning and electron microscopy provide complementary real-space imaging. Impact areas include grain growth, *in situ* deformation of metallic alloys that deform by slip and twinning on grain and subgrain length scales, stress fields of a propagating crack, domain flipping in ferroelectrics, and variant selection of single-crystal phase transformation under high pressure. The experimental data are crucial for the validation and development of physical models, such as subgrain-scale finite element calculations. The APS-U project will enable the following transformative capabilities: (1) simultaneous grain boundary

topology and stress-state mapping, (2) provide a thermomechanical sample environment that will enable measurements under realistic conditions, and (3) provide submicron beams that allow researchers to "zoom-in" on interesting features identified by the "tomographic" overview scans.

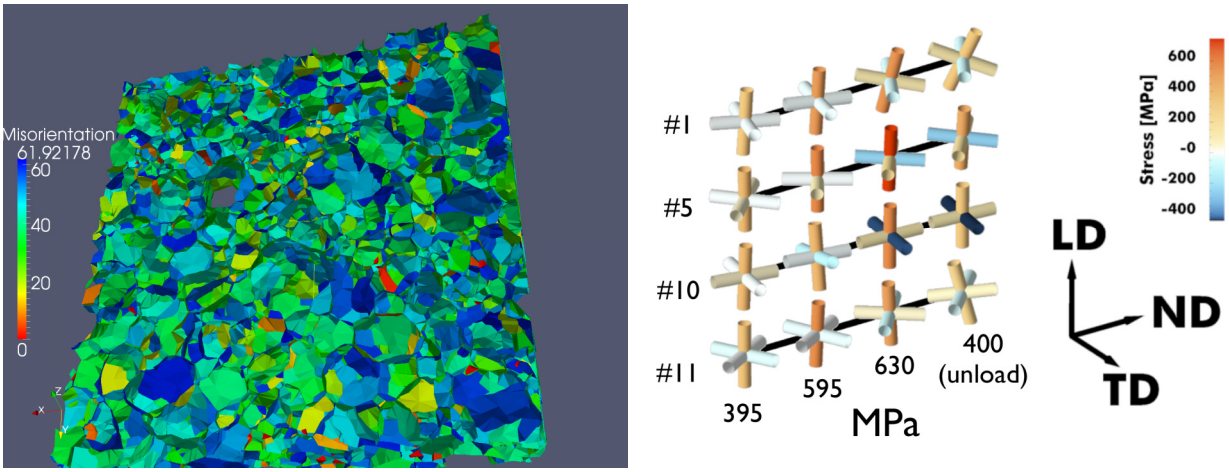

(a) (b)

Figure 4.5.4-1. Examples of non-destructive HEDM measurements: (a) grain map from bulk Ni with misorientations noted, (b) principal stress triads depicting the orientation and magnitude of the principal stresses experienced by four grains within a deforming titanium polycrystalline aggregate. The macroscopic (numbers) and grain-level (color bar) stress levels along with relevant directions are noted. Through the APS-U project, grain maps and stresses will be determined simultaneously.

4.5.4.2 Source Requirements

In order to increase capacity and performance of the high-energy beamlines, a 7.7-m straight section with canted undulators is specified. On the upstream end, a permanent magnet undulator(s) will be able to produce beams with continuous coverage in the energy range of 40-140 keV for the inboard (IB) line. A particularly attractive device will be the "revolving" undulator, which will allow use of discrete short periods (e.g., 2.1 cm and 2.3 cm) with a significantly longer length as compared to the alternative of two shorter undulators in series. While each of these short-period devices will yield higher brilliance than standard undulators (e.g., Undulator A) together they will permit continuous coverage over the desired energy range. On the downstream end, a superconducting undulator with a period and gap to produce a third harmonic at 60-75 keV will be employed for the monochromatic outboard (OB) line, such as the APS prototype 1.6-cm device. Reducing the minimum gap to below 10.5 mm will allow shorter periods and higher brilliances to be achieved. As opportunities evolve to obtain undulators (as is expected to occur during the APS-U project), these options will be revisited.

4.5.4.3 Beamline Description

The current single, monochromatic end station 1-ID-C will be replaced with two white-beam-capable hutches for the IB line, and two fixed-energy monochromatic hutches for the OB line (as shown in Figure 4.5.4-2). All hutches will be designed for seamless transfer between different sample stages/tables, with specialized optics to permit on-demand, microfocusing, diffracted beam apertures for 3D spatial mapping, and arrays of detectors for efficient and fast data collection. The 1-ID-D and 1-ID-E hutches will be used primarily for high-energy simultaneous SAXS/WAXS and HEDM studies, respectively. The 1-ID-D hutch is intended to house the Materials Test Systems load frame for thermomechanical studies, with a general-purpose table for other environmental chambers. The 1-ID-E

hutch will also include a load frame, diffractometer, and general purpose sample tables. These hutches can also be used for resonant diffraction studies. The side stations, 1-ID-F and 1-ID-G, will be served by the OB line. The F-hutch will include capability for high-energy surface scattering measurements of solid and liquid interfaces, as well as diffuse scattering measurements. The G-hutch will focus on *in situ* processing and microstructural kinetics, with some scope overlapping that of the D and E hutches in anticipation of continued user demand.

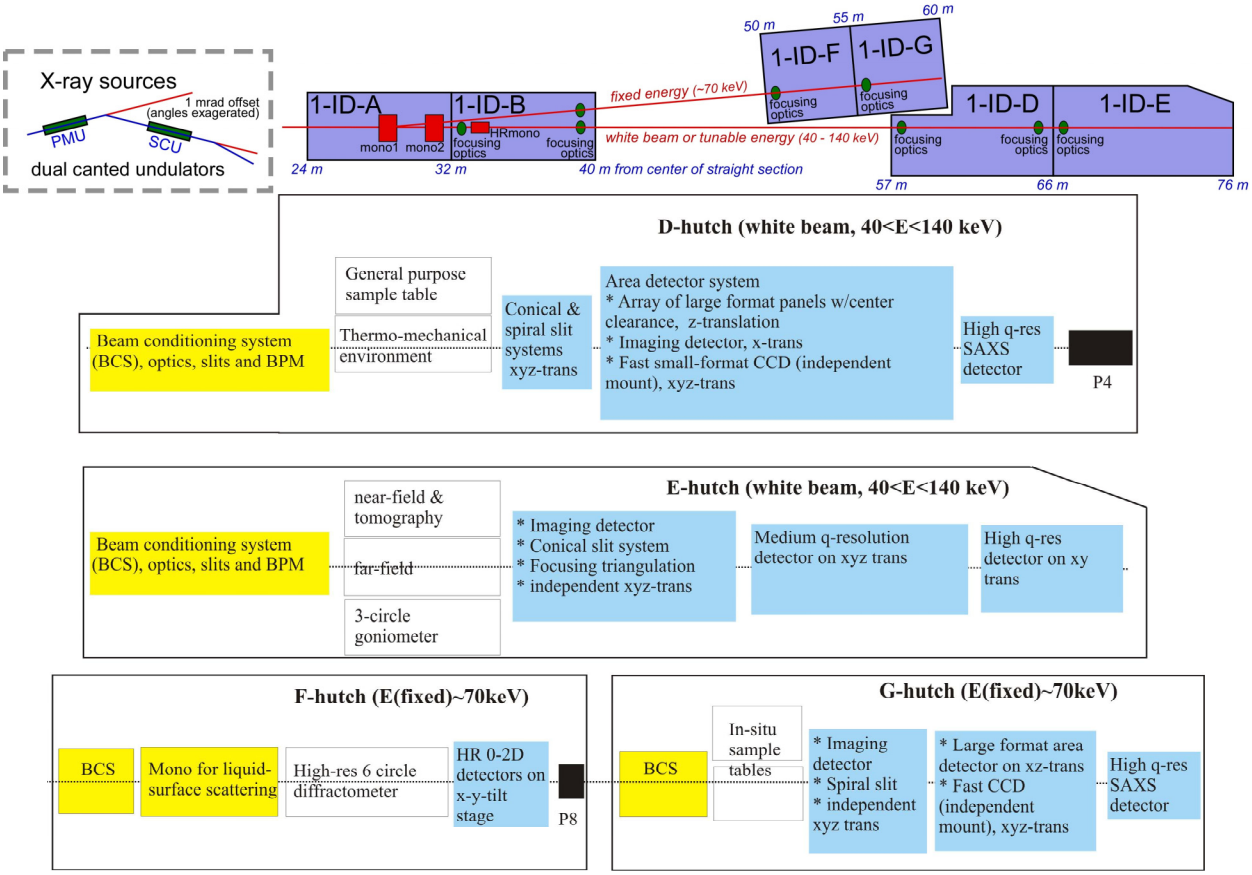

Figure 4.5.4-2. Schematic of 1-ID upgrade for enhanced high-energy scattering capability, including instrumentation for the four end stations.

The current single, monochromatic end station 1-ID-C will be replaced with two white-beam-capable hutches for the IB line, and two fixed-energy monochromatic hutches for the OB line (as shown in Figure 4.5.4-2). All htches will be designed for seamless transfer between different sample stages/tables, with specialized optics to permit on-demand, microfocusing, diffracted beam apertures for 3D spatial mapping, and arrays of detectors for efficient and fast data collection. The 1-ID-D and 1-ID-E hutches will be used primarily for high-energy simultaneous SAXS/WAXS and HEDM studies, respectively. The 1-ID-D hutch is intended to house the Materials Test Systems load frame for thermomechanical studies, with a general-purpose table for other environmental chambers. The 1-ID-E hutch will also include a load frame, diffractometer, and general purpose sample tables. These hutches can also be used for resonant diffraction studies. The side stations, 1-ID-F and 1-ID-G, will be served by the OB line. The F-hutch will include capability for high-energy surface scattering measurements of solid and liquid interfaces, as well as diffuse scattering measurements. The G-hutch will focus on *in situ* processing and microstructural kinetics, with some scope overlapping that of the D and E hutches in anticipation of continued user demand.

4.5.4.4 Optics

The 1-ID-A station will have: dual, independent white-beam slits to allow independent control of both IB/OB lines; a filter bank system to serve the IB/OB lines independently; and monochromators for both lines. The IB monochromator will consist of a bent, double-Laue crystal system in sequential Rowland conditions, as has been in use at 1-ID for 10 years to deliver a high-flux, fully tunable, fixed-exit beam with preserved source brilliance (i.e., size and divergence), as shown in Figure 4.5.4-3 [4.5.4-7]. In the current arrangement, the first crystal is in a vacuum tank and cryogenically cooled, whereas the second crystal is in air. In the upgrade scheme, both crystals will be in the same tank to permit a minimum energy of 40 keV and a maximum of at least 140 keV. The OB monochromator will consist of a cryogenically cooled, single-horizontal-reflection, bent Si Laue crystal (Figure 4.5.4-4), which will be located in its own tank (for vacuum isolation during maintenance) immediately upstream of the IB line monochromator and will provide a fixed-energy beam of roughly 70 keV to the F and G stations.

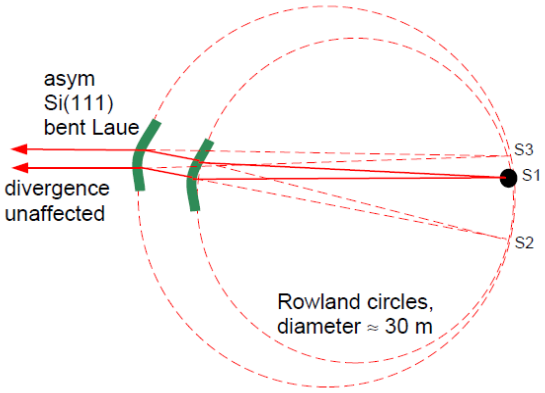

Figure 4.5.4-3. Tunable, fixed-exit monochromator (for the inboard branch stations 1-ID-D and -E) consisting of two vertically diffracting Laue crystals bent to Rowland conditions.

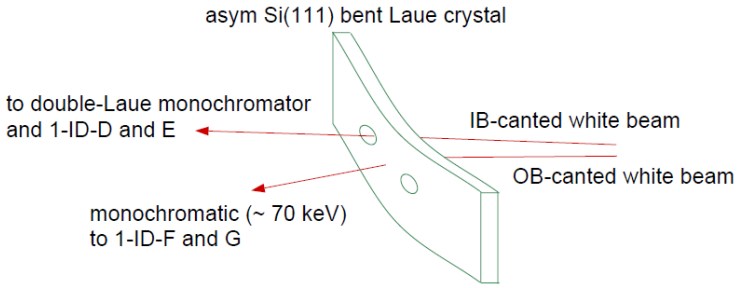

Figure 4.5.4-4. Single-reflection, bent Laue monochromator for the outboard branch side stations (1-ID-F and -G). A hole in the crystal lets the white beam pass through to the double-Laue monochromator and inboard line. With a lateral translation and a second pass-through hole, researchers can interchange delivery of the canted beams between the two lines.

The 1-ID-B station will contain long-focal-length (f > 10 m) focusing optics (most likely of the refractive type) for both lines' end stations (D, E, F, and G) and also a high-energy-resolution monochromator (HRM) system for the IB line that will optionally further monochromatize the beam delivered by the double-Laue system from $\Delta E/E \approx 10^{-3}$ down to 10^{-4}-10^{-5} levels of energy spread for high-resolution, reciprocal space diffraction studies or resonant scattering at heavy-element K edges. Such an

HRM has already been in operation at 1-ID for many years and consists of four flat Bragg crystal reflections in a (+--+) dispersive configuration [4.5.4-8] (Figure 4.5.4-5). When the HRM is in operation, the upstream focusing optics in 1-ID-B will be set for vertical beam collimation in order to enhance the throughput of the low-angular-acceptance HRM. In this mode, if focusing is also required with a narrow bandwidth, downstream focusing optics in 1-ID-B, -D, or -E can also be used (Figure 4.5.4-5).

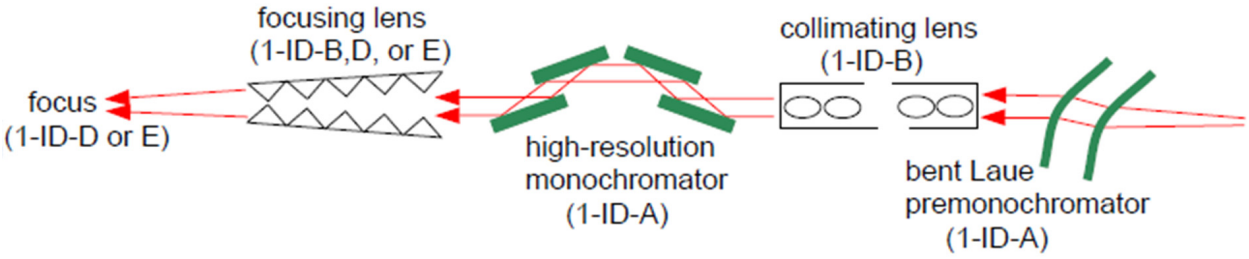

Figure 4.5.4-5. A four-reflection, high-energy-resolution monochromator. Upstream refractive lenses (shown here of the compound type) collimate the x-rays. Downstream lenses (shown here of the saw-tooth type) focus the beam.

Focusing optics for short focal lengths will be placed in stations D, E, and F to focus the beam into the same or immediately downstream station (Figure 4.5.4-2). These will mostly be parabolic refractive lenses of the compound-refractive or saw-tooth types. Saw-tooth refractive lenses have been used routinely for years at 1-ID to produce beams in the size range of 2-25 μm at 50- to 100-keV energies [4.5.4-9]. In addition to being effectively parabolic, they are continuously tunable in focal length or energy and have no attenuation on-axis. For the fixed-energy side stations F and G, researchers can sacrifice tunability for the benefit of enlarged spatial acceptance apertures by using kinoform lenses, which have lower attenuations off-axis compared to the compound or saw-tooth lenses.

The HEDM program residing in the E-station will also explore alternative focusing approaches than the refractive-based optics previously mentioned, namely bent Laue crystals and elliptically bent multilayers. Laue focusing is achieved by bending a crystal in an off-Rowland geometry with the source outside of the Rowland circle. By proper choice of crystal parameters, particularly the asymmetrical cut, one can eliminate the crystal thickness aberration and achieve theoretical source-size limited focusing in the vertical direction [4.5.4-10]. Because of the off-Rowland bending with the convex side facing the source, the focusing is inherently polychromatic (broadband), requiring incident white beam onto the Laue crystal. Addressing this need is one of the reasons for installing white-beam capability throughout the IB line all the way to the E-station. One feature of this type of focusing is the rectangular-function shape of the angular divergence profile, which is beneficial for certain HEDM studies. Another anticipated advantage of Laue focusing is its significantly larger spatial acceptance as compared to refractive lenses, a feature that becomes important far from the source, as is the case for the E-station. Larger spatial acceptances are also expected for elliptically bent multilayers [4.5.4-11], which can be used to capture and focus the horizontal undulator beam. To preserve the Bragg condition for a single wavelength over the elliptical profile, the multilayers will have a meridional gradient in their spacing. One can also take advantage of the broad bandwidth of multilayers, which will also require incident white beam.

Finally, discussion is presented of some specialized optics pertaining to the high-energy surface scattering (F-station) program. To measure x-ray scattering from liquid/gas and liquid/liquid interfaces, the incident beam must be steered out of the horizontal plane because liquid surfaces cannot be tilted. One compact design that can be incorporated into the beamline easily consists of a bent, double-Laue crystal assembly, which is very similar to the double-Laue monochromator described earlier but instead uses two different crystal reflections to obtain a nonhorizontal beam (i.e., one having a vertical component in its propagation direction). By coupling both crystals into a single-tilt stage that rotates about an axis parallel

to the incident beam, the exit beam can be made to sweep out a cone whose vertex, into which the beam is directed, is stationary and at the sample position [4.5.4-12]. Such a tilt degree of freedom results in the ability to vary the incidence angle of the x-rays with respect to the surface being studied. This design permits sample stability and increases measurement speed because the sample remains still. Using the Si(111) reflection for the first crystal and the Si(220) reflection for the second crystal enables the longitudinal scattering in reciprocal space to be measured up to 2.5 A^{-1} at 70 keV.

4.5.4.5 Anticipated Performance

Presently, 1-ID receives radiation from two 2.4-m, permanent magnet undulator sources, only one of which can be used at a given time—a 3.3-cm-period device and a 2.3-cm-period device. These sources, in conjunction with the bent double-Laue monochromator optics, deliver from 1-5 times 10^{12} photon s^{-1} mm^{-2} in $\Delta E/E \approx 10^{-3}$ energy spread over 50-100 keV into the current C-station (corresponding in location to the new D-station, Figure 4.5.4-2), with the higher fluxes occurring at the lower end of the energy range. In the APS-U project configuration, the ID line's end stations (D and E) should receive enhancement of more than an order of magnitude from small-gap, short-period permanent magnet undulators, resulting in from 1-5 × 10^{13} photon s^{-1} mm^{-2} of unfocused intensity. For the 70-keV, fixed-energy OB line, where an optimized short-period superconducting undulator is specified, a higher intensity of from 1-2 × 10^{14} photon s^{-1} mm^{-2} can be attained.

Long-focal-length focusing (i.e., from B into D/E or from B into F/G) will yield flux density gains of roughly 20 for the case of vertical focusing only, producing 12- to 25-μm line foci. Simulations show that there are marginal or no additional flux density gains if also focusing horizontally from the same location (i.e., also with the same long focal length). This result occurs because any gain anticipated from such horizontal focusing is lost by a combination of the weak demagnification of a much larger (by thirtyfold) horizontal source and the added horizontal attenuation profile of the additional refractive lens system. However, enhanced gains are indeed expected if conducting the vertical and horizontal focusing from different locations, with the latter at higher demagnification, to produce an image spot that is less eccentric (i.e., more circular) than the source. This action will be carried out by combining vertical focusing from B with horizontal focusing from D or F for the IB or OB lines, respectively. This approach is expected to increase the flux density gain by tenfold to roughly 200.

Short-focal-length focusing will be performed from stations D, E, and F into the same or immediately downstream station (Figure 4.5.4-2), achieving few μm-sized vertical foci, with a goal of 0.5 μm up to 100 keV. This approach should be accompanied by flux density gains of a few hundred. Achieving doubly focused beams with comparably sized horizontal foci will require using upstream beamline slits to define a small and effective source of appropriate horizontal size. While this approach may not yield larger flux density gains, the resulting beams will be small (μm-sized) in both dimensions, a result that is essential for numerous experiments.

4.5.4.6 Instrumentation

A wide variety of *in situ* sample environments will be made use of at 1-ID. The expanded number of hutches will permit greater dedication of instrumental setups, and further efficiency gains will be realized by rail mounts such that each instrument can be used with all relevant optics and detectors. One primary sample environment is thermomechanical loading, which is currently available at 1-ID with a servo-hydraulic fatigue load frame from MTS. The MTS provides a professional hardware/software system that is familiar to many users and can operate at high applied force of ±15 kN, with fatigue rates ranging up to kilohertz levels. The large distance between its two loading posts permits simultaneous use of a variety of additional sample environments. The MTS can be operated in concert with an infrared heating device that is capable of rapid heating to 1200°C. Users have also developed and successfully

demonstrated a cryogenic chamber for low-temperature operation. A number of improvements/additions to the system will be made through the APS-U project, primary among them the ability to attach additional environments to the sample. These include vacuum, water quenching, corrosive media, and controlled environments for radioactive samples. New loading modes (torsion and multi-axial loading) are also anticipated, most likely through development/use of new mechanical loading systems. Relatedly, high-pressure DACs coupled with high-temperature capability, which are under development at other beamlines (e.g., HP-CAT), can be utilized with 1-ID programs in cases when microfocused high-energy beams are needed.

A variety of user-supplied and user-inspired environments are anticipated for these upgraded hutches. These are, in a certain sense, limited only by the scientists' imagination, but may include studies of *in situ* processing (including welding, plasma deposition, and recrystallization) and *in operando* studies of operating batteries and fuel cells. In anticipation of these needs, the hutches will be constructed with exhaust ports and multipurpose sample tables. The use of two hutches for each branch line will permit extensive setup time in the free hutch, which will allow both for efficient operation and more complex environments to be utilized. These environments will be manipulated through high-load-capacity and high-resolution stages. For near-field and tomography applications in the E-hutch, for example, an airborne submicron concentricity rotation stage will be employed, with x-tilt and xyz-translations both below and above the rotation axis. The rotation axis control will be synchronized with a fast x-ray shutter and detector(s) to allow for rapid and efficient data acquisition.

The forward scattering associated with high-energy x-rays makes area detectors particularly efficient collectors of scattering data. Flat-panel pixel detectors, notably the Angio detector from General Electric, offer an excellent combination of size (40 × 40 cm^2, 2 k × 2 k pixels) and speed (7-Hz full frame, 30-Hz binned) for high-energy, wide-angle scattering data. These detectors (and/or their descendants) will be used in all of the hutches. While these detectors are primarily intended to be operated singly, they will also be utilized in a paneled mode, as shown in Figure 4.5.4-6. This setup will be operated on a z-translation stage to provide users with unique access to large q_{min} or very high q-resolution. The long sample-detector distances permitted (e.g., 4 m at 80 keV provides d_{min}~1 Å) will also provide high signal/background ratios, which is of particular importance for radioactive and/or highly fluorescing samples. An additional feature of the paneled design is the presence of a central hole, which will allow for simultaneous SAXS or full-field imaging measurements. For HEDM studies, a variety of detectors are will be utilized for different detection modes, as follows: (1) for near-field measurements, a two-screen, semi transparent "compound" imaging detector; (2) for far-field, medium q-resolution, a >16-Mpix, >10-frames/sec, 50-μm pixel size detector (such as split frame transfer CCD array [Rayonix], CMOS [Dexela 3529], or GE [Angio]); and (3) for far-field high q-resolution, a structured scintillator and CCD or CMOS with 500 × 4000 pixels and 20-μm pixel size. Similar attributes to (3) are desired for SAXS detectors, albeit with lower aspect ratios (2 k × 2 k pixels). While not crucial for experimental success, incorporation of energy discrimination for any of these detectors will be desirable to achieve higher signal/background levels. For surface scattering measurements, the detector system will permit easy transfer from a point counter, which is needed for "standard" surface scattering measurements (e.g., reflectivity, grazing-incidence diffraction) to an area detector. This capability is deemed especially useful for identifying scattering features of interest (using the point counter) and then determining kinetics by using the area detector. Finally, software with significant data reduction and analysis capabilities will be needed by Argonne staff scientists, and in cooperation with user groups, to maximize scientific output.

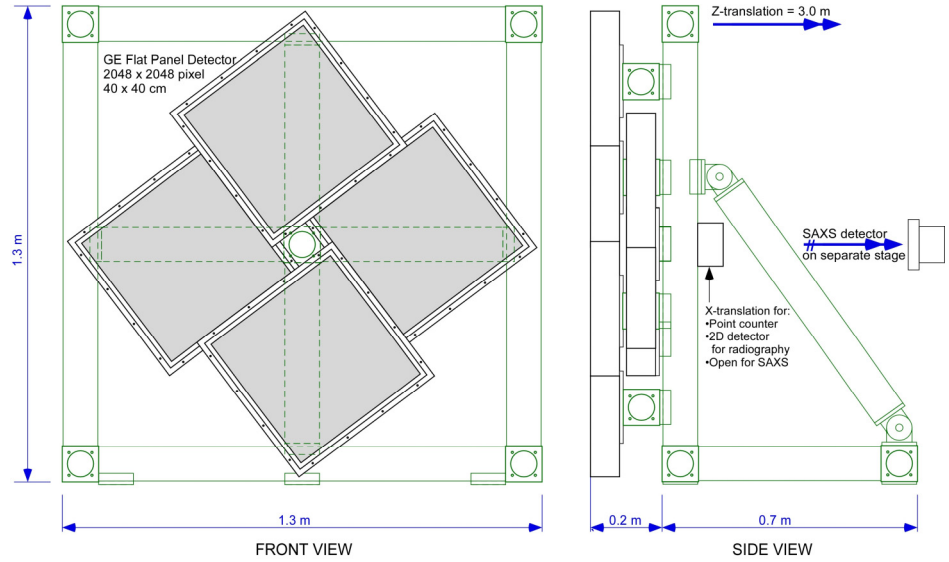

Figure 4.5.4-6. Schematic of a detector array system for high-energy x-ray scattering (SAXS/WAXS) and imaging.

Diffracted beam apertures for area detectors will also be developed as part of the APS-U project for 3D-resolved studies. When real materials in their operating sample containment environments are measured, the x-ray scattering arises from all materials present along the incident beam direction. Area apertures placed between the sample and detector can resolve the longitudinal position from which the signals originate, while providing information from a range of detector azimuths or sample orientations. This depth resolution is desired because (1) the material response often varies from the surface to its interior, and (2) it minimizes or eliminates scattering from sample containment. Sector 1, which currently uses one of the few conical slits available in the world, allows diffraction from a number of reflections to be recorded simultaneously, particularly for cubic crystal symmetries, and over almost full 360-degree azimuthal coverage. One factor limiting its use has been the lack of a dedicated setup, which has been dictated by the single 1-ID-C end station and multiple programs—and which APS-U project will ameliorate. Accordingly, this device, with longitudinal resolution of approximately 100- to 200-μm and focal length of 50 mm, will be supplemented with other conical systems (of different focal lengths), as well as spiral slit systems. In the case of the spiral slit, the signal can be measured as a function of depth simultaneously for all depths, albeit with less azimuthal orientation coverage than present in the conical slit. Spiral slits also cover a large, continuous range in scattering angles, so they can be used for all crystallographic space groups even for a fixed x-ray energy, which is particularly important for OB station use.

The smaller diffraction volumes associated with these 3D probes necessitate high-brilliance, focused, high-energy x-rays. Therefore, only a handful of x-rays beamlines exist in the world that are conducive to this technique, 1-ID being among this group. Utilizing these probes to rapidly determine structural properties of materials inside of real components provides a unique opportunity for the Argonne community to foster academic and industrial partnerships. By combining the measurements with simulations and material modeling, these enhanced APS-U project facilities will help researchers understand how materials operate, evolve, degrade, and fail during use and thereby provide opportunities for enhanced materials efficiency and discovery.

4.5.4.7 References

[4.5.4-1] K.D. Liss et al., Adv. Eng. Mater., **11**, 637 (2009).

[4.5.4-2] N. Lock et al., Chem.-Eur. J. **15**, 13381 (2009).

[4.5.4-3] X. Pan et al., J. Nucl. Mater. **398**, 220 (2010).

[4.5.4-4] M. Kerr et al. Acta Mater. **58**, 1578 (2010).

[4.5.4-5] D.J. Liu and J. Almer, Appl. Phy. Lett. **94** (2009).

[4.5.4-6] B. Jakobsen et al., Science **312**, 889 (2006).

[4.5.4-7] S.D. Shastri et al., J. Synch. Rad. **9**, 317 (2002).

[4.5.4-8] S.D. Shastri, J. Synch. Rad. **11**, 150 (2004).

[4.5.4-9] S.D. Shastri et al. J. Synch. Rad. **14**, 204 (2007).

[4.5.4-10] U. Lienert et al., J. Synch. Rad. **6**, 979 (1999).

[4.5.4-11] C. Schulze et al., J. Synch. Rad. **5**, 77 (1998).

[4.5.4-12] V. Honkimaki et al., J. Synch. Rad. **13**, 426 (2006).

4.5.5 Magnetic Spectroscopy Upgrade (4-ID) [U1.04.02.09]

Because of its element specificity and ability to probe extremely small sample volumes, x-ray spectroscopy has become an essential tool in understanding the magnetism of complex materials at ambient and extreme conditions. Over the past 10 years, the APS has played a key role in studying such complex magnetic systems using synchrotron radiation techniques, with many new types of measurements pioneered here. To remain at the forefront in new emerging areas of magnetism research, however, requires continued improvements to both the instrumentation and optics in order to provide greater flux, improved polarization control, and enhanced sample environments. This project involves upgrading both magnetic spectroscopy beamlines located on Sector 4. The major components of this upgrade as detailed in this section involve increasing the straight section cant to a full 1 mrad to eliminate cross-talk between beamlines; providing specialized insertion devices for each branch; replacing the beamline optics on 4-ID-C; installing focusing mirrors and expanding the experimental station on 4-ID-D; and providing new higher-field, cryogen-free magnets for each beamline.

4.5.5.1 Soft X-ray Magnetic Spectroscopy

The upgrade of the soft x-ray magnetism beamline (4-ID-C) will provide magnetic spectroscopy and imaging capabilities with a sensitivity level that is two orders of magnitude better than the current state of the art. This improvement will enable XMCD experiments on materials with dilute magnetic dopants, ultra-small induced magnetic moments, and interfacial structures. Enhanced sensitivity will be achieved through a combination of enhanced flux through more efficient optics and a specialized fast-switching source for lock-in detection of XMCD signals. Thus, the core features of this upgrade are the optical components up to the new grating monochromator and the fast-switching helical undulator.

4.5.5.1.1 Scientific Scope

In the 1990s, the rise of circularly polarizing insertion devices and associated soft x-ray beamlines with greatly improved flux and polarization control ushered in a new era of experiments with objectives that previously would have been unattainable. As a result, these techniques have become standard features in designing studies of magnetism, electronic ordering, and chiral systems, leading to a deeper understanding of the relationships between electronic structure at the atomic level and macroscopic properties, as well as to major technological advances. During this time, the field has progressed to the point where very subtle effects have become the crucial components in understanding the behavior(s) under study. These effects are at the current sensitivity limits of polarized x-ray beamlines even at third-generation synchrotrons.

The magnetization dynamics of spin-polarized carrier populations in semiconductors and metallic systems are among the most important questions for the use of these materials in spin-based devices. For example, induced magnetic moments in doped magnetic semiconductors are at the level of ~0.01 Bohr magneton/atom even for relatively high doping levels of between ~2-5% [4.5.5-1]. However, this doping level is high, and to truly understand the physics of an isolated dopant, it is essential to study samples with much lower concentrations, which are beyond the present limits of sensitivity. In addition, the much smaller spin asymmetries due to spin-injected or accumulated populations have not been detected so far. Other questions facing similar sensitivity limitations are the interplay between charge, magnetic, and structural order in complex oxide materials and in multiferroics [4.5.5-2]. The important materials chemistry here often involves small induced-moments on the oxygen atoms mediating charge and ferromagnetic order. Therefore, sensitivity to subtle changes in the oxygen K edge dichroic spectra is critical. All of these questions often involve interfacial moments that may be difficult to separate from the bulk contributions and thus also require high sensitivity.

Element-resolved studies of such phenomena are therefore critical, yet the effects are just barely observable with current sensitivity limits, making comprehensive, systematic studies, and especially time-resolved studies, difficult to achieve. Therefore, the ability of polarized x-ray techniques to contribute similar insights into the most compelling questions of the *next* 10-15 years will be limited without substantial increases in sensitivity over the current capabilities.

4.5.5.1.2 Source Requirements

Tunable radiation from 0.4-2 keV is needed to cover the absorption edges of interest for magnetic studies (nitrogen K, oxygen K, transition metal L, rare earth M, etc.). An additional requirement is >96% polarization, with circular and linear modes. To provide the highest sensitivity to small magnetic signals the ability to switch between modes quickly and at high repetition rates (~10 Hz) is required in order to employ lock-in detection methods. For this purpose, an electromagnetic variable polarizing undulator (EVPU) is ideal, similar to the device that is currently used on 4-ID-C [4.5.5-3]. Rapid circular polarization switching in such devices is accomplished by simply reversing the current polarity in vertical field coils while leaving the horizontal coil current fixed. The switching rate in the current 4-ID-C electromagnetic device, however, is limited to <1 Hz due to significant field errors in the magnetic pole pieces and the lack of suitable corrector coils at the end of the device. A new device with proper design for adjustment of individual field poles and corrector coils for complete compensation of beam motion would provide increased switching rates close to 10 Hz. Design studies for such a device are currently underway.

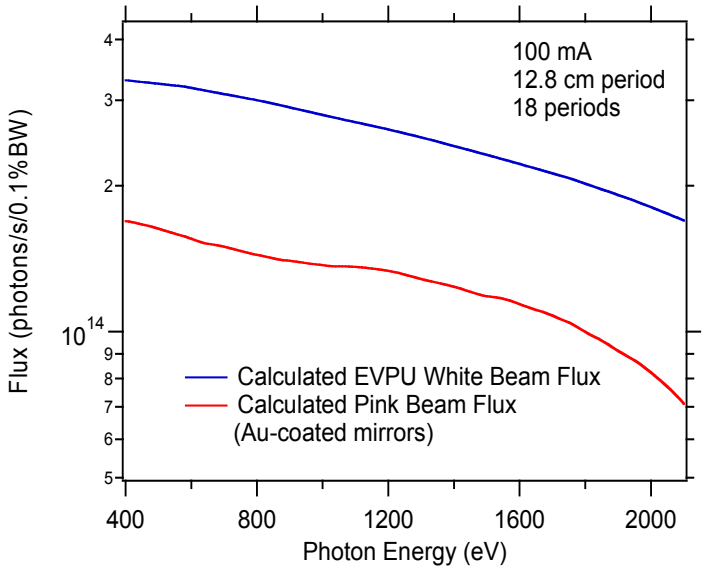

Figure 4.5.5-1. Estimated circularly polarized flux obtained from the 4-ID-C EVPU for 100-mA storage ring current (blue curve) and after reflection from three Au-coated mirrors with 1.0° incidence angles (red curve).

4.5.5.1.3 Beamline Description

The upgraded 4-ID-C beamline will occupy its current position in 4-ID, with the exception that the straight section will be modified for a full 1 mrad cant from its present cant of 270 μrad. With the current cant, the tail of the beam from the 4-ID-D source intercepts the first 4-ID-C branch mirror when operating near the minimum gap, which results in unwanted heating of this optic. The EVPU will occupy

the upstream section of the straight, while the hard x-ray Apple-II device for 4-ID-D will occupy the downstream section. In the first optics enclosure (4-ID-A), two horizontal mirrors deflect the soft x-ray beam outboard by 4° to separate it from the hard x-ray beam. Figure 4.5.5-2 shows the undulator arrangement in the 4-ID straight section.

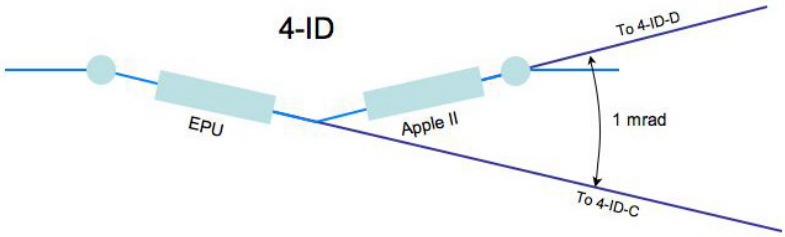

Figure 4.5.5-2. Undulator arrangement in 4-ID, showing full cant. Mirrors M0 and M1 in the FOE deflect the EPU white beam 4° outboard of the hard x-ray beam.

The layout of the 4-ID-C beamline is shown Figure 4.5.5-3. Only the enhancements to the main branch-line optics are included within the APS-U project. The main branch of 4-ID-C has three end-station positions. The first two will be occupied by an existing 1-Tesla octopole electromagnet and a new 9-Tesla horizontal-field magnet. The third station position will be shared among the current X-PEEM, PES/SPM instruments, and user-supplied experimental chambers, similar to the present 4-ID-C arrangement. The optical layout will permit a possible future upgrade option for adding a second branch line, shown in the inset of Figure 4.5.5-3. This future addition will provide much greater flexibility for user access and eliminate end-station changes in the third position of the main branch. Because of the additional costs associated with this option, however, it is not included within the present scope of the APS-U project.

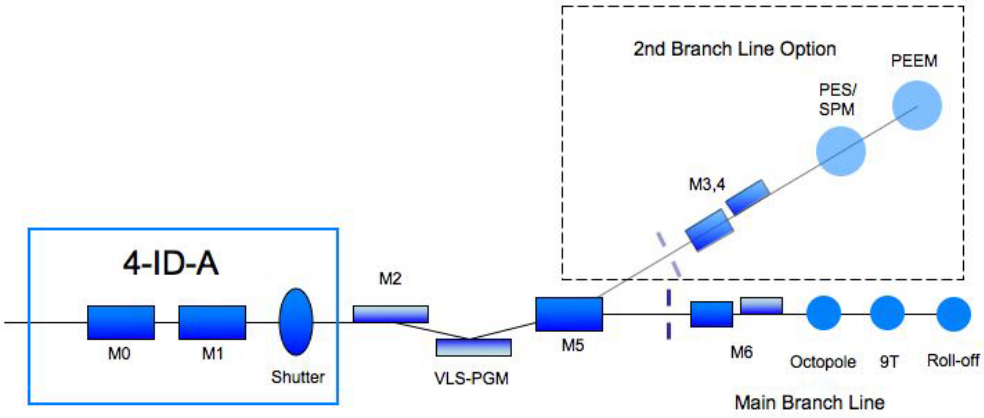

Figure 4.5.5-3. Diagram of the optics and instrumentation for the 4-ID-C beamline. The third "roll-off" position on the main-branch line will be shared by the PEEM and PES/SPM chambers. These instruments could be accommodated on a future second branch line option shown in the inset.

4.5.5.1.4 Optics

The first optics enclosure (4-ID-A) contains the first two mirrors for the 4-ID-C beamline (M0, M1), which will be replaced in this upgrade. These two mirrors intercept the EVPU beam and deflect it horizontally to the beamline, while allowing the hard x-ray Apple-II white beam to pass by. The current spherical grating monochromator on the beamline will also be replaced with a varied line-spacing grating

design (VLS-PGM), similar to that being installed on 29-ID [4.5.5-4]. This monochromator is an entrance-slitless design, with a vertical plane mirror (M2) and plane grating that are scanned together to preserve the incidence angle. This new design will result in an *~100× increase in flux* at 500 eV compared to that currently available on 4-ID-C. After the monochromator an exit slit is used to define the energy resolution, and a set of Kirkpatrick-Baez bendable mirrors (M6) are used to focus the beam. In a future upgrade to the beamline, a horizontal mirror (M5) downstream of the monochromator will deflect the beam 2.5° into a second branch line for surface magnetism studies requiring ultra-high vacuum environments and *in situ* scanning probe microscopy.

4.5.5.1.5 Anticipated Performance

The estimated flux from the EVPU in the 400 eV to 2000 eV range is 2×10^{14} photons/s/0.1% BW. This flux will be reduced prior to the grating by the reflectivities of the mirrors (M0, 1, 2). Assuming 80% reflectivity with Au coatings and integrating fully over the radiation cone gives $(2 \times 10^{14} \times (0.8)^3) = 1.0 \times 10^{14}$ photons/s/0.1% BW. The IEX CDR suggests that 20-35% grating efficiencies over this energy range are feasible. The refocusing optics further reduce the flux according to their reflectivities. This gives $(1.20 \times 10^{14} \times (0.2) \times (0.8)^2) = 1.3 \times 10^{13}$ photons/s/0.1% BW. The design goal for the monochromator will be a moderate to high resolving power of 10^4. The design goal for the fast-switching undulator will be a switching rate of ~10 Hz. Performance specifications are summarized in Table 4.5.5-1.

Table 4.5.5-1. Expected Beamline Performance

Feature	Expected Values
Energy range	0.4–2.0 keV
Resolution	2×10^{-4} ΔE/E
Beam size	100×200 μm^2
Flux	1.3×10^{13} photons/s at 700 eV
Polarization	Circular and linear (H and V) with 10 Hz

4.5.5.1.6 Instrumentation

The main branch of 4-ID-C will be equipped with two magnet end stations permanently installed on the beamline and a third position for the "roll-on" installation of various chambers. The magnet stations are dedicated to XMCD spectroscopy in moderate and high field. The "roll-off" instruments provide photoelectron spectroscopy and magnetic imaging capabilities and are also available to accommodate specialized user chambers. Only the high-field magnet station is being costed as part of this upgrade.

Octopole Magnet Station (existing): This existing instrument is an omnidirectional, eight-pole electromagnet capable of applying a ±1 T field along any direction. The magnetic poles are arranged to provide complete access to the horizontal plane for scattering measurements. The chamber is equipped with an integrated scattering detector. A liquid He cryostat provides sample temperatures of 4.2-350 K and four-axis motion (x, y, z, polar angle), with accuracies of 10 μm and 0.01°.

High-Field Magnet Station (upgrade): This instrument will be a new horizontal-field, split-coil superconducting electromagnet capable of a ±9 T field. A preliminary design for this magnet is shown in Figure 4.5.5-4. A liquid He cryostat provides sample temperatures of 2-350 K and two-axis motion (vertical, polar angle), with accuracies of 10 μm and 0.01°. The system is equipped with a He recirculation system for reaching effectively zero boil-off operation. This capability will greatly reduce the operational costs of running this magnet as compared to the helium-cooled, high-field magnet currently installed on the beamline. The magnet is fitted with an axial and radial access port, with 10°

angular acceptance along the beam axis for reflectivity studies and 5° angular acceptance on the radial ports for fluorescence measurements (x-ray and optical).

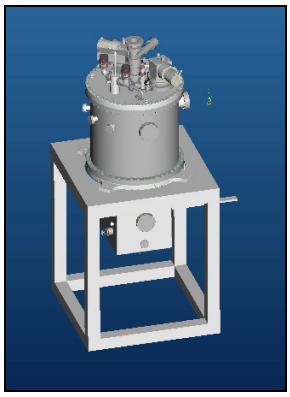

Figure 4.5.5-4. High-field magnet for the 4-ID-C spectroscopy branch (from Oxford Instruments).

Photoelectron Microscopy Station (existing): This existing instrument is an electrostatic PEEM used for magnetic imaging studies by using polarized absorption contrast with ~100-nm spatial resolution. Time-resolved imaging studies are possible by using pump-probe techniques to study domain dynamics. The instrument is equipped with a cryogenic sample stage for imaging between 25 and 325 K and has four-axis sample motion.

PES/SPM Station (future upgrade): This addition will be a new surface magnetism station combining high-resolution photoemission spectroscopy, scanning probe microscopy, and *in situ* prep and deposition. This instrument is for magnetic spectroscopy (absorption, photoelectron, and optical) experiments on ultraclean surfaces, with sample preparation and advanced surface analysis, all within the same UHV environment. The system is equipped with a high-resolution hemispherical electron spectrometer, variable temperature STM, and sample manipulator with four-axis motion (x, y, z, polar angle) with accuracies of 10 μm and 0.01°.

4.5.5.2 Hard X-ray Magnetic Spectroscopy

The upgrade of beamline 4-ID-D will enable x-ray absorption spectroscopy studies of electronic and magnetic materials under simultaneous high field (10 T) and pressure (>1 Mbar) conditions. An Apple-II insertion device will replace the current linear undulator in order to generate hard x-rays with variable polarization state directly at the source, circumventing the limitations of phase-retarding optics and resulting in large gains in flux and degree of x-ray polarization. New focusing optics will be installed to enhance high-pressure capabilities. Lastly, a large-bore superconducting magnet (10 T) capable of accommodating a membrane-driven diamond-anvil cell will be procured to enable x-ray magnetic circular/linear dichroism measurements under simultaneous extreme pressure and high magnetic field conditions.

4.5.5.2.1 Scientific Scope

Manipulating electronic states in condensed matter by driving atoms closer together at extreme pressure conditions provides a route to novel electronic materials with entirely different bulk properties. Recent developments in high-pressure methods now allow for changing inter-atomic distances in solids by up to a factor of two, with related density increases of over an order of magnitude. The resulting changes in bonding properties give rise to a host of new physical properties, including the creation of metals from materials possessing significant band gaps and the triggering of cooperative electronic

phenomena, such as the ordering of electrons into novel magnetic, ferroelectric, and superconducting states. Although the electronic structure and crystal structure are intimately connected, pressure-induced changes in electronic structure do not necessarily require a change in structural symmetry. Hence, determination of a material's structure and compressibility oftentimes does not provide sufficient information for unraveling important changes in electronic properties. X-ray absorption spectroscopy can offer unique information related to these phenomena, as it selectively probes the outer bonding electrons.

The element- and orbital-specificity properties inherent to the x-ray absorption process allow probing changes in valence state, orbital-occupancies, hybridization, charge transfer, and electronic ordering under extreme pressure conditions. Furthermore, when coupling the high-pressure environment with linearly and circularly polarized x-ray radiation and magnetic fields, the related x-ray magnetic linear and circular dichroism techniques can be used to yield information on spin-polarized electronic structure, orbital magnetization, and magnetic ordering. Recent efforts at beamline 4-ID-D demonstrated that the combined external stimuli of pressure (< 0.25 Mbar), magnetic fields (< 0.5 T) and moderately low temperature (10 K) can provide key insights into the inner workings of magnetocaloric materials [4.5.5-5], colossal magneto-resistive manganites (see Figure 4.5.5-5) [4.5.5-6], and materials for spintronics applications [4.5.5-7]. The upgrade of 4-ID-D will create a state-of-the-art x-ray spectroscopy capability by expanding the (P,H,T) range for transformational studies of electronic/magnetic materials to higher pressures (1-2 Mbar), higher fields (10 Tesla), and lower temperatures (2 K). The expanded pressure range allows exploration of phase diagrams into unchartered territory, especially in systems with relatively small compressibility and large energy scales (~0.5-1 eV) that are characteristic of many complex oxides. Furthermore, high pressures can induce novel ground states through the competition between spin-orbit and Coulomb interactions, which are particularly relevant in quasi-localized electronic systems such as actinides [4.5.5-8]. The new instrumentation for high-pressure x-ray spectroscopy under magnetic fields will be unique at the APS, as it falls outside the scientific scope of the other high-pressure beamlines.

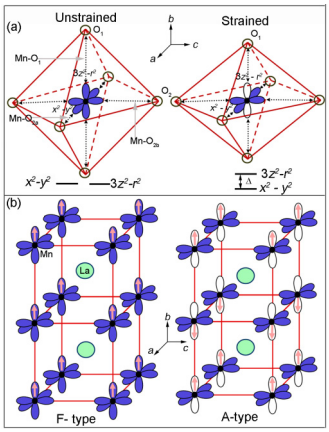

Figure 4.5.5-5. Redistribution of Mn 3d electronic states in CMR $La_{0.75}Ca_{0.25}MnO_3$ under pressure. The emergence of empty out-of-plane e_g states at high pressure suppresses ferromagnetic ordering and conductivity and promotes an insulating antiferromagnetic state.

4.5.5.2.2 Source Requirements

The experiments described above require a tunable (2.7- to 25-keV) source with variable polarization, such as an Apple-II device. Such an insertion device can generate CP x-rays directly at the source, circumventing the limitations of phase-retarding optics below about 5 keV (attenuation) and above 10 keV (small Bragg angles and low P_c). This source will enable XMCD/XMLD studies at the $L_{2,3}$ edges of 4d elements and $M_{2,3,4,5}$ absorption edges of 5d and 5f elements in the 2.7- to 5.0-keV range, and

the $L_{2,3}$ edges of 5f and 5d elements in the 10- to 25-keV range. It is currently either not possible or extremely inefficient to conduct these studies at 4-ID-D (see Table 4.5.5-2). In circular mode, the Apple-II device generates CP x-rays with Pc ~1 in its first harmonic (2.7-11 keV), which also includes the $L_{2,3}$ edges of rare-earths and the K-edges of first-row transition metals, both of which are heavily studied at this beamline. The increased flux and reduced asymmetry between incident left- and right-CP x-ray intensity relative to phase retarder optics will result in significant improvements to data quality and reduced data acquisition time. The Apple-II device generates elliptically polarized x-rays (Pc ~0.82) in the 10- to 25-keV range by using third and fifth harmonics, enabling XMCD/XMLD studies at the $L_{2,3}$ edges of 5d elements and actinides (Figure 4.5.5-6). Furthermore, this device does not produce on-axis higher harmonics in circular mode, which is an added advantage for high-pressure experimentation where the strong attenuation makes the measurements very sensitive to the harmonic contamination. A quasi-periodic (QP) option is being explored for harmonic rejection in linear mode. The QP option will reduce higher harmonic content to ~5%, albeit with a 20% reduction in 1st harmonic intensity. Phase-retarding optics will remain at the beamline for cases where fast helicity-switching, coupled with lock-in detection, is desirable (i.e., dichroic signals below 100 ppm).

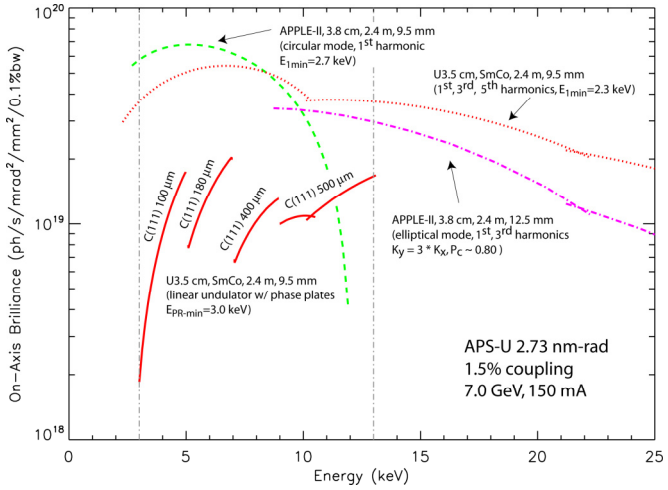

Figure 4.5.5-6. On-axis brilliance tuning curves for Apple-II undulator, compared with SmCo linear undulator with and without phase plates. The thickness of diamond phase plates currently used in the 3- to 13-keV range are also indicated. The Apple device covers 2.7–11 keV in circular mode and 10-25 keV in elliptical mode (Pc>82%).

4.5.5.2.3 Beamline Description

A diagram of the existing and specified components for the 4-ID-B,-D beamline are shown in Figure 4.5.5-7. All of the optics in the 4-ID-B station (i.e., slits, monochromator, phase retarders, and mirrors) will remain in their current locations and will continue to be used. The new/modified components are outlined in red. The current toroidal mirror will serve as a virtual source for the new KB focusing mirrors to be installed in the D station (see section 4.5.5.2.4). These mirrors will accept the full undulator beam and focus it down to a size of ~10 × 10 µm^2 for high-pressure spectroscopy measurements. A 10 Tesla superconducting magnet will be used for XANES/XMCD/XMLD studies at extreme pressures and fields under low-temperature conditions. The existing psi-diffractometer will remain in the station for resonant magnetic scattering experiments with circularly polarized x-rays (magnetic reflectivity for studies of interfacial magnetism and magnetic DAFS for studies of site-specific magnetism). To accommodate the diffractometer, new KB mirrors, superconducting magnet, and

cryogenics in the experiment station 4-ID-D will be expanded in all directions with a second door added in the outboard side.

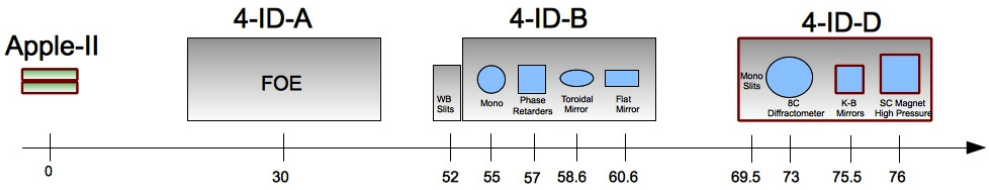

Figure 4.5.5-7. Optical layout for hard x-ray beamline 4-ID-B/D. New components are highlighted in red.

4.5.5.2.4 Optics and Instrumentation Enhancements

The current focusing at 4-ID-D (100 × 200 μm^2) provided by the toroidal mirror precludes efficient high-pressure XMCD/XMLD experiments to be carried out above 0.3 Mbar (30 GPa). At higher pressures, the reduced sample size necessitates beam slitting and results in compromised flux on the sample. This fact, coupled with the attenuation in phase-retarding optics and diamond anvils, renders experiments unfeasible at higher pressures. Experiments at or above 1 Mbar require ~10 × 10 μm^2 polarized x-ray beams. As part of this upgrade, 300-mm KB mirrors will be permanently installed in the D station to provide the required level of focusing (total demagnification × 30). The existing toroidal mirror will be used to create separate virtual sources in the horizontal (at 70.6-m) and vertical (at 86-m) directions (see Figure 4.5.5-8). The KB pair will feature different coatings (Pd & uncoated Si) for optimizing flux and harmonic rejection. This tandem configuration accepts the whole undulator beam and increases the flux available for 1-Mbar experiments by a factor of 240 (see Table 4.5.5-3).

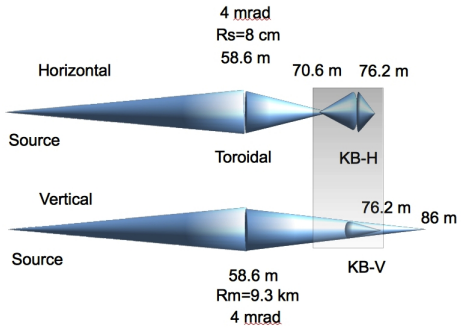

Figure 4.5.5-8. Schematic of tandem focusing using existing toroidal mirror and a 300-mm KB pair. The total demagnification is ~30 in both directions. Hatched area shows the boundaries of the expanded 4-ID-D experimental hutch.

The final major piece of equipment envisioned for this beamline is a large-bore superconducting magnet for high-pressure XMCD studies. This magnet will be cryogen-free in that it will be cooled down to its operating temperatures of ~4 K using a closed-cycle cryostat. Active shielding will be included to reduce stray fields to below 5 Gauss within 1.0 m from the magnet center in order to minimize shielding requirements on detectors and electronics. It will be a solenoid geometry with an inner warm bore of ~80 mm, large enough to accommodate a membrane-driven pressure cell. Multiple temperature inserts will enable sample cooling down to 2 K with a pressure cell and 300 mK without.

4.5.5.3 Anticipated Performance

The anticipated performance and expected flux density gains for high-pressure spectroscopy studies are summarized in the tables below.

Table 4.5.5-2. Expected Beamline Performance

Feature	Expected Values
Energy range	2.7-25 keV
Resolution	1.4×10^{-4} ΔE/E
Beam size	10×10 μm^2 with KB; 100×200 μm^2 without KB
Flux	2×10^{13} photons/s at 8 keV
Polarization	Circular and linear (any direction); fast (20-Hz) switching using PRs

Table 4.5.5-3. Flux Gains Realized by (1) Apple-II vs. Phase-Retarding Optics and (2) KB Focusing Optics

Energy range (keV)	Polarized flux gain (factor) from Apple-II	Polarized flux gain (factor) by focusing (P>0.3 Mbar)	Total flux gain (factor)
3-5	5-50	240	1200-12,000
6-10	2-10	240	480-2400
11-16	3-5	240	720-1200
17-25	Expanded energy range previously unavailable.		

4.5.5.4 References

[4.5.5-1] D.J. Keavney et al., Phys. Rev. Lett. **91**, 187203 (2003).

[4.5.5-2] Y. Tokura, Colossal Magnetoresistive Oxides, (Gordon and Breach Science, 2000).

[4.5.5-3] J.W. Freeland et al., Rev. of Sci. Instrum. **73**, 1408 (2002).

[4.5.5-4] Conceptual Design Report: Intermediate Energy X-Ray Collaborative Development Team (2009), http://www.aps.anl.gov/Sector4/IEX/IEX_CDR.pdf.

[4.5.5-5] Y.C. Tseng et al., Phys. Rev. B **78**, 214433 (2008).

[4.5.5-6] Y. Ding et al., Phys. Rev. Lett. **102**, 237201 (2009).

[4.5.5-7] N. Souza-Neto et al., Phys. Rev. Lett. **102**, 057206 (2009).

[4.5.5-8] K. Moore et al., Phys. Rev. B **76**, 073105 (2007).

4.6 Interfaces in Complex Systems

4.6.1 Introduction

Interfaces play a critical role in nearly every aspect of the science and technology involving condensed matter. The loss of translational invariance at an interface creates a nanometer-thick region in which the physical and chemical properties are modified from bulk properties. The reduced atomic coordination at interfaces (e.g., at terrace, step, and kink sites) modifies the intrinsic reactivity of these sites and simultaneously increases their accessibility to reactants and can lead to structural or compositional modification, such as symmetry-breaking surface reconstructions. Most generally, interfaces provide well-defined templates for the creation of new materials and/or sites for heterogeneous chemical reactions. The elementary processes that take place at interfaces (e.g., adsorption, growth/dissolution, solid state transformations/diffusion, charge transfer) control a vast array of industrial and commercial applications (e.g., novel materials growth, heterogeneous catalysis, corrosion inhibition, energy storage) and provide key controls over many processes in nature (biomineralization, contaminant sequestration, photosynthesis) and areas of overlap (e.g., biomimetic materials and geological repositories for spent nuclear fuel).

As a result, interfaces are central to many diverse fields of study. These include: *materials science*, where the control of the composition and structure of an interface can lead to new desirable materials properties; *geochemistry and environmental science*, where the transport and sequestration of nutrients and contaminants is often controlled by their interactions with mineral surfaces; *chemical science*, where the heterogeneous reactivity of interfaces in "supported" catalysts creates facile pathways that promote chemical reactions; *energy science*, where robust energy-storage technologies currently rely on the passivating layers at solid-electrolyte interfaces to prevent catastrophic failure; *nanoscience*, where the nanomaterial properties are modified by their surfaces due to their large surface-to-volume ratios; and *bioscience*, in which membrane proteins actively maintain chemical gradients necessary for sustaining life. Solid-solid, solid-fluid, or fluid-fluid interfaces are all relevant. The solids might be either "hard" (e.g., metals or semi-conductors) or "soft" (e.g., organic- molecular or model membranes), and the fluids might range from an aqueous solution to liquid metals or supercritical fluids.

Hence, modern interest in interfacial science is directly coupled with the need to understand and study interfaces within realistic environments. X-rays offer a unique opportunity to penetrate through many complex environments to probe the structure and chemistry of surfaces and internal boundaries in environments where other characterization tools are not appropriate. High-brilliance x-ray sources, such as the APS, enable these *in situ* studies and permit real-time investigations. The competitive advantage of the APS in hard x-ray brilliance is well suited to further development of this area, so the proposals that follow will exploit the characteristics of the upgraded APS source and build upon specific expertise of the research team members to produce a number of capabilities that will be unique worldwide to enable transformative research in interface science.

4.6.2 X-ray Interface Science Beamline [U1.04.02.11]

By its very nature, interfacial science brings together a diverse community with interests in catalysis, biomembranes, oxide film growth, semiconductors, geochemistry, surface physics, corrosion, nanoscience, tribology, electrochemistry, and in the development of the next generation of energy-related technologies. One of many grand challenges in this interdisciplinary field is to understand through observation and control the organization of atoms and molecules at well-defined surfaces in complex environments. Increasingly sophisticated *in situ* x-ray methods that exploit the inherent spatial, temporal, and spectral properties of undulator radiation are being developed to meet these challenges. A dedicated X-ray Interfacial Science (XIS) facility at a sector of the APS will fully exploit the unique capabilities of the APS to advance our understanding of this area. Within the baseline scope of the APS Upgrade plan, one new beamline will be designed, constructed, and operated in a new sector dedicated to interface science. This beamline will be widely tunable and will provide a flexible diffractometer instrument that will enable state-of-the-art x-ray interface scattering studies.

This new beamline also forms the core of a broader development plan for a comprehensive Interface Science 'Village' facility. The comprehensive XIS facility is considered within the alternate contingent scope of the APS Upgrade and will be described in a later section of this report.

4.6.2.1 Scientific Scope

Because of favorable cross sections, x-rays offer a unique opportunity to penetrate many complex environments (gas, liquid, or solid thin-film overlayers) to probe the structure and chemistry of surfaces and internal boundaries from macroscopic lengths down to the atomic level, in environments where traditional electron and other scanning probes are not applicable. High-brilliance x-ray sources, such as the APS, enable these *in situ* studies, permit real-time investigations to elucidate thin-film growth mechanisms, and allow molecular scale studies of important chemical interactions at internal boundaries using scattering, diffraction, resonance and absorption, fluorescence, standing-wave, and imaging techniques.

Interfacial Reactivity in Complex Environments: Reactive interfaces are found in a broad spectrum of technical fields ranging from energy storage (e.g., batteries [4.6.2-1]) to electrocatalysis (e.g., fuel cells [4.6.2-2]), geochemistry [4.6.2-3], hydrogen storage, catalysis [4.6.2-4] and corrosion at liquid-solid /gas-solid interfaces [4.6.2-5, 4.6.2-6]. Intrinsic to each of these areas are the divergent spatial (~Å-scale to >1 μm) and temporal scales (from ~1 ps to ~1 s) [4.6.2-7] describing interfacial reactivity. The coupling of these disparate spatial and temporal scales can lead to unexpected complexities that have been largely unexplored.

Electrochemical and Catalytic Interfaces: Understanding nanoscale mechanisms is the best way to transform a current trial-and-error approach to a knowledge-based rational design approach in discovering new revolutionary electrocatalysts, gas catalysts, or energy storage materials. Heterogeneous catalysis and electrocatalysis, among the energy conversion and storage processes, are pure interfacial phenomena. Therefore, the use of surface/interface x-ray techniques has been and will be critical in accelerating our understanding of nanoscale physical and chemical properties occurring at the surfaces of catalysts. This static view of catalysts dominates our understanding of catalysts. However, recent x-ray studies point to a highly symbiotic interaction between the reactants and catalysts, where the reactants even actively modify the catalysts resulting in a significant change in catalytic activities [4.6.2-8].

Interfacial Geochemistry: The mineral-fluid interface is the principal site of low-temperature geochemical processes at and near Earth's surface and exerts a powerful influence on the natural geochemical cycles in our environment. Mineral-fluid interface processes effectively control the

compositions of ground waters, surface waters, and, to a large extent, the atmosphere. A fundamental understanding of this area is critical to develop a predictive molecular-scale understanding of geochemical and environmental processes. Specific examples include the consequences of energy-related activities, such as subsurface CO_2 disposal by deep injection of liquid CO_2 into depleted oil and gas reservoirs, and the long-term isolation of high-level nuclear waste.

Emergent Materials Properties at Interfaces: Interfaces are not simply the place where two materials meet, with each of them retaining its own properties. There are abrupt changes in chemical and electrostatic potentials, as well as a lattice-mismatch, that exert significant stress on the material. Ionic and electronic reconstructions can occur at the interfaces of compound semiconductor heterostructures [4.6.2-9] and oxides leading to the emergence of entirely new physical properties and phenomena including correlated electron behavior.

***In situ* Materials Synthesis:** There are new scientific initiatives to establish the framework needed to unite materials synthesis with *in situ* characterization and theory and modeling, in order to design and create breakthrough materials and molecules. Synthesis of new, complex oxide materials are particularly promising because spatial confinement and nanoscale coupling between different epitaxial layers can result in a rich variety of physical phenomena including ferroelectricity, magnetism, multiferroicity, electronic and ionic conductivity, superconductivity, and coupled electric, magnetic, elastic, and optical properties. Whether fabricated with traditional methods or with new approaches, *in situ* time-resolved materials growth or processing x-ray studies are essential for controlling materials structure and understanding the resultant properties.

Supported Metal Nanostructures: Understanding the behavior of materials created on the nanoscale is a new frontier in the science of materials, because the small size of nanoscale materials can lead to unprecedented physical and chemical properties. These properties are not only fascinating from the perspective of fundamental scientific understanding, but nanostructures also present novel building blocks that can be transformative for technological applications. New electronic states [4.6.2-10] appear due to the quantum confinement of the conduction electrons, and this can affect the overall energetics of the nanoparticle. Second, the interfacial energy makes a large contribution to the total energy, particularly given that the nanostructure must be supported at an interface. Interfacial effects can alter the internal structure, as well as the surface chemistry, even leading to new catalytic properties [4.6.2-6, 4.6.2-11]. Finally, all of these effects can lead to pronounced changes in the statistical mechanics and kinetic behavior of nanostructures as compared to conventional systems. Exploring these effects, which are poorly understood, will be a critical aspect of future research in nanoscience.

This broad range of scientific opportunities requires the development of complex experimental systems, and integration with an optimally designed x-ray scattering facility. Because the demands for x-ray interfacial science capabilities are widespread, a significant effort will be made to maximize the impact of the sector. The large community of users and the diversity of the envisioned specialized capabilities make it compelling to consider a large-scale facility consisting of 11 experimental stations and centralized support facilities and staff.

4.6.2.2 Source Requirement

The weak scattering signals from 2D interface structures require that the XIS beamline has an optimized beamline and source selection. The XIS beamline requires the brilliance of an undulator with a fully overlapping tuning curve for energies between 4.0 and 40 keV. By using the first, third, and fifth harmonics of a 3.0-cm-period undulator, high performance and excellent brilliance over the energy range of 5-40 keV is achieved. To access energies below 5 keV, and to provide additional flux for energies above 5 keV, a second undulator will be installed in the straight section. This will be a 3.1-cm-period undulator that will be installed on a revolver mount. Experiments such as time-resolved interface

scattering generally do not require specific x-ray energy and are often performed at 10 keV or at higher energies such as 30 keV. So, for this experiment class, an undulator with higher brightness at approximately 10 keV (with a third harmonic of approximately 30 keV) is highly desirable. The existing design for a 2.7-cm-period undulator will be also be installed on the revolver to enhance the brilliance and flux delivered to those experiments that do not require access to specific energies.

4.6.2.3 Beamline Description

The XIS ID beamline will be fully tunable from 4-40 keV and provide beam to any one of three experimental stations that are dedicated to interfacial science studies using resonant scattering, interface diffraction, and various spectroscopy techniques. An extended first optics enclosure (ID-A) includes a cryo-cooled Si double-crystal monochromator and a cryo-cooled multilayer monochromator, and mirror optics are located in a downstream enclosure (ID-B). An instrumented experiment station (ID-D) is specially designed for studies of interfaces in complex environments (ICE). This ICE instrument will include a flexible general diffractometer with easily detachable specialized environmental cells or chambers and integrated gas-handling systems.

The beamline plans also include a hutch for x-ray interfacial microscopy (XRIM) (ID-C) and a hutch for real-time *in situ* environmental and materials fabrication and characterization (ID-E) with advanced and oxide MBE growth. These instruments will be developed in partnership with the user community. The floor plan for the XIS sector is depicted in Figure 4.6.2-1.

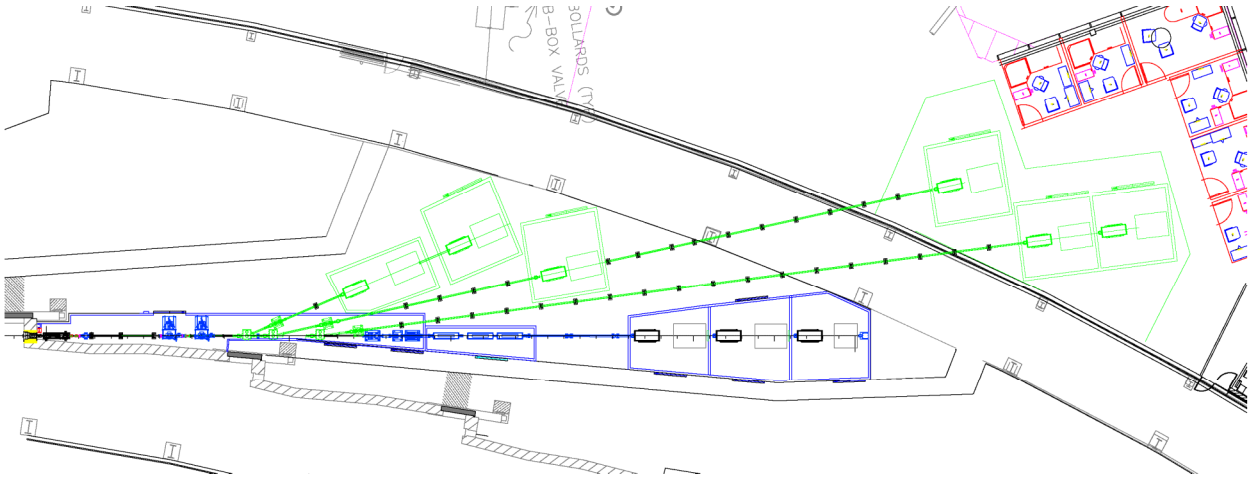

Figure 4.6.2-1. Sector layout for the XIS beamline (shown in blue), and the long-term plans to add a series of fixed-angle beamlines that complete a comprehensive Interface Science 'Village' (shown in green). The XIS beamline is widely tunable from 4.0 – 40 keV, and the fixed angle beamlines will operate at 10 keV and 30 keV.

4.6.2.4 Optics

The XIS beamline requires high performance over a very demanding energy range. To meet the requirements of diverse scientific objectives, this beamline will use a flexible, high-performance optical design. To select the monochromatic bandpass, a cryogenically cooled Si (111) crystal pair will be used. The energy bandwidth provided by this beamline optic is well matched to the lifetime broadened core hole width for all the K-shells between 4 and 40 keV and is substantially better than widths for the accessible L-shells. This is critically important for high resolution and for anomalous scattering experiments. Resonance is an important contrast mechanism often used to locate and identify atomic

species at buried interfaces or at surfaces in complex liquid or gaseous environments. The monochromator will use a fixed offset design and will include robust scanning capability to facilitate resonant studies. The first, third, or fifth harmonic energy of the undulator(s) will be used to span the operating energy range.

Because some interface science measurements are flux-limited and do not require excellent energy resolution, an additional multilayer monochromator is included in the beamline design. A pair of multilayer optics with 2-nm d-spacing (1% bandwidth) can produce an increase in photon flux of at least a factor of 64. This dramatic enhancement in flux performance will provide significantly increased dynamic range for imaging techniques, such as XRIM, or for studying surface kinetics/dynamics with time-resolved scattering studies. To provide flexibility with regard to beam focusing or collimation, dynamically bent mirrors are used. The mirrors also provide harmonic rejection. The first mirror will use a large horizontally deflecting surface with two material stripes, and will operate at 2 mrad. An Rh stripe will be used for energies as large as 20 keV, and a Pt stripe will be used for energies up to 40 keV. The mirror figure will be adjusted dynamically to allow horizontal focusing to any of the three experimental hutches or to provide a horizontally collimating (parallel) beam. This mirror will be located at ~46 m from the source and will require 2-mrad incidence. To accept the full horizontal beam of the central cone at this location will require a very long mirror length (~1.6 m).

This beamline is designed to operate with vertically deflecting mirrors that improve the harmonic rejection performance and provide vertical focusing or collimation at the experimental locations. Dynamically bendable mirrors with four coated stripes of various materials (Si, Cr, Rh, and Pt) provide excellent reflectivity and harmonic rejection for two different incident angles. For example, when operated at 3.5 mrad, the mirror pair is efficient for energies up to about 22 keV. For higher energies, the mirror pair will operate at 2 mrad. Because this beamline operates at only two distinct mirror angles, it is expected that wide energy changes will be easily achieved without affecting the beamline focusing performance. The quantitative spectral analysis for the high reflectivity of the fundamental wavelength and harmonic rejection is shown in Figure 4.6.2-2.

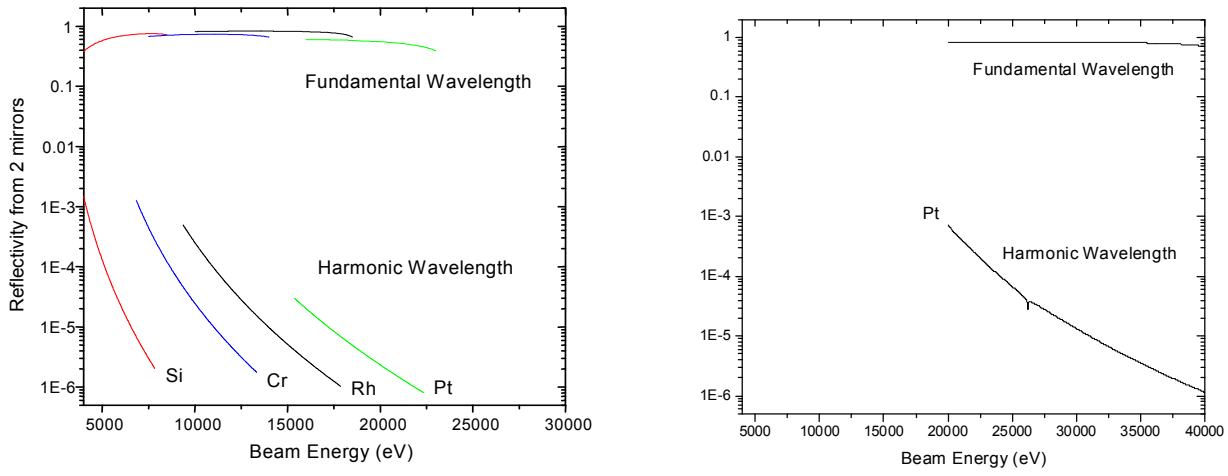

Figure 4.6.2-2. Mirror reflectivity shows that good peak throughput and harmonic rejection can be achieved over the range 4.0 keV – 22 keV for 3.5 mrad without changing mirror angle. Above ~22 keV, the mirrors perform well for 2.0-mrad incidence.

The XIS beamline may be operated in one of several focusing geometries. The mirrors may be set for focusing at the experiment location in any of the three hutches with the demagnification shown in Table 4.6.2-1. This mode is often used for surface and interface diffraction experiments that require

moderately small beams and high resolution. For focusing to smaller beam sizes, each experiment will include additional focusing capability, such as KB mirrors or zone plates that can be inserted as needed. For experiments such as X-ray Standing Waves, high collimation is required and the vertically deflecting mirror pair may be set to collimating geometry or optionally may be removed from the beamline.

4.6.2.5 Anticipated Performance

In the design and development of the beamline capabilities, particular attention will be given to x-ray beam stability and optical figure errors to better preserve the brightness of the APS undulator sources. This will allow for measurements that require outstanding beam stability and spatial resolution. The APS orbit stability is significantly better today than the original design specifications for the APS accelerator, and the emittance of the normal operation lattice with 1% coupling is 2.9 nm-rad. The size and stability of the beam delivered to the experimental hutches is generally limited by beamline optics and instabilities and not by APS accelerator beam motions or source size. The objective for XIS is to preserve the source flux and brightness as much as is practical through careful design and construction considerations. In addition, to enable studies that exploit coherent scattering techniques such as surface x-ray photon correlation spectroscopy (XPCS) and coherent diffractive imaging (CDI), efforts will be made to preserve the coherent flux delivered to the experimental hutches.

The typical source size and divergence at an APS straight section is 269.5 μm and 11.3 μrad in the horizontal plane, and 14.8 μm and 3.9 μrad in the vertical plane. The entire central cone of the undulator radiation will be accepted, so each optical element will be sized and cooled to accept the full beam (4σ of the source). The source demagnification at the experiment locations is between 2.3 and 5.5, so an estimate of the beam sizes and divergences at sample positions in the experimental stations can be made. The figure errors of the mirrors and other optical elements contribute the broadening of the beam size. For example, because the vertical source size is so small, the vertical beam size at the sample positions will be determined by the figure errors or aberrations of the optical elements. However, the horizontal beam size will be largely affected by the demagnification and the source size. Table 4.6.2-1 shows the demagnification and the beam sizes (FWHM) at each experimental station. These estimated beam sizes assume 1-μrad figure errors in the focusing optics. To estimate the focusing provided by local K-B mirror optics, a secondary source located 3 m upstream of the experiment sample location was assumed.

Table 4.6.2-1. Demagnification and the Beam Sizes (FWHM)

	Beamline Optics Focusing				Local K-B Mirror Focusing	
	Horiz. Demag.	Vert. Demag.	H Beam Size (μm)	V Beam Size (μm)	H Beam Size (μm)	V Beam Size (μm)
ID-C	4.4	5.5	164	63	18	7
ID-D	3	3.6	235	97	26	11
ID-E	2.3	2.7	306	130	34	15

Projecting reliable photon flux density at experimental stations requires full ray tracing. However, an estimate of the flux can be made from the experiences at existing beamlines.

4.6.2.6 Instrumentation

The range of capabilities provided with the ICE instrument will make it unique in the world and will enable forefront research in a wide range of interfacial sciences. The basic layout of the instrument, shown in Figure 4.6.2-3, incorporates a modular architecture. The modular aspect is important because

different chemistries can be highly incompatible and yet a vibrant user program requires the flexibility to rapidly switch between different environments. There are three main components to the instrument design: the diffractometer, the gas and liquid handling systems, and environmental chambers that must be integrated together. Appropriate gas/liquid monitoring and alarm systems are required to assure safe operation of the instrument.

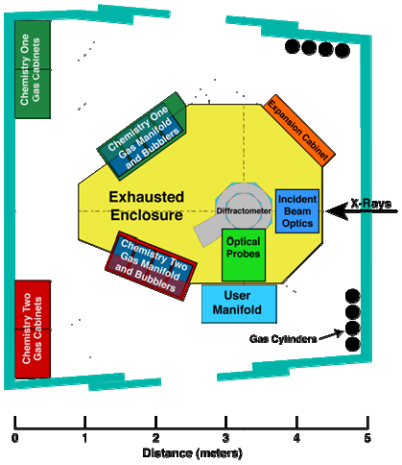

Figure 4.6.2-3. Concept for a general diffractometer with decoupled detector and sample motions for improved stability and flexibility. Robotic actuation will improve area detector flexibility for studies of interfaces in complex environments.

The ICE instrument will have two independent detector arms: a high-stability detector arm for high-resolution and imaging systems and a versatile robotic detector mover such as that used at LCLS for high speed, flexible diffraction using area detectors. The high-stability arm will be configured similar to a traditional diffractometer arm and will move sophisticated detectors with high accuracy but at fairly low speed. The robotic detector arm will employ a commercial robot arm to move a Pilatus area detector with 50-micron position repeatability (1/3 of a pixel) and with an angular resolution of 0.003° with the detector at 1 meter from the sample. This robotic arm will be mounted from an engineered support near the hutch roof to maximize the accessible parameter space and so that it can be moved out of the way to allow easy access to the sample chamber environment.

The sample and chamber mount will utilize a combination of a high-resolution goniometer to provide full 360° motion about the vertical axis together with a high-load hexapod for sample positioning in the three spatial coordinates and the two horizontal rotational axes with very high resolution and repeatability. This system will handle large sample chambers (< 200 kg), tilt them by ±15° degrees, and translate them ±25 mm vertically and ±50 mm horizontally. The hexapod mounts to a pair of high-load diffractometer circles that enable wide access to the sample reciprocal space.

The XIS facility will provide two sample chambers, for high and low x-ray energy studies, small environmental cells for heating and cooling, and a series of flow cells for surface studies in aqueous solutions. One chamber will have beryllium windows for ultra-high vacuum, low background and low photon energy measurements, along with provisions for optical and conductivity measurements. A second chamber will have a quartz tube reaction zone for chemical reaction studies. Both chambers will have heaters available for use in reducing or oxidizing atmospheres at temperatures up to 1000°C. The ICE instrument is capable of supporting a wide range of specialized environment chambers (e.g., user-supplied electrochemical cells and specialized atomic-layer deposition chambers).

The sophisticated gas/liquid handling system provides flexibility in choice of sample environment and computer control of gas composition so that complicated exposure sequences can be efficiently

implemented. This system will have channels for either directly flowing gasses or for flow employing bubblers. The reactive gas and bubbler channels have matched flow so that a nonreactive and reactive stream can be easily switched between a vent line that bypasses the chamber and a line to the chamber. Active pressure balancing between the vent and chamber lines will maintain uniform flows. The gas plumbing system will have two gas cabinets to separate incompatible chemistries for safety purposes. Permanent lines for standard gasses (Ar, He, N_2, O_2, CH_4, CO_2, CO, and H_2) along with four channels for experiment specific gasses, two of which will include the capacity for a dilution flow, are planned.

4.6.2.7 X-Ray Interface Science Fixed Angle Upgrade [CAS]

Many interface science studies do not require specific x-ray energies. Time-resolved *in situ* materials growth and processing studies can usually be effectively executed with a single x-ray energy. However, these studies require large, complex chamber systems for elaborate growth studies such as oxide molecular beam epitaxy (MBE). To effectively address these scientific opportunities, a large comprehensive facility dedicated to x-ray interface science is proposed. This comprehensive XIS 'village' facility will have two canted undulators producing four separate x-ray beams: one with variable energy and three with selectable fixed energies. The XIS facility will provide state-of-the-art x-ray scattering, spectroscopy, and microscopy tools for multilength-scale (from Ångstroms to microns), element-specific studies of vacuum/solid, gas/solid, liquid/solid, solid/solid interfaces and supported nanostructures. In addition to general-purpose spectrometers, custom-designed spectrometers developed in partnership with the user community will provide controlled environment and specialized growth chambers for sophisticated *in situ* studies.

4.6.2.7.1 Source Requirement

The XIS facility is based on a large suite of instruments that exploit the x-ray brilliance and hard x-ray flux of the APS. A canted undulator front-end source is required to supply radiation to two undulator beamlines. The XIS beamline requires an undulator with a fully overlapping tuning curve for energies between 4 and 40 keV using the first, third, and fifth harmonics, providing high performance and excellent brilliance over this energy range. The second undulator beamline will supply x-rays for three side-diffracting branch lines that will have fixed-angle (energy) operation, and therefore do not require overlapping first and third harmonics. So a 2.7-cm-period undulator with higher brightness at approximately 10 keV (with a third harmonic of approximately 30 keV) is better matched to the beamline design requirements. To permit other selectable energies on the fixed-angle beamlines, different crystals may be installed on the side-diffracting monochromator. This requires that the insertion device also has a variable energy spectrum. So, in addition to the 2.7-cm-period device, a 3.1-cm-period undulator will also be available on a revolver mount.

4.6.2.7.2 Beamline Descriptions

The canted ID beamline will provide beam to three horizontal diffracting branches that can accept x-rays simultaneously at fixed angles (energies). The experimental stations on each branch line are tandem with a flexible, general diffractometer in the upstream station and a specialized end station (perhaps a complex growth or processing chamber). The general diffractometers will accept small, easily detachable specialized environmental cells or chambers for *in situ* studies in reactive environments, flow-cell environments for liquid phase studies, and growth chambers for fundamental studies of materials synthesis. The layout for the sector is shown in Figure 4.6.2-1. This layout provides a large first optics enclosure for the canted undulator line that will contain the double-crystal monochromator for the fully tunable beamline, and the three single-crystal monochromators that will provide x-rays to the side-scattering branch lines. Each line will include a monochromatic shutter so that each operating experiment

can be accessed without affecting the other branch lines. In all, there will be nine experimental hutches on the ID line where four experiments can be performed simultaneously. Considered within the alternate contingent scope of the APS Upgrade are the three side-diffracting branch beamlines, optics, hutches, and three general diffraction instruments optimized and instrumented for interface science investigations. The highly specialized growth and processing chambers in the end stations require formation of partnerships to define the science, specify the instrument performance requirements, and help to develop an operation and procurement strategy. These highly specialized chambers remain outside the contingent additional scope.

4.6.2.7.3 Optics

Fixed-Angle Beamline Branch Line #1 (10 keV): This branch beamline will deliver 10-keV x-rays to tandem experimental stations (ID-F and ID-G) using a horizontal diffracting Si(111) monochromator to horizontally diffract the x-ray beam by 22.8° from the incident beam direction. The first harmonic of an optimized undulator source will be used. This monochromator crystal must be sufficiently thin to allow high transmission of the third-order harmonic for use in the downstream branch beamlines. To allow 85% transmission of the 30-keV photons, the Si must be no thicker than 100 μm. The Si monochromator crystal will be cooled with liquid nitrogen to perform with the high-power incoming beam. The development of a high-performance thin cryocooled Si monochromator will require R&D activities prior to commissioning. Alternatives to the thin Si crystal include using diamond rather than Si, or allowing a thick Si monochromator crystal to cut the incoming undulator beam in half and let the remaining half pass through to the subsequent branch line monochromators. The disadvantage of these alternatives is that the photon fluxes at all the side-bouncing monochromators will be significantly reduced. The third alternative employs a Laue Si(111) monochromator that will allow 86% transmission with a 0.5-mm-thick Si crystal. However, this will result in a 50% reduction of flux for branch line #1.

The fixed energy operation of the beamline permits use of Be compound refractive lenses (CRLs) for focusing to either experimental location along the beamline. The CRL focal length depends inversely on δ (decrement of index of refraction), which in turn depends on $1/E^2$. Although the focused point for 10 keV and 30 keV (the third harmonics) will be quite different, and slitting down the beam at the first harmonic focal point will accomplish some harmonic rejection, this rejection ratio is inadequate. So an additional harmonic rejection mirror will be required. Transmission through a parabolic Be CRL (R=0.6 mm, N=10/6) will be 62% and 77% for the upstream and downstream stations, respectively.

Fixed-Angle Beamline Branch Line #2 (30 keV): The second side-diffracting branch line will deliver 30-keV x-rays (to ID-H and ID-I) within the monochromator bandpass from the broad third harmonic of the undulator and allow the remainder of the spectrum to pass through to the subsequent branch line monochromator. A diamond (111) crystal will be employed with a deflection angle of approximately 11.51° from the incident beam direction. For this monochromator, a Bragg-diffracting geometry with water cooling will be utilized to avoid the complex engineering and logistics for the cryocooled monochromator.

An alternative is to use a Si(220) crystal with a diffracting angle of approximately 12.35°. A minor adjustment in the XIS sector layout will allow the change of the crystal from diamond to Si for the branch #2 monochromator.

A pair of dynamically bent, Pt-coated K-B mirrors will be used to focus (or collimate) the beam and to provide adequate harmonic rejection. The mirrors will be large enough to accept the entire central cone of radiation. A small vertically reflecting steering mirror will be located in each experimental station to level the beam.

Fixed-Angle Beamline Branch Line #3 (30 keV): The branch line #2 monochromator transmits a large fraction of the undulator third harmonic peak that is not within the bandwidth diffracted by the

C(111) crystal (to ID-J and ID-K). So, the final branch beamline will effectively use a wavelength that is close to but not the same as the branch #2 operational energy. For example, a difference of 10 eV is well within the harmonic envelope and well outside the notch removed by the C(111) diffraction. The final side-diffracting branch line will deliver x-rays at approximately 7.55^{o} from the incident beam direction. This results in 30.01-keV x-rays when using a Si(111) monochromator and the third harmonic of an optimized undulator source. A pair of dynamically bent, Pt-coated K-B mirrors will be used to focus (or collimate) the beam and to provide adequate harmonic rejection. The mirrors will be large enough to accept the entire central cone of radiation. A small vertically reflecting steering mirror will be located in each experimental station to level the beam.

Although each beamline is at a fixed angle from the incident beam direction, additional crystals may be included for each branch line so that different energies might be selected, as shown in Table 4.6.2-2. With alternate crystals, it may not be possible to effectively operate all three branch lines at the same time.

Table 4.6.2-2. Available Photon Energies (keV) with Alternate Crystals
(The fixed beamline angles are shown in parenthesis.)

	Si(111)	**C(111)**	**Si(220)**
Branch Line #1 (22.8)	10.0	15.2	16.3
Branch Line #2 (11.5)	19.7	30.0	32.2
Branch Line #3 (7.55)	30.01	45.8	49.0

A multilayer monochromator can be also implemented on the fixed-angle branch beamlines. For example, a multilayer optic with 1-nm d-spacing will deliver 9.4 keV on the fixed branch #3 for use with experiments that are flux-limited and do not require excellent energy resolution (such as many time-resolved or imaging studies). The choices of additional alternate optics for the fixed-angle beamlines will be carefully studied.

4.6.2.7.4 Anticipated Performance

A crucial factor is the bandwidth of the monochromator, which is determined by the crystal Darwin width. The polarization is also a factor for the horizontally diffracting monochromators of the side branch lines, where the reduction of flux is noticeable at lower energies. Table 4.6.2-3 shows the Darwin width and the polarization factors.

Table 4.2.6-3. Darwin Width and Polarization Factor for XIS Fixed Angle Beamlines

	Beamline Branch	#1	#2	#3
Darwin Width	10 keV (μrad)	26		
	30 keV (μrad)		5.9	8.5
Polarization Factor		0.85	0.96	0.98

As part of the APS-U project, beamlines are being designed for a ring current up to 200 mA. The cryocooled Si(111) double-crystal monochromators are expected to provide photon flux in excess of 10^{13} photons/s from 10 to 30 keV. Branch line #2 (30 keV) will deliver about 70% of the photon flux compared to branch line #3 because the diamond (111) crystal has a narrower Darwin width. The flux available at branch line #3 is also reduced to 85% by the absorption of the upstream branch #2 Si monochromator. And the branch #1 flux is reduced to 85% by the polarization factor. So, in all cases, there are only slight reductions of the delivered flux to the experiment locations, and excellent flux performance is anticipated for each beamline.

The undulator beamline optics with improved focusing are needed to illuminate smaller samples with higher flux and improved signal-to-noise ratios. Wherever possible, K-B mirrors or zone plates will be used in conjunction with secondary sources formed by beamline slits and the primary focusing optics. Through this approach, there will be further improvement of the optical performance stated above.

4.6.2.7.5 Instrumentation

The XIS facility will provide a large suite of state-of-the-art instruments for interface x-ray scattering, spectroscopy, and microscopy. The tandem design for each beamline will accommodate a general diffractometer in the upstream experimental hutch. These instruments will mount small, easily detachable standardized sample environmental cells and chambers, utilize new 2D detector configurations, and provide infrastructure for reactive gas experiments. Each will permit high-resolution measurements and incorporate rapid-scanning features. New 2D detectors, local focusing capabilities, and multiple detector schemes will be integrated with each instrument.

Although each general diffractometer will support interchangeable sample environments, each instrument will be optimized for somewhat specialized applications. For example, the general diffractometer in the clean room area in the LOM (ID-J) will focus on nanoscience applications, the general diffractometer on the high-energy side-diffraction branch #2 line will concentrate on liquid phase environments (ID-H), and the general instrument on the tunable beamline will be versatile for studies that require resonance or energy tunability (ID-D).

For these general diffraction instruments, conventional large-scale multicircle diffractometers with psi/kappa geometry or more traditional Huber 6+2 geometry will be considered (Figure 4.6.2-3). However, new concepts for separating detector motions from the sample goniometer using robotic detector arm actuation with 6 degrees of freedom will also be explored. For example, a kappa geometry goniometer for the sample and environment cell and a robotic detector actuation provides flexibility in the orientation of the surface normal and stability through decoupling of the detector and sample motions. Since the kappa geometry restricts the space available for environmental chambers, an alternate scheme with two orthogonal sample rotations can be combined with robotic detector actuation to allow very large incoming and outgoing angles to access large momentum transfer (Q_z) in the surface normal direction. For each of these choices, users can bring small sample cells or larger, customized processing or environmental chambers that can be easily attached to the diffractometer through a standardized mounting interface. Some specialized environmental cells and chambers will be developed for common *in situ* studies and will be made available to general users for use on the general diffraction instruments.

4.6.2.7.6 Instrumentation beyond the APS Upgrade

The vision for the completed XIS sector is expansive and requires significant involvement of the user community. In addition to the general diffractometers for interface studies, the completed XIS facility will incorporate specialized end-station instruments for materials synthesis, *in situ* processing, and interface imaging. The development of these specialized instruments requires strong partnerships. Proposals to develop experimental hutches on the XIS beamline have already been prepared and submitted. For example, one proposal for the end station on the tunable undulator beamline (ID-E) specifies a highly specialized environmental and materials fabrication and characterization instrument for real-time *in situ* x-ray characterization of advanced MBE growth (Figure 4.6.2-4). This system will include UHV sample transfer to and from an off-line UHV characterization system; sample heating to 1100 K; cooling to 140 K; MBE elemental source effusion cells with gate valves and shutters (5 mounted from an assortment of 15 total effusion cells of various types to enable a flexible choice among elements); molecular beam flux monitoring and control via quartz crystal monitor (QCM) and atomic absorption; purified ozone and oxygen plasma sources for oxide film growth; RHEED, GIXRD, GISAXS, GIWAXS,

XRR, and TR-XRF real-time characterization during growth; and XSW, CTR, XAFS, and hard x-ray photoelectron spectroscopy (HXPS) characterization primarily used for post-growth characterization.

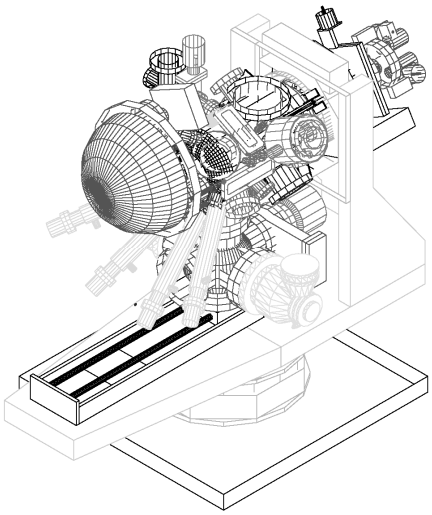

Figure 4.6.2-4. X-ray advanced MBE instrument showing coupling of vertical axis to horizontal axis to x-y-z translation stage to manipulator base. Inside the UHV chamber, the sample platen is on a heating and cooling stage that is mounted to the goniometer end of the manipulator. The upper UHV chamber has Be x-ray windows and ports for effusion cells, HXPS, ozone, RHEED, sample transfer, etc.

Another proposal has been prepared for developing advanced interface imaging techniques with x-rays in one experimental hutch (ID-C) on the tunable undulator beamline. There are powerful advantages to combining reciprocal space information from x-ray scattering measurements with high-spatial-resolution real-space imaging. For example, direct observations during new materials synthesis may be used to reveal where islands nucleate (at defects or step edges) and how they grow. The case for visualization of reactions, such as dissolution or growth, at buried boundaries is indeed compelling. The conversion of reciprocal space intensities to real-space structures has a significant limitation, namely probing properties that are statistically averaged over the sample (e.g., average defect spacing, general growth modes, height-height correlation functions), and this makes it difficult to investigate the behavior of isolated aperiodic structures, defects, or nucleation sites. Imaging elementary topography in real space demonstrates the ability to probe the behavior of individual structures. This capability has recently been demonstrated with XRIM (Figure 4.6.2-5) [4.6.2-12]. XRIM is similar to traditional full-field optical and x-ray microscopes, but uses the weak, interface-sensitive, specular-reflected or crystal-truncation-rod x-ray beams (with a reflectivity of $<10^{-5}$) to create an image. Since the reflectivity signal is interface specific, this leads to the ability to directly image interfacial topography and structures in *in situ* environments during growth or processing.

Potential partnerships have also been identified to develop the end stations on the fixed-angle beamlines. For example, the end stations that are located in the clean room facility may be instrumented for UHV studies of fundamental growth using quantum confinement effects (ID-I), and a specialized chamber for growth using MOCVD or ALD (ID-K). The clean room will be a cost-effective solution to provide an environment suitable for nano-fabrication and fundamental growth studies. A facility with both engineering and administrative controls is planned to provide better than class-10000 performance. The lower-energy branch line may also include a specialized growth or processing chamber—for example, PLD growth and laser annealing in ID-G. In each case, the end-station instrument will be

designed with appropriate growth control and characterization tools to make each instrument a state-of-the-art instrument for *in situ* studies.

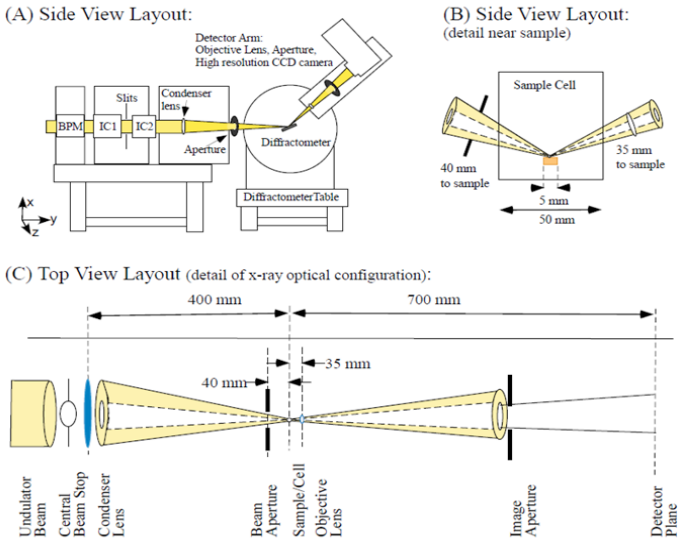

Figure 4.6.2-5. Schematic layout of the x-ray reflection interface microscopy instrument. The yellow regions indicate the x-ray beam, and the dimensions are approximate.

Surface-coherent x-ray scattering (SCXS) techniques [4.6.2-13, 4.6.2-14] are also now being developed at third-generation sources. Unlike phase-contrast microscopy, SCXS does not use an objective lens and therefore is limited only by the sample and beam characteristics, and the sampling of the diffraction images. The evolution of diffraction images can be analyzed to reveal temporal dynamics (e.g., relaxation times) and evolution using x-ray photon correlation spectroscopy (XPCS) [4.6.2-15, 4.6.2-16]. Alternatively, direct inversion of the diffraction pattern using phase-retrieval algorithms allows lensless imaging, known as coherent diffractive imaging (CDI). These capabilities will be integrated with both general and specialized diffraction instruments to enable simple changes from direct-space observations to reciprocal-space measurements. For example, the UHV growth chamber in ID-I will be designed with multi-technique *in situ* surface-imaging capabilities to provide imaging techniques of different length scales (0.1-1000 nm), such as x-ray microscopy, coherent diffraction imaging, and XRIM combined with STM/AFM in the same sample position. This will combine surface scattering and real-space imaging with *in situ* capabilities of MBE/CVD (metal/semiconductor/oxide/nitride) and gas phase catalytic reactions to further our understanding of growth and materials synthesis. A summary of the capabilities in the XIS sector is shown in Table 4.6.2-4.

Table 4.6.2-4 XIS Experimental Stations Emphasis

Hutch	Potential Instrument	Partnership Possibilities
ID-C	Interface Imaging	Yes
ID-D	Complex Gas Environments	
ID-E	Advanced and Oxide MBE	Yes
ID-F	Interface Diffraction/Scattering	
ID-G	Materials Synthesis (PLD/Laser MBE growth)	Yes
ID-H	Interface Diffraction/Scattering for Liquid-Solid Studies	
ID-I	Multi-technique UHV Surface Chamber	Yes
ID-J	Interface Diffraction/Scattering for nano-science	
ID-K	Materials Synthesis (Hybrid ALD/MBE or MOCVD)	Yes

In addition, dectectors and software development will enhance scientific productivity. Specialized 2D detectors are required for higher resolution, throughput, and sensitivity. There is demand for improved, user-friendly computer software for image processing (acquisition, visualization, and post-processing), and data manipulation and analysis. XIS will also exploit development of new algorithms for GISAXS-CDI, COBRA, and other direct methods for general users.

Analysis/Preparation Laboratory Space: Off-line characterization and sample preparation are recognized as critical to the scientific programs for the XIS facility. Optical microscopy, STM/AFM, and *in situ* SEM in sample preparation chambers are considered essential. Traditional electron probes such as XPS, AES, and LEEM/PEEM are also needed for surface characterization. These analysis capabilities in the laboratory space will compliment x-ray measurements and provide timely feedback to process-oriented experiments, thus improving the effectiveness of the facility for the synthesis and processing of new materials.

Many of the growth and environmental chambers will be used off line for new materials fabrication and to establish the parameters required prior to scheduled x-ray beam time. Specifications for the laboratory facilities will consider the capabilities available at the Center for Nanoscale Materials (CNM), and every effort will be made to coordinate with the CNM and with other resources available at the APS. Three hutches will be embedded in the laboratory spaces with clean room capabilities, and an LOM design to accommodate these is required. The fully developed XIS facility will be very active and will require appropriate laboratory and office facilities for the staff, users, and partner-user groups that will operate the general and specialized end-station instruments.

An alternative to a centralized XIS facility would include widely distributed beamline and support facilities. This distributed model is an excellent choice for science that requires unique x-ray tools and techniques such as polarization analysis for interfacial magnetism studies, advanced spectroscopy for catalysis studies, or very high energies (~100 keV) for penetrating into highly absorbing media. However, the efficiency and effectiveness of a centralized support structure (staff and facilities) is not realized in a distributed model. And, to effectively distribute the techniques that are planned for the fixed-energy branch lines at XIS would require several locations, positioned on three separate insertion-device beamlines, where the experiment hall floor space, undulator characteristics, and beam time would be available to permit these interface studies. Multiplexing three mutually compatible beamlines on one canted undulator port dedicated to interface science studies represents an effective approach.

This comprehensive XIS facility integrates greatly improved beamline optical performance and capabilities with a wide range of instruments for growth/environmental *in situ* studies and dedicated laboratory facilities to enable new research in diverse scientific areas. The increasingly sophisticated demands of a growing user community will be addressed by the XIS facility by providing state-of-the-art x-ray scattering, spectroscopy, and microscopy tools for multilength-scale, element-specific studies of vacuum/solid, gas/solid, liquid/solid, and solid/solid interfaces and supported nanostructures.

4.6.2.8 References

[4.6.2-1] J. Bard et al., J. Phys. Chem.-US **97**, 7147 (1993).

[4.6.2-2] V.R. Stamenkovic et al., Nat. Mater. **6**, 241 (2007).

[4.6.2-3] G.E. Brown, A. L. Foster and J. D. Ostergren, P. Natl. Acad. Sci. USA **96**, 3388 (1999).

[4.6.2-4] G. Ertl and H. J. Freund, Physics Today **52**, 32 (1999).

[4.6.2-5] Y. Kim et al., J. Phys. Chem. C **111**, 1874 (2007).

[4.6.2-6] P. Nolte et al., Science **321**, 1654 (2008).

[4.6.2-7] F.H. Ribeiro et al., Catal. Rev. **39**, 49 (1997).
[4.6.2-8] A. Menzel et al., Phys. Rev. B **75** , 035426 (2007).
[4.6.2-9] H. Ahn et al., Rev. Mod. Phys. **78**, 1185 (2006).
[4.6.2-10] D.-A.Luh et al., Science **292**, 1131 (2001).
[4.6.2-11] M. Valden, X. Lai and D. W. Goodman, Science **281**, 1647 (1998).
[4.6.2-12] P. Fenter et al., Nat. Phys. **2**, 700 (2006).
[4.6.2-13] I.A. Vartanyants et al., Phys. Rev. B **55**, 13193 (1997).
[4.6.2-14] L. Libbert et al., Phys. Rev. B **56**, 6454 (1997).
[4.6.2-15] K. Robinson et al., Phys. Rev. B **60**, 9965 (1999).
[4.6.2-16] M. Sutton et al., Nature **352**, 608 (1991).

4.6.3 *section deleted*

4.6.4 Sub-micron 3D Diffraction Upgrade (34-ID) [U1.04.02.12]

Diffraction tools are increasingly in demand to investigate the detailed structure (strain, orientation, phase, domain character, etc.) of materials at smaller and smaller length scales. Excellent spatial resolution permits structural diffraction studies in the interior of crystalline solids near defects, domain boundaries, and buried interfaces to understand how these affect the mechanical, electrical, and optical properties. Measurement techniques designed to probe the properties of matter at smaller length scales are critical to advance the forefront of condensed-matter and materials physics research [4.6.4-1]. X-ray diffraction measurements also provide a nondestructive, *in situ* structural probe that allows a direct link to theory, simulations, and multiscale modeling of structural evolution during deformation, or other strained states. Materials' properties depend largely on mesoscopic structure and evolution on length scales ranging from fractions of a micron to fractions of a millimeter, so structural characterization with submicron spatial resolution in all three dimensions is essential for understanding the properties of solid materials.

4.6.4.1 Scientific Scope

There are myriad applications where spatially resolved diffraction provides essential structural information for understanding fundamental materials questions. For example, electronic phase separation is observed in complex materials and has been linked to many types of exotic behavior, such as colossal magnetoresistance and high-temperature superconductivity [4.6.4-2]. In the area of advanced thermoelectric materials, nanoscale precipitates have been demonstrated to dramatically influence thermal transport properties by effecting phonon scattering and propagation. And in materials failure from Sn whisker growth, local strain gradients—not the strains themselves—provide the driving force for transporting Sn atoms to whisker nucleation sites [4.6.4-3]. Spatially resolved diffraction techniques are essential for phenomenological understanding of phase separation, strain gradient distribution, and the detailed structures at precipitates and phase (domain) boundaries.

Dislocation Cell Elastic Strain Distribution: The deformation behavior of metals is of central importance to the forming and eventual failure of many manufactured, fabricated components. Despite decades of intensive research, fundamental aspects of the evolution of dislocation structures are still poorly understood. Crucial, but otherwise inaccessible, information on the deformation process can be collected through spatially resolved microdiffraction experiments with hard x-rays. The evolution of local orientations and subgrain strains during the initial stages of deformation and the distribution on sub-micron length scales of elastic strains within deformed materials permits researchers and materials engineers to understand the fundamental mechanisms of crystal plasticity. Comprehensive studies of how and why dislocations are distributed heterogeneously in the form of "dislocation cells" in the crystal have presented the first quantitative, spatially resolved measurements of elastic strains within dislocation cells [4.6.4-4]. As the dislocation cell elastic strains originate as backstresses from the dislocation walls, the observed variation in the cell-interior strains strongly suggests that a similarly broad distribution may exist for the dislocation walls themselves. These measurements require spatial resolution of 50 nanometers or better, and will provide critical data for the development of detailed dislocation-based simulations and models.

Sn Whisker Growth Mechanism: The spontaneous growth of Sn whiskers in films is a long-standing and technologically critical question, which has plagued the electronics industry since the first attempts to replace Pb-based solders [4.6.4-3]. It is a surface relief phenomenon of creep, driven by a compressive stress gradient. The whiskers are electrically conductive, crystalline structures and have been observed to grow to lengths of several millimeters (mm) and are typically ~1 micron in diameter. Many electronic system failures have been attributed to short circuits caused by tin whiskers that bridge closely

spaced circuit elements maintained at different electrical potentials. Tin is only one of several metals that is known to form whiskers: others include zinc, cadmium, indium and antimony, so this represents a general issue in many metal systems. Earlier measurements of Sn whiskers with the unique 3D microdiffraction capabilities at APS 34-ID-E support new evidence for preferential grain orientations and a grain-boundary network near whiskers. To detect strain near the root of whiskers, the current spatial resolution of submicron x-ray beam is not sufficient. With a new 50 nanometer x-ray diffraction microscope probe, measurements will be greatly extended by the ability to map the strain field in the whisker root, which is the key to fully understanding the whisker growth mechanism.

Diffraction from Materials in Extreme Environments: Advances in high-pressure diamond-anvil cell (DAC) technology have opened many new areas in fundamental research for materials and earth sciences [4.6.4-5]. The maximum attainable and sustainable pressures can be reached by using nano-fabricated diamond anvil tips to reduce the pressurized volume. Ultrahigh-pressure investigations in the *terapascal* regime depend explicitly upon the ability to probe samples in a sub-100-nanometer scale through the anvils, and to distinguish sample signals from the background signals from the surrounding materials. The first study using a submicron x-ray probe at 34-ID-E has been very encouraging and obtained the first diffraction pattern at 270 GPa. The unique interchangeable white and monochromatic micro/nano-diffraction method provides a powerful way to probe submicron single crystals at ultrahigh pressure. The next breakthroughs will reach terapascal pressures and open vast new areas for discovery of novel materials and phenomena.

Phase Separation and Strained Domains in Manganite Systems: Current research on strongly correlated electron systems is driven by both scientific and technological interest in areas such as high-temperature superconductivity, colossal magnetoresistance (CMR), and spintronics. In particular, transition-metal oxide systems exhibit a variety of interesting and useful electronic and magnetic properties. Often, these physical properties arise from a subtle competition between competing phases with similar lattice structures. For example, lattice or charge distortions to an underlying cubic perovskite structure in manganite systems can lead to phase transitions between charge-ordered insulators and ferromagnetic metals. Near phase boundaries, spatially inhomogeneous microstructures and self-organized domains spontaneously appear. Understanding the complex electronic, structural and spin interactions between such coexisting nanoscale domains will likely provide the key to understanding the interesting physical properties in these systems.

The development of 3D spatially resolved x-ray nanodiffraction capabilities will enable the first quantitative measurements of the microstructure associated with phase domains in strongly correlated electron systems. Structural modulations, such charge and orbital ordering, are known to exist in manganites, but no technique has been available thus far to map the orientations or spatial distributions of phase domains. Similarly, theoretical models suggest that inhomogeneous strain fields couple to the electronic order and consequently play an essential role in phase coexistence [4.6.4-2]. For example, strain fluctuations may create pinning or nucleation centers for domain formation. The ability to nondestructively, quantitatively map structural modulations and strain distributions with nanoscale spatial resolution will represent a breakthrough for characterizing nanoscale phase separation. This tool will enable unique new studies, leading to significant advances in our understanding of strongly correlated electron systems.

A scanning nanodiffraction probe with suitable timing resolution and external field capability will also allow the dynamics of polarization and magnetization switching to be studied at the scale of single structural, ferroelectric, or magnetic domains [4.6.4-6]. Currently, this potential to study structural problems under large external fields on their fundamental scale is not available elsewhere.

Micro- and Nanoelectronic Devices: The rapid evolution towards CMOS devices that include integration of diverse materials with large crystallographic strains has taxed the tools used to evaluate

these structures. For example, strained silicon channels have been rapidly integrated in both PMOS and NMOS structures and have resulted in appreciable improvements in transistor performance due to enhanced mobilities of electrons and holes in devices [4.6.4-7]. The integration of strained SiGe source-drain regions can produce strains on the scales of large fractions of 1% in the transistor channel and yield 30% or more increases in currents by improving the mobility of charge carriers. It is highly desirable to measure and control strain in the present generation of 30-nm-scale devices using quantitative x-ray diffraction to have an adequate degree of understanding of composition and strain relaxation in the SiGe and the strain imparted into the channel. Nanodiffraction probes can provide strain and composition information that can be applied to generally applicable models of epitaxial growth, thermal stability, and imparted strain.

4.6.4.2 Source Requirements

A canted undulator beamline will be optimized for separate microbeam and nanobeam diffraction experiments. One branch of the beamline will continue to provide microbeam capabilities, and the other branch on a separately tunable undulator will provide x-rays to a new hutch that will include a nanoscale Laue diffraction platform.

To fully utilize the advantages of the Laue technique requires a wide-energy bandpass. However, a high-brightness monochromatic beam is also needed when the energy of a reflection is measured. So, in addition to high brightness, continuous energy tunability over the energy range 5-30 keV is essential for both undulator sources.

4.6.4.3 Beamline Description

To address the scientific opportunities in this area requires x-ray diffraction capabilities with excellent spatial resolution. To achieve this, the sector 34 ID beamline will be enhanced, and a dedicated x-ray polychromatic nanofocusing platform will be constructed. Canted undulators will allow for simultaneous and independent use of polychromatic microbeam diffraction and nanoscale diffraction facilities.

To focus the x-ray beam to the nanometer scale requires excellent optical performance, stability, and a significant demagnification of the x-ray source. A new hutch will be constructed at 34-ID for nano-scale diffraction using K-B mirrors. This facility will provide a unique capability for spatially resolved diffraction. The demands for environmental stability control of temperature, acoustic noise, and vibrations are challenging but must be addressed for successful nano-scale diffraction measurements.

Many of the components currently in use at 34-ID-E for the needs of the polychromatic microbeam diffraction instrument will remain [4.6.4-8], and a new optical enclosure (34-ID-F) and a new experimental hutch (34-ID-G) will be constructed and instrumented for the nanodiffraction experimental platform for K-B-mirror-based polychromatic nanoprobes to enhance capabilities for 3D diffraction investigations [4.6.4-9, 4.6.4-10]. Figure 4.6.4-1 shows a schematic drawing of the beamline layout. Because a project to cant the 34-ID beam line is already underway, other than adding a new hutch, there are no significant changes to the beam line required.

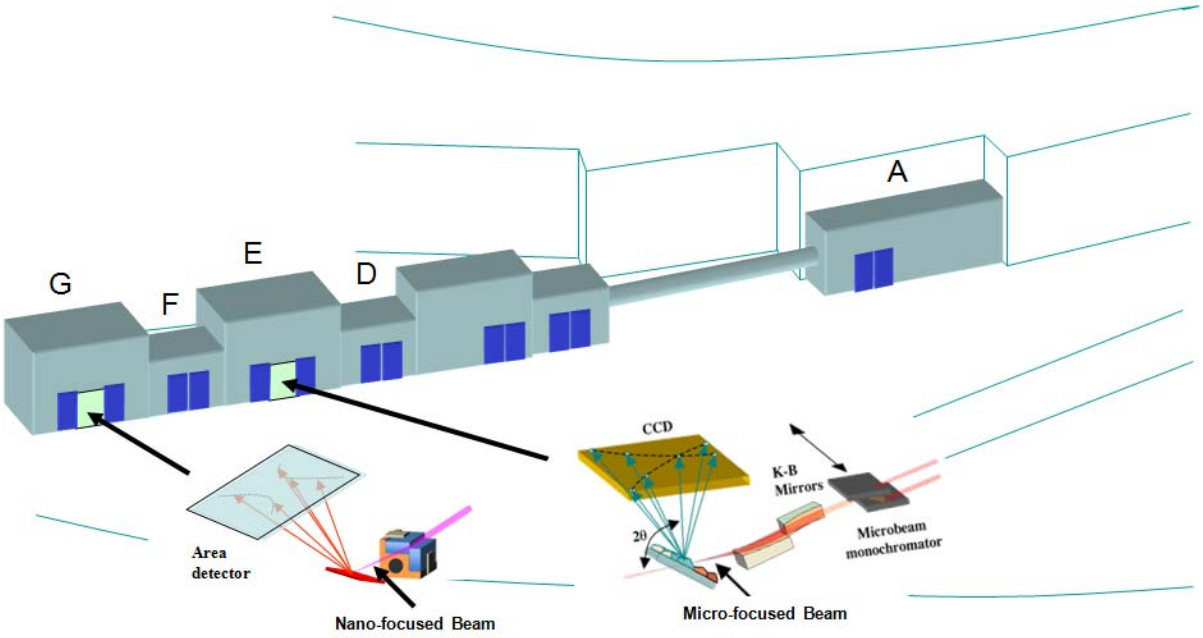

Figure 4.6.4-1. Schematic drawing of the upgraded 34-ID beamline.

4.6.4.4 Optics

Since the angle between beams of a canted insertion-device front end is only 1 mrad, a horizontal reflecting mirror in 34-ID-A will be used to further separate the 34-ID-F beamline from 34-ID-E beamline. The existing LN_2-cooled beam-splitting mirror, currently used for coherent diffraction experimental activities in hutch 34-ID-C will be modified for this purpose. A removable small-displacement Si(111) monochromator for the energy range of 5-30 keV will be installed at the downstream end of 34-ID-E to provide monochromatic x-rays to hutch 34-ID-E. The monochromator is designed to pass either a polychromatic beam or a monochromatic beam through the same exit slit. To achieve this, the beam offset in the monochromator is kept to 1 mm, which is within the dimension of the white-beam vertical profile entering the 34-ID-E hutch. To reduce the thermal load, a slit in front of the water-cooled monochromator restricts the incident beam in both polychromatic beam and monochromatic modes. The current microbeam monochromator in 34-ID-D will be relocated to the 34-ID-F to provide monochromatic x-ray beams to the 34-ID-G experimental hutch.

A new K-B nanofocusing mirror system will be installed in 34-ID-G for polychromatic and monochromatic Laue diffraction measurements. These ultra-precise mirrors require figure error of 0.1 μrad rms and surface roughness of 0.1 nm rms. This will assure diffraction-limited two-dimensional focusing for hard x-rays of 50 nm. The mirror control will use a high-stiffness high-precision tip-tilting stage system with small travel range and nanoradian multidimensional positioning resolution, using orthogonally configured laminar weak-link mechanisms.

4.6.4.5 Anticipated Performance

The beamline's canted undulator design will allow for simultaneous and independent use of the two diffraction stations for microbeam (34-ID-E) and for nanobeam (34-ID-G) structural studies. A dedicated, polychromatic microbeam diffraction instrument in 34-ID-E will continue to provide routine,

reliable hard x-ray beams focused to ~300 nm. The second canted undulator will be dedicated to the 34-ID-G nanoprobe station located downstream of the current microprobe station. Figure 4.6.4-2 shows a plan view of the layout for 34-ID. The K-B-mirror-based polychromatic focusing will have an initial focal spot of <80 nm and, with further development, beams of ~50 nm should be achievable in the future. This translates into a performance increase of more than one order of magnitude smaller x-ray beam cross sections compared with a currently available focus of 300-400 nm on the Laue diffraction instrument.

A key performance parameter is the working distance between the focusing optic and the sample field of view. The beamline demagnification and focal lengths are shown in Table 4.6.4-1. To address the 34-ID scientific objectives, specialized sample cells are needed for experiments at elevated or reduced temperatures, for real-time deformation studies of materials, or for other *in situ* studies. The working distance provides the flexibility needed to use these important sample environments.

Table 4.6.4-1. Parameters of the Beamline Focusing Optics

	Horiz focal length (mm)	Horizontal Demagnification	Vert focal length (mm)	Vertical Demagnification	Expected focal size (nm)
Microdiffraction 34-ID-E	60	575	130	496	300
Nanodiffraction 34-ID-G	30	1383	60	1191	50

Figure 4.6.4-2. Plan view of the layout for 34-ID showing the addition of a new optical enclosure (34-ID-F) and a new experimental hutch (34-ID-G), at the end of the existing beamline.

4.6.4.6 Instrumentation

To accomplish the scientific goals in this area, instrumentation development is required in addition to the beamline advances. New detectors will be deployed to increase the throughput and effectiveness of the facility. Improvements in mechanical motion control systems will be implemented to exploit the nanoscale-focused x-ray beams for state-of-the-art spatially resolved diffraction experiments.

The requirements for the area detectors for the nanoscale polychromatic diffraction instrument in 34-ID-G are different than those for the microbeam facility. Nanostructures provide intrinsically weak scattering signals, so the signal-to-noise performance of these area detectors is significantly more

important than for many other applications. Detectors that provide large area, moderate pixel size, good efficiency and readout performance, and excellent signal-to-noise ratios will be needed for nanoscale Laue diffraction applications.

Another challenge in nanoscale structural characterization concerns the accurate and precise manipulation of the sample. To fully exploit the nanoscale-focused beam sizes will require high-precision sample stages for translating samples. Nanometer resolution is required.

In addition, another considerable challenge for nanoscale structural research concerns vibration control and thermal stabilization for 34-ID-G. Once the stability requirements approach 100 nm below, the engineering designs must include vibration and thermal considerations.

Finally, beamline control hardware and software for 34-ID-G are required. Because the nanoscale Laue technique is relatively new and the software for data collection and analysis is not mature, efforts to improve this are essential for making the best use of this capability. In addition, the collection of large volumes of area detector images requires considerable computational and network infrastructure.

4.6.4.7 References

[4.6.4-1] Solid State Sciences Committee, "CONDENSED-MATTER AND MATERIALS PHYSICS: The Science of the World Around Us," National Research Council of the National Academies Committee on CMMP 2010 (2007).

[4.6.4-2] K.H. Ahn, T. Lookman, and A. R. Bishop, Nature **428**, 401 (2004).

[4.6.4-3] M. Sobiech et al., Appl. Phys. Lett. **94**(22), 221901-1 (2009).

[4.6.4-4] L.E. Levine et al., Nature Materials **5**, 619 (2006).

[4.6.4-5] L.Wang et al., Proc. Natl. Acad. Sci. USA **107** (14), 6140 (2010).

[4.6.4-6] P.G. Evans et al., Science **295**, 1042 (2002).

[4.6.4-7] S.E. Thompson et al., IEEE T. Semiconduct. M. **18**, 26 (2005).

[4.6.4-8] Final Design Report for Beamline Sector 34, Advanced Photon Source, October, 2000.

[4.6.4-9] W. Liu et al., Rev. Sci. Instrum. **76**, 113701 (2005).

[4.6.4-10] W. Liu et al., Nucl. Instrum. Methods A (2010); doi:10.1016/j.nima.2010.11.080.

4.6.5 Resonant Interface Scattering Upgrade (33-ID) [CAS]

For many compelling reasons, there is significant interest in surface and interface science, and a very active user community at the APS in this area. A new, dedicated x-ray interfacial science (XIS) facility at a sector of the APS (described in section 4.6.2) with exciting new capabilities, such as chemically sensitive 3D atomic mapping and new *in situ* materials growth capabilities is currently in the planning stages and has generated broad interest and enthusiasm. Surface and interface science activities have been developed and are growing in several APS sectors. For example, a canted beamline design will provide improved beam access for MOCVD and EEP programs in Sector 12. New dedicated facilities and canted source implementation is underway for the high-energy surface/interface programs at CARS in Sector 13, and the X-ray Science Division interface science activities in Sector 33 are continuing to flourish. However, as a consequence of the APS-U project, several other sectors and some surface and interface science experimental programs will no longer continue in their current locations. For example, the exciting new developments for LERIX and advanced spectroscopy tools in Sector 20 will make it impossible to continue active MBE growth research in that sector. Similarly, the upgrade of Sector 6 does not include continuation of the UHV growth studies ongoing in that sector. And additional surface and interface experimental programs utilizing general diffractometer instruments are not expected to continue at Sectors 11 and 6.

Sector 33 will continue as a center for surface and interface science activities at the APS and provides opportunity to build on the successes to date in this area and extend these to complement the development of the new XIS sector. With only one tunable undulator beamline for XIS, the need for additional capabilities at APS for resonant scattering experiments for interface science is anticipated. This upgrade of Sector 33 will include additional energy-scanning capabilities to meet anticipated need for resonant anomalous scattering for interface science. In addition, the expansion in Sector 33 will allow relocation of the interface science programs that will be displaced from other sectors as a result of the APS-U project.

4.6.5.1 Scientific Scope

One of many challenges in this highly interdisciplinary field is to understand and control the assembly of atoms and molecules at well-defined surfaces in complex environments. In the area of materials growth and synthesis, the ability to manipulate materials' properties (such as controlling composition or strain in thin films or nanostructures) is a central theme in engineering many new materials with novel chemical, magnetic, optical, mechanical, ferroelectric, thermoelectric, and electronic properties. Understanding the balance between mass transport and site-specific reactions at interfaces is critical to advancements in growth techniques (such as MOCVD, PLD, MBE, Laser MBE, ALD, and oxide MBE), and is essential to understanding chemical reactions and geochemical processes, such as etching, adsorption, dissolution, catalysis and precipitation. The relationship between atomic scale structure and catalytic function has important applications in fuel cells, hydrogen production and storage, and natural processes at biological membranes.

The mineral-fluid interface is the principal site of low-temperature geochemical processes at and near the Earth's surface, and influences the composition of groundwater, surface water, and to some extent the atmosphere. Environmental remediation strategies often require detailed knowledge of the structure and chemistry at these interfaces to establish effective procedures for environmental cleanup.

The role of interfacial magnetism in fabricated magnetic superstructures has received much recent attention, and a grand challenge today in highly correlated electron systems is the determination of the role surface and interface electronic structure in these complex materials. Indeed, the importance of surfaces and interfaces is becoming more widely appreciated in many different areas.

The use of elastic scattering of x-rays to probe the interfacial structure (e.g., x-ray reflectivity, crystal truncation rods, diffuse scattering) [4.6.5-1] is the central approach in this field. It has proven over the past two decades to be the most powerful approach for understanding interfacial structure, especially in complex environments and at buried interfaces. The use of resonant anomalous dispersion [4.6.5-2] extends interfacial scattering to probe elemental substructures through its inherent phase sensitivity and interfacial oxidation states through its chemical sensitivity (e.g., through changes to an atoms x-ray absorption near-edge structure). This powerful approach opens up new opportunities to locate elemental substructures (e.g., adsorbates at the solid-liquid interface, impurities within multicomponent films) and oxidation state distributions directly using elastically scattered x-ray beams [4.6.5-3].

Through changes in scattering angle, various aspects of interfacial structures may be highlighted, including defect distributions at buried solid-solid interfaces (e.g., dislocations), film growth, and the nucleation and growth of nanoparticles. The use of nonspecular crystal truncation rods provides sensitivity to lateral structures (e.g., reconstructed surface domains). Contrast derived from the resonant anomalous dispersion of x-rays will influence the crystal truncation rod (CTR) intensities and therefore can be used to specifically highlight elemental, chemical or magnetic features of an interface. These approaches should be widely applicable as a probe of various interfacial processes, such as ion adsorption, corrosion, catalytic reactions, magnetic and ferroelectric domain growth and switching.

4.6.5.2 Source Enhancements

The Sector 33 facility includes a set of instruments that exploit the x-ray brilliance and hard x-ray flux of the APS for interface science investigations. A canted undulator front-end source is required to supply radiation to two undulator beamlines. The first beamline requires an undulator with a fully overlapping tuning curve for energies between 4 and 40 keV using the first, third and fifth harmonic, providing high performance and excellent brilliance over this energy range. The second undulator beamline will supply x-rays for a side-diffracting double-crystal monochromator beamline that will operate between 10 and 20 keV. To span this energy range, a device with a 3.0-cm period is required.

4.6.5.3 Beamline Enhancements

A canted undulator beamline will be optimized for surface/interface experiments. One of the canted beamlines will be fully tunable over a wide energy range (4-40 keV) for experiments that require resonant contrast enhancement. This beamline will incorporate an upgraded double-crystal monochromator and new focusing mirrors for x-ray standing wave (XSW) studies, coherent Bragg-rod analysis (COBRA), and resonant CTR measurements. The other beamline will employ a double-crystal side-bounce monochromator with selectable energy over the energy range from 10 to 20 keV. The new side-bounce beamline will include focusing optics and an expanded experimental hutch with a new or relocated general-purpose diffractometer designed for integrated microscopy and scattering experiments, upgraded and enhanced PLD capabilities, and an upgraded UHV growth chamber. The beamline focusing optics for each beamline will provide excellent spot size at each experimental location using a secondary source (slit) for refocusing with easily installed KB mirrors or zone plate optics for experiments that require micron-scale beam spots (Figure 4.6.5-1).

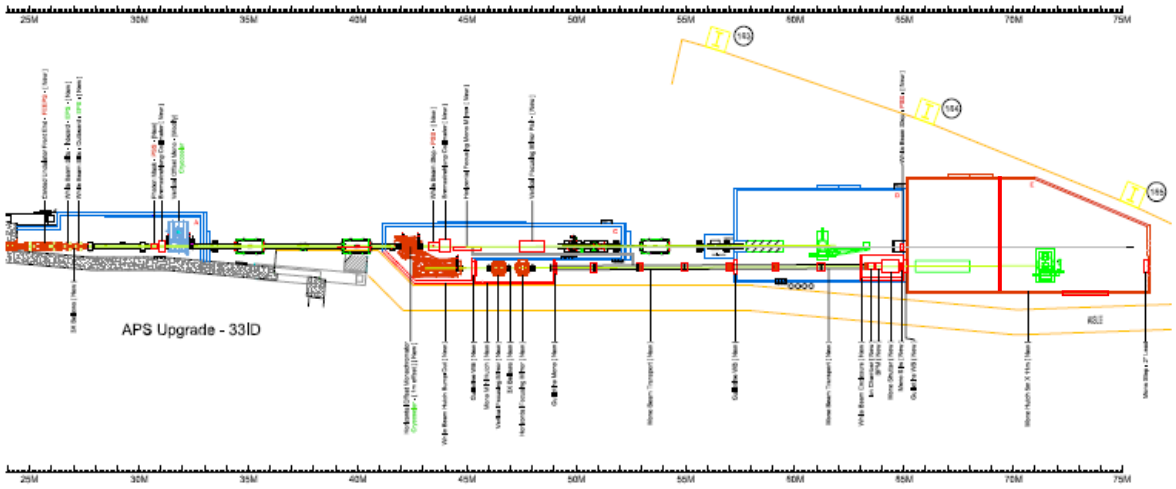

Figure 4.6.5-1. Layout of the canted Sector 33-ID beamlines showing the enlarged 33-ID-E hutch and expanded 33-ID-C optics enclosure.

The existing optics enclosure 33-ID-C will be modified to allow installation of a side-diffracting DCM and additional mirrors and shutter for the limited-energy-range beamline. This optics enclosure will also contain the shutter and new mirrors for the widely tunable beamline.

The existing experimental enclosure 33-ID-E will be enlarged. The new hutch footprint will allow three permanently installed experimental platforms for interface science studies. A wall will separate the general purpose diffractometer in the front from the dedicated instruments in the back to warrant access for those instruments.

4.6.5.4 Optics

The fully tunable beamline will use a cryocooled Si (111) double-crystal monochromator (upgraded Kohzu design) to span the energy range from 4-40 keV. This monochromator is a fixed offset design and has been demonstrated to effectively scan the incident beam energy for resonant studies. A new horizontally deflecting mirror at 45 m will be used to focus the beam to either the experiment location in the 33ID-D hutch or to a slit at 56 m that serves as a secondary source for further focusing. This mirror will also allow horizontal collimation of the beam for high-resolution measurements that require low angular divergence. Vertical focusing (or collimation) and harmonic rejection will be achieved with a pair of vertically deflecting mirrors located at 47.5 and 49 m. To effectively span a wide energy range, the vertical focusing mirror will operate at a range of incident angles and will have stripes of Si, Cr, Rh, and/or Pt, as well as a dynamically controlled radius.

The limited-energy-range beamline will use a cryocooled Si 111 side-diffracting double-crystal monochromator with at least 1 m horizontal offset. This beamline is anticipated to have energy selectivity between 10 and 20 keV. For this energy range, mirrors coated with Rh set at 3-mRad incidence will be effective for harmonic rejection. To position the focused beam at one of the three experiment locations in 33-ID-E will require dynamically bendable mirrors for both horizontal and vertical focusing. A small vertical steering mirror will be used just upstream of the experimental hutch to bring the beam to a horizontal direction (Figure 4.6.5-2).

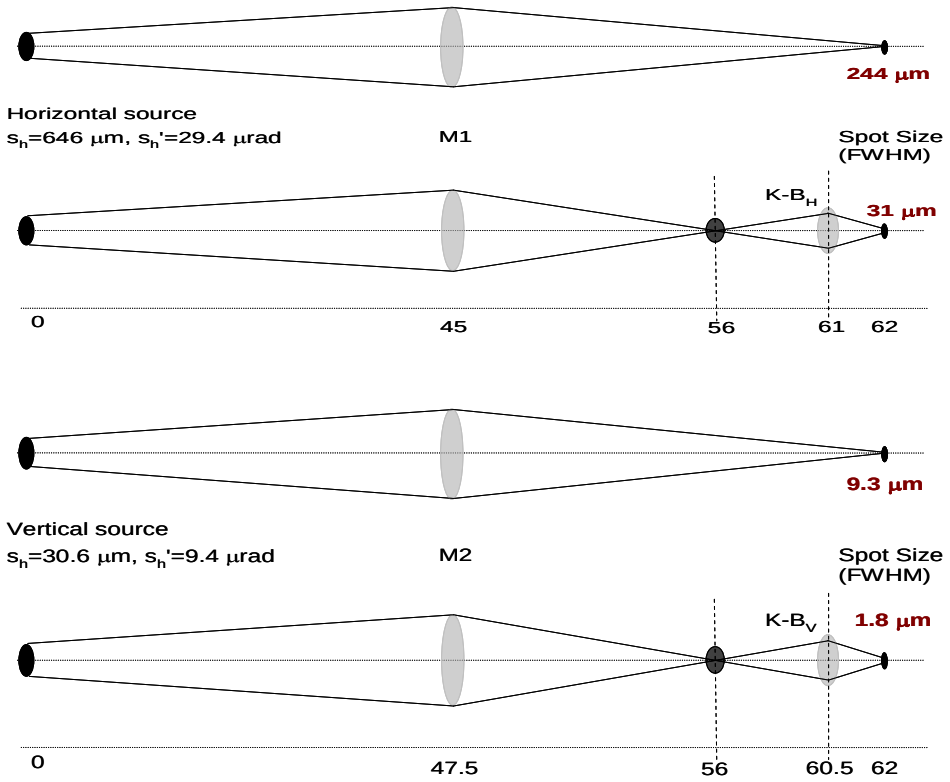

Figure 4.6.5-2. The optical configuration of the fully tunable beamline in Sector 33 is very flexible and will permit focusing in the horizontal plane, the vertical plane, or both. Additionally, the mirrors can be set to collimate the x-ray beam for applications that require low divergences.

4.6.5.5 Anticipated Performance

Mirrors are achromatic focusing elements and therefore are very appealing for use in wavelength-scanning applications. The optical design of the fully tunable beamline will allow energy scanning over a wide energy range without changes to the focus condition of the beam. This is important for studies involving small crystal surfaces or facets that require anomalous scattering techniques. The focused beam size will be affected by the mirror figure and other optical aberrations, so specifications for the mirror surfaces and figure will be considered as to their influence on the focus performance. The focusing limit with ideally performing optics are 244 × 9.3 μm (H × V) using only the beamline mirrors, and 31 × 1.8 μm if a K-B mirror pair is used to refocus the secondary source at 56 m. The long working distance of 1 m will allow access to large environmental chambers or cells. If needed, even smaller focused beams could be produced at the expense of working distance.

The cryocooled Si (111) monochromator provides a sufficiently narrow bandpass for resonant anomalous scattering studies for all accessible absorption edges between 4 and 40 keV. The Kohzu monochromator design has proven itself for scanning applications, so the currently used Kohzu will be upgraded for better vacuum performance and to use cryocooled Si optics.

4.6.5.6 Instrument Enhancements

Minor enhancements to the XSW platform and Newport diffractometer in 33-ID-D are expected to keep these operating at the forefront of interface science research. The general Newport diffractometer will be modified to accommodate small environmental cells and chambers with standardized interfaces to

permit use at the XIS facility. Software will be developed and refined to exploit widespread use of surface/interface scattering geometry and 2D detectors, resulting in improved temporal resolution and dramatically higher throughput. Sample handling, and off-line visualization and characterization infrastructure and associated specialized ancillary laboratory equipment will form an important element of this project.

An enlarged 33-ID-E experimental hutch will accommodate three permanently installed platforms for interface science studies on a beamline with 10- to 20-keV x-rays. The first will be a general diffractometer instrument—possibly relocated from another sector—to perform reflectivity, grazing incidence surface diffraction and crystal truncation rod measurements. This instrument will use 2D detectors, such as the Pilatus, and will also accommodate small environmental cells and chambers with standard interfaces that permit use at the XIS facility. The second platform in 33-ID-E will be an upgraded UHV growth chamber for surface diffraction studies of quantum controlled growth and other MBE growth studies. Improvements include growth chamber modifications to allow programs from Sector 6 and Sector 20 to continue in Sector 33. And the third platform in the expanded 33-ID-E station will be an existing PLD growth system with RHEED and an improved laser. The growth chambers will have enhanced capabilities, including additional sources (MBE, atomic oxygen, sputtering), sample transfer and separate prep/analysis capabilities, wider temperature-range stages, UHV-GISAXS capability, and provision for high-gas-pressure and high-temperature studies of material surfaces. Traditional electron and scanning probes will be included in the facility upgrade, including STM/AFM, *in situ* SEM for imaging and analysis, and LEEM/PEEM.

These improvements recognize the competitive advantage of APS, and exploit the great brilliance of the hard x-ray source. These improved x-ray facilities for *in situ* surface and interface science at the APS are based on a new canted undulator beamline design, and state-of-the-art beamline and focusing optics that will enable resonant scattering studies to determine structure and understand properties at surfaces and internal boundaries in fabricated systems, as well as those found naturally in our environment. Smaller beam sizes, faster detectors, and expanded dedicated capabilities will enable new research in diverse scientific areas. The upgrade will also enable experiments with smaller samples, involving *in situ* reactions and structures under nonambient conditions in controlled and complex environments. As interest in nonideal surfaces grows, small beams are often required to probe small crystal surfaces or facets. Improvements and enhancements to existing techniques will provide new capabilities and enable investigations not possible today. And from a practical perspective, the expanded facilities in Sector 33 will enable active and productive interface science programs to be relocated from other sectors to Sector 33.

4.6.5.7 References

[4.6.5-1] M. Mezger et al. Science **322**, 424 (2008).

[4.6.5-2] C. Y. Kim et al., J Phys. Chem. C **111**, 1874 (2007).

[4.6.5-3] A. Menzel et al., Radiat. Phys. Chem. **75**(1), 1651 (2006).

4.7 all sections deleted

4.8 General Beamline Upgrades

4.8.1 Introduction

Upgrades to the APS storage ring will present unique opportunities and challenges to all beamlines. Even if no upgrades are planned for a particular beamline, the increase in current from the present 100 mA to potentially 200 mA will result in a doubling of the beam power, and power density on beamline components for both bending magnet and insertion device beamlines. This power increase is in addition to the power loading that enhanced insertion device methodologies will create (e.g., multiple inline insertion devices, superconducting devices).

The power load challenges for all beamlines fall within three broad categories. The first category comprises the high-heat load safety-related components and must be verified and/or redesigned for the current power levels. These components include photon shutters, masks, and beamstops that are required to ensure that the beamline stays within the design safety envelope. The current material of choice for most high-heat load components is GlidCop Al-15. The current design criteria used for failure on these components, while being conservative, has a long history at the APS for designing safe components and is based on minimizing creep and fatigue failures in the components.

The second category includes those high-heat load beamline components that are not safety related but are required for beamline operations. These components include beam-defining apertures, slits, and windows.

The third, and final category, includes beamline optical elements that intercept the white beam from the synchrotron. These include x-ray crystal monochromators, multilayer monochromators, and x-ray mirrors. Unlike the previous two categories, where minor thermal distortions and drifts generally do not affect the function of the device, x-ray optics (especially monochromators) are extraordinarily sensitive to angular drifts on the order of microradians. Consequently, one of the major considerations of this last category is not only that the thermal distortions introduced by the x-ray beam power profile are acceptable, but that scattered power does not cause unacceptable distortion and drifting in the mechanics used to support and align the optics. In order to fully exploit the potential of the upgraded APS storage ring, insertion device beamlines will need to address all three categories, while bending magnet beamlines will primarily be considered with the last category.

4.8.2 Beamline Absorbers and Stops [U1.04.04.02]

4.8.2.1 Scope

Safe operation of APS beamlines requires that x-ray light be confined within a predetermined optical path and stopped using absorbers (e.g., shutters) and stops. These paths as well as the components are reviewed in accordance with a beamline safety design review committee as required by the APS Safety Assessment Document [4.8.2-1]. Components that confine or stop the white beam from the APS storage ring must be able to survive the heat load imposed by the beam created by that beamline's insertion device configuration. These components are listed as part of the APS radiation safety system configuration control program. Generally, bending magnet beamlines at the APS have not been designed to produce sufficient power densities that require significant high-heat-load power mitigation.

GlidCop Al-15 has been used as the material of choice for high-heat-load applications due to its excellent thermal and mechanical properties [4.8.2-2]. High-heat-load safety GlidCop components at the APS are designed so the material shall not exceed 300° C at the center of the beam footprint, the maximum temperature on the cooling wall where water flows shall not exceed the water boiling temperature (i.e., there is a requirement for single phase flow), and the maximum von Mises stress for photon shutters shall not exceed 400 MPa [4.8.2-2, 4.8.2-3]. Occasionally, components are made from other materials and they are considered on a case by case basis. While these criteria are conservative, they have proven successful in designing safe components on APS beamlines. Components are designed to spread the x-ray beam across the component, thereby spreading out the heat flux in order to insure that the above criteria are met. A program to better understand material and design constraints (see section 3.6.2.2) may alter these requirements. All current operational APS beamlines have been reviewed and can operate safely at a minimum of 100 mA of ring current with their insertion device types and configurations. An increase of ring current to 150 mA and/or a change in insertion device configuration to one that can produce higher power or power densities will necessitate a re-review of all of a beamline's safety components against the above criteria. High-heat-load safety-related components which do not meet the above criteria for GlidCop will require the implementation of one or more strategies for high-heat-load power mitigation.

In addition to the high-heat-load safety components, beamlines contain other components, including beam-defining slits and apertures as well as x-ray windows. While these may not be classified as safety systems, they have been designed for a particular x-ray beam profile and beamline operations may be affected if they are subjected to thermal loads beyond their design specifications. Consequently, beam-defining slits and apertures, as well as x-ray windows, also require evaluations to determine if a beamline requires a high-heat-load power-mitigation strategy.

4.8.2.2 Evaluation Process for Existing Beamline Components

Each beamline will be subjected to the following iterative process:

- The insertion device configuration and associated heat load that will be present after the APS--U project will be determined.
- The existing beamline review documentation will be examined for the high-heat-load components that are part of the APS configuration control program. This is done to determine if the existing components can meet the power and power-density requirements of the insertion device configuration for the beamline with a ring current of 150 mA.

- If the existing reviewed analysis does not reflect the higher power levels, then an engineering judgment will need to be made as to whether further analysis is cost effective or a mitigation strategy is warranted. If in good engineering judgment the component is likely to be acceptable at the higher power levels, then finite element modeling will be performed. If, after this analysis, the component is unacceptable, then a mitigation strategy will be utilized.
- Beamline components that are not related to safety (e.g., slits, apertures, and windows) will also be analyzed to determine if modifications are desirable for operational considerations.

After the analysis and the application of power-mitigation strategies, every attempt will be made to group any new required components to minimize the number of unique components that are produced. This may require modifications to create enough space so that the components can fit. The final beamline configuration will undergo a beamline safety design review.

4.8.2.3 Strategies for Power Mitigation

Power mitigation strategies for a beamline will be one of four types. The strategies that are chosen for a particular beamline will be the ones that are consistent with the scientific mission as well as being cost effective. Mitigation strategies will impact the overall beamline design and may trigger a reevaluation of existing beamline components (see section 4.8.2.2).

The first type of mitigation is the installation of a new high-heat-load-limiting aperture as part of the front-end exit table that will reduce the total power on the beamline. By implementing this as a controlled safety system device, components downstream are not required to intercept the full power of the x-ray beam. This strategy is useful when total power, rather than power density, is the limiting criteria on the beamline.

The second type of mitigation is to optimize the undulator configuration to better satisfy the scientific program and reduce the thermal limitations on the beamline. The power and power density of the x-ray beams produced by undulators increase as the undulator gap is lowered. By replacing the insertion device with one of a different period and/or limiting the closed gap limit of the device, the tradeoff between tunability, brightness, and power may result in a more optimum beamline configuration.

The third strategy is to develop operational power limiting systems for beamlines with multiple inline insertion devices. The power and power density of multiple inline devices add linearly. From a safety standpoint, the maximum power from all devices at their highest levels is the design power for safety beamline components. However, the scientific program of the beamline may not require that all devices be used at their highest power simultaneously. In these cases, a safety-rated power-limiting system that would limit the sum of the power from the devices rather than limiting the individual device power may result in a more optimum beamline configuration.

The fourth strategy is to redesign and replace components on the beamline. Redesign may increase the length of the components and therefore affect the overall beamline layout. Each beamline will need to be evaluated separately. If components are redesigned, full use will be made of different spreading geometries (e.g., spreading the beam along the vertical, rather than the horizontal direction as is currently used in the high-heat-load front-end (see section 3.6.1.3), as well as the results of new design parameters from development of high-heat-load components (see section 3.6.2.2). Furthermore, as much as possible, new components will be made so that a single design may be used in multiple beamlines.

4.8.2.4 References

[4.8.2-1] Advanced Photon Source Safety Assessment Document, APS-3.1.2.1.0. Rev. 3, Argonne National Laboratory, 2006.

[4.8.2-2] J. Collins, Thermal Fatigue of GlidCop Al-15 Experiments, ICMS Document No. APS_1409594, Advanced Photon Source, 2010.

[4.8.2-3] Y. Jaski, ANL/APS/TB-50, Advanced Photon Source, 2005.

4.8.3 Beamline and End Station Optics [U1.04.04.01]

The optics needs for the APS-U project can be divided into two categories: general beamline optics and end station optics. General beamline optics include high-heat-load optics, long-grazing-incidence mirrors, crystal monochromators, and to some extent, compound refractive lenses. End station optics includes mainly submicron optics and nanofocusing optics. The upgrade of beamline IDs and the APS storage ring present challenges for future beamline first optical components. The combination of customized IDs (e.g., superconducting devices), multiple IDs (made possible by longer straight sections), and higher beam currents may exceed the power density and/or heat load possible with current monochromator and mirror designs. The first beamline optical components must be optimized to withstand the heat load generated by the new IDs and storage-ring parameters with minimal strain and distortions.

Many of the emerging science beamlines will require some focusing optics for imaging spectroscopy, and micro- and nanodiffraction applications. When the APS was first built, imaging played a very limited role in the experimental program. The situation is quite different today since imaging is now combined with diffraction and with spectroscopy. Previously, it was assumed that the specimen under study was spatially homogeneous, but now, investigations are carried out about how the chemistry, strain, or other properties of the specimen vary over micrometer length scales. With the APS-U project, efforts will shift from the micro scale to the nanoscale, requiring a new generation of optics.

The range of x-ray experiments relying on beam coherence is clearly expanding, and with that, so does the challenge to preserve beam coherence as it passes through the optical trail to the experimental station. Optical surfaces and volumes that interact with the beam (e.g., mirrors, monochromators, windows, lenses, etc.) impose additional requirements. The options are either optical elements that preserve coherence or corrective (adaptive) optics to compensate for phase distortion. For example, whereas in the past, a monochromator surface was merely etched, now it should be etched and polished at the same time to provide a high-quality mirror surface with intact crystal structure. This is a challenge, especially for asymmetric monochromators, requiring developments in chemical-mechanical polishing, and other processes. Development of coherent preserving mirrors is also necessary. The APS effort will focus on working closely with qualified vendors to develop and test the needed optics.

This section describes the necessary development of optics that can handle the high-heat load of the upgraded APS, can preserve coherence, can deliver more stable monochromatic beams, and can provide nanometer-scale focused beams.

4.8.3.1 Scope

While most of the optical components, including standard-grazing-incidence mirrors, mirror bender assemblies, and compound refractive lenses will be acquired through specialized vendors, the expertise and capabilities acquired by the APS over the years in various areas of optics fabrication and metrology will be utilized to develop some of the advanced and highly specialized optical components, including multilayer Laue lenses, Kirkpatrick-Baez mirrors, multilayer optics, and crystal monochromators.

Argonne's crystal optics laboratories are equipped with comprehensive crystal fabrication and characterization facilities that are capable of fabricating various standard and customized crystals. Argonne scientists also carry out extensive R&D, including fabrication of ultra-smooth and strain and defect-free crystal surfaces; characterization of advanced crystal; development of novel high-energy-resolution monochromators; development of new crystal optics for Bragg diffraction imaging and phase-contrast imaging techniques; research into new crystals including sapphire, quartz, Germanium, and

others; modeling of diffraction physics; and other projects. To accommodate the expected large demand for crystal monochromators at the APS-U project, Argonne designers have begun upgrading various equipment and developing more efficient fabrication and characterization procedures. For example, a new advanced dicing saw (in addition to the existing one) for fast fabrication of high-quality IXS analyzers and high-precision crystals is being procured and more polishing facilities are in the planning stage. The facilities to test the specialized Si crystal optics in their mounted configurations are also being gradually improved.

The deposition facility will be utilized to develop thin-film optics including multilayer Laue lenses, graded multilayer, and others. Enhancement of or replacement of existing deposition facilities may be required in order to develop state-of-the-art optics.

The APS metrology laboratory carries out measurements for optics quality control and has played a significant role in providing data used in developing and fabricating profile-coated K-B mirrors. These activities will continue with the APS-U project. Significant improvement to the metrology laboratory will be needed to meet APS-U project optics measurement requirements. These include replacing the aging instruments, acquisition of new ones, and improving temperature stability around individual instruments. The Optics & Detector beamline at 6-BM will be used to perform complementary at-wavelength metrology measurements that are essential for optics development and characterization.

4.8.3.2 Description

General Beamline Optics: General beamline optics include mirrors, monochromators, and compound refractive lenses. A high-heat-load optic is generally the first optic in a beamline; this can be a monochromator or a grazing-incidence mirror. These elements are generally subject to large power loads and large power density and have to be efficiently cooled to minimize thermo-mechanical distortions. Due to the large incidence angle, crystal monochromators must sustain large power density for IDs, and as a result, they are typically cryogenically cooled.

Mirrors are operated at grazing-incidence angles and are typically water-cooled. Single crystal silicon is the main material for fabrication of both monochromators and mirror substrates because of its excellent physical and mechanical properties. Moreover, large-size high-purity Si crystal is readily available at a reasonable cost. Diamond type II has a better thermal conductivity and provides high peak reflectivity with a narrower bandwidth compared to Si and is therefore ideal for HHL applications. Thermal conductivity of natural diamond was measured to be about 22 W/cm•K. Monocrystalline synthetic diamond enriched in ^{12}C isotope (99.9%) has the highest thermal conductivity of any known solid at room temperature: 33.2 W/cm•K. However, the sizes of the specimens are very small (typically less than 1 cm × 1 cm) and although the quality of available synthetic crystalline diamond has improved over time, it still needs to be qualified, and as shown in Figure 4.8.3-1, it can contain major defects such as stacking faults [4.8.3-1]. Clearly a good source of diamond crystals is desired for HHL monochromators, windows, and other optical elements.

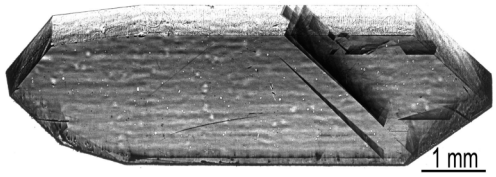

Figure 4.8.3.-1. X-ray topograph of a type IIa diamond showing a stacking fault.

Compound refractive lenses are becoming increasingly used as general beamline optics. They provide a simple and a cost effective means to collimate or moderately focus x-ray beams, and they are

particularly useful for efficiently microfocusing high-energy x-rays. The APS has developed several generations of CRLs, in Be, Al, and Li. Scattering from the bulk material is a limiting factor in focusing, and as a result, the proposal is to make lenses from single crystal beryllium. This requires the Be base material and working with qualified vendors to achieve high-quality x-ray lenses.

End-Station Optics: X-ray focusing optics are based on one of four different phenomena: specular reflection that works over a wide range of wavelengths at very high reflectivity, thin-grating diffraction such as in zone-plate optics with dispersion that scales with λ^{-1} (where λ is the radiation wavelength) and moderate efficiency, refraction (typically from compound lenses) with dispersion that scales with λ^{-2} and provides moderate efficiency, and volume-grating diffraction that is only tunable over a narrow energy range and provides high efficiency. For those experiments that involve energy tenability, such as spectroscopy, the APS-U project will concentrate on both K-B reflective optics and Fresnel zone plates; for those experiments that work at fixed energy, such as imaging, the APS-U project will concentrate on multilayer-coated K-B mirrors and multilayer Laue lenses based on chirped volume gratings.

K-B mirrors involve two elliptical mirrors at glancing angles to the x-ray beam, arranged 90° to each other to focus x-rays in the vertical and horizontal directions. Precise elliptical reflecting surfaces of the two K-B mirrors are essential to achieve diffraction-limited focusing. Figure errors remain an important barrier for fabrication of synchrotron x-ray K-B mirrors. The required precision increases as the x-ray wavelength decreases. The elliptical surfaces are asymmetrical and difficult to make, especially for hard x-rays. So far, computer-controlled optical surfacing and elastic emission machining techniques are the most known techniques used to produce the ultra-precise elliptical surfaces needed for synchrotrons [4.8.3-2, 4.8.3-3]. These techniques require many cycles of measuring and polishing to achieve a smooth and accurate surface profile. At the APS, a profile coating technique has been developed to convert readily available, inexpensive cylindrical and flat-Si substrates into precise elliptical mirrors [4.8.3-4]. Very precise elliptical K-B mirrors with sub-nm rms height errors have been obtained with one primary profile coating followed by a corrective profile coating. Focal spots as small as 70 nm have been achieved using a K-B mirror profile coated on a flat-Si substrate.

Fresnel zone plates produce a focus spot that is limited in Rayleigh resolution to 1.22 times the width of the narrowest, outermost zone. They are typically fabricated in a top-down manner by electron beam lithography, followed by high-aspect ratio etching and material deposition processes. Ideally, each zone imposes a phase shift of π on the incident wave, leading to an ideal thickness of a micrometer or more for ~10-keV x-rays. With today's fabrication processes, aspect ratios of only about 15:1 are achievable, leading to tradeoffs between resolution (as fine as 30 nm at present) and efficiency (only a few percent for the highest-resolution 10-keV zone plates). New processes might extend these limits; alternative strategies include stacking and aligning multiple zone plates, or overlay fabrication procedures.

Multilayer Laue lenses, pioneered at the APS, are a volume-grating form of FZPs used in transmission (Laue) geometry [4.8.3-5, 4.8.3-6]. By using thin-film deposition and sectioning plus thinning, the aspect ratio limitation to achieving high efficiency is eliminated; in addition, dynamic diffraction in the volume regime makes focusing with efficiencies of above 50% at high photon energies feasible. MLLs have demonstrated 1D focusing to 16 nm with 31% efficiency [4.8.3-7, 4.8.3-8] and theoretical calculations of idealized structures suggest that focal spots as small as 1 nm can be obtained [4.8.3-9]. Nanoscale 2-D imaging with a resolution of 25×40 nm^2 and an efficiency of 17% at a photon energy of 20 keV using two crossed MLLs has been recently achieved [4.8.3-10] as demonstrated in Figure 4.8.3-2.

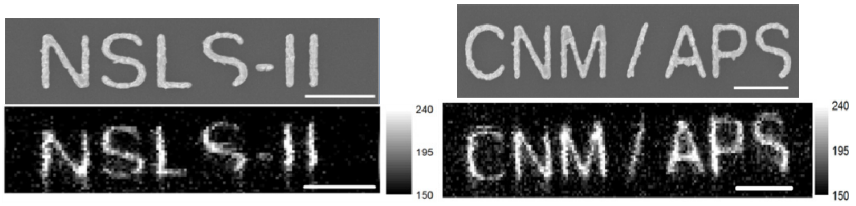

Figure 4.8.3.-2. X-ray scanning images (lower) obtained by MLL-based scanning microscope compared to the SEM images (upper). The pixel dimensions in the x-ray images are 20 × 20 nm^2. The signal collected is Au fluorescence obtained with incident x-rays at 19.5 keV. MLLs are in particular promising lenses for scanning probe beamlines that aim for a focus of below 10 nm.

Laboratory and Beamline Metrology (CAS): The X-ray Optics Metrology Laboratory of the APS has been in service since its commissioning in 1994. Its primary mission is to evaluate the surface figure and finish of optics for the benefit of the APS users and beamline scientists and to ensure that their surface quality is conformant with the APS specifications and requirements. This work is done by using an array of non-contact optical metrology instruments, including the long trace profiler [4.8.3-11], a laser Fizeau interferometer, and a roughness microscope interferometer. These instruments are housed in a Class 10,000 clean room with a well-controlled environment, located on the APS experiment hall floor, adjacent to the deposition and to the x-ray characterization laboratories. The tools played significant roles in fulfilling general requests as well as in providing data used in developing and fabricating profile-coated K-B mirrors. These activities will continue with the APS-U project.

In addition to laboratory measurements, an Optics & Detector beamline at 6-BM will carry out a variety of at-wavelength measurements essential to fully characterize nanofocusing and coherence preserving optics.

4.8.3.3 Research and Development

Optics and metrology R&D activities will be geared towards the needs of beamlines. For example, a better understanding of material properties and behavior during thin-film growth and under intense radiation will assist greatly in developing high-performance optics. The microstructure, orientations, defects, surface and interface roughness, and stress are all key areas to understanding the performance of x-ray optics. Aggressive research and development programs will be pursued in MLLs; nanofocusing mirrors; and high resolution, coherence preserving crystal optics. Research and development efforts will also be pursued in both laboratory and beamline characterization tools and techniques. The development of physical optical simulation codes is also essential for accurate design and for performance simulation of the advanced optics.

High Heat Load and General Optics: Although APS IDs produce beams with powers up to several tens of kW, only the central cone of radiation containing the harmonic radiation is most often of interest, and this is the part of the beam that is allowed to pass through apertures and traverse to the experimental station. The size of this beam, at the first encounter with any optical elements about 30 m from the source, is on the order of a few mm^2. For this reason, the multiple of the beam size and the peak-heat flux of the radiation emitted by an ID is a good proxy in the thermal management of x-ray optical systems. Presently, the peak-heat flux is typically on the order of 150 W/mm^2 with a beam size in the range of 1 to 9 mm^2. APS thermal management schemes, at best, can address this level of thermal load: 150 W/mm^2. With the APS-U project, where multiple in-line IDs are anticipated along with increased ring current to 150 mA, new designs and more efficient cooling schemes need to be evaluated to manage the increase in the heat flux. This effort is expected to mature in about four years, targeting monochromator development and design.

High-Resolution Crystal Optics: In the crystal optics area, improvements will be made to the fabrication capabilities, from orientating, cutting, grinding, polishing, and etching to characterization (with some work already started). The two major improvements include: (1) Upgrading the Rigaku Orientating Diffractometer to have a micro-focus source, a long collimating beam pipe, a high-precision automated goniometer, and ultrahigh-precision fixtures for mounting/cutting/grinding crystals, so as to achieve an orientation precision of <0.05° (compared with current precision of 0.1~0.2°). This upgrade is particularly critical for developing ultrahigh-resolution monochromators/ analyzers using highly asymmetric reflections that are aggressively pursued for modern IXS and related instrumentation. A commercial miscut measurement machine (e.g., Bruker D2 CRYSO bench-top crystal orientation analyzer) will be acquired. (2) Major improvement of crystal surface polishing from roughness (rms) of ~2 nm (currently the results from regular polishers) to routinely achieving a few angstroms while maintaining strain-free and defect-free crystal lattices. For critical crystals, the surface roughness will reach ~1 Å with flatness ~λ/20. Ultrasmooth crystal surfaces are crucial for coherence preservation in crystals and mirror substrates, and also for ultrahigh resolution monochromators. To achieve this goal, the advanced polisher will be upgraded to the Strasbaugh 6CM-CMP polisher, moving from pad polishing to pitch polishing. The upgrade cost is being estimated and may also require a dedicated technician position.

Upgrade of the interferometer for flatness measurement is also required. Optics, particularly monochromators designed for conventional energies, encounter problems when pushed to work at higher x-ray energies (> 50 keV). For example, the standard-double-crystal monochromator consisting of two flat-perfect-parallel crystals becomes inefficient at high energies. Far more efficient performance, with over an order of magnitude more flux, is obtained using bent-perfect crystals in the Laue geometry. Developing efficient crystals for high-energy x-rays is therefore essential. Research and development on surface treatment and crystal mounting will lead to available crystals for beamlines. Requisite topography will be performed either on the existing lab base source or at a new optics and detector test beamline. A CCD with a better resolution than the 60-micron pixel size of the CCD now in use will be needed at the laboratory source. Crystal characterization is an extremely important step for developing advanced crystal fabrication procedures and for diagnostics of optics. Currently the APS crystal optics laboratory is equipped with a rotating-anode double-crystal topography test unit (Cu target), which can measure lattice bending of ~0.5 μrad for large crystals up to three inches. This system will first be upgraded by improving the CCD resolution from 60 μm to ~3 μm so that it can reveal small defects (i.e., dislocation, etc., particularly for diamonds). Meanwhile, advanced topography and double-crystal diffraction techniques will be developed for photon energy 7-30 keV at the to-be-built metrology beamline 6-BM. At higher energy, these techniques will be able to detect tiny strains ($\Delta d/d$) or misorientations ($\Delta\theta$) on the order of 10^{-8}, and meanwhile, will be able to characterize almost all crystals (e.g., Si, Ge, diamond, sapphire, quartz, $LiNbO_3$, Be, Cu, Niobium, Tungsten, scintillating crystals, bent-perfect crystals, etc.).

Conventional x-ray topography has been focused on mapping lattice strains or misorientations, but the upgraded APS will heavily rely on coherence-preservation optics for a variety of beamlines. A new bright-field imaging technique (based on the Borrmann enhanced transmission effect) is in development that is extremely sensitive to phase contrast resulting from surface roughness, mechanical damages, and crystallographic defects. This technique will be implemented at beamline 6-BM for advanced crystal characterization with unprecedented sensitivity to strains and wavefront variations. In addition, this technique can provide a novel phase-contrast imaging method for general applications.

There is also active participation in the development of new crystal optics, including: (1) development of sub-meV medium-energy IXS optics with Yuri Shvyd'ko and NSLS-II, involving highly asymmetric and extremely long crystals, thin crystals, comb crystals, etc.; (2) development of new crystal analyzers for MERIX/RIXS to improve the resolution from ~100 meV to ~10 meV at (arbitrary) medium energies; (3) study of new crystals (e.g., sapphire, quartz, etc.) for IXS analyzers; (4) exploration of crystal optics (particularly diamond [4.8.3-12]) for special applications; and (5) development of

coherence-preserving crystals for the wide-field imaging beamline. In addition, in-depth research on crystal diffraction physics, using dynamical theory for designing and modeling multi-crystal diffraction (bandpass, angular acceptance, rocking curves in mono alignment, virtual sources [4.8.3-13], etc.) will be carried out. Meanwhile, computer programs and tools for modeling synchrotron optics are being developed [4.8.3-14].

Multilayer Laue lens (MLL) Optics: Future micro/nanoprobes will require focusing optics with high spatial resolution. The *in situ* Nanoprobe will require focal spot sizes of 20 nm with either zone plates or MLL optics and 50-200 nm with K-B mirrors. Currently MLLs have the highest promise to be used in current and future hard x-ray nanoprobes as focusing optics to achieve spot sizes of 20 nm or below at high (>10 keV) energy x-rays. The *in situ* Nanoprobe planned for the APS upgrade plans to use compact "monolithic" 2-D MLLs arrangements to achieve a spot size of 20 nm for photon energies of 10 – 30 keV (see section 4.3.7). In addition, efforts are being pursued to provide highest-resolution capabilities of below 10 nm in an MLL microscope. Optics for these applications require deposition of as many as 5000 double layers, for a total deposition thickness of 150 microns, with smallest features of 8 nm and a required accuracy of less than 3 nm over the entire course of the deposition.. Such optics will be capable of accepting the full coherent flux, while providing diffraction-limited resolution at high focusing efficiency. To push towards 5 nm, as imagined for an MLL microscope, yet more double layers must be deposited with higher accuracy, while also wedging the zones to locally satisfy the Bragg condition. Significant research and development and a more modern deposition system as are required to meet these goals.

Use of multilayer Laue lenses has been part of high-resolution optics research at Argonne for several years. MLLs have since been embraced by NSLS-II at Brookhaven, which has invested heavily in a new deposition facility aimed at producing 1-nm-resolution optics. While there is ongoing collaboration with Brookhaven on MLL development, the APS-U project will concentrate more on producing optics that are usable in practical experiments at higher photon energies. As an example, optics with a resolution limit of 5 nm at 20 keV will have a focal depth of 4 μm so that one can measure trace element concentrations within many confluent cell types, while optics with 1-nm resolution at 10 keV will have a depth of focus of only 80 nm, which is well within the allowed sample thickness for 0.2-nm-resolution electron microscopy studies. There are also efforts underway at the APS to use micromachining fabrication technologies to develop extremely compact alignment systems for bringing two linearly focusing MLLs together into a quasi-monolithic configuration. If such systems can be realized, then MLLs can be substituted for zone plates in the various nanoprobe instruments that will be part of the APS-U project.

K-B Mirrors: High-quality K-B mirrors are needed for various research programs such as nanodiffraction, spectroscopy, and imaging. K-B mirrors with various parameters capable of providing spatial resolutions from 50 to 400 nm need to be developed according to the requirement of individual beamlines. A dedicated, polychromatic microbeam diffraction instrument in 34-ID-E will be improved to provide routine, reliable hard x-ray beams focused to ~150 nm using a K-B mirror system (section 4.6.4.6). In addition, a K-B nanofocusing mirror system will be installed in 34-ID-F for polychromatic and monochromatic Laue diffraction measurements. K-B mirrors with ultraprecise figure error of better than 0.1 μrad rms and surface roughness of 0.1 nm rms will be required to achieve diffraction-limited two-dimensional focusing for hard x-rays below 50 nm. APS has successfully developed a method for fabricating fixed-figure K-B mirrors using a sputtered thin film profile coating. K-B mirror systems using the Montel (or nested) arrangement are very appealing for achromatic x-ray nanoscale focusing in conventional non-extra-long synchrotron beamlines. This system (see Figure 4.8.3-3, left), with two perpendicular elliptical mirrors aligned side by side, has the advantage of compactness, longer working distance, and larger collecting divergence than conventional sequential K-B optics. Monolitic Montel K-B mirrors made in a single piece are not feasible at this point. The profile coating technique [4.8.3-4] is well

developed to make the K-B mirrors for the arrangement shown in Figure 4.8.3-3, using either spherical or flat-Si substrates. Recent tests carried out at 34-ID-E delivered a two-dimensional focal spot size of 150 nm × 150 nm with either monochromatic or with broad-bandpass beam of energies up to ~30 keV [4.8.3-15]. The challenge is to produce a precise elliptical surface profile at the very edge where the two K-B mirrors meet. A wider mirror can be coated first, cut into two mirrors, and then the side of one of them can be polished before aligning them side by side. A very sharp edge, within a few microns variation, can be obtained. The metrology result (Figure 4.8.3-3, right) indicates that a high-precision elliptical profile remains in the mirror surface at the edge, and the measured profile is very close to the design.

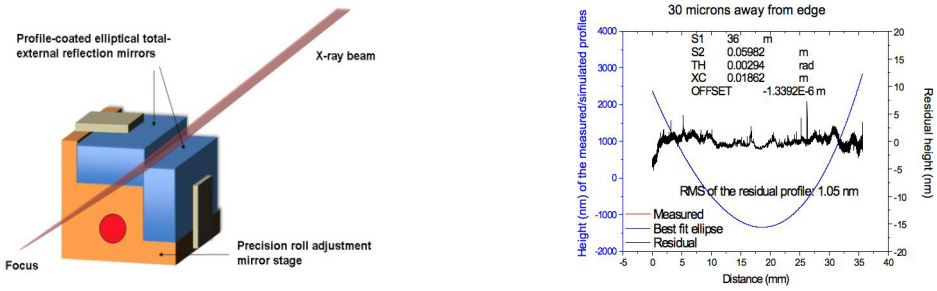

Figure 4.8.3-3. A sketch of the nested (Montel) K-B mirror setup (left), made by Pt-profile-coated K-B mirrors, and the measured Pt surface profile at 30 μm away from the edge after polishing (right). The measured residual height error after polishing is 1.05 nm rms from an ideal ellipse at the edge area. Here, the mirror size is 40 mm × 9 mm × 4.5 mm.

Further efforts are needed to find the most stable nested K-B system for extended high-energy x-ray radiation and to coat and polish larger K-B mirrors. On the equipment side, a larger deposition system and a large ellipsometer are needed. On the materials science front, still much work is needed to understand the mirror stability problem. K-B mirrors usually do not have radiation damage since they are total external reflecting optics. As a matter of fact, a Au-profile-coated K-B mirror using a flat-Si substrate and not-optimized dimensions (70 mm × 9 mm × 4.5 mm, long and thin) was successfully operated under normal conditions for almost two years until it was subjected to extended x-rays for several days with the slit fully open. The damage was attributed to a plastic deformation of the thin substrate due to x-ray induced stress relaxation of the Au film [4.8.3-16]. Since then, Pt has been used instead of Au because of its smaller film stress on Si. The substrate dimension has been optimized. Spherical Si substrates have also been used to reduce the coating thickness needed and thus, to further reduce the influence of film stress. There are still issues of mirror stability under extended x-ray radiation conditions. There are materials issues under extended x-rays that are not fully understood. The source of radiation damage to the Pt-coated mirror must be determined, as well as the exact cause for the deterioration of mirror performance. In addition to possible mirror material structural change, there are common C contaminations on the mirror. Figure 4.8.3-4 shows a stylus profiler scan across a C contamination line on a deteriorated Pt-profile-coated K-B mirror. A ~20-nm-high, 200-μm-wide bump is clearly visible. Efforts to reduce C contamination are needed.

Development of multilayer profile mirrors with ultralow figure errors is another area that will require much effort. While achromatic beams obtained through total reflection mirrors are important for some micro diffraction experiments, multilayer profile mirrors can yield smaller focal spots due to increased numerical aperture from multilayers. This type of optics is essential for many applications requiring nanoscale spot size <20 nm with large numerical apertures, such as differential phase contrast imaging with grating interferometry in the magnifying geometry (under consideration at 2-BM by Xianghui Xiao) and for studying material under extreme conditions. Laterally graded multilayer profile

mirrors can also be used as a polychromator in multiwavelength dispersive x-ray reflectometers. Further applications of multilayer profile mirrors are expected to grow with the APS-U project underway.

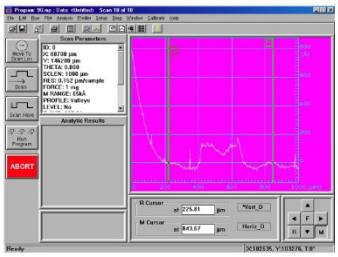

Figure 4.8.3-4. C contamination on a damaged K-B mirror as revealed by a stylus profiler.

To complement the profile coating technique in surface figuring, profile etching will be explored. Using a broad ion beam through an aperture mask to etch a moving substrate, in principle a profiled surface along the direction perpendicular to the moving direction can be created, just like the case in profile coating. Combining profile etching with profile coating, the coating thickness can be reduced (and thus the film stress). Then flat substrates can be used to produce profile mirrors and avoid the troublesome spherical profile of the spherical substrates.

To accommodate the demand of experimental samples, the APS deposition facility needs to be upgraded with new capabilities keeping up with new demands in both sample materials and structures. A new deposition system is needed to successfully fabricate the advanced MLLs and K-B optics. This system should be able to produce up to 200 mm-long K-B mirrors using the profile coating technique with much better deposition stability and transport property. The new deposition system should be capable of supporting future needs such as the superconducting detectors program led by Antonino Miceli. The APS superconducting detectors program will require deposition of thick stress-mitigated films (>~ 50 microns) in order to increase efficiencies at high energies. This requirement is similar to the needs for optics development.

Zone Plates: New zone plate optics and multilayer Laue lens optics will be installed at 34-ID (see section 4.6.5.5) to expand the energy range and efficiency for nanodiffraction on the diffractometer platform. Single-layer Freznel zone plates (FZPs) with zone widths down to 24 nm and aspect ratios of 15:1 are commercially available from a single vendor (Xradia Inc.), but no commercial roadmap to obtaining higher aspect ratios in single optics has been proposed. With the APS-U project, there will be at least six separate end stations that rely on high resolution zone plates, so it is crucial that there be an in-house program in zone plate development, concentrating on paths not taken by commercial vendors. Recent developments such as a zone-doubling technique have produced Fresnel zone plates with outermost zone widths down to 20 nm and aspect ratios higher than 25 [4.8.3-17]. Argonne's Center for Nanoscale Materials has a well-equipped nanofabrication lab that can be used for much of the work. The APS effort will center on two complementary approaches. The first approach is the use of materials growth processes (such as anodic aluminum oxide processes now being explored in collaboration with researchers in Materials Science and Energy Science at Argonne) that can produce higher aspect ratio structures. The second approach is the use of multiple-level fabrication processes that can multiply the highest achievable aspect ratio. This second approach requires capabilities that are not presently available at Argonne. One possible avenue is to collaborate with researchers at Cornell University, who have process technologies that are not yet available at Argonne and who will soon be receiving a first-of-its kind electron beam lithography system with unparalleled overlay accuracy. The effort should have a balance of research into new fabrication methods alongside timely delivery of optics

for scientific applications. This suggests a mix of student and postdoc research along with long-term staff members who can be counted on to deliver zone plates using successful processes.

Efforts must be continued on nanoscale multilayer x-ray masks for applications such as x-ray lithography, etc. Using the experience that Argonne gained in MLL fabrication, nanoscale gratings and x-ray masks were made. New applications need to be explored.

Laboratory and Beamline Metrology: When the APS was built, mirrors with 4-μrad rms slope error and 3- to 4-Å rms were considered to be the state-of-art, and metrology tools were developed or customized for the specific use at synchrotron radiation laboratories. Nearly twenty years later, the x-ray manufacturers are in the process of ramping up their capabilities to produce mirrors with slope errors that are more than an order of magnitude smaller (<0.5 mrad rms) and surface roughness more than a factor of 0.5 smaller (<1.5 Å rms). This level of surface quality is attainable using advanced deterministic polishing methods, where surface imperfections are precisely removed at the atomic or molecular level. The finite size of the tools used in deterministic fabrication methods can produce mid-spatial range imperfection and are outside the measurement range of the conventional Long Trace Profiler [4.8.3-11]. Developing a new generation of metrology tools that are capable of characterizing mirrors at all relevant length scales is now considered essential, especially for cases where coherence and wavefront preservation is required. For this reason, metrology based on stitching of interferometric data has now gained wide acceptance in industry and has been routinely utilized for the production of aspheric optics. At synchrotron radiation facilities, stitching of microscope interferometer data has been successfully used to deterministically fabricate diffracted-limited elliptical x-ray nanofocusing mirrors [4.8.3-18, 4.8.3-19]. However, because interferometers rely on internal optics and suffer from a variety of systematic errors, extension to the evaluation of large mirrors is challenging. To meet future needs, R&D effort is needed to improve existing techniques and develop a new generation of metrology tools that are robust and capable of measuring 2-D mirror surfaces with a high degree of precision at all length scales. A particular emphasis should be placed on developing innovative tools that do not rely on internal reference optics for measurement and are not affected by other environmental perturbations.

As useful as offline metrology is, there is no substitute for at-wavelength x-ray tests of optic performance. Since so many of the beamlines of the APS-U project depend on advances in optics to achieve their scientific goals, it is crucial to have frequent access to an optics testing end station (this end station could also serve needs for detector testing). By having a constant configuration, it is possible to compare optics to each other directly without having to take into account the variations between different beamlines where there could be brief time windows for optics testing among user science programs. This optics test end station should have a well-characterized illumination footprint, and precisely calibrated flux monitors both before and after the optic. More importantly, it should have a nanopositioning stage at the optic's focus and fluorescence detector for resolution tests using nanowires, and an area detector for measurement of the optic's far-field intensity pattern. By having a large, kinematic mount point, separate mounts for different optic types can be accommodated. One example is the multilayer Laue lens or MLL alignment platform developed by D. Shu, shown in Figure 4.8.3-5 [4.8.3-10]. This work will be initiated on the future Optics and Detector beamline. However, because nanofocusing optics require coherent illumination to achieve diffraction-limited performance, and because coherence makes available important test methods such as far-field diffraction reconstruction [4.8.3-20] and ptychography [4.8.3-21], it is essential to also develop a coherent optics testing end station that can use some fraction of the time of an ID beamline.

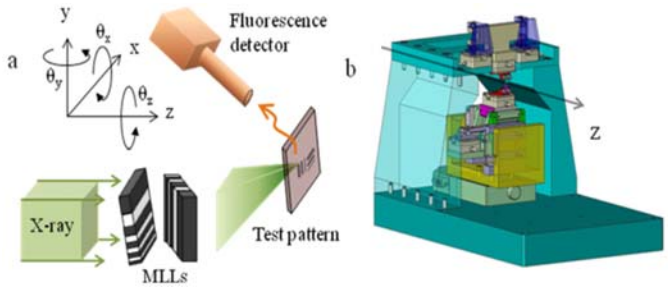

Figure 4.8.3-5. MLL manipulator implemented for two-dimensional focusing.

4.8.3.4 References

[4.8.3-1] X. Huang and A.T. Macrander, AIP Conf. Proc., (in press).

[4.8.3-2] Computer Controlled Optical Surfacing, Tinsley Laboratories Inc., 4040 Lakeside Dr. Richmond, CA 94806 USA; www.asphere.com.

[4.8.3-3] K. Yamamura et al., Rev. Sci. Instrum. **74**, 4549 (2003).

[4.8.3-4] C. Liu et al., SPIE **4782**, 104 (2002).

[4.8.3-5] C. Liu et al., J. Appl. Phys. **98**, 113519 (2005); US Patent 7,440,546, Oct. 21, 2008.

[4.8.3-6] H.C. Kang et al., Phys. Rev. Lett. **96**(12), 127401 (2006).

[4.8.3-7] A.T. Macrander et al., *Handbook of Optics* (McGraw-Hill Professional, 2009), Vol. V, Ch. 42.

[4.8.3-8] H.C. Kang et al., Appl. Phys. Lett. **92**(22), 221114 (2008).

[4.8.3-9] H. Yan et al., Phys. Rev. B **76**, 115438 (2007).

[4.8.3-10] H.F. Yan, V. Rose, D. Shu, et al., "Hard X-ray Microscopy at the Nanoscale," submitted (2010).

[4.8.3-11] P.Z. Takacs et al., Appl. Optics, **38**(25), 5468 (1999).

[4.8.3-12] Yu.V. Shvyd'ko et al., Nat. Phys. **6**, 196 (2010).

[4.8.3-13] X.R. Huang, A.T. Macrander, and P. Fernandez, submitted to J. Synch. Rad.

[4.8.3-14] X. R. Huang, J. Appl. Cryst. (in press).

[4.8.3-15] W. Liu, G. Ice, L. Assoufid et al., The 16th Pan-American Synchrotron Radiation Instrumentation Conference (SRI2010), September 21-24, 2010, Argonne National Laboratory, USA, (abstract submitted).

[4.8.3-16] C. Liu et al., SRI 2008 Conference Proceedings (2008).

[4.8.3-17] J. Vila-Comamala et al. Opt. Express **19**(1), 175 (2011).

[4.8.3-18] K. Yamauchi et al., Rev. Sci. Instrum.**74**, 2894 (2003).

[4.8.3-19] L. Assoufid et al., Proc. SPIE **6704**, (2007).

[4.8.3-20] H.M. Quiney et al., Nat. Phys. **2**(2), 101 (2006).

[4.8.3-21] K.M. Kewish, M. Guizar-Sicairos, L. Assoufid et al., XRM2010 Conference, Chicago, IL, August 2010, to be published.

4.9 Detector Development Capability [CAS]

4.9.1 Introduction

The APS-U project will have an appropriately sized detector capability component to ensure that the project science objectives are achieved. The two ingredients of this detector capability are the detector development efforts (section 4.9.2) and the enhancements to the existing APS Detector Pool (Section 4.9.3). The significant gains in beamline performance (e.g., brilliance, spot size, etc.) from the APS-U project will be largely wasted unless detectors at the APS are improved to keep pace.

Detector development efforts for the APS-U project will focus on expanding the capabilities for detection of hard x-rays (i.e., E > 20 keV), both in terms of efficiency and resolution, and pushing the readout speed of area detectors and diode arrays. The reasons for pursuing these avenues of development are rooted in the science case for the APS-U project. Faster, more efficient detectors (with improved resolution) are needed to realize the goals of studying real materials under real-time conditions and imaging matter at different length scales.

The expansion of the APS Detector Pool will support the goals of the APS-U project by providing cutting-edge commercial and quasi-commercial detectors to the APS user community. Quasi-commercial describes detectors developed at other universities or national laboratories that have not been commercialized. These detectors will be made available to the APS community through collaboration or contracts. We will also expand the services of the Detector Pool to provide enhanced support in detector characterization, maintenance, and use.

4.9.2 Detector Development

The APS-U project will have a strong detector development program to provide custom leading-edge detectors specifically suited for the needs of the project's science objectives. The APS-U project detector development effort will concentrate on three main areas: (1) hard x-ray detectors, (2) ultrafast picosecond detectors, and (3) column-parallel CCD cameras. Although these areas can be treated individually, much overlap occurs among them in technology, infrastructure for testing, and APS x-ray science applications. These projects will also tap the existing DOE-funded APS detector development for cryogenic high-energy resolution x-ray detection using superconducting MKIDs, designed and optimized for high count rate spectroscopic experiments. As the APS-U project moves forward and the scope of the project is refined, the detector development efforts described in this chapter will evolve and adapt to satisfy the requirements of the project.

4.9.2.1 Scope

The detector development work will proceed through collaborations with universities, industry, other national laboratories, and synchrotron facilities. Collaborations with universities involve graduate students and the use of university resources. Examples include the use of Northern Illinois University's clean room facility for semiconductor device fabrication and testing (Figure 4.9.2-1), Georgia Institute of Technology's radio frequency integrated circuit design and test capability, and DePaul University's femtosecond laser laboratory. (The cryogenic MKID work partners with the University of California, Santa Barbara.)

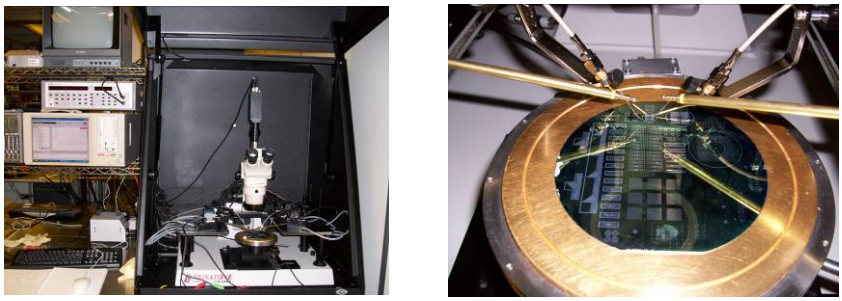

Figure 4.9.2-1. The Northern Illinois University Microelectronics Research and Development Laboratory facility is utilized to partially fabricate sensors and test wafers in a clean environment. The figure depicts (1) photodiode arrays being tested by using a semiconductor parameter analyzer and (2) an rf probe station inside a dark box. Many universities have suitable facilities; however, Northern Illinois University offers the advantage of a nearby location. The Optics and Detectors Group in the APS X-ray Science division has established a collaboration with Northern Illinois University to utilize their $8 M facility and to work on the design of custom ASICs.

Collaborations with industry can occur under DOE's SBIR program, or by contracting directly by using APS-U project funds. As customers (SBIR) or contract managers (APS funded), the detector needs of a beamline are matched to an industrial capability, perhaps in sensor or electronic circuit design. Success is measured by the delivery of detector systems that ultimately can benefit many synchrotron facilities (Figure 4.9.2-2).

Figure 4.9.2-2. This figure displays the disassembled parts of a pixel array detector that has been under development by Voxtel, Inc., for the past several years, as part of their Phase II SBIR. The detector was recently delivered to the APS. This particular detector has a 500-µm-thick silicon sensor, segmented to 48 ×48, 130-µm pixels. The sensors are similar to those being tested at Northern Illinois University, as shown in Figure 4.9.2-1 (overlaps in technologies are quite prevalent). The sensor is bump-bonded to a Voxtel-developed custom ASIC that for each pixel provides a user-defined energy window and two counters. The counters typically are meant for counting events with or without the laser pump in laser pump-x-ray probe experiments. The shaping times are on the order of 20 ns, far faster than any other PAD detector worldwide, and aimed at high count rate APS experiments or the 324-bunch mode. Working with companies can lead to rapid progress. However, it remains necessary to commit further resources to bring these fairly involved projects to the beamlines. The challenge will be to select the best of what industry has to offer and then support it.

Collaborations with other national laboratories and synchrotron facilities often involve technology exchange. An example is the joint development of a quasi-column-parallel CCD camera, which is discussed below.

Hard x-ray detectors: Hard x-rays are defined as photons for which 500-µm-thick silicon is 25% efficient or less; that is, 22 keV or higher [4.9.2-1]. To design an efficient hard x-ray detector, high-Z (atomic number) materials must be used in the form of a phosphor, scintillator, or direct detect semiconductor. Because indirect detection (using a phosphor and silicon sensor) has lower energy or spatial resolution, this development effort will focus on direct detection [4.9.2-2].

Development for hard x-ray applications will include research into sensor materials, fabrication of test devices, and coupling of the sensors to integrated or circuit board readout electronics. The sensor converts the incoming hard x-rays into electron-hole pairs. Since research in this area has been ongoing for decades, there are several materials of interest. Silicon is a primary sensor material and the mainstay of the integrated circuit industry. The next material of interest is germanium, which also is available in large-size, high-quality crystalline wafers. Other materials that can be used for hard x-ray sensors include many of the III-V or II-VI compounds. In addition, worldwide research has been conducted on the heterojunction superlattice structure.

One role in sensor research will be to evaluate new ideas from industry and universities by building on an expanding capability in the testing and characterization of materials. This task will involve improving the test stands that determine parameters of interest, such as the speed and mobility of the material as a function of temperature and electric field, the lifetime of carriers, the quality of the crystal and hence its suitability for energy dispersive detectors, the effectiveness of diode-type structures, the point spread function, etc.

A second emphasis will focus on the theoretical and system models of sensors and detector structures being created by industry, universities, etc., with the goal of guiding development toward sensors for hard x-rays. For example, companies that work in infrared applications may not be aware that the same materials (e.g., GaAs and InSb) can be used for hard x-ray applications if the sensor could be made thicker.

A third emphasis will be to evaluate and selectively fund work for emerging sensor concepts, such as photo-electron-collecting microstrips, possibly combined with work on photocathode materials (here overlapping with the ANL High Energy Physics ultrafast detector work [4.9.2-3]); TFTs deposited on high-Z substrates or sensors; and high-Z CCDs.

Ultrafast picosecond detectors: Picosecond x-ray timing development work will be tailored to pump-probe experiments, where the sample is first excited with a sub-picosecond duration laser pulse and then investigated with x-rays from the ~100-ps APS x-ray bunch. Development will include gaining an understanding of fast sensor materials, working with electronic packaging, and examining ultrafast integrated circuit electronics. The resulting detectors can be set up at multiple beamlines, and their development will tap the large industrial base in integrated circuit design.

By mimicking existing detectors that work at the microsecond [4.9.2-4, 4.9.2-5] or nanosecond range, picosecond detectors will often be fabricated as a pixel array detector—a hybridization of a semiconductor sensor bonded to the readout ASIC. Other groups, especially in high-energy physics, are also investigating the use of electron multiplication (e.g., microchannel arrays) coupled to fast microwave strip lines. In either path, extensive care must be paid to packaging for low-inductance, fast signals. Ultrafast detectors typically are tested or calibrated with femtosecond laser pulses and specialized rf test equipment. The test capabilities at the APS beamlines will be utilized, as will the DePaul University Physics Department's femtosecond laser laboratory.

For precision timing, it is essential to have low jitter or uncertainty between the reference, or start, signal and the collected, or stop, signal. In most cases, the same laser pulse that excites the sample starts the internal "stop-watch," thus eliminating this source of jitter. Such detection schemes are not affected by jitter in the timing clocks derived from the rfs used in the synchrotron or storage ring. Precision timing also requires ultrafast electronics, beyond what can be done on a printed circuit board, and leads to the use of modern SBIR processes.

Presently, collaboration with the electrical engineering department at the Georgia Institute of Technology is under way to develop ultrafast SiGe electronics [4.9.2-6]; this effort is funded by current APS resources. Simulations show that integrated electronics can pass signals with delays of about 7 ps, thus setting this as a range for timing resolution. Furthermore, the necessary SiGe-based BiCMOS electronics can fit under a pixel size of 100-200 μm square. (Small pixels are necessary for good spatial and timing resolutions.) This effort takes advantage of the IBM8HP Bi-CMOS commercial process.

Column-parallel CCD cameras: CCDs have a long history and play an important role in x-ray science. They offer advantages by providing a path to small pixel size and excellent energy resolution. As part of the APS-U project, the large body of work done on CCD detectors will be leveraged to continue extending and improving their capabilities as x-ray detectors. The APS has a standing collaboration with the ALS at LBNL, known as the "Fast CCD Collaboration," to develop fast frame rate CCDs for synchrotron applications [4.9.2-7]. These detectors use a quasi-column-parallel CCD chip developed by LBNL. As part of the APS-U project, the Fast CCD Collaboration will continue to develop fully column-parallel cameras for use at both facilities (Figure 4.9.2-3).

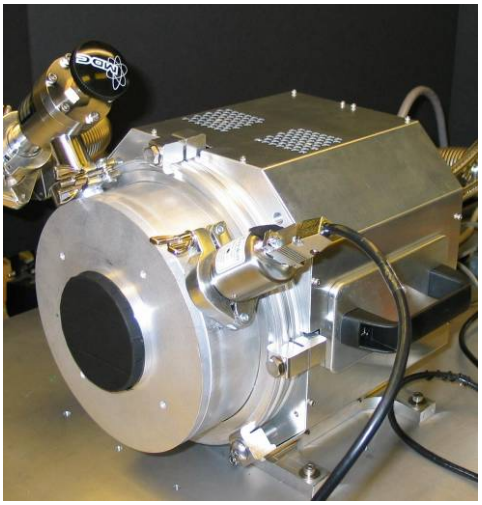

Figure 4.9.2-3. This figure shows the existing Fast CCD detector routinely in use at the APS. This detector is the result of a successful partnership with LBNL technical groups.

4.9.2.2 Description

Hard x-ray detectors: There are many options here that must be carefully evaluated. For detection of hard x-rays with medium spatial resolution, a collaborative development of a high-Z PAD will be considered. Examples of this architecture include the Pilatus and Medipix systems [4.9.2-4, 4.9.2-5]. At this point, some estimates are in hand for the amount of electronics that can be pushed into a pixel's footprint, based largely on APS work with industry. Each pixel's read-out electronics takes up space, so 2D PAD pixel sizes typically range from 80 μm and up, while 1D strip detector pitch is limited by sensor charge spreading. (Dimensions are steadily dropping, for example, as 3-D CMOS circuitry becomes more common, and it will be necessary to revise these estimates.)

For high-spatial-resolution (perhaps < 1 μm) imaging of hard x-rays, a double-sided microstrip detector based on research at Risø-DTU by Poulsen et al. [4.9.2-8] will be considered. This detector, called the "NanoDetector," is fashioned by creating fine strip electrodes of 1-μm pitch on both the top and bottom of a 1 mm × 1 mm, high-Z semiconductor sensor (InP), with the top and bottom strips being perpendicular. As single x-ray photons generate electron-hole pairs in the sensor, signals generated in the electrodes can be used to determine the centroid of the photon-generated charge cloud (Figure 4.9.2-4).

Recent developments from Professor Karim Karim at the University of Waterloo will also be considered. He has demonstrated that amorphous silicon TFTs can be integrated with crystalline photodiode sensors to produce direct-detection hard x-ray detectors [4.9.2-9] (Figure 4.9.2-4).

InSb is also a high-Z material. Industry has already used it for photodiode arrays and CCD structures for infrared applications. Finally, germanium is a candidate high-Z semiconductor, and collaboration with ongoing industrial work for Ge-PADs [4.9.2-10] will continue.

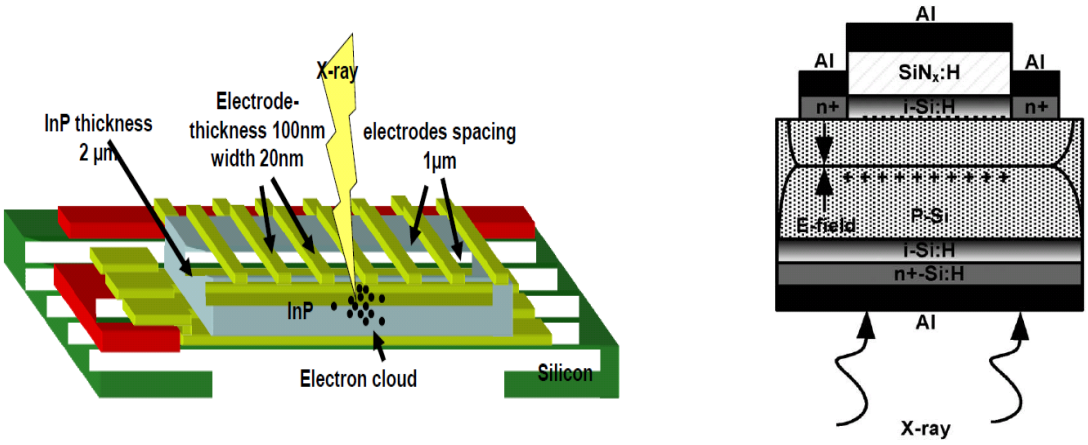

Figure 4.9.2-4. The left figure details the schematic of the Risø NanoDetector concept. Two sets of orthogonal gold strip lines are patterned with e-beam lithography on an InP diode sensor. The red boxes on the edges are the readout electronics (ASIC) (courtesy of Henning Friis Poulsen [4.9.2-8]). The right figure shows a single-pixel schematic of a-Si TFT architecture merged with the crystalline Silicon PIN diode [4.9.2-9], © 2010 IEEE.

Ultrafast picosecond detectors: Ultrafast detectors must be carefully packaged. If long signal connections are necessary, they must be made with attention to proper rf matching and line impedance. Amplifier and signal processing bandwidths often fall in the gigahertz range, and cable transmission losses can be significant. It seems very likely that most electronics for ultrafast picosecond detectors will be done with custom integrated circuits, i.e., ASICs, or a hybrid technology where the silicon die for a commercial integrated circuit is bonded to a custom printed circuit board.

Currently, the fastest electronics are based on SiGe heterojunction bipolar transistors; therefore, attention has been focused there. Foundries worldwide have put considerable R&D into this technology, resulting in rapid gains in the clock speeds of ICs. For signal processing in mixed mode (analog and digital) integrated circuits, the basic clock speeds have moved into the 100s of GHz range. Today, SiGe transistors have unity gain frequencies (fT) of 300-500 GHz. Feature sizes continue to drop, and they are now 110 nm for the IBM8HP BiCMOS process used by Georgia Tech collaborators [4.9.2-6, 4.9.2-11].

Column-parallel CCD cameras: The goal of the Fast CCD collaboration between APS and ALS/LBNL is to maximize the usefulness of CCDs in x-ray detectors. To this end, LBNL has developed quasi-column-parallel CCDs and custom readout chips, which increase the speed and QE of CCDs in x-ray applications. The first prototype of these quasi-column-parallel Fast CCD detectors features a 480 × 480 pixel CCD, a 30-µm × 30-µm pixel size, an almost column-parallel readout with 96 output ports (48 on top and 48 on bottom), a fully depleted 200-µm-thick substrate, a pixel conversion time of 1.6 µsec, and a readout time of 5 msec.

The version of the Fast CCD detector currently under development will be larger. It will have a 1920 × 960 pixel CCD; 192 output ports; the ability to operate in a frame transfer mode, with an image size of 960 × 960 pixels; a pixel conversion time of less than 1 µsec; and a readout time of 5 msec.

As part of the APS-U project, for the future extension of the Fast CCD detector, a CCD with a fully column-parallel readout will be developed. This advance will allow the fastest readout rate possible for a CCD, while maintaining its QE energy resolution and small pixel size.

4.9.2.3 Research and Development

Hard x-ray detectors: To address this large subject, multiple options (especially pixel detectors) will be considered at the system model level. Pixel detectors, such as the Pilatus, Medipix, or Voxtel systems, that utilize bump-bonded 1-D CMOS readout electronics have a pixel size limited to greater than ~80 μm. Alternatively, readout circuitry has been realized as TFTs deposited by using a PECVD system directly on the sensor. Because thin-film electronics generally are very simple compared with bump-bonded electronics, pixel sizes may be much smaller, perhaps down to 10 μm (the tradeoff often is lower speed). For this reason, the use of thin-film electronics bonded to a high-Z semiconductor is being considered. Of particular interest is the depositing of TFT electronics on crystalline silicon, thereby creating a high-quality detector [4.9.2-9]. Research will be needed to examine the deposit of TFT electronics on high-Z materials, such as crystalline CdTe and GaAs, for area detectors of less than 400 mm^2. For detectors with a larger area, amorphous selenium will be investigated.

For high-spatial-resolution hard x-ray imaging, design based on the NanoDetector [4.9.2-8] will be considered. This detector is currently in the prototype stage, and additional R&D will be required before a system can be used at a beamline. However, it could lead to high spatial resolution (~1 μm or less). Spatial resolution generally involves a tradeoff for efficiency, since highly efficient detectors tend to be thick and therefore have poor spatial resolution. A proper balance between spatial resolution and efficiency must be achieved. Because the NanoDetector features readout electronics on the periphery, it is possible to stack several detectors to improve efficiency. The Risø-DTU group needs assistance in the area of readout electronics, which could lead to collaboration. The main limitation for this detector is the maximum flux rate. This aspect can be improved with faster readout electronics, such as those using wavefront analysis techniques.

As part of R&D efforts in this area, development will continue on the capabilities of the cryogenic (20 K to 300 K) test stand. This test stand will be used to evaluate sensor materials and devices for hard x-ray detectors. Semiconductor device modeling codes will be implemented to enable simulation of devices and fabrication (foundry) processes. To manage the procurement of hard x-ray devices through outside vendors (if necessary), it is crucial that foundry processes are well understood.

Ultrafast picosecond detectors: As described above, custom ASICs are developed by utilizing the fastest industrial IC processes and relying on industrial CAD tools that model circuit performance. This has been one of the motivations for the establishment of in-house IC design capability, as well as for work with universities. Also in need of development are the sensor and the process to bond it to the ASIC. This work can proceed in steps (i.e., small arrays first, etc.). Further, commercial processes, such as bump bonding and packaging, will be mastered. Much of the test equipment will overlap that needed by others working at the GHz level (i.e., rf network analyzers, etc.).

Column-parallel CCD cameras: The development of fully column-parallel CCDs will enable scientists to take advantage of the upgrade, which will allow them to collect data faster and more efficiently. To make a fully column-parallel x-ray detector, a custom CCD chip and a custom readout chip must be designed. One challenge in making the CCD chip is that the output circuitry must be small enough to fit into the width of the 30-μm pixel. The readout chip must have a large number of CDS converters to accommodate the 1920 outputs that a 1920 × 960 CCD will have. The readout chip must be able to fit each CDS converter into the 30-μm pixel width to enable its inputs to line up with the outputs of the CCD chip. The acquisition system will need to be fast enough to collect the raw data stream, which can be as much as 4000 Mbytes/sec. Storing this amount of data is impracticable, so methods to reduce the data in real time will become extremely important. Any data reduction algorithms will most likely become an integral part of the detector to reduce the amount of data being stored.

4.9.2.4 Design

Hard x-ray detectors: There is a great deal of synergy between these detectors and ultrafast detectors. Typically, the system involves the sensor (which is often done by outside groups) and readout electronics. To the extent that the electronics are done on-ASIC, they can be designed in-house or externally (i.e., collaborations, hired consultants, universities, back to those who designed the sensor, etc.). There are standard paths to read-out the ASICs into a computer and hence into beamlines, based on commercial digital electronics. This last piece can be considered off-the-shelf.

Ultrafast picosecond detectors: These detectors follow the pattern of slower pixel array detector— sensor bonded to the underlying ASIC. However, now the packaging problems are challenging, especially if the sensor must be cooled.

Column-parallel CCD camera: While the details change, the overall design of the column-parallel readout detector does not change from the present Fast CCD detectors. The main components are a detector head, back end electronics, a vacuum system, a cooling system, and an interlock system. It is advantageous to reduce the total size of the detector so it is more portable, as well as to continue making improvments to the user interface in an effort to make the detector a seamless part of the experiment.

4.9.2.5 Anticipated Performance

Hard x-ray detectors: Various high-Z materials have excellent stopping power up to ~100 keV (Fig 4.9.2-5). Pixel sizes of 45 μm are anticipated via the use of Si TFT electronics deposited on high-Z materials. A pixel detector with such architecture on a 200-μm-thick sensor of CdTe would provide about 15% efficiency at 60 keV. Based on the performance of current TFT-based area detectors, the detector could provide >30 frames per second. Because CdTe exhibits fluorescence x-rays in the energy range of interest, GaAs has been shown to be a better choice for medium-resolution pixel detectors. However, as a trade, CdTe comes in high-quality wafers, which are available from Acrorad Corporation in Japan [4.9.2-12].

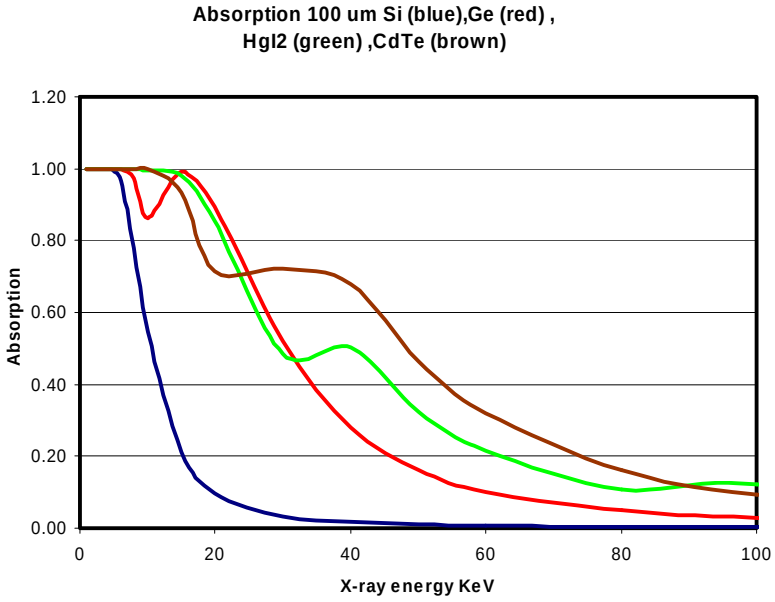

Figure 4.9.2-5. This figure shows the x-ray stopping power of various materials at an arbitrarily chosen thickness of 100 μm. Sensor thickness affects x-ray efficiency, timing, spatial resolution, and mechanical packaging.

There are fundamental limits to sensor spatial resolution as a function of sensor thickness. Still, with centroiding of the detected signals, spatial resolutions in the micron range are anticipated for some architectures.

Ultrafast picosecond detectors: As with hard x-ray detectors, there are fundamental trades of sensor thickness and time resolution. The speed of an electron carrier in most semiconductor materials is in the range of 10^7 cm/s. An x-ray stopping at the top of a 5-μm-thick silicon sensor will create a signal ~50 ps later than an x-ray stopping at the bottom of the sensor. This leads to an approximate 14-ps RMS spread, which is lower (hence better) if faster materials such as GaAs or InSb are used, and a bit lower still if they are cooled. The processing electronics can work with a time resolution of <10 ps, as demonstrated by delay line architectures and wave form sampling integrated circuits. Such circuits are being simulated; they can lead to pixel sizes in the range of 100-200 μm square, if a 2D PAD is expected.

Column-parallel CCD cameras: The anticipated performance of the column-parallel Fast CCD detector is shown in Table 4.9.2-1. The major improvement over the existing CCD x-ray detectors is in achieving the faster readout speed while maintaining the high QE, read noise, and small pixel size.

Table 4.9.2-1. Performance of the Column-Parallel Fast CCD Detector

Quantity	Description of Feature
1920 × 960	Number of CCD pixels
30 μm × 30 μm	Pixel size
200 μm	CCD thickness
1920	Number of outputs, 960 on top and 960 on bottom
500 ns	Pixel conversion time
2000 fps	Frame rate in 960 × 960 frame transfer mode
0.5 ms	Readout in 960 × 960 frame transfer mode
4000 MB/s	Raw data rate in 960 × 960 frame transfer mode

4.9.2.6 References

[4.9.2-1] Lawrence Berkeley Laboratory, Filter Transmission Website (2010); http://henke.lbl.gov/optical_constants/atten2.html.

[4.9.2-2] G. Knoll, *Radiation Detection and Measurement*, 3rd ed., (John Wiley and Sons, Inc., New York, NY, 1999).

[4.9.2-3] H. Frisch et al., Argonne National Laboratory and the University of Chicago Collaboration on High Energy Physics Detectors, various internal reviews (2009, 2010).

[4.9.2-4] E.F. Eikenberry et al., Nucl. Instrum. Methods A **501**, 260 (2003).

[4.9.2-5] S.R. Amendolia et al., Nucl. Instrum. Methods A **422**, 201 (1999).

[4.9.2-6] J.D. Cressler and G. Niu, *Silicon-Germanium Heterojunction Bipolar Transistors*, 1st ed., (Artech House, Boston, MA, 2003).

[4.9.2-7] P. Denes et al., Rev. Sci. Instrum. **80**, 083302 (2009).

[4.9.2-8] H.F. Poulsen et al., Mat. Sci. Forum **467-470**, 1363 (2004).

[4.9.2-9] K. Wang and K.S. Karim, Electron Device Lett. **31**, 147 (2010).

[4.9.2-10] Voxtel, Inc., Portland, OR, private communication (or refer to the DOE SBIR website) (2010); http://www.er.doe.gov/sbir/.

[4.9.2-11] R. Krithivasan et al., IEEE Electron Device Lett. **27**, 567 (2006).

[4.9.2-12] Acrorad Corporation, “Development of CdTe Detectors in Acrorad” (2010); http://www.acrorad.co.jp/_skin/pdf/Development_of_CdTe_detectors.pdf.

4.9.3 Detector Pool

A significant fraction of APS-U project detector needs will be satisfied by purchasing commercial off-the-shelf equipment or by contracting with companies, universities, and/or national labs for the fabrication of custom or non-commercially available detectors. Most of these detectors will be procured for dedicated use at specific beamlines, but some will be placed in the APS Detector Pool for use by the entire APS user community. A significant amount of effort will involve the evaluation of potential x-ray detectors from the medical imaging industry and other non-synchrotron industries. The resources dedicated to each of these activities will depend on the actual scope of the APS-U project beamline upgrades and related detector needs. The APS Detector Pool currently includes more than 50 x-ray detectors and satisfies over 300 user requests per calendar year (Figure 4.9.3-1).

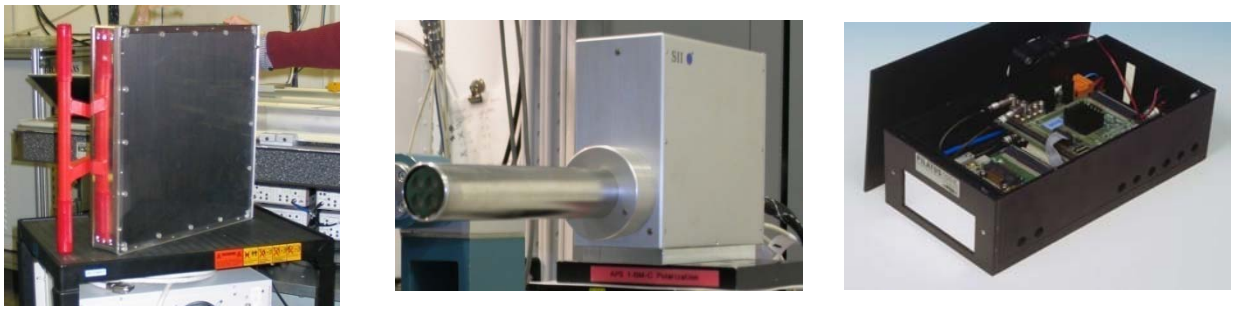

Figure 4.9.3-1. Examples of existing equipment in the APS Detector Pool. From left to right: amorphous silicon detector (GE Healthcare); 4-element silicon drift detector (SII NanoTechnology); and Pilatus 100-K silicon pixel array detector (Dectris).

Most of the commercial detectors to be procured are fast large-area detectors, either amorphous silicon (a-Si) flat panels for E > 40 keV or Pilatus silicon PADs for lower energies, including the next-generation Pilatus XFS, which will be faster (~ 10 kHz) and have smaller pixels (75 μm). Additional commercial detectors that will be procured include CCDs and scientific CMOS cameras with varied specifications, CMOS flat panel detectors, silicon strip detectors, and assorted single-element photon counting detectors. There is also a strong science case for custom-designed energy dispersive SDD arrays; these custom detectors, with a modest number of elements, can be purchased from commercial suppliers.

Newer commercial technologies, especially from the medical field, will also be evaluated for adoption at the APS. Examples include the amorphous selenium flat panel detectors used in mammography systems and the high-resolution, high-energy detectors from the dental imaging market [4.9.3-1, 4.9.3-2].

Under consideration as part of the APS-U project is the expansion of APS Detector Pool services to include the maintenance and repair of silicon PADs. This activity will entail training the appropriate personnel and stocking spare parts. Given the expected proliferation of PADs at the APS, providing this service may prove to be efficient and cost effective. In addition, capabilities to quickly characterize and recalibrate PADs and other area detectors will be part of the Optics & Detectors beamline at 6-BM, which is currently in the planning and design phase. This beamline will also house a program to develop and characterize novel x-ray optics. The detector testing, characterization, and calibration activities at 6-BM will complement the work performed using the Detector Pool optical and fixed x-ray tube test stands.

4.9.3.1 References

[4.9.3-1] Hologic (2010); http://www.hologic.com/en/breast-imaging/digital-mammography/selenia/.

[4.9.3-2] Hamamatsu Corporation, Solid State Division (2010); http://sales.hamamatsu.com/en/products/solid-state-division/image-sensors/dental-ccd.php.

Chapter 5

Enabling Technical Capabilities

5.1 Overview

For a significant facility upgrade such as the APS-U project, consideration must be given to the increased demand upon that facility's foundational infrastructures. This chapter describes several areas where capabilities must be improved to maximize the potential of the APS-U project.

Enabling technical capabilities encompasses three main areas: front ends, physical infrastructure and information technology infrastructure. The front ends are essential for all beamlines to condition the beam prior to entering the experiment stations. Information technology infrastructure underpins the whole of the APS: the accelerator, the beamlines, and the engineering and administrative activities of the organization. Physical infrastructure is essential to ensure that enough power, heating, cooling, and other services are available to meet the demands of machines, instrumentation, and staff throughout the facility.

This section gives an overview of these Enabling Technical Capabilities and describes why they are important to the APS-U project.

5.1.1 Front End

Most of the front ends at APS were designed more 15 years ago and have been in operation since then. The bending magnet front ends were designed to handle the power from APS operating at 300 mA current at 7 GeV. The insertion device front ends were originally designed to handle 100 mA of beam from a 2.4-m-long undulator A. Recently the APS has designed a front end to handle higher heat loads. The APS Upgrade will refurbish the existing front ends to handle a minimum of 150-mA stored current. In addition, beamlines using more than one undulator as well as beamlines being canted and special-case beamlines will require new front ends.

5.1.2 Physical Infrastructure

The APS physical infrastructure, which for this discussion includes electrical power, primary and secondary cooling, temperature control, and ventilation of enclosed spaces, dates back to the original facility construction more than 20 years ago. Since that time it has been maintained and improved where necessary. The APS-U project will bring with it much new equipment and instrumentation. This section addresses the need for physical infrastructure enhancements (i.e., additional utility capacity, the operation of utilities to tighter tolerances, or both) to support such additions. Also included are considerations of the work required to provide new structures for items such as a long beamline.

5.1.3 Information Technology Infrastructure

Information technology (IT) infrastructure encompasses computer networking, storage, and resources required to support operations at the APS. This infrastructure is a fundamental building block on which any successful modern organization functions. The IT infrastructure of the APS was designed approximately 20 years ago. Although it has undergone periodic refreshes since then, the underlying architecture is basically unchanged. Due to increased demands additions to the IT infrastructure are needed and are addressed in the following sections.

5.2 Front-End Upgrades [U1.05.02]

5.2.1 Introduction

A major goal of the upgrade is to increase the flux and brightness of x-rays delivered by the APS. One factor in doing this is provision of higher beam current, with the minimum upgrade value being 150 mA. In addition, some programs require longer undulators or several in-line devices. Such changes will significantly increase the x-ray power loads on front-end and beamline components. Hence, an essential enabling condition is an upgrade of those components. In this section, we discuss the front-end upgrade.

The function of the beamline front ends is to constrain the synchrotron radiation and bremsstrahlung radiation to a defined opening angle and to provide a means of stopping and absorbing the radiation upstream of the ratchet wall to allow personnel access to equipment downstream in the first optical enclosure. The beamline front ends are located primarily within the storage ring enclosure.

The major components of the beamline front ends are photon masks and shutters, beam-defining apertures and/or slits, bremsstrahlung collimators and shutters, vacuum valves for machine protection and isolation, x-ray beam position monitors, and beryllium or CVD diamond windows that isolate the vacuum systems while transmitting x-rays.

The front end starts at the storage ring exit valve and extends to the beamline isolation valve. The usable length of the front-end area in the tunnel is about 7.6 m (24.9 ft) for the insertion device (ID) beamlines and 13.3 m (43.6 ft) for the bending magnet (BM) beamlines. The front end also includes the ancillary systems such as vacuum pumps and gauging; provision for residual gas analysis; utilities distribution including water, compressed air, and electrical power; the Personnel Safety System (PSS); and the Front-End Equipment Protection System (FEEPS).

5.2.2 Design Limits of Front-End Components

Front-end designs are constrained by the available space and the thermal limits of the x-¬ray-absorbing components. Undulators and wigglers used at third-generation x-ray synchrotrons are extremely bright sources, producing copious x-rays in tightly collimated beams. The core of the x-ray beam is used by experiments but much of the power must be absorbed by beam-defining and absorbing elements. Synchrotron radiation x-ray absorbers, in the form of shutters and masks, are used to protect the bremsstrahlung-and x-ray-shielding components used for personnel protection. Power handling in absorbers relies on the ability to conduct the power away from the absorbing surface while withstanding repeated thermal cycling without fatigue failure. High-strength copper alloy is used for maximum yield strength and maximum thermal conductivity. Designs utilize glancing incidence, to spread the high power over a larger area and optimized cooling.

The demands of experiments require increasingly brighter and higher-power sources. A considerable challenge of beamline engineering is to manage the high power produced by these beams to

keep the thermally induced stresses and deformations in the components within acceptable limits. While the total power of the x-ray beam on a component is considerable, it is often the peak power density that produces thermal gradients in the material, causing excessive stresses and deformations. For example, at minimum gap a single 3.3-cm-period undulator used at the Advanced Photon Source with 100 mA of stored electron beam produces up to 5.3 kW of x-rays and 157 kW/mrad^2. Typically, only a few watts of monochromatic beam will reach the target while the remainder must be safely removed by absorbers and optics. When the beam is shuttered to allow experimenter access to a sample, the entire power of the beam must be absorbed. At the position of the first photon shutter in the APS front end the peak heat flux at normal incidence is 562 W/ mm^2. Thermal fluxes of this magnitude are greater than encountered in rocket nozzles and fusion reactors [5.2-1]. To achieve higher photon fluxes at the target, longer insertion devices and higher stored-beam current are planned for the APS Upgrade. Both changes will result in higher thermal loads on the front ends.

Existing design limits for thermal loads imposed at the APS have prevented thermal failures of absorbing components over the lifetime of the facility. These limits are as follows:

- The maximum surface temperature, generally occurring at the center of the beam footprint, shall not exceed 300°C in order to prevent creep.
- The maximum temperature on the cooling wall shall not locally exceed the water boiling temperature, and thus only single-phase water is allowed. The typical pressure after going through two-thirds of the length of a component is about 60 psig, corresponding to a water boiling temperature of around 153°C.
- The maximum von Mises stress for photon shutters shall not exceed 400 MPa, the room temperature yield stress of plate stock GlidCop Al-15. The maximum stress allowed on fixed masks at extreme missteering conditions is relatively relaxed since such missteering cases are very rare.

Recently, efforts have been underway to re-examine these criteria. Several research studies have been conducted, including work at the Advanced Photon Source (APS) [5.2-2], at the European Synchrotron Research Facility (ESRF) [5.2-3, 5.2-4] in collaboration with the APS, and at SPring-8 [5.2-5]. These are geared towards establishing new design guidelines based on a thermal fatigue life corresponding to a finite number of thermal cycles. Elastic-plastic analysis of the cyclic stress-strain imposed by thermal gradients in absorbing components suggests that higher loads than allowed by traditional design limits may be tolerated while maintaining acceptable fatigue lifetimes. X-ray beam tests have been conducted but were inconclusive due to inadequate sample size or uncontrolled variables [5.2-6]. Further lifetime tests with a larger number of samples are planned.

Critical heat flux (CHF) is a thermohydraulic phenomenon that manifests itself in a sudden and severe drop in heat transfer efficiency. In the heat exchanging systems where the heat flux is controlled, once the heat flux reaches its critical level, even a very small further increase of heat flux leads to a very large and almost instantaneous increase in the temperature of the heat exchanger, which can cause catastrophic material failure known as burn-out. This phenomenon is caused by the sudden creation of a thin layer of vapor at the heat exchanger walls, which separates the walls from the bulk liquid. Thus, CHF can occur only in those heat exchanging systems that are characterized by both phase change and very high heat flux values. Several hundred papers have been published in the past 60 years with hundreds of empirical and semi-empirical correlations for predicting CHF in heat exchangers. Unfortunately, due to the large number of thermo-hydraulic parameters that can affect CHF and due to the broad variety of operating conditions of the heat exchangers that can potentially suffer from CHF, a general correlation that would accurately predict the occurrence of CHF for a broad variety of geometries and operating conditions of heat exchangers is yet to be devised. The discrepancies in the results of existing CHF correlations are so large that the research effort continues but with a different goal. Instead of focusing on

one general correlation that would give accurate predictions for the broad range of situations, researchers are now concentrating on correlations that are optimized for the conditions of particular interest. A very detailed report on the effort invested in bettering the understanding and prediction of CHF can be found in [5.2-7, 5.2-8]. The application of CHF to synchrotron-radiation-absorbing components at the APS has been reviewed by Brajuskovic [5.2-9].

Water-cooled front-end and beamline components at APS belong to the class of heat exchangers with controlled heat flux. Although the overall exchanged heat in these components does not exceed several tens of kWs, due to the localized interaction of the beam and the intercepting surfaces, the peak densities of the heat load in these components can exceed 15 MW/m^2. Until recently we did not consider CHF as one of the possible causes of catastrophic failures of front-end components because of the design criteria (see above) that the temperature of the cooling channel walls remain below the saturation temperature in order to prevent a phase change (one of two necessary conditions for the occurrence of CHF). However, the temperature of the cooling channel walls of some of the older versions of photon shutters at APS could reach and exceed the saturation temperature in operating conditions with multiple insertion devices or with higher stored beam current. For these conditions, the maximum computed cooling channel wall temperatures exceed the saturation temperature and the heat fluxes from the walls to the coolant exceed the CHF values computed by one of the correlations widely regarded as among the most accurate.

5.2.3 APS Front Ends

Several types of front ends have been developed at APS for particular ID and BM beamlines [5.2-1, 5.2-10], but all share common properties. The photon beam is either transmitted through the front end or stopped on one of two cooled movable photon shutters. Missteered photon beams are intercepted by cooled apertures (masks). Bremsstrahlung produced by the electron beam interaction with the residual gas or by accidental beam dumps is shielded by the combination of copper masks, photon shutters, lead and tungsten collimators, and tungsten movable stops. Although the operational philosophy of the BM front end is the same as the ID front end, the power and the power density that are handled by various components in the BM front end are significantly lower. The original APS insertion device beamlines were designed to accommodate a 2.4-m-long, 3.3-cm-period undulator (UA33) or, alternatively, an 8.5-cm-period wiggler, for a stored beam current of 100 mA. The bending magnet front ends were designed for a stored beam current of 300 mA. Over the years designs have been developed for higher x-ray power and power density [5.2-11] and for a canted undulator configuration [5.2-12, 5.2-13] that allows two beamlines to be operated from a single straight section. Table 5.2-1 lists the power and power density limits for the front-end designs in use presently at the APS.

Table 5.2-1. Maximum Power and Power Density of APS Front Ends

Front-end Type	Max Power (kW)	Max Power Density ($kW/mrad^2$)
Original APS FE	6.9	198
Undulator Only FE	8.9	245
Canted FE	20	281
HHL FE	21	590

5.2.3.1 High Heat Load Front End

The APS high heat load front end (HHLFE) was designed to allow two 2.4-m-long undulators with a 3.3-cm period to be operated simultaneously in a collinear geometry with a stored beam current of up to 200 mA. This is primarily achieved by changing the incidence surface from horizontal to vertical

and reducing the angle of incidence to between 0.9 and 1.0 degree. The power density that can be absorbed by a vertical surface is much higher than by a horizontal surface when the plane of electron oscillation in the undulator is horizontal. The beam footprint will be thin and long versus wide and short when the beam is incident to a horizontal surface. For grazing incidence components such as masks and shutters, the beam footprint can be treated as a line heat source. The power per unit length of the footprint governs the heat transfer. The maximum power density that can be handled by the absorbing surfaces of the HHL front-end components ranges up to 32 W/mm^2. Figure 5.2-1 shows the layout of components in the HHL front end.

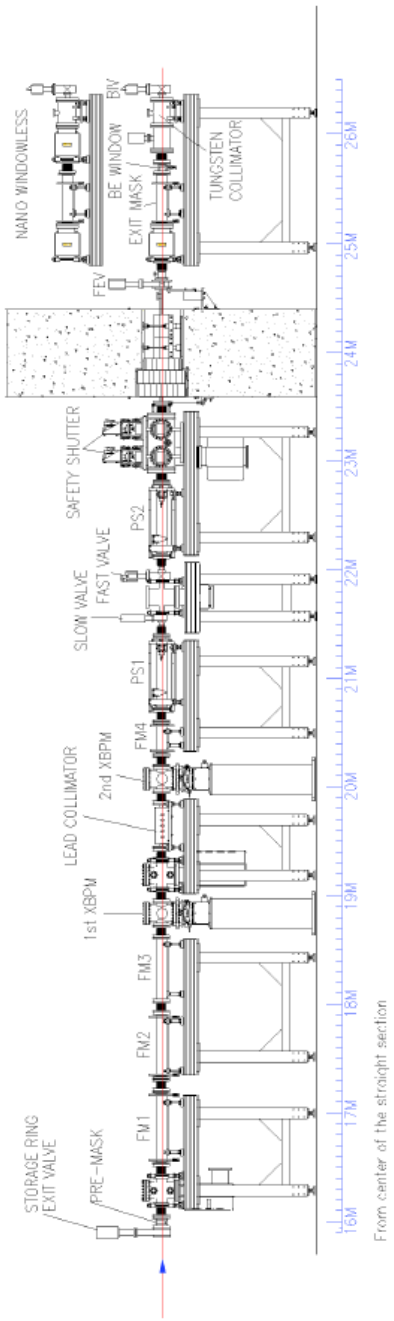

Figure 5.2-1. Layout of the HHL front end.

5.2.3.2 Canted Undulator Front End

In order to operate two beamlines from two insertion devices in a single straight section, a canted undulator front end (CUFE) was developed. In this configuration, the dipole correctors on either side of the straight section and an additional electromagnetic dipole between the undulators are used to create a chicane to deflect the electron beam. The beam is deflected first outward, then inward, and finally back to the original trajectory. Figure 5.2-2 shows this schematically. In this way, two x-ray beams separated by 1.0 mrad are created. The corrector and beam position monitor (BPM) between the undulators allow independent steering of the two x-ray beams. Some undulator length (0.2 m each) is sacrificed to allow space for the center dipole and the corrector.

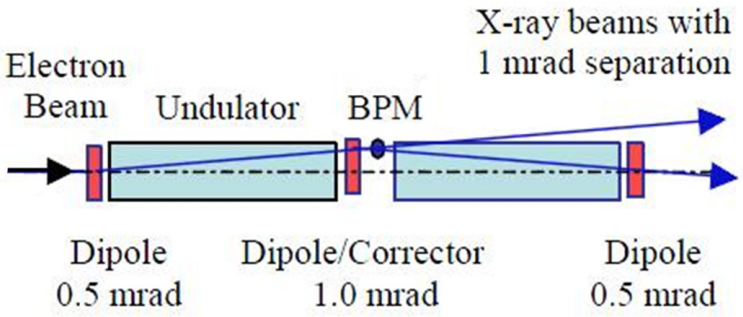

Figure 5.2-2 Canted undulator straight section.

5.2.4 Upgrade Plan

5.2.4.1 Upgraded Beamline Sources and Front-End Requirements

The APS Upgrade will involve a number of changes that require the installation of new front ends. The number and type of front ends that will be installed are summarized in Table 5.2-2. Table 5.2-3 lists the tasks involved in upgrading a typical new front end.

Table 5.2-2. Type and Number of Existing and New Front Ends

Type	Status	Existing	New
Original	Existing design	16	0
Undulator only	Existing design	4	0
Canted (CUFE)	Existing design	7	4
High Heat Load (HHLFE)	Existing design	3	4
Long Straight Canted (ACUFE)	New design	0	1
Retrofit FEv1.2 for 150 mA	New design	0	10
Very High Heat Load (VHHLFE)	New design	0	1
Bending Magnet	Existing design	23	1

Table 5.2-3. Tasks Involved in Upgrading a Typical Front End

Design	Procurement	Fabrication	Assembly	Installation
Conceptual FE Design	Vacuum pumps	Pre-mask	FE Utilities	Remove water lines
Preliminary Design	Vacuum gauges	TSP housing	In-tunnel water manifolds	Remove air lines
Final Design	RGA system	RGA housing	In-tunnel air manifolds	Remove vacuum components
	Vacuum valves	Vacuum components	FE PSS & EPS	Remove mechanical components
		Fixed Masks (3)	FE controls	Install table assemblies
		Photon BPMs (2)	Table assemblies	Install vacuum hardware
		Photon Shutters (2)		Install cabling
		Safety shutter		Install pneumatics
		Horizontal collimator		Install cooling lines
		Wall collimator		
		Exit mask		
		Exit collimator		
		X-ray window		
		FE EPS cables		
		FE EPS components		
		PSS components		
		PSS cables		

Acronyms: EPS - Equipment Protection System
PSS - Personnel Protection System
TPS - Titanium Sublimation Pump
RGA - Residual Gas Analyzer

The APS Upgrade will include increasing the stored beam current to at least 150 mA. All front ends will be upgraded to be compatible with the higher current. For those beamlines with Vs1.2 front ends that are not undergoing source upgrades, a modified front end will be installed that increases the thermal load capacity. Modified Vs1.2 front ends will be made compatible with 150 mA of stored beam and one UA33. The synchrotron radiation intercepting components of these front ends will be replaced with CUFE-style masks and photon shutters. All shielding components will be retained. Some vacuum components will be replaced. Many beamlines will make changes to the source, e.g., change of insertion device magnetic period or increasing the length. Four straight sections will be lengthened to allow up to 7.7 m of insertion device. To accommodate the larger thermal loads and the new beamline configurations, and to be compatible with future upgrades, new front ends will be upgraded to be compatible with a stored beam current of up to 200 mA. In many cases, existing designs of the CU or HHL front ends will

be used with minor modifications. Some source configurations will require more extensive modifications or new designs. Examples of such configurations are longer straight sections with multiple undulators with very high heat load (VHHLFE) and asymmetric canted straight sections where one beamline has a longer undulator (ACUFE).

The front end for the short pulse x-ray (SPX) beamline has special requirements. It must transmit the beam in short-pulse mode (large vertical size, low-power density) and in normal mode (small vertical size, high-power density). For the assumed maximum deflecting voltage of 4 MV, the deflected beam vertical size at 25.4 m (front-end exit mask location) is about 30 mm (±15 mm). Current planning is for one of the beamlines to transmit 1.0-mrad of vertical divergence while the other beamline will accept the beam transmitted through a 2-mm vertical aperture.

One of the goals of the APS Upgrade is to improve x-ray beam stability (see section 3.3). Part of the plan to meet that goal includes installation of new hard x-ray beam position monitors in the front ends that will be less sensitive to parasitic radiation from focusing elements than the currently installed diagnostics. One concept is the grazing-incidence x-ray beam position monitor (GRID-XBPM), shown in Figure 5.2-3, which combines the limiting aperture of the front end with an x-ray fluorescence detector. Research and development are underway to design and fabricate a prototype and to test it with x-ray beam in Sector 29 this year. If successful, the GRID-XBPM will be incorporated into new HHLFE designs. The horizontal orientation of the photon-absorbing surface in CUFE shutters will require additional design effort.

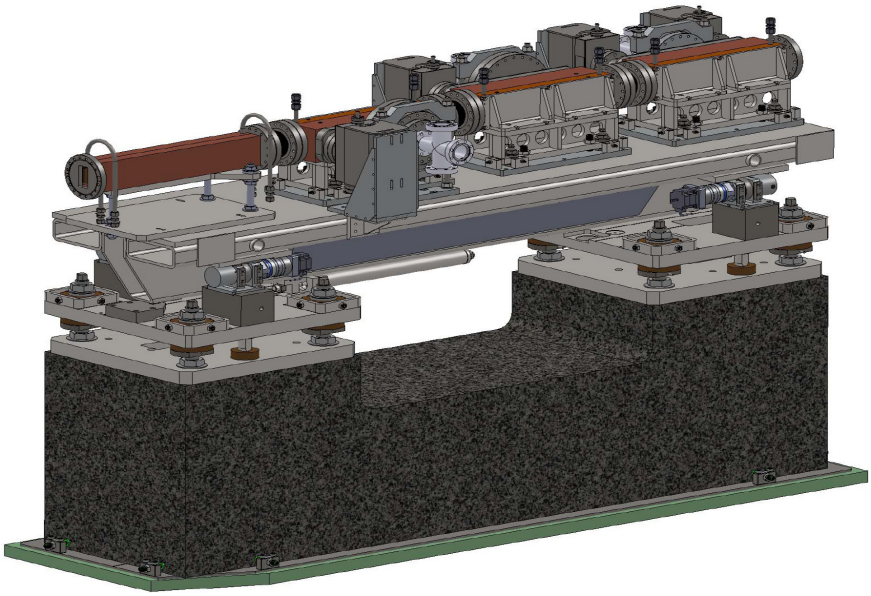

Figure 5.2-3. GRID-XBPM.

5.2.4.2 High Heat Load R&D

The choice of conservative criteria for stress and temperature limits of x-ray absorbers at the APS has been successful in avoiding component failures over the present life of the facility at the operating thermal loads. Some of the proposed source configurations may produce significantly higher thermal loads on x-ray absorbing components than have been seen at any synchrotron radiation facility. For example, a possible 3.5-m-long superconducting undulator with a 2.0-cm period would be a remarkable source of radiation but cannot be accommodated even by the HHL front end. Advanced superconducting undulators (ASCU) may create thermal loads as much as 10 times the current limits of the HHL front end.

In order to expand the possibilities open to beamlines in choosing new devices, the APS will continue to perform R&D during the early years of the project to better define the thermal limitations and to optimize the thermal criteria and component lifetime. A two-pronged approach is proposed whereby tests can be performed both in a laboratory using a bench-top HHL testing system utilizing a fiber laser source, as well as in one of the remaining available APS ID sectors with ID x-rays. Whereas beamtime can be limited and sample changing can be time-consuming on a beamline, a table-top laboratory experiment will enable rapid sample turnaround and higher throughput. The x-ray beam experiments will be used to benchmark the laser experiments.

Future experimental work at the APS will include enough samples to develop a comprehensive statistical data base. Five different peak surface temperatures should be included in the study ranging from 400°C to 600°C in 50°C increments. For each peak surface temperature condition, three different surface finishes should be considered since fatigue crack initiation probability can be related to surface finish. Fiber optic lasers produce a beam with a power distribution that is a near-perfect Gaussian with $m^2 < 1.1$; therefore, the power distribution is very well defined. For modeling purposes, it is absolutely essential to know the actual beam power distribution in order to create a model that represents the actual test conditions.

It is also essential to have sufficient power density. As an example, SPI Lasers UK Limited offers a 400-watt cw/modulated fiber-optic laser source. For the bench-top HHL testing system, three such 400-watt lasers will be necessary to deliver the required total power to the test sample. Each of these lasers comes equipped with a built-in laser pointer used for sighting and positioning the beam spot. The three laser heads can be mounted into angularly adjustable vacuum feedthroughs so that the beam outputs from the three lasers can be aligned onto the same target spot on the test piece. Different focusing/expanding optics could be used to custom tailor the energy distribution within the beam spot. The vacuum test chamber will be approximately 2 meters in length with the laser heads mounted inside the chamber at one end and the test piece mounted at normal incidence to the beams at the other end of the chamber on a manual positioning stage. Therefore, very small angular positioning of the three lasers will be required to align them all coincident on the same target spot on the test piece. A CCD camera mounted outside of the vacuum chamber will be positioned to look through a window at the test piece so that the laser positions can be aligned onto the same target spot even when the vacuum chamber is closed. A light source inside the vacuum chamber will allow the target spot to be clearly seen.

Elastic-plastic analysis will be performed on the most critical APS HHL components, such as the photon shutters, to determine the total strain range as a function of the mean temperature, which will allow the SPring-8 thermal fatigue life prediction model to be used to estimate the thermal fatigue life as a function of peak power density. It is expected that the front end and source of the IEX (sector 29) beamline will be available for test purposes in early 2011 and will remain available for HHL tests for about a year. This will allow sufficient time to test as many as 28 samples. An additional 50 samples can be tested with the laser setup in the same period. The two combined experiments will allow as many as ~ 75 samples, each with 10,000 thermal cycles, to be tested in a one-year period.

5.2.5 References

[5.2-1] D. Shu et al., Nucl. Instrum. Methods A, **319**, 63, (1992).

[5.2-2] V. Ravindranath et al., Proc. of MEDSI 2006, Himeji, Japan, (2006).

[5.2-3] L. Zhang et al., Proc. of MEDSI02, Argonne, IL, ANL-03/7 (2002).

[5.2-4] L. Zhang et al., Proc. of MEDSI2006, Hyogo, Japan, (2006).

[5.2-5] S. Takahashi et al., J. Synchrotron Rad., 15(Part 2), 144–150, (2008).

[5.2-6] J. Collins. Technical report, (2010).

[5.2-7] D. D. Hall and I. Mudawar, International J. of Heat and Mass Trans., 43(14), 2605 (2000).

[5.2-8] D. D. Hall and I. Mudawar, International J. of Heat and Mass Trans., 43(14), 2573 (2000).

[5.2-9] B. Brajuskovic. Technical report, Advanced Photon Source, (2010).

[5.2-10] T. Kuzay. Technical Report TB-5, Advanced Photon Source, (1993).

[5.2-11] Y. Jaski, T. Warwick et al., editors, Proc. of SRI 2004, AIP Conf. Proc. **705**, 356 (2004.

[5.2-12] C. Benson et al., Proc. of SRI 2004, AIP Conf. Proc. **705**, 466 (2004).

[5.2-13] P. Den Hartog et al., Proc. of PAC'03, Portland, OR., (2003); http://www.JACoW.org.

5.3 Physical Infrastructure

5.3.1 Introduction

Conventional facilities provide control over the critical environmental envelope necessary for optimum operation of the APS accelerator, storage ring, and beamlines. These include the building structural systems, primary electrical power and distribution systems, and mechanical systems and associated temperature controls. These conventional facility systems are a dedicated and integral part of the overall accelerator and beamline equipment and operation.

5.3.2 Storage Ring Tunnel - Building 400 [CAS]

One of the activities for the APS-U project is to improve beam stability, as discussed in section 3.6. In order to enhance beam stability to meet the criteria for the upgrade of the APS storage ring, the temperature controls systems for both the space air temperature and the vacuum chamber deionized water cooling systems will be upgraded. This upgrade will result in an increase in the precision and stability of each system's operating temperature and greater temperature stability of the storage ring vacuum chamber. Table 5.3-1 is a comparison of the current vs future needs for temperature stability requirements for the storage ring air temperature and the vacuum chamber deionized cooling water.

Table 5.3-1. System Temperature Stability Requirements

Storage Ring Space Air Temperature Tolerance (° F)		Vacuum Chamber DI Cooling Water Temperature Tolerance (° F)	
Current	Upgrade	Current	Upgrade
$\pm$0.5 ° F	$\pm$0.25 ° F	$\pm$0.20 ° F	$\pm$0.1 ° F

The existing storage ring tunnel temperature control system consists of 20 individual air handling units dedicated to tunnel temperature control. These units are located in the experiment hall mechanical mezzanine and each unit controls the space temperature in two individual sectors. The air temperature control systems will be modified to include a reheat stage capable of providing extremely fine control of the temperature or the air stream supplied to the tunnel. The existing temperature control coils and devices will be reconfigured to supply a constant-supply air temperature upstream of this new reheat coil, providing a first stage of control (course adjustment) with the new coil providing the final temperature control (fine) adjustment. The new reheat coil will be an electric resistance device utilizing silicon-controlled rectifiers to provide rapid cycling (on the order of 0.1 s or less) to infinitely adjust power output to the new coil. Figure 5.3-1 is a schematic representation of the planned modification to the storage ring air temperature control system.

The deionized cooling water to the storage ring vacuum chambers provides direct cooling to maintain temperature stability of the chambers to inhibit dimensional changes resulting from thermal expansion and contraction. Water is supplied to a pair of sectors from individual cooling water skids located in the experiment hall mechanical mezzanine. To increase the stability of the cooling water temperature, each skid will be modified to include an additional stage of temperature control to be provided by electric heating coils controlled by SCR controllers and integrated into the existing Allen-Bradley temperature control system. As described above for the air temperature control, these devices will be capable of rapid cycling to make infinitely small adjustments to the temperature of the water supplied to the vacuum chambers. Figure 5.3-2 is a schematic of the modification to the deionzied water cooling circuit for the storage ring vacuum chamber.

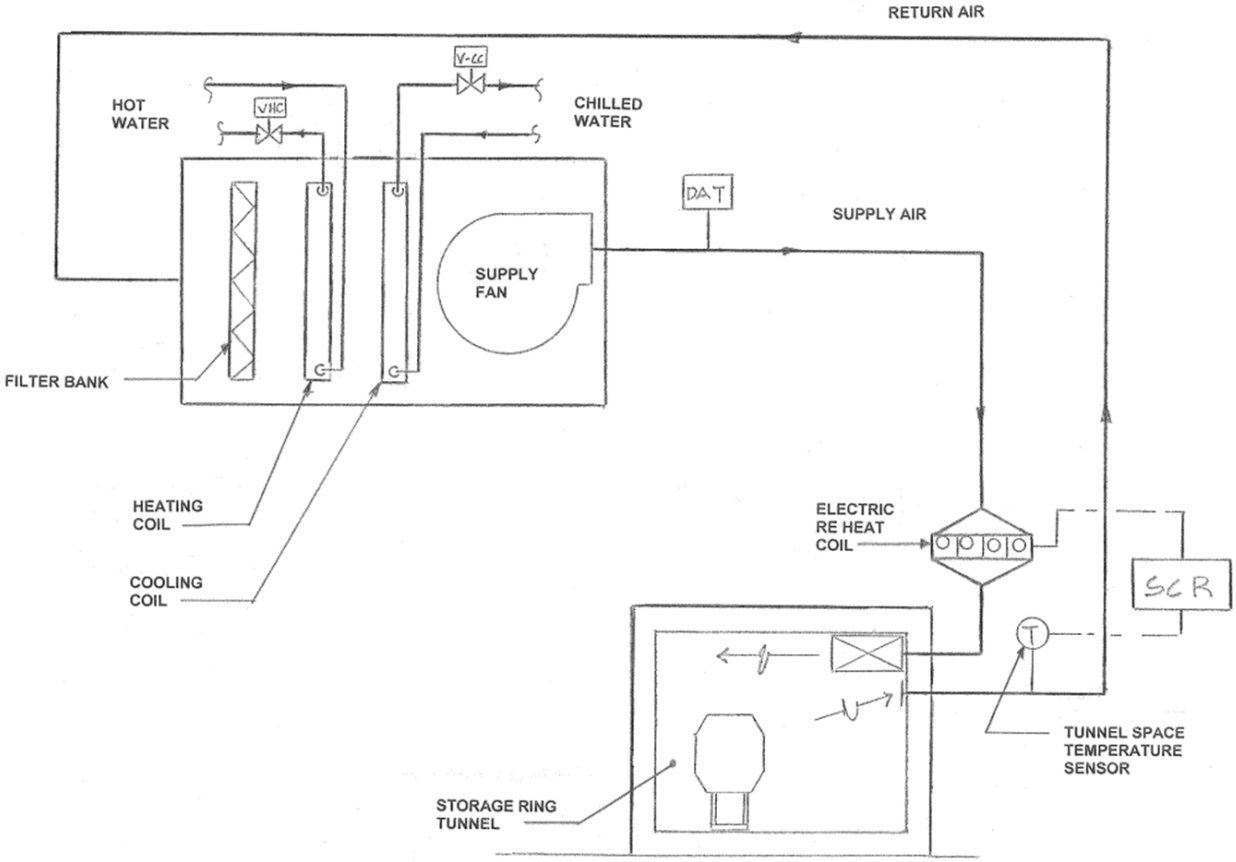

Figure 5.3-1. Diagram of modifications to the storage ring tunnel air temperature control system.

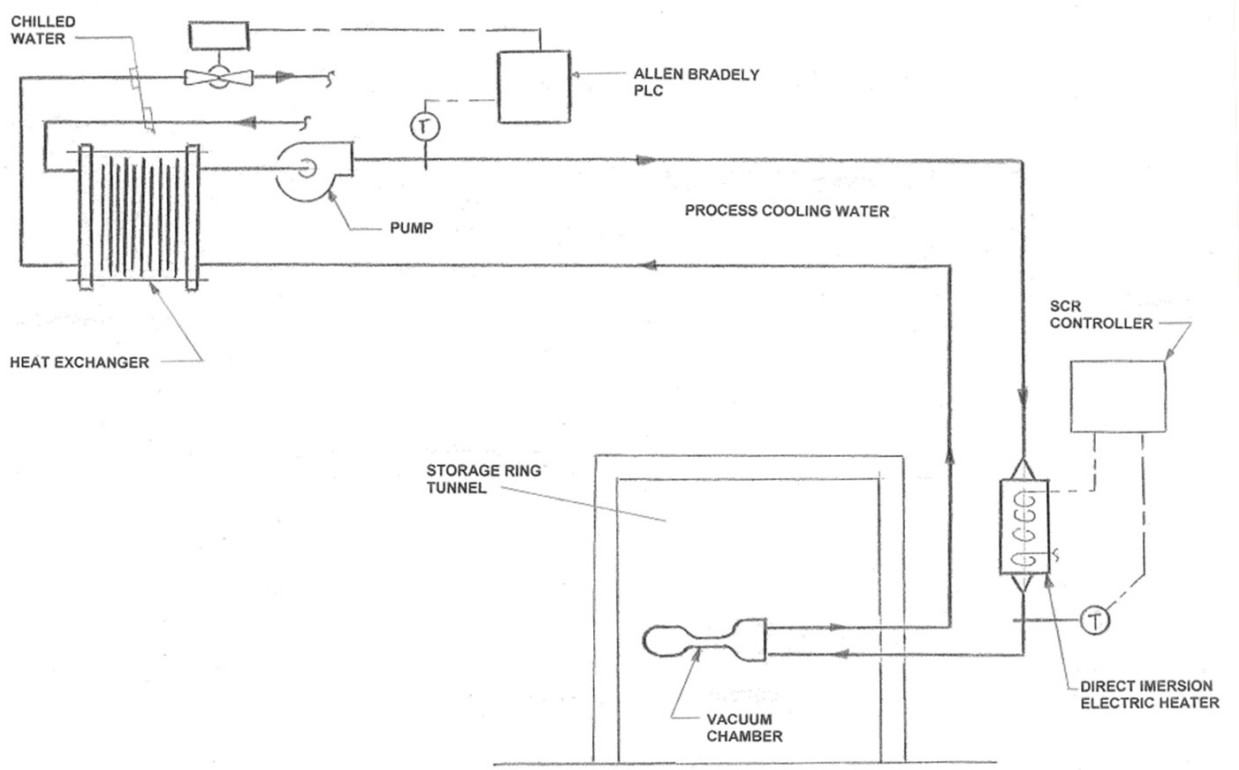

Figure 5.3-2. Diagram of modifications to storage ring tunnel vacuum chamber temperature control system.

5.3.3 Conventional Facilities for the Wide-Field Imaging Beamline [U1.05.03.01]

The wide-field imaging beamline, as discussed in section 4.3.2, has an end station at about 250 m from the insertion device source. The beamline will further extend about 160 m outside of the existing experiment hall. The end stations will be housed in a building about 130 m away from the experiment hall. The end-station building will be connected to the experiment hall through a beam transport utility corridor. The new building enclosures (e.g., end-station building, corridor) will be designed and constructed in a manner similar to that of the APS facility and will provide the appropriate vibration protection, temperature and dimensional stability, and life-safety systems. Figure 5.3-3 is a site plan with the wide-field imaging beamline located at Sector 19 (in red).

End-Station Building: The end station building will be a high-bay-style building to house the experiment stations and a small control area for the stations. The approximate dimensions are 12 m wide × 35 m long × 7 m high. The building will also have a mechanical room and a large door lock access. The building will be air conditioned similar to the experiment floor.

Beam Transport Utility Corridor: A beam transport corridor will connect the experiment hall to the end station building. The corridor will be about 3 m wide × 130 m long × 4 m high and will house the beam transport. In addition, all service lines (power lines; Tel/Data lines; DI, chilled, and hot water; cable trays, etc.) to the end station building will be inside the corridor. There will be room for a pedestrian walkway along the beam transport connecting the 400 building with the end station building.

Infrastructure and Modifications to Existing Facility: The long beamline will disrupt the layout of the experiment hall. The sighting of the long beamline is to minimize the disruption to the experiment hall and the lab/office module laboratories and the office space. The location of Sector 19 for the long beamline will be least disruptive of all possible scenarios. The long beamline will penetrate through a corner of one of the building 435 end laboratories. The truck lock and the liquid nitrogen storage area will also be disrupted and will require relocation.

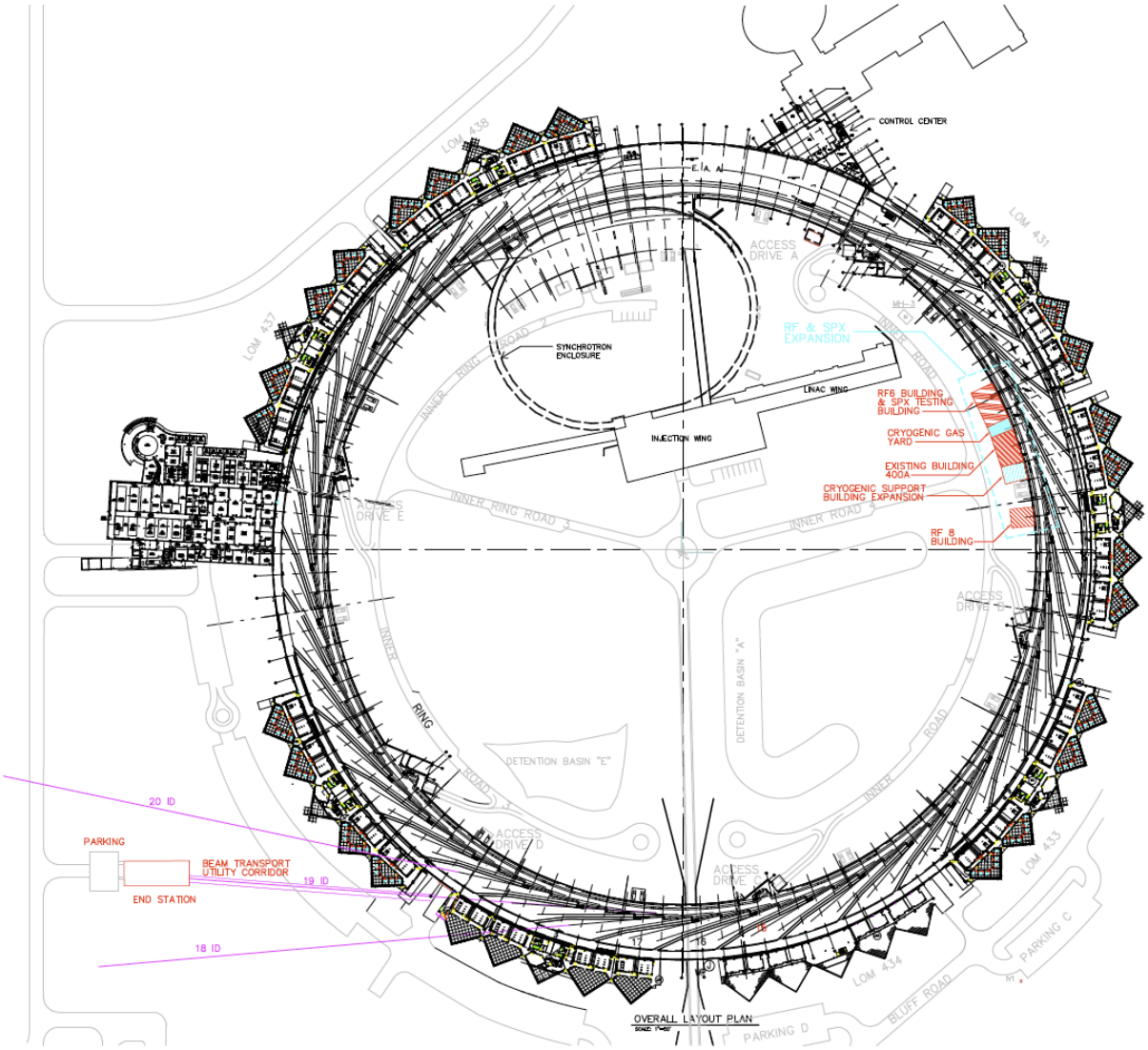

Figure 5.3-3. Proposed APS site plan with the SPX radio frequency building (blue) and the wide-field imaging beamline (red).

Alternate Beamline Analysis: In addition to Sector 19, two more beamlines were also considered, at Sectors 18 and 20. A comparison of the merits and cost of each of the three options was performed. The two alternate locations will significantly impact the adjacent building 435(for Sector 18) or 436 (for Sector 20). The proposed beam lines will go through the office suite, electronics and chemistry laboratories, causing significant disruption and requiring that adequate new substitute spaces be

constructed. The cost estimate for Sector 19 was also lower than the other two alternates. Thus, from conventional facilities prospective, Sector 19 is the option recommended for adoption by the APS-U project.

5.3.4 Conventional Facilities for the XIS Beamline [CAS]

The x-ray interfacial science (XIS) beamline is to be located at Sector 28. The beamline, as discussed in section 4.6.2, will have two branches, which will extend past the experiment hall into Building 437, where there will be three end stations. A planned Class-10000 clean room will coexist with the three end stations.

The existence of two beamlines extending past the experiment hall corridor will impose some restrictions to foot traffic and material movement in the experiment floor. To overcome this problem a pedestrian path will be established that meets the Americans with Disabilities Act requirements. To allow for scheduled occasional vehicular access, the beamlines will be installed with removable segments. The scope of conventional facilities is limited to providing the basic infrastructure and utilities (e.g., power, HVAC mains, process water, means for handicapped access, etc.) needed to support the later installation of end stations and clean room inside Building 437.

5.4 Information Technology Infrastructure [CAS]

5.4.1 Introduction

Computing infrastructure is the electronic backbone on which both the beamlines and the accelerator are completely dependent. Enhancement of this infrastructure is required in order to support the huge demands placed on the APS computing and network infrastructure by the combination of additional beamlines and increased amount of data generated by faster and larger detectors resulting from the APS-U project. These factors, coupled with the ever-advancing speed of computing hardware, require investment by the APS to provide sufficient future capacity for data collection, analysis, storage, and transfer.

An effective IT strategy, closely aligned with the APS-U project strategies and objectives, is fundamental and will assure that the required IT enabling infrastructure, skills, and systems are in place and operational.

The results of new computing research will be rapidly incorporated into the APS operational network. This approach is particularly important because the network services envisaged in APS-U project scientific research plans are so advanced that the technological path for providing them has yet to be defined. Many of the fields represented at the APS will need grid computing. These range from now-emerging computational grids required by computationally intensive fields (e.g., molecular orbital calculations and many modeling and simulation tasks) to the proposed virtual data grids needed by data-intensive fields. Meeting these requirements will take a challenging interplay among the operation of the production network, computing, and testing and deployment of new capabilities on a rapid schedule. Close contact with the research and technical communities is essential.
Continuation of the indispensable benefits of APS computing and networking to the APS programs depend on efforts in the following areas and require sufficient funding to meet the program goals.

The APS networking will expand performance levels to meet the escalating program requirements. Network rate capability is expected to need exponential growth of a factor of two per year, on the basis of past experience and programmatic predictions. The APS must also expand and enhance the services that allow programmatic users to use the network for collaboration.

Because many programs will rely on grid-type distribution of computing and data resources for the next research advance while others require on-demand high-performance computing, APS IT will work closely with the research and development projects aimed at creating these capabilities. In this regard, a focus on uses of the network to support research is vital to the future success of the APS.

Detector technology increases in resolution and acquisition rates every year. The APS is engaged in leading-edge science, and APS scientists are constantly pushing the envelope of available and upcoming technologies. New beamline detectors are capable of generating terabytes of data per day, thus requiring IT to support petabyte-scale disk storage in order to have the capacity for all XSD beamlines.

Finally, the APS will continue to provide cybersecurity services to protect users and to prevent unauthorized intrusion and preserve system integrity. To this end, IT requires full management support in enforcing configuration control for existing systems and preventing the proliferation of nonstandard hardware and software. Adding nonstandard products adds hours of staff time to the installation of these devices. This time can be more profitably spent in other areas of support.

This strategic IT plan is based on the needs of both the beamline scientists and the staff that use the APS computing facilities. Future trends in computing and networking are addressed, with a particular emphasis on continued support for world-class science while keeping information technology costs within the available budget. This document serves as a blueprint for continued progress in support of new instrumentation, including entire beamlines, and advances in administrative applications.

5.4.2 High-Performance Computing

5.4.2.1 Prospective Science

Scientific Rationale

The general rationale for APS-hosted high-performance computing (HPC) infrastructure is that beamline experiments will need to run data reduction, analysis, and visualization on-demand during the actual scheduled beam time. The computation during beam time is needed in part to validate the quality of data taken to allow for modifications to the experiment on the fly. The computation may also be needed for pipelined data reduction to reduce enormous volumes of data to a reasonable size without requiring that all data be acquired before reduction may begin. The HPC resource must be dedicated, and therefore APS-hosted, to guarantee predictable, consistent throughput.

A more specific rationale for APS-hosted HPC infrastructure are the existing uses of the current cluster that are expected to continue and grow in scale, as well as a number of future applications envisioned by the scientists. Currently, the existing cluster is utilized on-demand to run a tomography reconstruction code (TomoMPI) for sectors 1, 2, and 32, and an autocorrelation code (MPICorrelator) for x-ray photon correlation spectroscopy for sector 8. The tomography beamline described in section 4.3.4 and the HEDM beamline described in section 4.5.4 both have expressed a need for 3D visualization tools such as ParaView, which are designed to run on GPU-enabled nodes in an HPC cluster, as described in this section. Such visualization is needed on demand during the experiment to validate data quality. The coherent diffraction imaging beamline described in section 4.3.3 will utilize iterative phase retrieval algorithms that require rapid processing of large data sets during the experiment.

Enabling Software Infrastructure

Making use of an HPC cluster in an on-demand environment requires a host of supporting software. At a minimum, appropriate cluster scheduling and disk resource management software must be selected, installed, and integrated with the larger experiment workflow. The disk space on the parallel file

system must be managed with data management software. The goal of data management is to track the creation and movement of data, metadata, and execution logs from local acquisition disks through data reduction and analysis (local or HPC) and on to more permanent storage. Large-scale movement of data will require software transfer agents, such as the GridFTP server, at every endpoint, and software to orchestrate the entire data movement and processing workflow. Visualization will require the installation, configuration, and tuning of complex applications such as ParaView. Closer to the hardware, we must supply parallel programming libraries such as MPI and OpenCL as a service to the scientists.

5.4.2.2 Requirements (Preliminary)

The following list describes the requirements for beam line data storage in the general sense. More specific requirements for performance levels, capacity, uptime, etc., will be added as the data needed for such analysis becomes available.

HPC for XSD Beamlines

The HPC system needs to provide on-demand computer resources with sufficient file storage for beamline data. The data should only reside there for the purpose of analysis. The disk space needs to be large enough to accommodate current and future users, along with advancements in detector technology. The compute node requirements need to provide “per sector” availability. Therefore, each beamline would be dedicated to a set of nodes. These nodes should provide whatever compute resources are appropriate for the problems being solved by each beamline. There are some algorithms that run well on a graphics processing unit (GPU), for example, while others require a single node with a large amount (100GB) of system memory. Other computational tasks only require a more common compute node, providing many standard processing cores and more conventional amounts of memory.

The current Orthros system has only twenty-five compute nodes with 102 terabytes of disk storage. The typical space usage is about 50% or 51 terabytes. A distributed file system should not be filled past 85% or a significant and noticeable slowdown in performance will occur. Therefore, an HPC system needs to have at least 20% more disk space than will ever be in use at one time.

Considering new detectors (and techniques) will be generating four to ten times more data, it is reasonable to conclude that the data storage space on the HPC storage system will need to be increased from 100 terabytes to at least 400 terabytes. This would allow for growth of current users, plus additional users.

The compute node requirements are more difficult to project. Some applications don't scale linearly, while others do. Compute nodes must be assigned on a per sector basis. This is the only way to guarantee compute access while a beam line is operating experiments. A typical beamline today uses 6 to 10 computer nodes. This is a limitation based on the number of nodes in the cluster today. It is expected that each beamline could have access to 20 or more compute nodes based on today’s technology. Extrapolating from current to projected beamline usage there should be a pool of 20 or more nodes with GPUs and a pool of 20 nodes with a lot of memory. Based on these preliniary results the cluster would have 200 or more standard compute nodes.

The above system would provide state of the art compute power to the APS user community. However, it is imperative that software development resources are put in place to build the necessary tools.

HPC for the APS Accelerator

The APS accelerator support group (ASD-OP) currently uses two clusters for simulations and analysis of accelerator characteristics. The current accelerator HPC systems have a combined 520

computational cores with 75TB of storage. These two clusters will be combined into a single accelerator HPC environment. This will simplify overall system management and resource allocation. The accelerator HPC system will provide an on-demand computational resource similar to the accelerator Control System. Due to projected growth and complexity of undulator design, a cluster with 1000 compute cores and 150TB of distributed storage would be a minimal system.

While at first glance, it would appear that the beamline and accelerator HPC systems could share the same compute nodes and storage, they should not. The accelerator HPC system typically runs much larger and more resource-demanding computations. If the two systems shared the same infrastructure, one could "starve" the other for network and I/O bandwidth. Also, by keeping the two systems separate, tuning for one type of job does not degrade the performance of the other.

A note about cores and physical CPUs: With the introduction of many-core CPUs, e.g., 6 and 8 cores per chip, it leads one to believe that fewer physical CPUs would be necessary. In other words, having 10 8-core nodes would be equivalent to 20 4-core nodes. This is not necessarily the case. A typical HPC scheduler runs only one or two jobs per physical node, due to potential internal system bottlenecks, such as context switching, RAM and I/O bandwidth. For example, if a node has 16 GB of RAM and two jobs are each using 12 GB of RAM, a lot of time can be lost during context switches.

5.4.2.3 Alternative Analysis

High-Performance Computing Infrastructure

The primary goal of the APS high-performance computing environment is to provide an on demand compute resource to allow near real-time analysis of beamline data. The difference between on-demand vs. batch computing is described below.

During an accelerator run, selected compute nodes are dedicated to a beamline and remain idle until processing is required by the beamline experiment. This ensures "fast" turn-around for data analysis, because beamlines are not competing for processing power. In contrast, production HPC computing environments measure their effectiveness and efficiency by the overall load, or utilization of the cluster. Their goal is to provide a constant high utilization of the CPU power by keeping their queues filled with a large number of batch jobs, thus delaying the data analysis for a particular beamline.

To minimize large data copies between systems, the HPC systems will be integrated into the centralized distributed storage system. This will minimize the number of transfers that must be done to process and store data. In addition, the HPC environment will have two local storage pools available: a "fast" storage system for APS internal analysis, such as non-XSD data processing or accelerator analysis; and a "slower" storage system for access by external users.

For example, based on current and projected usage, the fast storage will consist of 250 TB of SAS-disk-based storage. The SAS disk technology is nearly twice as fast as a typical SATA drive. The slow storage will be 250 TB of SATA disks. The storage pools will be part of a Lustre distributed file system with approximately 20 storage nodes (Figure 5.4.2-1), each consisting of two failover servers. Each node will be connected to a mixed SAS and SATA disk array system.

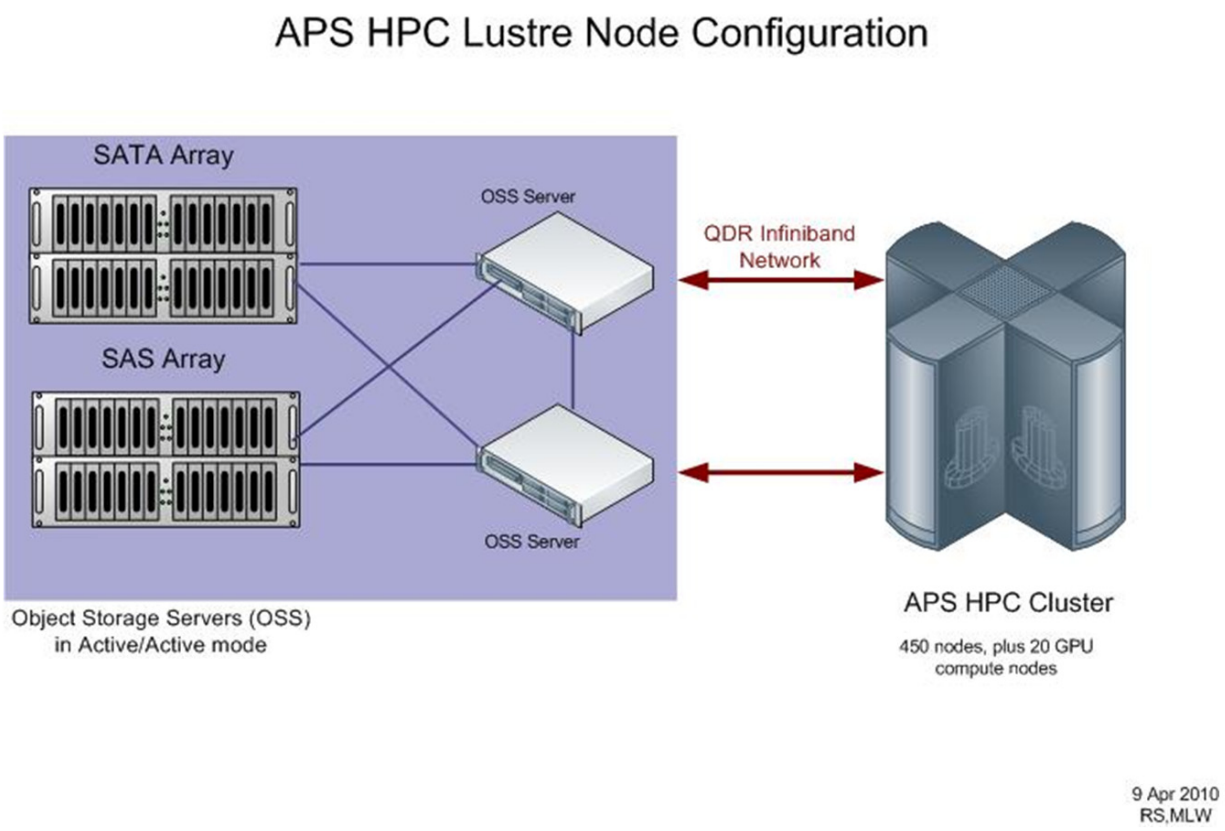

Figure 5.4.2-1. APS HPC Lustre node configuration.

Compute Nodes

Most HPC systems utilize "commodity" 1U compute nodes. Though cheap, these nodes use a great deal of physical space and require more physical infrastructure (e.g., cabinets, cables, power runs etc.). By utilizing a blade chassis technology, 200+ compute nodes can fit in two racks. Blade systems cost more, but that cost is offset by the ease of growth, and future infrastructure requirements can be determined more precisely. Also, blade systems have sophisticated power management systems to minimize energy usage.

Hybrid Nodes

Graphics processing units designed to accelerate graphics applications are highly parallel processors capable of being utilized for nongraphical, high-performance computing. Graphics computing is becoming more commonplace at the APS, so the APS HPC environment will provide nodes with GPU-compute capabilities as required by the beamlines. These nodes can also be used for advanced visualization techniques.

HPC Network

Infiniband is switched fabric interconnect technology used primarily in high-performance computing for connecting compute nodes and storage systems. Its features include quality of service, failover, and scalability, and its architecture defines high data-rate connections between processor nodes and high-performance I/O nodes such as parallel storage devices. The APS HPC environment will use a

standard quad data rate 40-Gb/s Infiniband network as its primary data path. This network will connect to the local HPC storage pools and the centralized beamline data-storage system (Figure 5.4.2-2).

Interprocess communications (compute nodes exchanging messages with other nodes within the cluster) require a high-performance Ethernet network to facilitate the exchanges. The internal APS HPC network will consist of a switched fabric Ethernet switch capable of 10 Gb/s and possibly 100 Gb/s in the near future. Clarification: the switch itself needs to support 10-Gb/s Ethernet, not the entire HPC internal network.

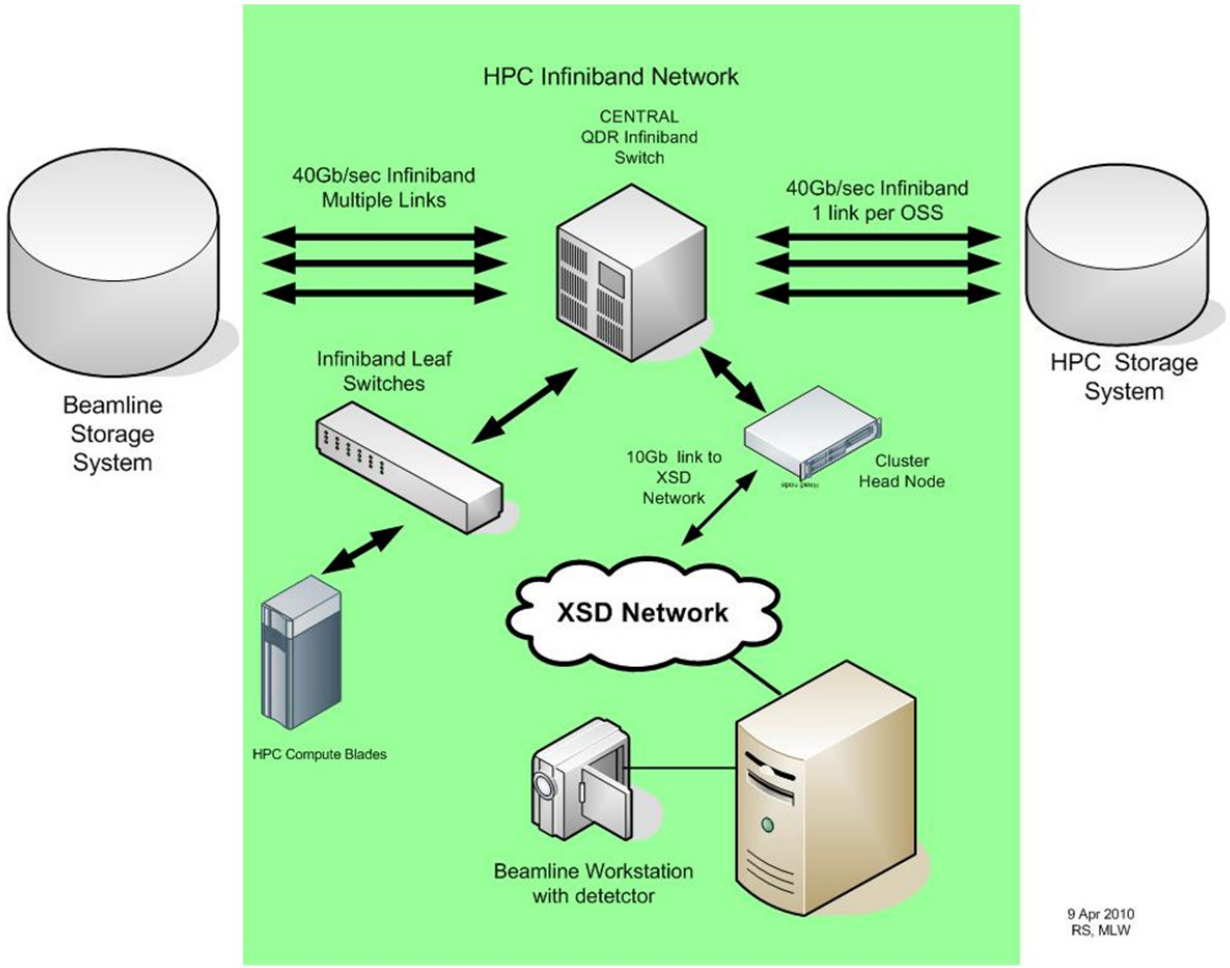

Figure 5.4.2-2. An APS HPC Infiniband network.

Storage Technology

The current "state of the art" is considered to be a solid state drive (SSD) connected via SATA protocol. The current cost of SSD drives, prohibits their use in large arrays. However, as any technology matures, those costs will go down and they will be used in large arrays. This will open a major bottleneck in storage I/O, the time to physically write to disk. Modern disk arrays use a writeback cache to immediately send write acknowledgements back to the computer. But, this cache is typically small, under 1GB. Using an SSD based array will significantly reduce the need for a cache. Now the bottleneck is the

path from memory to the storage, whether it is fiber channel, iSCSI, etc. The data must go through the PCI bus and an adapter card. The next generation bus technology called "Light Peak" will greatly simplify the path from system memory to external device. The specification will be capable of 10-Gb/s speeds over copper and as high as 100 Gb/s over optical fiber. This technology will be introduced in the first half of 2011.

Data Transfer

Another challenge is the movement of large volumes of data within the APS network and to external user institutions. One solution is to use GridFTP, a high-performance, reliable data transfer protocol optimized for high-bandwidth, wide-area networks. It is based on the file-transfer protocol and defines extensions for high-performance operation and security. Moving data throughout the APS facility will be done via a set of GridFTP servers. These servers will be connected to the HPC slow-storage pool (Figure 5.4.2-3). The GridFTP client software has the ability to "stripe" requests across multiple gridFTP servers.

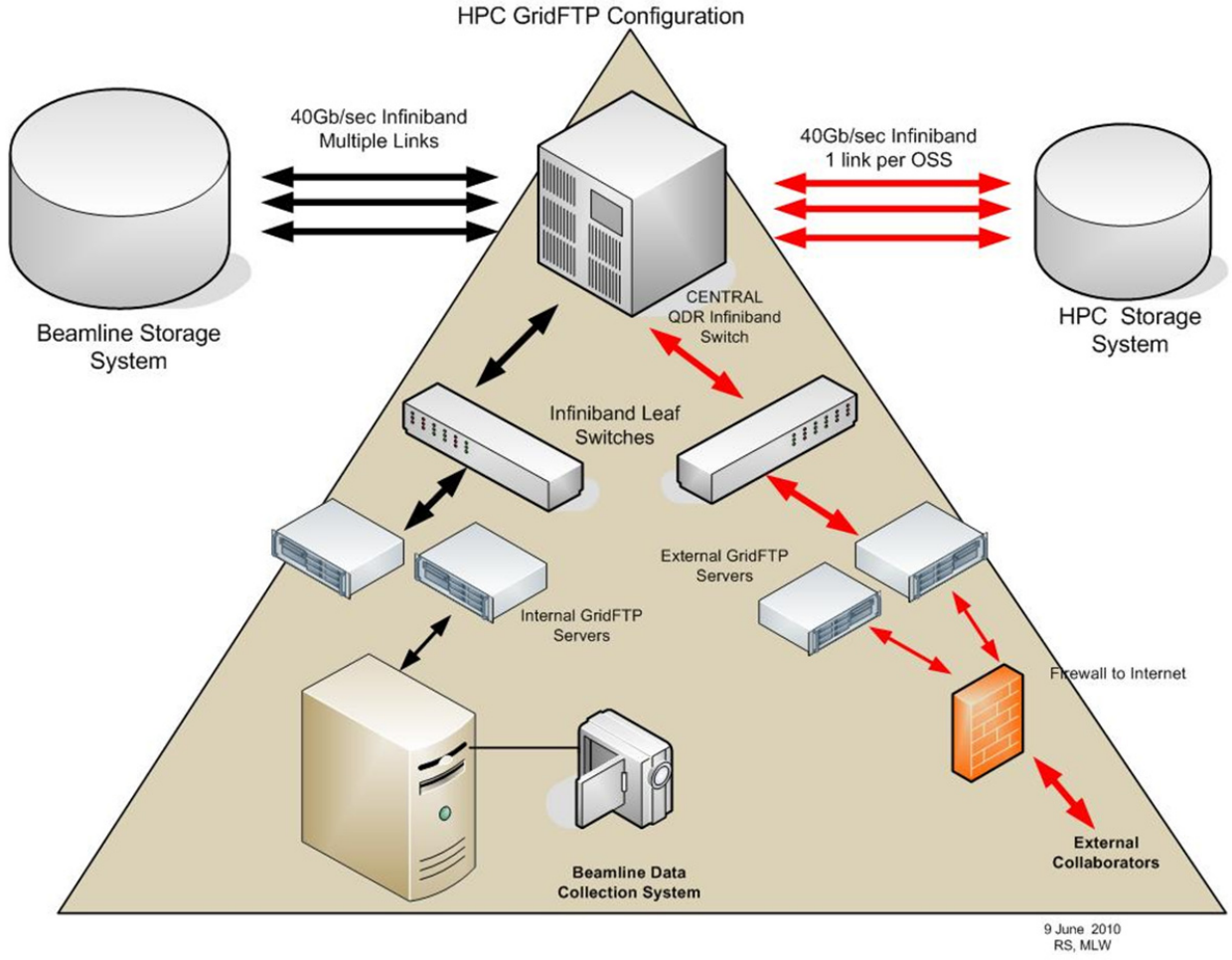

Figure 5.4.2-3. APS HPC GridFTP configuration.

5.4.2.4 Alternative HPC Technologies

Cloud Computing

The use of "Cloud Computing" has received a lot of attention in recent months. It is attractive for a number of reasons, among them cost and easy access for external users. However, it should be viewed for what it is, a form of out sourcing. Cloud computing is cheap due to economy of scale. Which means, if an APS user has a problem "in the cloud," that user is no longer 1 of 50 with direct access to a system administrator. That user is now one of thousands waiting on hold in the call center.

ALCF Computing Resources

Argonne's Leadership Computing Facility (ALCF) provides some of the most advanced HPC resources in the world. However, their environment is a batch system (described earlier) and, as such, does not fit the on-demand needs of the APS beamline user community.

Myrinet and 10G Networking

The internal low latency network for most HPC systems is Infiniband (IB). However, two other alternatives exist, Myrinet and 10-G Ethernet. Myrinet is a proprietary network technology that has evolved to be a variant of 10-G Ethernet. Myrinet has very low latency, about 0.5 to 1.1 microseconds. At one time, Myrinet's low latency gave it an advantage over IB and 1-G Ethernet. However, that has changed, and few HPC systems currently use Myrinet. Another technology is 10-G Ethernet running iWARP. The iWARP protocol allows RDMA (remote direct memory access) over Ethernet. Combined with TCP offload, a data transfer can be performed without CPU intervention. However, Infiniband is now available with 40 Gb/s rates and combined with its inherent low latency, IB out performs 10 G. However, 10-G Ethernet could be used on the Lustre nodes to provide beamline (or other) systems with high-speed access via the Lustre protocol over TCP.

5.4.3 Petabyte Storage System

5.4.3.1 Prospective Science

The sectors that are supported by APS IT fall into two general categories, from the perspective of data handling: high performance and medium performance. Medium-performance beam lines typically generate data at the rate of megabytes or a few gigabytes per day. High-performance beamlines can generate anywhere from hundreds of gigabytes to one or more terabytes of data per day. For the sake of the analysis of the requirements for upgrading the capacity and performance of beamline data-storage systems, the storage needs of medium-performance beamlines are so overwhelmed by their high-performance counterparts that our analysis will focus on only the requirements of the latter.

Sector 1: An Example

The APS IT staff recently undertook an analysis of the dedicated storage needs of Sector 1 for the next two years. Since many of the high-performance beamlines will use equipment similar in capabilities and quantities to Sector 1, it can be used as a template for the analysis of the remaining high-performance sectors.

Sector 1 is currently purchasing General Electric area detectors. These detectors generate images with a resolution of 2048 × 2048 pixels, with 2 bytes of data per pixel. Each frame is 8 MB in size. The General Electric detectors can operate at a maximum rate of 10 frames per second, for a total data rate of

80 MB of data per second. Sector 1 is purchasing four of these detectors. Figure 5.4.3-1 depicts the logical configuration of the Sector 1 beamline, in terms of the movement of data.

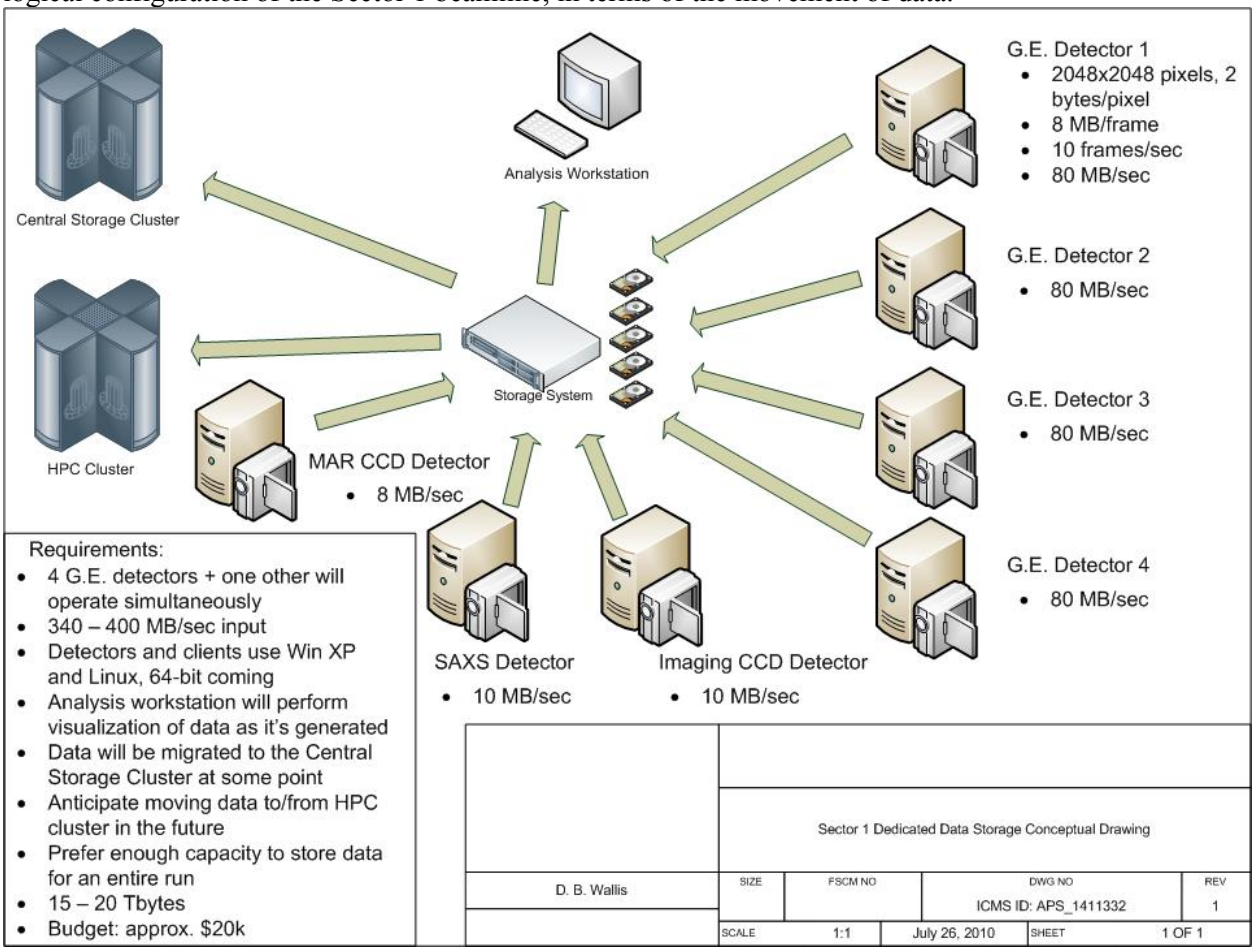

Figure 5.4.3-1. Data movement at Sector 1.

Working with Sector 1 staff, the following requirements for beamline storage were established:

- Beamline needs to support the simultaneous operation of up to four General Electric detectors (maximum data rate of 80-MB/sec each) and one MAR, SAXS, or imaging CCD detector (max 10-MB/s).
- Local storage needs to spool detector data at up to 330 MB/s.
- Enough capacity to store all the data for an entire run.
- Analysis and/or visualization of data can be performed while experiments are running.
- Detector computers and beamline workstations that will access the data storage system will run Windows and Linux operating systems.
- Beamline staff anticipates the need to move data to/from an HPC cluster at some point in the future.
- Data will be migrated from the local data storage to a central server at some point.
- Prefer 15-20 TB of disk space.

The following analysis shows the sector's storage needs based on the performance of the detectors and the beamline operating parameters. The analysis estimates the quantity of data that could be generated during a typical run. For the purposes of this task, a "run" was defined as averaging 73 days of

24/7 operation, and takes into account scheduled maintenance periods called “studies” days, that last 24 or 48 hours each.

Max data rate for Sector 1= data rate/detector × number of detectors

= 80MB/sec × 4 + 10MB/sec × 1

= 330 MB/sec

≈ 333 MB/sec (assumed for this exercise)

= 30GB/min

= 1.2 TB/h

Collection time per run = hours per day of data collection × days of data collection

Assume the beamline takes data 8 h/day;

Assume takes data on ½ the days beam is available during a run:

= 8 × 73 × 0.5

= 292 h

This is equivalent to data being collected for 16.6% of available beam time.

Data collected per run: = Data rate × collection time

= 1.2 TB/h × 292 h

= 350.4 TB

Thus, assuming that the experiment is operated at the maximum frame rate the detectors are capable of (10 fps), approximately 350 TB of storage per run is required by ***one beamline*** using detectors that are ***currently*** being procured. Figure 5.4.3-2 shows graphically, the data generated per run by GE detectors. However, these experiments are frequently operated in a mode where the detector is allowed to integrate data over as many as 10 frames. When operated in this manner, the actually rate of data generation is reduced by a factor of 10, resulting in the experiment generating roughly 35 TB of data per run.

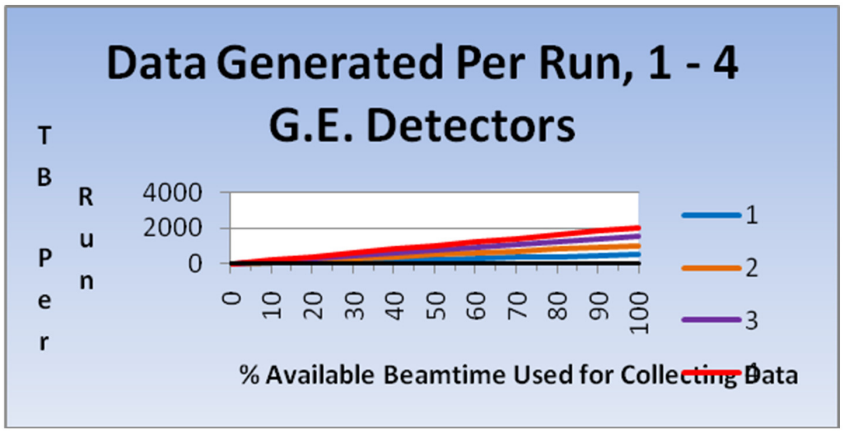

Figure 5.4.3-2. General Electric detector data per run.

Some detectors being procured for other beamlines have even higher data rates. For example, Pilatus 100K detectors are capable of a maximum ~535 MB/s. By the time detectors are procured for the

APS-U project, still higher data rates can be expected. Clearly, significant amounts of data will need to be handled.

5.4.3.2 Requirements (Preliminary)

The following list describes the requirements for beam line data storage in the general sense. More specific requirements for performance levels, capacity, uptime, etc., will be added as the data needed for such analysis becomes available.

Meet the beamlines' needs: First and foremost, a large data-storage system must meet the differing needs of the many beamlines it serves. In particular, it must be adaptable to the wide range of performance requirements of the various beamlines, from a few gigabytes per hour up to one terabyte per hour and potentially more. It is desirable for a storage system to both minimize the need for moving large volumes of data between systems and provide a means to automatically move data when necessary. Any method for moving large data sets must provide adequate performance so as to not hamper further data collection at the beamline. Also, the storage system must support the easy movement of data from within the APS to outside users and collaborators.

Scalability: The petabyte storage system must be scalable both in terms of data volume and performance. The storage needs of XSD beamlines constantly increase, as does their ability to generate data at ever increasing rates. In order to be practical, a storage system must have the ability to grow without the need for replacement. The performance characteristics must also scale to meet the requirements of each beamline without, for example, requiring low-bandwidth experiments to purchase expensive high-performance storage hardware that they do not need.

Maintainability: The petabyte storage system must be maintainable and very reliable, and must have extremely high up-time performance. The design of such a system must allow for individual component failures in such a way that they do not render the entire storage system unusable. The system must allow for "self healing" (the ability to work around single component failures) to the largest extent possible.

Upgradability: The petabyte storage system will be expensive to build, and must provide service for many years. It must therefore be designed in such a way that components can be upgraded in stages; upgrading capacity or performance by replacing the storage system will not be practical. Implementing the storage system with a rolling upgrade strategy in mind will help extend the useful life of the system, as well as reducing the overall cost and minimizing downtime due to upgrades.

Data archiving: The long-term storage of scientific data derived from the APS-U project must be taken into consideration. In order to specify hardware, decisions must be made as to data retention and media used for storing data, plus any regulatory data-retention requirements. Salient questions must be answered, such as how often will access to this data be required and what is the expected response time for data access.

5.4.3.3 Alternative Analysis

Current Data Storage Strategy

Ever since the first XSD beamline was commissioned in 1995, they have tended to operate independently, with each beamline choosing how and where to store experiment data, how long to keep it, whether to archive it, etc.

The APS Engineering Support Division IT Group provides and maintains two clustered file servers with approximately 50 TB of storage, much of it dedicated to storing data from XSD beamline experiments. However, some beamlines choose to store data locally, on disk storage appliances or disk

drives installed in beamline workstations. File backups are accomplished via Symantec's Netbackup software and a single tape library with 10 LT0-3 tape drives and approximately 300 tape slots.

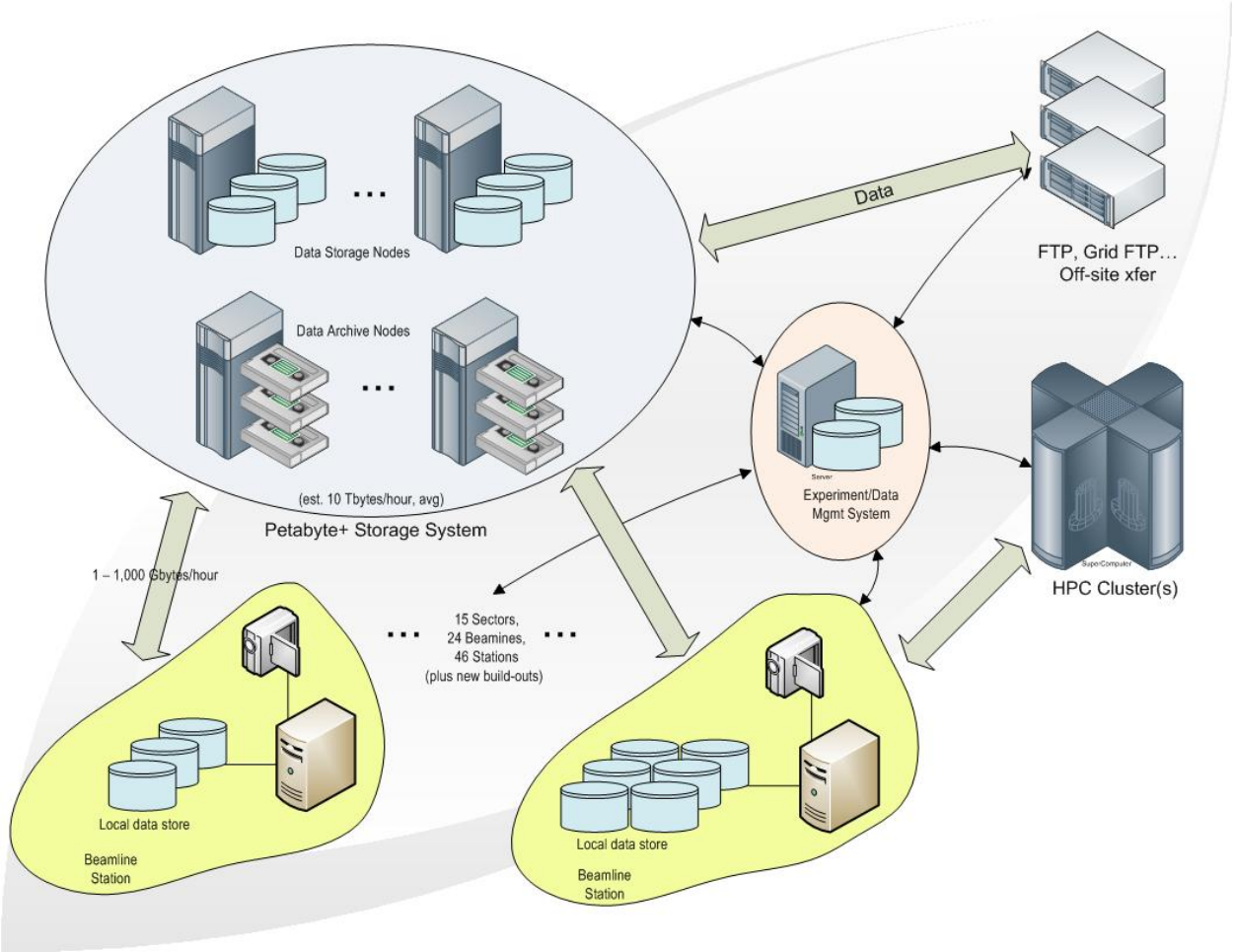

Figure 5.4.3-3. Petabyte storage system diagram.

As XSD has grown and matured, the need for a common data storage system has become apparent. XSD scientists and external APS users frequently work at more than one beamline. As the quantity of data being generated at APS beamlines continues to grow at ever increasing rates, it becomes more and more important to provide a common solution to storing and moving large volumes of data. At the same time, the APS has never had a standard method for archiving experiment data—that has been left up to the individual beamlines. A common data storage structure will make it easier for APS users and staff to operate on multiple beamlines, without the need to learn multiple storage and archival strategies. A petabyte data store that is engineered to meet the data volume and performance requirements of each beamline addresses this problem (Figure 5.4.3-3).

It is anticipated that the latest storage, network, and file system technology available will be used when the storage system is actually implemented. Based on current storage technology, it is clear that a distributed storage system, such as the Lustre file system, will be advantageous. A distributed storage system allows for scalable data-storage volume by adding additional disk drives, as well as scalable performance by adding additional storage server nodes.

Hierarchical storage systems that allow for rules-based control of data storage on multiple layers of storage hardware, each engineered to meet performance requirements, will provide many advantages for a petabyte data storage system. Hierarchical file systems reduce the total cost of storage by moving little-used files to less-expensive storage media, while providing high-performance media for new and frequently accessed data. At the same time, a hierarchical system provides a simple solution to making backups of large volumes of data, since it allows for a magnetic tape layer in its hierarchy. In addition, this storage system automatically migrates files to tape as they are added or changed, eliminating the need for high-performance tape systems capable of writing hundreds of terabytes of data to tape on a weekly basis.

It is also anticipated that solid state drives will be utilized in this storage system, as well as SATA disk drives and SAS disk drives. The SSD devices provide much higher read and write performance than physical disk drives, and thus perform well as cache devices for a large storage system. Read-optimized and write-optimized SSD devices are now becoming available and will be included in the petabyte storage system design.

Regardless of the technology that is used to implement the petabyte storage systems, it is paramount that it be designed in such a way that it addresses the performance and storage needs of each beamline, and that it facilitates connectivity as well as the movement of data between beamlines, archival storage, HPC systems, and external users.

Applicable Technologies

The following paragraphs describe some currently existing technologies that are applicable to the discussion of a large-scale, high-performance data storage system for APS beamlines. They are representative of what is available at the time of the writing of this document and are not intended to be a complete list of products. It is understood that storage technology is a rapidly changing industry, and there are likely to be new techniques and products as the time to implement a petabyte storage system nears.

Lustre File System

The Luster file system is one example of a distributed file system that is capable of scaling in both storage capacity and performance. Lustre is currently an open source product, although there are companies that sell integration services and support for Luster.

A Lustre system consists of one or more meta-data servers and a number of storage servers. Each storage server provides some amount of storage space and the input/output resources to handle reading and writing data to its storage. The capacity of a Luster system is increased by adding more disk space to one or more storage nodes, while I/O capacity is increased by adding additional storage nodes.

Isilon IQ Platform

Isilon is a storage technology company that sells hardware/software storage solutions. Their IQ Platform product is a scalable storage product that provides a number of different classes of storage nodes, depending the the performance and storage requirements of the application. IQ nodes are similar to Luster storage nodes, in that they provide a computer and attached storage, and storage volume and I/O capacity are increased by adding storage to IQ nodes, or adding additional nodes, respectively.

The IQ platform differs from Lustre in that the file system (“OneFS”) does not use separate meta-data servers, but rather replicates meta data across the IQ nodes. The IQ platform currently supports up to about 10 petabytes in a single file system.

Hewlett Packard X9000 Storage System

Hewlett Packard is marketing a new storage solution, the X9000, that will become available later this year or early next year. The system builds on existing products to create a storage system that has similar scaling cabailities as the Lustre file system and the Isilon IQ Platform. The HP system utilizes their blade server chassis for computer resources, and their SmartArray disk array chassis for storage resources. An operating system tailored specifically to handling storage management runs on one or more blade servers. Each blade server may have one or more SmartArray trays connected to it. Thus, storage capacity is increased by adding additional trays, and I/O capacity is increased by adding additional blade servers to the blade chassis.

Chapter 6

ES&H and QA

6.1 Environment, Safety & Health

Title 10 of the Code of Federal Regulations (CFR), Part 851, referred to as 10 CFR 851, *Worker Safety and Health Program*, requires the development of a Worker Safety and Health Program (WSHP) for every covered Department of Energy (DOE) site. The purpose of the program is the prevention of injuries and illnesses to workers at the covered sites. This rule is substantively similar to DOE Order 440.1A *Worker Protection Management for DOE and Contractor Employees* that most sites have been working under as a DOE directive that was incorporated into the operating contract for the site.

The contract for UChicago Argonne, LLC to operate Argonne National Laboratory also includes the requirement for an Integrated Safety Management System (ISMS). DOE's ISMS requirements are described in 48 CFR 970.5223-1, *Integration of ES&H into Work Planning and Execution*. In turn, these requirements are promulgated across the DOE by DOE P 450.4, *Safety Management System Policy*.

Fundamental to the ISMS process is the application of Guiding Principles and Core Functions. Guiding Principles are a series of best-management practices, or "basic philosophy," that ensure start-to-finish management of environment, safety, and health (ES&H) issues. Core Functions provide the necessary structure that describes the scope of work, identifies and analyzes work hazards, develops and implements hazard controls, allows work to be performed within the controls, and uses feedback from the work performed to improve the safety system.

In addition DOE Order 450.1A, *Environmental Protection Program*, in conjunction with Executive Order 13423, *Strengthening Federal Environmental, Energy, and Transportation Management*, levy specific environmental protection requirements on DOE contractors.

It is Argonne National Laboratory policy and objective to integrate ES&H protection into management and work practices at all levels, so that the Laboratory's mission is accomplished while protecting the worker, the public, and the environment. To achieve this objective, Argonne has developed and implemented both a Worker Safety and Health Program (WSHP) and an Integrated Safety Management System (ISMS). WSHP and ISMS description documents communicate the policies and procedures that together comprise the functional WSHP and ISMS at Argonne in compliance with 10 CFR 851 and the DOE P 450.4. The WSHP and ISMS description documents are implemented by the policies and procedures of the Laboratory-wide documents. In this document, these Laboratory-wide implementing policies and procedures collectively are referred to as the "ESH and QA program." The policies and procedures are placed in a common format and are associated with essential functions within Argonne through the Laboratory Management System (LMS).

Argonne also has developed an Environmental Management System (EMS). An EMS description communicates the policies and procedures that together comprise the EMS at Argonne in compliance with DOE Order 450.1A. Argonne has chosen to develop and implement its EMS to meet the requirements of International Organization for Standardization (ISO) 14001:2004, *Environmental Management Systems*.

The ESH and QA policies at Argonne apply to all employees, users, research visitors, students, and subcontractors at every level, as well as suppliers, and are presented in LMS-POL-1, *Safety and Health*; LMS-POL-2, *Environmental Protection*; and LMS-POL-9, *Quality Policy*.

In addition Argonne policies contain the safety policy for specific topics such as: ARGPOL-7.4, *Radiological, Nuclear, and Accelerator Safety Policy;* LMS-POL-4, *Emergency Management Planning*; LMS-POL-5, *Establishing and Balancing Priorities*; LMS-POL-6, *Traffic Safety*; LMS-POL-8, *Aviation Management and Safety*: and, ANL-POL-10, *Working Alone*..

Everyone at Argonne must fully comply with the applicable procedures, instructions, and directives in order to perform safe, environmentally compliant work that protects the health and safety of the worker and the public while meeting quality requirements and preserving the integrity of DOE assets. Argonne's ESH and QA program is described in and implemented through documents that prescribe ESH and QA requirements. The main source for ESH requirements are the LMS procedures in the ESH series, previously published as the *ESH Manual* and LMS procedures associated with the safety and health core process.

6.1.1 APS Hazard Analysis Methodology

The potential hazards associated with the operation of the APS facility and generic x-ray beamlines have been addressed in a Safety Assessment Document (SAD) [6.1-1]. The SAD eventually will be revised to reflect implementation of the APS-U project by incorporating information from this conceptual design report (CDR) and the APS-U Project Preliminary Hazards Analysis Report (PHAR).

An important result of the APS SAD was the establishment of the safety envelope for the components of the APS. In the operating range of the APS, the maximum radiation dose rate increases as particle beam power increases in each of the injector components. For this reason, the safety envelope for injector components has been defined in terms of maximum beam power. The safety envelope for the storage ring in injection mode is also defined in terms of maximum beam power. In stored beam mode, the storage ring safety envelope is related to loss of the entire beam, and is therefore defined in terms of the maximum stored energy in the beam, measured in joules. The safety envelope for the beamlines is defined differently in that it requires a set of controls be in effect which taken together ensure radiation exposures inside Building 400 and outside the beamline enclosures are maintained As Low As Reasonably Achievable (ALARA). The safety envelopes are all based on parameters used in calculating the consequences of a maximum credible incident (MCI) for each component of the APS. The MCIs and their consequences are discussed in the APS SAD Chapter 4. The safety envelope is provided in the APS SAD Chapter 5.

The hazard analysis process for the APS-U project involves developing a PHAR which documents the study of potential hazards— including radiation, energy sources, hazardous materials, and natural phenomena—associated with the proposed modifications to the APS facility and x-ray beamlines. The hazards from the APS-U project are the same as those addressed in the APS SAD. The analysis of each hazard is based on a bounding-event approach in which the most severe case of each hazard category is analyzed to identify the worst-case result. If the result is bounded by the existing hazard analysis in the APS SAD, then the SAD adequately addresses the hazard and the only change involved with the SAD will be descriptive text. If the result is not bounded by the existing analysis in the APS SAD, then a new event analysis must be developed that includes determination of the initiating occurrence, possible

detection methods, safety features that could prevent or mitigate the event, probability of occurrence, and the possible consequences. Initial review has not identified any new analyses which are likely to result in consequences worse than those previously evaluated in the SAD.

Table 6.1.1-1 provides a summary of the PHAR analyzed hazards, their probability level as described in Table 6.1.1-2, and their consequence level as described in Table 6.1.1-3. Figure 6.1.1-1 provides an overall risk matrix with resultant risk levels given in Figure 6.1.1-2. The last column in Table 6.1.1-1 corresponds to the risk levels shown in Figure 6.1.1-2.

6.1.2 APS Upgrade Project Safety Design

The design and development of the APS-U project and its technical components involve an iterative review process. The safety of the design and the effects of the operation of the technical components are included in the conceptual development of the APS-U. This process begins with the identification and evaluation of hazards, development of control or alternative mechanisms to address the identified hazards, and where necessary, a revision of the design to assure that the hazards are eliminated or appropriately mitigated. The safety review and revision process will continue as designs progress and became more detailed. This same process was used for the original APS project.

6.1.2.1 Codes and Standards

DOE 10 CFR 851, *Worker Safety and Health Program*, requires the incorporation of specified codes and standards into contractor's WSH programs. These in turn are referenced by various Argonne safety requirements documents, such as the Argonne LMS procedures in the ESH series, previously published as the *ESH Manual* and LMS procedures associated with the safety and health core process. The APS design review process includes determining whether the appropriate codes and standards have been applied. Some codes and standards of note that apply to the APS-U project include:

- ANSI Z136.1, Safe Use of Lasers, (2000) [as implemented via Argonne Laboratory-wide Procedure ESH-6.2, Nonionizing Radiation Protection – Laser Safety, Rev. 2, 6/10/09]
- National Fire Protection Association (NFPA) 70, National Electrical Code, (2005) [as implemented via Argonne Laboratory-wide Procedure ESH-9.1, Electrical Safety Program – General, Rev. 1, 7/21/08]
- NFPA 70E, Standard for Electrical Safety in the Workplace, (2004) [as implemented via Argonne Laboratory Wide Procedure ESH-9.2, Electrical Safety program – Electrical Worker Safety, Rev. 1, 7/21/08]
- American Society of Mechanical Engineers (ASME), *Boiler and Pressure Vessel Code, Sections I through XII including applicable Code Cases*, (2004) [as implemented via Argonne Laboratory-wide Procedure ESH-13.1, *Pressure Safety – Systems*, Rev. 1, 10/1/06]

Table 6.1.1-1. APS-U Risk Determination Summary

HAZARD (Off-Normal)	**PROBABILITY LEVEL**	**CONSEQUENCE LEVEL**	**RISK LEVEL**
Ionizing Radiation			
Accelerator Systems	Low	Low	ExtremelyLow
X-ray Beamlines	Low	Medium	Low
Nonionizing Radiation	Extremely low	Low	Extremely Low
Chemical	Medium	Low	Low
Cryogenic	Low	Low	Extremely Low
Electrical	Low	Medium	Low
Fire	Medium	Low	Low
Magnetic Fields	Low	Low	Extremely Low
Oxygen Deficiency	Extremely low	Medium	Extremely Low
Noxious gases			
Accelerator Systems	Medium	Low	Low
X-ray Beamlines	Low	Medium	Low
Mechanical	Medium	Low	Low
Vacuum and Pressure	Medium	Low	Low

Table 6.1.1-2. Hazard Probability Rating Levels

Category	**Estimated Range of Occurrence Probability (per year)**	**Description**
High	>10-1	Event is likely to occur several times during the facility or operation lifetime.
Medium	10-2 to 10-1	Event may occur during the facility or operation lifetime.
Low	10-4 to 10-2	Occurrence is unlikely or the event is not expected to occur, but, may occur during the life of the facility or operation.
Extremely Low	10-6 to 10-4	Occurrence is extremely unlikely or the event is not expected to occur during the life of the facility or operation. Events are limiting faults considered in design.
Incredible	<10-6	Probability of occurrence is so small that a reasonable scenario is inconceivable. These events are not considered in the design or SAD accident analysis.

Table 6.1.1-3. Hazard Consequence Rating Levels

Consequence Level	Maximum Consequence
High	Serious impact on-site or off-site. May cause deaths or loss of the facility/ operation. Major impact on the environment.
Medium	Major impact on-site or off-site. May cause deaths, severe injuries, or severe occupational illness to personnel or major damage to a facility/ operation or minor impact on the environment. Capable of returning to operation.
Low	Minor on-site with negligible off-site impact. May cause minor injury or minor occupational illness or minor impact on the environment.
Extremely Low	Will not result in a significant injury or occupation illness or provide a significant impact on the environment.

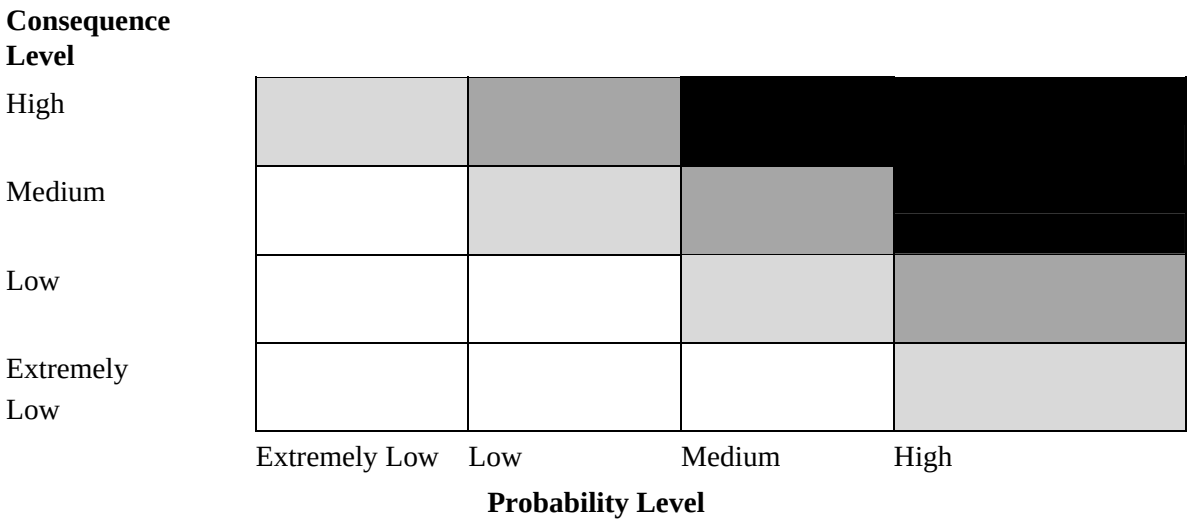

Figure 6.1.1-1 Risk Matrix

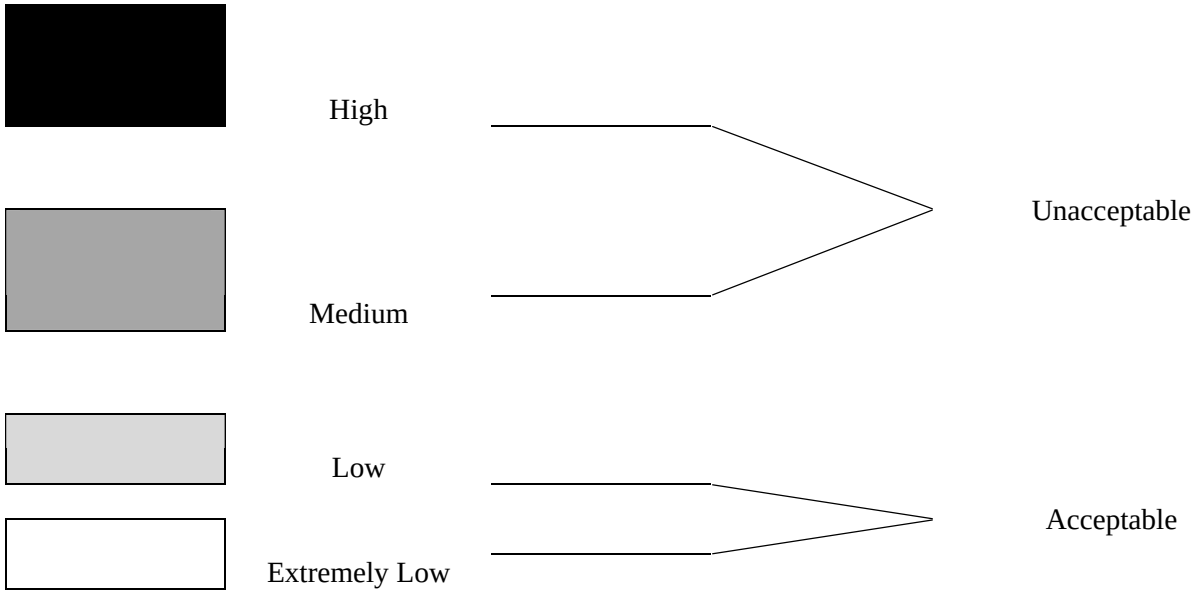

Figure 6.1.1-2 Risk Determination

6.1.2.2 Design Reviews

The *APS Design Review Procedure*, AP&P 3.1.01, latest revision is being followed by the APS-U project. This procedure defines a uniform approach for the APS staff when designs are being reviewed. The procedure applies to designs for new projects or modifications to existing APS systems, including mechanical, pressure, cryogenic, electrical, electronic, software, safety, and shielding systems. This same procedure is applied to designs brought to the APS from external parties, e.g., partner users. In this case, the review focuses on safety, although recommendations regarding technical issues may be included in the report. APS management uses a graded approach to determine the appropriate level of formality to be applied to design reviews. Any improvements or modifications to an APS safety system must follow a formal review process.

The x-ray beamline review process is currently managed by the Beamline Safety Design Review Steering Committee (BSDRSC). From the onset, the safety of the beamline components has been evaluated as the components are designed. When assembled, the beamline components are inspected by the Beamline Commissioning Readiness Review Team and the appropriate APS safety committees. Comments and guidance from each of these reviews provide input to the iterative process of safety design and procedures improvement.

The BSDRSC conducts its evaluation in a systematic manner using the expertise of the committee members as well as the committee advisors. The initial safety analysis for each beamline is prepared by the group managing the beamline. The estimated effect of each hazard is evaluated by the BSDRSC with regard to its potential impact on personnel and on operation of the facility.

6.1.2.3 Natural Phenomena Hazards Mitigation

The design of the APS addressed mitigation of hazards posed by natural phenomena and the same considerations are being applied to the APS-U project:

- Seismic risk at Argonne is considered low, as defined by the International Building Code (IBC), and the IBC does not impose any additional seismic design requirements.
- Wind-loading requirements on the building (per the IBC) are specified in the structural design, calculations, and specifications, as well as being specified for all building exterior enclosure systems. Tornado shelters are designated per Argonne guidelines at interior protected locations of the APS buildings.
- Flooding is not considered to be a likely hazard because the APS is not in a flood zone, is on high ground, and has few subsurface areas, which all have dedicated sump pumps.
- Lightning protection and grounding have been included in the design for the entire APS facility, per IBC, National Fire Protection Association and National Electrical Code requirements.

6.1.3 ES&H Management of Installations and Operations

6.1.3.1 Equipment Installation

APS-U project management recognizes that equipment installation activities can directly and indirectly pose significant hazards. Thus, management will ensure that APS-U project activities and associated hazards are evaluated before work starts in conformance with the latest revisions of Argonne Laboratory-wide Procedures LMS-PROC-64, *Non-Experimental Work Planning and Control*, LMS-PROC-65, *Non-Experimental Skill-of-the-Worker*, and LMS-PROC-79, *Experimental Work Planning and Control*. APS management prefers the use of written procedures for equipment installation or modification. The procedures identify hazards and the hazard controls to be followed. The hazard controls typically involve specifying personal protection equipment that must be worn during work activities. Storage ring and infrastructure modifications will be performed during scheduled maintenance periods and will be planned and carried out using existing APS work planning and control processes. Beamline installations or modifications may be carried out during operating periods if the work is being performed outboard of the storage ring ratchet wall, with the beamline safety and photon shutters fully closed.

APS-U project management also will ensure that installations involving supplier personnel are managed in conformance with the requirements established in Argonne procedures ESH-17.1 *Contractor Safety – General Requirements*, ESH-17.2 *Contractor Safety – Technical Representative and Contractor ESH Representative Requirements*, and ESH-17.3 *Contractor Safety –Hazard Identification through Job Planning*.

6.1.3.2 Operations

This CDR chapter addresses the environment, safety, and health aspects of the APS-U project and does not address how operations will be conducted once upgrade equipment/modifications are completed. Accelerator facility operation requires a high degree of flexibility for the effective execution of unique and complex research and development programs. At the same time, these activities must be conducted in a safe and environmentally sound manner. The Advanced Photon Source Conduct of Operations Manual [6.1-2] was prepared in accordance with DOE O5480.19 Change 2, *Conduct of Operations Requirements for DOE Facilities*, July 9, 1990. The APS manual implements the 18 chapters of DOE O 5480.19 in sequence and supplements the requirements of the Order with Argonne site procedures where applicable. As required by the Order, within the APS organization a graded approach is to be followed in determining which of the chapters or elements of chapters are applicable to any activity or unit. This means that the elements of the chapters are applied to each activity at a level of detail that is commensurate with the operational importance of the activity and its potential environmental, safety, and/or health impact.

For example, initial operation of the storage ring following upgrade modifications will be conducted as part of the machine studies period that precedes the start of each operations run. Machine studies are covered in the APS Conduct of Operations Manual, Chapter 2, *Shift Routines and Operating Practices*.

DOE 0580.19 has since been replaced by *Conduct of Operations* Directive O 422.1. This directive is applicable to nuclear facilities and to other facilities as designated by DOE Field Element Managers. The DOE Argonne Site Office Manager has not designated this directive to apply to the APS as of preparation of this CDR section, but APS management has decided to continue to use the existing APS Conduct of Operations Manual. If Directive O 422.1 is made applicable to APS, the necessary information will be prepared and submitted to DOE, and the manual will be revised as necessary to comply with the directive.

6.1.3.3 Emergency Planning

The APS participates in the Argonne Comprehensive Emergency Management Plan and has developed local-area emergency plans for all APS buildings. The emergency management program incorporates documentation, including maps with designated tornado shelters and fire rally points, assignment of area emergency response responsibilities, and periodic drill requirements. The APS-U project modifications will be incorporated into the emergency management program as the modifications are implemented.

6.1.4 APS Upgrade Project ES&H Considerations

6.1.4.1 Summary

The APS-U project involves a variety of facility changes that will be implemented or installed over a multiyear effort and involving different portions of the facility. As such, the various changes are no different than facility modifications that must be evaluated for ES&H considerations prior to installation or use. The ISMS Core Functions provide the necessary structure that describes the scope of work, identifies and analyzes work hazards, develops and implements hazard controls, allows work to be performed within the controls, and uses feedback from the work performed to improve the safety system. Argonne uses its Laboratory-wide work planning and control procedures to implement the Core Functions for work performed at Argonne. These procedures will be followed by the APS-U project.

The APS-U PHAR will address the types of ESH consideration involved with different portions of the APS-U Project.

6.1.4.2 Potential Actinide Facility Project

A workshop on the nuclear energy community's synchrotron facility needs was held January 27-28, 2010 at Argonne. The workshop assessed the potential contribution of synchrotron experiments to the scientific needs of the nuclear energy science and engineering community in the context of the APS-U project. Several recommendations resulted from the workshop, including construction at the APS of specialized beamlines and a dedicated facility for handling radioactive samples. The construction of dedicated high-energy (> 60-keV) x-ray beamlines for experiments on radioactive samples would accommodate the relevant requirements associated with handling nuclear materials (radiation levels, safety, security) and provide capabilities unavailable elsewhere in the world. This recommendation is consistent with capabilities being planned for the APS-U project. The recommendation that a dedicated facility be built for handling radioactive samples is outside of APS capabilities, including those being planned for the APS-U project. A separate project would be required to construct a stand-alone building located adjacent to the APS to permit open-sample manipulation and

serve as a home base for the nuclear energy systems community (both of these needs were identified by the user community). As such the ES&H considerations of this potential facility are not addressed in this CDR.

6.1.5 Anticipated Hazards

The following subsections summarize the potential hazards that may result from the APS-U project including the procedures and equipment used to control the hazard and reduce the risk levels to ensure safe operation. The PHAR will provide a more detailed discussion of the hazard analyses.

The potential hazards are: (1) ionizing radiation, (2) non-ionizing radiation, (3) chemical, (4) cryogenic, (5) electrical, (6) fire, (7) magnetic fields, (8) oxygen deficiency, (9) noxious gases, (10) mechanical, and (11) vacuum and pressure.

Table 6.1.5-1. APS-U Project Hazards and Associated Controls

Hazard	Associated Controls
Ionizing Radiation:	
Accelerator Systems	Shielding, Access Control and Interlock System (ACIS), Argonne Radiation Protection Program (radiological surveys, dosimetry, posting & labeling), procedures, training
X-ray Beamlines	Shielding, Personnel Safety System (PSS), Argonne Radiation Protection Program, (radiological surveys, dosimetry, posting & labeling), procedures, training
Nonionizing Radiation:	
Radio-Frequency	Shielding, interlock system, field surveys, posting & labeling, work procedures, training, standards
Laser	Shielding, interlock system, permit process, posting & labeling, personnel protective equipment (PPE), procedures, training, standards
Visible/UV Light	Shielding, optics, PPE, procedures, training, standards
Chemical	Designated storage areas, ventilation hoods, APS Chemical Hygiene Plan, Material Safety Data Sheets (MSDS), Chemical Management System (CMS), satellite waste-accumulation areas, posting & labeling, PPE, procedures, training, standards
Cryogenic	Containment design, oxygen-deficiency hazard (ODM) monitors, ventilation, PPE, procedures, training, standards
Electrical	Barrier design, interlocks, equipment inspection, hot work permit process, posting & labeling, PPE, procedures, training, standards
Fire	Barriers, detectors (smoke & heat), alarms, sprinkler system, ventilation, emergency egress routes, Fire Department, limiting combustibles, flammable liquid storage cabinets, open flame permit, procedures, training, evacuation drills, standards
Magnetic Fields	Field surveys, posting & labeling, procedures, training, standards
Oxygen Deficiency	Ventilation, ODH monitors, alarms, confined space entry permit, posting & labeling, procedures, training, standards
Noxious Gases	Ventilation, procedures, training, standards
Mechanical	Design, barriers (machine guards), equipment inspection, posting & labeling, PPE, training, standards
Vacuum & Pressure	Design, pressure relief devices, monitors/gauges, flow & pressure control devices, posting & labeling, PPE, training, standards

6.1.6 Environmental Protection

The National Environmental Policy Act of 1969 (NEPA) established a national environmental policy that promotes consideration of environmental factors in federal or federally-sponsored projects. NEPA requires that the environmental impacts of proposed actions with potentially significant effects be

considered in an environmental assessment or environmental impact statement. DOE has promulgated regulations in 10 CFR Part 1021 that list classes of actions that ordinarily require those levels of documentation or that are categorically excluded from further NEPA review. In accordance with the DOE requirements, the environmental impact of the construction and operation of the APS facility was addressed by an environmental assessment document originally issued in February 1990. This document was later revised to address addition of the Center for Nanoscale Materials, as a separate building adjoining the APS, and a bio-safety level 3 facility on a APS beamline. The revised environmental assessment was issued in June 2003. In addition to these documents, the DOE Argonne Site Office has issued specific categorical exclusions related to APS operations. One such categorical exclusion, ASO-CX-216, applied to the SPX building constructed in 2007.

These documents provide the bounding environmental protection analyses for APS construction and operation. All present APS operations and experimental activities are within these analyzed boundaries. The APS-U project also must be evaluated to determine if the existing boundaries remain bounding or if new boundaries must be established. The evaluation process is described in LMS-PROC-11, *National Environmental Policy Act Implementation*. Once the priorities for the various proposed changes have been defined and a more definitive project scope prepared, an environmental review form will be prepared and submitted to the DOE Argonne Site Office. The DOE Argonne Site Office then will determine whether the APS-U project can be addressed under a categorical exclusion or will require preparation and submittal of a revised environmental assessment document.

Given the proposed accelerator systems and beamline modifications described in this CDR, APS operations with those modifications installed are highly likely to remain within those bounded by the existing documentation. However, various minor construction activities associated with installation of a long imagining beamline and expansion of the existing SPX building will need to be further evaluated against the existing analyses. The most likely areas for further evaluation involve earth grading and drainage considerations. In particular the potential impact on the wetland area northwest of the APS must be evaluated.

6.1.7 References

[6.1-1] Advanced Photon Source Safety Assessment Document, APS-3.1.2.1.0, Rev. 3 (2006); http://centraldocs.aps.anl.gov/reference/docs/APS_1188832.pdf.

[6.1-2] Advanced Photon Source Conduct of Operations Manual, APS-3.1.1.1.0, Revision 3 (2006); http://centraldocs.aps.anl.gov/reference/docs/COO.pdf.

6.2 Quality Assurance

The Quality Assurance (QA) requirements for the APS-U project originate from DOE Order DOE O 413.3B, *Program and Project Management for the Acquisition of Capital Assets*, which requires the APS-U project to address the QA criteria in 10 CFR 830 Subpart A and DOE O 414.1C, *Quality Assurance*. The contractor requirements document in Attachment 2 of DOE414.1C requires the APS-U project to develop a QA program that implements 10 DOE QA criterion, suspect/counterfeit item prevention, and safety software QA using a graded approach. The 10 DOE QA criteria are as follows:

1. Quality Program
2. Personnel Qualification and Training
3. Quality Improvement
4. Documents and Records
5. Work Processes
6. Design
7. Procurement
8. Inspection and Acceptance Testing
9. Management Assessment
10. Independent Assessment

DOE also recommends following the information in DOE G 413.3-2, Quality Assurance Guide for Project Management, and DOE G 414.1-2A, Quality Assurance Management System Guide for Use with 10 CFR 830 Subpart A Quality Assurance Requirements, and DOE O 414.1C, when developing a QA Program.

The APS-U project will implement the DOE QA requirements and recommendations using the Argonne Laboratory Management System (LMS), which has been certified to ISO9001:2008 Quality Management Systems Requirements.

Argonne LMS-POL-9, *Quality Policy*, states that the quality policy of Argonne National Laboratory is to pursue continual improvement in products and services and in relationships internally and with its customers, and that Argonne is committed to the following:

- Providing exceptional products and services in support of the Laboratory's mission, customer requirements, and country.
- Providing an environment - through empowerment, training, and recognition - that will challenge and reward employees.
- Maintaining a safe and healthy for employees and for anyone who may be affected by the employee's organization.

The LMS will be supplemented by a Project QA Program included in the Project Implementation Plan. The project QA program will provide the following:

- Efficient, value-added processes in line with DOE and Argonne requirements, guidelines, and expectations
- Training for project staff and administrative personnel
- Procedures to communicate clear requirements and minimize delays

- A robust assessment program to identify project quality improvement opportunities

DOE Order 413.1B also contains a requirement for the APS-U project to integrate safety at all levels of the project, including QA, and to use the DOE Integrated Safety Management System (ISMS).

The APSU project will implement the DOE ISMS requirements by following the LMS ISMS Description Document, which addresses how the principles of ISM and their associated QA requirements are integrated into the daily processes of the Laboratory.